N.T.

1972 VENUS FLYBY/ENTRY PROBE MISSION STUDY

FINAL TECHNICAL REPORT

BOOK II

- Entry Probe Aeroshell Technology Study Addendum
- Flyby Probe Synthesis
- Program Schedule, Cost, Effectiveness and Risk Summary
- Appendix I

Prepared for

JET PROPULSION LABORATORY
4800 OAK GROVE DRIVE
PASADENA, CALIFORNIA 91101

April 1968

CONTRACT JPL 951 964

GPO PRICE $ _____
CFSTI PRICE(S) $ _____
Hard copy (HC) 3.00
Microfiche (MF) .65
ff 653 July 65

AVSSD-080-68-RR

AVCO SPACE SYSTEMS DIVISION
AVCO CORPORATION

MAY 1968
RECEIVED
NASA STI FACILITY
INPUT BRANCH

FACILITY FORM 602
N68-21888 (ACCESSION NUMBER) (THRU) 1
504 (PAGES) (CODE) 30
CR#94234 (NASA CR OR TMX OR AD NUMBER) (CATEGORY)

Reproduced by the CLEARINGHOUSE for Federal Scientific & Technical Information Springfield Va. 22151

1972 VENUS FLYBY/ENTRY PROBE MISSION STUDY

FINAL

TECHNICAL REPORT

BOOK II

Prepared By

AVCO SPACE SYSTEMS DIVISION
AVCO CORPORATION
LOWELL, MASSACHUSETTS

CONTRACT JPL 951 964

APPROVED

Philip Levine
Philip Levine
Project Manager

AVSSD-080-68-RR

Prepared For

THE JET PROPULSION LABORATORY
PASADENA, CALIFORNIA

ACKNOWLEDGMENTS

AVCO SPACE SYSTEMS DIVISION

H. B. Winkler	Entry Probe System Project Engineer
D. P. Fields	Mission Definition Project Engineer
C. K. Wilkinson	Mission Analysis
W. W. Wilkinson	Mission Analysis
R. I. Moskowitz	Entry Probe Electronic Subsystems
S. J. Brzeski	Program Definition Project Engineer
E. R. Carrubba	Reliability Project Engineer
O. L. Zappa	Aerodynamics Technical Leader
A. Robb	Aerodynamics Analysis
B. M. Morgan	Aerodynamics Analysis
D. M. Moodie	Thermodynamics Technical Leader
J. W. Graham	Thermodynamics Analysis
J. J. Bonasia	Thermodynamics Analysis
B. Laub	Thermal Analysis
G. C. Gasser	Thermal Analysis
H. F. Steinle	Thermal Control Technical Leader
A. J. Stratton	Entry Probe Science Technical Leader
T. H. Rider	Sterilization Requirements
J. J. Hayes	Communications Technical Leader
Chi hau Chen	Communications Analysis
R. E. Herskind	Antenna Analysis
A. J. Grubis	Communications Analysis
J. B. Lazow	Communications Analysis
J. J. Dowd	Power Analysis
W. R. Midgley	Structures Technical Leader
R. Wray	Structural Analysis
D. G. Munro	Entry Probe Design Technical Leader
J. C. Harris	Entry Probe Design
H. M. Burnham	Entry Probe Design
T. R. Ellis	Systems Analysis Technical Leader
W. J. Coderre	Systems Analysis
M. M. Hopkins, Jr.	Systems Analysis

NORTHROP SYSTEMS LABORATORY

D. H. Herman	Project Manager
S. O. Bresin	Flyby Probe Project Engineer
L. F. Burnbach	Program Definition
R. D. Tooley	Flyby Science/Mission Effectiveness Technical Leader
A. F. Caprioglio	Flyby Configuration Design
T. J. Gant	Flyby Probe Design Technical Leader
J. M. Hudson	Mission Analysis
R. J. Calof	Flyby Probe Design
B. D. deBaryshe	Flyby Systems Analysis
G. M. Reppucci	Systems Analysis
J. Peterson	Systems Analysis
W. Dennis	Systems Analysis
A. Welkowsky	Systems Analysis
V. Sobczynski	Communications Analysis
W. B. Ellein	Systems Analysis
B. J. Russell	Communications Analysis
J. Hamer	Systems Analysis

PRECEDING PAGE BLANK NOT FILMED.

PREFACE

This report presents the results of a study of a 1972 Venus Flyby/Entry Probe Mission, primarily aimed at improving man's knowledge of Venus and its atmosphere. Atmospheric measurements are obtained from complementary entry probe and flyby probe experiments, trapped radiation and magnetic field experiments, and multiple wavelength radiometric measurements of the planet are part of the flyby mission. The entry probe mission terminates at impact.

The study was initially oriented to selection of a preferred mission and defining the system and subsystem functional requirements. As the study progressed, the study objectives were modified to examine several alternate missions to compare their cost, effectiveness, and development requirements. Alternative missions which favored the flyby probe experiments, particularly the RF occultation experiments, and which favored the entry probe, particularly low entry velocities to reduce the heating rates, were evolved. Various combinations of science payloads and flyby and entry probe configurations were studied and their impact on cost and effectiveness defined.

The final report consists of four documents:

1. Technical Report
2. Mission Definition Supplement
3. Entry Probe Synthesis Supplement
4. Flyby Probe Synthesis Supplement

The Technical Report is divided into Books I and II. Book I contains the Introduction, Mission Definition and Entry Probe Synthesis; Book II contains the Entry Probe Aeroshell Technology Study Addendum, Flyby Probe Synthesis and Program Schedule, Cost, Effectiveness and Risk Summary. The Supplements contain detailed supporting information evolved during the course of the study and only partially summarized in the Technical Report. Copies of the three Supplements may be obtained by request from the Jet Propulsion Laboratory, Pasadena, California.

SUMMARY

Three candidate Mariner Venus 1972 Missions have been evolved, using an Atlas SLV-3C/Centaur launch vehicle, a modified Mariner Mars 1969 spacecraft and an entry probe capable of entry from the approach trajectory. The first mission, optimizes the Venus encounter geometry favoring the requirements of the flyby experiments and particularly those of the RF occultation experiment; hence this mission is designated the Best RF Occultation Probe Mission: both direct link and relay link configurations have been considered. The second mission, the Minimum Flyby/Entry Probe Mission, minimizes the cost and program development requirements by reducing the science payload, and mechanization complexity and selecting launch and arrival dates that result in the lowest entry velocity commensurate with launch energy requirements. The third mission favors the entry probe, employing an enhanced science payload on the entry probe and the same low entry velocity launch period as for the Minimum Flyby/Entry Probe Mission; this mission is designated the Best Entry Probe Mission.

The system requirements for each mission are defined including: the entry probe ballistic parameter required to deploy instruments above the cloud tops, the stowed configuration requirements for launch, the flyby probe maneuver requirements necessary to separate the entry probe, the flyby and entry probe communication link requirements, the aerothermal environments due to Venus entry, and the science experiment operation requirements. There are eight baseline experiments for the entry probe; composition (mass spectrometer), temperature, pressure, density, scale height (accelerometers),

scattering (photometry), impact, and speed of sound measurements. There are seven baseline experiments for the flyby probe; magnetic field, trapped radiation, UV, IR, microwave and RF occulation measurements. A key structural interface exists between the flyby and entry probe due to the Centaur shroud constraints on the launch configuration. The Minimum Flyby/Entry Probe Mission considered a sufficiently small entry probe, 43 inches in diameter, that the existing adapter could be used and no articulation of the flyby probe elements are required. The Best Entry Probe Mission, with a larger payload (including a radar altimeter) has a 48 inch diameter entry probe, requiring small modification to the launch adapter. The Best RF Occulation Mission, with a 54 inch entry probe, requires a significantly larger adapter and articulation of the low gain antenna on the flyby probe. A number of system requirements stem from the mission peculiar constraints, including: a nose mounted rocket for the entry probe for the Best RF Occulation Mission as opposed to a tail mounted rocket for the other missions, a second articulated low gain antenna on the flyby for the Best RF Occulation Mission versus a single body fixed low gain antenna for the other missions, and high entry velocities for the Best RF Occulation Mission, 38,670 fps versus 35,800 fps for the alternate missions.

Communication link performance and mechanization analyses for the entry probe indicate that a direct link is favored due to the high surface pressures of the Venus atmosphere which causes a long descent time. Long descent time favors a direct link, but aggravates the relay link mechanization requirements as the line of sight essentially goes from horizon to horizon. The

relay link can be improved at the cost of complexity or design compromise; examples include a large deployable antenna on the flyby and/or an entry probe with a large ballistic parameter. A direct link was selected although such a selection constrains the entry probe targeting to the vicinity of the subearth point, since evaluation of the science benefits derived from targeting indicated no particularly strong targeting requirements.

Entry probe configurations were studied parametrically, considering a family of spherically blunted or sharp cones quantized with 30, 45 or 60 degree cone (semi apex) angles. The study results show that the 30 degree cone is unfavorable due to its (1) higher ballistic parameter, (2) smaller ratio of roll to transverse moments of inertia, and (3) sensitivity to spin up due to asymmetries during entry. The 60 degree cone packaged in an optimal manner and has the lowest M/C_DA, but the critical nature of its dynamic stability requires partial despin prior to entry. At the high entry speeds for the Best RF Occulation Probe Mission, the 60 degree cone was found to have large radiation heating rates on the cone, whereas for the lower speed Minimum Mission, the 60 degree cone has low convective and radiative heating rates, admitting the use of a low density ablator such as Avcoat 5026-39 HC/G that is being used on Apollo; hence the 60 degree cone was selected for the Minimum Flyby/Entry Mission to capitalize on existing technology. The 45 degree cone, with a nose radius, 25% of the base radius was selected for the Best RF Occulation Probe Mission and Best Entry Probe Mission, as it favorably compromised the competing requirements of ballistic parameters, stability, radiative heating, ratio of roll to transverse moment of inertia, packaging, and response to winds and gusts.

Flyby probe configuration studies resulted in a high gain antenna location on one of the solar panels due to the competing view angle requirements of the large 3 cm wavelength microwave spectrometer/imager antenna and the high gain antenna for the Best RF Occulation Probe Mission. The subsystem modifications required to adopt the Mariner Mars 1969 spacecraft are presented. A second articulated low gain antenna is required for the Best RF Occulation Probe Mission in order to maintain communications during the course of the entry probe release maneuver. The RF subsystem is shown to have adequate margin for all communications modes during the entire mission using the 85 ft DSIF antenna with one exception, that during the course of the entry probe release maneuver, the 210 ft DSIF antenna must be specified to insure link integrity with the low gain antenna. From the flyby probe point of view, key development areas are the combined multi-frequency Microwave/Spectrometer/Imager and a non-cryogenically cooled IR Spectrometer. Additional flyby simplification could result if flight qualified digital recorders were developed with a higher bit packing density.

Results of Mission effectiveness and cost analyses are presented which indicate that the Best RF Probe Occulation Mission is the most effective and costly mission, and as expected the Minimum Flyby/Entry Probe Mission is the least costly and effective mission. The major result of the cost effectiveness study is that cost reduction by reducing the complexity and size of the flyby science payload is preferable to entry probe payload reduction as the effectiveness is most dependent on the entry probe experiments.

Book I

CONTENTS

1.0 INTRODUCTION 1-1

1.1 Study Objectives 1-1

1.1.1 Mission and System Definition for 1972 Launch 1-1

1.1.2 Synthesis of Entry Probe Design 1-2

1.1.3 Synthesis of a Flyby Probe Design 1-2

1.1.4 Evaluation of Alternate Science Payloads 1-2

1.1.5 Define Technology and Program Requirements 1-3

1.2 Study Guidelines 1-3

1.2.1 Baseline Science Payloads 1-3

1.2.2 Mariner Mars 1969 Concepts and Design 1-4

1.2.3 Launch Vehicle Performance 1-4

1.2.4 Sterilization Specification 1-4

1.2.5 JPL Trajectory Data 1-4

1.2.6 Venus Atmosphere Data 1-4

1.2.7 Deep Space-Net Capability 1-5

1.2.8 Reliability 1-5

1.2.9 Entry Probe Impact Survival 1-5

1.2.10 Mission Risk 1-5

1.3 Study Plan 1-6

1.3.1 Study Plan Approach 1-6

1.3.2 Task Breakdown and Documentation 1-9

1.3.3 Study Schedule 1-10

1.4 References 1-12

2.0 MISSION DEFINITION

2.1 Mission Objectives 2-1

2.1.1 Best RF Occultation Mission 2-3

2.1.2 Minimum Flyby/Entry Probe Mission 2-4

2.1.3 Best Entry Probe Mission 2-6

2.1.4 Mission Summary 2-8

2.2 Science Objectives 2-9

2.2.1 Best RF Occultation Mission 2-9

2.2.2 Minimum Flyby/Entry Probe Mission 2-14

2.2.3 Best Entry Probe Mission 2-16

2.3 Engineering Objectives 2-18

2.3.1 Flyby Probe 2-18

2.3.2 Entry Probe 2-19

2.4 Value Assignments 2-21

2.4.1 Value Criteria 2-21

2.4.2 Evaluation of Alternate Missions 2-33

2.4.3 Discussion of Mission Values 2-40

2.5 Mission Reliability Requirements 2-43

2.5.1 Launch Period Duration 2-43

2.5.2 Launch Configurations 2-49

2.5.3 Mission Phase Goals 2-54

2.6 Mission Constraints 2-61

2.6.1 Launch Vehicle 2-61

2.6.2 Ascent Constraints 2-61

2.6.3 Canopus/Sun Occultation 2-63

2.6.4 Planet Quarantine 2-63

2.7 Encounter Geometry Requirements 2-67

2.7.1 Entry Probe Targeting 2-67

2.7.2 Flyby Science Encounter Requirements 2-75

2.7.3 Comparative Encounter Geometries 2-86

2.7.4 Entry Probe Separation Requirements 2-88

2.8 Transfer Trajectories to Venus During the 1972 Launch Opportunity 2-107

2.8.1 Launch and Arrival Date Parameters 2-107

2.8.2 Spacecraft-Earth/Sun Geometry 2 11

2.8.3 Midcourse Maneuver Requirements 2-122

2.9 Best RF Occultation Transfer Trajectory Selection 2-124

2.9.1 Optimization Analysis 2-124

2.9.2 Aim Point 2-130

2.9.3 Venus Cone and Clock Angles 2-132

2.10 Minimum and Best Entry Probe Transfer Trajectory Selection 2-134

2.10.1 Optimization Analysis 2-134

2.10.2 Aim Point 2-139

2.10.3 Venus Cone and Clock Angles 2-142

2.11 Alternate Mission During the 1973/74 Launch Opportunity 2-144

2.11.1 Transfer Trajectories 2-144

2.11.2 Mission Constraints 2-147

2.12 Type II Interplanetary Trajectories 2-149

2.12.1 Launch and Arrival Date Parameters 2-149

2.12.2 Mission Constraints 2-149

2.13 References 2-153

3.0 ENTRY PROBE SYNTHESIS

3.1 Objectives and Approach 3-1

3.1.1 Ballistic Parameter, M/C_DA Tradeoffs 3-1

3.1.2 Entry Velocity Tradeoffs 3-3

3.1.3 Entry Angle Tradeoffs 3-5

3.1.4 Entry Probe Configuration Considerations 3-5

3.2 Entry Probe System Constraints and Requirements 3-6

3.2.1 Venus Atmosphere Models 3-6

3.2.2 Venus Cloud Tops 3-9

3.2.3 Winds and Gusts 3-9

3.2.4 Atlas/Centaur Payload Capability 3-10

3.2.5 Shroud Limitations 3-12

3.2.6 DSIF Performance 3-12

3.2.7 Flyby Probe Interfaces 3-15

3.2.8 Reliability Requirements 3-21

3.2.9 Entry Probe Science and Engineering Instrumentation Requirements 3-42

3.2.10 Sterilization Requirements 3-58

3.2.11 Entry Probe Stability Requirements 3-58

3.2.12 Heat Shield Development Requirements 3-60

3.2.13 Payload Module Requirements 3-61

3.2.14 Communications Link Constraints and Requirements 3-62

3.3 Entry Probe Configurations 3-63

3.3.1 Entry Probe Configuration Selection Factors 3-63

3.3.2 Entry Probe Configuration for Best RF Occultation/Probe Mission - Direct Link 3-66

3.3.3 Entry Probe Configuration - Minimum Flyby/Entry Probe Mission 3-72

3.3.4 Entry Probe Configuration - Best Entry Probe Mission 3-76

3.3.5 Entry Probe Configuration for Best RF Occultation Probe Mission - Relay Link 3-81
3.3.6 Configuration Summary 3-86

3.4 Flight Sequence 3-92

3.4.1 Entry Probe Separation and Entry Sequence 3-92

3.4.2 Flyby/Entry Probe Flight Sequence - Best RF Occultation Probe Mission 3-96

3.5 Aerodynamics 3-105

3.5.1 Aerodynamic Coefficients 3-105

3.5.2 Heat Transfer Methods 3-123

3.5.3 Entry Trajectory Results 3-128

3.5.4 Selected Mission Configurations and Entry Conditions 3-142

3.5.5 Heat Transfer Predictions for the Three Alternate Missions 3-145

3.5.6 Steady Wind and Gust Effects During Terminal Descent 3-159

3.6 Heat Shield Subsystem 3-171

3.6.1 Functional Requirements 3-171

3.6.2 Heat Shield Subsystem Definition 3-171

3.6.3 Functional Description 3-322

3.7 Structure Subsystem 3-233

3.7.1 Functional Requirements 3-233

3.7.2 Structure Subsystem Definition 3-237

3.7.3 Functional Description 3-255

3.8 Payload Module Subsystem 3-260

3.8.1 Functional Requirements 3-260

3.8.2 Payload Module Subsystem Definition 3-260

3.8.3 Functional Description 3-287

3.9 Sterilization Canister Subsystem 3-294

3.9.1 Functional Requirements 3-294

3.9.2 Sterilization Canister Definition 3-295

3.9.3 Functional Description 3-297

3.10 Radio Frequency Subsystem 3-299

3.10.1 Functional Requirements 3-299

3.10.2 RF Subsystem Definition 3-299

3.10.3 Functional Description 3-407

3.11 Power Subsystem 3-410

3.11.1 Functional Requirements 3-410

3.11.2 Power Subsystem Definition 3-411

3.11.3 Functional Description 3-431

3.12 Data Handling Subsystem 3-433

3.12.1 Functional Requirements 3-433

3.12.2 Data Handling Subsystem Definition 3-433

3.12.3 Functional Description 3-444

3.13 Sequencer Safing and Initiation Subsystem 3-446

3.13.1 Functional Requirements 3-446

3.13.2 Sequencer Subsystem Definition 3-446

3.13.3 Functional Description 3-452

3.14 Propulsion Subsystem 3-457

3.14.1 Functional Requirements 3-457

3.14.2 Propulsion Subsystem Definition 3-457

3.14.3 Functional Description 3-462

3.15 Attitude Control Subsystem 3-464

3.15.1 Functional Requirements 3-464

3.15.2 Attitude Control Subsystem 3-464

3.15.3 Functional Description 3-478

3.16 Thermal Control Subsystem 3-483

3.16.1 Functional Requirements 3-483

3.16.2 Thermal Control Subsystem Definition 3-483

3.16.3 Functional Description 3-511

3.17 Pyrotechnic Subsystem 3-515

3.17.1 Functional Requirements 3-515

3.17.2 Pyrotechnic Subsystem Definition 3-515

3.17.3 Functional Description 3-515

3.18 Cabling Subsystem 3-522

3.18.1 Functional Requirements 3-522

3.18.2 Cabling Subsystem Definition 3-522

3.18.3 Functional Description 3-522

3.19 Radar Altimeter Subsystem 3-530

3.19.1 Functional Requirements 3-530

3.19.2 Radar Altimeter Subsystem 3-530

3.19.3 Functional Description 3-540

3.20 Impact Detector Subsystem 3-544

3.20.1 Functional Requirements 3-544

3.20.2 Impact Detector Subsystem Definition 3-544

3.20.3 Functional Description 3-552

3.21 References 3-554

Contents, Book II

4.0 ENTRY PROBE AEROSHELL TECHNOLOGY STUDY ADDENDUM

4.1 Study Scope and Objectives 4-1

4.2 Aerothermal Environment 4-1

4.2.1 Study Criteria. 4-1

4.2.2 Sharp Cone Analysis 4-2

4.2.3 Blunt Cone Analysis 4-4

4.2.4 Discussion of Flow Field Results. 4-17

4.2.5 Boundary Layer Analysis 4-17

4.2.6 Discussion of Boundary Layer Study Results. 4-20

4.2.7 Radiation Heating Analysis 4-22

4.2.8 Discussion of Radiation Heating Study 4.42

4.3 Prediction of Materials Performance 4.43

4.3.1 State of the Art Survey 4.43

4.3.2 Thermochemistry Study 4.58

4.3.3 Survey of Boundary Layer Transpiration Studies 4.68

4.4 Survey of Failure Modes 4.82

4.4.1 Study Scope and Objectives. 4.82

4.4.2 Cold Soak Thermal Stresses. 4.84

4.4.3 Membrane Stresses Due to Combined Mechanical and Thermal Loads of Venus Entry. 4-106

4.4.4 Complete Aeroshell Stress Evaluation During Entry 4-128

4.4.5 Fabrication and Bonding 4-137

4.4.6 Structures Development Program Requirements 4-146

4.4.7 Failure Mode Summary

4.5 Candidate Heat Shield Materials 4-153

4.5.1 Data Correlations: Carbon Phenolic 4-153

4.5.2 Data Correlations: Avcoat 5026-39/HC-G 4-190

4.5.3 Heat Shield Performance Analysis. 4-230

4.5.4 Shear and Pressure Gradient Effects on Avcoat 5026-39/HC-G . . 4-247

4.6 Development Testing Simulation 4-250

4.6.1 Introduction. 4-250

4.6.2 Simulation Considerations 4-252

4.6.3 Trajectory Requirements and Facility Capabilities 4-259

4.6.4 Ground Test Limitations 4-268

4.6.5 Selection of Test Facilities - Phase I 4-281

4.6.6 Phase I Test Program - Summary. 4-289

4.6.7 Phase II - Characterization of Material for Design. 4-291

4.6.8 Phase III - Materials Screening 4-314

4.6.9 Evaluation of Flight Test Simulation. 4-319

4.7 References 4.320

5.0 Flyby Probe Synthesis

5.1 System Requirements and Constraints. 5-1

5.1.1 Mission Invariant Requirements and Constraints. 5-1

5.1.2 Best RF Occultation (Baseline) Mission Requirements and Constraints 5-2

5.1.3 Alternate Mission Requirements and Constraints. 5-2

5.2 System and Configuration Design. 5-3

5.2.1 Best RF Occultation Mission 5-3

5.2.2 Alternate Missions. 5-12

5.3 Subsystem Design 5-22

5.3.1 Structure and Mechanical Subsystem. 5-22

5.3.2 Scan Platform Subsystem 5-26

5.3.3 Attitude Control Subsystem. 5-30

5.3.4 Thermal Control Subsystem 5-36

5.3.5 Power Subsystem 5-46

5.3.6 Midcourse Propulsion Subsystem. 5-49

5.3.7 Flight Telemetry Subsystem. 5-51

5.3.8 Flight Command Subsystem. 5-55

5.3.9 Radio Frequency and Antenna Subsystem 5-57

5.3.10 Central Computer and Sequencer Subsystem. 5-68

5.3.11 Data Automation Subsystem 5-70

5.3.12 Data Storage Subsystem. 5-74

5.3.13 Cabling Subsystem 5-77

5.3.14 Pyrotechnic Subsystem 5-77

6.0 PROGRAM SCHEDULE, COST, EFFECTIVENESS AND RISK SUMMARY

6.1 Introduction 6-1

6.2 Work Breakdown Structure 6-1

6.3 Schedule Ground Rules 6-3

6.4 Program Schedule 6-5

6.4.1 Total Program Considerations 6-5

6.4.2 Special Flyby Probe Considerations 6-8

6.4.3 Special Entry Probe Considerations 6-10

6.4.4 Summary 6-13

6.5 Costing Ground Rules 6-13

6.5.1 Primary Entry Probe System Ground Rules 6-14

6.5.2 Primary Flyby Probe System Ground Rules 6-15

6.6 Program Costs 6-16

6.6.1 Cost Summary 6-16

6.6.2 Flyby Probe Configuration Summary 6-16

6.6.3 Entry Probe Configuration Summary 6-19

6.6.4 Expenditure Plan 6-24

6.7 Cost Effectiveness for Alternate Approaches 6-24

6.7.1 Effectiveness Criteria 6-24

6.7.2 Cost Effectiveness Summary 6-29

FIGURES

Figure No.	TITLE	Page
1.1	Study Plan Flow Diagram	1-7
1.2	Study Schedule	1-11
2.1	Mission Analysis Diagram	2-2
2.2	Entry Probe Experiment Regimes	2-13
2.3	Probability of Launch Within Given Launch Opportunity Duration	2-50
2.4	Probability of Mission Success	2-51
2.5	Atlas/Centaur Separated Payload Capability	2-62
2.6	Operational Constraints for Planet Quarantine	2-66
2.7	Definition of 0° Longitude on Venus	2-68
2.8	Impact Contours for Constant Entry Angle	2-70
2.9	Entry Angle Requirements for Subearth Point Targeting	2-71
2.10	Latitude and Longitude of the Approach Asymptotes	2-77
2.11	Flyby Orbit Inclination Required for Diametric Occultation	2-78
2.12	Sun-Earth-Canopus Occultation Zones	2-81
2.13	Encounter Trajectory Ground Tracks (Far Side Flyby)	2-83
2.14	Comparative Flyby Encounter Trajectories	2-87
2.15	Separation and Encounter Geometry	2-89
2.16	Entry Probe Separation Velocity Requirements for Best RF Occultation Probe Mission	2-92
2.17	Entry Probe Thrust Vector Orientation for Best RF Occultation Probe Mission	2-94
2.18	Entry Probe Separation Range for Best RF Occultation Probe Mission	2-96

(Figures continued)

2.19	Entry Probe Separation Velocity Requirements for the Minimum Flyby/Entry Probe Mission and Best Entry Probe Mission	2-101
2.20	Entry Probe Thrust Vector Orientation for Minimum Flyby/Entry Probe Mission and Best Entry Probe Mission	2-102
2.21	Entry Probe Thrust Vector Orientation for Minimum Flyby/Entry Probe Mission and Best Entry Probe Mission	2-104
2.22	Summary of Trajectory Data for Venus, 1972, Type I	2-108
2.23	Flyby/Entry Probe - Earth/Sun Geometry	2-117
2.24	Flyby/Entry Probe - Planet/Sun Distances	2-118
2.25	Vehicle Centered Coordinate System	2-120
2.26	Interplanetary Cone - Clock Angles	2-121
2.27	Launch Window for Best RF Occultation Probe Mission	2-125
2.28	System Tradeoffs for Best RF Occultation Probe Mission	2-126
2.29	Aim Point Diagram for Best RF Occultation Mission	2-131
2.30	Venus Cone - Clock Angles for Best RF Occultation Probe Mission	2-133
2.31	Launch Window for Minimum Flyby/Entry Probe Mission and Best Entry Probe Mission	2-135
2.32	Injected Payload Weight and Entry Velocity Data for Type I Trajectories	2-137
2.33	Minimum Flyby/Entry Probe Mission and Best Entry Probe Mission System Tradeoffs	2-138
2.34	Aim Point Diagram for Minimum Flyby/Entry Probe Mission and Best Entry Probe Mission	2-141
2.35	Venus Encounter Cone-Clock Angles for Minimum Flyby/Entry Probe Mission and Best Entry Probe Mission	2-143
2.36	Summary of Pertinent Trajectory Data for Venus 1973-74 Type I	2-145
2.37	Launch Window for 1973-74 Mission	2-148

(Figures continued)

2.38	Summary of Pertinent Trajectory Data for Venus 72, Type II	2-150
2.39	Launch Window for Type II Trajectories	2-152
3.1	Entry Probe Synthesis Logic Diagram	3-2
3.2	Centaur Nose Fairing and Spacecraft Dynamic Envelope	3-13
3.3	Maximum Entry Probe Envelope Configuration	3-14
3.4	Flyby/Entry Probe Adapter Interface Comparison	3-16
3.5	Entry Probe Inboard Profile for Best RF Occultation Mission - Direct Link	3-68
3.6	Entry Probe Inboard Profile for Minimum Flyby/Entry Probe Mission	3-75
3.7	Entry Probe Inboard Profile for Best Entry Probe Mission	3-80
3.8	Entry Probe Inboard Profile for Best RF Occultation Probe Mission - Relay Link	3-85
3.9	Sequence During Separation, Best RF Occultation Probe Mission - Direct Link	3-93
3.10	Sequence During Entry, Best RF Occultation Probe Mission - Direct Link	3-95

(Figures continued)

3.11	Axial Force Coefficient - 60 Degree Cones	3-117
3.12	Normal Force Coefficient - 60 Degree Blunt Cone	3-118
3.13	Center of Pressure - 60 Degree Blunt Cone	3-119
3.14	Damping Coefficient - 60 Degree Blunt Cone	3-120
3.15	Comparative Zero Angle of Attack Drag Coefficients	3-122
3.16	Radiation Intensity Data Correlation	3-124
3.17	UV Contribution to the Radiation Heating	3-127
3.18	Effect of Entry Velocity on Radiative Heating	3-130
3.19	M/C_DA and Entry Angle Dependence on Maximum Heat Rates	3-131
3.20	60 Degree Cone Performance	3-138
3.21	Effect of Mass Asymmetries - 30 Degree Cone	3-139
3.22	Effect of Mass Asymmetries - 45 Degree Cone	3-140
3.23	Effect of Mass Asymmetries - 60 Degree Cone	3-141
3.24	Stagnation Point Enthalpy, Pressure and Convective Heating (Minimum Flyby/Entry Probe Mission)	3-146
3.25	Stagnation Point Radiation Heating - Minimum Flyby/Entry Probe Mission	3-147
3.26	Heating at End of Cone - Minimum Flyby/Entry Probe Mission	3-148
3.27	Stagnation Point Enthalpy, Pressure and Convective Heating - Best Entry Probe Mission	3-152
3.28	Stagnation Point Radiative Heating - Best Entry Probe Mission	3-153
3.29	Heating at End of Cone - Best Entry Probe Mission	3-154
3.30	Stagnation Point Enthalpy, Pressure and Convective Heating - Best RF Occultation Probe Mission	3-155

Figures (Cont'd)

3.31	Stagnation Point Radiative Heating - Best RF Occultation Probe Mission	3-157
3.32	Heating at End of Cone - Best RF Occultation Probe Mission	3-158
3.33	Wind Shear Effects on Entry Probe Attitude (Zero Spin Rate)	3-165
3.34	Gust Effects on Maximum Angle of Attack	3-168
3.35	X-6300 Temperature Histories After Mach 0.5	3-190
3.36	Effects of Entry Angle on Stagnation Point Heat Shield Thickness - Blunt Cone - X6300 Unstaged	3-191
3.37	Effects of Entry Angle on Stagnation Point Heat Shield Thickness - Blunt Cone - X6300 Staged	3-192
3.38	Effects of Entry Angle on Stagnation Point Heat Shield Thickness - Blunt Cone - OTWR Unstaged	3-193
3.39	Effects of Entry Angle on Stagnation Point Heat Shield Thickness - Blunt Cone - OTWR Staged	3-194
3.40	Stagnation Point Ablated and Total Heat Shield Thickness - Blunt Cone	3-195
3.41	Effects of Entry Velocity on Stagnation Point Ablator Thickness - Blunt Cone - Unstaged	3-197
3.42	Effects of Entry Velocity on Stagnation Point Ablator Thickness - Blunt Cone - Staged	3-198
3.43	Effects of M/C_DA on Heat Shield Thickness - Stagnation Point - Blunt Cone - Unstaged	3-199
3.44	Effects of M/C_DA on Heat Shield Thickness - Stagnation Point - Blunt Cone - Staged	3-200
3.45	Effects of Entry Angle on Mid-Cone Heat Shield Thickness - Blunt Cone - X6300 Staged	3-202
3.46	Effects of Entry Angle on Mid-Cone Heat Shield Thickness - Blunt Cone - X6300 Staged	3-203
3.47	Effects of Entry Angle on Mid-Cone Heat Shield Thickness - Blunt Cone - OTWR Unstaged	3-204
3.48	Effects of Entry Angle on Mid-Cone Heat Shield Thickness - Blunt Cone - OTWR Staged	3-205

Figures (Cont'd)

3.49	Mid-Cone Ablated and Total Heat Shield Thickness - Blunt Cone -	3-206
3.50	Effects of Entry Velocity on Mid-Cone Heat Shield Thickness - Blunt Cone - Unstaged	3-207
3.51	Effects of Entry Velocity on Mid-Cone Heat Shield Thickness - Blunt Cone - Staged	3-208
3.52	Effects of M/C_DA on Mid-Cone Heat Shield Thickness - Blunt Cone - Unstaged	3-209
3.53	Effects of M/C_DA on Mid-Cone Heat Shield Thickness - Blunt Cone - Staged	3-210
3.54	Effects of Entry Angle on Mid-Cone Heat Shield Thickness - Sharp Cone - X6300 Unstaged	3-212
3.55	Effects of Entry Angle on Mid-Cone Heat Shield Thickness - Sharp Cone - X6300 Staged	3-213
3.56	Effects of Entry Angle on Mid-Cone Heat Shield Thickness - Sharp Cone - OTWR Unstaged	3-214
3.57	Effects of Entry Angle on Mid-Cone Heat Shield Thickness - Sharp Cone-OTWR Staged	3-215
3.58	Effects of Entry Velocity on Mid-Cone Heat Shield Thickness - Sharp Cone - Unstaged	3-216
3.59	Effects of Entry Velocity on Mid-Cone Heat Shield Thickness - Sharp Cone - Staged	3-217
3.60	Effects of M/C_DA on Mid-Cone Heat Shield Thickness - Sharp Cone - Unstaged	3-218
3.61	Effects of M/C_DA on Mid-Cone Heat Shield Thickness - Sharp Cone - Staged	3-219
3.62	Avcoat 5026-39/HC-G Bond Line Temperature Profile	3-231

(Figures continued)

3.63	Maximum Entry Deceleration Loads	3-238
3.64	Aluminum Aeroshell Structural Weights 30 Degree Cone	3-242
3.65	Aluminum Aeroshell Structural Weights 45 Degree Cone	3-243
3.66	Aluminum Aeroshell Structural Weights 60 Degree Cone	3-244
3.67	Titanium Aeroshell Structural Weights 30 Degree Cone	3-245
3.68	Titanium Aeroshell Structural Weights 45 Degree Cone	3-246
3.69	Titanium Aeroshell Structural Weights 60 Degree Cone	3-247
3.70	Steel Aeroshell Structural Weights - 30 Degree Cone	3-248
3.71	Steel Aeroshell Structural Weights - 45 Degree Cone	3-249
3.72	Steel Aeroshell Structural Weights - 60 Degree Cone	3-250
3.73	Beryllium Aeroshell Structural Weights, 10-50 psi - 60 Degree Cone	3-252
3.74	Steel Aeroshell Structural Weights, 10-50 psi - 60 Degree Cone	3-253
3.75	Entry Probe Structural Comparison	3-261
3.76	Thermal Conductivity as a Function of Temperature for AV-50 Atmosphere	3-272
3.77	Heat Transfer Coefficient for AV-50 Atmosphere	3-273
3.78	Insulation Thickness as a Function of Payload Temperature Rise for Min-K and a Linde Superinsulation for Probe M/C_DA Values of 1, 5, and 15 slugs/ft^2	3-280
3.79	Insulation Thickness as a Function of Payload Temperature Rise for Min-K 1301 and a Linde Superinsulation for Probe M/C_DA Values of 1, 5, and 15 slugs/ft^2	3-281
3.80	Insulation Thickness as a Function of Insulation Weight	3-282
3.81	Insulation Thickness as a Function of Payload Temperature Rise for a Linde Superinsulation	3-284
3.82	Entry Probe Payload Module, 20 Inch Diameter Module	3-288

(Figures continued)

3.83	Attenuation Due to Venus Atmosphere	3-303
3.84	Galactic Noise	3-304
3.85	Receiver Solid Angle Geometry of Venus	3-305
3.86	System Noise Model	3-307
3.87	Candidate Modulation Schemes	3-310
3.88	Comparison of Coded and Uncoded Modulation Schemes	3-311
3.89	Required E/N_o for Noncoherent Orthogonal Coded Modulation Schemes	3-313
3.90	Comparison of Coherent and Noncoherent Coded Modulation Schemes(TA=1 min)	3-317
3.91	Comparison of Coherent and Noncoherent Coded Modulation Schemes (TA=5 min)	3-318
3.92	Multipath Loss	3-325
3.93	Circular Aperture Radiation Characteristics	3-327
3.94	Circular Aperture Gain	3-330
3.95	Transmitter Power Required for 10 BPS Mission	3-331
3.96	S-Band Parametric Antenna Weights	3-333
3.97	S-Band Transmitter Weight	3-336
3.98	S-Band Transmitter Efficiency	3-337
3.99	Battery Weight Requirements	3-338
3.100	RF Subsystem Weights	3-340
3.101	Frequency Selection - Propagation Loss and System Noise	3-348
3.102	Frequency Selection - Propagation Loss, System Noise, Antenna Efficiency	3-350
3.103	Frequency Selection - FCC Allocations	3-351
3.104	Synchronization in Data Channel	3-357

(Figures continued)

3.105	Synchronization in Separate Channels	3-357
3.106	Autocorrelation of Serial Coded Systems	3-361
3.107	Autocorrelation Functions of Separate Sync. Channel Systems	3-362
3.108	Ratio of IF Bandwidth-to-Data Rate ($b_o \tau$)	3-365
3.109	Comparison of Coherent and Non-coherent Coded Modulation Schemes	3-367
3.110	Relative Mission Data, Coherent vs. Noncoherent	3-369
3.111	Communication Look Angle Geometry	3-373
3.112	Flyby Probe Geometry	3-374
3.113	Actual and Allowed Descent Time Variations	3-376
3.114	Elevation Angle Constraints on Minimum Allowable M/C_DA	3-377
3.115	Range Improvement From Mach 0.5 to Impact	3-379
3.116	Entry Probe Look Angles	3-380
3.117	Transmitter Antenna Gain at Impact	3-382
3.118	Transmitter Antenna Gain at Mach 0.5	3-383
3.119	Probe Antenna Gain Improvement from Mach 0.5 to Impact	3-384
3.120	Maximum Flyby Probe Antenna Gain Degradation from Mach 0.5 to Impact	3-385
3.121	Flyby Probe Look Angles	3-387
3.122	Relay Link Performance - T_{Lead} = 56 minutes	3-388
3.123	Relay Link Performance - T_{Lead} = 60 minutes	3-389
3.124	Relay Link Performance - T_{Lead} = 64 minutes	3-390
3.125	Relay Link Performance - T_{Lead} = 68 minutes	3-391
3.126	Relay Link Performance - T_{Lead} = 72 minutes	3-392
3.127	Optimum Relay Link Performance	3-393

(Figures continued)

3.128	Relay Link Transmitter Power Requirements	3-395
3.129	Relay Link Performance - Mach 0.5 to Impact	3-398
3.130	Pre-Entry Probe Look Angles	3-400
3.131	Relay Link Performance Comparison - 25 and 50 Bar Atmospheres	3-404
3.132	Entry Probe Power Profile	3-420
3.133	Battery Voltage History During Constant Current and Impedance Discharge	3-424
3.134	Simulation of Venus Temperature Profile	3-425
3.135	Characteristic Entry Probe Power Profile	3-426
3.136	Battery Voltage History During Discharge	3-427
3.137	Power Conditioning System for Simple Payloa	3-429
3.138	Power Conditioning System for Complex Payload	3-430
3.139	Entry Probe Data Handling Subsystem	3-439
3.140	Entry Probe Data Collection and Transmission Profile	3-441
3.141	Block Diagram of Sequencing, Safing, and Initiation Subsystem for Best RF Occultation Mission - Direct Link	3-450
3.142	Block Diagram of Sequencing, Safing, and Initiation Subsystem for Best Entry Probe Mission	3-453
3.143	Pyrotechnic Initiator Functional Block Diagram	3-455

(Figures continued)

3.144	Typical Entry Probe System Temperature Profile	3-487
3.145	Probe Temperature as a Function of Cone Angle-Cruise Mode	3-494
3.146	Temperature of Sun Oriented 45 Degree Cone Configuration - Cruise Mode	3-498
3.147	Power Required to Raise the Temperature of the Sun Oriented 45 Degree Cone Configuration During Cruise Near Earth	3-499
3.148	Temperature of Space Oriented 45 Degree Cone Configuration - Cruise Mode	3-501
3.149	Effect of Heat Shield Coating α/ϵ Variation on Probe Temperature During Port Separation, 45 Degree Cone Configuration	3-507
3.150	Effect of Solar Exposure Angle Variation on Probe Average Temperature During Post Separation	3-508
3.151	Temperature Gradient Across Probe During Post Separation	3-510
3.152	Thermal Control System Summary	3-512
3.153	Interface Wiring Diagram, Best RF Occultation Probe Mission - Direct Link	3-523
3.154	Interface Wiring Diagram, Best Entry Probe Mission and Best RF Occultation Mission - Relay Link	3-525
3.155	Frequency Effects on Radar Altimeter Power Requirements	3-533
3.156	Radar Altimeter Antenna System Block Diagram	3-534
3.157	Quarter Loop Coupling Antenna	3-535
3.158	Radiation Pattern - E Plane, Quarter Loop Coupling	3-536
3.159	Radiation Pattern - H Plane, Quarter Loop Coupling	3-537
3.160	Generic ICW Range Tracker	3-541
3.161	CW Fuze Block Diagram	3-547

BOOK II

FIGURES

Figure No.	Title	Page No.
4.1	Blunt Body Shock Shapes	4-6
4.2	Blunt Body Pressure Distributions	4-7
4.3	Blunt Body Temperature Profiles	4-8
4.4	Stagnation Point Thermodynamic Properties	4-10
4.5	Specie Concentration Profiles at the Stagnation Point	4-11
4.6a	Thermodynamic Properties in the Shock Layer of a 30° Blunt Cone	4-12
4.6b	Specie Concentration Profiles in the Shock Layer of a 30° Blunt Cone	4-13
4.7a	Thermodynamic Properties in the Shock Layer of a 45° Blunt Cone	4-14
4.7b	Specie Concentration Profiles in the Shock Layer of a 45° Blunt Cone	4-15
4.8	Continuum Spectral Absorption Coefficients in the UV Region	4-24
4.9	Continuum Radiation Intensity in the UV Region	4-25
4.10	Line and Continuum Spectral Radiation Intensity	4-33
4.11	Oxygen Multiplet Distribution	4-34
4.12	CO (4+) Emissivity - KBF Results	4-36
4.13	CO (4+) Intensity - MOT Results	4-38
4.14	CO (4+) Spectral Absorption Coefficient - HW Results	4-39
4.15	Equilibrium Composition - AV-50 ATM	4-60
4.16	Equilibrium Composition at Gas/Solid Carbon Interface - AV-4 ATM	4-61
4.17	Equilibrium Composition at Gas/Solid Carbon Interface - AV-10 ATM	4-62

Figure No.	Title	Page No.
4.18	Equilibrium Composition at Gas/Solid Carbon Interface - AV-50 ATM	4-63
4.19	Equilibrium Composition at Gas/Solid Silica Interface - AV-4 ATM	4-65
4.20	Equilibrium Composition at Gas/Solid Silica Interface - AV-10 ATM	4-66
4.21	Equilibrium Composition at Gas/Solid Silica Interface - AV-50 ATM	4-67
4.22	Comparison of Experimental Heat Transfer Results for N_2, He, and H_2O Coolants	4-71
4.23	Comparison of the Effectiveness of Air and He in Reducing Skin Friction	4-72
4.24	Effect of Mach Number on the Reduction in Skin Friction with Air Injection	4-74
4.25	Comparison of Heating Reduction Expressions for Air-Air Injection	4-79
4.26	Comparison of Turbulent Heating Reduction for Air-Air Injection	4-81
4.27	Heating Reduction for Laminar Flat Plate and Stagnation Point Air-Air Injection	4-83
4.28	X6300 Tensile Modulus	4-85
4.29	X6300 Tensile Proportional Limit	4-86
4.30	X6300 Ultimate Tensile Strength	4-87
4.31	X6300 Longitudinal Thermal Strain	4-88
4.32	X6300 Circumferential Thermal Strain	4-89
4.33	X6300 Compressive Modulus	4-90
4.34	X6300 Compressive Proportional Limit	4-91
4.35	X6300 Ultimate Compressive Strength	4-92
4.36	X6300 Thermal Strain at $0^{\circ}F$	4-94
4.37	5026-39/HC-G Stiffened Titanium Composite Strain Distribution, $-100^{\circ}F$	4-101

Figure No.	Title	Page No.
4.38	5026-39/HC-G Stiffened Steel Composite Strain Distribution, -100°F	4-102
4.39	5026-39/HC-G Steel Honeycomb Composite Strain Distribution, -100°F	4-103
4.40	5026-39/HC-G Tensile Modulus	4-108
4.41	5026-39/HC-G Tensile Poisson's Ratio	4-109
4.42	5026-39/HC-G Compressive Modulus	4-110
4.43	5026-39/HC-G Compressive Poisson's Ratio	4-111
4.44	5026-39/HC-G Thermal Strain	4-112
4.45	5026-39/HC-G Temperature Profiles During Entry	4-114
4.46	5026-39/HC-G Stiffened Steel Composite Circumferential Ablator Strain	4-116
4.47	5026-39/HC-G Stiffened Steel Composite Meridional Ablator Strains	4-117
4.48	5026-39/HC-G Steel Honeycomb Composite Circumferential Ablator Strain	4-118
4.49	5026-39/HC-G Steel Honeycomb Composite Meridional Ablator Strain	4-119
4.50	5026-39/HC-G Stiffened Titanium Composite Circumferential Ablator Strain	4-120
4.51	5026-39/HC-G Stiffened Titanium Composite Meridional Ablator Strain	4-121
4.52	X6300 Temperature Profiles During Entry	4-124
4.53	X6300 Steel Honeycomb Composite Circumferential Ablator Strains	4-125
4.54	X6300 Steel Honeycomb Composite Meridional Ablator Strains	4-126
4.55	Analytical Model of Avco 1322 Shell Program Analysis	4-130
4.56	Dimensional Schematic of Aeroshell	4-132
4.57	Substructure Stress Distribution - Program 1322 Solution	4-133

Figure No.	Title	Page No.
4.58	Circumferential Strain Distributions in Ablator - Program 1322 Solution	4-134
4.59	Meridional Strain Distributions in Ablator - Program 1322 Solution	4-135
4.60	R6300 Thermal Conductivity Functions - Test Data	4-160
4.61	R6300 Thermal Conductivity Functions - Simulated	4-163
4.62	R6300 Enthalpy - Temperature Data	4-164
4.63	R6300 Specific Heat Variation	4-166
4.64	R6300 Density-Temperature Relationship	4-167
4.65	R6300 Predicted and Measured Thermal Response - Rovers Test 1	4-168
4.66	R6300 Predicted and Measured Thermal Response - Rovers Test 2	4-171
4.67	R6300 Predicted and Measured Thermal Responses - Rovers Test 3.	4-172
4.68	R6300 Predicted and Measured Thermal Response - Rovers Test 8	4-173
4.69	R6300 Final Density Profile - Test	4-174
4.70	R6300 Wall Enthalpy Correction	4-177
4.71	R6300 Model 500 Arc Ablation Rate Data	4-179
4.72	R6300 Test Specimen Geometry	4-182
4.73	R6300 Reaction Rate Data	4-183
4.74	R6300 Thermal Radiation Decay After Shutdown	4-186
4.75	Vapor Pressure of Carbon	4-187
4.76	R6300 Ablation Histories Comparison with Ground Tests	4-188
4.77	5026-39/HC-G Surface Temperature - Radiant Heating Tests - Air	4-206
4.78	5026-39/HC-G Surface Temperature - Radiant Heating Tests - Argon	4-207

Figure No.	Title	Page No.
4.79	5026-39/HC-G Surface Temperature - Radiant Heating Tests - Nitrogen	4-208
4.80	5026-39/HC-G Surface Temperature - Radiant Heating Tests - 5% O_2, 95% N_2	4-209
4.81	5026-39/HC-G Surface Temperature - Radiant Heating Tests - 10% O_2, 90% N_2	4-210
4.82	5026-39/HC-G Mass Loss Rate - Radiant Tests - Air	4-212
4.83	5026-39/HC-G Mass Loss Rate - Radiant Tests - Argon	4-213
4.84	5026-39/HC-G Mass Loss Rate - Radiant Tests - Nitrogen	4-214
4.85	5026-39/HC-G Mass Loss Rate - Radiant Tests - 5% O_2, 95% N_2	4-215
4.86	5026-39/HC-G Mass Loss Rate - Radiant Tests - 10% O_2, 90% N_2	4-216
4.87	5026-39/HC-G Mass Loss - Giannini Splash Tests	4-219
4.88	5026-39/HC-G Mass Loss - Brightness Temperature Correlations	4-220
4.89	5026-39/HC-G Mass Loss - Overs Tests	4-224
4.90	5026-39/HC-G Thermal Conductivity	4-225
4.91	5026-39/HC-G Specific Heat	4-227
4.92	5026-39/HC-G Thermogravimetric Data	4-228
4.93	5026-39/HC-G Stagnation Point Surface Recession History	4-232
4.94	5026-39/HC-G Stagnation Point Temperature Histories	4-234
4.95	5026-39/HC-G Stagnation Point Density Profiles	4-235
4.96	X6300 Mid-Cone Point Surface Recession History	4-237
4.97	X6300 Mid-Cone Point Temperature Histories	4-238
4.98	X6300 Mid-Cone Point Density Profiles	4-239
4.99	X6300 Stagnation Point Surface Recession History	4-242
4.100	X6300 Stagnation Point Temperature Histories	4-243

Figure No.	Title	Page No.
4.101	X6300 Insulation Weight	4-245
4.102	Effects of Shear on Avcoat 5026-39/HC-G Surface Recession	4-248
4.103	Effects of Pressure Gradient on Mass Loss Rate of Avcoat 5026-39/HC-G	4-251
4.104	Stagnation Convective Heating - Gas Enthalpy Environment	4-253
4.105	Stagnation Convective - Radiative Heating	4-254
4.106	Convective - Radiative Heating on Cone	4-255
4.107	Turbulent Shear Stress Simulation	4-258
4.108	Future Ablation Test Facilities Capabilities	4-260
4.109	Stagnation Heating and Pressure Simulation	4-283
4.110	Convective Heating - Enthalpy Trajectory Profile, V_E = 38,250 fps γ_E = -60°	4-292
4.111	Convective Heating - Pressure Trajectory Profile, V_E = 38,250 fps, γ_E = -60°	4-293
4.112	Convective - Radiating Heating Trajectory Profile, V_E = 38,250 fps, γ_E = -60°	4-294
4.113	Convective Heating - Enthalpy Trajectory Profile, V_E = 35,600 fps, γ_E = -60°	4-295
4.114	Convective Heating - Pressure Trajectory Profile, V_E = 35,600 fps, γ_E = -60°	4-296
4.115	Convective - Radiant Heating Trajectory Profile, V_E = 35,600 fps, γ_E = -60°	4-297
4.116	Convective Heating - Enthalpy Simulation, V_E = 38,250 fps, γ_E = -60°	4-298
4.117	Convective Heating - Pressure Simulation, V_E = 38,250 fps, γ_E = -60°	4-299
4.118	Convective - Radiative Heating Simulation, V_E = 38,250 fps, γ_E = -60°	4-300
4.119	Convective Heating - Enthalpy Simulation, V_E = 35,600 fps, γ_E = -60°	4-301

Figure No.	Title	Page No.
4.120	Convective Heating - Pressure Simulation, V_E = 35,600 fps, γ_E = -60°	4-302
4.121	Convective - Radiative Heating Simulation, V_E = 35,600 fps, γ_E = -60°	4-303
5.1a	Flyby Configuration 10a, Stowed	5-7
5.1b	Flyby Configuration 10a, Deployed	5-8
5.2a	Flyby Configuration 20a, Stowed	5-9
5.2b	Flyby Configuration 20a, Deployed	5-10
5.3	Launch Configuration of Flyby/Entry Probe - Best RF Occultation Mission	5-13
5.4a	Flyby Configuration - Minimum Mission - Alternate 1, Stowed	5-20
5.4b	Flyby Configuration - Minimum Mission - Alterante 1, Deployed	5-21
5.5a	Flyby Configuration - Minimum Mission - Alternate 2, Stowed	5-23
5.5b	Flyby Configuration - Minimum Mission - Alternate 2, Deployed	5-24
5.6	Structural Interface of Flyby/Entry Probe	5-27
5.7	Scan Platform Functional Block Diagram	5-29
5.8	Attitude Control Requirements	5-31
5.9	Attitude Control Mechanization	5-33
5.10	Attitude Control Functional Block Diagram with Canopus Occultation at Planet	5-37
5.11	Thermal Control Subsystem Requirements	5-39
5.12	Thermal Blanket Performances.	5-41
5.13	Effect of Solar Array on Louvers	5-43
5.14	Bay VI Temperatures	5-44

Figure No.	Title	Page No.
5.15	Thermal Control Subsystem Summary	5-45
5.16	Mariner Venus 1972 Power Subsystem Functional Block Diagram	5-48
5.17	FTS Block Diagram	5-53
5.18	FCS Block Diagram	5-56
5.19	RFS Block Diagram	5-59
5.20	Normalized Carrier Performance	5-60
5.21	Cruise Data Subcarrier Margin	5-61
5.22	Data Mission Profile	5-62
5.23	CC & S Block Diagram	5-69
5.24	DAS Block Diagram	5-73
5.25	DSS Block Diagram	5-77
5.26	Pyrotechnic Subsystem Block Diagram	5-80
6.1	Entry Probe System - Work Breakdown Structure	6-2
6.2	Venus 72 Project Flyby/Entry Probe Schedule	6-6
6.3	Flyby Program Schedule Reference - Mariner Mars 1969	6-9
6.4	1972 Flyby Program Schedule - Baseline and Alternate I Configurations	6-11
6.5	1972 Flyby Program Schedule - Alternate 2 Configuration	6-12
6.6	Entry Probe Program Task Comparison - Cost/Payload Option	6-20
6.7	Entry Probe Subsystem Comparison - Cost/Payload Option.	6-22
6.8	Entry Probe Expenditure Plan	6-25
6.9	Flyby Probe Expenditure Plan	6-26
6.10	Alternate Mission Cost and Effectiveness	6-31

Book I

TABLES

Table No.	TITLE	Page
2.1	Summary of Instrument Weightsfor Alternative Missions	2-8
2.2	Value Coefficients - Flyby Probe (Atmospheric Objectives)	2-23
2.3	Value Coefficients - Entry Probe (Atmospheric Objectives)	2-24
2.4	Value Coefficients - Flyby Probe (Planetology Objectives)	2-25
2.5	Value Coefficients - Entry Probe (Planetology Objectives)	2-26
2.6	Value Coefficients - Flyby Probe (Particles/Fields and Interplanetary Objectives)	2-27
2.7	Intrinsic Value Summary	2-29
2.8	Commonality Coefficients	2-31
2.9	Experiment Value - Best RF Occultation Probe Mission	2-34
2.10	Experiment Value - Minimum Flyby/Entry Probe Mission	2-37
2.11	Experiment Value - Best Entry Probe Mission	2-39
2.12	Value Estimate for Combined Mariner V and Venera 4	2-39
2.13	Summary of Mission Values	2-42
2.14	Launch Configuration Elements - Estimated Recycle Times	2-44
2.15	Number of Recycles During Launch Opportunity	2-46
2.16	Launch Configuration Mission Success Diagrams and Reliability Mathematical Models	2-51
2.17	Launch Configuration Element Reliability Values	2-53
2.18	Mathematical Model for Reliability Goals	2-56
2.19	Mission Reliability Goals	2-58
2.20	Mission Phase Reliability Goals	2-60
2.21	Flyby/Entry Probe Contamination Allocations	2-65

(Tables continued)

2.22	Influence of Entry Probe Thrust Application Angle on Pre-Entry Communications	2-97
2.23	Influence of Thrust Application Angle on Pre-Entry Communication, Entry Dispersion and Rocket Location	2-99
2.24	Separation and Entry Parameters for Minimum Flyby/Entry Probe Mission and Best Entry Probe Mission	2-105
2.25	Best RF Occultation Probe Mission Profile	2-129
2.26	Minimum Flyby/Entry Probe Mission and Best Entry Probe Mission Profiles	2-140
3.1	General M/C_DA Trade-off Parameters	3-4
3.2	General Entry (Approach) Velocity Trade-Off Parameters	3-4
3.3	General Entry Angle Trade-Off Parameters	3-4
3.4	Reference Atmospheric Parameters	3-7
3.5	Model Atmosphere Comparison	3-8
3.6	Injection Energy Requirements for 1972 Venus Missions	3-11
3.7	Value Judgement Criteria for Reliability Allocation	3-23
3.8	Probe Subsystem and Assembly Reliability Goals	3-25
3.9	MV '72 Entry Probe Failure Modes, Effects, and Criticality Analysis	3-28
3.10	Summary of Entry Probe Potential Functional Weak Links	3-34
3.11	Entry Probe Reliability Prediction Model	3-36
3.12	Entry Probe Reliability Feasibility Prediction	3-37
3.13	Entry Probe Subsystem Reliability Predictions and Allocations	3-38
3.14	Entry Probe Mission Reliability Profile	3-39
3.15	Reliability Enhancement Techniques for Potential Weak Links	3-40
3.16	Summary of Baseline Entry Probe Experiment Requirements	3-44
3.17	Entry Probe Payload Instrumentation Bit Accuracy	3-55
3.18	Comparison of Accuracy of Measurement with Error Caused by Sampling Interval	3-57
3.19	Direct Communications Link Parameters for Alternate Missions	3-62

(Tables continued)

3.20	Configuration Selection Factors	3-64
3.21	Entry Probe Characteristics for the Best RF Occultation Probe Mission - Direct Link	3-67
3.22	Entry Probe Weight and Power Summary for the Best RF Occultation Probe Mission - Direct Link	3-70
3.23	Entry Probe Mass Properties for the Best RF Occultation Probe Mission - Direct Link	3-72
3.24	Entry Probe Characteristics for Minimum Flyby/Entry Probe Mission	3-74
3.25	Entry Probe Weight and Power Summary for Minimum Flyby/Entry Probe Mission	3-77
3.26	Entry Probe Mass Properties for Minimum Flyby/Entry Probe Mission	3-78
3.27	Entry Probe Characteristics for Best Entry Probe Mission	3-79
3.28	Entry Probe Weight and Power Summary for Best Entry Probe Mission	3-82
3.29	Entry Probe Mass Properties for Best Entry Probe Mission	3-83
3.30	Entry Probe Characteristics for Best RF Occultation Probe Mission - Relay Link	3-84
3.31	Entry Probe Weight and Power Summary for Best RF Occultation Probe Mission - Relay Link	3-87
3.32	Entry Probe Mass Properties for Best RF Occultation Probe Mission - Relay Link	3-88
3.33	Entry Probe-Flyby Probe Weight Summary	3-89
3.34	Flyby/Entry Probe Weight Combinations	3-90
3.35	Entry Probe Overall Dimensions	3-91
3.36	Venus 1972 Flyby/Entry Probe Flight Sequence - Best RF Occultation Probe Mission	3-97

(Tables continued)

3.37	Normal Shock Density Ratios for Three Atmosphere Models	3-106
3.38	Axial Force Coefficients - 30 Degree Cones	3-108
3.39	Normal Force Coefficients - 30 Degree Sharp Cone	3-109
3.40	Normal Force Coefficients - 30 Degree Blunt Cone	3-110
3.41	Center of Pressure Variation - 30 Degree Cones	3-111
3.42	Damping Coefficients - 30 Degree Cones	3-111
3.43	Axial Force Coefficients - 45 Degree Cones	3-112
3.44	Normal Force Coefficients - 45 Degree Sharp Cone	3-113
3.45	Normal Force Coefficients - 45 Degree Blunt Cone	3-114
3.46	Center of Pressure - 45 Degree Cones	3-115
3.47	Damping Coefficients - 45 Degree Cones	3-115
3.48	Heating Rate Summary for Parametric Configuration Study	3-133
3.49	Configuration Summary Data Used in Parametric Stability Study	3-135
3.50	Spin and Diameter Effects	3-136
3.51	Entry Conditions for Selected Missions	3-143
3.52	Internal Thermal Properties - X6300 and OTWR	3-180
3.53	Surface Ablation Properties - X6300 and OTWR	3-181
3.54	Internal Thermal Properties - Avcoat 5026-39/HC-G	3-182
3.55	Surface Thermal Properties - Avcoat 5026-39/HC-G	3-183
3.56	Venus Entry Probe Heat Shield Thickness at Stagnation Point, Blunt Cone	3-220
3.57	Venus Probe Heat Shield Thickness at Mid-Cone Point, Blunt Cone	3-221
3.58	Venus Probe Heat Shield Thickness at Mid-Cone Point, Sharp Cone	3-222
3.59	Aerodynamic Shear Summary	3-227
3.60	Heat Shield Summary	2-232

(Tables continued)

3.61	Summary of Mission Independent Design Conditions for the Entry Probe Structure	3-234
3.62	Scale Height of Venus Model Atmospheres	3-239
3.63	Single Pressure Vessel Structural Weight Comparison	3-264
3.64	Comparison of Total Entry Probe Structural Weight	3-264
3.65	Profiles for Descent into the AV-50 Atmosphere	3-268
3.66	Profiles for Descent into the AV-4 Atmosphere	3-269
3.67	Total Descent Time Through Atmosphere	3-270
3.68	Entry Probe Payload Mass	3-275
3.69	Total Internal Power Dissipation	3-276
3.70	Insulation System Design Characteristics	3-277
3.71	Electrical Paths Across the Insulation Barrier	3-291
3.72	Payload Module Design Characteristics	3-293
3.73	Sterilization Canister Summary Data	3-298
3.74	Leakage Gas Requirements	3-298
3.75	Sterilization Canister Weight Schedule	3-298
3.76	Assumptions and Constraints - Direct Link Modulation Selection	3-309
3.77	Assumptions and Constraints - Direct Link Performance	3-321
3.78	Entry Probe Direct Link Communications Angles	3-323
3.79	S-Band Transmitter Characterisitcs	3-335
3.80	Direct Link Design Control Chart	3-341
3.81	Selected Transmitter Characteristics, Direct Link	3-345
3.82	Assumptions and Constraints - Relay Link Modulation Selection	3-355
3.83	Table of Values of (K) Versus (n)	3-359
3.84	Comparison of Coded Systems	3-364

(Tables continued)

3.85	Assumptions and Constraints - Relay Link Performance Study	3-372
3.86	Relay Link Design Control Table	3-396
3.87	Relay Link Design Control Table -- 25 Bar Atmosphere	3-406
3.88	RF Subsystem Characteristics	3-408
3.89	Entry Probe Full Load Power Requirements	3-431
3.90	Entry Probe Power Summary	3-432
3.91	Data Handling Modules	3-443
3.92	Entry Probe Data Rates	3-445
3.93	Sequence of Entry Probe Events for Best RF Occultation Mission	3-447
3.94	Weight and Power Consumption of SS & I Subsystem	3-456
3.95	Deflection Rocket Motor Design Data	3-459
3.96	Propulsion Requirements for Entry Probe Missions	3-463
3.97	List of Symbols for Propulsion Subsystem Error Analysis	3-470
3.98	MARC 18A1 Spin Rocket Motor Characteristics	3-475
3.99	Entry Probe Mass and Dimensional Characteristics for Calculation of Spin-Thrust System Performance	3-479
3.100	Entry Probe Spin-Thrust System Performance	3-480
3.101	Yo-Yo Despin Subsystem Characteristics	3-482
3.102	General Design Conditions and Requirements - Entry Probe Thermal Control Subsystem	3-484
3.103	Temperature Limitations for Structural Members and Components	3-488
3.104	Comparison of Sun Oriented and Space Oriented 45 Degree Cone Configuration	3-502
3.105	Summary of Post Separation Parameters and Study Results, 45 Degree Cone Configuration	3-504

(Tables continued)

3.106	Entry Probe Pyrotechnic Devices	3-516
3.107	Radar Altimeter Comparison	3-539
3.108	ICW Altimeter Design Control Chart	3-543

BOOK II

TABLES

Table No.	Title	Page No.
4.1	Sharp Cone Inviscid Shock Layer Results	4-3
4.2	60 Degree Cone Inviscid Shock Layer Results	4-16
4.3	30 Degree Cone Boundary Layer Results	4-17
4.4	30 Degree Cone Boundary Layer Interaction Estimates	4-18
4.5	45 Degree Cone Boundary Layer Results	4-19
4.6	60 Degree Cone Boundary Layer Results	4-19
4.7	Line and Multiplet Radiation Heating	4-31
4.8	Survey of Class I Programs	4-46
4.9	Survey of Class II Programs	4-49
4.10	Survey of Class III Programs	4-53
4.11	Summary of Experimental Turbulent Data on Gas Injection	4-70
4.12	X6300 Computed and Allowable Cold Soak Stresses at $0^{\circ}F$	4-95
4.13	X6300 Computed and Allowable Cold Soak Stresses at $-20^{\circ}F$	4-97
4.14	5026-39/HC-G Mechanical Properties at $-100^{\circ}F$	4-99
4.15	5026-39/HC-G Computed and Allowable Strains at $-100^{\circ}F$	4-105
4.16	X6300 Arc Test Data	4-155
4.17	X6300 Thermal Conductivity Test Data	4-159
4.18	X6300 Thermal Conductivity Multipliers	4-161
4.19	Rovers Test Environment	4-169
4.20	Thermocouple Locations - Rovers Tests	4-169
4.21	Determination of Free Stream Oxygen Fraction	4-176

Table No.	Title	Page No.
4.22	Results of Diffusion Analysis .	4-180
4.23	Areas of Material Property Investigation Required for Carbon Phenolic Utilization in the Venus Environment	4-191
4.24	5026-39/HC-G Ablation Data - Radiation Tests	4-193
4.25	5026-39/HC-G Ablation Data - Giannini Tests	4-217
4.26	5026-39/HC-G Ablation Data - Overs Tests	4-222
4.27	Aerodynamic Environment for Avcoat 5026-39/HC-G Performance Calculations	4-231
4.28	Aerodynamic Environment for JPL Comparison Case	4-241
4.29	Development Test Plan - Phase I	4-264
4.30	Lo Rho MHD Boost Performance	4-282
4.31	Simulation Requirements V_E = 35,600 fps, γ_E = -60°	4-305
4.32	Simulation Requirements V_E = 38,250 fps, γ_E = -60°	4-306
4.33	Comparison of Ground Test Capabilities and Simulation Requirements, V_E = 35,600 fps, γ_E = -60°	4-307
4.34	Comparison of Ground Test Capabilities and Simulation Requirements, V_E = 38,250 fps, γ_E = -60°	4-308
4.35	Development Test Plan - Avcoat 5026-39/HC-G	4-312
4.36	Development Test Plan - Carbon Phenolic	4-313
4.37	Cut Bar Conductivity Measurements	4-315
4.38	Method of Mixtures Specific Heat Measurements - Carbon Phenolic	4-316
5.1	Invariant Requirements and Constraints	5-1
5.2	Best RF Occultation Mission Requirements and Constraints	5-2
5.3	Alternate Mission Requirements and Constraints	5-3
5.4	Configuration Trade Analysis - Representative Configurations	5-5
5.5	Baseline Mariner 72 Weight Table	5-14
5.6	Minimum Mission Weight Table - Alternate 1	5-15

Table No.	Title	Page No.
5.7	Minimum Mission Weight Table - Alternate 2	5-17
5.8	Principal Inertial Characteristics of Mariner Venus 1972 Spacecraft	5-34
5.9	Velocity Increment with Mariner 1969 Propulsion Subsystems	5-51
5.10	Functional Modifications from Mariner 1969 FTS	5-45
5.11	Command Requirements Comparison	5-57
5.12	Design Control Table - Day 104 - Entry Probe Deployment.	5-64
5.13	Design Control Table - Post Encounter	5-66
5.14	Data Rate Summary	5-72
5.15	Pyrotechnic Subsystem Requirements	5-79
5.16	Pyrotechnic Subsystem Variation from MM '69	5-80
6.1	Flyby Probe/ Entry Probe Costs	6-17
6.2	Baseline and Alternate Flyby Probe Configuration Cost Summary	6-18
6.3	"A" & "B" Entry Probe Task Comparisons	6-21
6.4	"A" & "B" Entry Probe Subsystem Comparisons	6-23
6.5	Summary of Major System Differences for Alternate Missions	6-28
6.6	Cost-Effectiveness Comparison	6-30

Glossary of Symbols*
(Units given where invariant.)

C_3 - Canopus - probe (spacecraft) - near limb of Venus angle employed to define Venus centered Canopus occultation zones

C_f - Local skin friction coefficient

c_p - Specific heat, Btu/lb-^oF

CPV, - Twice the total energy per unit mass and defined by $C_3 = V_{HL}^2$

DLA - The declination of the outgoing asymptote of the escape hyperbola

EPV - Earth - probe (spacecraft) - near limb of Venus angle

F - Normalized injection rate; F =

GP - The angle between the incoming arrival hyperbolic - excess velocity vector V_{HP}, and its projection onto the target planet's orbital plane

H - Total enthalpy, Btu/lb

H_v - Effective heat of vaporization, Btu/lb

M - Mass, Mach number, molecular weight

M/C_DA - Probe ballistic parameter

N - Number density, particles/cc

P - Pressure; spin rate

q_c, q_s - Local and stagnation point convective heat rate, Btu/ft^2-sec

q_R - Radiative heating rate, Btu/ft^2-sec

Q_c, Q_s, Q_r - Integrated heating (same notation as heat rates), Btu/ft^2

r_a - Aim point of the incoming approach hyperbolic - excess velocity vector defined by $r_a = r_p \sqrt{1 + \frac{2\mu_v}{r_p V^2}}$

r_c - Communication distance

r_E - Probe entry radius defined as 6500 km

R_{ex} - Reynolds number based on boundary edge conditions and streamline distance from the stagnation point

R_N - Nose radius

r_p - Spacecraft periapsis radius

r_o - Spacecraft/probe range from Venus at time of probe separation

* local usage can supercede this glossary when so noted

SG1	The semi-major axis of the error ellipse formed by projecting the three-dimensional error ellipsoid onto the T-R plane
SG2	The semi-minor axis of the error ellipse
SPV	Sun-probe (spacecraft) - near limb of Venus angle employed to establish the Venus centered Sun occultation region
t_f -	Flight time from launch to encounter
t_L -	Probe lead time defined as the spacecraft time from periapsis at probe entry into the atmosphere
t_{SEP}	Spacecraft time from periapsis passage at probe release
u -	Local streamline velocity
V_{HL} -	The launch hyperbolic excess speed
V_{HP}, V	The hyperbolic excess speed at Venus
W_p -	The total spacecraft/entry probe weight
x -	Streamline distance from stagnation point
X -	Axial coordinate from nose
ZAE -	the Earth - probe (spacecraft) - Venus angle several days prior to encounter
ZAP -	the Sun - probe (spacecraft) - Venus angle several days prior to encounter
γ_E -	probe entry angle defined as the angle between the entry velocity vector and the local horizon where entry angles greater than -90^o indicate the probe and spacecraft are flying by opposite sides of the planet
θ_{op} -	the thrust application angle defined as the angle between the approach asymptote and the probe deflection velocity vector
μ_v -	gravitational parameter of Venus taken as 324583.4 km^3/sec^2
ϕ_E -	range angle traversed by the probe from separation to entry
Δt_E -	uncertainty in entry time produced by perturbations in the separation parameters
ΔV -	magnitude of the probe deflection velocity
$\Delta\gamma_E$ -	uncertainty in the entry angle produced by perturbations in the separation parameters

μ_λ - spectral absorption coefficient, cm^{-1}

λ - wavelength

μ - microns; also absorption coefficient

ρ - density, $slugs/ft^3$

θ_{FC} - communication angle between axis of entry probe antenna and line of sight from entry probe to receiver

$$\theta_{FC} = \theta_D + \theta_W + \bar{\alpha} + \theta_E \text{ (for direct link)}$$

θ_D - contribution to θ_{FC} due to entry angle dispersion

θ_W - contribution to θ_{FC} due to winds

θ_E - plane-to-centric range angle between impact point and sub-Earth point

$\Delta\phi_E$ - uncertainty in the range angle produced by perturbations in the separation parameters

β_i - elevation angle below which communications is considered impossible

$\bar{\alpha}$ - angle of attack envelope value

δ - boundary layer thickness

δ^* - boundary layer mass - defect thickness

Δ^* - effective displacement thickness

Δ - shock stand off distance

η - transpiration factor

θ_c - semi-apex cone angle; also communication angle

θ_{eff} - effective cone angle

σ - mean standard deviation; also absorption cross section

ξ - stand off distance normal to body normalized by nose radius

Subscripts

c - coolant, cone or convective heating

E - conditions at entry (entry radius defined as 6500 km)

e - conditions at edge of boundary layer

w - conditions at wall

o - zero injection conditions

s - stagnation point

i - refers to i th specie

IV. ENTRY PROBE

AEROSHELL TECHNOLOGY STUDY ADDENDUM

4.0 ENTRY PROBE AEROSHELL TECHNOLOGY STUDY ADDENDUM

4.1 Study Scope and Objectives

The study consisted of five key technology areas:

(1) Prediction of aerothermal environment

(2) Prediction of material performance

(3) Failure mode identification

(4) Define preferred materials candidates

(5) Development testing simulation.

The technology areas noted above are multidisciplined in many respects, involving aerodynamics, thermodynamics, stress analysis, materials, and test; however, the emphasis on the study lies in the thermodynamics area. The objectives of the study include,

(1) An assessment of the uncertainties in the technology areas and of their effects on material selection and heat shield performance.

(2) Comparative performance of candidate materials.

(3) Recommended thermal and mechanical material property specifications necessary for a direct Venus entry.

(4) An assessment of the limitations of ground and flight testing and a recommended heat shield materials ground test/simulation plan.

4.2 Aerothermal Environment

4.2.1 Study Criteria

The flow field analyses were performed for a flight condition selected early in the mission study. The selected flight condition is 36,243 fps at an ambient density of 4.3×10^{-6} slugs/ft^3, and the mixture selected for detailed study was a 50 percent CO_2, 50 percent N_2 combination. The choice of the flight condition was made to coincide closely with the point in a trajectory where the maximum ultraviolet line and continuum radiation was predicted. The results are applicable to the final reference design heating for the Best RF

Occultation Mission which is for the AV-4 atmosphere, an M/C_DA of 0.475 slugs/ft^2 an entry velocity of 38,250 fps and an entry angle of -60 degrees. The peak UV radiation component occurred at 37,600 fps and an ambient density of 2×10^{-6} slugs/ft^3; at 36,243 fps, the density was 4×10^{-6} slugs/ft^3 and the UV radiation was 75 percent of the maximum value.

The flow field analyses considered a family of cones with semi-apex angles of 30, 45, and 60 degrees, which were either sharp cones or blunted with a spherical nose radius 25 percent of the base radius.

4.2.2 Sharp Cone Analysis

Sharp cone solutions were obtained using Feldmans' constant density hypersonic approximation for the shock layer, which has been found to compare well with exact concial flow solutions. The resultant conical shock angles were computed parametrically as a function of the shock density ratio and the species concentrations in the shock layer were obtained and are given : Table 4.1 for the selected flight conditions.

The sharp cone calculations provide useful information for interpreting blunt cone solutions, as for small bluntness the bow wave angle and surface pressure distributions should approach the sharp cone values asymptotically. The pressure coefficients on the cone surface are,

Cone Angle	Pressure Coefficient at Surface
30	.496
45	1.00
60	1.50

As can be seen, the pressure coefficients are well predicted by Newtonian theory; there is less than one percent variation in pressure across the shock layer.

TABLE 4.1

Sharp Cone Inviscid Shock Layer Results

Cone Angle (deg)	30	45	60
Shock Angle (deg)	30.83	46.55	62.74
Pressure (psf)	1404	2827	4241
Density (scf)	$.851 \times 10^{-4}$	$.844 \times 10^{-4}$	$.858 \times 10^{-4}$
Temperature (deg.K)	4477	6971	8291
Speed of Sound (fps)	4531	6150	7651
Molecular Weight	24.30	18.63	15.05
Number Density of Species (molecules lcc)			
e^-	1.354×10^{13}	1.45×10^{15}	1.05×10^{16}
C	8.76×10^{12}	1.15×10^{17}	3.08×10^{17}
CN	4.51×10^{12}	4.14×10^{15}	2.74×10^{15}
CO	3.65×10^{17}	2.43×10^{17}	5.05×10^{16}
CO_2	1.79×10^{15}	1.74×10^{13}	1.47×10^{12}
C_2	2.35×10^{7}	1.62×10^{13}	2.51×10^{13}
N	6.31×10^{15}	3.94×10^{17}	6.67×10^{17}
NO	1.69×10^{16}	3.87×10^{15}	1.70×10^{15}
NO_2	3.00×10^{11}	7.21×10^{9}	2.22×10^{9}
N_2	3.55×10^{17}	1.62×10^{17}	3.38×10^{16}
N_2O	5.37×10^{11}	1.21×10^{11}	2.82×10^{10}
O	3.36×10^{17}	4.80×10^{17}	6.87×10^{17}
O_2	5.99×10^{15}	1.31×10^{14}	8.78×10^{15}
C^+	1.15×10^{8}	9.40×10^{14}	8.78×10^{15}
CN^+	6.01×10^{3}	6.86×10^{10}	3.66×10^{11}
CO^+	2.11×10^{10}	1.04×10^{14}	1.60×10^{14}
N^+	6.51×10^{7}	5.12×10^{13}	7.09×10^{14}
NO^+	1.35×10^{13}	2.89×10^{14}	2.63×10^{14}
N_2^+	2.69×10^{8}	5.23×10^{12}	1.35×10^{13}
O^+	7.93×10^{9}	6.08×10^{13}	5.78×10^{14}
O_2^+	1.09×10^{10}	3.22×10^{11}	8.18×10^{11}

The flow Mach number behind the shock is:

Cone Angle	Flow Mach Number Behind Shock
30°	6.9
45°	4.1
60°	2.1

The high flow Mach number behind the shock for the 60° cone indicates that on a spherically blunted 60° cone, the bow shock layer consists of mixed (subsonic-supersonic) flow. The shock angle corresponding to Mach 1 is 76 degrees, and further indicates that on the blunted 60 degree cone, the sonic line traverses the whole length of the cone and the subsonic region is quite restricted.

The species concentrations indicate that C, N, O atoms are the most populous on the 60 degree cone, C, N_2, CO, N, O on the 45 degree cone, and CO, N_2, O on the 30 degree cone.

4.2.3 Blunt Cone Analysis

Blunt body solutions for the 30 and 45 degree cones were obtained using the inverse method of Lomax and Inouye[2,3] and the method of characteristics coupled in Avco computer program 1646D.

An exact solution for the hypersonic flow field about a blunt 60 degree cone presented difficulty because of the transonic character of the flow over the entire forebody. It was necessary, therefore, to devise a semi-empirical, semi-analytical approach to the problem, taking full advantage of all existing information on this body. A pressure distribution was furnished by Mr. P.J. Bobbitt[4] of NASA/Langley for a solution at Mach 10 and constant ratio of specific heats of 1.22 (ideal gas). The shock shape was obtained from a NASA/Ames Schlieren photograph of a hypersonic flow field in a 50 percent N_2, 50 percent CO_2 atmosphere. In addition, Avco computer program 1646D was utilized to obtain streamlines in the nose cap using the proper atmospheric mixture.

Beginning with these streamlines, a simple streamtube analysis, using the continuity equation, was performed.

The forward portions of the shock shapes are shown in Figure 4.1. The stagnation point shock stand-off distance is approximately five percent of the nose radius. Also shown are the asymptotic limits for each shock shape. For the 60 degree cone, the shock angle rapidly converges to 63° with little evidence of over-expansion. This value compares well with the sharp cone value, computed as 62.74°. The 45 degree cone shock shows a more pronounced over-expansion region. The asymptotic limit of the 46.5 degrees is virtually identical to the sharp cone value of 46.55 degrees. The 30 degree cone shock exhibits somewhat unusual behavior in that a large gas cap forms forward of the over-expansion region and the limiting angle of 31.5° is relatively far from the sharp value of 30.8°. No entirely satisfactory reason for this behavior has been found; the computer program (1646D) is known to be quite accurate. It is believed that the dissociation chemistry may affect the flow in this region.

Pressure distributions for the three blunt cones are shown in Figure 4.2. Also indicated are the sharp cone levels for reference purposes, as are the mid-cone ordinates. The 45 degree and 30 degree cone pressure levels approach the sharp cone levels rather slowly, whereas the 60 degree cone distribution, which is subsonic over the entire cone, shows the expected fall to the sonic pressure level at the shoulder. The shock layer temperature profiles for the three cone mid-points and the common stagnation point are plotted in Figure 4.3.

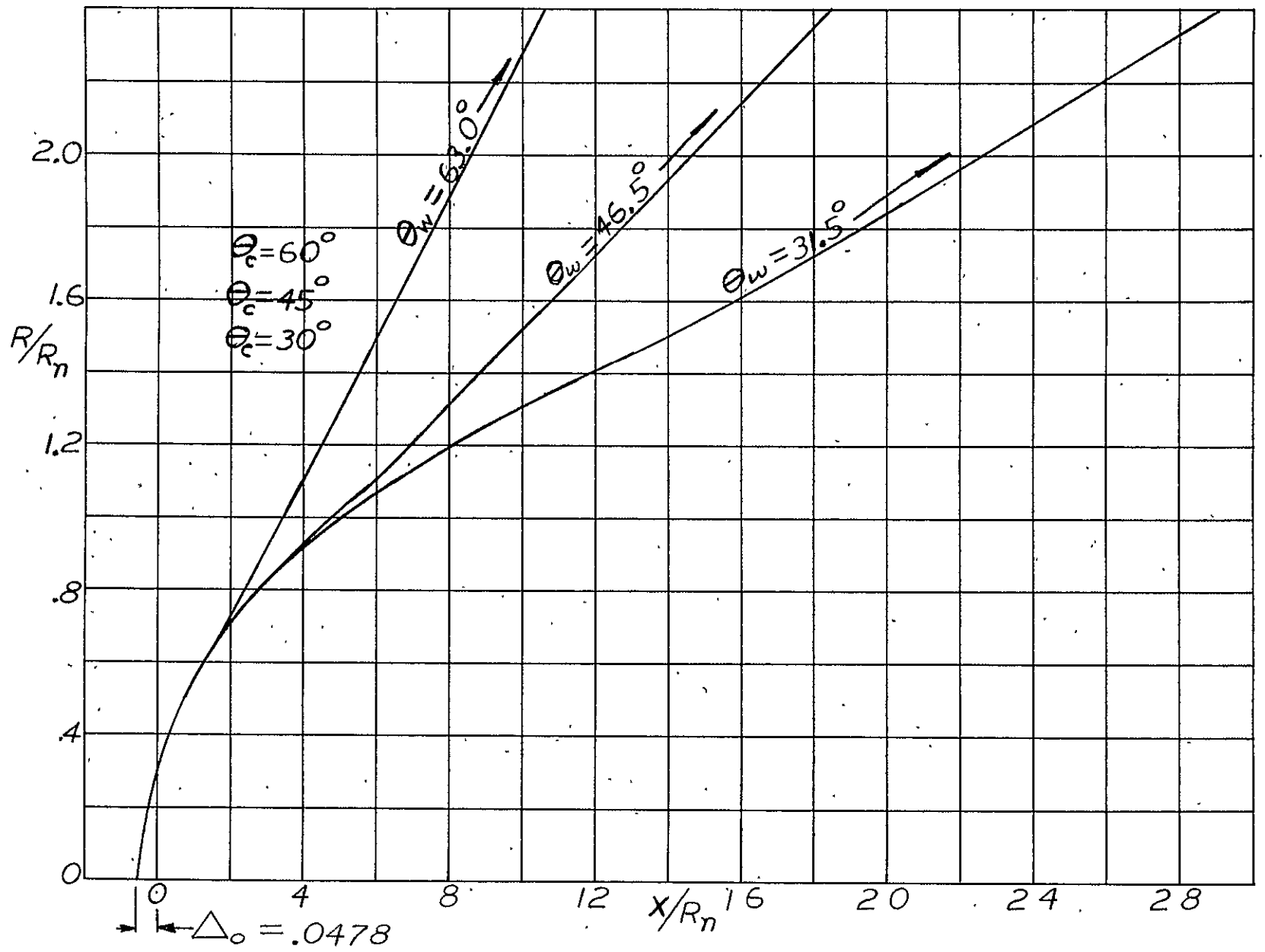


Figure 4.1 Blunt Body Shock Shapes

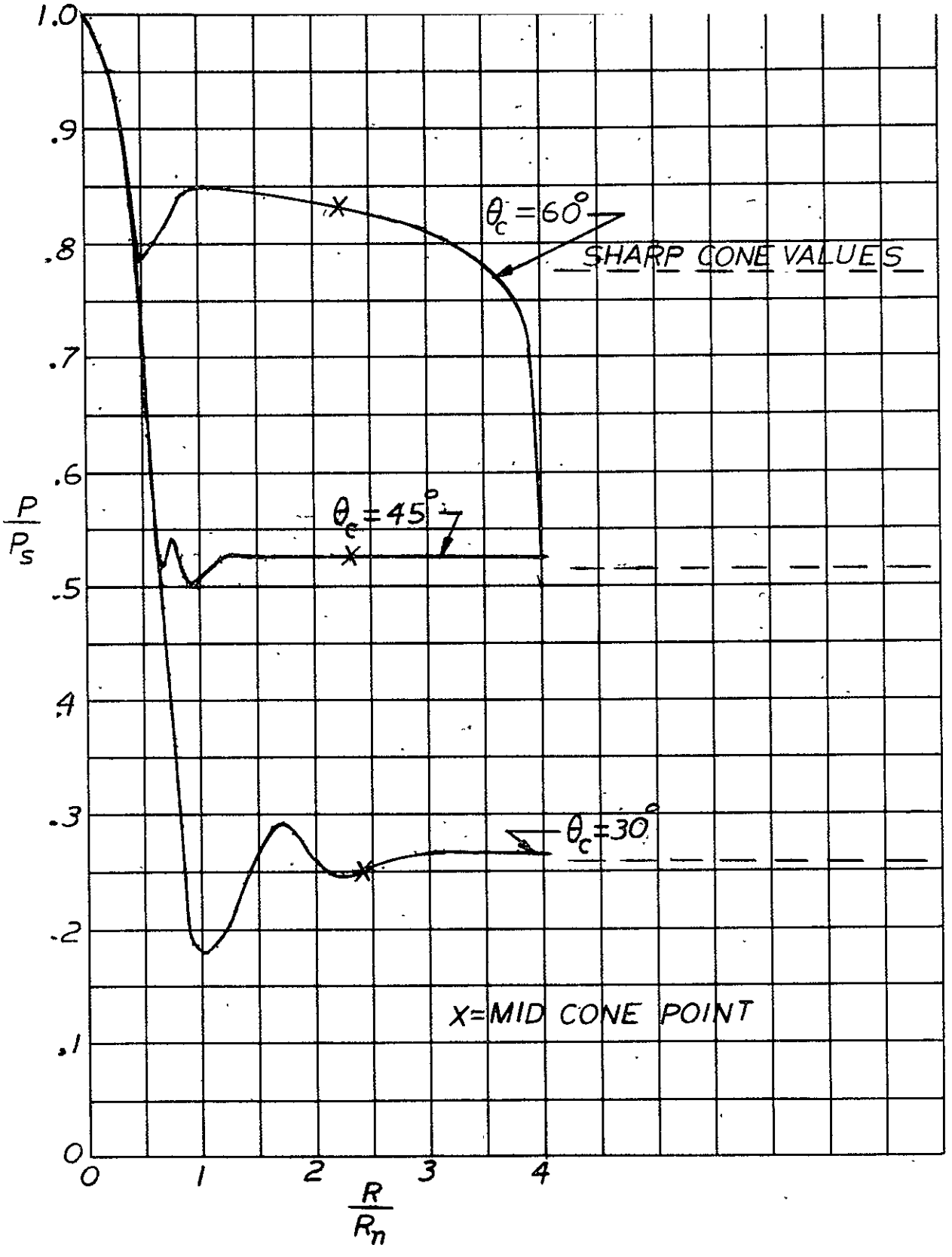


Figure 4.2 Blunt Body Pressure Distributions

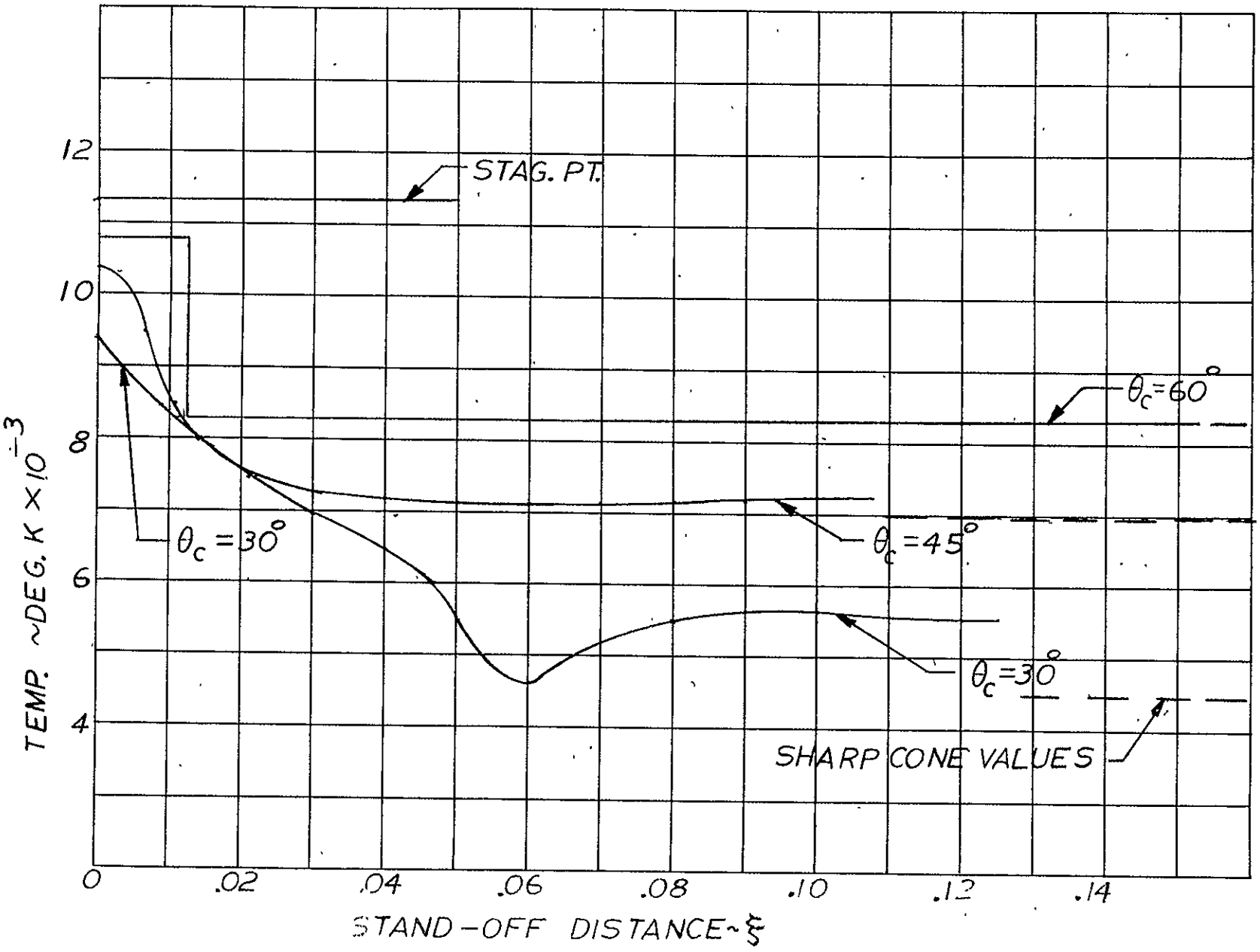


Figure 4.3 Blunt Body Temperature Profiles

Also shown are the sharp cone values. The 30 degree cone temperature profile is seen to wander due to the compression-expansion system occurring. On the 45 degree cone, the expansion system has been essentially damped out, and the high temperature region is confined to the entropy layer. A two part temperature profile is seen to be a good approximation and was assumed to synthesize the 60 degree cone flow field. The entropy layer was defined by balancing the mass flow through the nose shock with entropy layer mass flow and a uniform, high temperature layer was obtained. The outer portion of the flow was then taken as the equivalent sharp cone condition. The over-expansion region, being small in extent, was ignored. As shown, the entropy layer also effects a very small portion of the flow field, but must be considered in radiation calculations.

The thermodynamic properties at the stagnation point are shown in Figure 4.4 as a function of shock standoff distance. The parameter ξ is the ratio of distance from and normal to the body, divided by the nose radius. Pertinent stagnation point values are:

$$P_s = 5482 \text{ lbs/ft}^2 = 2.59 \text{ atm.}$$

$$\rho_s/\rho_\infty = 16.9$$

$$T_s = 11371^\circ K$$

The chemical concentrations, shown in Figure 4.5 are essentially constant across the stagnation region.

Figures 4.6 a,b and 4.7 a,b show the thermodynamic and specie profiles across the shock layer normal to the surface of the 30 degree and 45 degree blunt ($R_N/R_B = .25$) cones at the mid-cone point. The 60 degree cone flow field was divided into two temperature layers as discussed above; the resultant thermochemical data for each layer is given in Table 4.2.

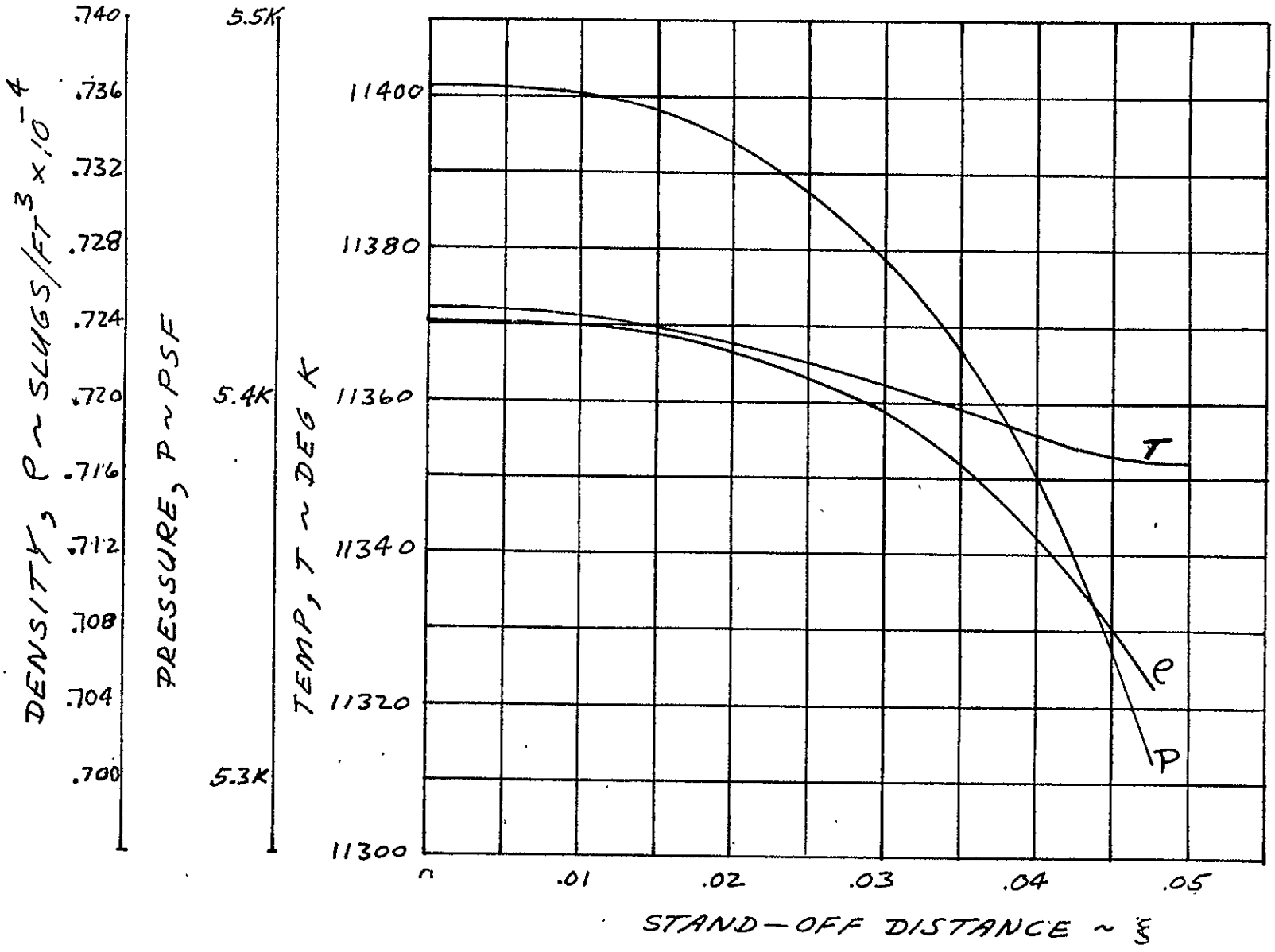


Figure 4.4 Stagnation Point Thermodynamic Properties

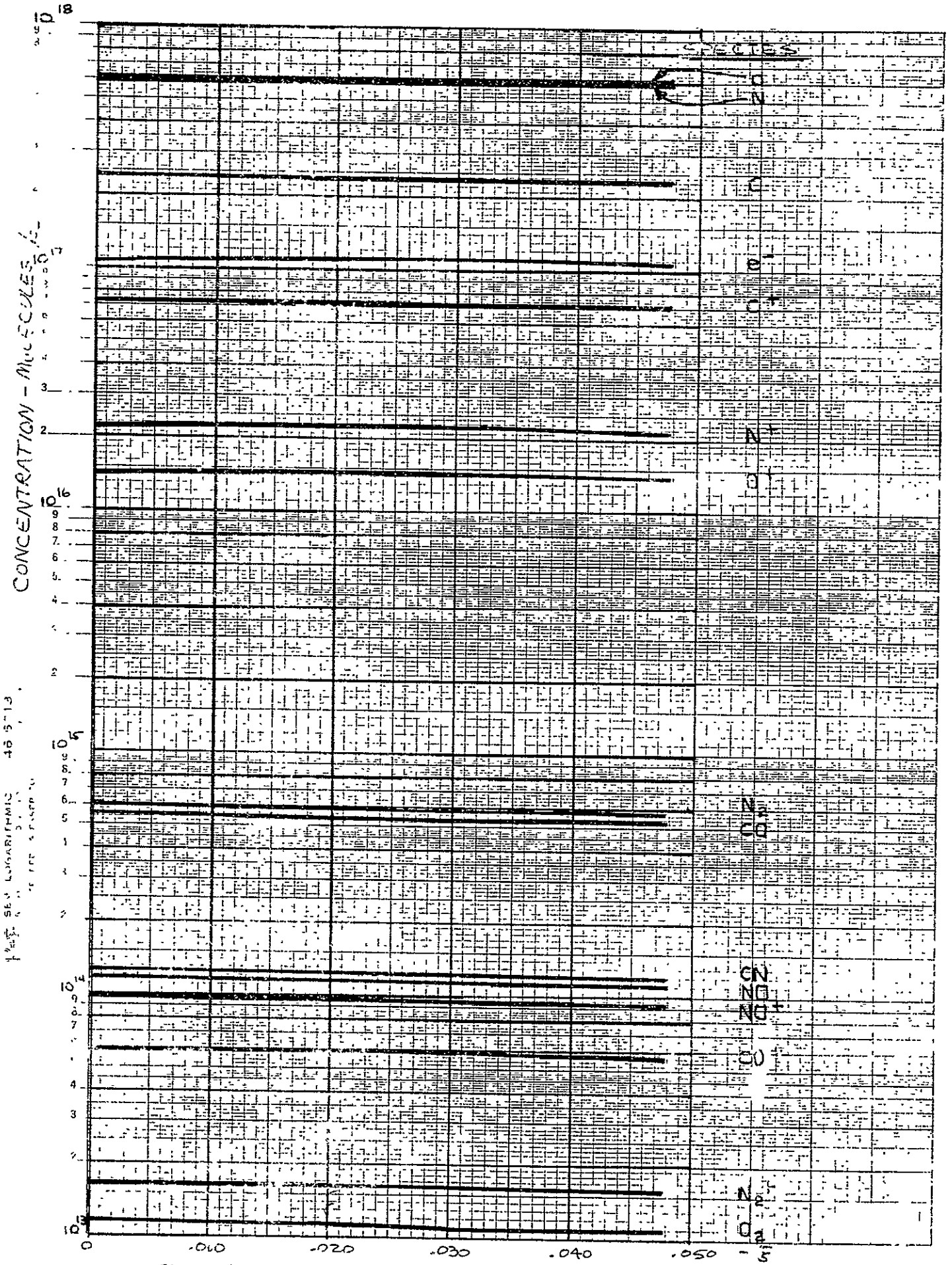


Figure 4.5 Specie Concentration Profiles at the Stagnation Point

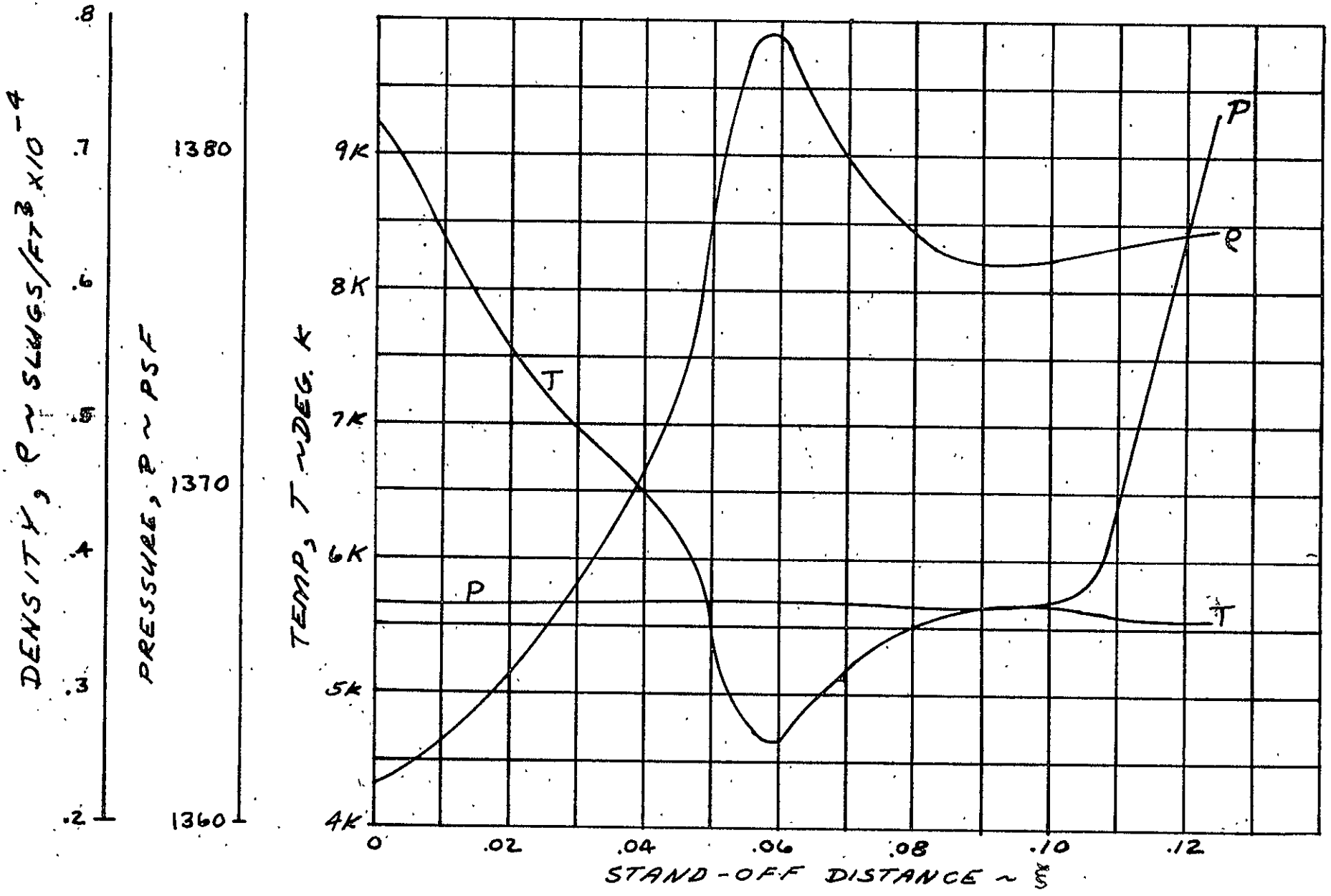


Figure 4.6a Thermodynamic Properties in the Shock Layer of a 30° Blunt Cone

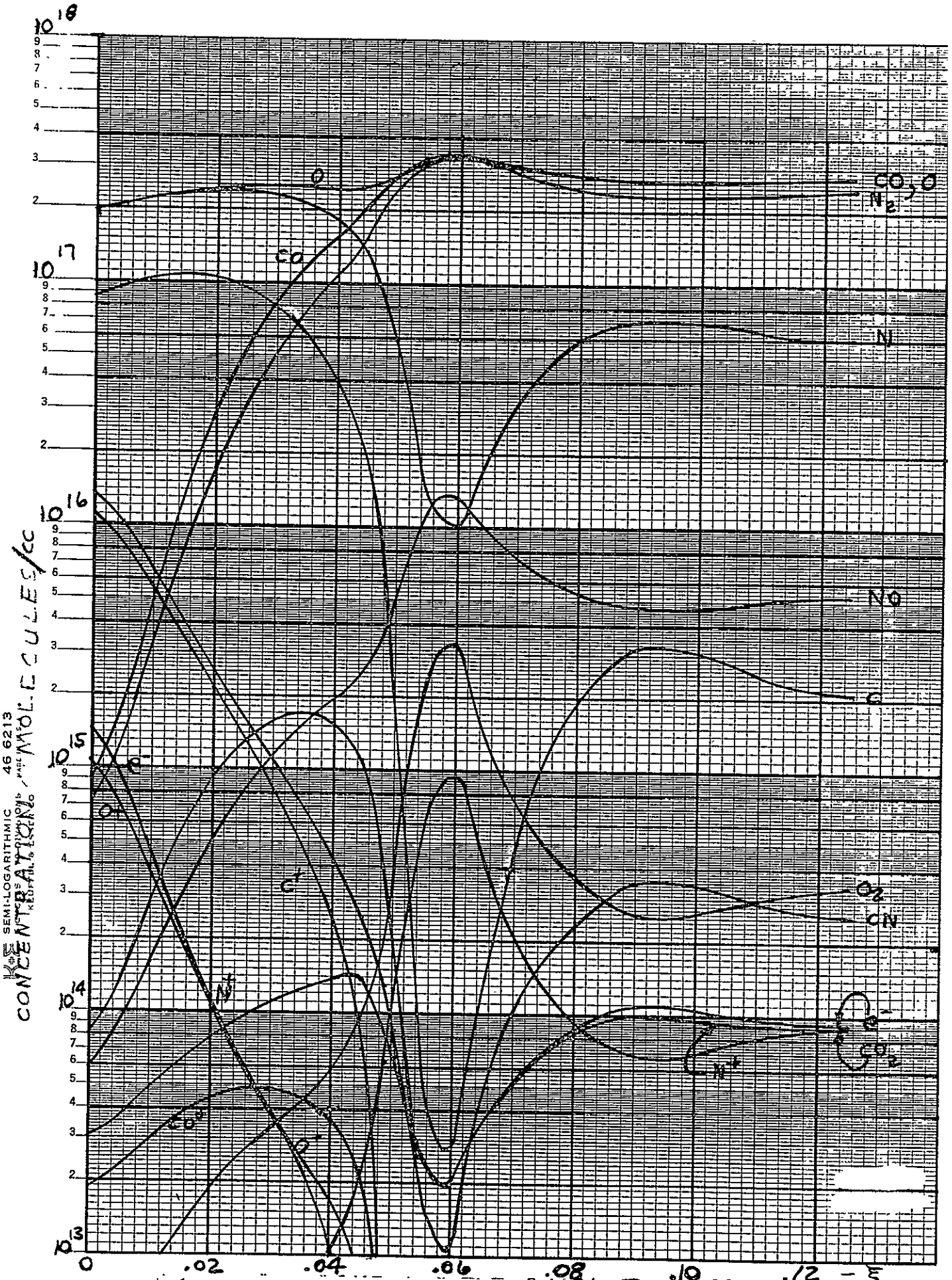


Figure 4.6b Specie Concentration Profiles in the Shock Layer of a 30° Blunt Cone

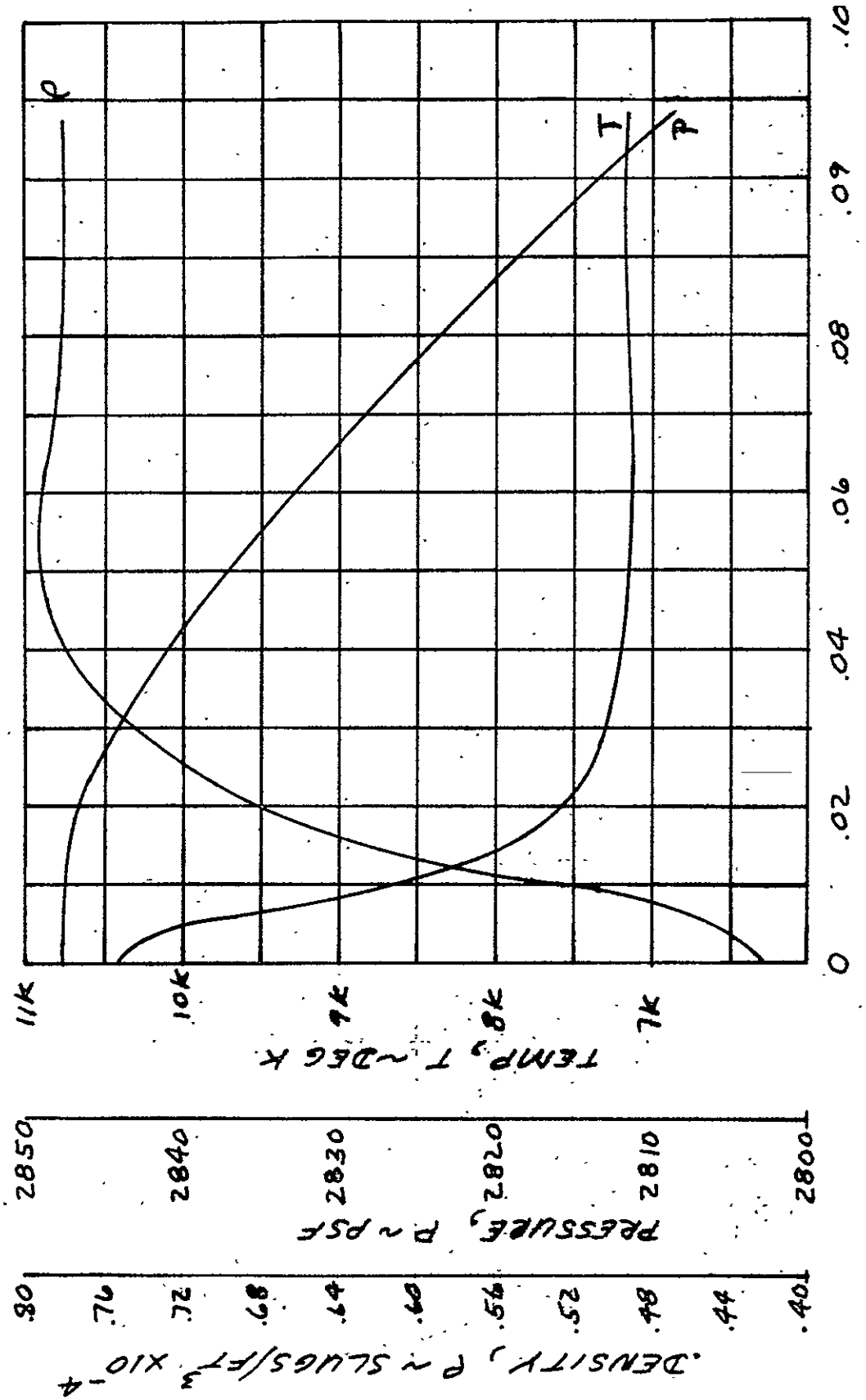


Figure 4.7a Thermodynamic Properties in the Shock Layer of a 45° Cone

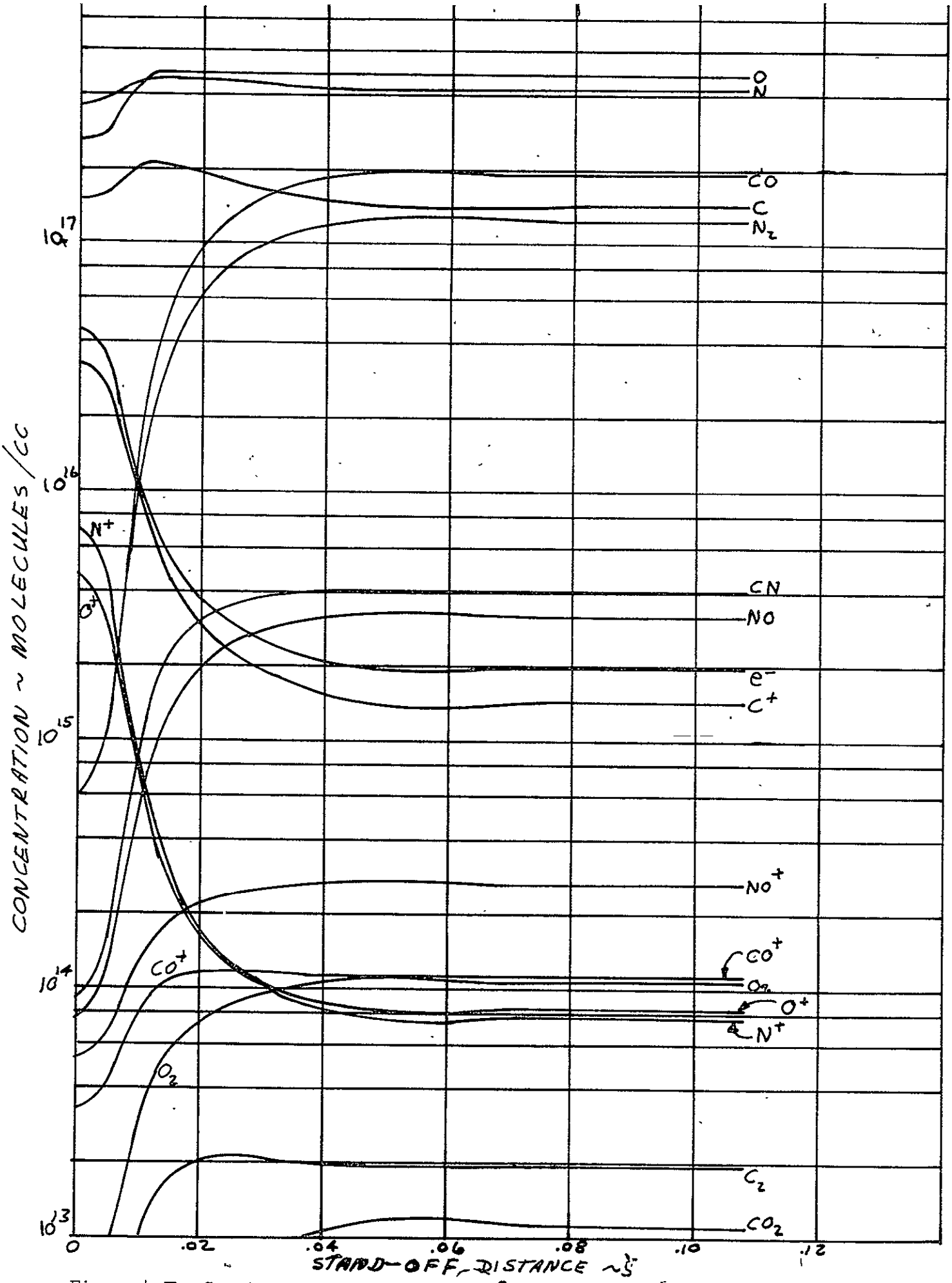


Figure 4.7b Specie Concentration Profiles in the Shock Layer of a 45° Blunt Cone

60 DEGREE CONE INVISCID SHOCK LAYER RESULTS

Table 4.2.

Distance from Body, η	$0 \leq \eta \leq .0125$	$.0125 \leq \eta \leq .153$
pressure (lb/ft^2)	4560	4241
density ($slugs/ft^3$)	$.61 \times 10^{-4}$	$.858 \times 10^{-4}$
temperature (degree K)	10,800	8291
Number density of species in molecules/cc		
e^-	7.3×10^{16}	1.05×10^{16}
C	2.3×10^{17}	3.08×10^{17}
CN	1.6×10^{14}	2.74×10^{15}
CO	8.4×10^{14}	5.05×10^{16}
CO_2	4.4×10^{9}	1.47×10^{12}
C_2	2.2×10^{12}	2.51×10^{13}
N	5.4×10^{17}	6.67×10^{17}
NO	1.4×10^{14}	1.70×10^{15}
NO_2	5.9×10^{8}	2.22×10^{9}
N_2	8.5×10^{15}	3.38×10^{16}
N_2O	4.4×10^{9}	2.82×10^{10}
O	5.5×10^{17}	6.87×10^{17}
O_2	1.8×10^{13}	7.71×10^{13}
C^+	5.2×10^{16}	8.78×10^{15}
CN+	4.6×10^{11}	3.66×10^{11}
CO+	5.7×10^{13}	1.60×10^{14}
N+	1.3×10^{16}	7.09×10^{14}
NO+	9.1×10^{13}	2.63×10^{14}
N_2^+	1.3×10^{13}	1.35×10^{13}
O+	8.4×10^{15}	5.78×10^{14}
O_2^+	1.3×10^{12}	8.18×10^{11}

4.2.4 Discussion of Flow Field Results

The blunt 60 degree cone results are felt to be of particular significance as the shock shape indicates that the sonic line traverses the whole length of the forebody. The over-expansion and subsequent recompression of the flow in the shock layer of the 60 degree cone downstream of the nose cap will cause a boundary layer disturbance locally. As the amount of subsonic flow is so small, it is not clear how the flow behaves and it is suspected that it may well be unsteady with the possibility of an imbedded transonic zone downstream of the nose cap. It is recommended that experimental testing be performed at high shock density ratios (say 20) to assess the stability of the flow.

The detailed over-expansion and recompressions downstream of the nose cap are bothersome as their effect on heating and stability is not clearly understood. An analytical study of alternative nose shapes, possibly having continuous second (or higher) order derivatives, is recommended to see if these effects can be eliminated by a modest shape change.

4.2.5 Boundary Layer Analysis

The flow field results provide adequate information to compute the boundary layer thickness, displacement thickness and laminar heat transfer distribution. Table 4.3 contains the boundary layer results, based on laminar flow and local similarity. Correlations of transport properties for the mixture of interest given by Van Tassel[5] show that they are close to air up to 8000°K.

Table 4.3

30 Degree Cone Boundary Layer Results

X/R_N	Pe/Ps	$\rho_e U_e$*	$R_{ex}(10^{-6})$	Mach	q_c/q_s	δ (in.)	Remarks
0	1.00	0	0	0.00	1	0.162	Stag PT
0.1953	0.570	0.43	0.03	1.00	0.72	0.210	Sonic PT
0.50	0.197	0.28	0.03	1.78	0.35	0.432	Tangent PT
3.22	0.250	0.32	0.15	1.64	0.22	0.69	Mid-cone
5.94	0.260	0.33	0.26	1.61	0.17	0.88	End of cone

* lbm/ft^2-sec

The local Reynolds number (R_{ex}) and boundary layer thickness (δ) are given for a 54-inch diameter body and a wall temperature of 2000°K.

In order to obtain at least a crude estimate of the rotational flow effects on the boundary layer and heating, the boundary layer edge coordinates were located within the calculated inviscid flow field and the momentum, ρu, calculated. The results are given in Table 4.4.

Table 4.4

30 Degree Cone Boundary Layer Interaction Estimates

X/R_N	$\rho u/\rho_e u_e$
0	1.0
0.1953	1.8
0.50	1.95
3.22	6.25
5.94	6.05

The results show that the local Reynolds number can be markedly higher, up to a factor of six, and the local heating can vary up to a factor of 2.5. The crude manner of estimating the interaction effects shows a potentially serious boundary layer interaction, due primarily to the high flight Mach number and low M/C_DA vehicles which lead to low Reynolds numbers. The case for the 30 degree cone is not as bad as might appear from the results above, as the selected flight conditions were for a low M/C_DA (0.6 slugs/ft^2) vehicle, whereas the 30 degree cone has M/C_DA's on the order of 2.5 slugs/ft^2 with concurrently higher Reynolds numbers by a factor of 4 and lower boundary layer thicknesses by a factor of 2, at peak heating.

The results of boundary layer analyses on the blunted 45 degree cone are shown in Table 4.5.

Table 4.5

45 Degree Cone Boundary Layer Res...

X/R_N	Pe/Ps	$\rho_e u_e$	$R_{ex}(10^{-6})$	Mach	q_c/qs	δ (in.)	Remarks
0	1.00	0	0	0.00	1	0.162	Stag Pt
0.1953	1.57	0.43	0.03	1.00	0.72	0.210	Sonic Pt
0.30	0.41	0.39	0.033	1.27	0.61	0.36	Tang Pt
1.95	0.52	0.42	0.14	1.10	0.33	0.66	Mid-cone
3.33	0.52	0.42	0.24	1.10	0.25	0.86	End of cone

Examining the flow interaction as before at the midpoint and endpoint, we find, at these two stations,

X/R_N	$\rho u/\rho_e u_e$
1.95	5.2
3.33	4.7

The 45 degree cone exhibits a considerable interaction effect on the local Reynolds number and laminar heating.

Boundary layer results for the 60 degree cone are shown in Table 4.6.

Table 4.6

60 Degree Cone Boundary Layer Results

X/R_N	Pe/Ps	$\rho_e u_e$	$R_{ex}(10^{-6})$	Mach	q_c/qs	δ (in.)	Remarks
0	1.0	0	0	0	1	0.162	Stag Pt
0.134	0.78	0.34	.019	0.62	0.81	0.166	Tan Pt
1.15	0.83	0.31	.084	0.55	0.38	0.44	Mid-Cone
2.15	0.57	0.43	.214	1.00	0.34	0.49	End of cone

The rotational flow effects for 60 degree cone were estimated by a stream tube analysis which indicates that the mid and end points correspond to streamlines entering the conical shock region, whereby we have

X/R_N	$\rho u / \rho_e u_e$
1.15	4.5
2.15	3.25

The rotational flow effects are further reduced on the 60 degree cone compared to the other two cases.

4.2.6 Discussion of Boundary Layer Study Results

It should be emphasized that the flight conditions selected correspond to a case for $M/C_DA = 0.627$ slugs/ft^2, entry angle $\gamma_E = -50^o$, entry velocity of 38,250 ft/sec, and the time of peak (radiative plus convective) heat rate. This peak rate occurs slightly before peak laminar heating.

Sizeable effects of flow interaction have been noted, affecting the local Reynolds number and the transition time, and the heat rate. Further, more refined theoretical studies considering the matching conditions at the edge of the boundary layer and supporting test studies are needed in the very high speed regime, i.e., 30,000 fps.

The effect of increased convective heat rate on the aeroshell weight will be attenuated, for the selected configurations of 45 and 60 degrees have significant radiation on the side of the cone which causes blockage of the convective heating during ablation.

The potential boundary layer interaction effects due to the small (25%) bluntness of these shapes is of concern. Increasing the bluntness as on the Minimum Probe Mission has a powerful effect on the interaction problem; it can be readily shown that the entropy gradient normal to the surface is inversely proportional to the square of the nose radius. Because of the high radiative and convective heating rates, the effects of ablation on the flow field are of concern, as the injection of ablation products into the boundary layer will perturb the flow field.

The effect of ablation is to increase the displacement thickness, as

$$\Delta^* = \delta^* + \int^x \frac{\rho_w u_w}{\rho_e u_e} \, dx$$

where

Δ^* = effective displacement thickness

δ^* = usual mass-defect thickness

$\rho_w u_w$ = injected mass flux per unit area

$\rho_e u_e$ = mass flux per unit area at edge of boundary layer

x = coordinate along streamline

The effective shape, or cone angle is then,

$$\theta_{eff} = \theta_c + \frac{d\delta^*}{dx} + \frac{\rho_w u_w}{\rho_e u_e}$$

In the case of no injection, δ^* is much less than the boundary layer thickness; local similarity solutions indicate that it is about 10 percent of the boundary layer thickness. Inspection of the boundary layer results given above indicates that $d\delta^*/dx$ is small, in the order of one degree. The effect of ablation will clearly be small for material with a high thermochemical heat of ablation such as carbonaceous materials; for example, for carbon phenolic at high enthalpy, the convective heat of ablation is approximately ηH, where η (transpiration factor) is 0.76 and ηH = 20,000 Btu/lb and the heat of vaporization is 11,400 Btu/lb so the material is effective for both the convective and radiative components. At the stagnation point the convective heat rate is 3350 Btu/ft^2-sec. The radiation heating contribution as deduced from correlation of experimental data is 1550 Btu/ft^2-sec, combined with the UV prediction of 982 Btu/ft^2-sec totals 2532 Btu/ft^2-sec. (See Section 4.2.7).

The weight loss rate at the stagnation point is estimated by

$$\rho_w u_w = \frac{q_R}{H_v} + \frac{q_c}{\eta H} \; e^{-\eta H \, q_R/H_v q_c}$$

and is 0.27 lbs/ft^2-sec, the bulk of this from radiation due to the blockage of the convective mode. On the side of the cone, the weight rate loss rate will be less, and so $\frac{\rho_w u_w}{\rho_e u_e} < .027$, which corresponds to < 1.5 degrees increase in the cone angle.

No serious flow changes are foreseeable as a result of this increase, but rather a perturbation to the drag and heating.

4.2.7 Radiation Heating Analysis

4.2.7.1 Study Objectives

The bulk of radiation experiments have been performed where the optical properties of the medium between the source and the detector, and/or the detector itself cut off all radiation below 0.2 μ. For Mars entry or entry from Earth orbit, the stagnation temperature seldom exceeds 7000°K. At 7000°K, the total blackbody radiative contribution from wavelengths less than 0.2 μ is only 100 Btu/ft^2-sec. For the present case, where the stagnation temperature is 11,370°K, the total blackbody contribution for wavelengths less than 0.2 μ has increased to a possible 10,000 Btu/ft^2-sec. As the mission studies were handicapped by lack of theoretical predictions in the UV region, emphasis was placed on this portion of the radiation heating problem. Experimental data correlations (Section 3.5.2) were used for wavelengths > 0.2 μ. Three sources of UV radiation were considered,

(1) continuum radiation resulting from flow ionization,

(2) atomic line radiation resulting from neutral and ionized atoms, and

(3) molecular bands, especially CO (4+).

4.2.7.2 Continuum Radiation

Definition of the continuum radiation at the stagnation

point was based upon the thermodynamic and thermochemical data cited above. Only the four most populous species were considered, these being the carbon atom and ion, and atomic nitrogen and oxygen. Since the overall object of the study was to determine the UV radiant intensity, it was hypothesized that consideration of the four species listed would define whether (a) both continuum and line spectral emissions would require consideration, or (b) the continuum radiation would be sufficiently close to blackbody over a portion of the spectrum that line considerations could be narrowed to a lesser range.

The absorption coefficient was obtained from the product of the species number density and its photo-ionization cross section,

$$\mu = N\sigma$$

The cross-section values were obtained from Wilson and Nicolet.[9]

Absorption coefficients for C, N, O, and C^+ are presented in Figure 4.8 over the range of interest. These values of μ result in the intensity values of Figure 4.9, using a shock stand-off distance, Δ, of .82 cm. Blackbody radiation is also shown in the latter figure. The proximity of the carbon continuum to blackbody radiation below .11 microns insures the validity of the blackbody assumption for these wavelengths. For $.11\ \mu < \lambda < .2\ \mu$, the total radiation from the species considered is closely approximated by the carbon system. Since these values fall far below the blackbody radiation, the contributions of the strongest lines must be considered.

4.2.7.3 Line Radiation

Only the most populous four species were investigated, the atomic forms of carbon, oxygen and nitrogen, and the singly ionized carbon atom. Briefly, the analysis is carried out for an infinite slab of radiating

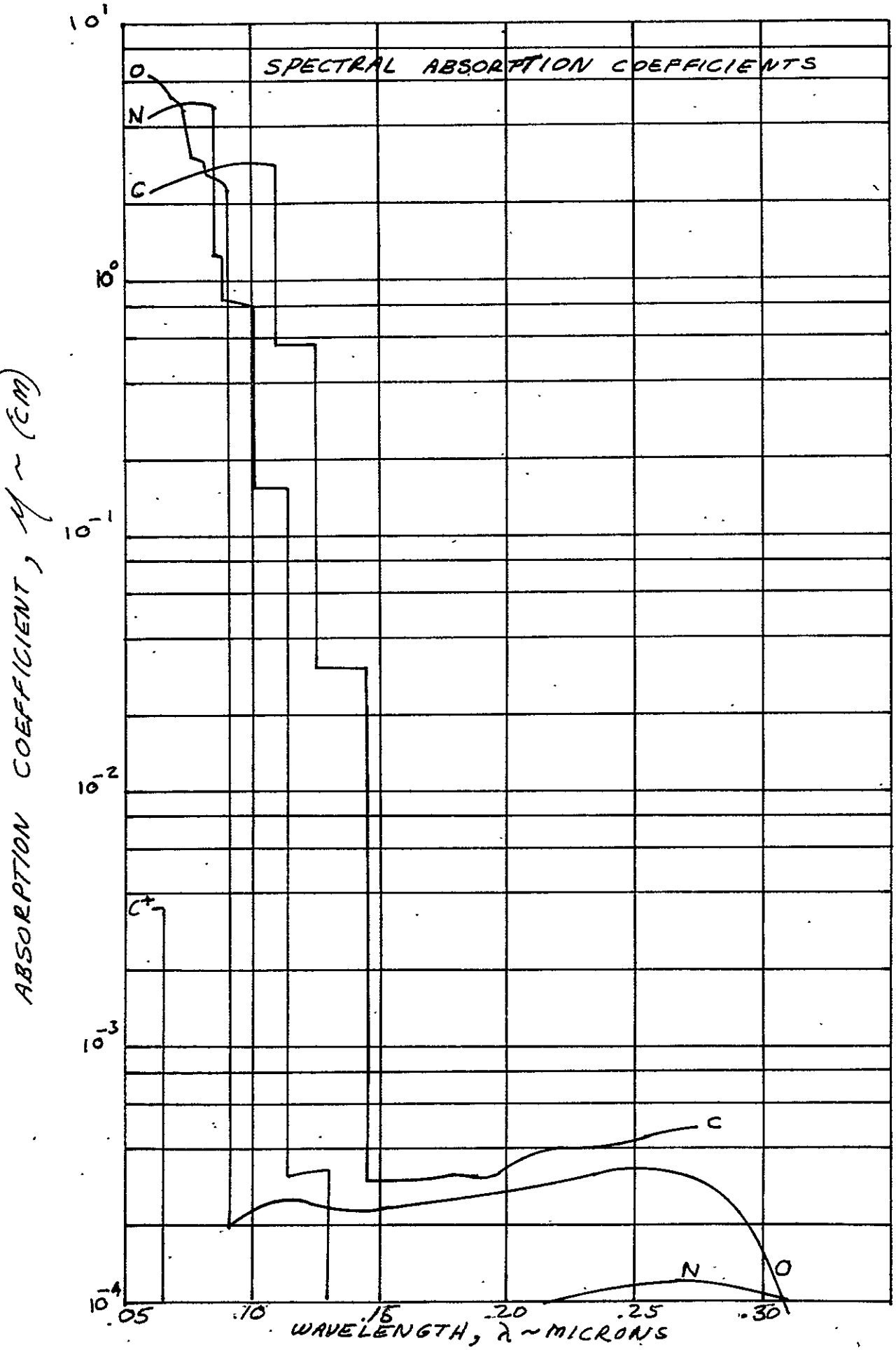


Figure 4.8 Continuum Spectral Absorption Coefficients in the UV Region

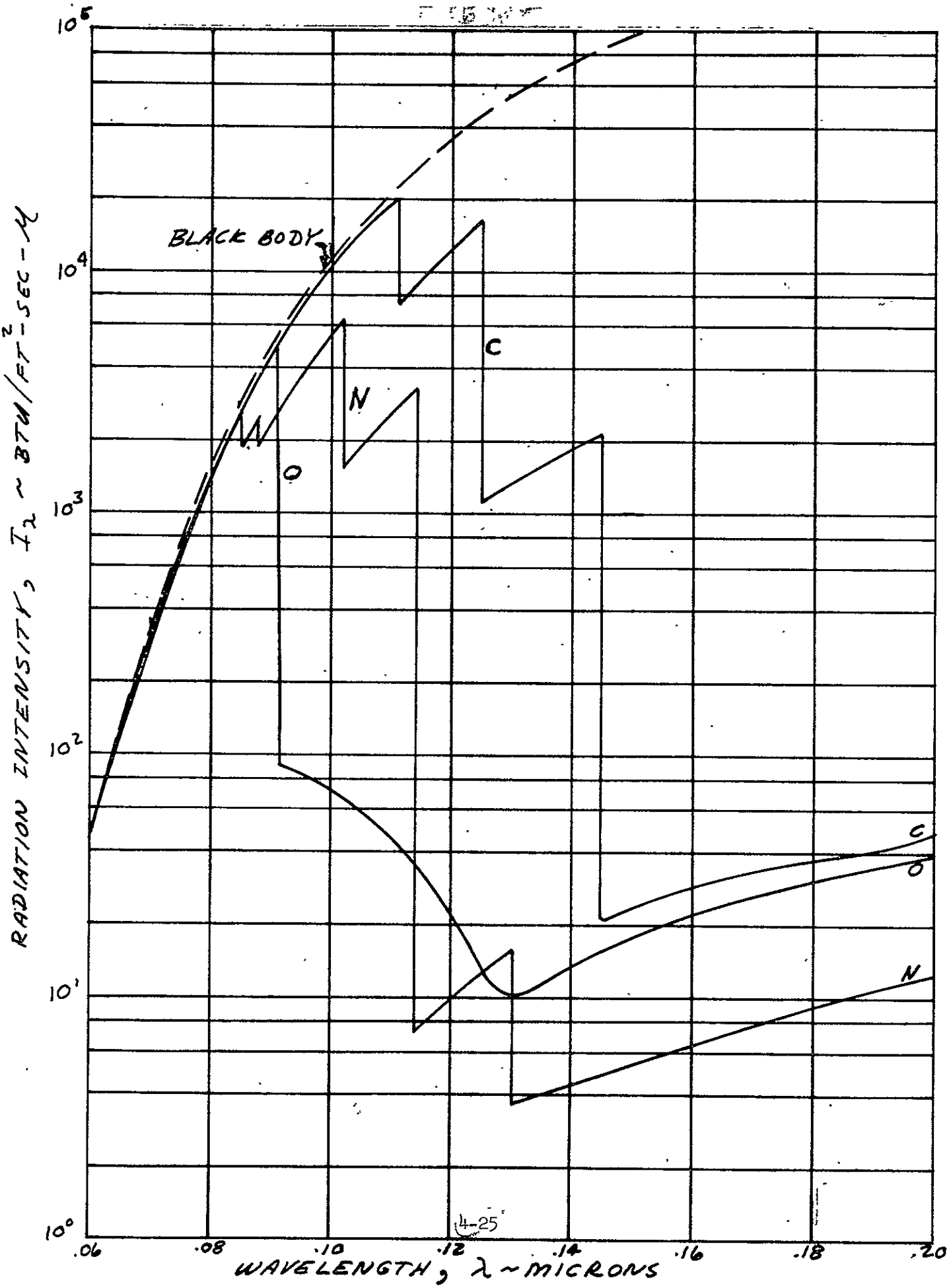


Figure 4.9 Continuum Radiation Intensity in the UV Region

gas, .82 cm thick, at a temperature of 11,400°K. The species concentrations are listed below:

Species	Concentration (particles/cc)
C	2.4×10^{17}
N	5.9×10^{17}
O	6.2×10^{17}
C^+	7.2×10^{16}
e^-	1.1×10^{17}

Since it is desirable to be able to predict the UV contribution (below 2000 Angstrom units) to the radiation heating by some simple means, and since the blackbody expression provides an ideal method for so doing, it is pertinent to inquire how closely blackbody radiation approximates the actual total radiation from the continuum and line spectra of the various constituents of the gas.

As shown above, continuum radiation dominates the ultra-violet spectrum in the wavelength range between 0 and 1100 Å. At the latter point the continuum radiation from the carbon neutral atom decreases sharply. At 1250 Å, the second carbon cut-off occurs, and the total continuum intensity drops by an order of magnitude. Below 1100 Å, the continuum radiation of all species is sufficiently close to the blackbody limit that the simple blackbody expression may be used to predict radiant heat transfer. Between 1100 Å and 2000 Å it is therefore necessary to consider the line contributions of the various species.

The total energy radiated by a line from optically thick plasmas depends strongly upon line shape. As the shape is of considerable importance in radiant transfer problems, a computer program has been generated to handle this transfer.

Avco has programmed for solution on an IBM 7094 computer expressions which describe the Stark broadening of isolated lines of neutral and singly ionized atoms (i.e., lines from levels where components with different orbital momenta are well separated) in terms of their intensities and absorption coefficients. Pressure broadening, which is much less important for conditions of interest is ignored. The model for collisional dominated conditions is based on line profiles which include the more important interactions (as those between radiating systems and plasma ions or electrons) and include effects caused by the presence of electric fields. The expressions utilized in the program are given below.

4.2.7.3.1 Line Profile

With the quasi-static approximation for ions, the line profile for Stark broadening is given as:*

$$L(\lambda,T) = \frac{1}{\pi W_{\frac{1}{2}\frac{1}{2}}} \int_0^\infty \frac{d\beta\, W(\beta)}{1+(x-\alpha^{4/3}\beta^2)^2} \qquad (1)$$

where $W_{\frac{1}{2}\frac{1}{2}}(T)$ is the electron impact half (half) width; $W(\beta,T)$ is the ion field strength distribution function at neutral points or singly charged ions; β is the ratio of the electric field strength produced by the perturbing ions to the normal field strength for singly charged ions; $\alpha(T)$ is an ion broadening parameter; and x is defined as:

$$x = \frac{(\lambda - \lambda_0 - d)}{W_{\frac{1}{2}\frac{1}{2}}} \qquad (2)$$

*Details can be found in "Plasma Spectroscopy," by H.R. Griem, McGraw-Hill, 1964.

where $d(T)$ is the electron-impact shift and λ_o is the wavelength of the line in question.

4.2.7.3.2 Emission Coefficient

The emission of a bound-bound transition in an optically thin gas is in terms of power per unit volume solid angle and wavelength interval:

$$\epsilon(\lambda, T) = \frac{hc}{2\pi\lambda} A N_u L(\lambda, T) \qquad (3)$$

where $L(\lambda, T)$ is the line profile, A is the transition probability for spontaneous emission and N_u is the density of atoms or ions in the upper state of the line. Assuming LTE, the upper density term may be related to the total density 'N' of atoms or ions by employing the proper Boltzmann factor. In addition, the spontaneous emission transition probability may be expressed in terms of the absorption oscillator strength 'f'. With these substitutions, equation (3) can be rewritten as:

$$\epsilon(\lambda, T) = \frac{2\pi r_o h c^2}{\lambda^3} f g_L \frac{N(T)}{U(T)} L(\lambda, T) \exp\left(\frac{-E_u}{kT}\right) \qquad (4)$$

where the constants k, r_o, h and c have their usual meaning; N(T) is the total number density; f is the absorption oscillator strength; g_L is the statistical weight of the lower state of the line; U(T) is the internal partition function of the atoms or ions; E_u is the excitation energy of the upper state of the line; and T is the absolute temperature.

4.2.7.3.3 Absorption Coefficients

The effective absorption coefficient, i.e., the difference between true absorption and induced emission coefficients in a spectral line is:

$$K' = \sigma^a N_L - \sigma^i N_u \qquad (5)$$

where N_L and N_u are respectively the number densities of the lower and upper states of the line, and σ^a and σ^i are respectively the absorption and induced

emission cross sections. In LTE, it can be shown that

$$K' = \epsilon / I_T \qquad (6)$$

where ϵ is the emission coefficient and I_T is the familiar Planck's blackbody function. Hence, for collision-dominated plasmas in LTE:

$$K' = \pi r_0 \lambda^2 g_L f \frac{N(T)}{U(T)} L(\lambda, T) \exp\left(-\frac{E_u}{KT}\right)\left[\exp\left(\frac{hc}{K\lambda T}\right) - 1\right] \qquad (7)$$

4.2.7.3.4 Total Emission and/or Effective Absorption Coefficients

The above mentioned computer problem has been programmed to read from tape the free-free, free-bound results of a continuum program. This previous program has been modified slightly to yield continuum absorption as well as the continuum emission coefficients as a function of wavelength. The present line program is capable of superimposing its results onto the continuum and thus provides a spectrum of total emission and/or absorption coefficients.

This program was used to compute the line contributions of carbon neutral, which is the greatest source of line radiation in the wavelength range $1100 \leq \lambda \leq 2000$ Å. The required data for the lines and multiplets was obtained from references 6 and 7. Only the strongest contributors, as set forth in the NBS report, were considered. Of the oxygen lines, only the 1305 Å multiplet system was investigated. The carbon ion radiation, amounting to only one multiplet around 1335 Å, was not investigated.

Although theoretical solutions provide a convenient means of determining the unknown spectral intensities, no theory has been sufficiently adequate to duplicate experimental results in every case. It is therefore worthwhile to rely as much as possible on test data. Fortunately, a considerable effort has been expended by J. Morris and R. Krey of Avco in determining the spectral intensities of atomic nitrogen. Their experimental values[8,9] of normal emissivity have been used exclusively herein in calculating the strong nitrogen neutral lines.

The contributions of the individual line systems to the radiation heating are shown in Table 4.7. Carbon is seen to produce approximately 70 percent of the radiation. The total contribution of the line systems to the radiant heat transfer is 853.3 Btu/ft^2-sec, in the UV wavelength range from 1100 Å to 2000 Å. From the previous section which presents the continuum radiation, the contribution of the continuum radiation between zero and 1100 Å is 110.5 Btu/ft^2-sec. The total radiation in the UV range is, therefore, 963.8 Btu/ft^2-sec. Total blackbody radiation for this range of wavelengths is on the order of 10^4 Btu/ft^2-sec, and this assumption is, therefore, not adequate for predicting radiant heat transfer in planetary atmospheres.

The mission parametric analysis assumes a fraction of blackbody radiation, specifically, the portion below 1440 Å, for the UV contribution. For this particular temperature, this value is 2000 Btu/ft^2-sec or a factor of two larger than the theoretical estimate.

The spectral radiation intensity profile in the UV region is shown in Figure 4.10. A sample line profile is shown in Figure 4.11, for an oxygen multiplet.

4.2.7.4 CO (4+) Radiation

Three methods for evaluation of the CO (4+) radiation were investigated. The first two give values of total radiation intensity. The third includes the effects of self-absorption with a fairly simple mathematical calculation procedure.

The K-B-F Method: This method was first proposed by Kivel and Bailey in 1957.[10] It was later modified by Flinn[11] for the particular band system of interest. The emissivity per unit thickness is expressed as

$$\frac{\epsilon}{L} = \frac{C_i N_i e^{-T_i/T}}{5.4 \times 10^{19}} \left(\frac{T}{10^4}\right)^{-n_i} \qquad (8)$$

Table 4.7

LINE AND MULTIPLET RADIATION HEATING

Wavelength (Å)	J	f	Upper Energy (eV)	Half-Half Width (Å)	Heating Increment (BTU/ft^2-sec)
SPECIES: CARBON NEUTRAL CI					
1260.75	0.0	.02	9.836	.001946	
1260.90	0.0	.066	9.836		
1260.96	1.0	.064	9.836		
1261.12	2.0	.086	9.835		
1261.40	1.0	.011	9.836		
1261.56	2.0	.026	9.835		41.7
1277.15	1.0	.078	9.709	.001616	
1277.27	2.0	.058	9.710		
1277.40	1.0	.02	9.709		
1277.62	3.0	.063	9.711		
1277.77	2.0	.012	9.710		
1277.80	1.0	.00075	9.709		45.5
1328.88	1.0	.208	9.332	.0000475	
1329.10	1.0	.053	9.332		
1329.10	0.0	.0696	9.332		
1329.10	2.0	.0857	9.332		
1329.58	2.0	.155	9.332		
1329.58	1.0	.0513	9.332		19.8
1459.05	1.0	.000746	9.762	.00235	2.5
1463.33	3.0	.0625	9.738	.002241	37.0
1470.20	3.0	.0142	9.699	.00454	25.6
1481.77	2.0	.011	9.632	.001998	13.3
1560.31	1.0	.283	7.947	.0002232	
1560.70	2.0	.20	7.948		
1560.70	1.0	.071	7.948		
1561.29	2.0	.043	7.948		
1561.30	1.0	.0028	7.947		
1561.40	3.0	.24	7.947		92.0
1656.26	2.0	.08	7.489	.001005	
1656.92	1.0	.026	7.484		
1657.0	2.0	.027	7.489		
1657.37	1.0	.035	7.484		
1657.89	0.0	.045	7.481		
1658.11	1.0	.105	7.484		142.8
1751.90	1.0	.0748	7.686	.00338	91.0
1764.0	1.0	.0031	9.714	.006553	7.5
1765.0	1.0	.0141	9.709	.006553	19.6
1930.93	1.0	.0729	7.686	.00176	63.0

TOTAL CARBON CONTRIBUTION = 601.3 BTU/ft^2-sec.

Table 4.7 continued

Wavelength (Å)	J	f	Upper Energy (eV)	Half-Half Width (Å)	Heating Increment (BTU/ft^2-sec)
SPECIES: OXYGEN NEUTRAL, OI					
1302.17	1.0	.031	9.51855	.000394	
1304.87	1.0	.032	9.51855		
1306.04	1.0	.031	9.51855		49.7

TOTAL OXYGEN CONTRIBUTION = 49.7 BTU/ft^2-sec.

SPECIES: NITROGEN NEUTRAL, NI

Wavelength (Å)	Emissivity @ 13200°K	Emissivity @ 11,400°K	Heating Increment (BTU/ft^2-sec)
1134	.39	.28	6.0
1143	.185	.15	3.4
1163	.28	.2	5.0
1168	1.0	1.0	25.6
1176	.465	.35	9.4
1200	1.0	1.0	30.2
1243	.51	.36	13.2
1310	.142	.11	5.2
1319	.75	.51	24.8
1411	.058	.04	2.6
1492	-	.485	38.3
1742	-	.23	38.6

(Nitrogen Data at $5x10^{17}$ Atoms/cm^2)

TOTAL NITROGEN CONTRIBUTION = 202.3 BTU/ft^2-sec.

TOTAL LINE RADIATION = 853.3 BTU/ft^2-sec.

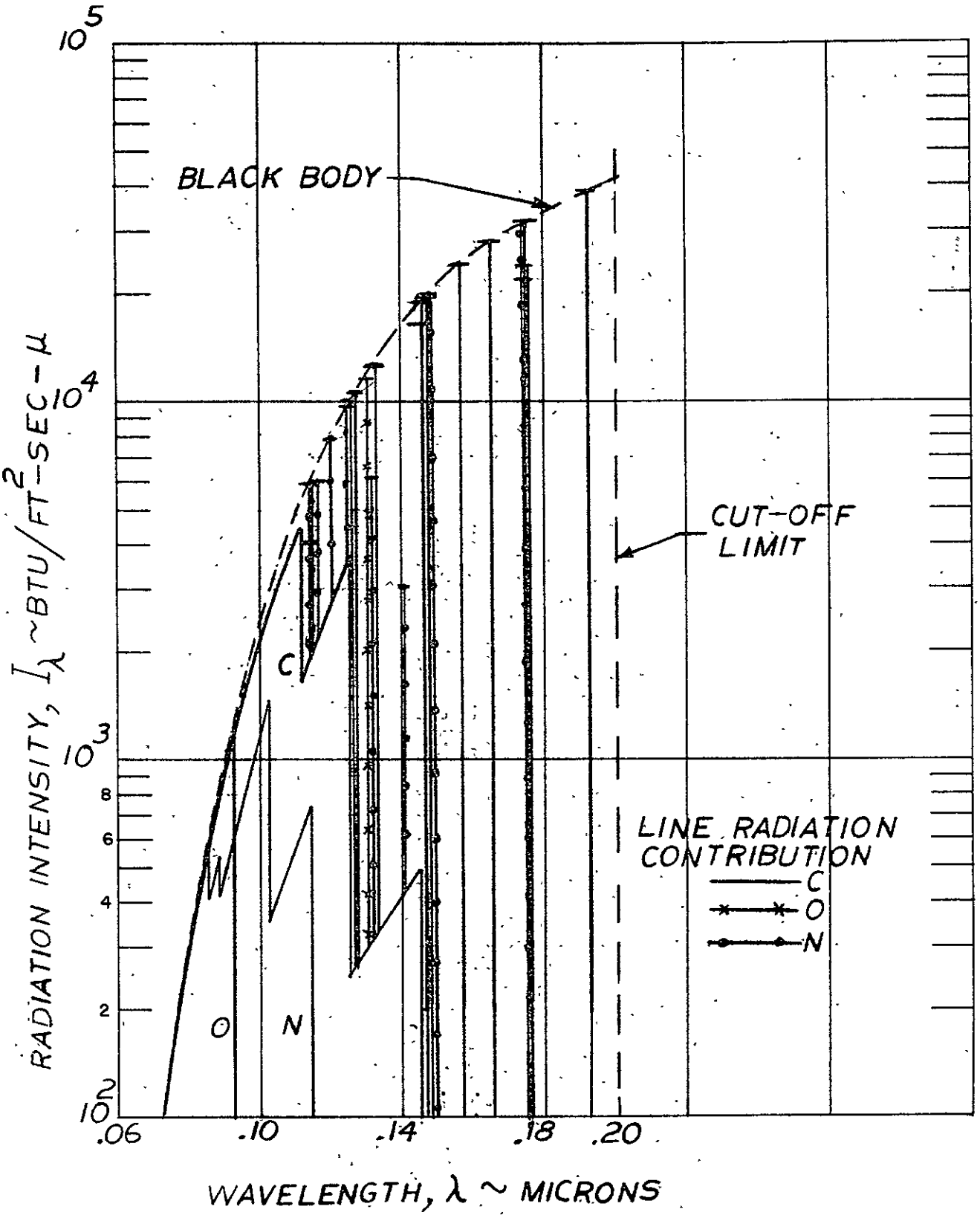


Figure 4.10 Line and Continuum Spectral Radiation Intensity

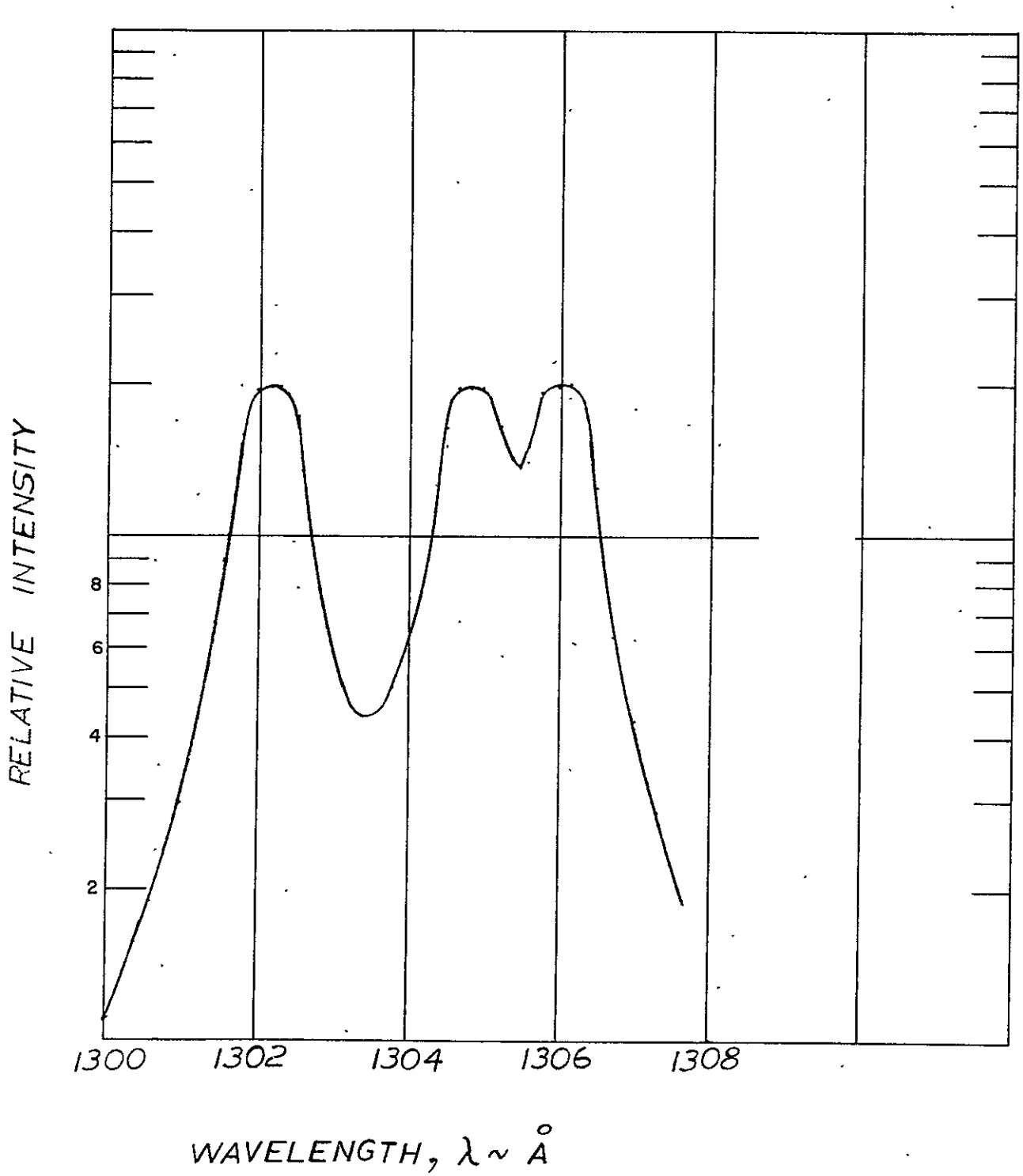


Figure 4.11 Oxygen Multiplet Distribution

where

N_i = species concentration (molecules/cc)

T = gas temperature (^oK)

C_i, n_i = empirical constants from experiment

T_i = energy of emitting state, ^oK.

For CO (4+), Flinn gives these values as

$C_i = 2.27 \times 10^5$

$T_i = 93{,}000^oK$

$n_i = 4$

The oscillator strength (f-number) implied by the above value of C_i is .01. In this study, a value of .15 has been used for f since it is now generally popular in the literature. It is noted, however, that Wentink[12], et al have reported f = .19, for the ground state.

By dividing both sides of the above equation by the moledular concentration of CO, an expression for specific emissivity results which is purely a function of temperature. The specific emissivity is plotted in Figure 4.12. Thus, knowing the molecular concentration, temperature, and gas layer thickness (in centimeters), the total CO (4+) radiation intensity may be calculated (based on an optically thin layer).

Such a development ostensibly omits self-absorption. However, the constants involved are derived from test data, and may include this effect to some extent.

(MOT) Curve-Fit Method: The second method is based on the curves presented by Myer, Ohrenberger, and Thompson (MOT)[13]. CO molecule concentrations given in Reference 13, were used to effectively universalize the radiation intensity results in terms of composition and collapse them to the envelope presented in

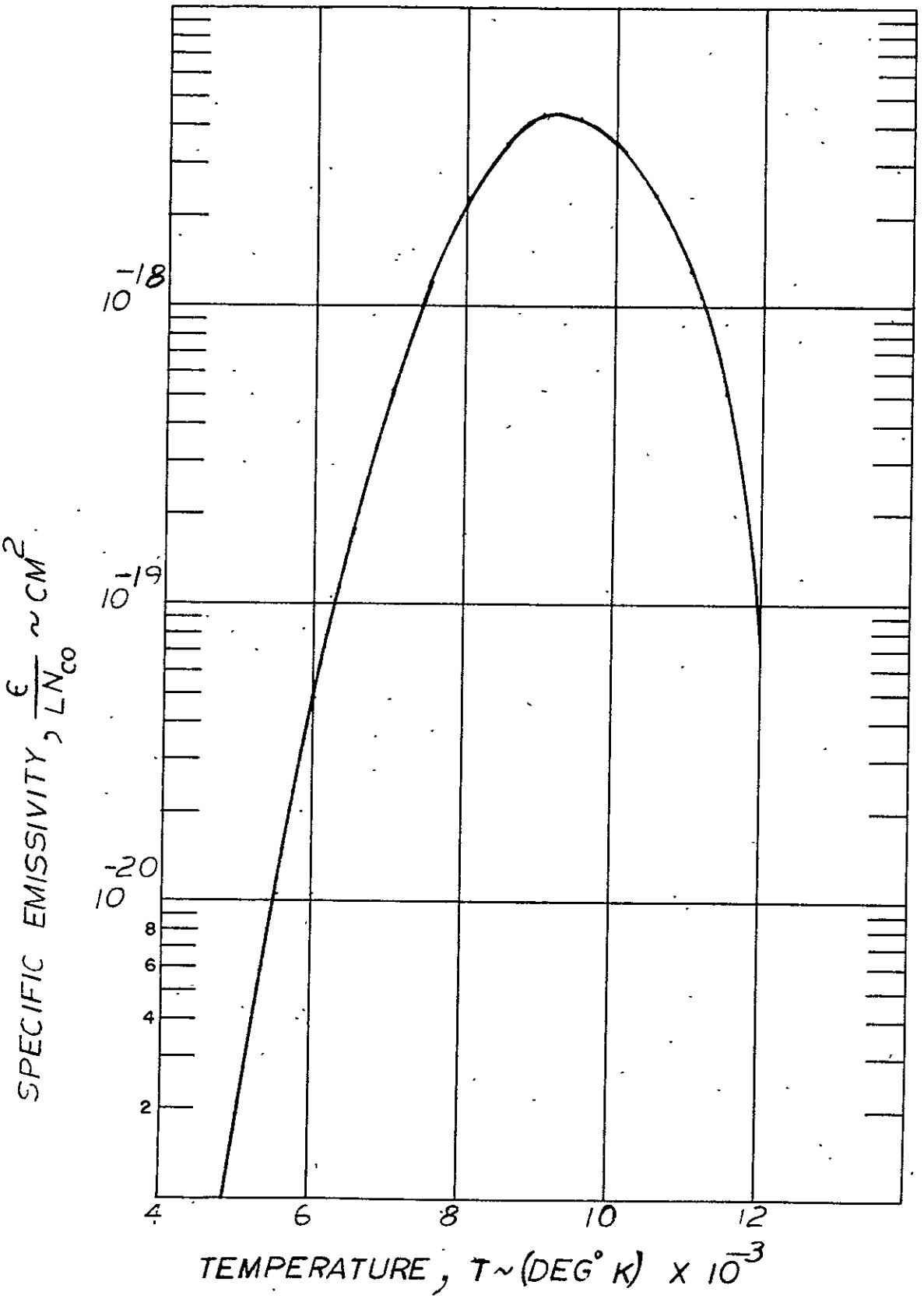


Figure 4.12 CO (4+) Emissivity - KBF Results

Figure 4.13. The effects of self-absorption, given in charts[13] for an 85% N_2--15% CO_2 mixture indicate that because of the high velocity at the flight condition studied, the self-absorption is negligible; however, at lower speeds (lower temperatures) self-absorption is important.

Hoshizaki and Wilson: Hoshizaki and Wilson[14] present an expression for obtaining the absorption coefficient:

$$\mu_\lambda = 6.67 \times 10^{-16} \, f \, N_{CO} \exp\left(-\left|\frac{1.243 \times 10^{-4}}{\lambda} - 8.25\right|^2\right) \qquad (9)$$

where λ is the wavelength in centimeters. Figure 4.14 shows a plot of μ_λ versus λ for the vehicle stagnation point conditions. The intensity at any wavelength is computed from

$$I_\lambda = I_{B\lambda}\left(1 - e^{-2\mu_\lambda L}\right) \qquad (10)$$

where $I_{B\lambda}$ is the blackbody value. A comparison of the parabola with that presented in Reference 13 shows very good agreement for f = .15. Each of the three methods were applied to the stagnation point of the vehicle, assuming an infinite slab of radiating gas, equal in thickness to the standoff distance (.82 cm). The resultant values of radiation heat transfer to the stagnation point were as follows:

Kivel and Bailey/Flinn - q_R = 27.2 Btu/ft^2-sec

Myer/Ohrenberger/Thompson - q_R = 29.6 Btu/ft^2-sec (absorption neglected)

Hoshizaki and Wilson - q_R = 37.0 Btu/ft^2-sec

The agreement between the K-B-F and the M-O-T values is striking. However, at other conditions the two do not agree within 50 percent. The CO (4+) UV radiation is insignificant for the stagnation point, at the high temperatures (1100°K); at lower temperatures (~7000°K) the carbon monoxide molecule constitutes a large fraction of the gaseous system and will produce a considerable amount of radiation.

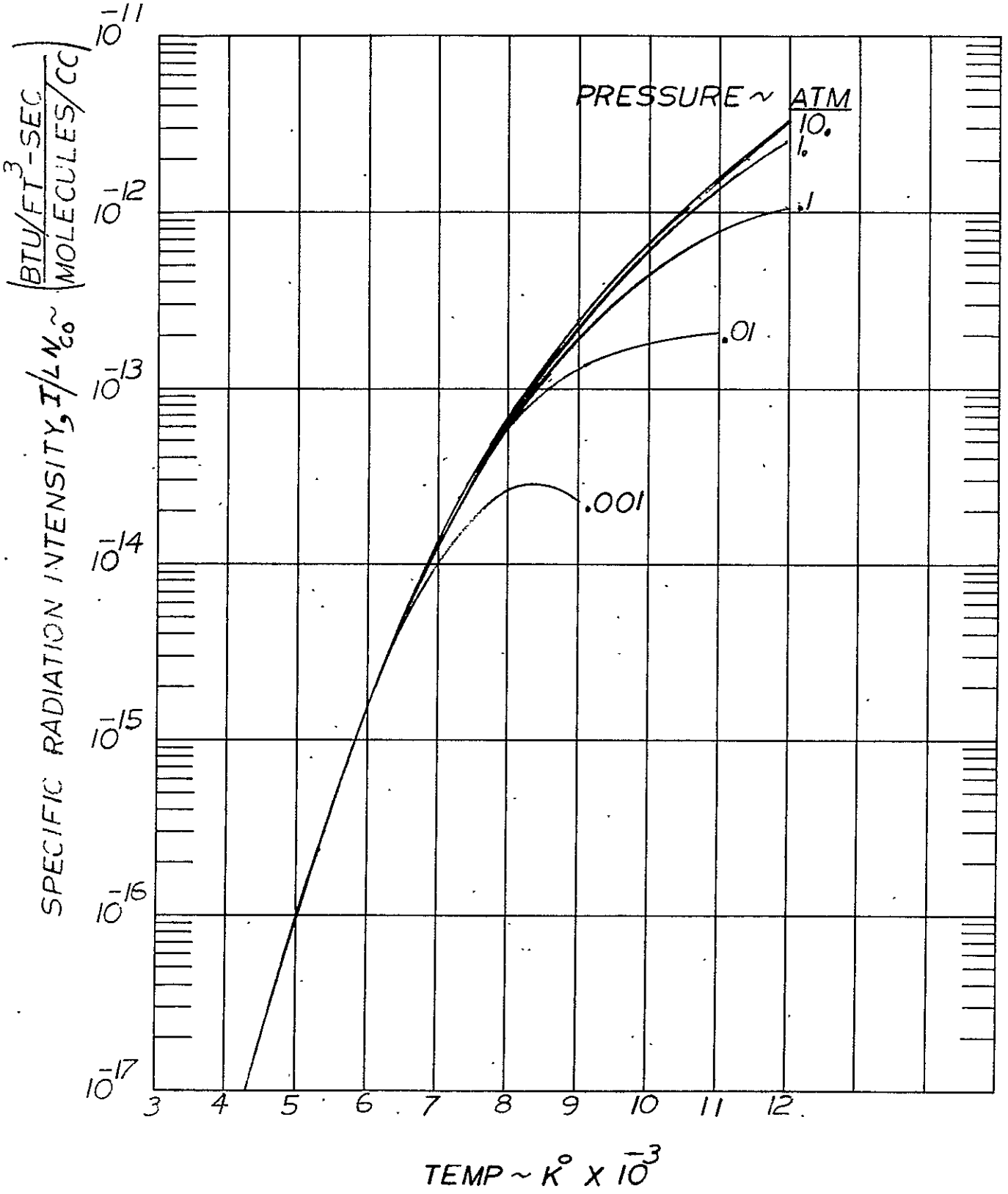


Figure 4.13 CO(4+) Intensity - MOT Results

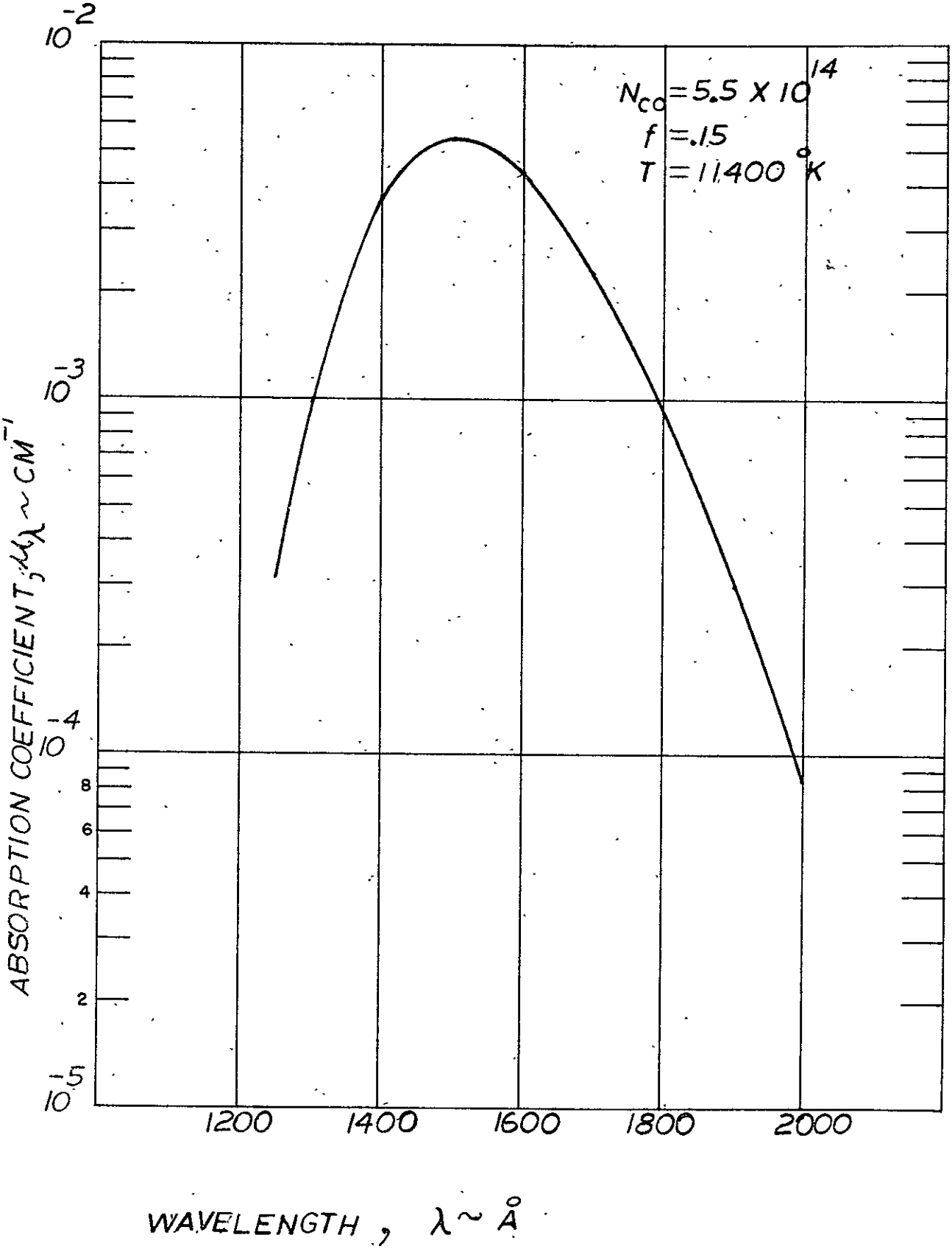


Figure 4.14 CO(4+) Spectral Absorption Coefficient - HW Results

4.2.7.5 Other Considerations

The radiation contribution for wavelengths $\lambda > 0.2\ \mu$ was found by scaling experimental data,[15,16,17,18] assuming the shock layer to be optically thin in this wavelength region. The small continuum photon cross sections given in Reference 6 for wavelengths $> 0.2\mu$, three orders of magnitude smaller than the UV values, support the optically thin approximation. The results for line radiation from air, given by Allen[19], at a corresponding temperature and density show a linear dependence of the radiation with shock layer thickness up to 10 cm, and hence the assumption of an optically thin layer for wavelengths $> 0.2\ \mu$ does not appear to be unduly conservative. The radiation contribution for wavelengths $> 0.2\ \mu$ is predicted to be 1500 Btu/ft^2-sec based on experimental data. The results of Allen[19] indicate that roughly half of this radiation is due to line radiation and half is due to continuum radiation.

The total energy in the flow is $\frac{1}{4}\rho v^3$ and for the present case is 67,000 Btu/ft^2-sec, and the total radiative heat rate loss from the flow is less than one percent of this value, and so the energy coupling is small.

Comparison of the present results with those of Allen[19] for air is shown in the table below, for $\lambda < 0.2\ \mu$,

	Radiation Heat Rates, Btu/ft^2-sec	
	Present	Allen[19]
Σ lines	853	460
continuum	115	110
Total	968	570

The carbon lines apparently contribute more heavily to the present mixture resulting in close to a factor of two increase over the air predictions.

4.2.7.6 Heating Distributions

The mission studies indicated that the low M/C_DA compact configurations were more favorable as opposed to the 30 degree cone. The temperature profile across the shock layer of the 45 degree cone approaches a step function, and for ease of computation this was used; similarly for the 60 degree cone.

As seen above, on the 45 degree cone, a hot layer at 10,400°K and 0.02 cm thick exists near the surface at the mid cone point. To estimate the heating at the mid cone point, the parametric study for line radiation ($\lambda < .2\ \mu$) from air (Ref. 19) was utilized, which considered the effect of layer thickness, temperature and density on the line radiation, and yields a factor of 15% of the stagnation point line contribution magnitude. For the continuum there is also an order of decrease and this becomes negligible.

On the 60° cone, the results are similar as the thickness of the higher temperature layer is small; the oblique shock layer temperature of 8200°K will yield negligible UV radiation (Ref. 19 predicts about a 2 orders of magnitude decrease in the UV in going from 11,400 to 8200°K).

The radiative contribution at wavelengths larger than 0.2 μ was found from experimental correlation as normal shock stagnation point data $q_R(\rho, v, \Delta)$ and can be recast as (optically thin) (see Section 3.5.2 for correlation with data)

$$q_R \sim P^{1.4} h^{2.12} \Delta \qquad (11)$$

where P and h are the static pressure and enthalpy which define the state of the gas. Dividing the shock layer into 'N' iso-enthalpy layers, the distribution is approximated by (optically thin)

$$\frac{q_{RC}}{q_{RS}} = \left(\frac{P_c}{P_s}\right)^{1/4} \sum_N \frac{\Delta}{\Delta_s} \left(\frac{h}{H_s}\right)^{2.12} \qquad (12)$$

For a two layer approximation, the 45 degree cone result is, at the mid-point,

$$\frac{q_{RC}}{q_{RS}} = 0.30, \text{ or } 450 \text{ Btu/ft}^2\text{-sec}$$

The 60 degree cone, using a similar calculation, yields $\frac{q_{Rc}}{q_{Rs}} = 0.77$, or 1150 Btu/ft^2-sec.

The CO (4+) radiation is of special interest as the lower temperatures on the side of the cone promote an increase in CO concentration. Using the MOT correlation discussed above (optically thin)

$$\frac{q_{Rc}}{q_{Rs}} = \frac{1}{(I/\Delta N_{CO})_s} \sum_N \frac{I}{L N_{CO}} \cdot \frac{\Delta N_{CO}}{\Delta s} \frac{}{N_{COs}} \qquad (13)$$

Applying the above approach, using the flow field data calculated yields for the 45 degree cone, the ratio of radiative heating from the CO (4+) band, 45 degree cone

$$\frac{q_{Rc}}{q_{Rs}} = 10.1, \quad q_{Rc} = 185 \text{ Btu/ft}^2\text{-sec}$$

and the 60 degree cone

$$\frac{q_{Rc}}{q_{Rs}} = 13.3, \quad q_{Rc} = 250 \text{ Btu/ft}^2\text{-sec}$$

The mid-cone locations are shown in Figure 4.2.

4.2.8 Discussion of Radiation Heating Study

The flow field results on the conical shapes considered indicate that the high temperature (entropy) layer is thin (about 20 percent of the shock standoff distance at the nose) which suppresses the radiative contribution from this layer. In fact, for the small bluntnesses studied, a good deal of boundary layer interaction is predicted in which case much of this layer would be engulfed by the boundary layer. In consonance with the small thickness of the high temperature layer, a large reduction in the line and continuum UV components was observed.

The importance of the CO (4+) and contributor was found to be important on the sides of the cones primarily due to the increased particle density of CO at the lower temperatures.

Because of the small bluntness, the radiative heating rates appear modest and strong absorption for $\lambda > 0.2\ \mu$ and energy coupling effects are not

predicted.

The supplementary work done on the aerothermal environment indicates that, for the same factors considered, the radiative heating calculations used in the mission study are conservative, the amount of conservation being greater for the Best Occultation Mission, which based on the flight condition studied indicates a 40 percent factor on the peak radiative rate.

Experimental work is needed to develop confidence in the radiative predictions for gas mixtures of high CO_2 content. In particular, radiation data are needed for the UV region.

4.3 Prediction of Materials Performance

4.3.1 State-of-the-Art Survey

4.3.1.1 Scope of Survey

The objective of the survey was to provide a comparison of existing transient ablation analysis techniques; in particular, to assess the methods used to handle the problem areas of prime importance to a thermodynamic analysis of entry into the Venus atmosphere.

The computer codes discussed herein are representative of the available analyses. It is not necessary to describe every program in use since the differences are in detail rather than formulation. Some analyses are company proprietary and detailed information is not available. Among the screening criteria was the requirement that the analysis and solution has been programmed for at least a second generation digital computer.

The survey was limited to one-dimensional transient analyses of charring ablation materials. Multi-dimensional analyses are available, but present computer core limitations necessitate rather simplified models.

4.3.1.2 Survey Results

In general, the one-dimensional analyses can be classified as belonging to one of three classes; (1) detailed models for the internal

material response with simplified approximations for the surface boundary condition; (2) convective transfer coefficients with detailed surface chemistry; or, (3) coupled, ablator-boundary layer solutions.

For the first class of analyses, the conventional approach has been to focus attention on the in-depth charring ablator response, utilizing empirical correlations such as, heat of ablation or ablation-rate versus surface-temperature relationships or correlations of theoretical solutions (e.g., oxidation kinetics) to provide the surface boundary condition. This method has been effective when applied to conditions which do not differ significantly from the test conditions at which the empirical relationships were derived, but there is no valid basis for extrapolation to other conditions since the highly nonlinear coupling between the various phenomena cannot be scaled. Typical of this type of analysis are programs originated at Avco (Ref. 20), Boeing (Ref. 21), NASA-MSC (Ref. 22), and NASA-LRC (Ref. 23 and 33).

A somewhat more sophisticated approach has been to represent the boundary-layer heat and mass transfer processes by convective transfer coefficients while considering detailed chemical interactions and coupled mass and energy balances at the surface. Because detailed surface physics can be retained in the formulation, this method is better suited for application at conditions beyond the range of available experimental data. However, it is still limited in this regard since the effects of nonsimilarities between boundary-layer profiles cannot be treated precisely. Thus, mass addition, chemical reactions, and multicomponent diffusion effects can be taken into account only in an approximate manner, and upstream effects, thermal diffusion, and radiation-convection coupling cannot be considered except, possibly, through correlations of boundary-layer solutions. Typical of this type of analysis are programs originated at Lockheed (Ref. 24), Vidya (Ref. 25), and Rocketdyne (Ref. 26).

The only coupled transient charring ablation problem which has

been attempted has been at Aerotherm (Ref. 27-32). The following computer programs have been developed at Aerotherm:

a) Charring material ablation program (CMA)

b) Boundary-layer integral-matrix procedure program (BLIMP)

c) Surface thermochemistry programs based on convective transfer coefficients: Aerotherm chemical equilibrium (ACE) and Aerotherm chemical equilibrium with selected surface reaction kinetics (ACE-KINET)

d) Coupled ablator/boundary layer/environment program (CABLE).

The CMA program can be operated independently for obtaining the in-depth response of charring materials for a variety of approximate boundary conditions. The ACE and ACE-KINET programs can be operated independently to compute steady-state ablation of arbitrary material-environment combinations or can be used to provide tables of surface-thermochemistry information as input to the CMA program for transient charring ablation calculations, again for arbitrary material-environment combinations. The BLIMP program can be operated independently to provide boundary-layer solutions for a variety of coupled, partially-coupled or uncoupled steady-state ablation surface boundary conditions. Finally, the CABLE program calls upon the BLIMP and CMA programs as subroutines to provide fully coupled transient charring ablation and boundary-layer solutions.

A comparison of the pertinent features of the Class I programs discussed above is shown in Table 4.8. Taking into consideration the fact that many approximations to the physics of the problem must be made to use this class of programs, it appears that Avco's Program 1600 is the best among this type simply due to generality and versatility (e.g., the inclusion of in-depth pressure and radiation attentuation calculations).

A comparison of the pertinent features of the Class II programs discussed above is shown in Table 4.9. Although this type of analysis is more representative of the physics of the problem, it still requires many approximations. It appears that the Rocketdyne program is the best among this class

TABLE 4.8

SURVEY OF CLASS I PROGRAMS

MODEL	AVCO	BOEING	NASA-MSC	NASA - LRC
1. Internal Response				
a. Class of materials	Any charring or noncharring material	Any charring or noncharring material	Any charring or noncharring material	Any charring or noncharring material
b. Geometry	One-dimensional conduction with approximations for cylindrical or spherical shells as special cases.	One-dimensional conduction	One-dimensional conduction	One-dimensional conduction
c. Thermal properties	State and temperature dependent	State and temperature deptendent	Temperature dependent	Temperature dependent
d. Pyrolsis Kinetics	Three independent Kinetic reactions; thermal equilibrium between the char and pyrolysis gas assumed	Four independent Kinetic reactions; thermal equilibrium between char and pyrolysis gas assumed	One Kinetic reaction; thermal equilibrium between char and pyrolysis gas assumed	Discontinuous density change at pyrolysis temperature; thermal equilibrium between char and pyrolysis gas assumed.
e. Internal pressure distribution	Pressure distribution through the char calculated a posteriori using Darcy's law	Not calculated	Not calculated	Not calculated

TABLE 4.8 (cont.)

MODEL	AVCO	BOEING	NASA -MSC	NASA - LRC
d. Radiation flux	Incident flux considered to pass through boundary layer without attenuation	Incident flux considered to pass through boundary layer without attenuation	Incident flux considered to pass through boundary layer without attenuation	Incident flux considered to pass through boundary layer without attenuation.
e. Environmental gas	Arbitrary nitrogen-oxygen composition	Air	Air	Air
3. General				
a. Backup materials	Several noncharring materials; variable thermal properties; air gaps allowed between materials.	Several noncharring materials; variable thermal properties	Several noncharring materials; variable thermal properties air gaps allowed between materials	Several noncharring materials; variable thermal properties
b. Rear boundary	A variety of rear boundary conditions	A variety of rear boundary conditions	A variety of rear boundary conditions	A variety of rear boundary conditions
c. General inputs	All properties can be functions of state and/or functions of time, distance, reversible or irreversible functions of temperature.	Most properties can be functions of state and/or reversible functions of temperature.	Most properties can be reversible functions of temperature.	Some properties can be reversible functions of temperature.

TABLE 4.8 (cont.)

MODEL	AVCO	BOEING	NASA-MSC	NASA - LRC
f. In-depth radiation	Internal self glowing and exponential attenuation of external radiant flux.	Not calculated	Not calculated	Not calculated
g. Numerical technique	Implicit-explicit finite difference	Implicit finite difference	Implicit finite difference	Explicit finite difference
2. Surface Phenomena				
a. Surface recession	Constant ablation temperature; or, programmed function of surface temperature; or oxidation Kinetics with high temperature sublimation	Oxidation Kinetics with high temperature sublimation	Empirical function of temperature	Constant ablation temperature
b. Mechanical removal	Empirical function of temperature	Tabular input	Not calculated	Not calculated
c. Transpiration correction	Exponential function of dimensionless blowing parameter	Tabular function of dimensionless blowing parameter	Linear function of dimensionless blowing parameter	Second-order function of dimensionless blowing parameter

TABLE 4.9

SURVEY OF CLASS II PROGRAMS

MODEL	LOCKHEED	VIDYA	ROCKETDYNE
Internal Response			
a. Class of Materials	Any charring or noncharring material.	Any charring or noncharring material.	Any charring or noncharring material.
b. Geometry	One-dimensional conduction	One-dimensional conduction; cylindrical coordinates.	One-dimensional conduction.
c. Thermal properties	Functions of state and temperature.	Functions of state and temperature	Functions of state and temperature.
d. Pyrolsis Kinetics	Three independent Kinetic reactions: equilibrium composition of pyrolsis gas calculated.	One Kinetic reaction; thermal equilibrium between the char and pyrolysis gas assumed.	One Kinetic reaction; reaction zone broken into six components, virgin plastic, char, reinforcement, solid product of char-reinforcement reaction, stable gas and unstable gas
e. Internal pressure distribution	Not Calculated	Not Calculated	Calculated using modified momentum equation for slow flow through porous media.
f. In-depth radiation	Not calculated	Not Calculated	Not Calculated.

TABLE 4.9 (cont.)

MODEL	LOCKHEED	VIDYA	ROCKETDYNE
2. Surface Phenomena			
a. Boundary Layer Assumptions	Equal diffusion coefficients, Le=Pr=1 , approximated by transfer coefficients.	Equal diffusion Le=Pr=1, approximated by transfer coefficients.	Equal diffusion coefficients Le=Pr=1, approximated by transfer coefficients.
b. Surface recession	Limited reaction Kinetics for C, O, H,N system.	Reaction Kinetics for C, O, H,N system. Pyrolysis gases frozen in boundary layer.	Low temperature reaction Kinetics; thermal equilibrium at surface at high temperatures for arbitrary chemical system.
c. Mechanical removal	Not calculated	Not calculated	Shear removal of liquid layer.
d. Transpiration correction	Linear function of dimensionless blowing parameter	Linear function of dimensionless blowing parameter	Linear function of dimensionless blowing parameter.
e. Radiation flux	Incident flux considered to pass through boundary layer without attenuation.	Incident flux considered to pass through boundary layer without attenuation.	Incident flux considered to pass through boundary layer without attenuation.
f. Environmental gas	Arbitrary nitrogen-oxygen composition	Arbitrary C,O, H,N chemical system	Arbitrary C. O, H,N chemical system

TABLE 4.9(cont.)

MODEL	LOCKHEED	VIDYA	ROCKETDYNE
3. General			
a. Backup materials	Several noncharring materials; variable thermal properties.	Several noncharring materials; variable thermal properties	Several noncharring materials; variable thermal properties.
b. Rear boundary	A variety of rear boundary conditions	A variety of rear boundary reactions	A variety of rear boundary conditions.
c. Special features	None	None	Includes calculations of coking reactions and char-inforcement reactions.

of programs, again, due to generality and versatility (e.g., the inclusion of coking and char-reinforcement calculations).

Since, at present, the Aerotherm program is unique, no comparison is available. All of the features of the BLIMP and CMA programs pertinent to the coupled program are retained in the CABLE program. The models employed in the CABLE program are presented summarily in Table 4.10. The operational status of the various aspects of the computational procedure are also summarized therein. Certain aspects of the boundary-layer solution cannot be considered fully operational until the procedure is checked out for the wide variety of materials, environments, and flight conditions for which it is presumably applicable. Some aspects of the ultimate boundary-layer program have not been fully implemented at this time.

Specific materials with important additional subsurface events are not well described by any of these programs. Physical events here include coking and subsurface char erosion due to interaction with the pyrolysis gas, chemical kinetics of pyrolysis-gas cracking reactions as the gas flows through the char, thick liquid-layer runoff, additional subsurface chemical reactions such as carbon-silica reactions, thermal expansion effects, and mechanical damage to weak chars.

It is very important to note that many boundary-layer phenomena are not presently included in the Aerotherm program and may severely limit its usefulness until such time as they are available. Among these are: extension to a turbulent boundary layer, inclusion of radiation absorption and emission within the boundary layer, inclusion of general nonequilibrium, inclusion of an entropy layer, and, extension to a non-adiabatic inviscid flow field. For many materials and/or flight conditions none of these phenomena is important. For other materials and/or flight conditions, the relative importance of these additional aspects has generally not been determined. The importance of these phenomena should be

TABLE 4.10

SURVEY OF CLASS III PROGRAMS

BOUNDARY-LAYER-EDGE CONDITIONS

Phenomena	Model	Operational Status
a. Flight conditions	Transient or steady-state;boundary layer-edge conditions around the body can be specified, or pressure distribution around the body and either conditions upstream of the shock or local stagnation conditions can be specified.	Fully operational
b. Environmental gas	Arbitrary elemental and molecular composition.	Fully operational
c. Chemical state	General mixed equilibrium-nonequilibrium	See Item II (e)
d. Incident radiation	Angular dependent incident radiation from inviscid shock layer	See Item II (g)
e. Entropy Layer	Edge velocity allowed to be a function of stream function as well as streamwise location.	Incorporated into program logic, but option has never been exercised; presently, flow field is considered isentropic or the presence of an entropy layer approximated by assignment of edge velocity as well as pressure but with zero shear at the boundary-layer edge.
f. Radiation coupled inviscid flow field	Total enthalpy allowed to be a function of stream function as well as streamwise location.	Requires rearrangement of some program logic before option can be implemented; presently flow field is considered adiabatic or non-adiabatic flow field approximated by assignment of total enthalpy but with zero heat flux at the boundary-layer edge.

TABLE 4.10 (cont.)

II. BOUNDARY LAYER

Phenomena	Model
(a) Boundary-layer type	Laminar nonsimilar with discontinuous mass injection
(b) Nature of solution	Numerical procedure capable of yielding accurate solutions.
(c) Body geometry	General planar or axisymmetric flow around blunt or sharp bodies; three-dimensional boundary layers can be approximated by streamtube considerations.
(d) Chemical system	Arbitrary elemental and molecular composition
(e) Chemical state	General mixed equilibrium-nonequilibrium with arbitrary homogeneous and heterogeneous (surface) reaction kinetics
(f) Transport properties	Incorporates bifurcation approximations for unequal diffusion and thermal diffusion coefficients and approximations for mixture viscosity and thermal conductivity of the Sutherland-Wassilijewa type.
(g) Radiation absorption and emission	One-dimensional radiation absorption and emission with accurate frequency integrations for molecular, ionic and atomic species resulting from ablation products and their interaction with boundary-layer edge gas

TABLE 4.10 (cont.)

Phenomena	Model	Operational Status
III SURFACE PHENOMENA		
(a) Coupling considerations	The boundary layer and charring ablator solution fully coupled; transient solution at a given streamwise station completed before proceeding to next station.	One solution as been obtained; some further checkout is required before the coupling can be considered fully operational for all materials and environments for which it is presumably applicable.
(b) Chemical interactions	Chemical reactions between char, pyrolysis gas, and boundary-layer species allowed; these reactions are assumed to be in equilibrium except for specified rate-controlled reactions.	Equilibrium operational; some solutions have been obtained for selected rate-controlled reactions.
(c) Mechanical removal mechanisms	Each candidate surface condensed phase material (e.g. , SiO_2*, C*, SiC*) assigned a fail temperature, above which that species cannot appear as the surface material (this is equivalent to specifying, for example, a zero liquid viscosity for SiO_2* and zero strength for C* above their respective fail temperatures).	Operational for those surface materials which have been considered; occasionally leads to chemistry convergence difficulties
(d) Other considerations	Velocity slip and temperature jump at the surface not allowed.	
IV IN-DEPTH RESPONSE OF EXPOSED (ABLATING) MATERIAL		
(a) Class of materials	Any charring or noncharring material for which thermochemical data are available or can be estimated.	Fully operational
(b) Geometry	One-dimensional conduction but area change due to material curvature taken into account in a generalized manner, with planar, cylindrical, and spherical geometries as special	Fully operational

TABLE 4.10 (cont.)

Phenomena	Model	Operational Status
IV IN-DEPTH RESPONSE OF EXPOSED (ABLATING) MATERIAL (cont.)		
(c) Thermal properties	Temperature dependent	Fully operational
(d) Pyrolysis kinetics and subsequent internal chemical events	Pyrolysis can be specified by three independent kinetic reactions; thermal equilibrium between the char and pyrolysis gas assumed; formulation consistent with general pyrolysis-gas cracking, the user employing pyrolysis-gas enthalpy as function of temperature; char density buildup due to coking not calculated.	Fully operational
(e) Internal pressure distribution	Pressure distribution through the char calculated a posteriori using Darcy's law with momentum correction, the user specifying char permeability as a function of temperature to simulate char-density buildup due to coking reactions.	Fully operational
(f) Numerical technique	Implicit finite-difference, except that gas generation is partially explicit.	Fully operational
(g) Other numerical considerations	Variable grid spacing with nodelets used in decomposition zone. Nodes dropped from rear of ablation material.	Fully operational
V IN-DEPTH RESPONSE OF BACKUP MATERIALS		
General	Several noncharring materials with variable thermal properties are allowed, with interfacial contact resistance (including air gaps) between materials, and variable rear surface boundary conditions.	Fully operational

defined through well-planned experimentation and post-test model examination coupled with performance predictions with the existing computer programs.

The general philosophy when using the programs as described in Table 4.8 is to take presently existing data, obtain gross material property correlations and, if necessary, extrapolate to design conditions. The use of the programs as described in Tables 4.9 and 4.10 makes the extrapolation more accurate but at the same time complicates the determination of the necessary constants simply because of the number of variables. Indeed it is possible that with presently existing data the programs of Table 4.1 are really the only meaningful type to use for engineering design purposes since the proper use of the more sophisticated programs would require an extensive amount of additional testing and data interpretation.

It is concluded therefore that while the degree of sophistication required for the design of the Venus probe has not been defined, the use of a method similar to Avco's Program 1600 for the design of the Venus probe is compatible with the present state-of-the-art. The use of the more complex mathematical models at the present time should be restricted to the evaluation of the effects of parameter trends rather than to the levels.

3.1.3 Summary

The survey of computer programs indicates that there are three levels of sophistication starting from methods similar to the Avco design technique (program 1600) adding some coupling procedures and ending with a coupled method as developed by Aerotherm. Several variations in the first two levels are described briefly and others not mentioned here exist throughout the country but were not included since the intention here was to provide a reasonable look at the state-of-the-art and not be involved with minor variances. Evaluation of the pros and cons of the various techniques

leads to the conclusion that at the present time the state-of-the-art is compatible with the lower level of sophistication simply due to the additional work required to define the increasing number of parameters involved with the more complex methods. The advanced program concepts, although more complex and not useful for design calculations at the present time, are valuable in assessing the effects of parameter variations.

4.3.2 Thermochemistry Study

4.3.2.1 Study Scope

The objective of the study was to evaluate the possible reactions between the surface constituents of candidate ablation materials and the Venus atmosphere. Among the uncertainties in the heat shield thickness study is the evaluation of the potential for oxidation of carbonaceous materials during hypersonic entry. Current practice utilizes a conservative value for the oxygen concentration (which is assumed invariant with surface temperature and pressure) at the gas/solid interface and results in over-estimate of the potential for oxidation. Thus, a weight penalty is imposed upon carbonaceous materials in certain cases.

To evaluate the possible reactions between the surface constituents of candidate ablation materials and the Venus atmosphere thermochemical equilibrium calculations were performed for each of the atmospheric models (AV-4, AV-10, and AV-50) with an excess of particular elements to simulate the presence of a condensed phase material. For example, to simulate a solid carbon surface in contact with the AV-4 atmosphere (75% CO_2, 25% N_2 by volume) one mole of gas was included in a system containing an excess (10 moles) of the element carbon. At low temperatures, where no reactions occur, the equilibrium mixture contains 0.75 moles CO_2 and 0.25 moles N_2 in the gaseous phase and 10 moles of carbon in the condensed phase. Similar calculations were performed for SiO_2 (silica) as the condensed phase material.

These calculations were performed for the pressure range from 0.01 to 10.0 atmospheres for temperatures from 600°K to 4200°K. The results of these calculations were compared with the baseline results obtained in which the gas-phase equilibrium chemistry of the atmospheric models was studied in the absence of a condensed phase.

4.3.2.2 Study Results

The variation of the mole fraction of the principal species of the AV-50 atmosphere (neglecting mass addition) over the temperature range from 0°K - 4200°K is illustrated in Figure 4.15 for a pressure of 1.0 atmospheres. These results are typical of those obtained for a range of pressures from 0.10 to 10.0 atmospheres.

The results of the equilibrium calculations for the study of interactions with solid carbon surfaces is presented as plots of mole fraction of the gas phase species as a function of temperature and is illustrated (for each atmospheric model and 1 atm. pressure) in Figures 4.16 - 4.18. The results indicate that if carbon dioxide reaches the surface, it will react with condensed phase carbon to produce carbon monoxide by the reaction:

$$C\ (s) + CO_2\ (g) \rightleftharpoons 2\ CO\ (g) \qquad (14)$$

It is unlikely that any appreciable amount of carbon dioxide will reach the surface. The previous results show that carbon dioxide dissociates to carbon monoxide and molecular oxygen, and the molecular oxygen, in turn, dissociates to atomic oxygen. In either case, the solid carbon is removed by oxidation reactions and up to temperatures of approximately 3000°K is the only mechanism of chemical removal. Above 3000°K the condensed phase begins to sublime to gaseous species C, C_2, C_3, C_4, and C_5. The results indicate that carbon in the condensed phase does not react with molecular nitrogen and it is only at temperatures where gaseous carbon species are produced that cyano (CN) production

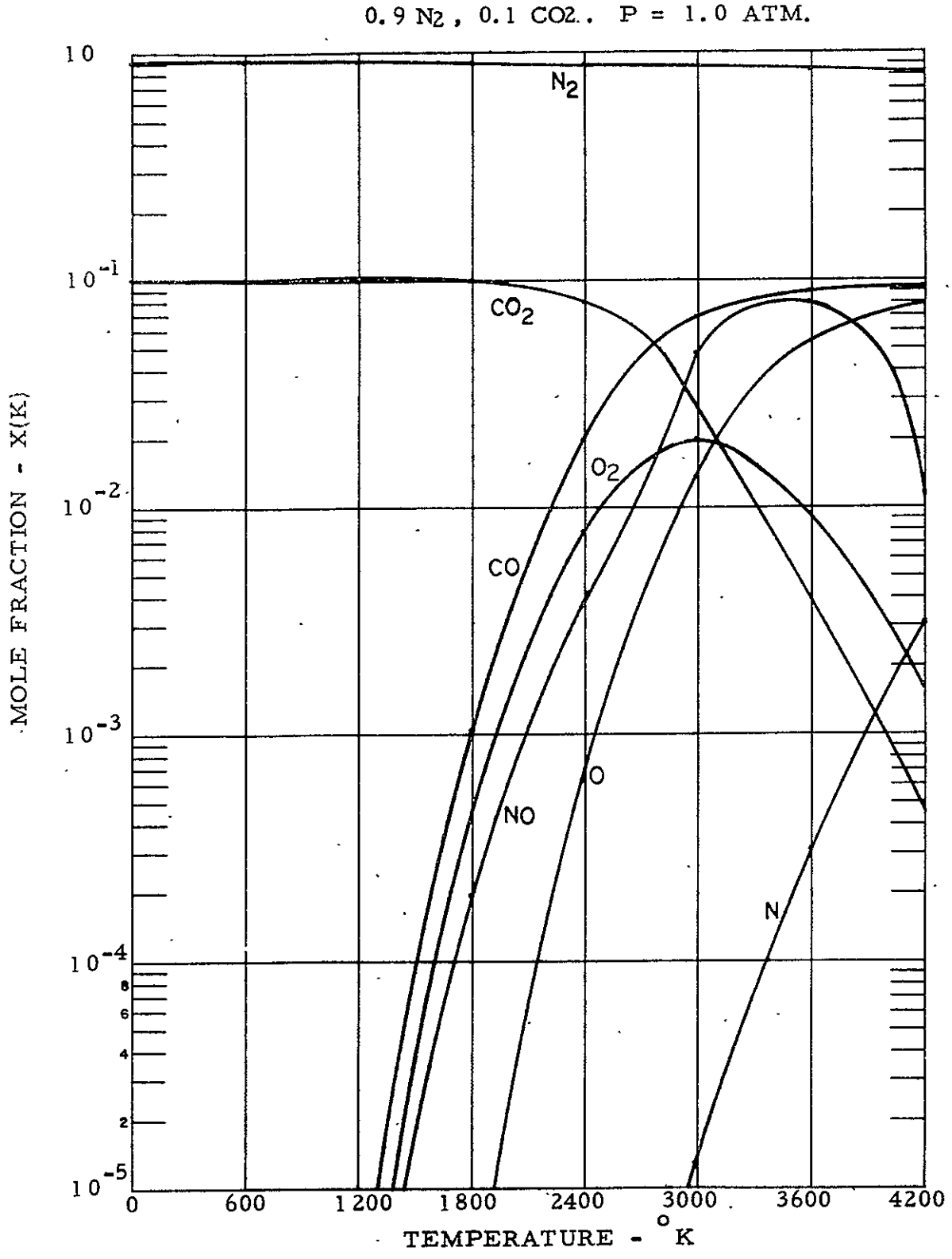


Figure 4.15 Equilibrium Composition - AV-50 ATM

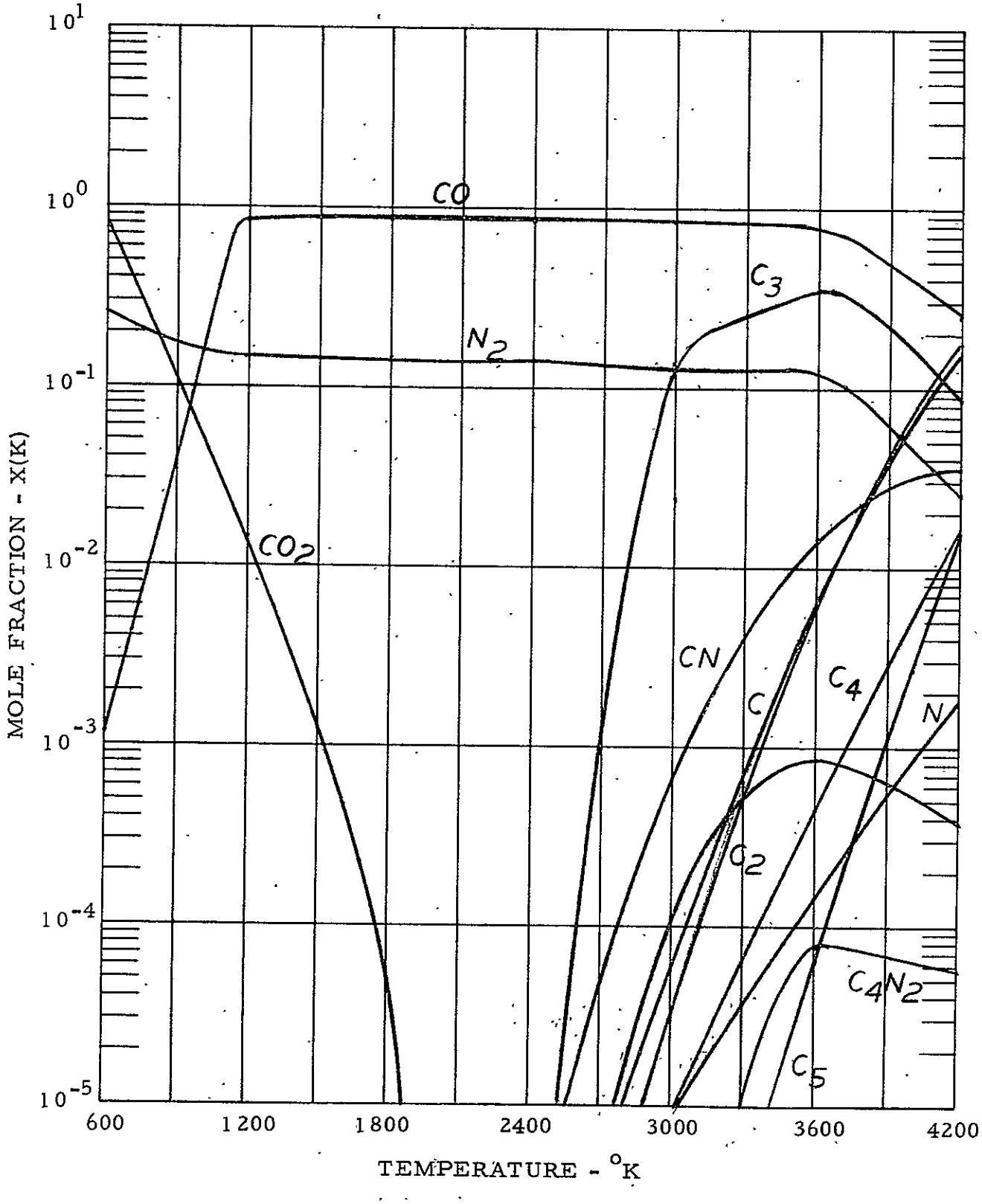


Figure 4.16 Equilibrium Composition at Gas/Solid Carbon Interface - AV-4 ATM

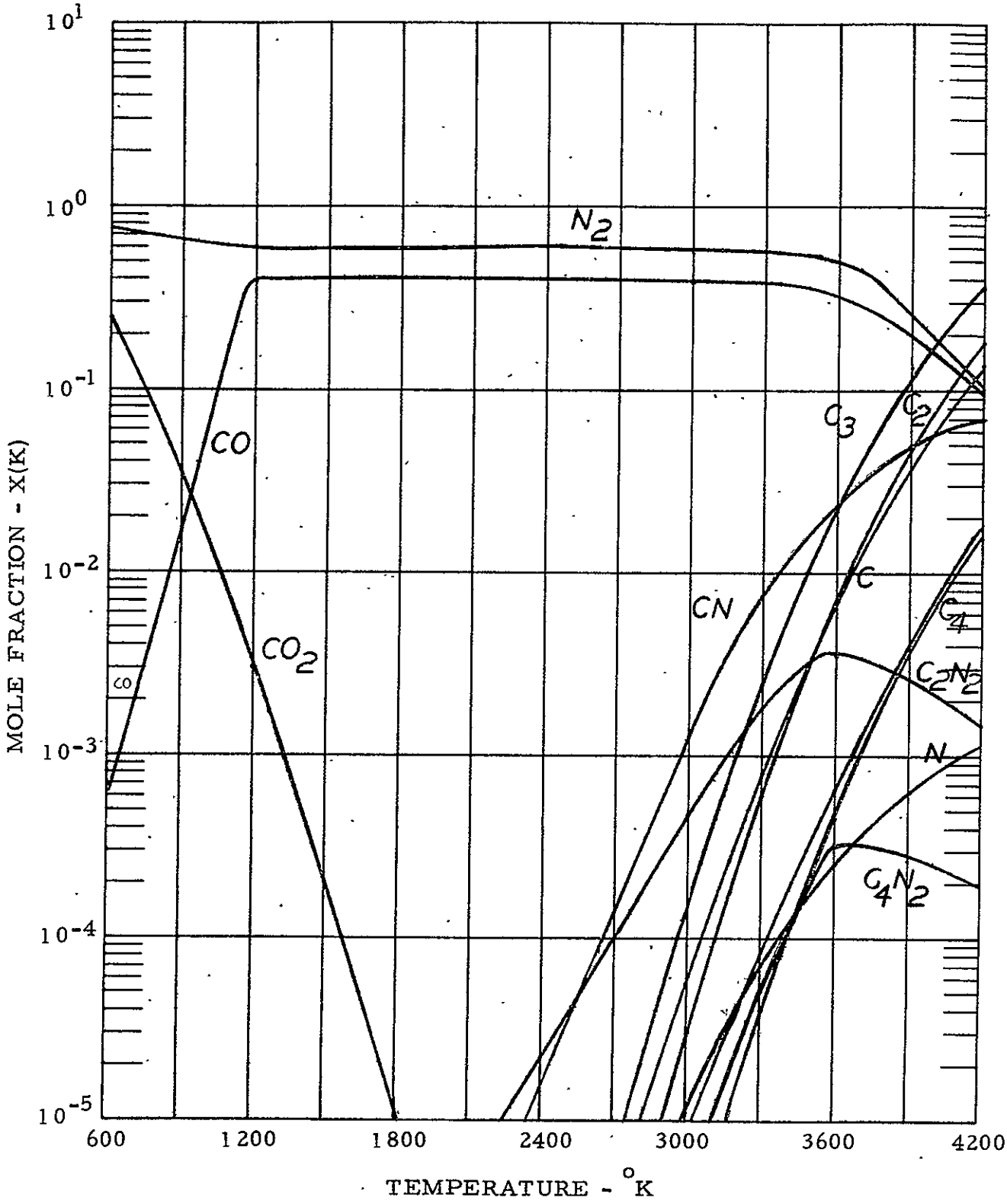


Figure 4.17 Equilibrium Composition at Gas/Solid Carbon Interface, AV-10 ATM

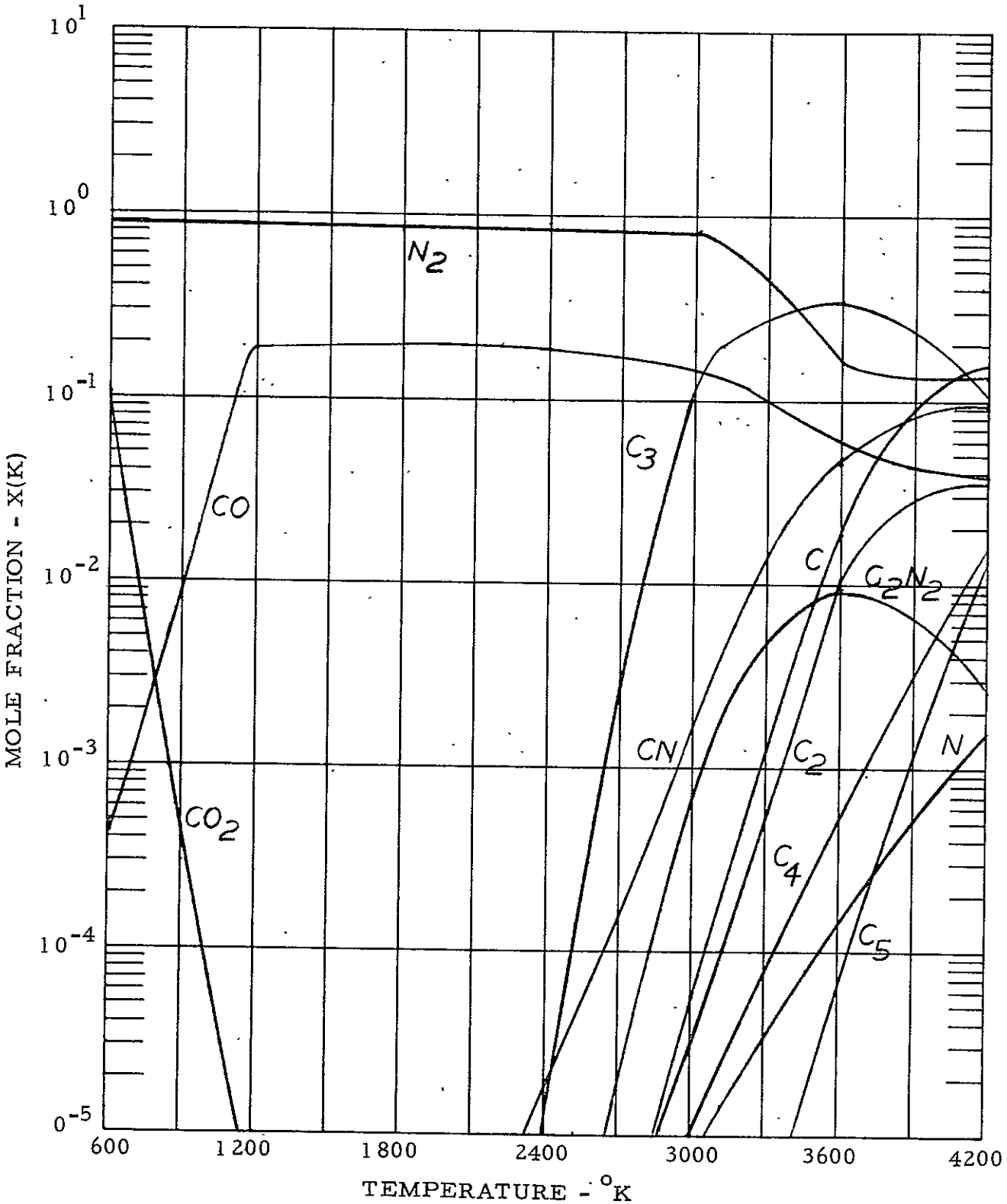


Figure 4.18 Equilibrium Composition at Gas/Solid Carbon Interface - AV-50 ATM

occurs. An examination of the results leads one to conclude that nitrogen reactions do not contribute to the chemical erosion of a carbonaceous surface. The only evident mechanisms for chemical removal of carbonaceous surfaces appears to be oxidation at temperatures below approximately 3000°K and sublimation at higher temperatures.

The results of the equilibrium calculations for the study of interactions with solid silica surfaces is presented as plots of mole fraction of the gas phase species as a function of temperature and is illustrated (for each atmospheric model and total pressure) in Figures 4.19-4.21. The results indicate that the molal concentrations of the atmospheric species is unaffected by the presence of silica in the condensed phase, i.e., the removal of condensed silica is a very weak function of environmental composition. The removal mechanism is vaporization and is governed by two reactions:

$$SiO_2\ (s) \rightleftharpoons SiO\ (g) + \tfrac{1}{2}\ O_2\ (g) \qquad (15)$$

and,

$$SiO_2\ (s) \rightleftharpoons SiO_2\ (g) \qquad (16)$$

The results of this study indicate that the Venus atmosphere does not introduce additional analytical problems for siliceous materials. However, the study of the interactions with a carbonaceous surface reiterates the importance of the oxidation kinetics and sublimation characteristics of carbon. The equilibrium assumption indicates that the presence of condensed phase carbon depletes all of the oxygen in the stream including the starvation of the boundary layer of the oxygen required for the normal nitric oxide reactions. The equilibrium assumption is only valid at high temperatures where reaction rates are extremely large. To determine if the oxidation potential is as severe at lower temperatures (which is indicated by the present results) requires an analysis of the reaction kinetics coupled to the flow field with a

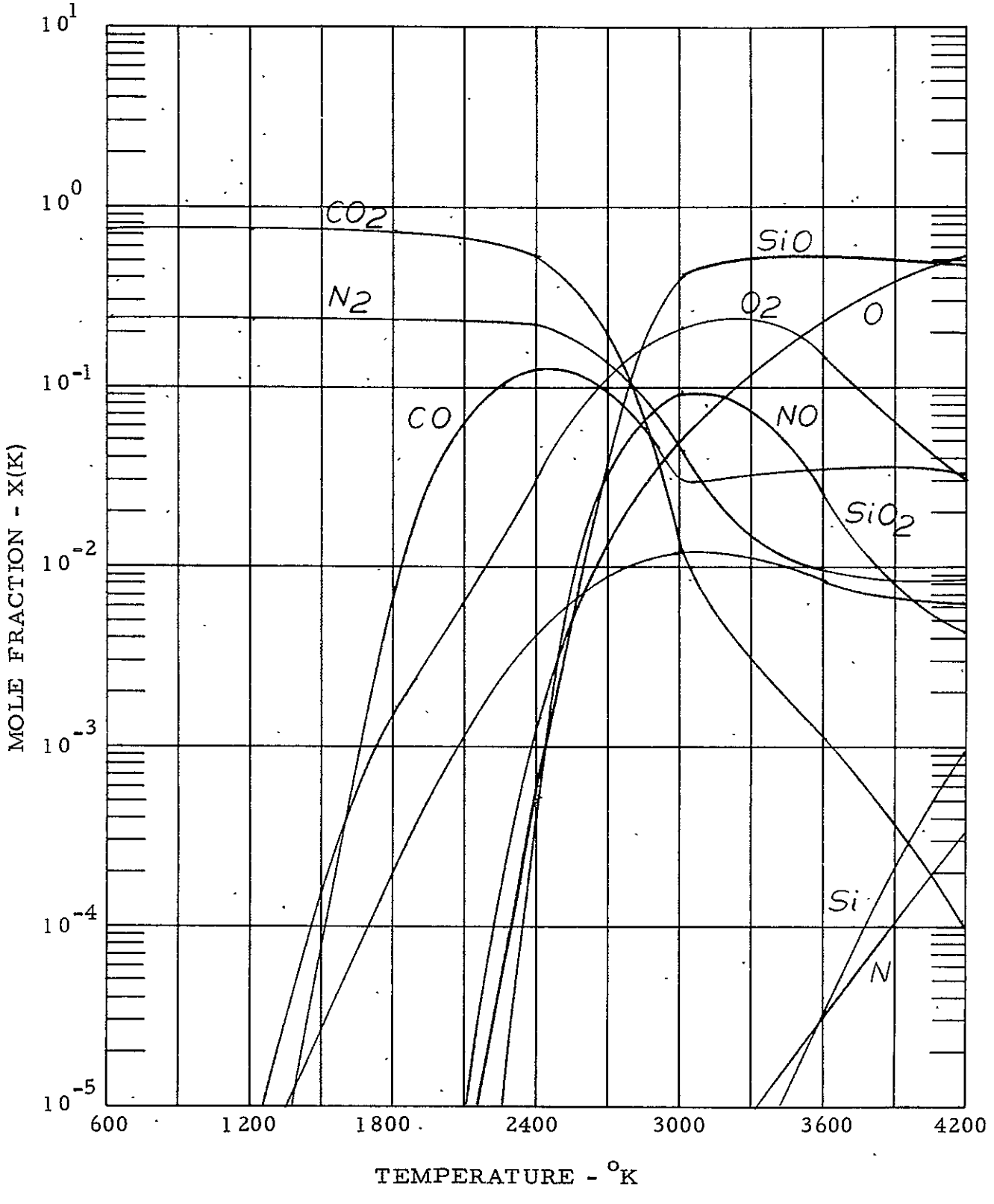


Figure 4.19 Equilibrium Composition at Gas/Solid Silica Interface - AV-4 ATM

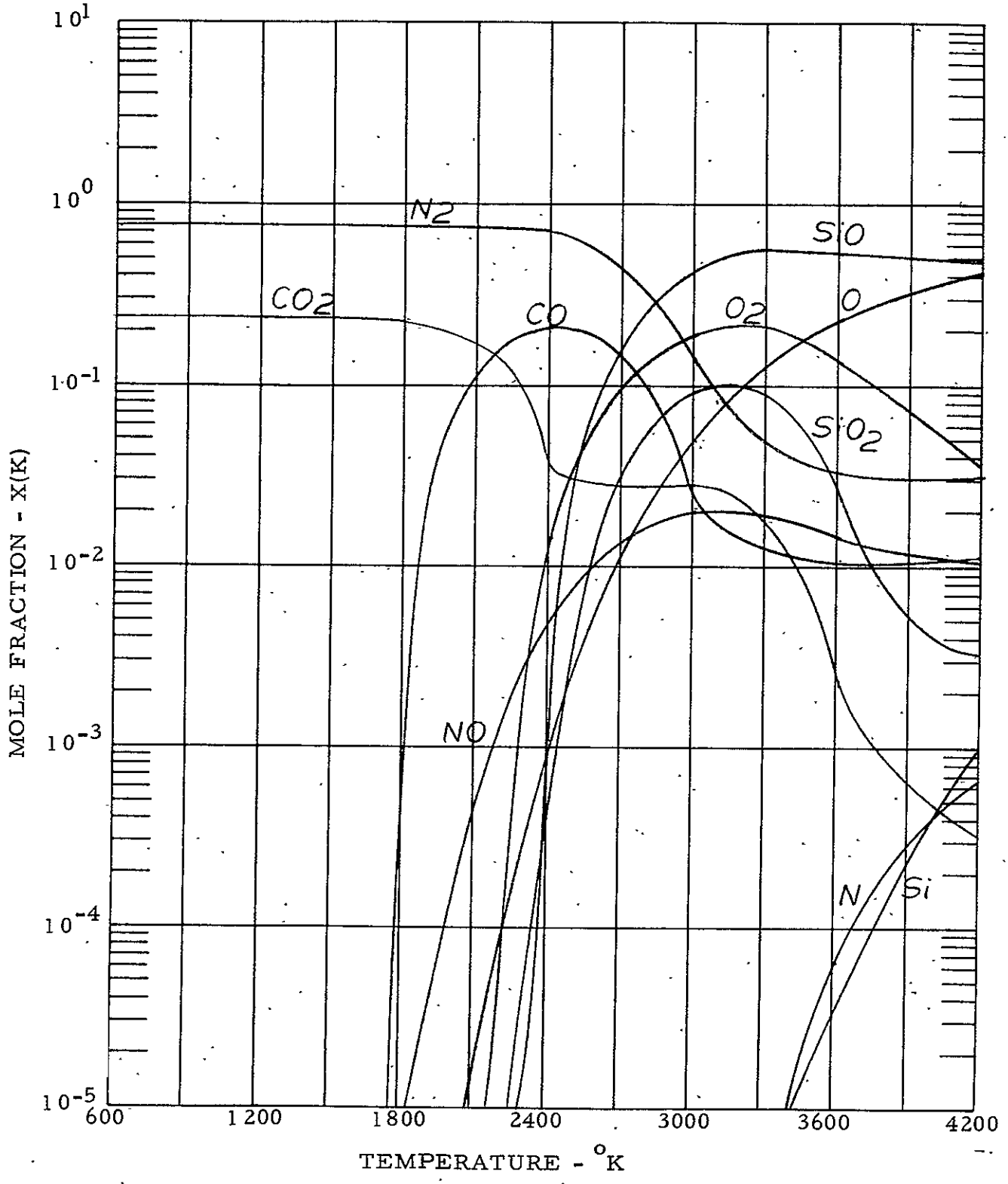


Figure 4.20 Equilibrium Composition at Gas/Solid Silica Interface - AV-10 ATM

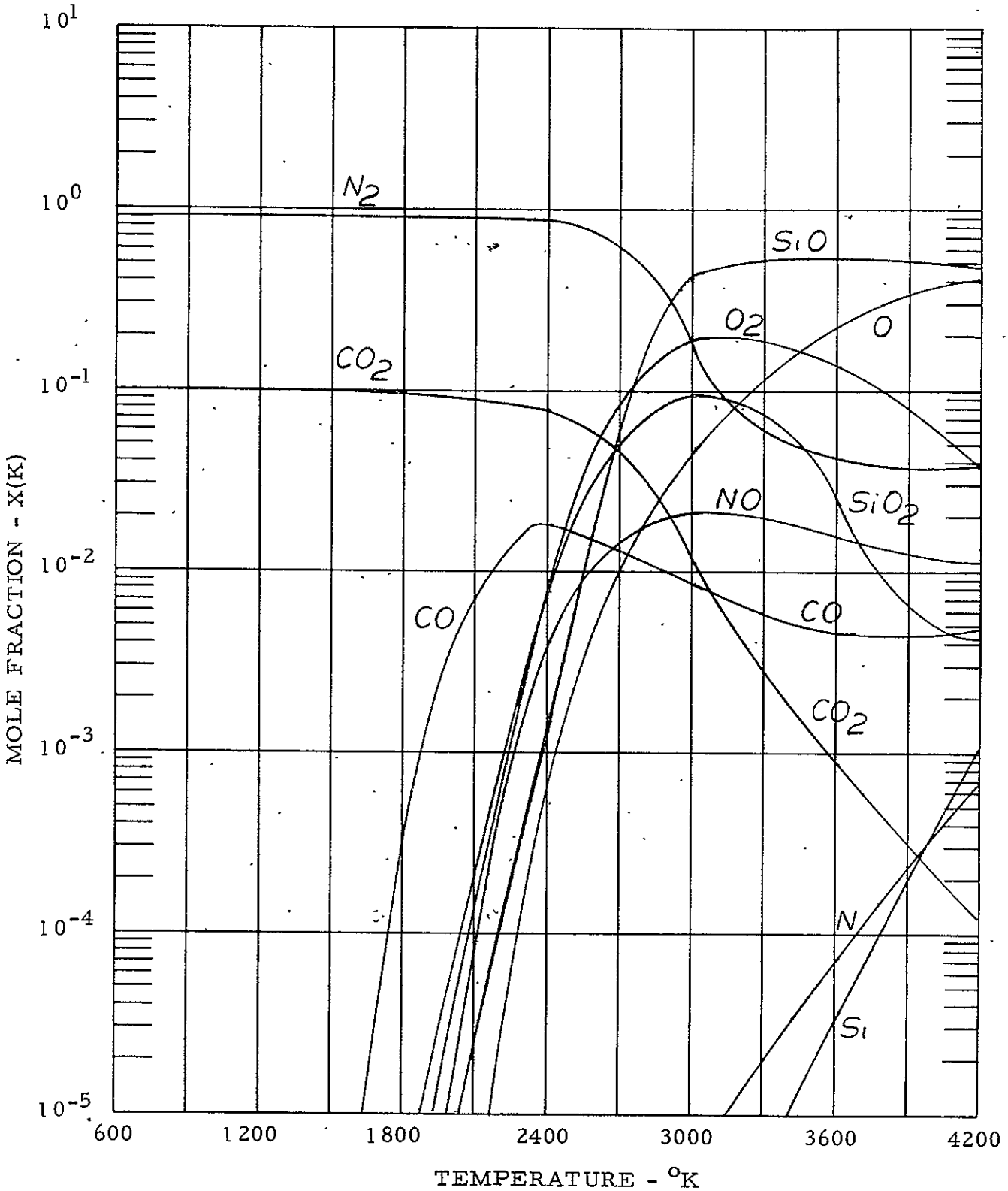


Figure 4.21 Equilibrium Composition at Gas/Solid Silica Interface - AV-50 ATM

reacting carbon dioxide stream.

4.3.2.3 Summary

Evaluation of the reactions between the boundary layer gases and the heat shield disclosed the key thermodynamic surface recession processes. For carbonaceous materials the removal process appears to be dictated by oxidation up to temperature levels of 3000°K and by sublimation of carbon to gaseous species (C, C_2, C_3, C_4, C_5) at higher temperatures. In addition, the equilibrium calculations indicate that nitrogen does not react with carbon in the condensed phase and CN is only formed when gaseous carbon is present. For the silica materials, the results indicate that the removal mechanism is a very weak function of the environment and the removal rate is dictated by the vaporization rate of silica.

4.3.3 Survey of Boundary Layer Transpiration Studies

4.3.3.1 Survey Scope

The objective of the survey was to examine the extensive literature pertaining to transpiration cooling and to assess the state-of-the-art in the following subject areas:

a. The theoretical analyses pertaining to the correlation of mass injection rates with heat transfer;

b. The experimental investigation relating to the verification of existing theories and the development of empirical correlations for determining the effects of mass injection on surface heat transfer and skin friction.

A survey by Kelley and L'Ecuyler (46) compared the significant analytical and experimental investigations of transpiration cooling of a turbulent boundary layer. Some of the following observations can be attributed to them but they did not discuss some of the more recent investigations. A summary of the

pertinent experimental investigations is illustrated in Table 4.11. A more detailed discussion of the results of these studies is given below.

4.3.3.2 Survey Results

Most of the experimental investigations have been concerned with air-air injection. Only recently have studies been made of foreign gas injection, but, almost always, have been limited to an air boundary layer. Woodruff and Lorenz (35) measured heat transfer on a flat plate with helium, air and argon injected into an air boundary layer. Their data extended the range of non-dimensional blowing rate (F/St_o) to 18. The data is well correlated by an expression due to Bartle and Leadon (40). The effects of various injectants is apparently eliminated from the data by modifying the blowing rate (F/St_o) by the ratio of the specific heat of the injectant to the specific heat of the freestream (evaluated at the edge of the boundary layer). Romanenko and Kharchenko (37) also conducted flat plate tests with helium, air, Freon-12, and carbon dioxide as injectants. They correlated their data with a simple exponential equation and also found that the same specific heat modification was applicable. Brunner (38) conducted tests on a cone with nitrogen, helium, and water as coolants and attempted to verify the correlation of Stewart (49) who modifies the blowing rate by the specific heat ratio to the 0.6 power. A comparison of Brunner's data and the theories of Stewart and Rubesin and Pappas (51) is illustrated in Figure 4.22. The agreement is more in trend rather than absolute magnitude. Pappas and Okuno (36) conducted tests on a cone with helium, air, and Freon-12 as injectants. Some typical results are shown in Figure 4.23 which compares the skin-friction ratio for the three injectants with the theoretical predictions of Rubesin and Pappas (51). The data is shown to fall below the predictions but the fact that the effectiveness of low molecular

TABLE 4.11

SUMMARY OF EXPERIMENTSL TURBULENT DATA ON GAS INJECTION

REFERENCE	CONFIGURATION	TEMPERATURE MEASUREMENTS	BOUNDARY LAYER MEASUREMENTS	ENVIRONMENTAL GAS	INJECTED GAS	RANGE OF BLOWING RATE	RANGE OF REYNOLDS NO.	MACH NO.	FREESTREAM TEMPERATURE °F	Ψ
Fogaroli & Saydah (34)	Porous Cone 7.5° half-angle 12" Base diam.	Yes	Pressure and Temperature	Air	Air	.001 to .018	3×10^6 and 2.2×10^6 Re_∞/ft	5.3 and 8.1	350 and 1430*	$\left[\left(\frac{m\Delta H}{2q_o}\right)^2 + 1\right]^{1/2} - \frac{m\Delta H}{2q_o}$ Culick
Woodruff & Lorenz (35)	Flat plate α = 0°,-5°,-10°	Yes	No	Air	N_2,He,A	0 to .0258	0.29×10^6 to 0.45×10^6 Re_∞/ft	6.77 to 8.02	875*	$\frac{c_{Pc}/c_{Pe} \times F/St_o}{\left[1 + 1/3 \times c_{Pc}/c_{Pe} \times F/St_o\right]^3 - 1}$ Bartle & Leadon
Pappas & Okuno (36)	Cone	No	No	Air	He, Air Freon-12	0 to .00285	0.9×10^6 to 5.9×10^6	0.3, 0.7, 3.5, 4.7	Ambient	Compared with Rubesin
Romanenko and Kharchenko (37)	Flat Plate	Yes	Pressure and Temperature	Air	He, Air, Freon-12, CO_2.	.0001 to .007	1×10^5 to 5×10^5	0	350, 530	$\exp(-A_T B_T)$ $B_T = \frac{c_p\rho u)_w}{c_p\rho u)_e \times St_o}$ A_T=1.7 for He, 0.64 for Air, 0.32 for CO_2 and 0.2 for Freon
Brunner (38)	Cone	Yes	No	Air	N_2,He,H_2O	.002 to .06	1.4×10^6	2.5	2040*	$(1+2/9\ Fc_p^*/St_o)^{-3}$ $c_p^* = (c_{pc}/c_{p\infty})^{0.6}$ Stewart
Mickley & Davis (39)	Flat Plate	No	Pressure	Air	Air	0 to .01	4×10^4 to 3×10^6	0	Ambient	Compared with theory of Rubesin
Bartle & Leadon (40)	Flat Plate	Yes	Pressure and Temperature	Air	N_2	0 to .0016	1×10^6 to 5×10^6	2.0,3.2	42.5,73.6	Compared with theory of Rubesin Dorrance and Dore and van Driest
Tewfik (41)	Cylinder	No	Pressure	Air	Air	0 to .00312	1×10^5 to 1.1×10^6	0	Ambient	Compared with theory of Rubesin
Danberg (42)	Flat Plate	Yes	Pressure and Temperature	Air	Air	0 to .0025	8×10^6 to 19×10^6	6.7	527*	Compared with theory of Rubesin and van Driest

*Stagnation temperature

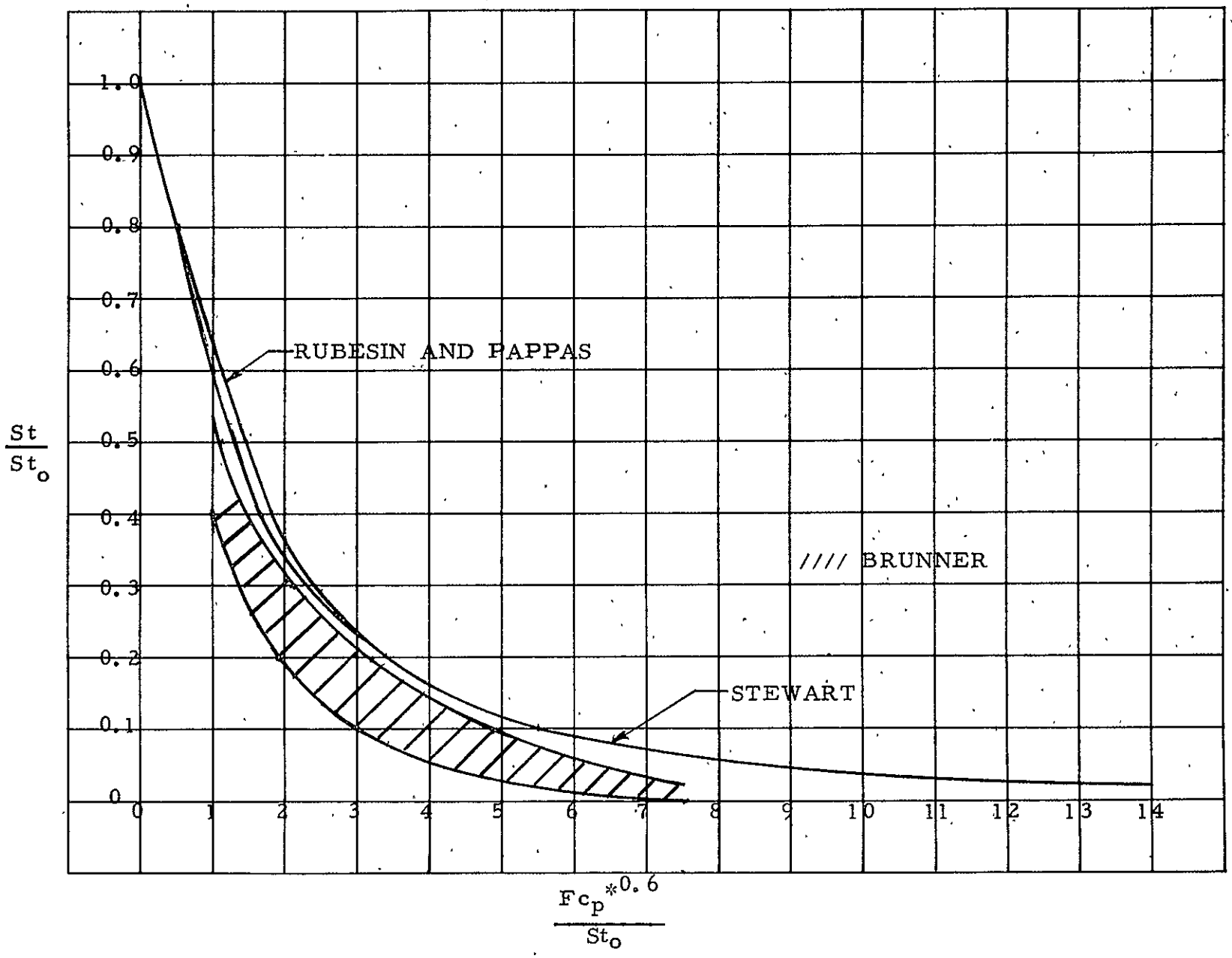


Figure 4.22 Comparison of Experimental Heat Transfer Results for N_2, He, and H_2O Coolants

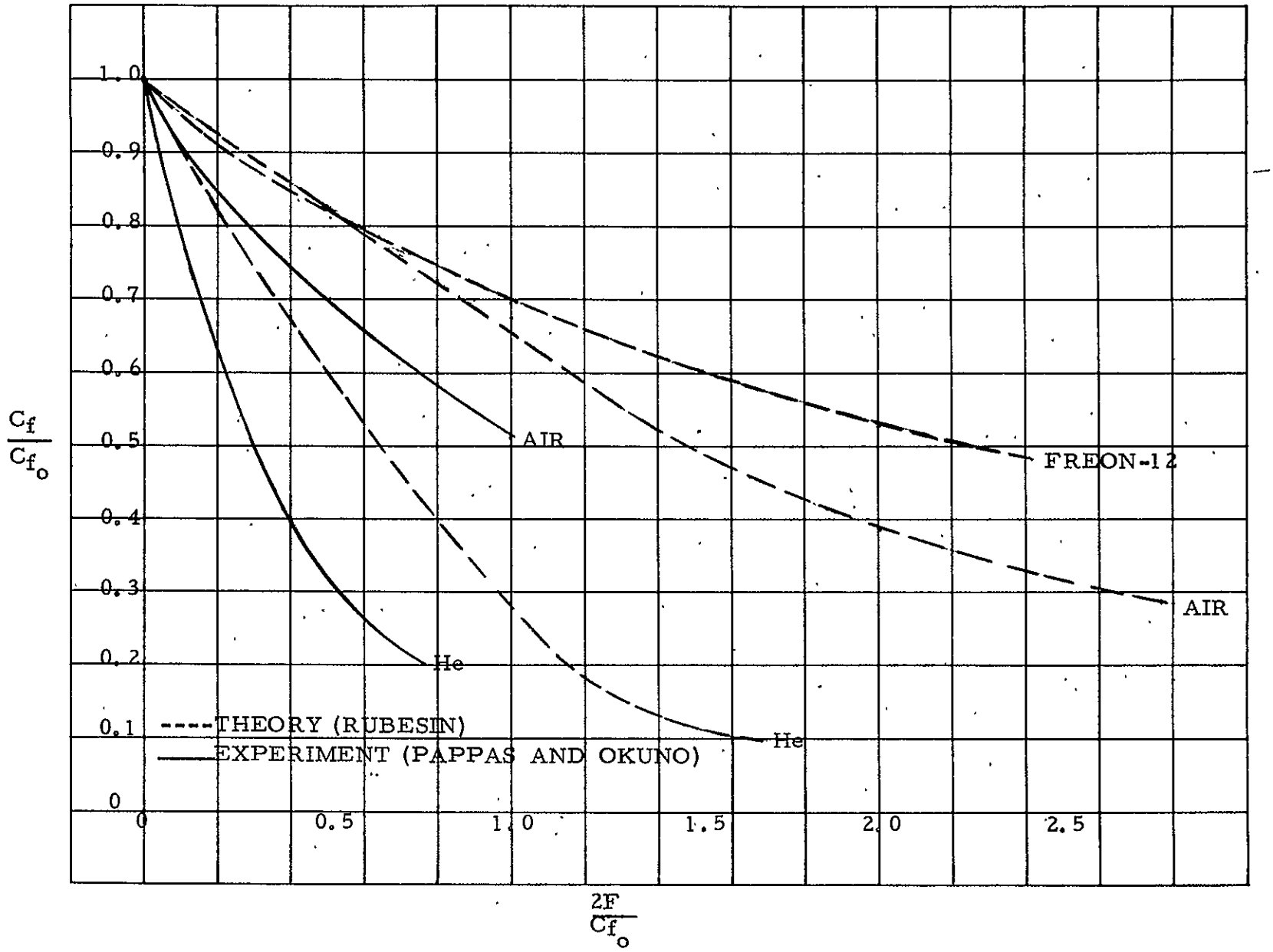


Figure 4.23 Comparison of the Effectiveness of Air and He in Reducing Skin Friction

weight injectants is superior is demonstrated. One of the disturbing consequences of the data of Pappas and Okuno is that air is shown to be superior to Freon-12. Since the specific heat of Freon-12 and air are almost equivalent, one would expect the heating reduction to be similar according to the correlations of Bartle and Leadon, Romaneko and Kharchenko, and Stewart. Since they are not, one might conclude that the effects of molecular weight are more pronounced than specific heat.

It has been found that if the experimental data for the Stanton number and the skin friction coefficient are presented in terms of the ratios St/St_o and C_f/C_{fo} as a function of the dimensionless blowing rate parameter (F/C_{fo} or F/St_o), then the influence of the independent variables, Rex and Tw/Te , and the flow geometry (flat plate, cone, etc.) is satisfactorily eliminated from those correlations.

Pappas and Okuno (36) found that the higher the blowing rate, the more pronounced the effect of Mach number becomes. They also found that the effect of Mach number diminished at hypersonic speeds and in all cases for F/C_{fo} = constant, C_f/C_{fo} either decreased slightly or approached a constant as the Mach number was increased above 4.5 Danberg's (42) results indicated that this indeed was the case. The data of Mickley and Davis (39), Pappas and Okuno (36), and Danberg (42) are presented in Figure 4.24 to illustrate the effect of Mach number on the skin friction coefficient. It should be noted that between a Mach number of 2.5 and 5.0, the effect is relatively insignificant. In the subsonic regions of the curves, the effect becomes somewhat more pronounced. Romanenko and Kharchenko (37) conducted subsonic tests to study the effects of blowing upon both skin friction and heat transfer. Their results for skin friction lie within the range indicated for all other subsonic results except Tewfik's (41). Their results are in general agreement with those of Bartle and Leadon (40) and indicate that the effect of Mach number on

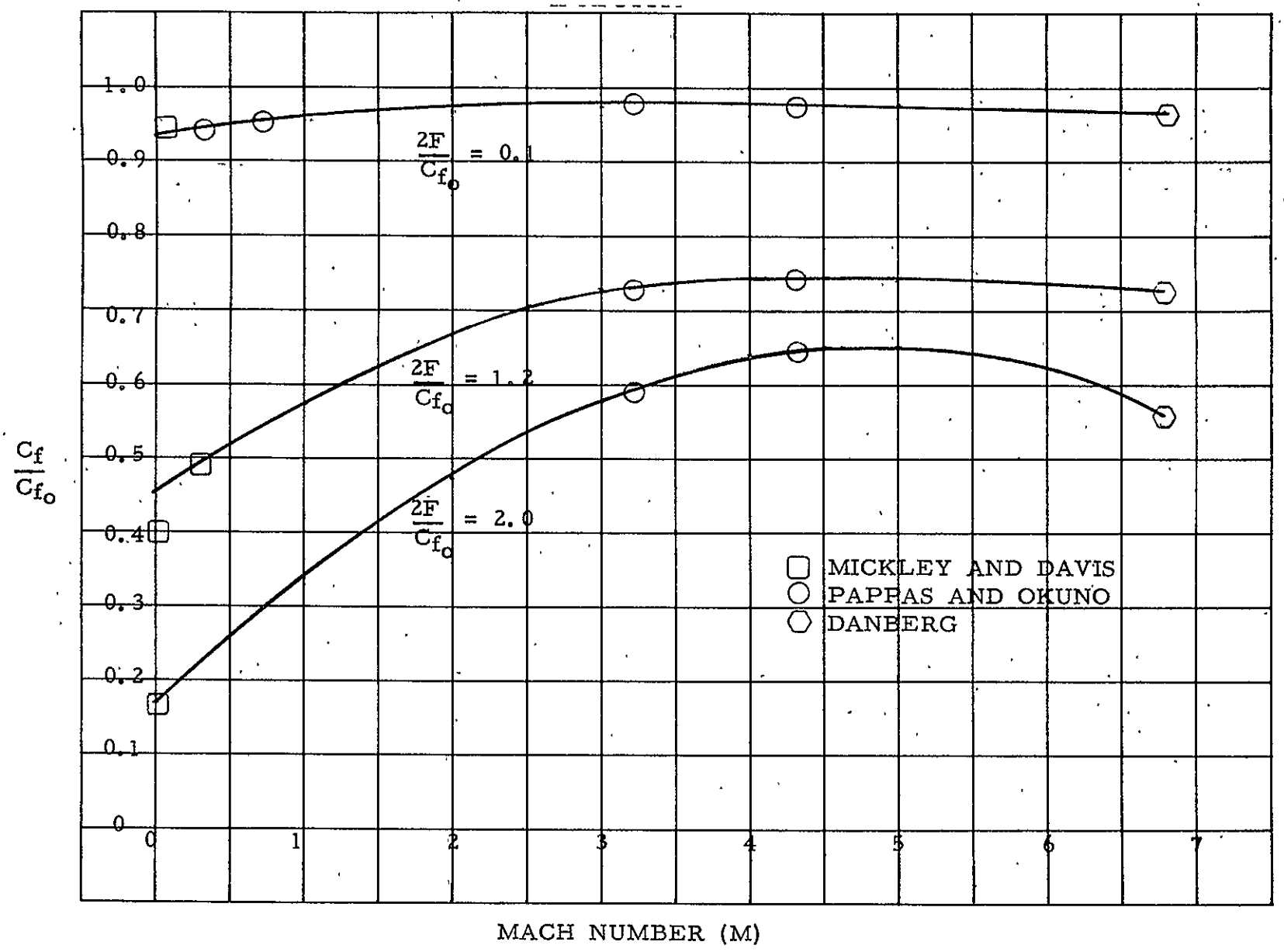


Figure 4.24 Effect of Mach Number on the Reduction in Skin Friction with Air Injection

skin friction coefficient is significant. However, it is also concluded that the effect of Mach number upon the Stanton number ratio is not significant when plotted as St/St_o vs. F/St_o. Fogaroli and Saydah (34) conducted tests in a hypersonic wind tunnel and conclude that the effect of mass injection upon heat transfer is independent of Mach number. Woodruff and Lorenz (35) saw no apparent effects of Mach number on their heat transfer results. It can be concluded that the effect of Mach number on St/St_o is less significant than its effect on C_f/C_{f_o}. In regard to the foregoing conclusion, at high supersonic Mach numbers ($2 < M < 7$), the influence of Mach number on St/St_o or C_f/C_{f_o} has been observed to be minor and the correlation of Spalding et al (50) as well as the theories of van Driest (45) and Rubesin (43) are in good agreement with existing data. On the other hand there is considerable disagreement among the data regarding the influence of Mach number in the low supersonic and subsonic regimes; the results of Tewfik (41) indicate a negligible influence of Mach number on C_f while the data of Mickley and Davis (39), Pappas and Okuno (36), and Romanenko and Kharchenko (37) exhibit a pronounced influence of Mach number.

The effects of a freestream pressure gradient on skin friction and heat transfer have been evaluated experimentally by Romanenko and Kharchenko (37). Again, though a significant influence of a moderate longitudinal pressure gradient on the skin friction coefficient ratio was demonstrated, it has only a negligible influence on the relative reduction in Stanton number.

Fogaroli and Saydah (34) obtained data for air-air injection for blowing rates up to $F/St_o = 20$. They always obtained a finite value for St/St_o and although an asymptotic limit is not that evident, it appears that a value of St/St_o between 0.05 and 0.10 is a reasonable lower bound. They also found that the solution due to Culick (47) fits the data well for the range of mass injection rates. Woodruff and Lorenz (35) present turbulent heat transfer data

using nitrogen, helium, and argon as the injected gases. The maximum value of the blowing rate they obtained was $F/St_o = 18$. Their results are well correlated by an empirical relation due to Bartle and Leadon (48). Again a minimum value of St/St_o appears to be between 0.05 and 0.10.

The numerous theoretical analyses for predicting the influence of mass injection on the heat transfer and skin friction coefficients have exhibited qualitative agreement with the trends indicated by experimental data but there is no theory which adequately accounts for the influence of all variables of importance. The disagreement can be attributed to:

a) inherent limitations of necessarily simplified theoretical analyses; and

b) the limited accuracy and scope of existing experimental data.

The analyses of Rubesin (43), Dorrance and Dore (44), and van Driest (45), are essentially similar. However, each of these analyses requires the calculation of heat transfer as a function of Reynolds number, Mach number, and wall to free-stream temperature ratio. This scheme is not readily adaptable to present thermodynamic analysis techniques. Kelley and L'Ecuyler (46) conclude that the semi-empirical analysis of Spalding, et al (50) provides the most readily applied method for predicting the reduction in heat transfer or skin friction due to mass addition. This analysis is based upon and therefore is representative of the majority of the existing experimental data. Kelley and L'Ecuyler feel that the predictions obtained from this analysis are as accurate (or moreso) than those obtainable from other existing theories. But, utilization of this method requires evaluation of various parameters from tabular solutions and thus is not readily adaptable to present techniques.

Fogaroli and Saydah (34) found that the solution of Culick (47) fits their air-air injection data very well for the range of mass injection rates they attained. The general solution due to Culick can be written in the form:

$$St/St_o = \left[(F/2St_o)^2 + \lambda_w\right]^{\frac{1}{2}} - (F/2St_o) \qquad (17)$$

where λ_w is a function of the ratio of the density-viscosity product of the injectant to the density-viscosity product of the freestream gas. For air-air injection, $\lambda_w = 1$, but for other injectants, λ_w is a function of the concentration of the species at the wall and thus becomes a function of injection rate. For this and other reasons, the solution of Culick is not compatible with present thermodynamic analysis techniques and is not recommended.

Brunner (38) found that his heat transfer results for transpiration cooling with helium, nitrogen, and water were reasonably well correlated by an equation due to Stewart (49). Stewart's equation can be written as:

$$St/St_o = (1 + \frac{2}{9} Fc_p^*/St_o)^{-3} \qquad (18)$$

where $c_p^* = (c_{pc}/c_{p_e})^{0.6}$. This correlation is a reasonable form for engineering use, but a comparison of this equation with the experimental results of Fogaroli and Saydah (34) and Woodruff and Lorenz (35) shows that Stewart's equation overpredicts the heating reduction at the high blowing rates.

Woodruff and Lorenz (35) found that their transfer data for the transpiration cooling of the boundary layer with nitrogen, helium, and argon could be correlated with an expression due to Bartle and Leadon (48). This equation can be written as:

$$St/St_o = \frac{c_{pc}/c_{pe}\ F/St_o}{\left[1 + 1/3\ c_{pc}/c_{pe}\ F/St_o\right]^3 - 1} \qquad (19)$$

It is seen that this equation becomes indeterminant at $F/St_o = 0$. However, comparison of this equation with the experimental data of Fogaroli and Saydah (34) and Brunner (38) shows that it is a reasonable representation of the data for all blowing rates and if anything, is a bit conservative.

A comparison of the solutions of Bartle and Leadon (48), Culick (47) and Steward (49) is illustrated in Figure 4.25 for the case of air-air injection It is seen that the Bartle and Leadon correlation is conservative with respect to the others while the Stewart correlation is the least conservative. Also shown on this plot is the present equation used in Avco Program 1600. This equation can be written as:

$$\Psi = q_c/q_{c,o} = \exp\ (-f(1 + \alpha f)) \qquad (20)$$

where $f = \eta\ F/St_o$ and η is a transpiration coefficient dependent upon the molecular weight of the injectant. It is seen that the equation presently being used is unconservative at high blowing rates. The value of α used in this equation presently is 0.618 and was obtained as a fit to transpiration data for values of F/St_o to approximately 1.0. It is seen that for this range of blowing rates, the equation is a reasonably good representation.

In comparing the solutions of Bartle and Leadon, Culick, and Stewart, it is concluded that the relation of Bartle and Leadon is the best representation that can be made of the present experimental data. There is some doubt as to whether the specific heat ratio is the best correlating parameter for foreign gas injection. The Bartle and Leadon curve can be approximated in Avco Program 1600 by simply changing the value of α. Using the present equation, a value of α was found that reasonably represents the Bartle and Leadon curve for air-air injection. Unlike the Bartle and Leadon equation, the effect of foreign gas injection is contained in the term η The value of η was chosen to be:

$$\eta = 0.347\ (M_e\ /M_c)^{0.1} \qquad (21)$$

according to Munson et al (52). Using this value of η, one finds the value of α to be -0.097. The equation has an inflection point and thus is only

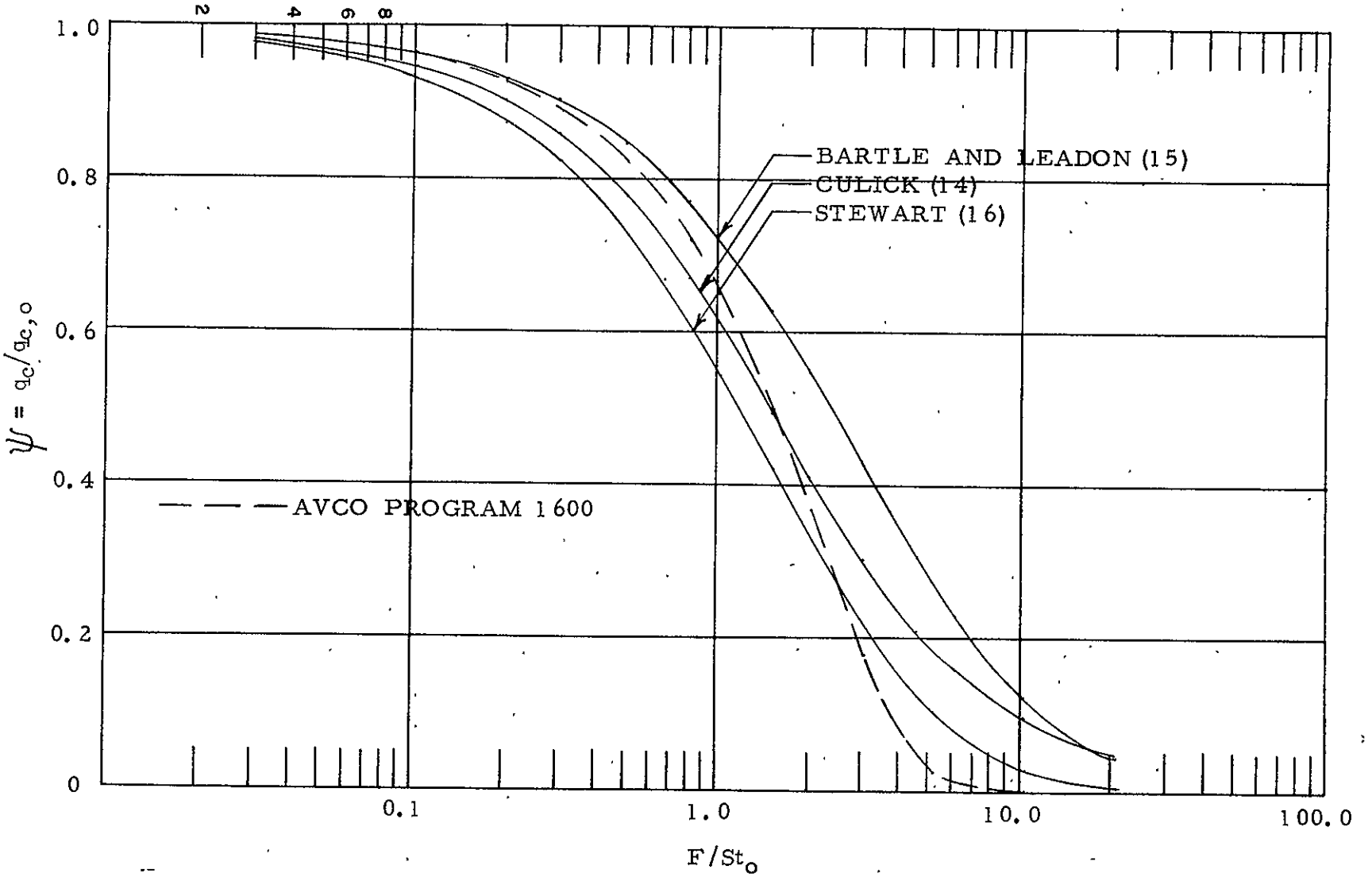


Figure 4.25 Comparisons of Heating Reduction Expressions for Air-Air Injection

applicable in the range of blowing rates from $F/St_o = 0$ to a maximum value of $F/St_o = 14.8$. If it is desired to use an asymptotic limit in the analysis it is possible to find a value of α to fit the Bartle and Leadon curve once the value of the asymptotic limit is specified. Use of an asymptotic limit would require a minor program modification. A comparison of the curve fit with the Bartle and Leadon correlation is illustrated in Figure 4.26.

The study of transpiration cooling of a laminar boundary layer is quite different than that for the turbulent case. Whereas, the turbulent boundary layer is not readily amenable to analysis, the laminar boundary layer is. The result of this distinction has been a multitude of experimental studies of the turbulent boundary layer as contrasted with very limited experimental data for transpiration cooling of a laminar boundary layer. However, extensive analytical solutions have been obtained for continuous and discrete injection into a laminar boundary layer on a flat plate and at an axisymmetric stagnation point.

The results of these studies have been summarized by Gross, Hartnett, Masson, and Gazley (53). The analyses were limited to low blowing rates and the heat transfer results can be correlated as a linear reduction of heating with dimensionless blowing rate (F/St_o). These correlations have been generalized by Mascola (54) for injection of various gases and it is shown that the theoretical results for injection into a laminar boundary layer on a flat plate with zero pressure gradient or at an axisymmetric stagnation point is well represented by the equation presently incorporated in Program 1600.

$$\Psi = \exp(-f(1 + \alpha f)) \qquad (22)$$

where $f = \eta F/St_o$ and $\alpha = 0.618$

and $\eta_{LFP} = 0.764 (M_e/M_c)^{1/3}$

$\eta_{SP} = 0.603 (M_e/M_c)^{1/3}$

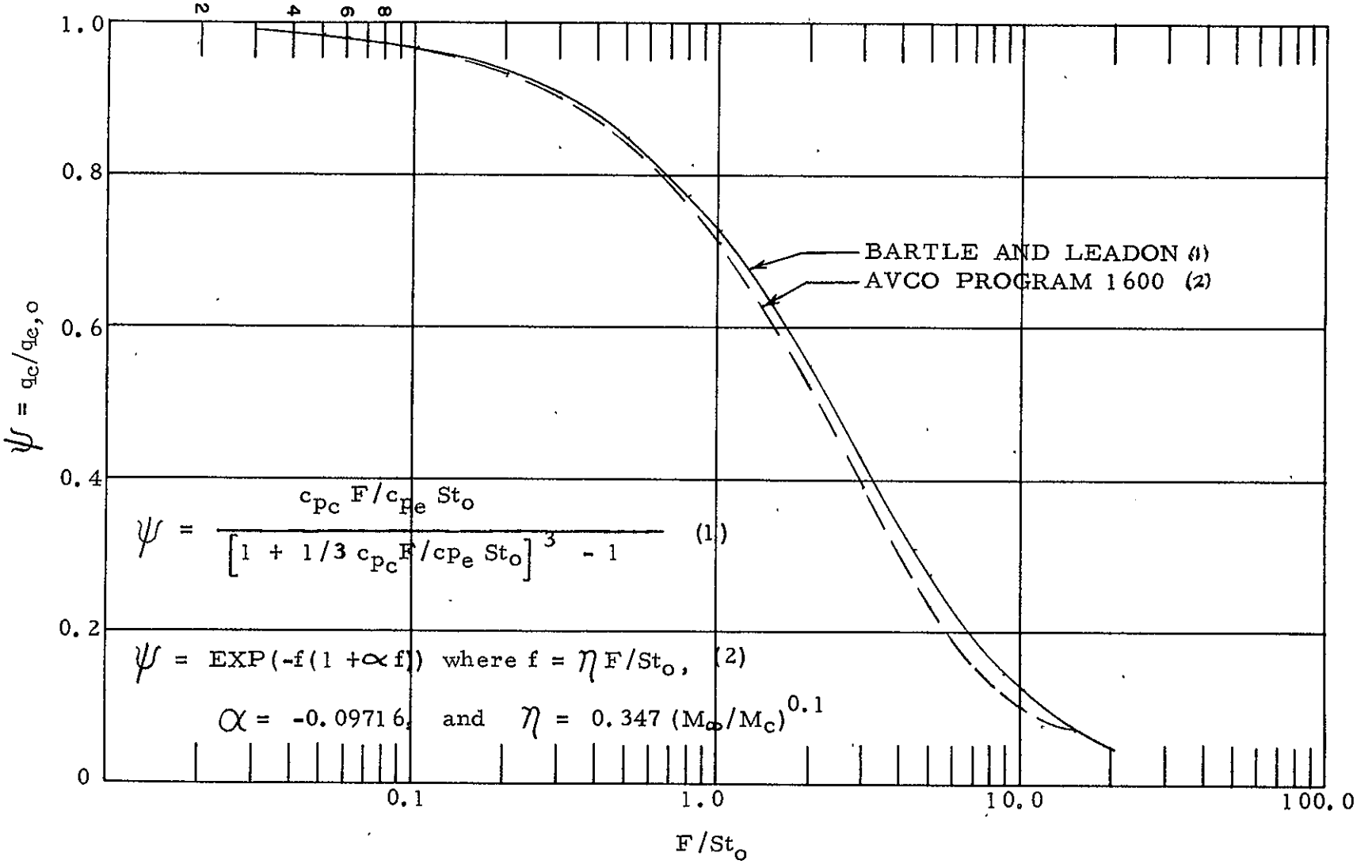


Figure 4.26 Comparison of Turbulent Heating Reduction for Air-Air Injection

The exact solutions for both the laminar flat plate and the stagnation point is compared with the Avco equation in Figure 4.27. Since the tendency of a laminar boundary layer is towards transition to turbulence at moderate blowing rates and separation at high rates, inclusion of a scheme to predict transition in the design analysis would be significant.

4.3.3.3 Summary

The survey of the effects of mass addition on heat transfer and skin friction shows an influence of Mach number on skin friction; a lack of this influence on heat transfer is indicated. The effects of large blowing rates result in limiting $q_c/q_{c,o}$ between 0.05 and 0.10. An empirical value of the blocking parameter used in Program 1600 to describe the effect of mass addition was obtained which matches the data at high blowing rates. The modified value of the blockage factor is more conservative at high blowing rates.

4.4 Survey of Failure Modes

4.4.1 Study Scope and Objectives

The objective of this study on the survey of failure modes was to assess the likelihood of mechanical failure of candidate heat shields for th Venus mission and to identify problem areas. The heat shield materials considered in the study were a carbon phenolic (X6300), a high density ablator and 5026-39/HC-G, the Apollo heat shield material, a low density ablator.

The structural analyses performed on the heat shield systems in the study included a cold-soak thermal stress analysis, a membrane stress analysis considering the combined mechanical and thermal loads associated with entry into the Venus atmosphere, and a detailed stress analysis of the entire aeroshell of the minimum payload probe for the most critical entry condition in terms of combined mechanical and thermal loads.

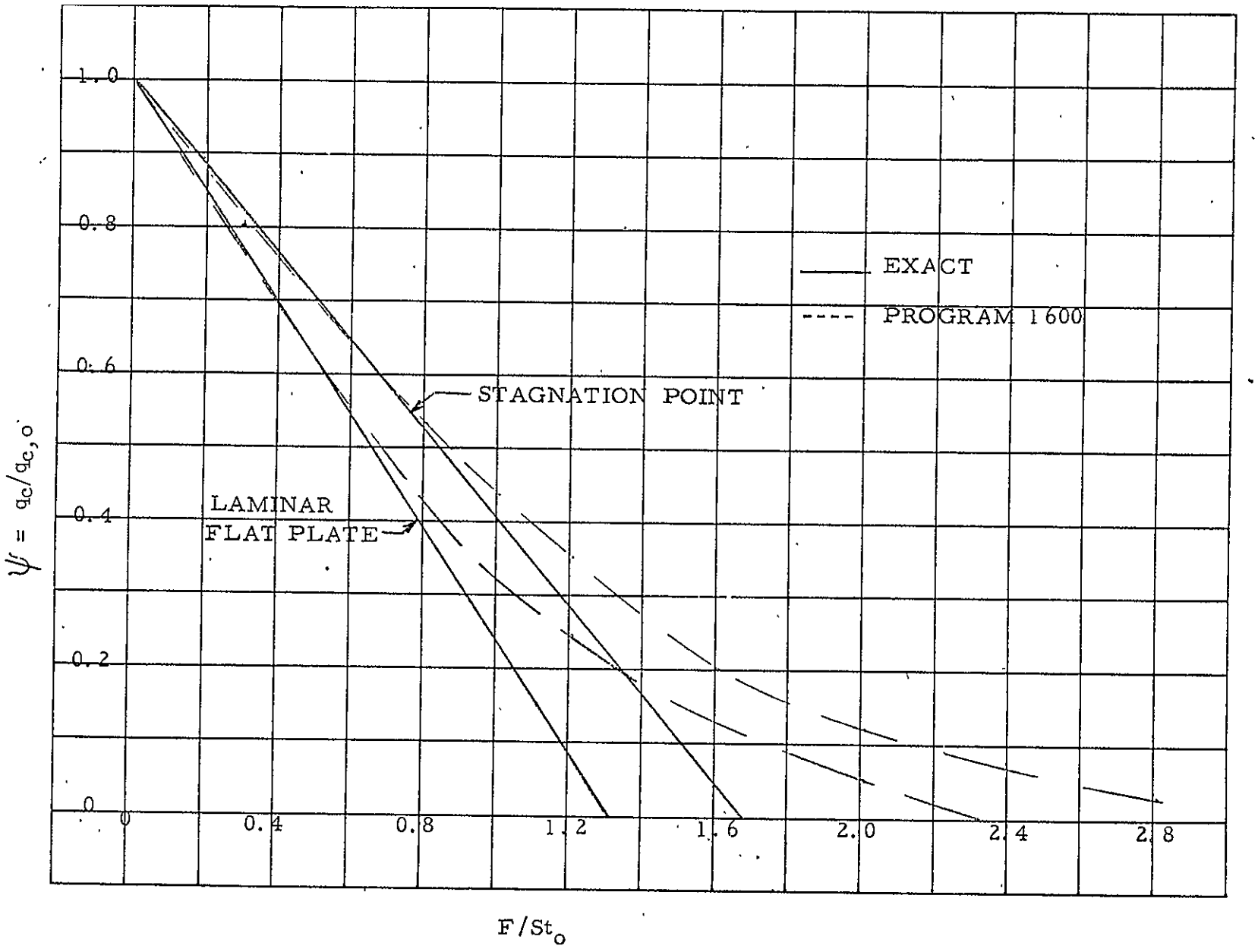


Figure 4.27 Heating Reduction for Laminar Flat Plate and Stagnation Point Air-Air Injection

Although detail bond stress analyses were not performed, some calculations were made to indicate where a problem area may exist; in addition, a general discussion or evaluation of the bond systems is presented based on available data and experience.

Finally, a structural development requirements are presented, as it was apparent from the analyses that were performed, that early development testing was necessary in several areas to ensure the availability of the heat shield system for the Venus mission.

4.4.2 Cold Soak Thermal Stresses

4.4.2.1 Carbon Phenolic (X6300)

Thermal stresses have been computed in the X6300 ablator and in a candidate titanium substructure for a cold-soak, inflight transportation criteria and compared with allowable stresses in order to be assured of the structural integrity of the composite.

The following results were computed from mechanical properties obtained from unsterilized specimens of X6300 (carbon phenolic) tape wound at 20 degrees to the axis. No properties are available for X6300 material that has been subjected for three cycles at thirty-six hours per cycle to 275°F dry heat sterilization. The available properties were primarily obtained at room temperature, 160°F, 300°F, and 500°F; whereas thermal strain was measured over the range of 0°F to 500°F. Since thermal strain data was available between room temperature and 0°F, the mechanical properties for 0°F were either extrapolated to 0°F or taken equal to those at room temperature. Figures 4.28 through 4.30 show tensile modulus, tensile proportional limit, and ultimate tensile strength versus temperature respectively for both the longitudinal and circumferential directions. Figures 4.31 and 4.32 show thermal strain versus temperature in the longitudinal and circumferential directions respectively. Figures 4.33 through 4.35 show compressive modulus, compressive

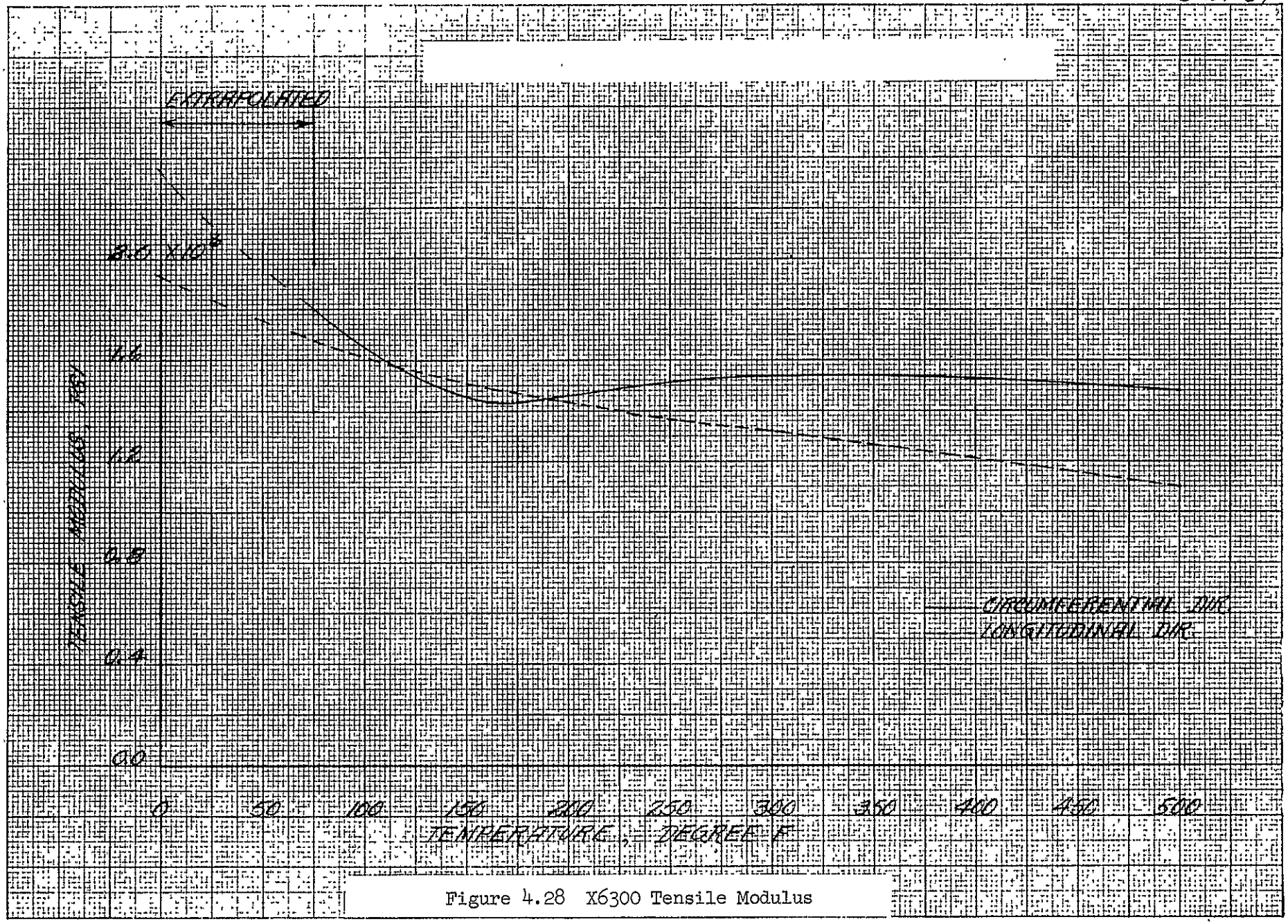


Figure 4.28 X6300 Tensile Modulus

8-24-67

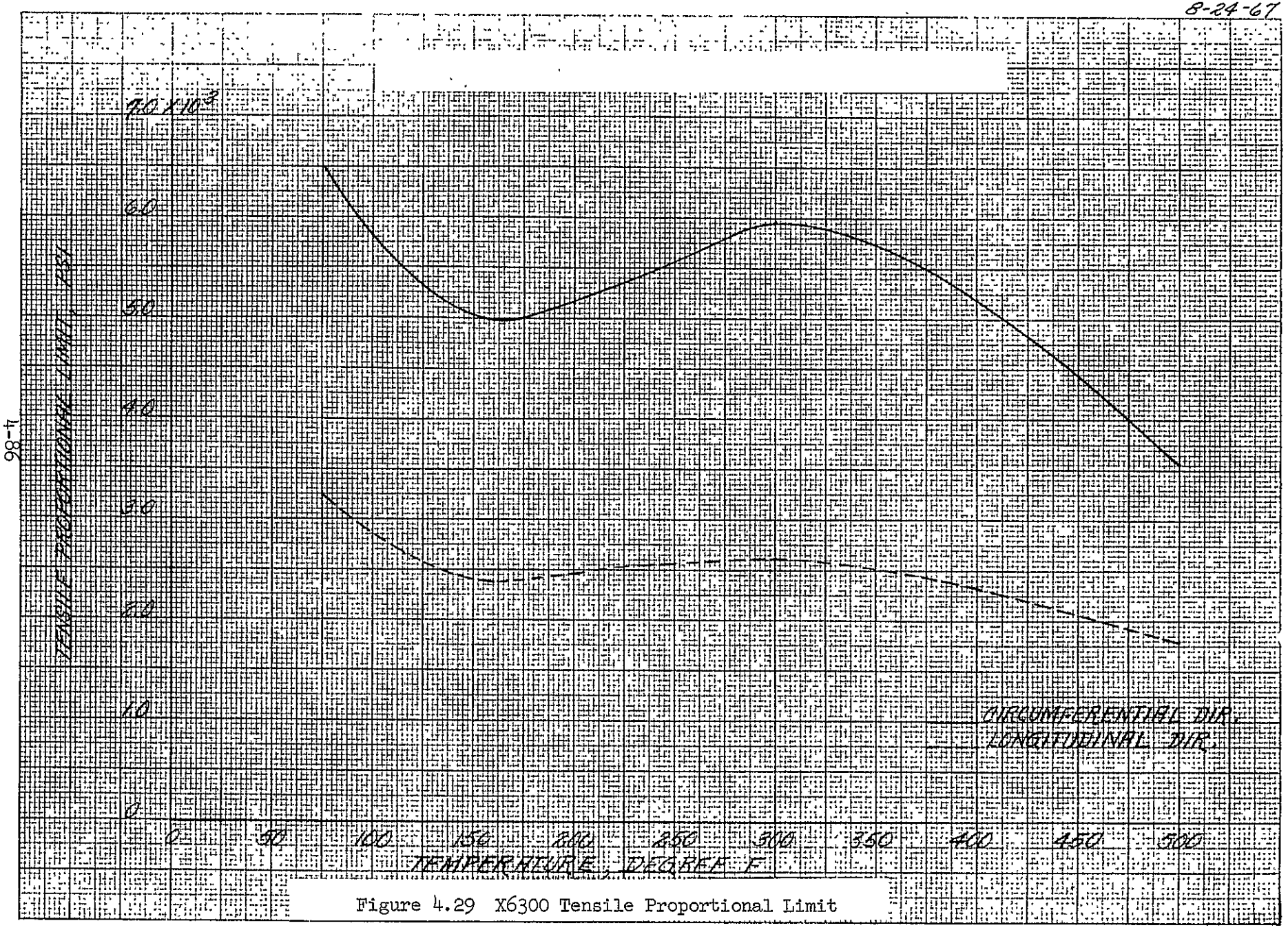


Figure 4.29 X6300 Tensile Proportional Limit

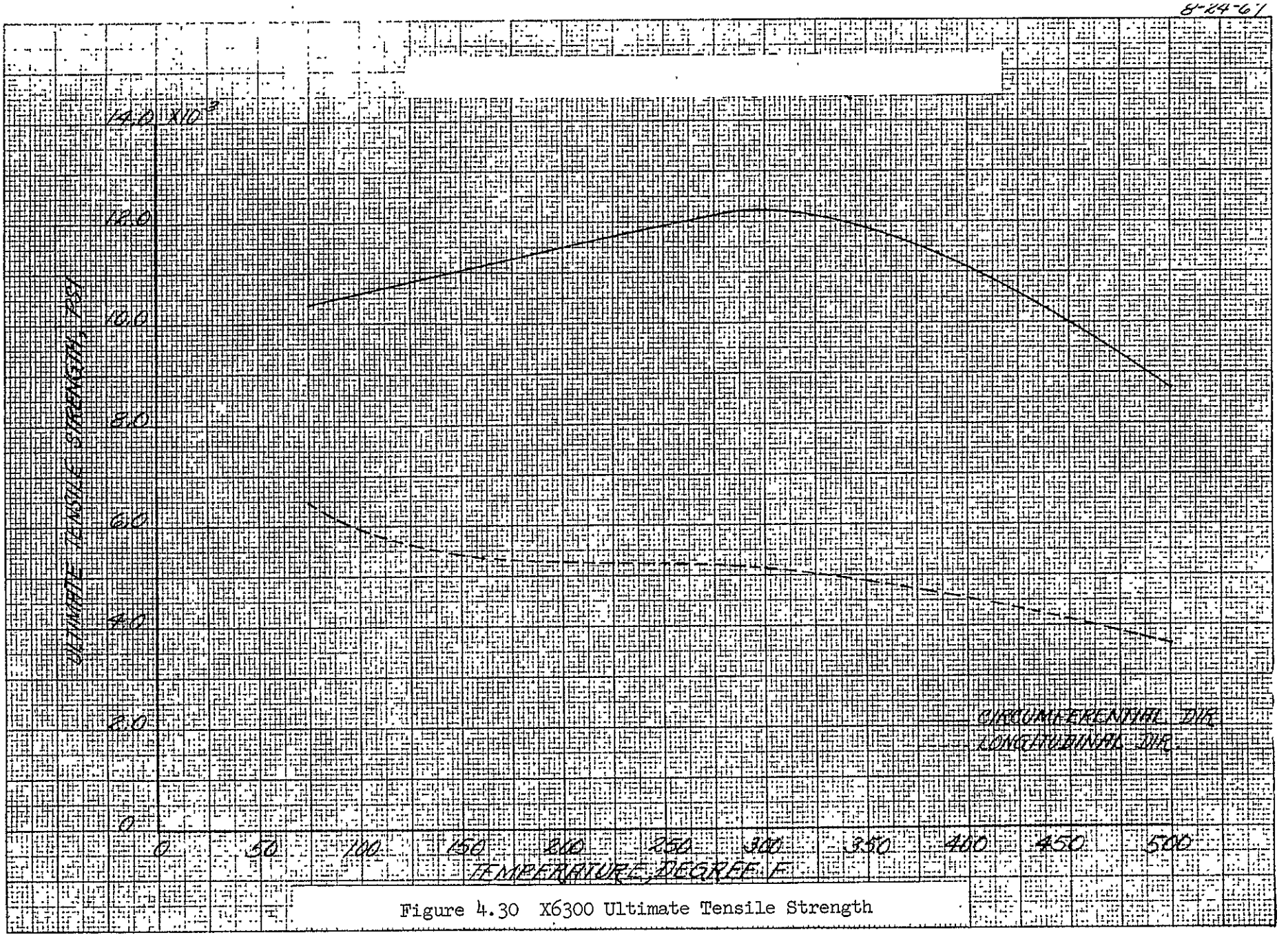


Figure 4.30 X6300 Ultimate Tensile Strength

8-23-67

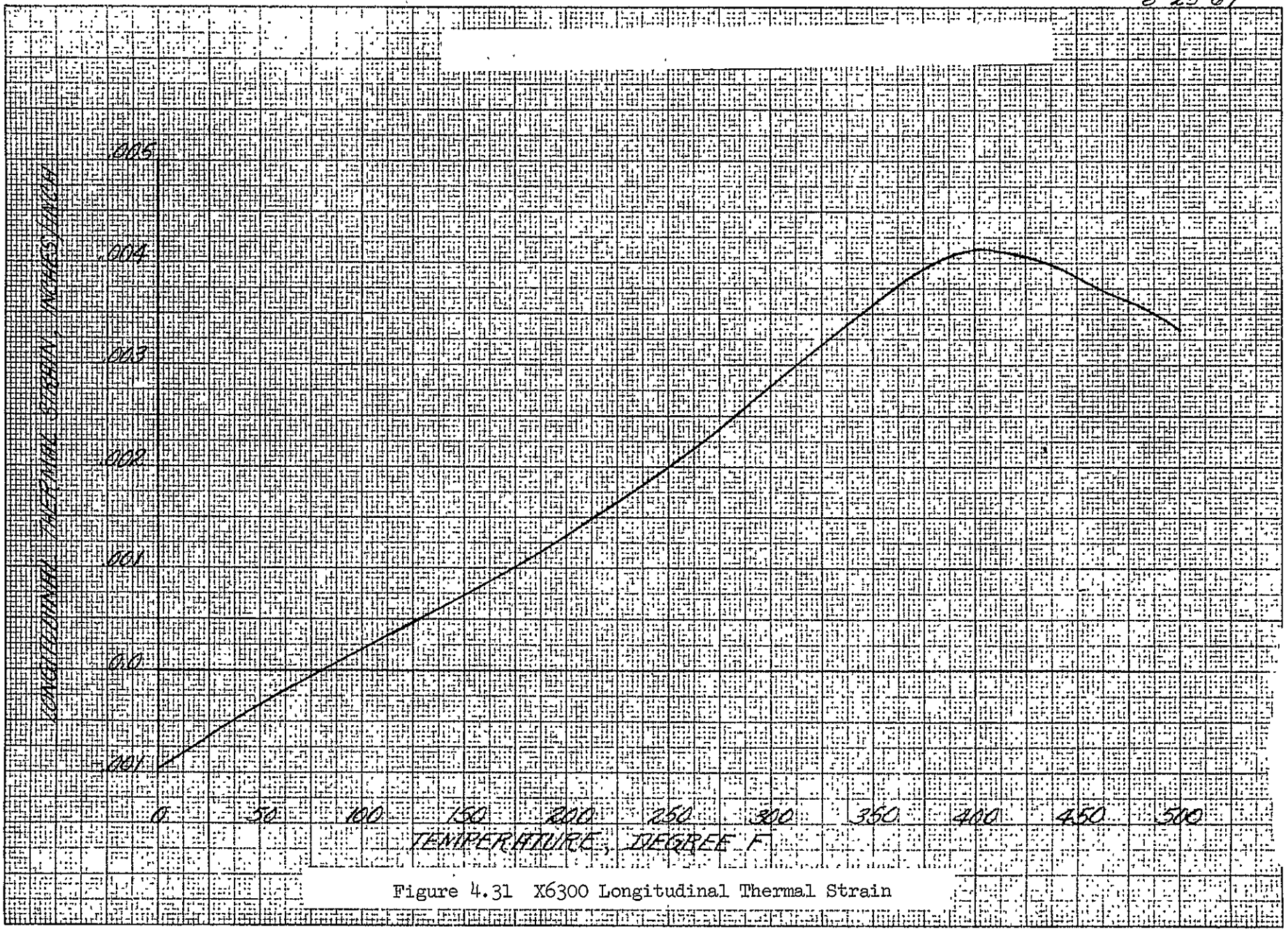


Figure 4.31 X6300 Longitudinal Thermal Strain

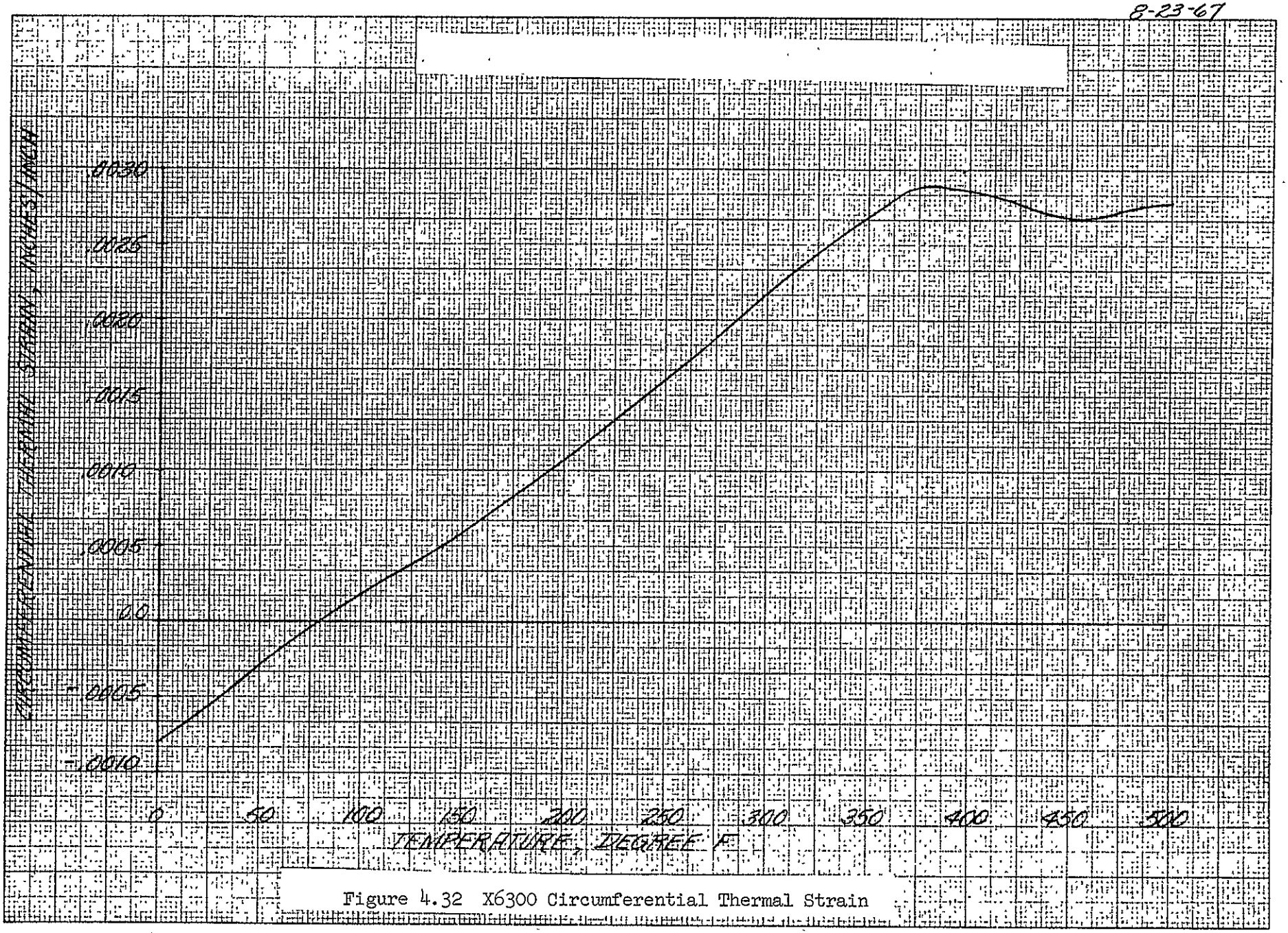


Figure 4.32 X6300 Circumferential Thermal Strain

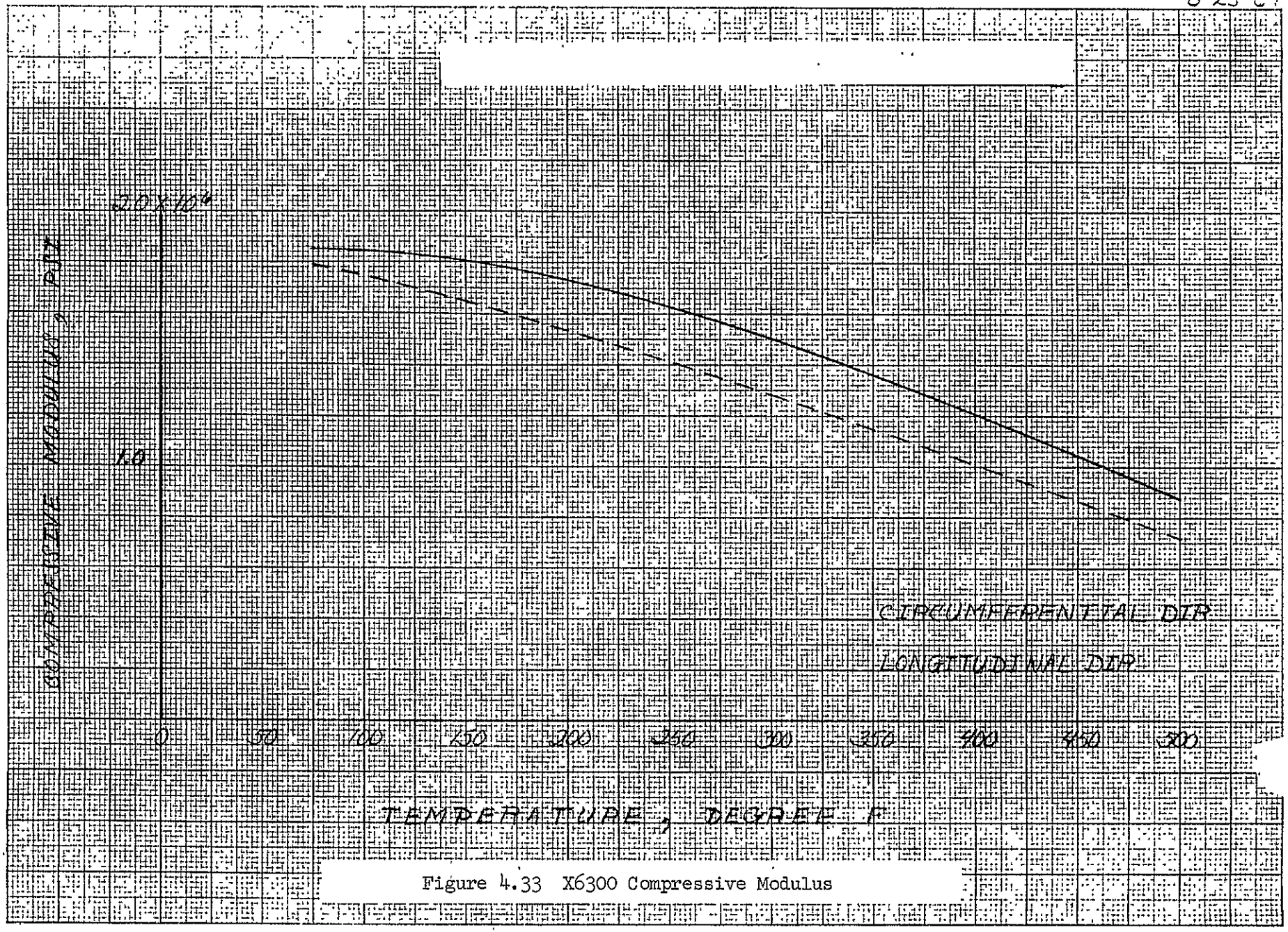


Figure 4.33 X6300 Compressive Modulus

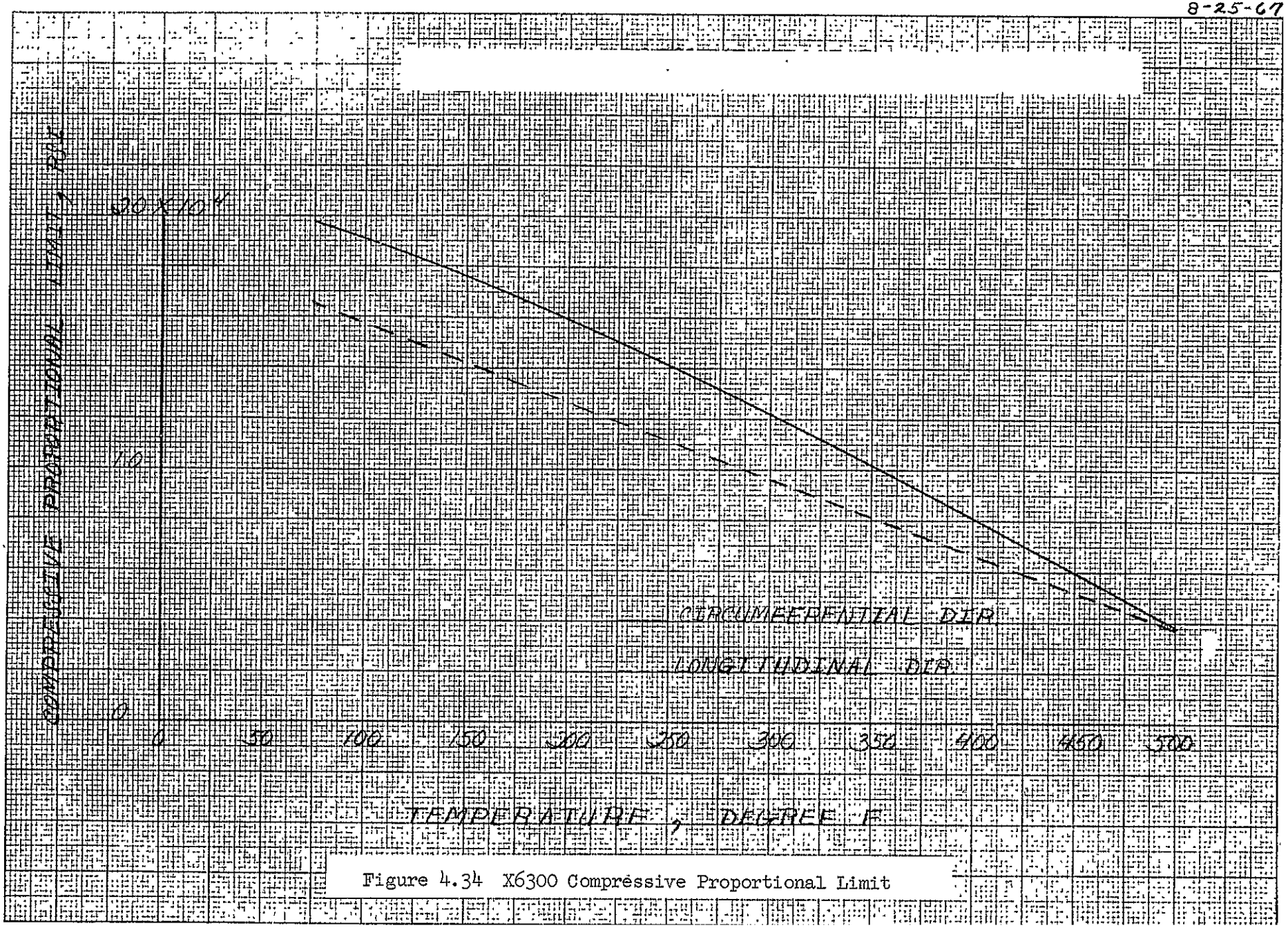


Figure 4.34 X6300 Compressive Proportional Limit

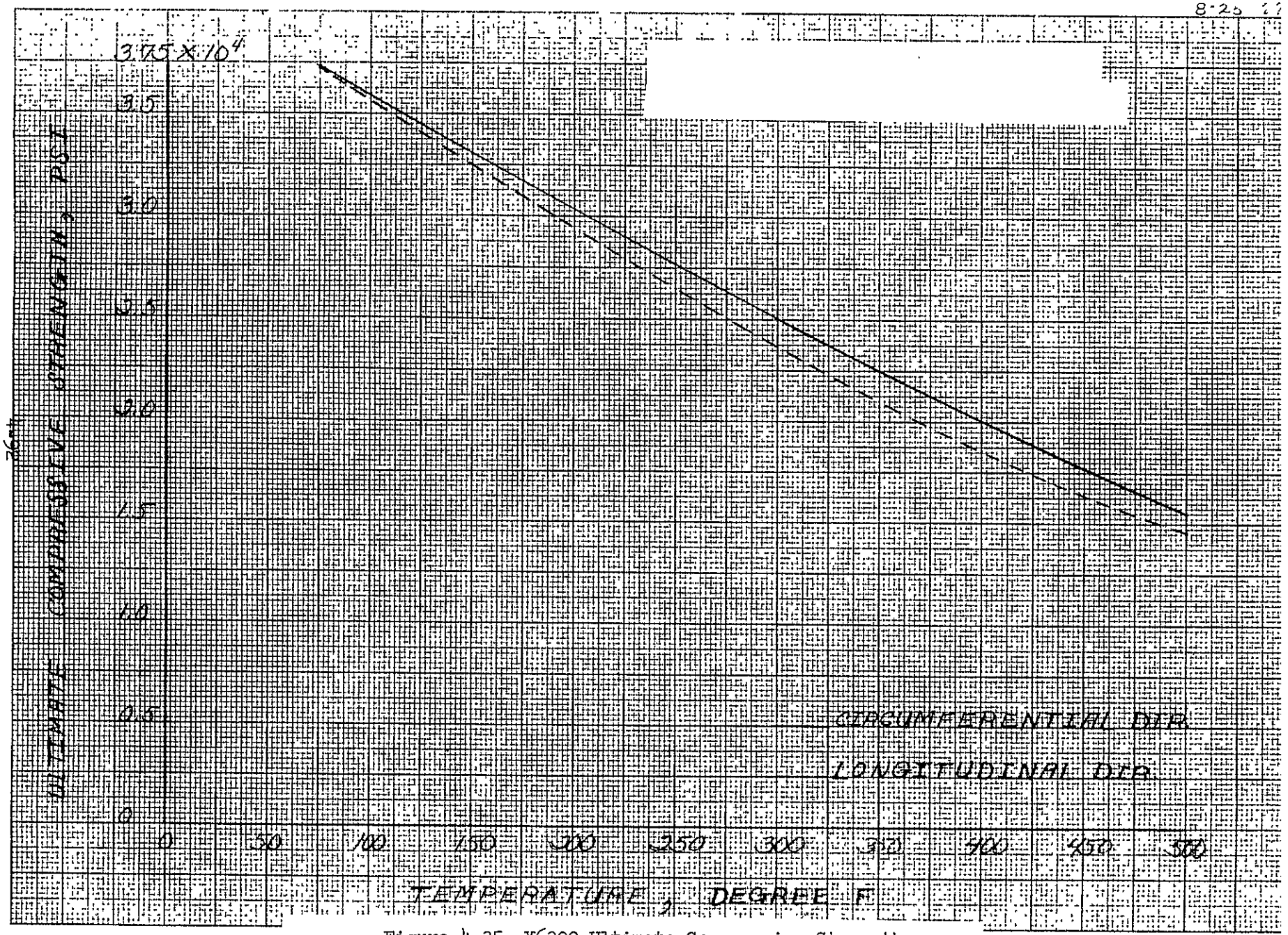


Figure 4.35 X6300 Ultimate Compressive Strength

proportional limit, and ultimate compressive strength versus temperature respectively in both the longitudinal and circumferential directions.

Thermal stresses were computed for a 0°F cold-soak temperature rather than say -100°F because no data has been obtained for X6300 below room temperature and 0°F. The zero stress temperature for the ablator was assumed to be 175°F since the substructure is tape wound at room temperature, and then the temperature of the composite is raised one degree F per minute to 300°F and held for two hours and then allowed to cool. An ablator thickness of one-half inch and a 0.24-inch titanium (Ti-13V-11Cr-3Al) substructure were assumed. The thermal stresses were computed by means of a plate solution with unrestrained curvature.

Figure 4.36 shows a plot of the mechanical thermal strains (a uniaxial solution) in both the longitudinal and circumferential direction. Table 4.12 shows a comparison of the computed with the allowable stresses based on a plate solution. As is apparent from the Table 4.12, the most critical condition for the ablator is in the longitudinal direction where the ratio of the allowable to the computed stress is 2.68. However, it should be pointed out that the allowable is the proportional limit at room temperature rather than at 0°F. The substructure stresses are, of course, negligible.

The thermal stresses in the X6300 ablator were also computed assuming restrained curvature, i.e., zero bending stress. The restrained curvature solution produced uniform ablator tensile stresses of 1390 psi and 810 psi in the longitudinal and circumferential directions respectively. These ablator stress levels, although slightly higher than the maximum levels computed by means of the unrestrained curvature solution are still well within the allowable limits of the X6300 material. The maximum ablator stress of 1390 psi for the longitudinal direction results in a ratio of allowable to computed stress of 2.34.

From these results, it would appear that the X6300 attached to titanium

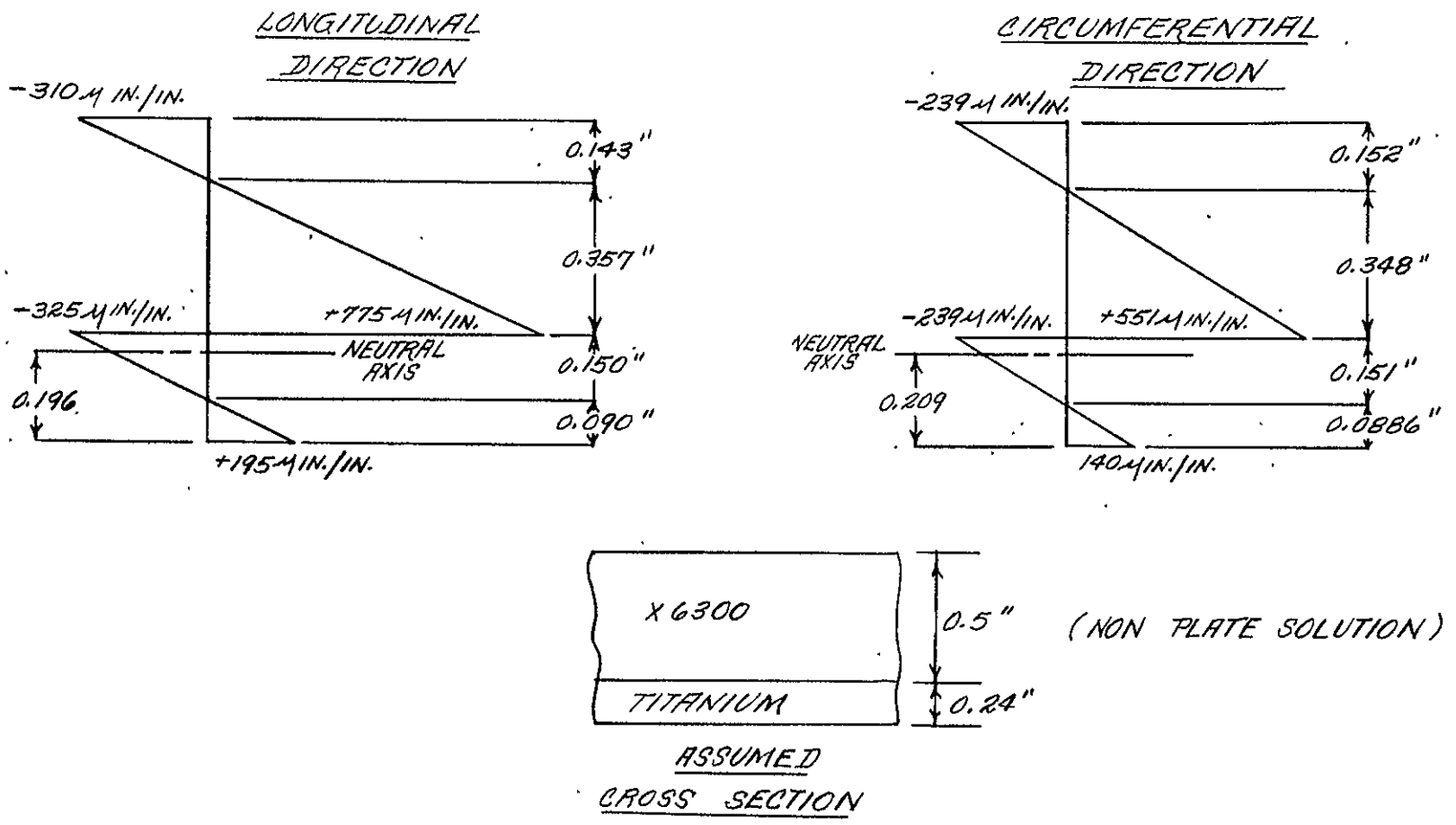


Figure 4.36 X6300 Thermal Strain at 0°F

TABLE 4.12

X6300 Computed and Allowable Cold Soak Stresses at 0°F

ABLATOR STRESSES

Tension or Compression	Direction	σ Computed, psi	σ Allowable, psi	$\frac{\sigma \text{ Allowable}}{\sigma \text{ Computed}}$
Tension	Longitudinal	1,210	3,250(1)	2.68
	Circumferential	766	6,500(1)	8.48
Compression	Longitudinal	477	16,500(1)	34.6
	Circumferential	350	19,800(1)	56.6

(1) Proportional Limit at Room Temperature

TITANIUM STRESSES

Tension	Longitudinal	2,480	170,000(2)	68.5
	Circumferential	1,410	170,000(2)	120
Compression	Longitudinal	4,110	160,000(2)	38.9
	Circumferential	2,450	160,000(2)	65.3

(2) Yield Strength at 0° F

would be structurally sound for a cold-soak criterion of 0°F and a zero-stress temperature of 175°F.

Since the ablator stresses for the cold-soak condition will increase as the zero-stress temperature for the composite increases, the effect of a higher zero-stress temperature than 175°F is considered. The dry-heat sterilization temperature of 275°F is higher than the proposed bond cure temperatures of 200°F and, hence, represents the maximum zero-stress temperature that can exist for the composite. In addition, a cold-soak temperature of 0°F was initially assumed instead of -100°F since extrapolation of material properties to -100°F was considered unreasonable. Based on systems studies, however, the cold-soak limit for the aeroshell during the entire cruise phase now appears to be -20°F. Consequently, the ablator stresses were calculated for a zero-stress temperature of 275°F and a cold-soak temperature of -20°F.

The results are presented in Table 4.13. The maximum levels shown in Table 4.13 are still acceptable based on the stress allowables. The stress allowables used are the proportional limits at room temperature. As seen in Figure 4.29, however, the proportional limits at 0°F and -20°F are probably higher than the room temperature levels, and this would tend to make a comparison of the actual and allowable stresses more conservative when based on room temperature allowables. From these overall results, it would appear that the X6300 attached to titanium would still be structurally adequate for a cold-soak temperature down to -20°F based on a maximum zero-stress temperature of 275°F. A check of ablator stresses for the extreme cold-soak of -150°F and a zero-stress temperature of 275°F indicates that the ablator would not fail based on total strain to failure, but would experience some yielding as the stresses do exceed the proportional limit. However, because of the relatively high rigidity of the X6300 at this low temperature, it is questionable that a hard inflexible bond such as epoxylite (X5403) would survive whereas a soft bond,

TABLE 4.13

X6300 Computed and Allowable Cold Soak Stresses at -20°F

COLD SOAK = -20°F ZERO STRESS TEMPERATURE = 275°F

(a) UNRESTRAINED CURVATURE SOLUTION

TENSION OR COMPRESSION	DIRECTION	$\sigma_{COMPUTED, PSI}$	$\sigma_{ALLOWABLE, PSI}$	$\frac{\sigma_{ALLOWABLE}}{\sigma_{COMPUTED}}$
TENSION	LONGITUDINAL	2050	3250 (1)	1.59
	CIRCUMFERENTIAL	1290	6500 (1)	5.04
COMPRESSION	LONGITUDINAL	805	16,500 (1)	20.50
	CIRCUMFERENTIAL	590	19,800 (1)	33.56

(b) RESTRAINED CURVATURE SOLUTION

TENSION OR COMPRESSION	DIRECTION	$\sigma_{COMPUTED, PSI}$	$\sigma_{ALLOWABLE, PSI}$	$\frac{\sigma_{ALLOWABLE}}{\sigma_{COMPUTED}}$
TENSION	LONGITUDINAL	2350	3250 (1)	1.38
TENSION	CIRCUMFERENTIAL	1365	6500 (1)	4.76

(1) PROPORTIONAL LIMIT AT ROOM TEMPERATURE

would readily deform to absorb the thermal mismatch.

The effect of thinning down or optimizing the X6300 ablator would tend to increase the ablator stresses of Tables 4.12 and 4.13. The reason is that the decrease in extensional rigidity of a thinner ablator would cause it to absorb more of the total thermal growth mismatch between the ablator and substructure.

All computations in this analysis and subsequent entry analysis are based on extrapolated data for unsterilized material; material properties must be obtained for X6300 carbon phenolic (after sterilization) over the full range of temperatures required to evaluate the entire Venus mission.

4.4.2.2 5026-39/HC-G Avcoat

An analysis was performed to determine the mechanical thermal strains in the 5026-39/HC-G ablator for a cold-soak, in-flight criterion of -100°F. The substructure designs considered in the analysis include a ring-stiffened titanium, a ring-stiffened steel, and a steel honeycomb shell. The zero stress temperature for all composites investigated was 185°F, a value established from actual test data in the Apollo Program. The physical and mechanical properties of 5026-39/HC-G, titanium and steel at -100°F are shown in Table 4.14.

The current design properties of 5026-39/HC-G are used in the analysis; however, the requirement for sterilization of the Venus Probe will alter the cure and post cure temperature levels for the 5026-39/HC-G, namely, to increase them by approximately 100°F over present levels to 300°F and 350°F, respectively. In the analysis it was assumed that the modified cure and post cure cycles as well as ETO and dry-heat sterilization would not significantly alter the properties of the 5026-39/HC-G. Preliminary investigations (Ref. 55) indicate that these higher temperature environments may affect the mechanical properties; and, consequently, it is recommended that material testing be

TABLE 4.14

5026-39/HC-G Mechanical Properties at -100°F

MECHANICAL PROPERTY	5026-39/HC-G		TITANIUM	STEEL
	MERIDIONAL	CIRCUMFERENTIAL		
MODULUS OF ELASTICITY, E, LBS./IN.^{2}	$.139 \times 10^6$	$.169 \times 10^6$	15.5×10^6	30×10^6
COEFFICIENT OF THERMAL EXPANSION, α, IN./IN./°F	19.47×10^{-6}	13.68×10^{-6}	4.8×10^{-6}	6.0×10^{-6}
POISSON'S RATIO, ν	0.18	0.15	0.25	0.30

performed to determine the effect of these environments on the current design properties.

The uniaxial (strip) solutions for mechanical thermal ablator strains in both the meridional and circumferential directions are shown in Figures 4.37 to 4.39 for the various substructures investigated. Unrestrained curvature was considered in each case in order to account for the component of strain due to the thermal moment. Figure 4.37 is the case of the .30-inch thick 5026-39/HC-G ablator on a titanium ring-stiffened monocoque substructure; Figure 4.38, the same ablator on a steel ring-stiffened monocoque; and Figure 4.39, on a steel honeycomb structure. The uniaxial strain distribution through the thickness of the composites shown in Figures 4.37 to 4.39 are computed by the elementary formula:

$$\epsilon = \frac{P_T}{\bar{E}\bar{A}} + \frac{M_T Y}{\bar{E}\bar{I}} - \alpha \Delta T \qquad (23)$$

where, for the isothermal cold soak condition

P_T (thermal thrust) = $E_a A_a \alpha_a \Delta T + E_s A_s \alpha_s \Delta T$

M_T (thermal moment) = $E_a A_a \alpha_a \Delta T \bar{Y}_a + E_s A_s \alpha_s \Delta T \bar{Y}_s$

E = modulus of elasticity

A = unit cross-section area

α = coefficient of thermal expansion

ΔT = difference between the actual temperature and the reference zero stress temperature

$\bar{E}\bar{A}$ (total extensional stiffness) = $E_a A_a + E_s A_s$

$\bar{E}\bar{I}$ (total flexural stiffness) = $E_a A_a \bar{Y}_a^2 + A_s E_s \bar{Y}_s^2 + E_a (\bar{I}_a) + E_s (\bar{I}_s$

$\bar{Y}$ = distance from composite neutral axis to centroid of either ablator or substructure

Y = distance from composite neutral axis

Subscripts "a" and "s" refer to ablator and substructure, respectively

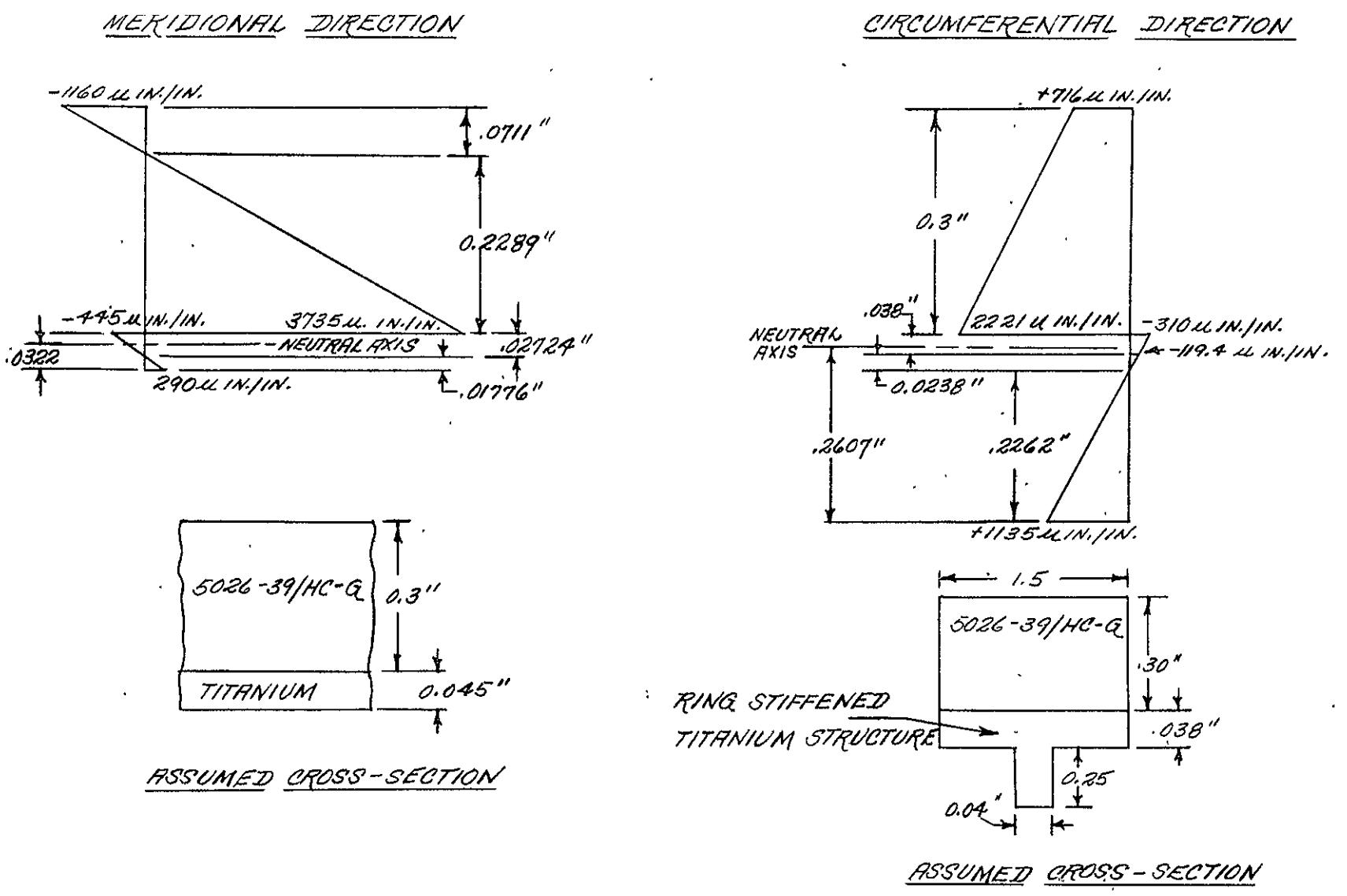


Figure 4.37 5026-39/HC-G Stiffened Titanium Composite Strain Distribution, -100°F

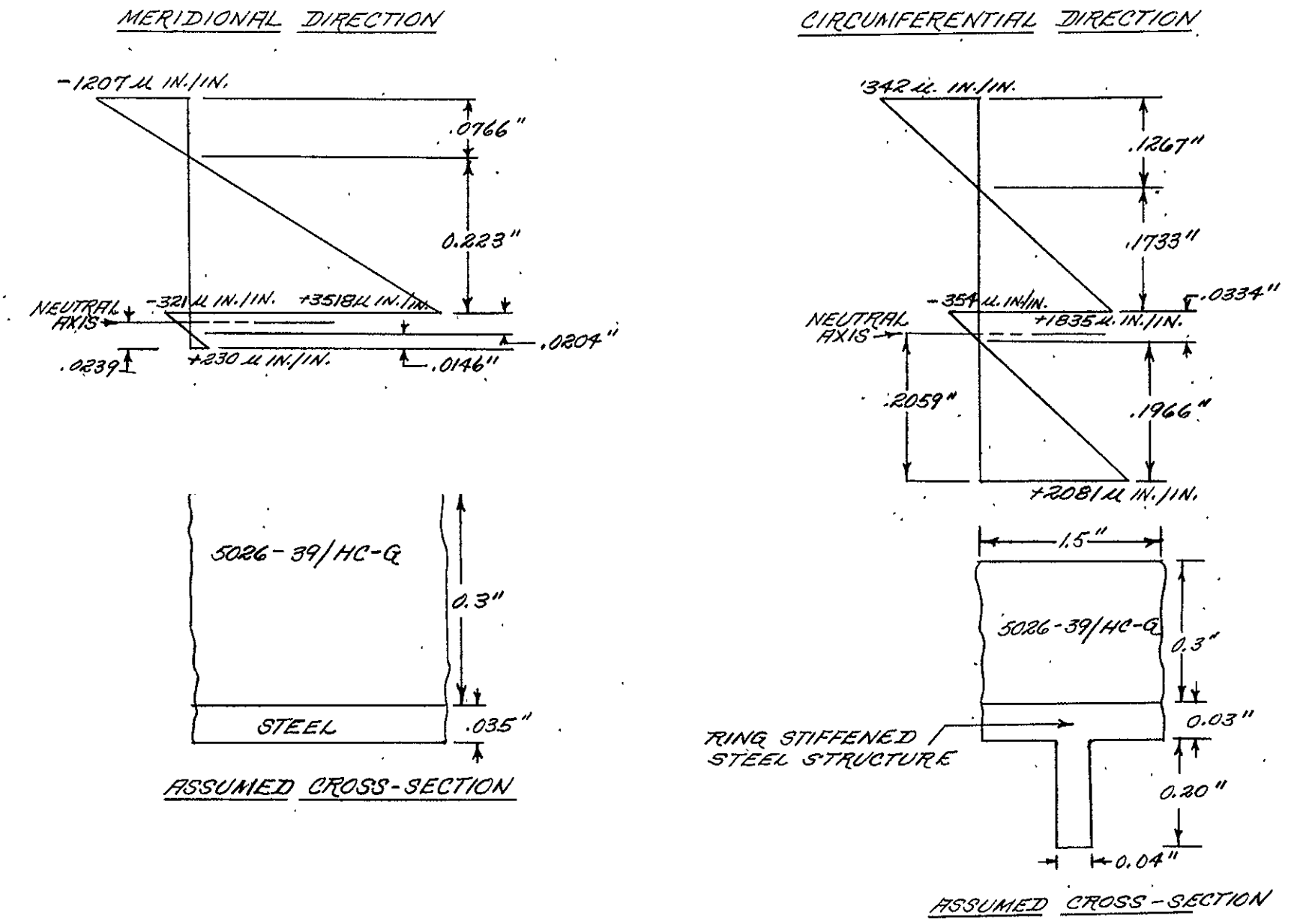


Figure 4.38 5026-39/HC-G Stiffened Steel Composite Strain Distribution, -100°F

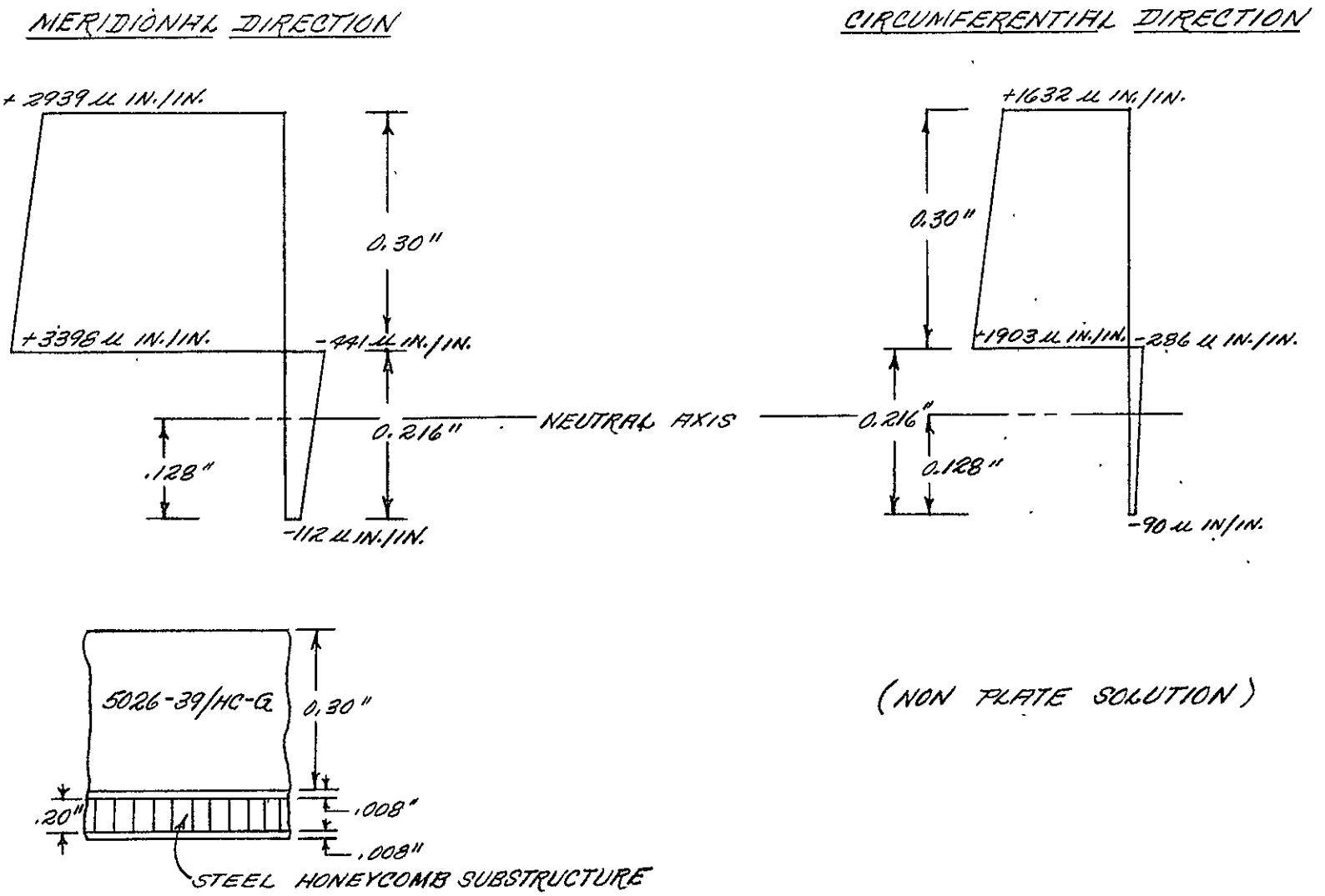


Figure 4.39 5026-39/HC-G Steel Honeycomb Composite Strain Distribution, -100°F

$\bar{I}$ = moment of inertia of either ablator or substructure about its own centroid.

Table 4.15 is a summary of the maximum computed ablator strains for the three composite designs based on a plate solution. The plate solution strains were computed from the uniaxial strains by the expressions

$$\epsilon_\theta = \epsilon_\theta \text{ (uniaxial)} - \nu_{\theta\xi}\, \epsilon_\xi \text{ (uniaxial)}$$

$$\epsilon_\xi = \epsilon_\xi \text{ (uniaxial)} - \nu_{\xi\theta}\, \epsilon_\theta \text{ (uniaxial)}$$

The margins of safety based on ultimate strain to failure are also presented in Table 4.15. The substructure stresses are not tabulated since they are small relative to the yield strengths of the substructure materials.

A check of ablator strains based on the restrained curvature solution, i.e., no bending strain component from thermal moment, produced only slightly higher maximum tensile strains (in general, no more than 5 per cent higher) than the maximum tensile strains given in Table 4.15.

From the results of this study, it appears that the 5026-39/HC-G ablator would survive a cold-soak of -100°F for any of the substructure designs considered. It should also be noted that systems studies indicate that the cold-soak limit for the entire cruise phase of the Venus mission is -20°F rather than -100°F and, hence, the cold-soak analysis performed is very conservative.

In the analysis, it was assumed that the bond system was reliable and would survive a cold-soak of -100°F. For the standard method of bonding, the 5026-39/HC-G ablator to the substructure as specified for the Apollo Program, i.e., bonding the honeycomb to the substructure before gun-filling with ablative material, a high reliability has been demonstrated. Again, because of the sterilization requirement, it is proposed in this program that the ablator would first be fabricated and cured either in large segments or as smaller tiles and then bonded onto the substructure. Since it is not known whether the bond structural characteristics are affected, it is recommended that the

TABLE 4.15

5026-39/HC-G Computed and Allowable Strains at -100°F

SUBSTRUCTURE (MATERIAL & CONSTRUCTION)	RADIAL LOCATION	MERIDIONAL			CIRCUMFERENTIAL		
		COMPUTED STRAIN, %(1)	ALLOWABLE STRAIN, %	MARGIN OF SAFETY (2)	COMPUTED STRAIN, %(1)	ALLOWABLE STRAIN, %	MARGIN OF SAFETY (2)
TITANIUM (RING STIFFENED MONOCOQUE)	OUTER SURFACE	-.13	10.0	A	+.09	.60	A
	INTERFACE	+.33	.57	.727	+.16	.60	A
STEEL (RING STIFFENED MONOCOQUE)	OUTER SURFACE	-.10	10.0	A	-.12	3.25	A
	INTERFACE	+.32	.57	.781	+.13	.60	A
STEEL (HONEYCOMB)	OUTER SURFACE	+.26	.57	A	+.12	.60	A
	INTERFACE	+.31	.57	.838	+.14	.60	A

(1) MINUS SIGN IMPLIES COMPRESSIVE STRAIN
PLUS SIGN IMPLIES TENSILE STRAIN

(2) MARGIN OF SAFETY (M.S.) = $\frac{\text{ALLOWABLE STRAIN}}{\text{COMPUTED STRAIN}} - 1$
AMPLE (A) IMPLIES M.S > 1.0

development program also include cold-soak tests of panels typical of the Venus aeroshell composite in order to substantiate the structural integrity of the actual system for the specified cold-soak environment.

As a final note to this study, restrained curvature calculations were made to determine ablator strains for an extreme cold-soak of -150°F. The results for the 0.3-inch 5026-39/HC-G ablator over the ring-stiffened steel monocoque substructure shown in Figure 4.38 show strains of .362 percent and .17 percent in the meridional and circumferential directions, respectively. The ultimate tensile strains at -150°F for the meridional and circumferential directions are .55 and .58 percent, respectively. These results indicate a minimum margin of safety in the meridional direction of 0.52.

4.4.3 Membrane Stresses Due to Combined Mechanical and Thermal Loads of Venus Entry

A restrained curvature analysis using Avco computer program 1368 was performed for both the low density ablator 5026-39/HC-G and the high density ablator X6300 for critical Venus design entry environments. Program 1368 solves for the thermal membrane stresses and strains in a thin multi-layered shell of revolution subjected to radial temperature gradients and composed of materials which display both orthotropic and temperature-dependent material properties. Additional hand calculations were made to determine the membrane stress and strain components caused by combined aerodynamic pressure and inertia forces and these were superimposed on the Program 1368 thermal strains to obtain the total membrane solution.

4.4.3.1: 5026-39/HC-G Ablator Analysis

For the analysis of the 5026-39/HC-G ablator, the probe aeroshell configuration considered was a 60 degree cone with a basic diameter of 43 inches. The aeroshell entry heating, aerodynamic pressure, and inertia load imposed for the ablator model were representative of the AV-4 atmosphere

and trajectory parameters of V_E = 35,600 fps, γ_E = -50°, and M/C_DA = .15 slugs/ft^2 (Preliminary Design Estimates). This entry model results in the most severe entry loads for the minimum-payload low M/C_DA probe. Three different substructure designs were considered under the .30-inch thick 5026-39/HC-G ablator. These consisted of a ring stiffened steel monocoque shell, which for this study was converted to an equivalent .035-inch steel monocoque shell by equating the extensional stiffnesses, a steel honeycomb with 8-mil face sheets and a .2-inch core, and a ring-stiffened titanium shell which also was converted to an equivalent .045-inch monocoque shell. The actual cross section of the ring-stiffened shell showing the ring dimensions and spacing are shown in the circumferential views of Figures 4.37 and 4.38 for the titanium and steel, respectively. The ring dimensions and spacing shown are based on both general and local instability of the aeroshell for entry pressure loads. The mechanical properties of the 5026-39/HC-G ablator used in the analysis are given in Figures 4.40 to 4.44. Since 5026-39/HC-G is an orthotropic material, two sets of properties are presented; one for the direction oriented parallel to the ribbons of the fiberglass honeycomb and the other for the direction perpendicular to the ribbons. On the probe, the parallel properties apply to the circumferential direction and the perpendicular, to the meridional direction. These properties shown in Figures 4.40 and 4.44 are current design values. However, higher cure temperatures will be required on the Venus program to stabilize the material against the effects of sterilization and these higher temperatures may affect the mechanical properties of the 5026-39/HC-G as preliminary data seem to imply (Reference 55). A test program is required to determine conclusively the effect of sterilization on the mechanical properties of the 5026-39/HC-G.

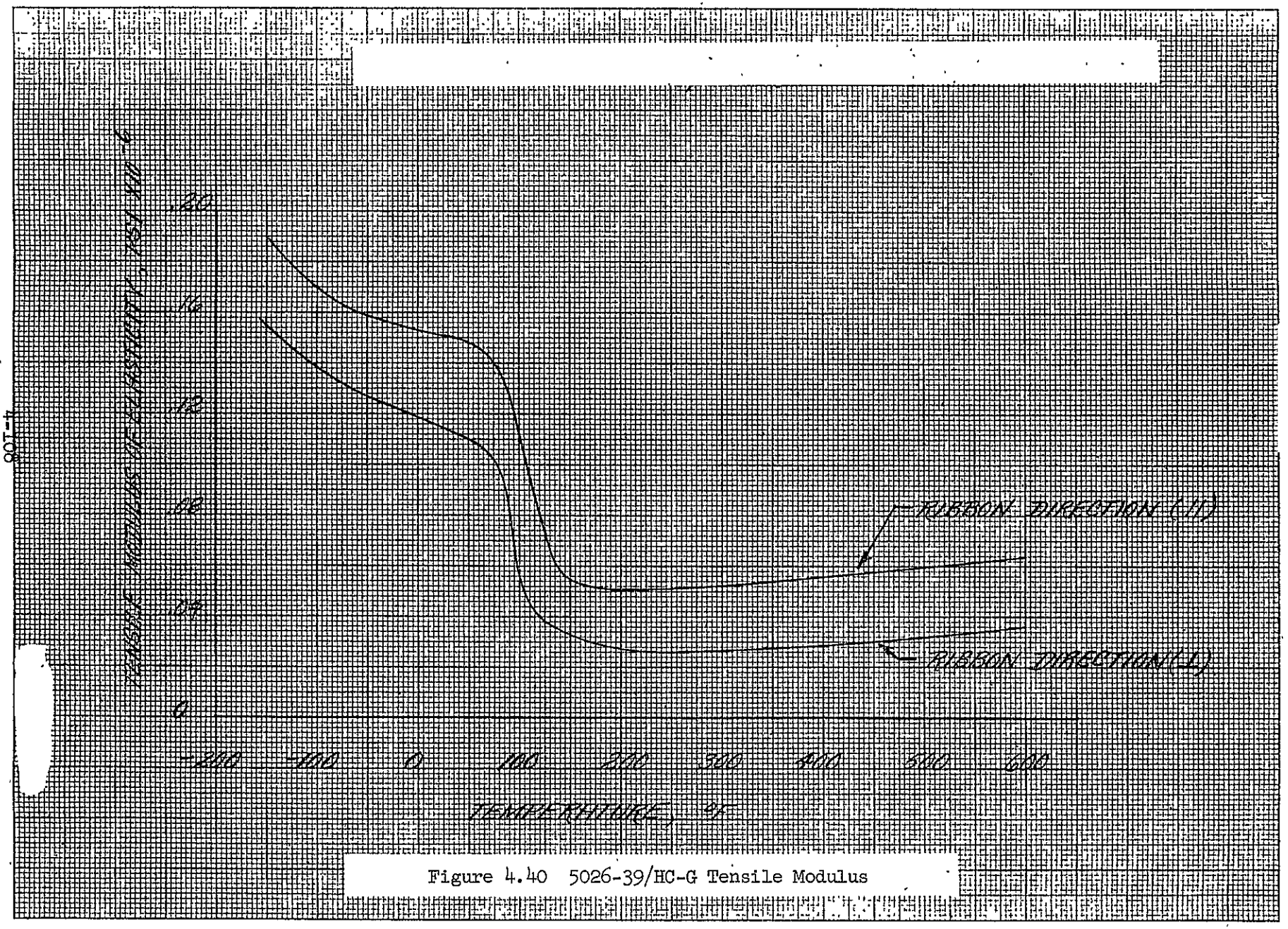


Figure 4.40 5026-39/HC-G Tensile Modulus

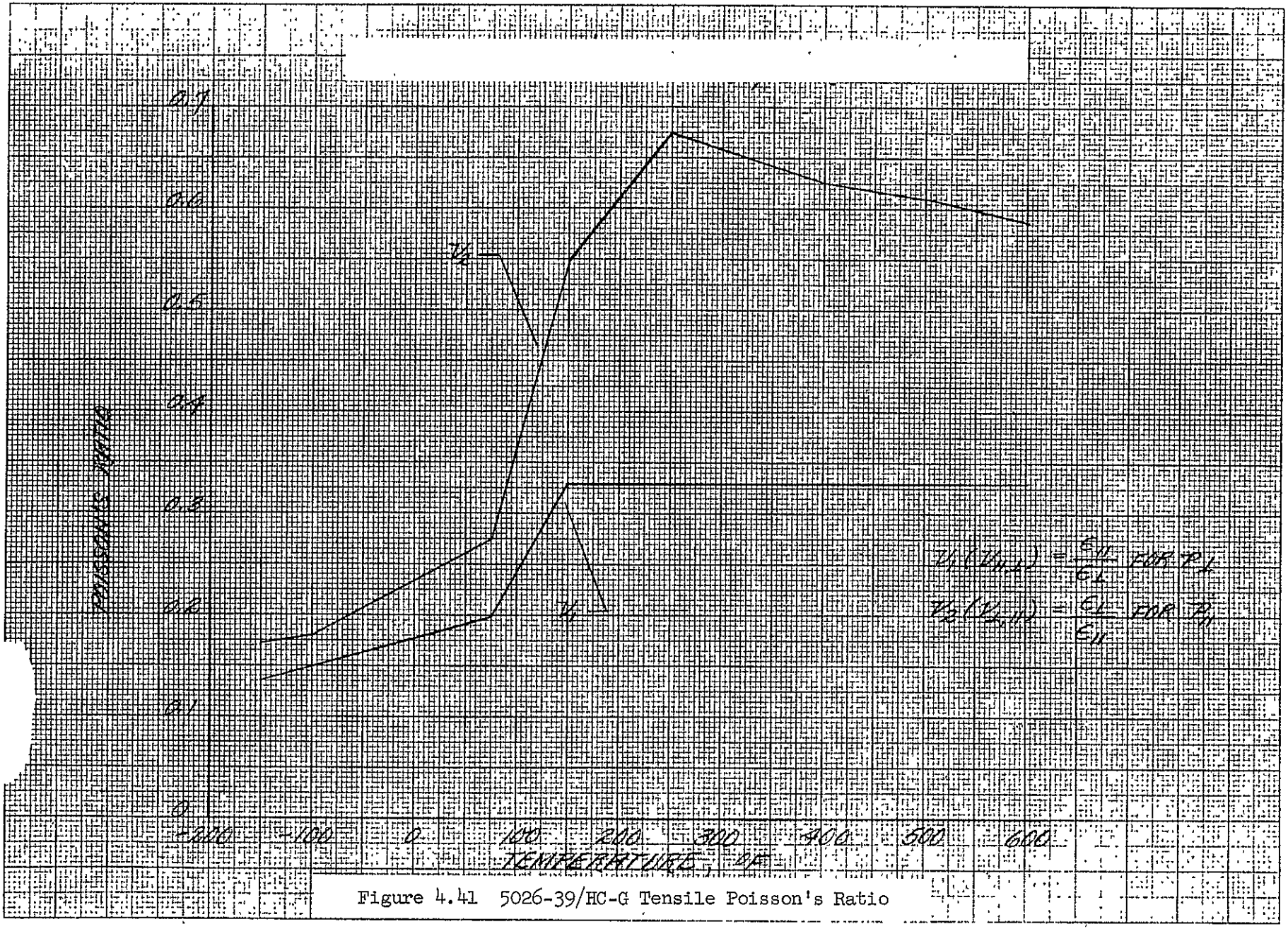


Figure 4.41 5026-39/HC-G Tensile Poisson's Ratio

Figure 4.42 5026-39/HC-G Compressive Modulus

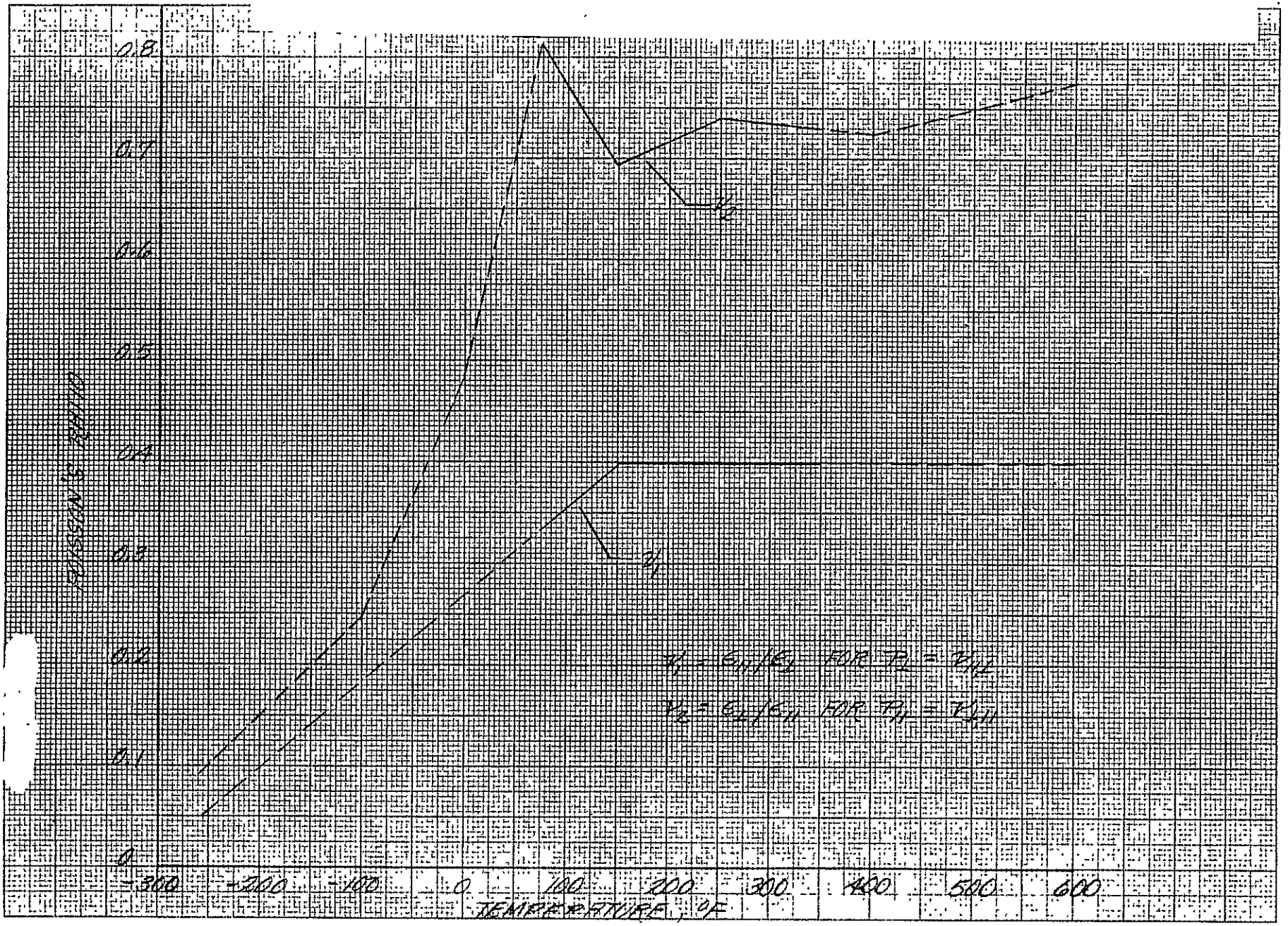


Figure 4.43 5026-39/HC-G Compressive Poisson's Ratio

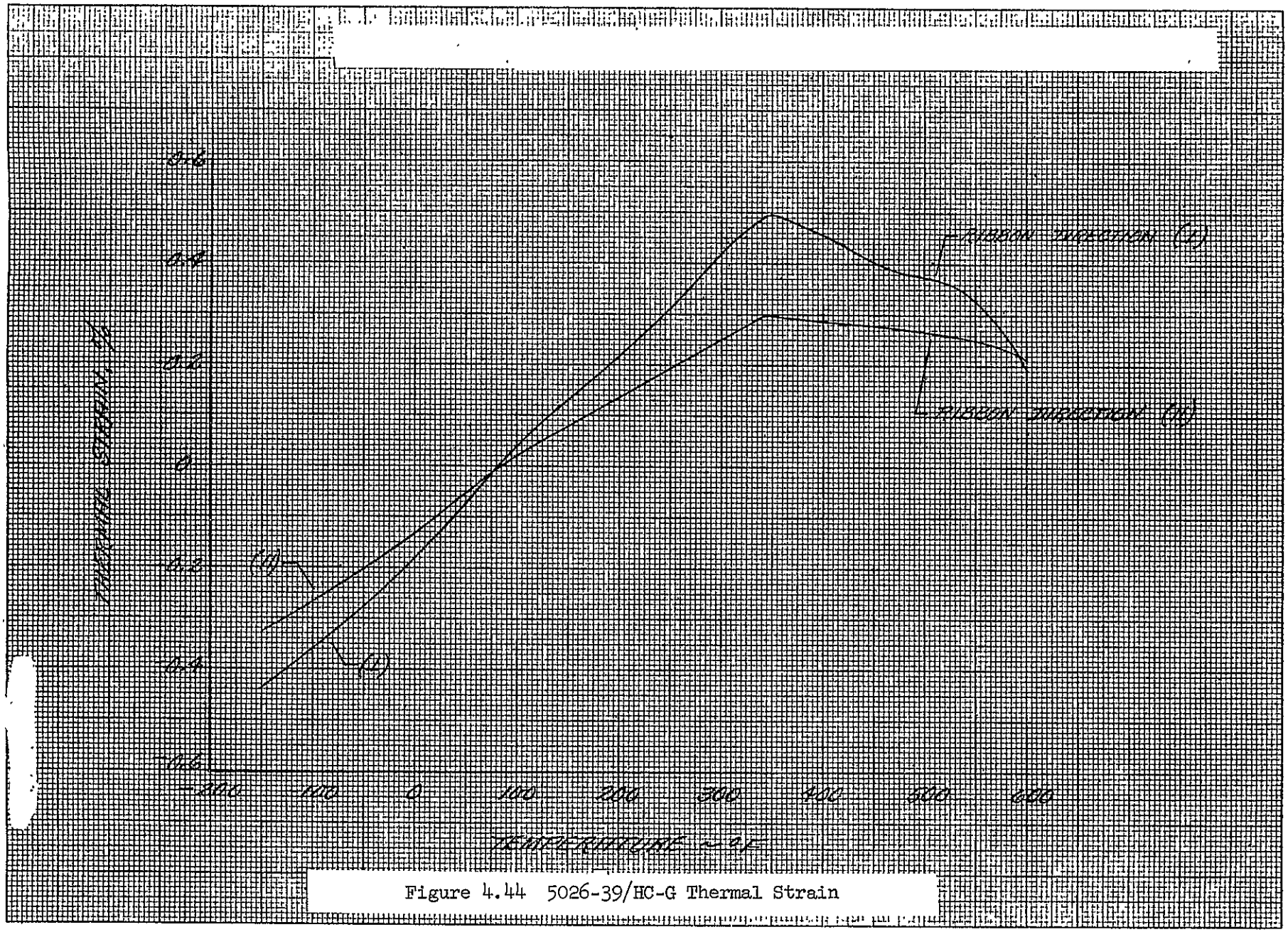


Figure 4.44 5026-39/HC-G Thermal Strain

The initial entry temperature of the 5026-39/HC-G composites was assumed to be 40°F. In the study, two entry times were evaluated, initial heating when the surface temperature reaches or exceeds 600°F and the time of maximum re-entry loads. The temperature profiles in the ablator for these times are shown in Figure 4.45; the same ablator temperature profiles were used for the three different substructure cases as the influence of the substructure on the temperature profiles is negligible. Although these temperature profiles were determined for a station at the base of the cone, they are considered to be a good representation for the overall cone. In addition to the temperature profile for the load condition, the aeroshell was also subjected to a symmetrical external pressure of 20.2 psi and a total payload inertia load of 15,450 pounds distributed uniformly to the shell through the payload support ring which for this analysis was assumed to be at the junction of the spherical nose cap and the cone. This combined loading produces meridional and circumferential membrane forces of 440 pounds/inch and -435 pounds/inch respectively in the aeroshell at the payload support ring. This is the region of maximum membrane force in the meridional direction. On the other hand, the pressure load will produce a maximum membrane force of -865 pounds/inch in the circumferential or hoop direction at the base of the aeroshell.

The components of ablator strains resulting from these maximum membrane forces were superimposed on the mechanical thermal strains to obtain the maximum combined ablator strains for the overall shell. The mechanical thermal strains in the ablator computed by Computer Program 1368 are the result of both the thermal growth mismatch between composite materials and the thermal gradient. The zero-stress temperature for the composite was assumed to be 185°F.

Certain strain components have not been included in this analysis, however, since they are either considered negligible or are unknown. Radial compressive

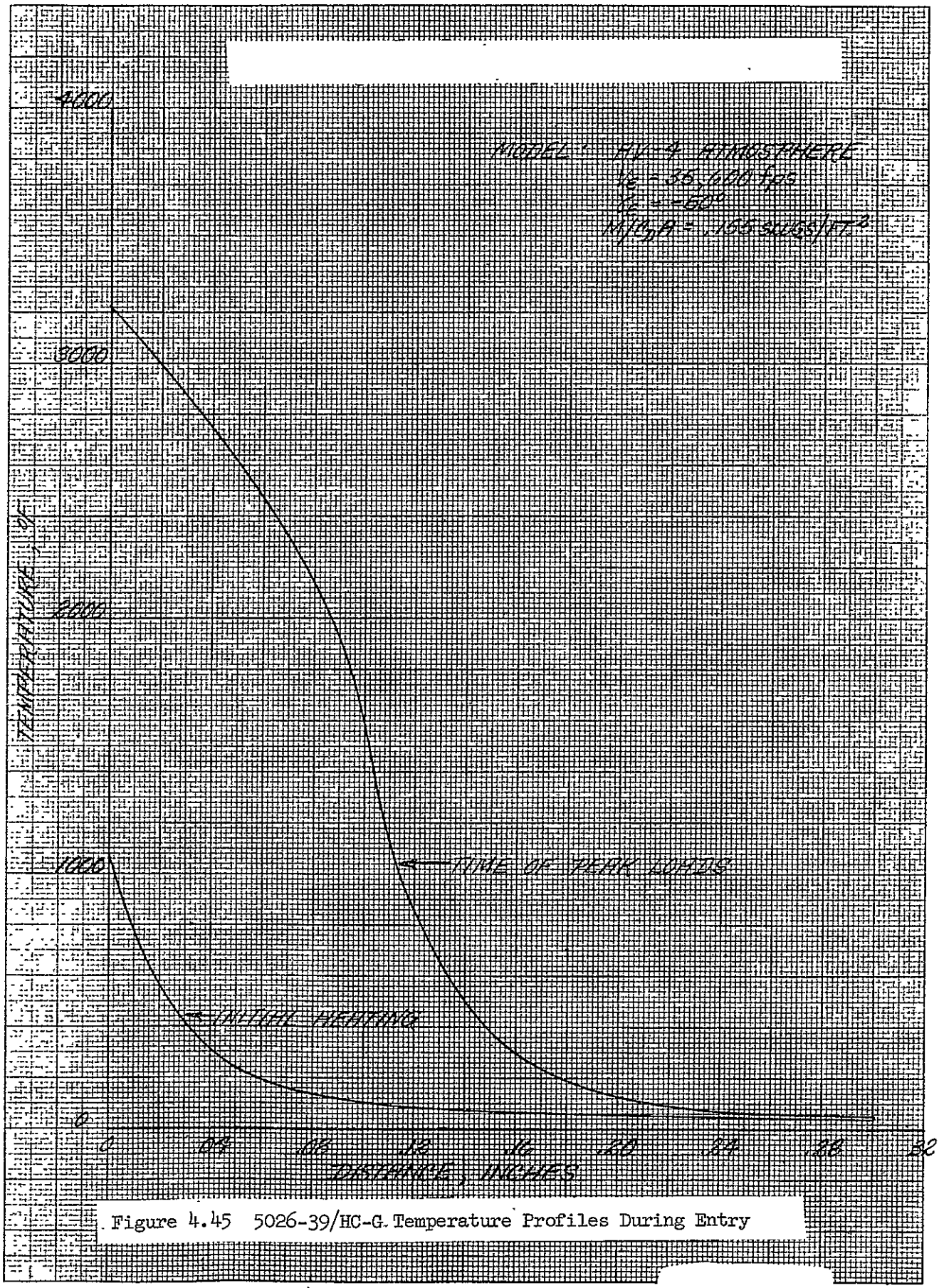


Figure 4.45 5026-39/HC-G Temperature Profiles During Entry

strains due to aerodynamic pressure and aerodynamic shear strains, for instance, are considered negligible. Residual strains due to ablator shrinkage during sterilization are also assumed negligible since the ablator will be stabilized against such effects before attaching to the substructure. The effect of internal pressure due to outgassing of the 5026-39/HC-G and the bond is not known; however, it is not anticipated to be a problem based on Apollo experience. Also, the level of vibrational induced strain is not known since dynamic analysis has not been made of the probe aeroshell. However, in the final design, the aeroshell would be designed such that the minimum shell natural frequency would be higher than the anticipated forcing frequency during entry and consequently no appreciable dynamic response would be expected. The combined strain results are presented in Figures 4.46 to 4.51 in the form of an envelope of maximum total strain versus temperature in the ablator. Figures 4.46 and 4.47 show the envelope of maximum total strain versus ablator temperature in the circumferential and meridional direction respectively for the .035-inch steel monocoque structure design; Figures 4.48 and 4.49, the envelope of maximum total strain in the circumferential and meridional directions respectively for the steel honeycomb design; and Figures 4.50 and 4.51, the circumferential and meridional directions respectively for the titanium substructure design. The envelopes of strain shown in Figures 4.46 to 4.51 include the results of both entry times as well as maximum membrane force effects for the peak load case. Ablator strains for temperatures above 600°F are ignored as 600°F is considered the threshold temperature at which the ablator begins to char and no structural failure criterion other than aerodynamic shear is considered for the char.

The maximum aerodynamic shear force for the minimum payload probe is 9.5 pounds per square foot (psf) whereas the threshold shear limit for the 5026-39/HC-G char before any degradation in normal ablator performance is approximately

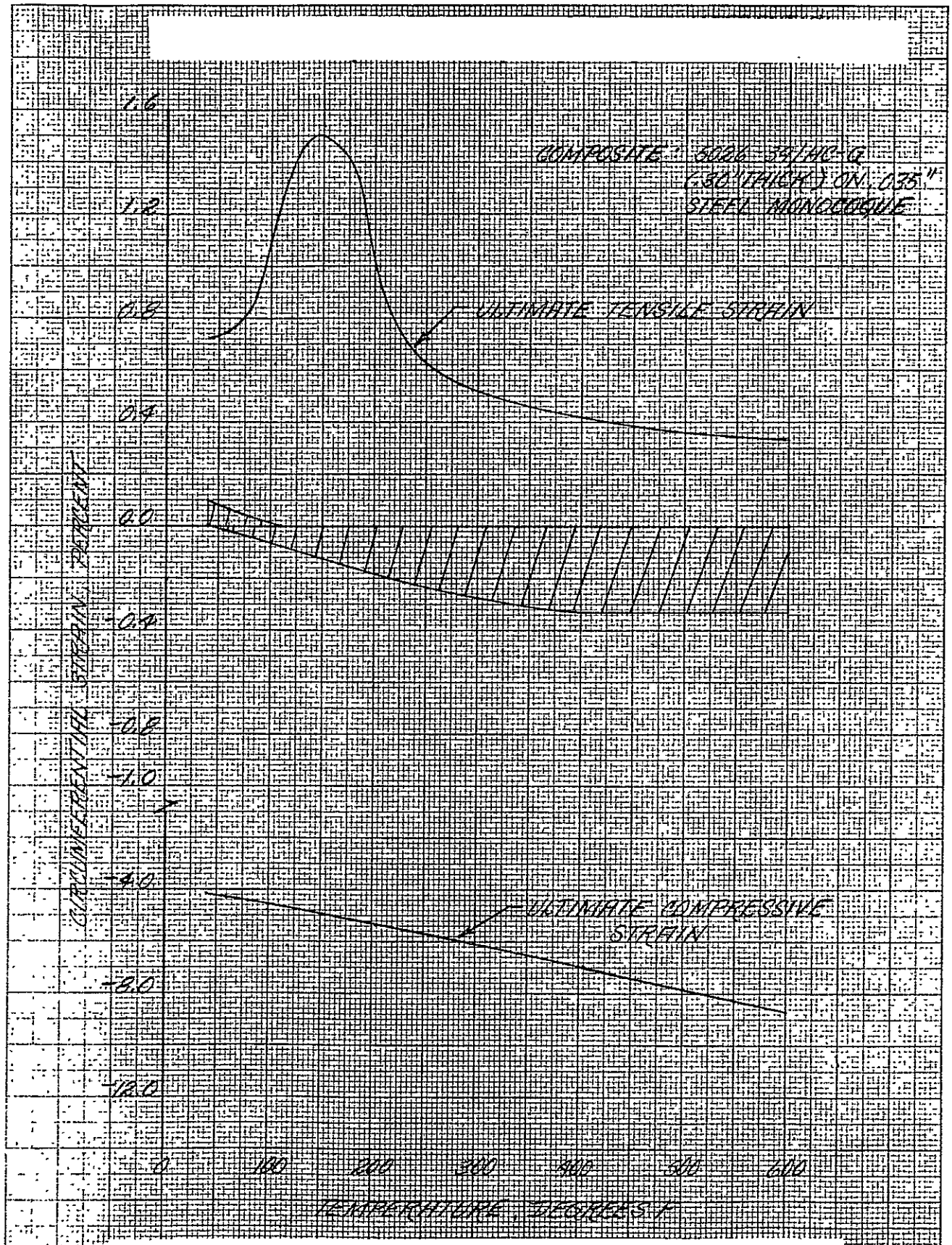


Figure 4.46 5026-39/HC-G Stiffened Steel Composite Circumferential Ablator Strain

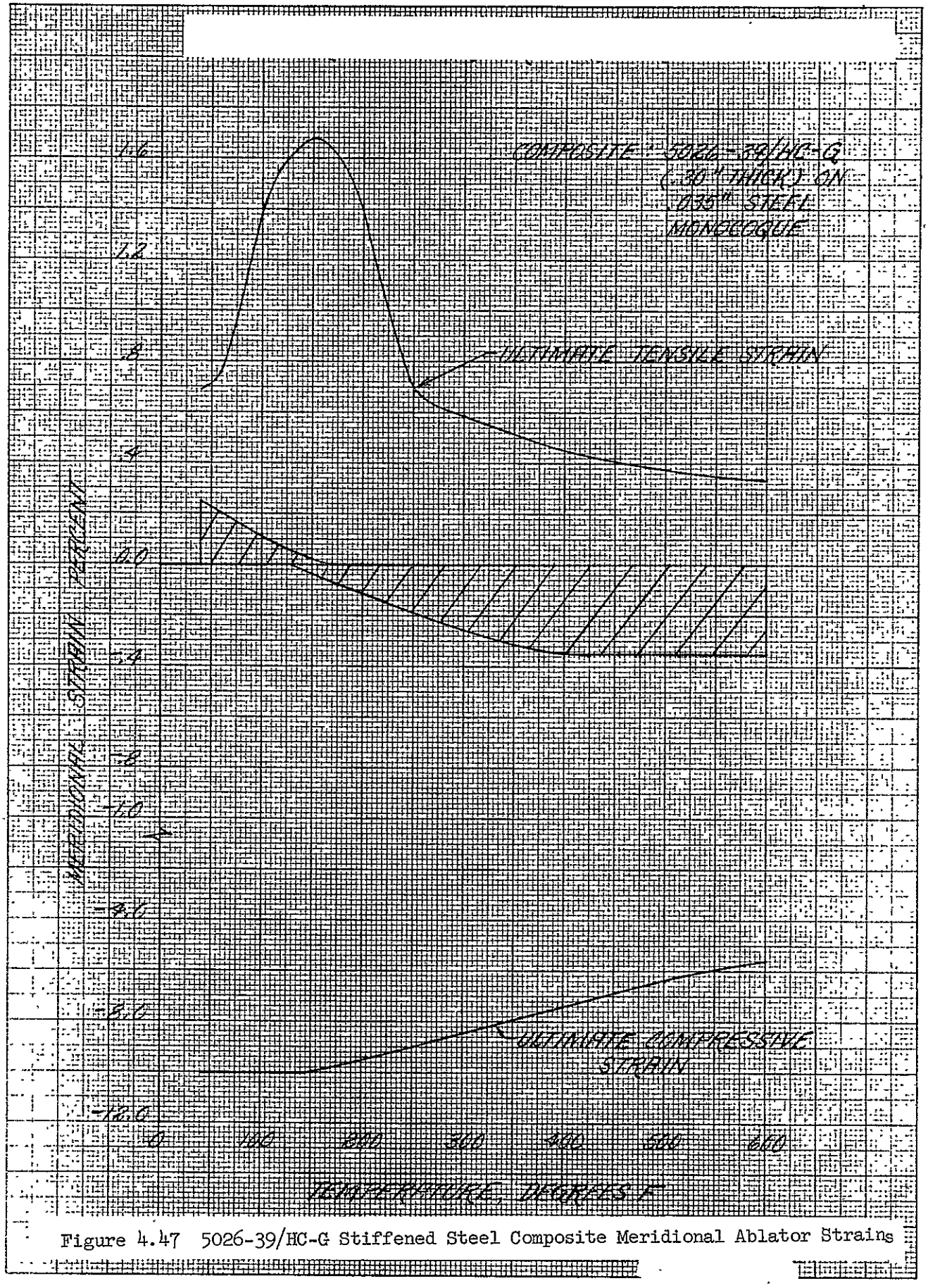


Figure 4.47 5026-39/HC-G Stiffened Steel Composite Meridional Ablator Strains

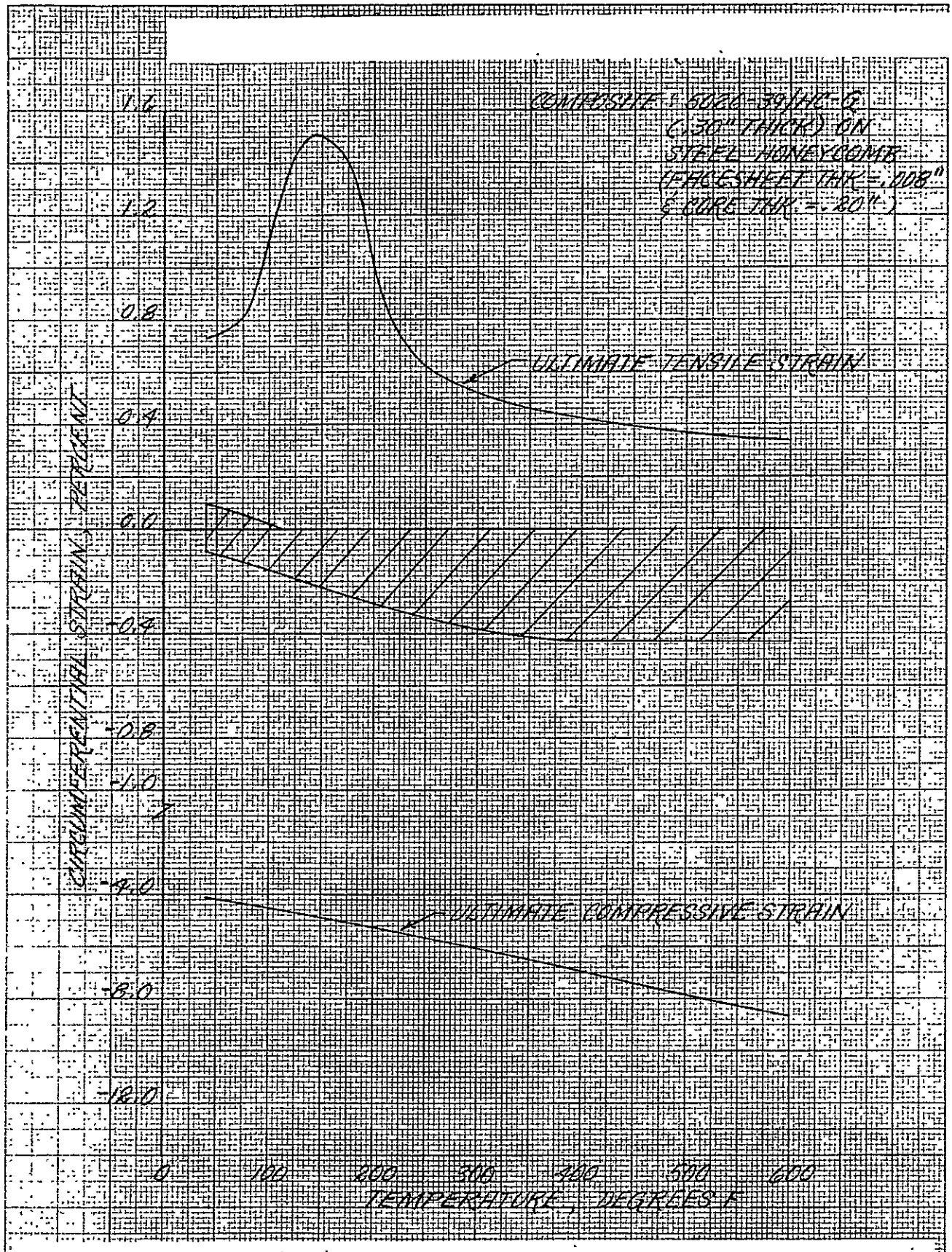


Figure 4.48 5026-39/HC-G Steel Honeycomb Composite Circumferential Ablator Strain

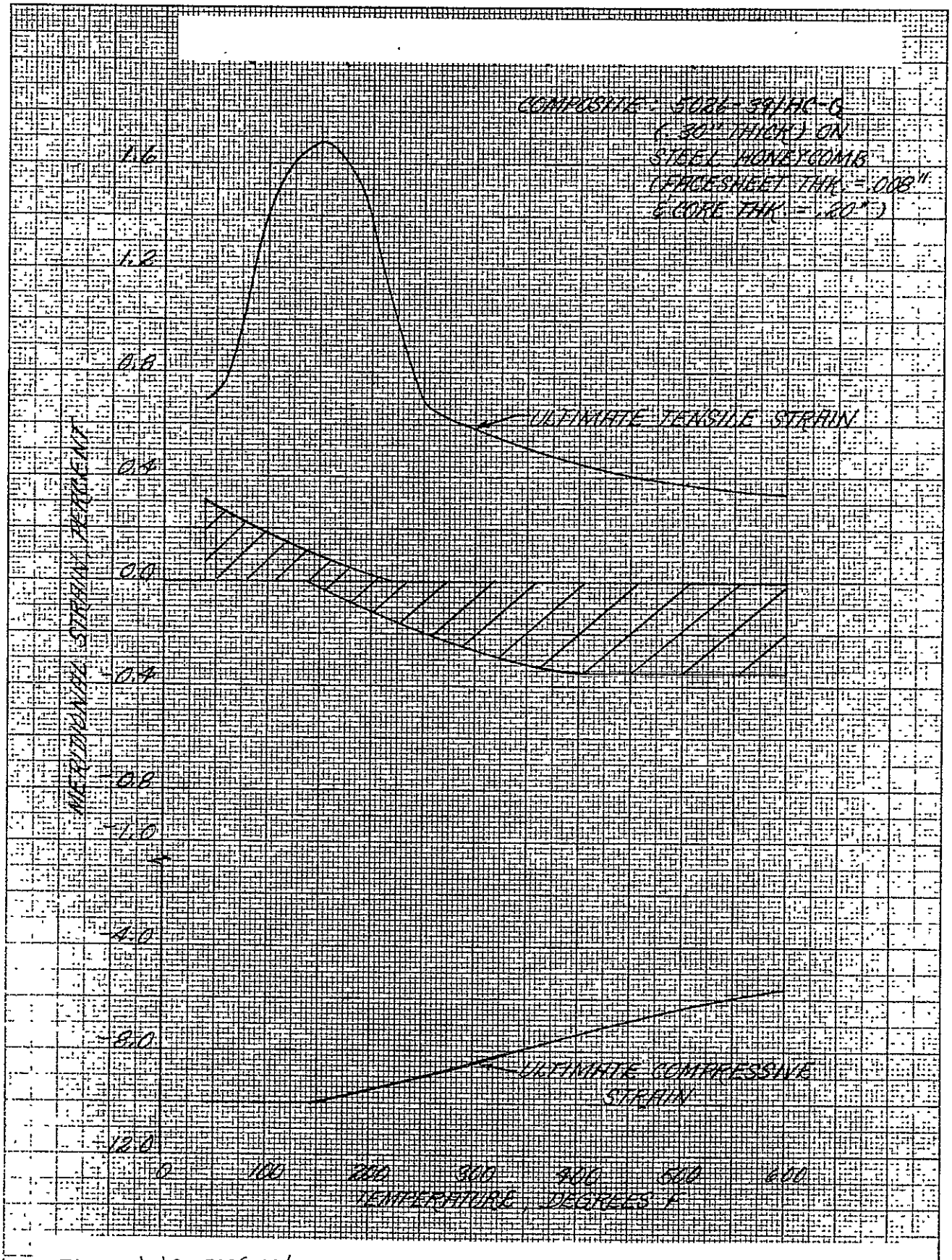


Figure 4.49 5026-39/HC-G Steel Honeycomb Composite Meridional Ablator Strain

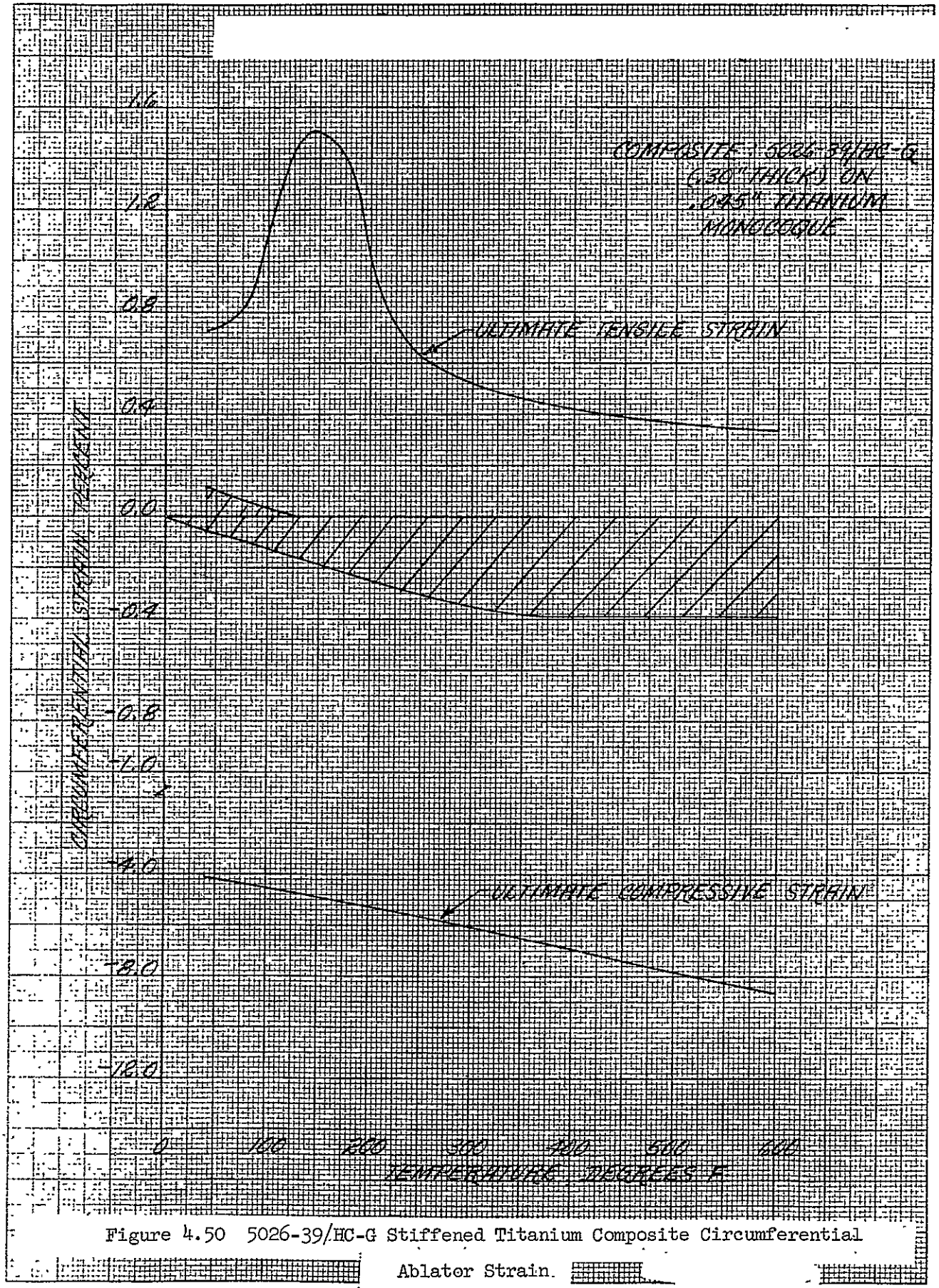


Figure 4.50 5026-39/HC-G Stiffened Titanium Composite Circumferential Ablator Strain.

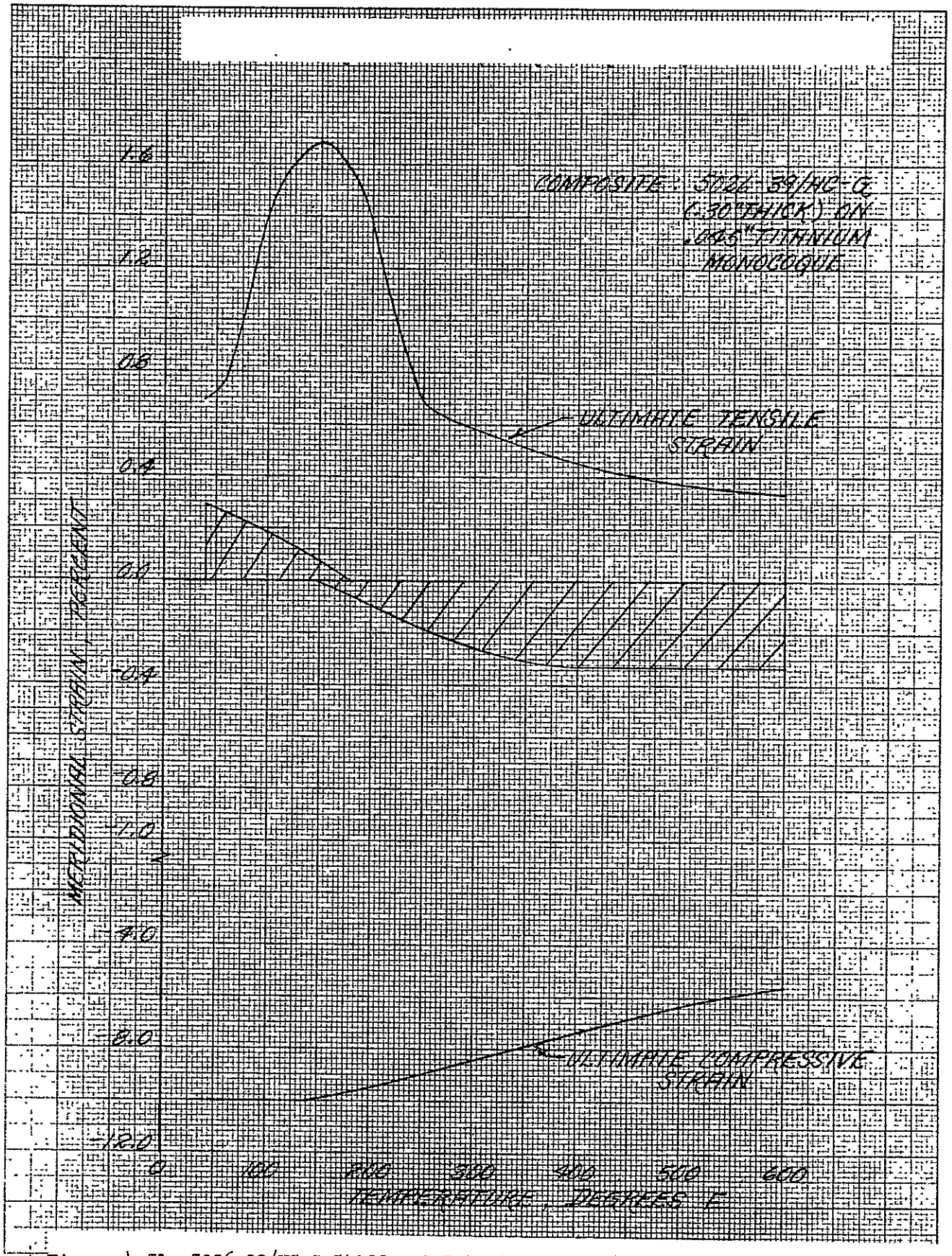


Figure 4.51 5026-39/HC-G Stiffened Titanium Composite Meridional Ablator Strain

15.0 psf. Consequently, mechanical erosion of the surface char due to aerodynamic shear forces is not anticipated.

The allowable strain curves are also shown in Figures 4.46 to 4.51 to indicate the structural margin of safety in the 5026-39/HC-G ablator. Based on the comparison of actual strains and allowable strains, it appears that the regions of the aeroshell away from local discontinuities present no structural problems for the 5026-39/HC-G ablator designs and entry conditions evaluated.

In addition to the two entry cases mentioned, an additional calculation ablator strain for a 600°F soak-out condition was made assuming restrained curvature. The equivalent .035-inch steel monocoque shell was assumed as the substructure. It was determined that the ablator strains in the meridional and circumferential directions for this case are tensile and equal to .16% and .07%, respectively. The 5026-39/HC-G ablator is in tension since the mean coefficient of thermal expansion of the ablator from 185°F, the zero-stress temperature, to 600°F is less than for steel. The margins of safety based on total strain to failure at 600°F are 1.1 and 3.8 for the computed meridional and circumferential strains respectively which indicates that the 5026-39/HC-G will survive the 600°F soak-out as well.

A complete detailed shell analysis has been performed utilizing Avco Computer Program 1322D. The detailed analysis was performed to solve for the complete (membrane and bending) stress and strain distributions in the composite aeroshell. The analysis and results of this detailed shell analysis are presented in Section 4.4.4. The proposed heat shield application for the Venus probe is different from the current Apollo technique and, consequently, the critical failure modes and strength characteristics of the bond could also be different. Failure modes as well as strength data for the actual bond system must be determined by testing in order to design for a reliable system. Moreover, environmental testing (i.e., cold soak followed by re-entry) of an

actual composite section would also be needed as a final verification of the aeroshell design.

4.4.3.2 X6300 Carbon Phenolic Heat Shield

For the thermostructural study of the X6300 heat shield, the aeroshell composite design investigated consisted of a .47-inch thick layer of X6300 on a steel honeycomb substructure with .01-inch facesheets and a .6-inch core. The aeroshell configuration considered was a 45 degree cone with a 42-inch base diameter. The aerodynamic heating, radial temperature distributions and loads imposed the aeroshell were representative of the AV-4 atmosphere and trajectory characteristics of V_E = 38,254 fps, γ_E = 50°, M/C_DA = 1.1 slugs/ft^2. The initial entry temperature of the composite was assumed to be 80°F. The zero stress temperature, i.e., the temperature at which thermal forces in the composite are zero, was assumed to be 275°F. The mechanical properties of X6300 used in this analysis are given in Section 4.4.2.1. Again, two entry times were evaluated; the time at which the surface temperature reached or exceeded 600°F (while the bulk of the heat shield is still cool) and the time of peak entry loads. The temperature profiles for these times are shown in Figure 4.52.

Figures 4.53 and 4.54 summarize the results of this analysis again in the form of an envelope of maximum total strain versus temperature in the X6300 material for the circumferential and meridional directions respectively. The total strain levels include both thermally induced strains and maximum mechanical strains produced by the aerodynamic pressure and payload inertia loads. The pressure in this case is 113 psi and the payload inertia load is approximately 2330 pound/inch applied at the payload support ring where the radius normal to the shell axis is 11.0 inches. The overlap of tensile and compression strains which is most evident for the meridional direction, Figure 4.54, is the result of the different entry environments and cone locations considered. Whereas

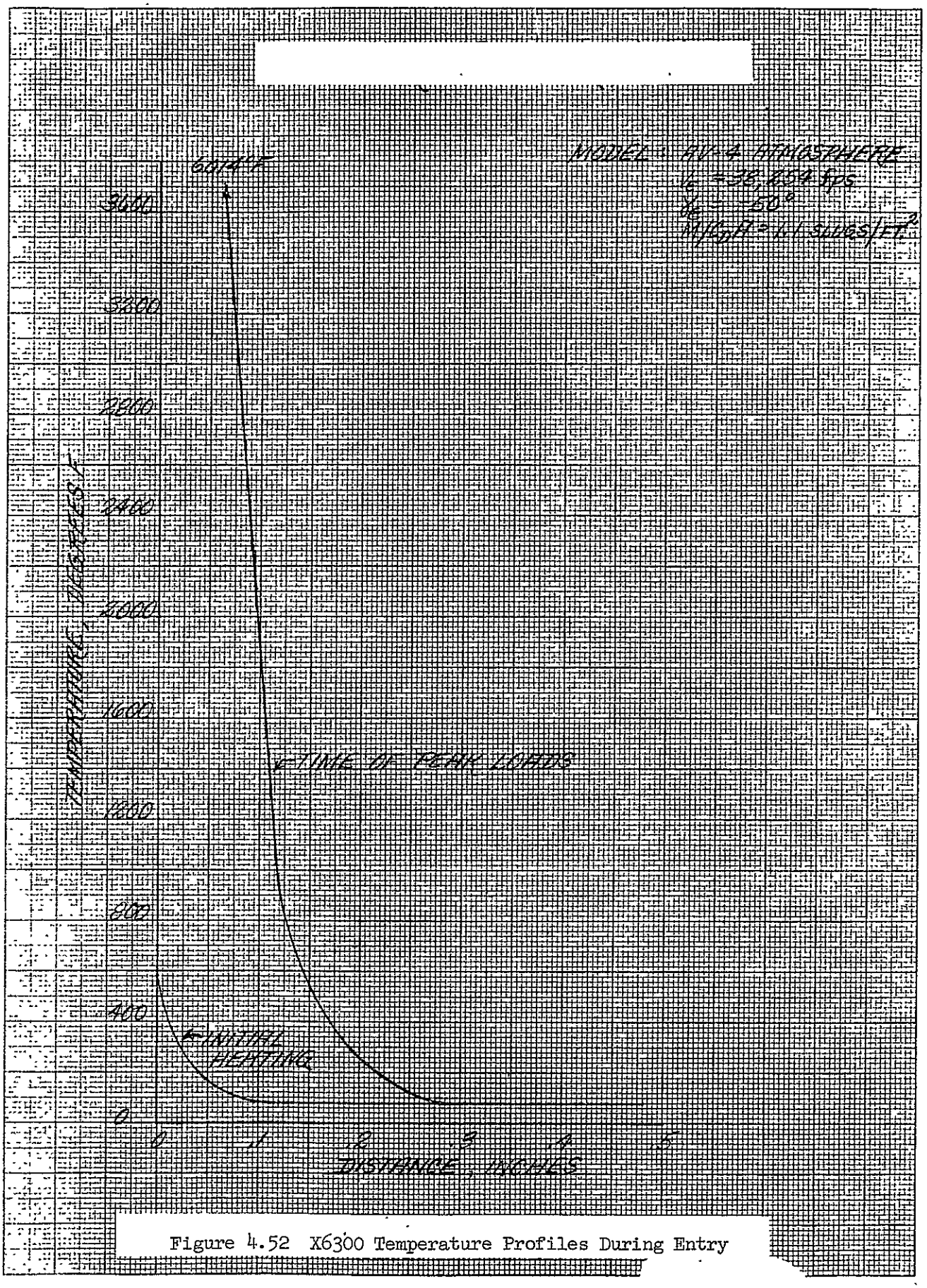


Figure 4.52 X6300 Temperature Profiles During Entry

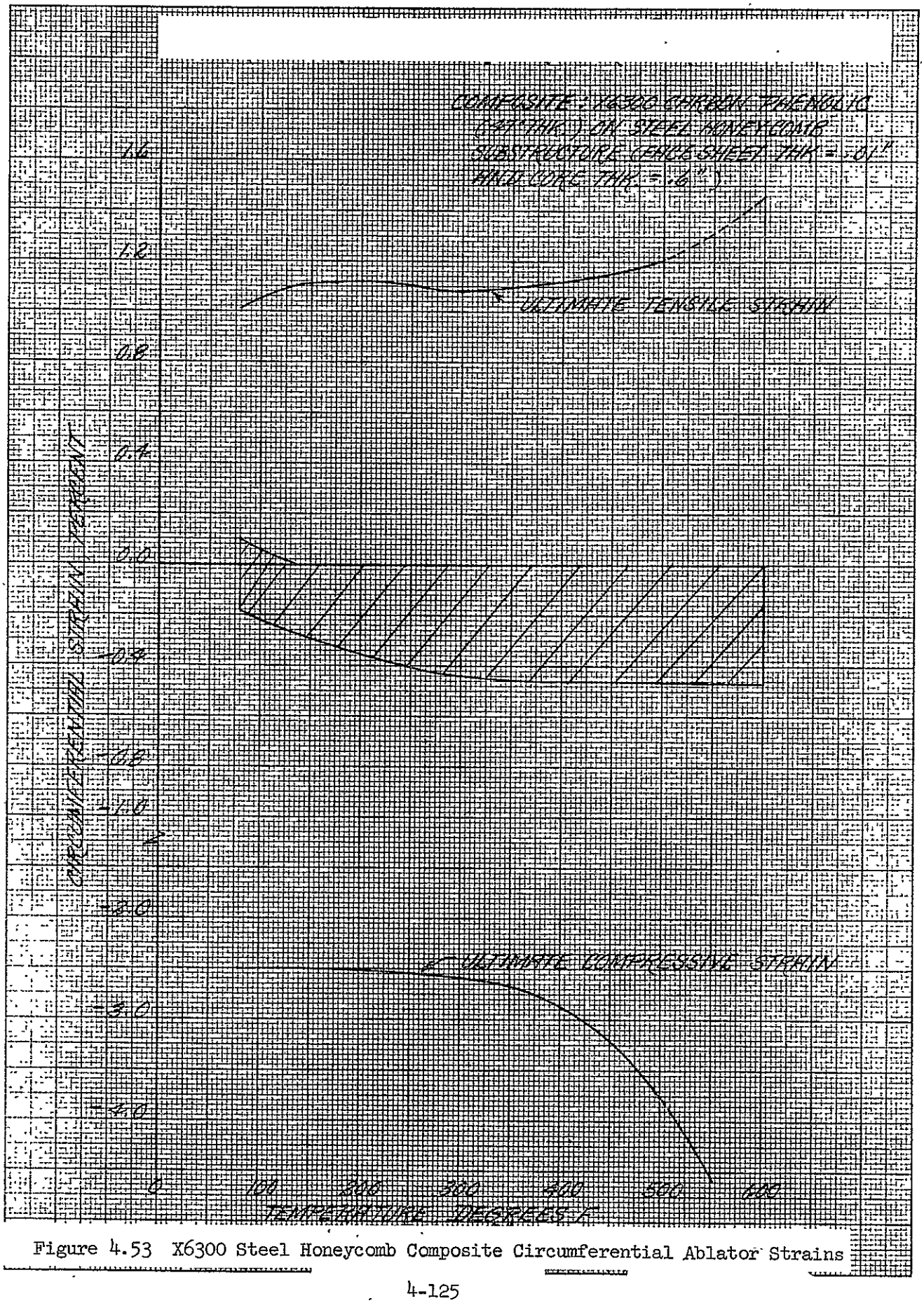


Figure 4.53 X6300 Steel Honeycomb Composite Circumferential Ablator Strains

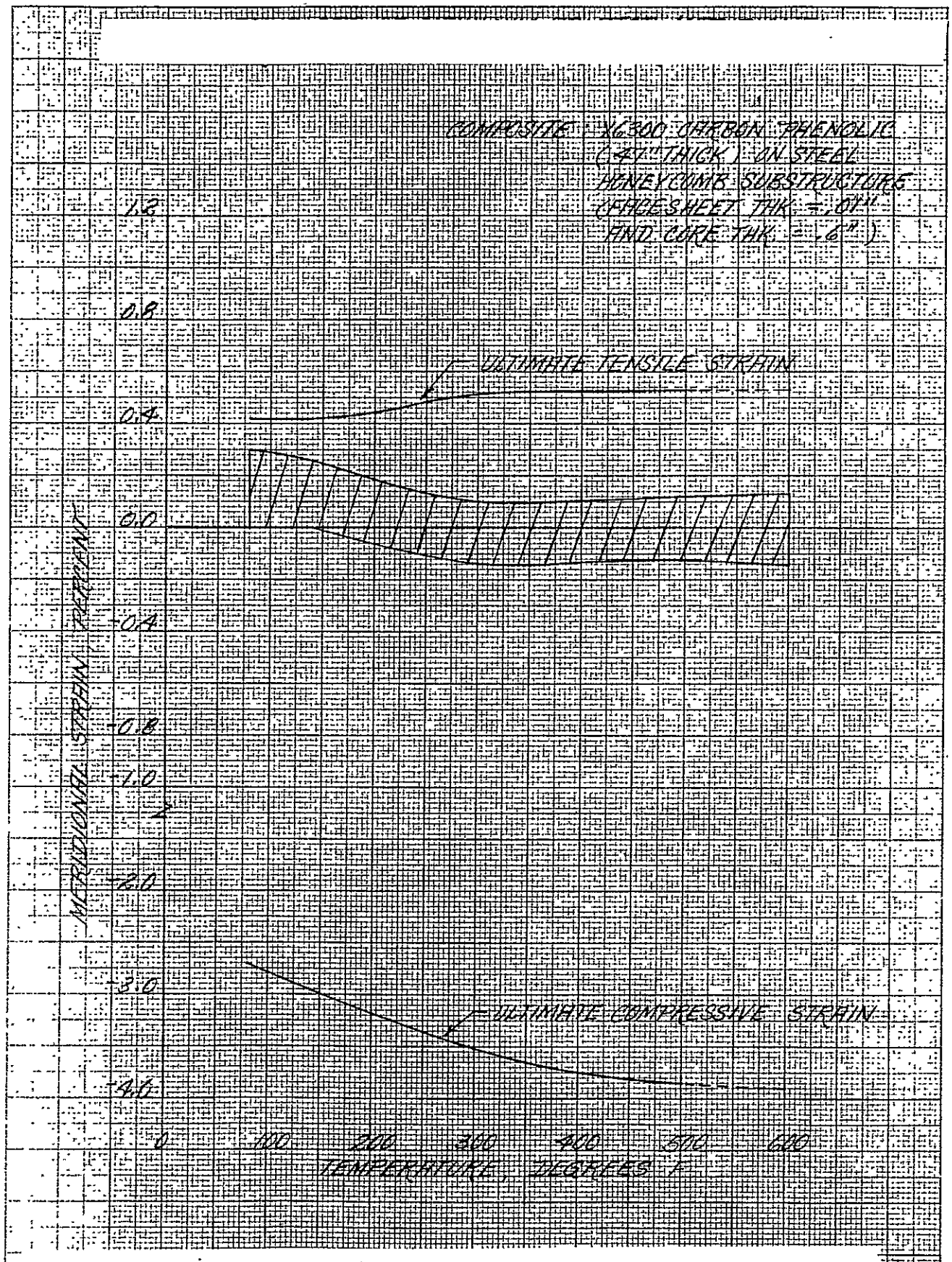


Figure 4.54 X6300 Steel Honeycomb Composite Meridional Ablator Strains

the specified temperature profiles alone would normally produce tensile strains in the area of the bond line where temperatures are below the zero stress temperature and compressive strains in the higher temperature regions, the combined net meridional strains in the region of the payload ring are tensile for the complete X6300 layer because of the large tensile strain due to the inertia load of the payload.

The allowable strain curves are also shown in Figures 4.53 and 4.54 to indicate the margin of safety in the X6300 for the assumed conditions. Ablator strains in the surface layer which experiences temperatures above 600°F during entry heating are ignored since, at these temperatures, the X6300 has either charred or experienced severe mechanical degradation and no structural criteria other than aerodynamic shear stability is considered.

The maximum aerodynamic shear force experienced by the X6300 is 19 ps The X6300 material, however, has been tested at shear levels in excess of 100 psf (Reference 56), and no problem of mechanical erosion of the char exists for the anticipated conditions.

The maximum meridional tensile strain of .30 percent shown in Figure 4.54 is primarily caused by the payload inertia load and occurs in the payload support region. Local beefing-up of the substructure at the interface region, although it would somewhat increase the thermally induced strains in the X6300 because of the increased extensional rigidity of the substructure, would result in a lower net tensile strain because it would lower the more significant membrane strain produced by the loads.

As in the 5026-39/HC-G analysis, radial compressive strains due to pressure, aerodynamic shear strains, and residual strains were ignored since they are negligible. The effect of outgassing of the phenolic carbon heat shield and the bond, particularly for the soak-out phase where interior

temperature may reach 600°F was not considered in this analysis. However, outgassing can be evaluated from the proposed small panel tests and the full-scale proof-test of the phenolic- carbon-ablator system for the heating and soak-out environments as outlined in Section 4.4.6.

A calculation for the 600°F soak-out condition was performed. Tensile strains of .035 percent and .04 percent were computed for the meridional and circumferential directions respectively. Based on the ultimate strain to failure of the carbon phenolic at 600°F, the margins of safety are 13.8 and 29.0 respectively for the above strain levels. Based on the presented results, it would appear that the X6300 is structurally adequate for the Venus entry heating environment and the composite design considered.

4.4.4 Complete Aeroshell Evaluation During Entry

A complete detailed shell analysis utilizing Avco Computer Program 1322D has been performed for the 60 degree cone minimum-payload probe in order to evaluate the total stress distribution in the substructure and the total strain distribution in the ablator resulting from the combined thermal and mechanical loads.

The membrane stress analysis of the 5026-39/HC-G ablator on a steel substructure indicated that based on a non-bending solution, the heat shield composite was structurally adequate. However, a more detailed stress analysis was performed to evaluate the total stresses, both membrane and bending, from the combined thermal and mechanical loads. The purpose of the analysis is to substantiate the adequacy of shell thicknesses that are based on buckling stability or membrane stress and determine where increased thickness and rigidity are required to ensure both acceptable substructure stresses and ablator strains. Of particular interest are the payload support interface, local geometric discontinuities and joints.

In addition, the results of the analysis will provide a preliminary estimate of the additional structural weight which results from the requirements for local stiffening.

The detailed aeroshell composite stress analysis was performed using Avco Computer Program 1322D. Computer Program 1322D solves for the stresses and strains of a thin-elastic, multi-layered, multi-region orthotropic shell of revolution under axisymmetric pressure loads and temperature distributions; the program is capable of handling temperature-dependent mechanical properties.

The axisymmetric shell solution is applicable to the Venus probe since the angle-of-attack history at the point of peak loading is low enough to result in essentially symmetrical loading.

The aeroshell composite schematic, radial temperature profile, and symmetrical pressure distribution considered in the analysis are shown in Figure 4.55. The geometry is representative of the minimum-payload, low M/C_DA probe configuration and the temperature profile and pressure distribution shown represent the peak load conditions for the most severe entry trajectory (i.e., the AV-4 atmosphere, V_E = 35,600 fps, $\gamma_E = -50^o$, and M/C_DA = .15 slugs/ft^2). The resultant axial force, obtained by integrating the external pressure over the aeroshell surface, causes deceleration which, in turn, produces an inertia load which is directly related to the total mass of the entry probe. The inertia forces due to the mass of the aeroshell tend to reduce the net pressure load acting on the shell and, hence, are beneficial. The inertia load due to the mass of the payload, however, will be transmitted through the payload support ring to the aeroshell. The concentrated reaction of the payload inertia load produces high bending and shear stresses in the aeroshell in the proximity of the circle of application.

For this reason, the aeroshell thickness was arbitrarily tapered from the nominal .05-inch to .25-inch as shown in Figure 4.55. The circumferential

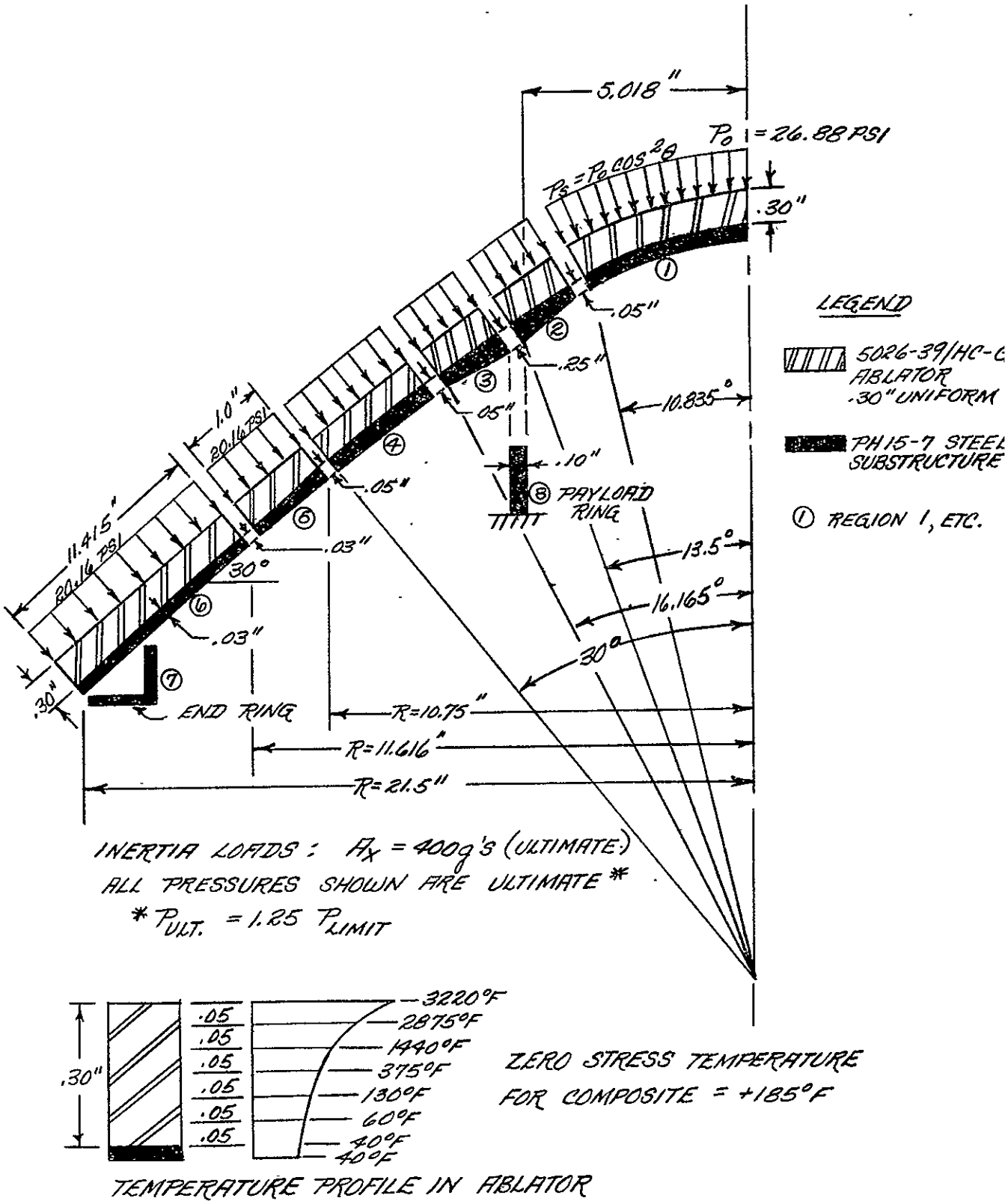


Figure 4.55 ANALYTICAL MODEL OF VENUS AEROSHELL 1322 PROGRAM ANALYSIS

ring stiffeners which are required to resist buckling in the .03-inch conical substructure shell from the external pressure are not included in this detailed analysis. Since inclusion of these rings would have caused only minor fluctuations in the computed stress and strain distributions, they were ignored in order to facilitate the analytical model.

Both inertia and pressure loads used in the analysis are ultimate; the ultimate levels are computed by multiplying the limit or actual loads by a factor of 1.25. The thermal forces, however, do not include a safety factor of 1.25 since they are computed internally in the program from the temperature profile and the composite properties. Although the radial temperature profile shown in Figure 4.55 is actually for a station at the cone base, it is considered a reasonable representation for the overall shell. The mechanical properties of the 5026-39/HC-G ablator are those given in Section 4.4.2.2. The mechanical properties of the PH15-7Mo steel substructure are as follows: $E = 30 \times 10^6$ lbs/in^2, $\alpha = 6.1 \times 10^6$ in/in/$^\circ$F, and $\nu = 0.3$.

A dimensional schematic of the aeroshell is shown in Figure 4.56; this schematic is helpful in matching the substructure stresses and ablator strain to aeroshell location. Both the meridional stresses (σ_ξ) and circumferential stresses (σ_θ) in the steel substructure are shown in Figure 4.57. Subscripts "i" and "o" refer to the inner and outer surfaces respectively of the substructure. As can be seen from the stress distributions, the payload support ring attachment region is most critical. However, the assumed taper of the shell region adjoining the payload support ring was sufficient to keep the substructure stresses well below the allowable yield limits as can be seen in Figure 4.57.

The ablator strain distributions for the circumferential (ϵ_θ) and meridional (ϵ_ξ) directions are presented in Figures 4.58 and 4.59 respectively.

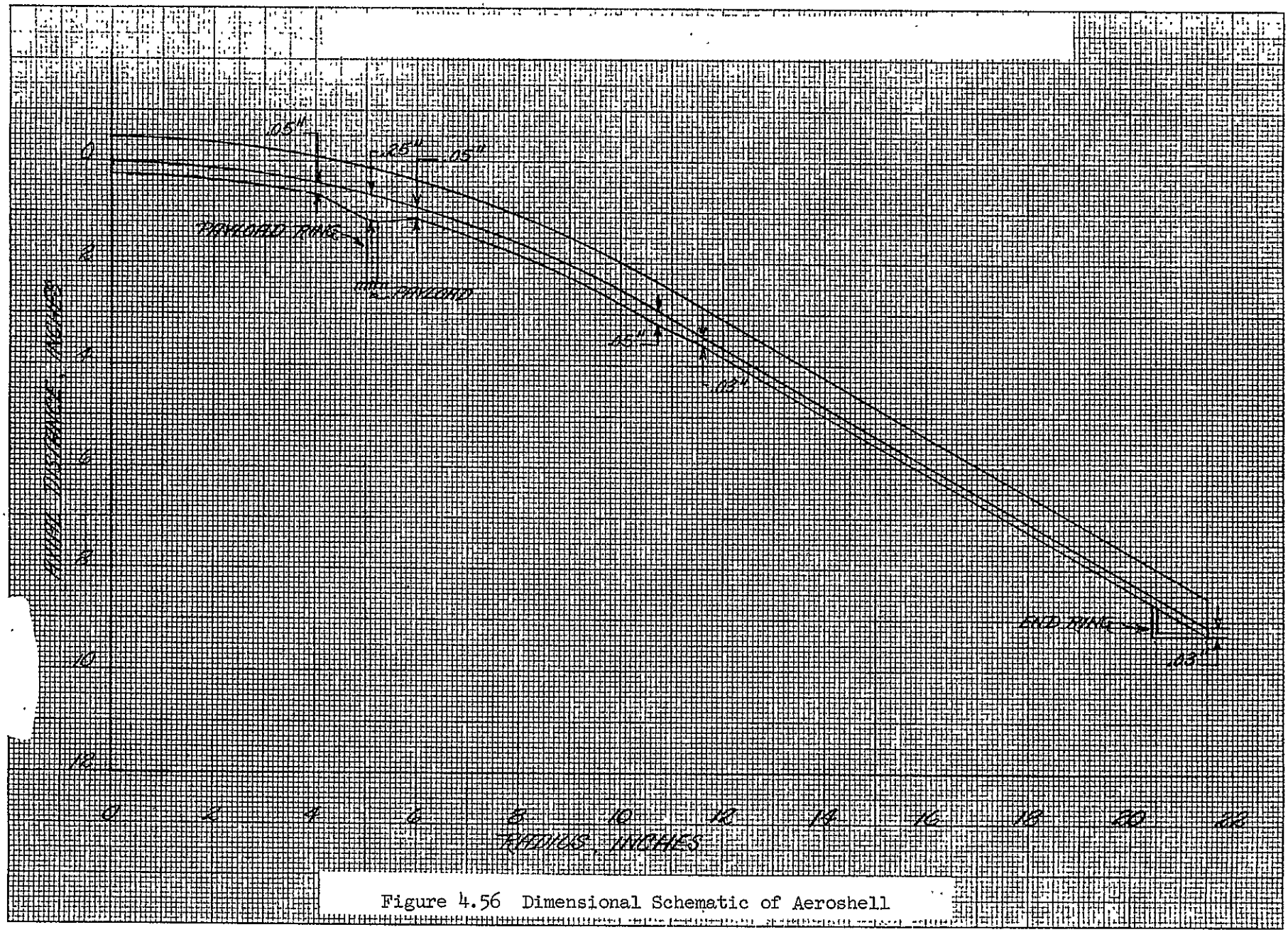


Figure 4.56 Dimensional Schematic of Aeroshell

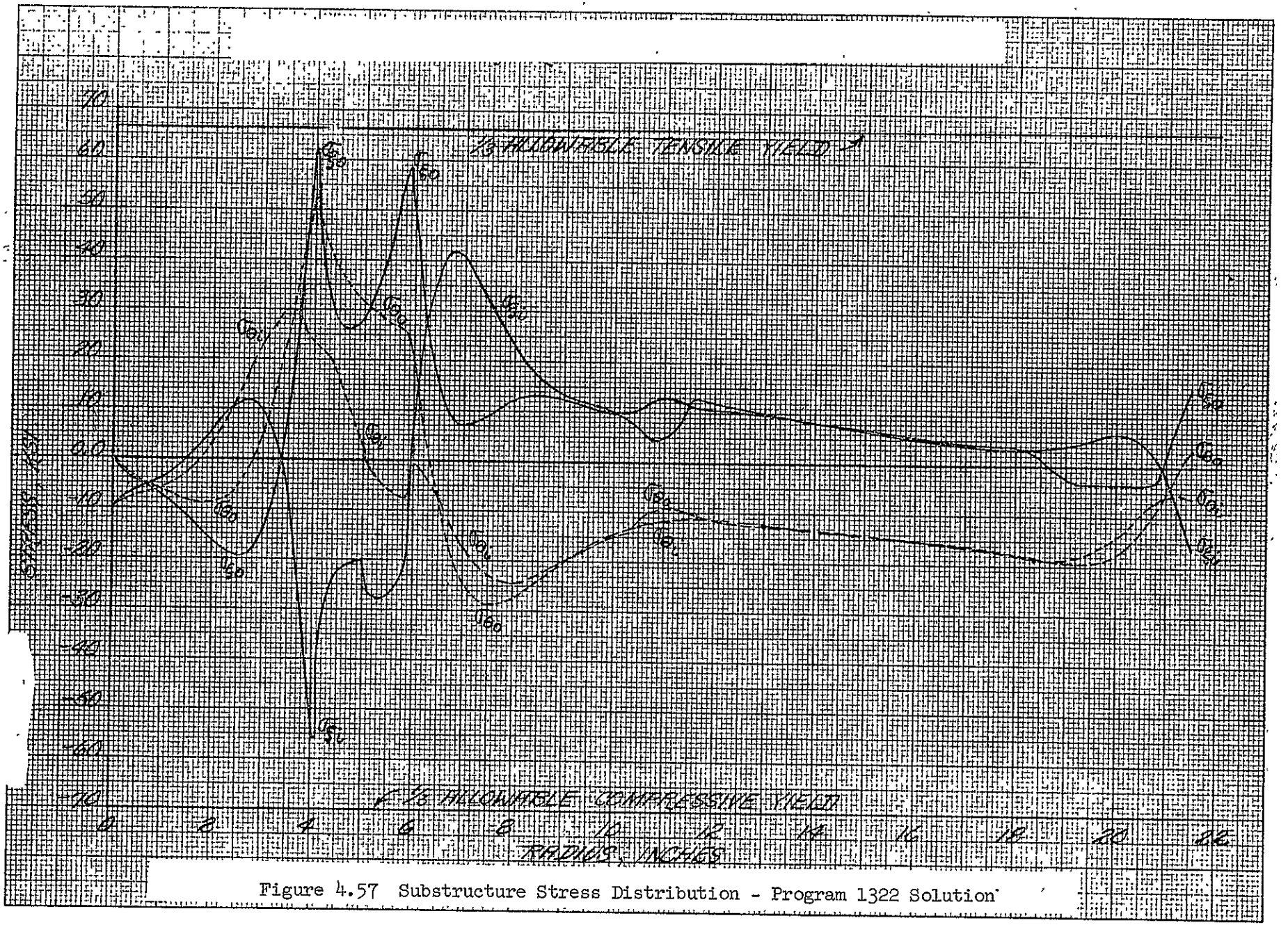


Figure 4.57 Substructure Stress Distribution - Program 1322 Solution

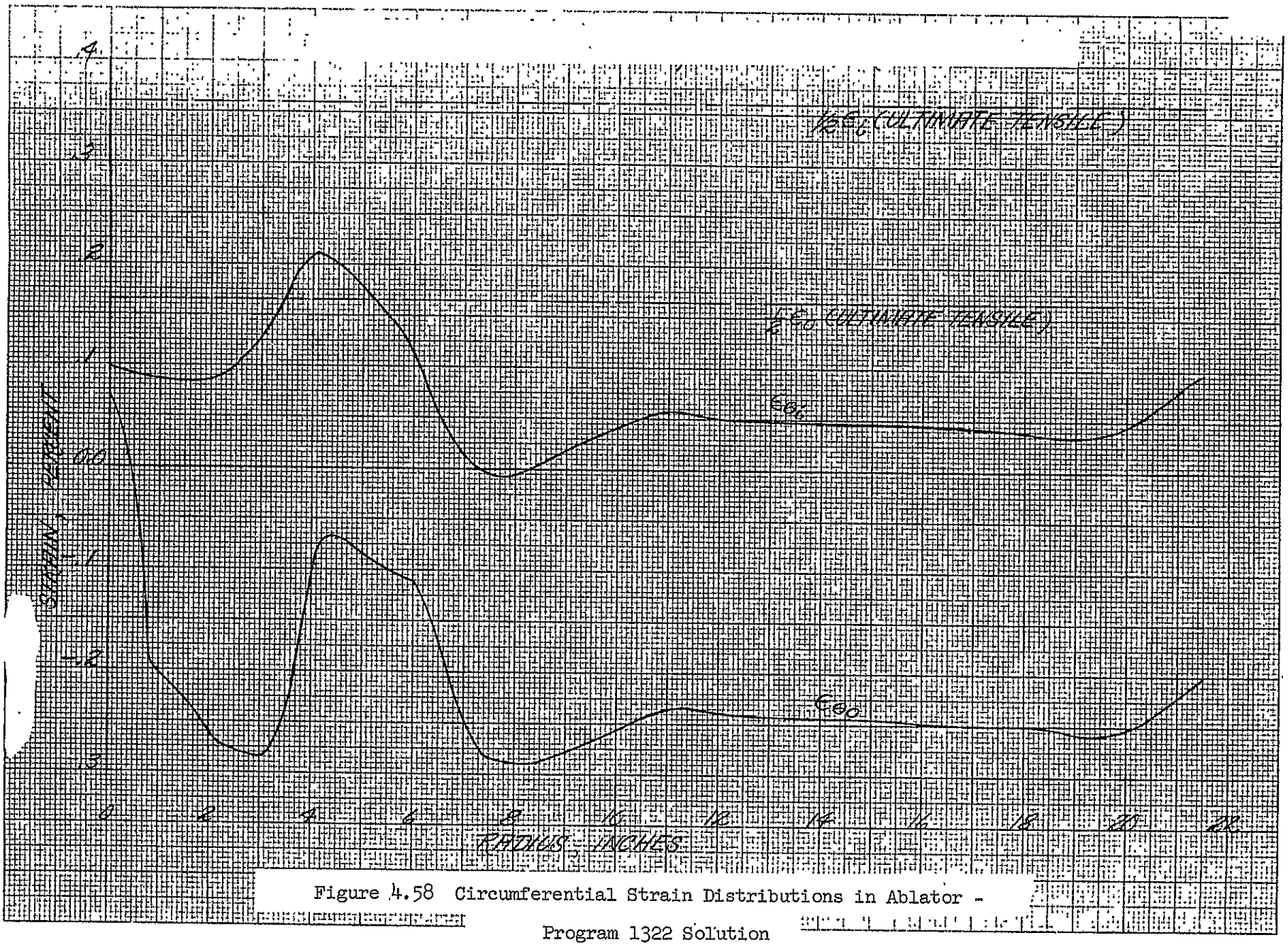
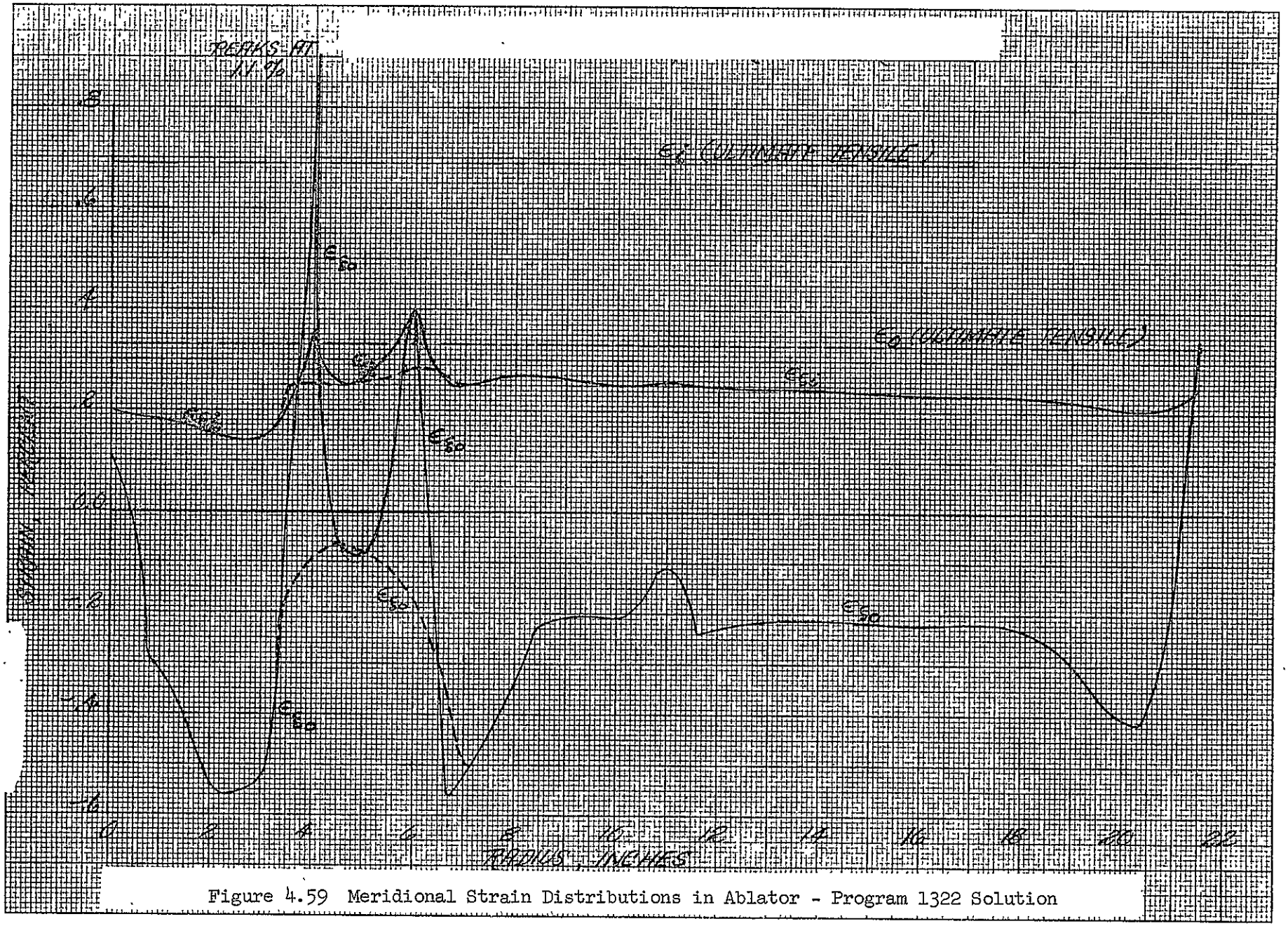


Figure 4.58 Circumferential Strain Distributions in Ablator - Program 1322 Solution


RADIUS IN %
ϵ_x CIRCUMFERENTIAL TENSILE
ϵ_θ MERIDIONAL TENSILE
ϵ_{50}
ϵ_{50}
ϵ_{50}

The subscript "i" refers to the inner surface of the ablator and the "o" refers to an internal surface where the ablator is at 600°F. The 600°F surface at the entry time considered, i.e., peak load, is approximately .13-inch from the actual outer surface. The ablator strains for temperatures above 600°F are ignored as 600°F is considered the threshold temperature at which the ablator begins to char and no structural criterion other than aerodynamic shear is considered for the char.

In general, the strain distributions in Figures 4.58 and 4.59 represent the maximum strain limits in the uncharred ablator layer between the inner surface and the 600°F temperature line. Without exception, these curves represent the maximum tensile strains anywhere in the ablator; but, there are somewhat higher compressive strains than indicated by the 600°F temperature strain plots in regions where the mechanical moments are low. In these cases, however, the margins of safety based on the ultimate compressive strains still exceed 10.0 and, hence, the maximum compressive strains not shown by Figures 4.58 and 4.59 are just as trivial as those that are shown. For these reasons, the strain results of Figures 4.58 and 4.59 can be used to indicate where the 5026-39/HC-G ablator is or is not structurally adequate for the specified configuration and environment.

In Figure 4.58, one-half of the ultimate tensile strain for the circumferential direction is plotted for both the inner surface where the temperature at peak loading is approximately 40°F and the 600°F temperature line denoted by subscript "o". It appears from the comparison of the actual maximum tensile strains and the allowable strains that the 5026-39/HC-G ablator is structurally adequate in the circumferential direction for the overall aeroshell. The ultimate compressive strains for the ablator are not plotted; at 600°F, however, the ultimate compressive strain in the circumferential

direction is 7.6 percent which indicates that the circumferential compressive strains in the overall ablator are well below the ultimate limit.

In the meridional direction, the results of Figure 4.59 indicate that the ablator tensile strains do peak close to or higher than the tensile ultimate strain. This is due to the high local bending deformations in the aeroshell composite in the proximity of the payload attachment structure. The two critical strain peaks occurring at radii of 4.0 and 6.0 inches indicate that the assumed taper of the substructure must be extended beyond one inch in both directions from the payload attachment point at radius of 5.0 inches. Hand calculations were made for the case of a shell taper from .25-inch at the payload attachment point to .05-inch in a length of two inches in each direction. The resulting meridional strain distributions for this case are shown in Figure 4.59 by dashed lines. It can be seen that the extended shell taper has reduced the meridional strains in the critical region to acceptable levels. Figure 4.59 also indicates that a small shell taper may be warranted at the base ring location as well since the meridional strain for the 600°F line approaches the ultimate strain due to local bending.

The additional structure weight resulting from the required shell taper at the payload attachment amounts to approximately 3.5 pounds; this is not considered a prohibitive weight increase for the overall aeroshell.

4.4.5 Fabrication and Bonding

4.4.5.1 Avcoat 5026-39/HC-G

4.4.5.1.1 Fabrication Techniq...

The recommended method of application for Avcoat 5026-39/HC-G is a modification of the technique presently utilized in manufacturing the Apollo heat shield. Previous test programs on the ablator have shown that dimensional changes do occur (with the material fabricated by the

standard procedure) during sterilization that could induce stresses that will affect the performance of the structure during cold soak conditions. The following procedure will be utilized to attempt to minimize (or eliminate) this problem.

The honeycomb core will be fabricated to the desired shape by bonding to a fiberglass face sheet that simulates the shape of the probe structure. After cleaning and priming the honeycomb, the ablator will be gunned into the cells, inspected and vacuum bagged cured at 200°F. The face sheet will then be removed and the heat shield positioned on a fixture and heat stabilized above the temperature encountered during sterilization. The fixture used for stabilization will allow adequate movement of the heat shield composite to reduce stress formation. The composite will then be inspected for ablator integrity, machined to the required internal contour and bonded to the structure. The bond between the structure and heat shield will be ultrasonically inspected and the external surfaces contoured.

4.4.5.1.2 Bonding Technique

Several adhesive systems are available for bonding Avcoat 5026-39/HC-G to the structure. The most commonly used one is Cyanimid's HT-424 film adhesive and is recommended for this application. An alternate system is Epoxylite 5403, a filled epoxy material, made by Epoxylite Corporation.

The HT-424 film would be applied to either the heat shield or the structure and the parts mated and cured under pressure. The use of Epoxylite 5403 would require a more complicated bonding procedure. The heat shield would be positioned on the structure with shims and the adhesive pumped into the bond line. The cure temperature employed with either adhesive would be selected after a series of tests are performed to determine the conditions required to minimize the zero stress temperature and to prevent movement or distortion of the adhesive during sterilization.

4.4.5.1.3 Evaluation of Ablator Bond

Accurate bond stress calculations were not made for either 5026-39 Avcoat or X6300 ablator because it was deemed more important to determine the ablator strains during this phase of study. Bond stress calculations can be performed by the Rohm and Haas computer program. Furthermore, it is considered more important to perform tests on specimens and finally to perform a full scale test on the probe to prove the satisfactory performance of the bond rather than to perform bond-type analyses. However, both tests and analyses should eventually be performed prior to flight.

HT 424 bond strength between 5026-39 HC/G, hand-gunned ablator and the stainless steel substructure for a cold soak at -150°F for a significant number of Apollo test specimens is large enough such that a bond failure has not occurred. Furthermore, ablator cracking has been produced in specimens by lowering the temperature until a crack occurs or by loading beam specimens while at -150°F, and in no specimen has a bond failure occurred. Bond line temperatures of -350°F have been reached on Apollo mockups of an S-band antenna and a fuel tank without any evidence of delamination.

HT 424 bond strength for a specimen of 5026-39M (molded) ablator bonded to a titanium substructure and subjected to a cold soak of -150°F, was large enough such that again a bond failure did not occur. The bond strength of four specimens of 5026-39M bonded to stainless steel (PH 15-7 Mo) substructures and subjected to a cold soak of -280°F, was large enough such that a bond failure did not occur. After the specimen having the titanium substructure and after those having stainless substructure were cold soaked, the temperature of each was raised until the bond line temperature reached 600°F; again, no bond line failure occurred. After the other three specimens having stainless substructure were cold soaked, the temperature of each was raised to 250°F and each was then subjected to a simulated re-entry

temperature profile; the bond line temperature reached a peak value of 580°F and no bond failure occurred. However, it is likely that these molded ablator specimens were tested under uniaxial conditions rather than biaxial conditions since the sizes of the specimen were about 12 inches long by 2 inches wide by $1\frac{1}{4}$ inches to $1\frac{1}{2}$ inches thick.

The bonding procedure for the Venus probe is, however, different than Apollo, as discussed, and hence, the bond strength characteristics may, in turn, be somewhat different. To prove the realiability of the Avcoat bond for the Venus probe, biaxial restrained curvature specimens should be subjected to a 600°F soak and similar specimens should be subjected to the most critical Venus entry temperature profile from both the cold and hot transportation temperatures. Furthermore, these "entry" tests should indicate whether or not the ablator is sufficiently porous such that outgassing pressures caused from a further cure (above about 300°F) of the ablator and bond could cause a catastrophic bond failure. However, this is not anticipated because such a problem was not experienced with Apollo specimens having ablator thicknesses of up to 2.5 inches and entered from -150°F; the Apollo re-entry trajectories should be somewhat similar to the Venus trajectories. Also, since the ablator will be cured at higher temperatures than was done with Apollo, less shrinkage or outgassing should occur.

Hand calculations were performed to evaluate the peak-edge shear stress in the 5026-39/HC-G bond for both a cold-soak of -20°F and a post-heating hot-soak of 600°F. These critical edge shear stresses were computed by the shear-lag principle presented by Gatewood in Reference 57. For the cold-soak of -20°F, the computed edge shear stress in the HT 424 bond was 163 psi as compared to an ultimate shear strength of 1,550 psi. For the 600°F hot-soak the edge shear computed was 130 psi, as compared to an ultimate shear strength of 340 psi.

4.4.5.2 X6300 Carbon Phenolic

4.4.5.2.1 X6300 Carbon Phenolic Fabrication Technique

As a result of extensive materials evaluation and process studies under the REST program (Contract AF 04(694)-687), Avco/SSD has developed a carbon/phenolic heat shield material designated as X6300. Fabrication of heat shields for the types of Venus probes being considered is well within the state-of-the-art using this material.

Two basic fabrication techniques are used to fabricate carbon/phenolic heat shield materials. These include tapewrapping and compression molding. The following is a description of these techniques as applied to the Venus probes under consideration:

4.4.5.2.1.1 Tapewrapping

This technique is suitable for cylindrical or conical shapes. It involves the wrapping of a resin impregnated fabric tape onto a mandrel at a controlled angle to the axis or surface of the mandrel. Temperature, tension, compaction pressure and positioning of the tape are important processing variables that are controlled during this operation. Photo 4-1 illustrates the tapewrapping process using resin impregnated quartz tape in the Avco/SSD plastics processing laboratory. Carbon tape would be processed using the same procedure. Following the wrapping operation, a rubber bag is applied over the mandrel and the entire assembly is placed into a hydroclave. The part is cured in the hydroclave at 200 to 1000 psi at temperatures up to 275°F. The part is then removed from the mandrel and post cured for several hours in an oven at temperatures up to 350°F. The part is then machined to final dimension and is ready for bonding to the probe structure.

4.4.5.2.1.2 Compression Molding

The blunt probe design is not suitable for the use of a tapewrapping fabrication technique. In this case a

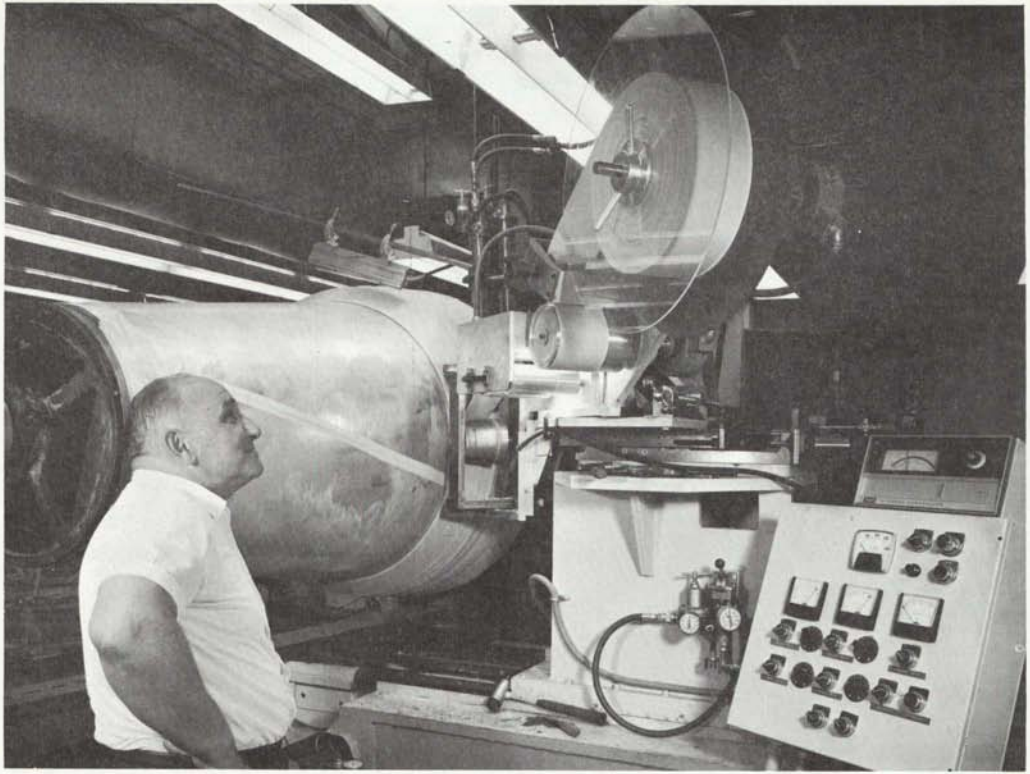


Photo No. 4-1. Avco Tape Wrapping Process

compression molding technique is recommended. This would involve the cutting of resin impregnated carbon fabric to the desired shape, positioning this fabric in the female portion of a matched metal mold and curing under heat and pressure in the mold. This type of mold, mounted in a hydraulic press is shown in photo 4-2. Moldings of carbon phenolic are usually cured at 200 to 1000 psi at temperatures up to 300°F. The part is then removed from the mold and postcured for several hours up to 350°F. After postcure, the heat shield is machined to final shape and is ready for bonding to the probe structure.

4.4.5.2.2 Bonding Technique

Several adhesive systems have been evaluated for bonding carbon/phenolic heat shield materials to metal structures. In general, low cure temperatures are required for these bonds to achieve a low heat shield-structure zero stress temperature. In addition, a 600°F bondline temperature is anticipated. Obtaining an adhesive with low cure temperature and elevated temperature performance is difficult. The only material that has been found to come close to meeting these requirements is Epoxylite 5403 (product of Epoxylite Corp., El Monte, Calif.). This is a filled epoxy material that is cured at 200°F for 16 hours. This adhesive loses strength rapidly above 350°F but maintains minimal properties (~100 psi) up to 600°F. Another adhesive HT 424 (product of American Cyanamid Co.) has shown good properties up to 600°F but this material should be cured to at least 300°F to exhibit the desired properties. Sterilization temperatures should complete the cure for both of these adhesives but this may also raise the zero stress temperature.

Cleaning and surface preparation procedures for bonding carbon/phenolic to various metals have been established, and no problems are anticipated in achieving good adhesion to these surfaces. Obtaining a void-



Photo No. 4-2. Avco Compression Molding Technique

free bond line is not as straightforward. The best technique found to date with Epoxylite 5403 is to assemble the heat shield to the structure with small spacers to establish a bond line thickness. The adhesive is then pumped into the bond line and cured in an oven. The HT 424 is a film adhesive. This is applied to one of the surfaces to be bonded and the heat shield and structure are then joined. Since this adhesive foams during cure, any bond line variations will be taken care of.

4.4.5.2.3 Evaluation of Ablator Bond

Calculations were also performed to predict the bond shear stress between the X6300 and the substructure for a -20°F transportation condition and a zero stress temperature of 275°F. The computed peak shear stress occurring at an edge was about 7000 psi. The allowable shear strength at -20°F is about 10,000 psi. Therefore, it appears that the bond is satisfactory. However, to prove the reliability of the bond biaxial restrained curvature specimens should be cold soaked at -20°F.

Similar calculations were performed for a bond temperature of 600°F. The computed peak edge shear stress was about 640 psi. The allowable shear-strength at 600°F is about 300 psi (projected from a curve plotted from measured values at -35°F, R.T., 160°F, 350°F, and 1000 psi at 500°F). Therefore, it does appear that a bond failure could occur. The calculation of this peak shear stress which occurs only at an edge may, however, be over conservative since any bond deformation will result in a more favorable distribution of the edge shear over a larger distance and, hence, lower this peak level significantly.

In order to truly ascertain the structural reliability of the bond system, a cold soak restrained curvature specimen mentioned above should be subjected to the most critical entry condition and allowed to soak

until the bond temperature reaches 600°F. This procedure assumes, of course, that no failure of the specimens occurred during cold soak.

The test results from both the entry and hot soak conditions should indicate the reliability of the X6300 and the bond. Since the cure temperature of X6300 is 300°F, and since the temperature will be raised above 300°F during entry, the phenolic resin will continue to cure or degrade with time at temperature. A significant change in mechanical and thermal strain properties occurs at 400°F and the amount of change is dependent on time. Furthermore, a similar outgassing occurs with the Epoxylite bond which is also time dependent. As a result, significant pressures could be built up within the bond which could cause a tension failure in a conical type carbon phenolic heat shield bonded to a metal substructure.

Such a failure could occur on the Venus probe, but would depend on the re-entry heating rates and the heat shield thickness. To prove whether such would occur, a full scale test of the probe should be performed. It first should be subjected to a cold soak and then thermally cycled for the most critical trajectory and then allowed to soak out at 600°F.

4.4.6 Structures Development Program Requirements

It is apparent from the studies discussed above that early development testing is desirable in several areas. Consequently, this section outlines a test program which in conjunction with the analytical evaluation would substantiate the structural reliability of the ablator-structure composite for all critical environments related to the Venus mission. The 5026-39/HC-G Avcoat and X6300 carbon phenolic development test programs are discussed separately in the following paragraphs.

4.4.6.1 Avcoat 5026-39/HC-G

The test effort for the 5026-39/HC-G ablator, to define the mechanical properties for the material after stabilization and sterilization,

consists of small composite panels tests, beam delamination tests, and finally, a full scale aeroshell test under the critical thermal and mechanical load environments.

4.4.6.1.1 Mechanical Properties

As discussed in both Sections 4.4.2.2 and 4.4.3.1, the requirements of sterilization of the Venus probe will effect the cure and post cure temperature of 5026-39/HC-G, specifically, the cure and post cure temperatures must be raised approximately 100°F over current levels to 300°F and 350°F respectively in order to stabilize the material against the effects of sterilization. However, it is not anticipated that stabilization at the modified cure and post cure temperatures along with sterilization will significantly alter the material's mechanical properties, and hence, only limited testing for mechanical properties is proposed. Belief that the properties will not significantly change is based on:

a) the mechanical properties ultimate strength and total strain, measured at room temperature after both stabilization and sterilization (Reference 55) fall within the scatter band of total data for the material;

b) long time exposure at 250°F, which results in some degree of stabilization, does not appear to degrade properties.

Test for mechanical properties data include the following:

a) Tensile tests which will yield modulus of elasticity, ultimate tensile stress and total strain to failure in two directions (parallel and perpendicular to the ribbons of the honeycomb); typical specimens of both directions at -30°F*, R.T., 250°F, and 700°F.

b) Compressive tests to obtain same properties in compression

Thermal strain specimens to obtain coefficient of thermal expansion data for both directions (parallel and perpendicular to honeycomb ribbons) over a temperature range of -30°F* to 700°F.

It should be stated that the foregoing test effort represents a minimum that would be required if properties are not significantly different from Apollo.

4.4.6.1.2 Small Specimen Tests

The need of small specimen tests, in view of the great deal of Apollo experience which exists, results from the fact that the ablator bonding assembly procedure for the Venus probe will be different from Apollo as discussed in Section 4.4.5 and, hence, the bond strength characteristics may in turn be different.

Restrained curvature panel tests are proposed in order to evaluate both the structural performance of the ablator and the bond system for the critical temperature environments. Prior to the test environments, the panels will be subjected to the higher cure and post cure temperatures which are required to stabilize the ablator and then to sterilization.

Environmental testing includes restrained curvature panels at -20°F or another prescribed cold soak temperature. The same specimens would then undergo simulated entry heating of Venus and allowed to soak out to 600°F or less depending on thermal predictions.

In addition, restrained curvature panels would be taken

* -30°F is specified since system studies indicate a maximum cold soak of -20°F. If a more severe cold soak is prescribed, additional data will be required to bracket the cold soak limit which is established.

to +40°F or the minimum pre-entry soak temperature and then subjected to entry heating followed by a soak-out to either 600°F or the maximum predicted soak-out temperature. The size of the panels will depend on ablator thickness but for the case of a uniform ablator thickness of 0.3 inch, which appears to be the ablator design for the minimum payload mission, a 9 x 9 (inches) panel is considered large enough for edge effects to damp out.

In addition to the restrained curvature panels, beam delamination tests are a vital part of the test program. If a crack should occur in the 5026-39/HC-G ablator, it is essential that the bond system be capable of surviving the remaining mission environments without delamination. The bond, by not delaminating, would allow the ablator to still function properly. For this reason, bond delamination tests are recommended in order to ensure bond integrity in the event a crack does occur. Beam delamination tests are required at each of the following temperatures: -20°F, R.T., 250°F, and 600°F.

4.4.6.1.3 Full-Scale Aeroshell Proof Test

As the final verification of the reliability of the ablator-structure composite aeroshell, a full-scale test model would be subjected to the following sequence of combined thermal and mechanical load environments:

a) a cold soak @ -20°F (no mechanical loads)

b) combined simulated pressure and inertia loads applied at the most critical predicted conditions.

c) heating representative of the selected entry trajectory.

d) soak out @ 600°F or the most severe predicted level.

Prior to these environments, of course, the test assembly would be subjected to the proper cure and post cure cycles for stabilization and then sterilization.

4.4.6.2 X6300 Carbon Phenolic Ablator

The test program for the X6300 ablator is very similar to that described above for the 5026-39 material.

4.4.6.2.1 Mechanical Properties

Mechanical properties are needed for X6300 in the post-sterilized state over the same range of temperatures as 5026-39/HC-G. However, since existing data for X6300 is relatively thin, it is necessary to define specimens statistics for each type of test, specimen, direction, and temperature. Since the X6300 is orthotropic, both longitudinal and circumferential properties are required.

The test plan is summarized below:

Type of Tests: tensile, compressive, and thermal strain

Material Orientation: both longitudinal and circumferential

Test Temperatures: -30°F*, R.T., 250°F, 500°F, and 700°F

In addition, at least one restrained curvature specimen and beam specimen would be required to establish the zero-stress temperature for the X6300-substructure composite after the bond cure and sterilization cycles.

4.4.6.2.2 Small Specimen Tests

The small specimen test program for X6300 assumes that there exists an available bond system which can meet the environmental requirements for the Venus mission and, hence, no bond development effort is

*-30°F again specified since system studies indicate a maximum cold soak of -20°F. A lower cold soak criteria will necessitate obtaining the required mechanical properties at least to, and more preferably, just beyond the established limit.

specified here.

This phase of the program is identical with that specified in 4.4.6.1 for the 5026-39 ablator in the type of tests (both restrained curvature panels and beam delamination tests), types of test specimens and thermal environments imposed. Since the entry conditions for the X6300 ablator probe are different than those for the minimum payload probe with the 5026-39 ablator the simulated entry heating will, of course, be different.

4.4.6.2.3 Full-Scale Aeroshell Proof Test

As in the case of the 5026-39/HC-G, a full-scale test model would be built, undergo sterilization, and then be subjected to the same sequence of simulated test environments as shown in 4.4.6.1 for the 5026-39 material, namely, a cold soak, the critical design entry loads and heating and finally soak-out.

4.4.7 Failure Mode Summary

The cold-soak thermal stress analyses indicated that both the X6300 and 5026-39/HC-G ablators would survive a cold-soak temperature of -20°F which systems studies indicated to be the lower limit. Also, a check of ablator stress and strain for the extreme cold-soak temperature of -150°F indicated that both ablator materials would survive without cracking. The analyses, however, were based on available mechanical properties of the material for the unsterilized condition; in the case of X6300, mechanical properties also had to be extrapolated and a zero-stress temperature assumed for the X6300 composite.

For these reasons, it is recommended that post-sterilization mechanical properties be obtained for both ablator materials for a range of temperature to include the final predicted cold-soak limit.

Preliminary bond stress calculations indicated that the bond for each

ablator would be capable of withstanding the -20°F cold-soak. The bond systems for the 5026-39/HC-G and X6300 ablators were assumed to be HT 424 and Epoxylite (X5403) respectively. Although the reliability of the HT 424 bond system used to secure the 5026-39/HC-G ablator on Apollo has been adequately demonstrated for the extreme cold-cold temperature of -150°F, it was pointed out that the bonding procedure proposed for the Venus probe is different than Apollo and as a result the bond strength characteristics may be affected. As for the X6300 system, no composite cold-soak test data is available although Epoxylite bond strength data does exist for the unsterilized condition. Consequently, it was also proposed in the development test program to conduct restrained curvature composite panels tests and beam delamination tests to substantiate the analytical evaluation and ensure the reliability of the ablator systems for the predicted Venus environments.

Structural analyses of the X6300 and 5026-39/HC-G ablator materials were also performed for the critical Venus entry environments using membrane stress theory. The total ablator stresses and strains computed in these analyses included components due to thermal mismatch, thermal gradients, and combined aerodynamic pressure and inertia forces. The results indicated that both 5026-39/HC-G and X6300 ablator designs evaluated would survive the Venus entry environment including the soak-out. However, these membrane stress analyses, just as the cold-soak analyses were based on available mechanical properties (unsterilized material). In addition, the effect of outgassing of both the heat shield material and the bond during the soak-out period, when the interior temperatures increase well beyond the cure temperature levels, could not be evaluated in these analyses. Although it is not anticipated that outgassing poses a problem for the 5026-39/HC-G system based on Apollo experience, it may be a problem in the case of the X6300 ablator system.

For these reasons, both small specimens tests and a full-scale proof-test is proposed to ensure the structural integrity of the final heat shield design for all critical environments including cold-soak, entry, and soak-out.

In addition to the membrane stress analyses, a detailed analysis including combined membrane and bending stresses was performed for the minimum payload probe design. The most critical entry condition evaluated as determined from the membrane stress analyses was the time of peak loads. The analysis indicated that local substructure stiffening in the form of shell tapering was required at the payload attachment point and the base ring junction. The additional structural weight required, however, was not critical. Nevertheless, it was recommended in the development program that a full-scale proof-test be conducted for the combined critical thermal and mechanical loads.

4.5 Candidate Heat Shield Materials

This section contains all of the ground test data considered as part of the evaluation of carbon phenolic, typical data correlations, and references of flight test data.

4.5.1 Data Correlations: Carbon Phenolic

A survey was made to collect all available ground and flight test data for carbon phenolic and to assess the data relative to the Venus entry problem and to the thermal analysis model used for heat shield design. It was discovered that no radiant heating test data exist for carbon phenolic. It is noted that Section 4.5.1.1 and 4.5.1.2 of this document are extracted directly from Reference 58 (with the exception of re-numbering) since this reference contains the best available properties correlation study for carbon phenolic ground tests. In addition, the Venus probe study has referred to carbon phenolic as X6300, while Reference 58 used R6300 for nomenclature of this material.

Table 4.16 contains all of the arc test data which were accumulated during this study and which serve as the basis for the correlations as taken from Reference 58.

4.5.1.1 Internal Properties Determination and Comparison with Tests

4.5.1.1.1 Internal Properties Determination

Internal properties have been determined for R6300. Functional relationships between these properties and temperature have been empirically formed and the resulting functions used to produce a favorable comparison between predicted temperature responses and measured responses on samples tested in the ROVERS facility. These property determinations have been made for the RT-29 test specimen series molded at 200 psi.

4.5.1.1.2 Thermal Conductivity

Measurements of thermal conductivity were made on virgin and precharred samples (700°, 1000°, 1500°, 2000°F) with a "guarded hot plate" device. These measurements were made at several different temperature levels and the resulting test data including density values are given in Table 4.17.

Examination of the test data indicated the possibility of curve-fitting the values of conductivity as a function of temperature for each sample pre-char condition. The following function was used where KM is the thermal conductivity multiplier (K = 1.00):

$$KM = TB1 + TB2\ TEMP\ (x,\ t)^{1.0} + TB4\ (10.0)^{TB6}$$

The resulting curve fits of the test data are shown in Figure 4.60. Constant values of conductivity are assumed at temperatures below 250°F since limited test data are available at this temperature level and there is no justification for the rapidly decreasing values of KM calculated by the functions which are curve fits of existing data only.

X6300 ARC TEST DATA

TABLE 4.16

Specimen Identification			Geometry	Length			Density	$\dot{q}_c$	$\dot{q}_r$	H_s	P_{Surf}	Time	Shear Stress	Surface Temp.	q_{rr} $\epsilon_\sigma T_c^4$	ϵ	Weight			$\dot{s}$	$\dot{m}$	Char Thick	Fluid Medium	Remarks
No.	Mat.	Config.	W	Dia.	Pre	Post	△										Pre	Post	△					Facility and Explanatory Notes
			Lbs.	In.	Inches			Lbs/Ft^3	BTU/Ft^{2}Sec		BTU/Lb	Atmos	Secs	Psf	°R	BTU/Ft^{2}Sec		Grams		In/Sec	Lb/Sec	In.		
B07703	X6300	CYLINDER		.75			0.145	70.5	445		2680	1.22	40.4		—	169	—			2.423	0.00468	0.016		AIR	MODEL 500; HIGH PURITY
B07704							0.174		442		2846	1.23	40.4		5040	171	0.56			2.763	0.00487	0.016		
B07702							0.135		316		2160	1.21	41.5		4550	115	0.58			2.175	0.00344	0.016		
B07703A							0.123		400		2660	1.22	34.4		4970	146	0.59			2.311	0.00408	0.016		
B07701A							0.140		171		2030	1.04	36.6		3970	69	0.58			1.332	0.00100	0.007		
B07705							0.037		158		1846	1.04	40.3		3830	66	0.65			1.294	0.00106	0.007		
B07701	↓	↓		↓			0.078	↓	213		2700	1.08	40.0		4550	96	0.47			1.893	0.00214	0.010	↓	↓
B07201	X6300	CYLINDER		.75			0.062	83.8	1325		10620	1.03	30.3		6620	790	0.86				0.00260	0.00384		AIR	MODEL 500; HIGH PURITY,
B07202							0.158		1390		8300	1.14	30.5		6650	763	0.82				0.00593	0.00803			COMPRESSION MOLDED.
B07203							0.239		1435		6710	1.35	30.3		6720	778	0.86				0.00830	0.0136			
B07204							0.215		1100		4990	1.46	30.6		6440	653	0.80				0.00745	0.0172			
B07205							0.195		776		3270	1.44	30.8		6040	462	0.72				0.00818	0.0201			
B07206							0.174		1390		8290	1.14	30.6		6720	790	0.81				0.00578	0.00810			
B07301	X6400	CYLINDER		.75			0.081	85.5	1325		7860	1.03	30.3		6690	798	0.83				0.00402	0.00400			MODEL 500; HIGH PURITY,
B07302							0.161		1390		8190	1.14	30.6		6690	750	0.78				0.00643	0.00814			TAPE WRAPPED
B07303							0.260		1435		6440	1.34	30.3		6430	657	0.81				0.00868	0.0140			
B07304							0.233		1100		4950	1.48	30.4		6480	627	0.74				0.00740	0.0170			
B07305							0.216		776		3360	1.48	30.6		5910	441	0.76				0.00778	0.0201			
B07306							0.162		1390		8120	1.14	30.5		6620	723	0.89				0.00617	0.00814			
B07401	X6300	CYLINDER		.75			0.071	89.2	1325		10310	1.03	30.5		6520	710	0.83				0.00240	0.00378			
B07402							0.142		1390		8510	1.14	30.5		6530	765	0.89				0.00524	0.00672			
B07403							0.199		1435		6130	1.37	30.7		6440	707	0.84				0.00753	0.0140			
B07404							0.188		1100		4910	1.48	30.6		6160	582	0.84				0.00685	0.0172			
B07405	↓	↓		↓			0.166	↓	776		3420	1.48	30.2		5680	403	0.81				0.00628	0.0201	↓	↓

ABLATION DATA

TABLE 4.16 (CONT)

Specimen Identification			Geometry		Length			Density	$\dot{q}_c$	$\dot{q}_r$	H_s	P_{Surf}	Time	Shear Stress	Surface Temp.	q_{rr} $\epsilon_{\sigma} T_c^4$	ϵ	Weight			$\dot{s}$	$\dot{m}$	Char Thick	Fluid Medium	Remarks
No.	Mat.	Config.	W	Dia.	Pre	Post	Δ											Pre	Post	Δ					Facility and Explanatory Notes
			Lbs.	In.	Inches			Lbs/Ft^3	BTU/Ft^2Sec		BTU/Lb	Atmos	Secs	Psf	°R	BTU/Ft^2Sec		Grams			In/Sec	Lb/Sec	In.		
B02501	X4300	CYLINDER		.75			0.072	85.5	1170		10230	1.03	30.6		6450	678	0.82			2.795	0.00332	0.00360		AIR	MODEL 500; TAPE WRAPPED
B02502							0.241		1380		14700	1.34	30.7		6530	706	0.82			3.207	0.00617	0.0136			
B02503							0.186		770		3590	1.45	30.7		5130	410	0.80			2.605	0.00633	0.0197			
B02504							0.184		1170		10390	1.04	30.7		6540	697	0.80			2.554	0.00424	0.00383			
B02505							0.229		1380		6760	1.34	30.6		6570	708	0.80			3.147	0.00825	0.0137			
B02506							0.181		770		3560	1.45	30.7		5150	408	0.78			2.606	0.00640	0.020			
B02601	X4300	CYLINDER		.75			0.042	91.0	1110		9600	1.04	30.3		6450	685	0.83			2.189	0.00350	0.00381		AIR	MODEL 500; COMPRESSION MOLDED
B02602							0.200		1382		6580	1.35	30.4		6490	684	0.81			3.172	0.00850	0.0139			
B02603							0.163		766		3670	1.46	30.5		5820	415	0.76			2.646	0.00608	0.020			
B02604							0.062		1110		10040	1.05	30.4		6500	689	0.81			2.070	0.00314	0.00464			
B02605							0.197		1380		6700	1.34	30.4		6500	654	0.77			3.094	0.00752	0.0137			
B02606							0.158		760		3690	1.46	30.4		5760	393	0.75			2.618	0.00597	0.020			
B05601	X4300	CYLINDER		.75				81.3	1180		10770	1.03	30.3		6440	698	0.85				0.00363	0.00390		AIR	MODEL 500; TAPE WRAPPED
B05602									1360		8290	1.14	30.8		6420	695	0.82				0.00542	0.00802			
B05603									1382		6980	1.37	30.6		6420	662	0.82				0.00746	0.0138			
B05604									1490		5870	1.54	30.4		6320	643	0.85				0.00938	0.0171			
B05605									790		3540	1.48	30.6		5690	364	0.73				0.00611	0.0210			
B05606									1360		8730	1.15	30.4		6540	700	0.80				0.00618	0.00825			
B05701	X4300	CYLINDER		.75				87.5	1182		9980	1.03	30.6		6450	696	0.84				0.00266	0.00414		AIR	MODEL 500; TAPE WRAPPED
B05702									1362		7980	1.14	30.5		6520	701	0.82				0.00572	0.00819			
B05703									1383		6700	1.34	30.6		6450	494	0.60				0.00712	0.0137			
B05704									770		4920	1.43	30.4		6010	496	0.77				0.00622	0.0172			
B05705									770		3920	1.46	30.3		5110	366	0.72				0.00547	0.0201			
B05706									1360		8290	1.14	30.5		6490	679	0.81				0.00514	0.00814			

ABLATION DATA

TABLE 4.16 (CONT.)

Specimen Identification			Geometry		Length			Density	$\dot{q}_c$	$\dot{q}_r$	H_s	P_{Surf}	Time	Shear Stress	Surface Temp.	q_{rr} / $\epsilon_\sigma T_c^4$	ϵ	Weight			$\dot{s}$	$\dot{m}$	Char Thick	Fluid Medium	Remarks
No.	Mat.	Config.	W	Dia.	Pre	Post	Δ											Pre	Post	Δ					Facility and Explanatory Notes
			Lbs.	In.	Inches			Lbs/Ft^3	BTU/Ft^2Sec		BTU/Lb	Atmos	Secs	Psf	°R	BTU/Ft^2Sec		Grams			In/Sec	Lb/Sec	In.		
B01801	X6300	CYLINDER		.75				87.4	1170		10210	1.04	30.8		6560	683	0.77				3.43×10^{-3}			AIR	MODEL 500, PURIFIED BY FIBERITE
B01802								87.4	1340		8510	1.14	30.7		6640	730	0.79				5.94				
B01803								87.4	1380		6700	1.35	30.5		6590	760	0.78				8.39				
B01804								87.4	1100		5250	1.44	30.6		6350	600	0.77				7.15				
B01805								87.4	771		3540	1.45	30.6		5740	393	0.76				6.08				
B01806								87.4	1340		8740	1.14	30.8		6650	715	0.77				5.97				
B01901	X6300	CYLINDER		.75				89.2	1170		10350	1.04	30.6		6530	662	0.76				3.98×10^{-3}				
B01902								89.2	1340		8400	1.14	30.7		6610	706	0.77				8.06				
B01903								89.2	1380		6690	1.35	30.6		6540	675	0.77				13.89				
B01904								89.2	1100		5180	1.44	30.5		6370	615	0.78				17.01				
B01905								89.2	771		3470	1.46	30.6		5770	401	0.77				19.95				
B01906								89.2	1340		8750	1.14	30.8		6450	689	0.74				8.06				
B07801	X6400	CYLINDER		.75				87.9	1330		9970	1.03	30.8		6520	697	0.81				3.45×10^{-3}			AIR	MODEL 500
B07802								87.9	1400		8690	1.14	30.5		6550	661	0.75				6.26				
B07803								87.9	1420		6540	1.35	30.6		6530	646	0.75				7.29				
B07804								87.9	1110		4980	1.44	30.7		6270	570	0.77				6.93				
B07805								87.9	729		3330	1.44	30.3		5630	360	0.75				5.99				
B07806								87.9	1400		8220	1.14	30.7		6480	655	0.78				6.10				
B07901	X6400	CYLINDER		.75				93.5	1330		9700	1.03	30.3		6070	483	0.75				5.62×10^{-3}				
B07902								93.5	1400		8260	1.14	30.2		6120	483	0.72				1.11				
B07903								93.5	1420		6560	1.35	30.5		6060	467	0.73				1.59				
B07904								93.5	1110		5310	1.44	30.2		5970	457	0.75				1.58				
B07905								93.5	729		3290	1.44	30.6		5520	317	0.71				1.44				
B07906								93.5	1400		8570	1.14	30.2		6060	490	0.76				8.68				
B08001	X6400	CYLINDER		.75				86.1	1330		9750	1.03	30.2		6360	670	0.86				2.76×10^{-3}				
B08002								86.1	1400		8530	1.14	30.2		6650	708	0.76				5.98				
B08003								86.1	1420		6300	1.34	30.3		6440	666	0.81				8.79				
B08004								86.1	1110		5040	1.44	30.5		6200	554	0.79				7.20				
B08005								86.1	729		3220	1.44	30.4		5720	314	0.71				6.95				
B08006								86.1	1400		8470	1.44	30.2		6570	640	0.77				5.99				

ST-211

ABLATION DATA

TABLE 4.16 (cont.)

Specimen Identification			Geometry		Length			Density	$\dot{q}_c$	$\dot{q}_r$	H_s	P_{Surf}	Time	Shear Stress	Surface Temp.	q_{rr} $\epsilon_\sigma T_c^4$	ϵ	Weight			$\dot{s}$	$\dot{m}$	Char Thick	Fluid Medium	Remarks
No.	Mat.	Config.	W	Dia.	Pre	Post	△											Pre	Post	△					Facility and Explanatory Notes
			Lbs.	In.	Inches			Lbs/Ft^3	BTU/Ft^{2}Sec		BTU/Lb	Atmos	Secs	Psf	$^\circ$R	BTU/Ft^{2}Sec		Grams			In/Sec	Lb/Sec	In.		
1	X6300	SQUARE							525		9108	3.80	10.08	17.3						8.4				AIR	TEN MEGAWATT ARC TEST; HIGH PURITY, TAPE WOUND
2		PIPE							529		9176	3.82	10.09	17.3						4.1					
3									485		6840	4.05	10.03	19.5						9.5					
4									495		6995	4.07	10.04	19.6						8.8					
5									490		3523	4.19	10.02	29.1						8.2					
6									480		3623	4.19	10.05	29.1						8.2					
1	X6400	SQUARE							539		9345	3.83	10.17	17.4						7.0				AIR	TEN-MEGAWATT ARC TEST; HIGH PURITY
2		PIPE							539		9345	3.83	10.20	17.4						7.0					
3									497		7043	4.10	10.07	19.7						7.2					
4									491		7043	4.10	10.06	19.7						7.5					
B14301	X6300	CYLINDER		.75			0.163	78.7	1310		9740	1.03	45.7		6860	780				—	0.0036	0.004		AIR	MODEL 500.
B14302							0.282	81.0	1220		5140	1.44	39.6		6510	640				4.050	0.00740	0.0265			
B14303							0.300	81.0	860		3980	1.44	45.8		6040	455				4.270	0.00704	0.01905			
	X6300	SONIC PIPE									4673	12.1	5.00							22.6			0.05	AIR	10 MW ARC

TABLE 4.17

THERMAL CONDUCTIVITY TEST DATA
(R6300)

Char Temperature (°F)	Char Density (lb/ft^3)	Test Temperature (°F)	Thermal Conductivity (Btu/ft-hr-°F)
RT	85.7	212	0.390
		300	0.430
		485	0.435
700	80.9	240	0.335
		490	0.360
		665	0.425
1000	74.9	240	0.292
		640	0.374
		895	0.385
1500	73.9	230	0.435
		625	0.555
		880	0.585
2000	68.2	240	0.500
		615	0.675
		870	0.710

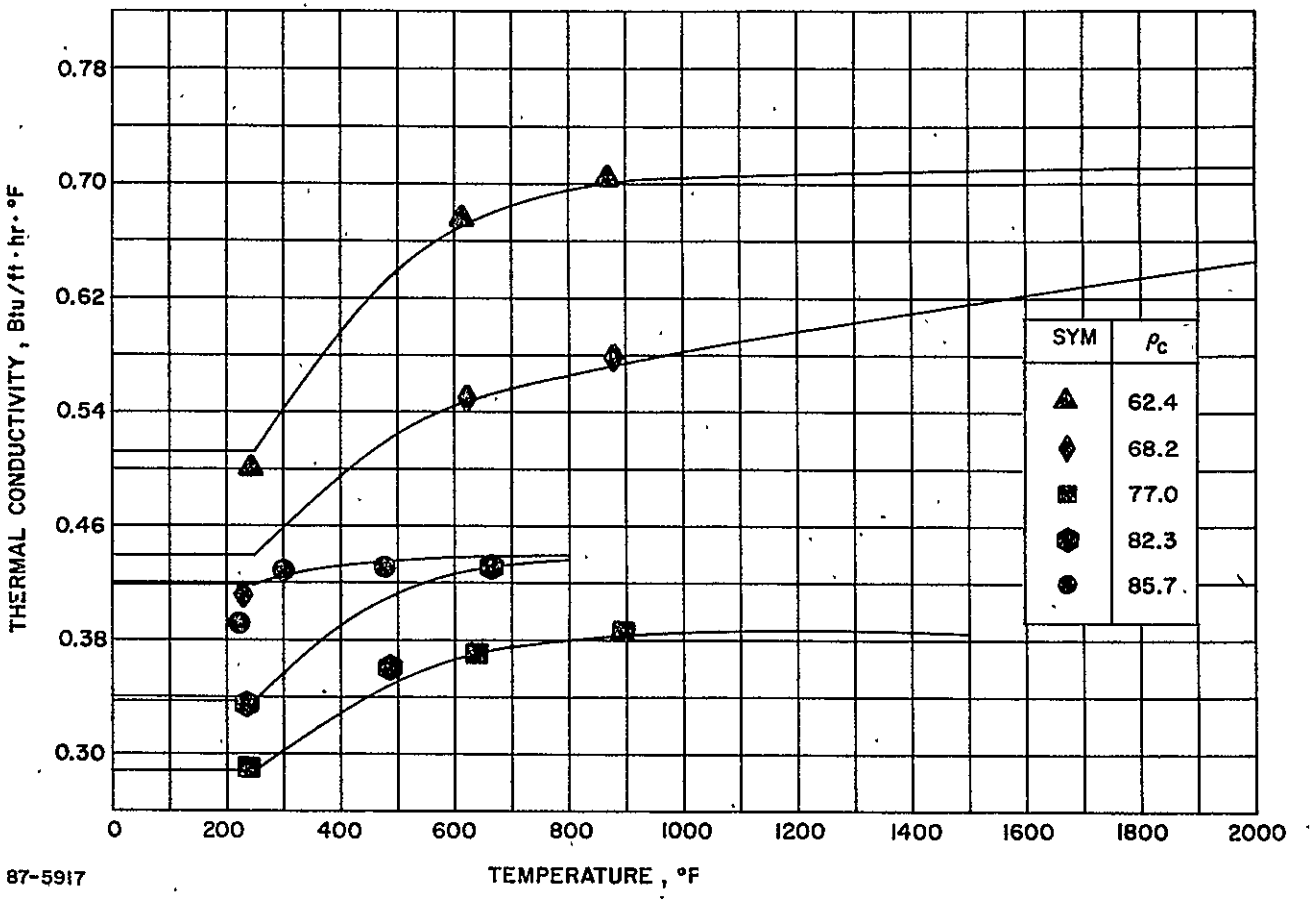


Figure 4.60 . THERMAL CONDUCTIVITY FUNCTIONS AVCO R6300 - ORIGINAL TEST DATA CURVE FITS

Table 4.18

THERMAL CONDUCTIVITY MULTIPLIERS -- R6300

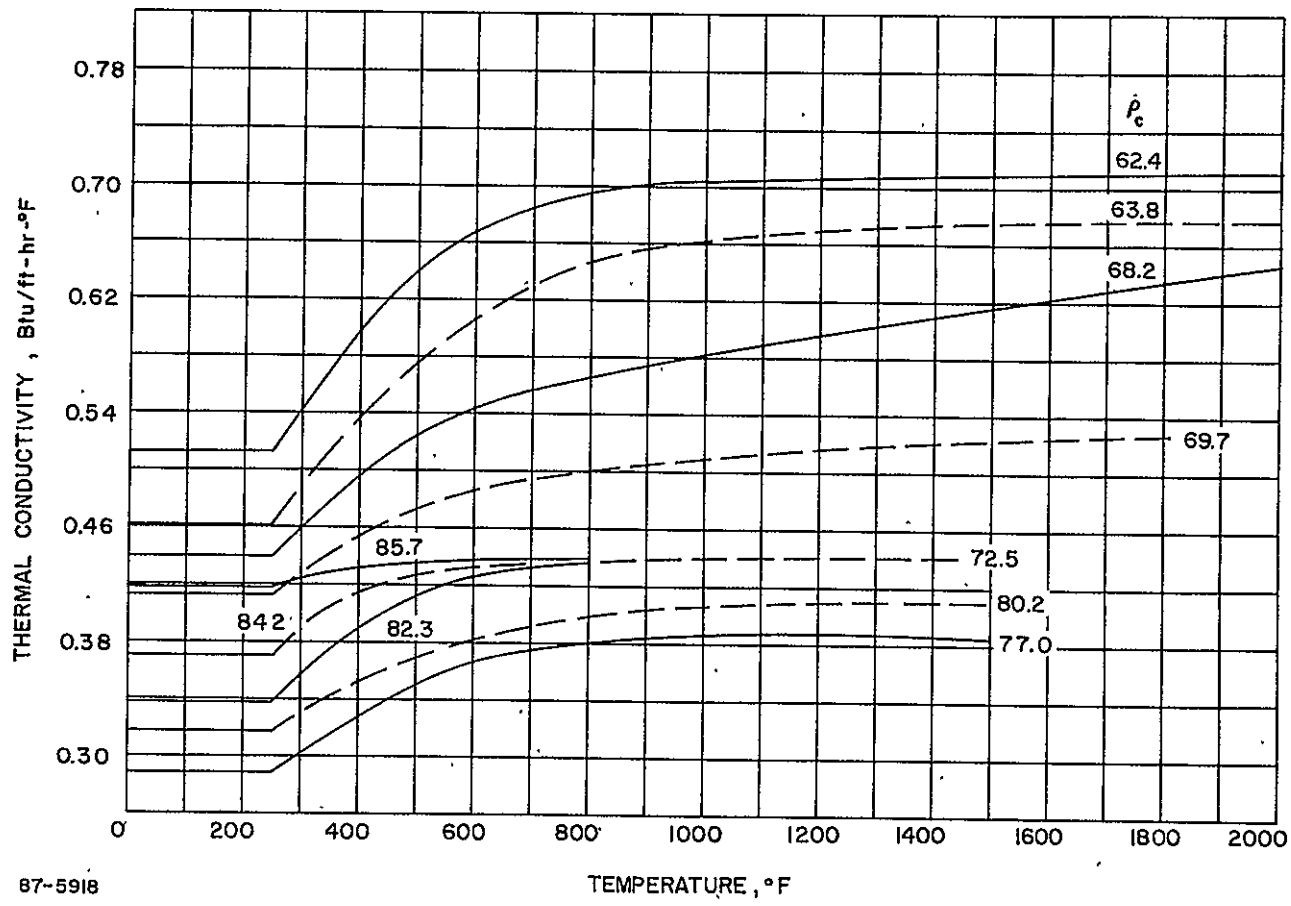
ρ	$\Delta\rho$	k ($T_{x,\ t} \leq 610°$ R)	KM Function ($T_{x,\ t} > 610°$ R)
85.7	85.70 - 84.50	0.418	$0.438 - 128.74\ (10.0)^{-5.105} \times 10^{-3}\ T$
84.2	84.49 - 83.30	0.370	$0.440 - 19.796\ (10.0)^{-2.688} \times 10^{-3}\ T$
82.3	83.29 - 82.00	0.337	$0.440 - 2.261\ (10.0)^{-1.905} \times 10^{-3}\ T$
80.2	81.99 - 79.30	0.317	$0.409 - 1.553\ (10.0)^{-1.660} \times 10^{-3}\ T$
77.0	79.29 - 74.40	0.288	$0.385 - 2.480\ (10.0)^{-2.007} \times 10^{-3}\ T$
72.5	74.39 - 71.60	0.337	$0.440 - 2.261\ (10.0)^{-1.905} \times 10^{-3}\ T$
69.7	71.59 - 69.10	0.412	$0.508 + 1.25 \times 10^{-6}\ T - 1.896\ (10.0)^{-1.826} \times 10^{-3}\ T$
68.2	69.09 - 66.20	0.438	$0.498 + 6.0 \times 10^{-5}\ T - 2.378\ (10.0)^{-1.971} \times 10^{-3}\ T$
63.8	66.19 - 63.30	0.461	$0.675 - 4.449\ (10.0)^{-1.704} \times 10^{-3}\ T$
62.4	63.29 - 58.00	0.512	$0.710 - 4.515\ (10.0)^{-1.898} \times 10^{-3}\ T$

Although it is obvious to assume that the thermal conductivity of R6300 is a continuous function of char density and temperature, the task of simulating conductivity in the KM form as a continuous function is highly complicated, because of the number of coefficients and the problems associated with predicting the individual rates of change of these coefficients with temperature and char density. In order to simplify this problem, a number of additional KM functions were derived for intermediate char densities and superimposed on the original test data curve fits resulting in the set of curves shown in Figure 4.61. The equations for all functions are given in Table 4.18. The assumption is then made (for the sake of computer simulation) that each function is applicable over a small range rather than continuous functions which would (in theory) require an infinite number of expressions. The $\Delta\rho$ column in Table 4.18 indicates the density range of application for each KM function.

4.5.1.1.3 Specific Heat

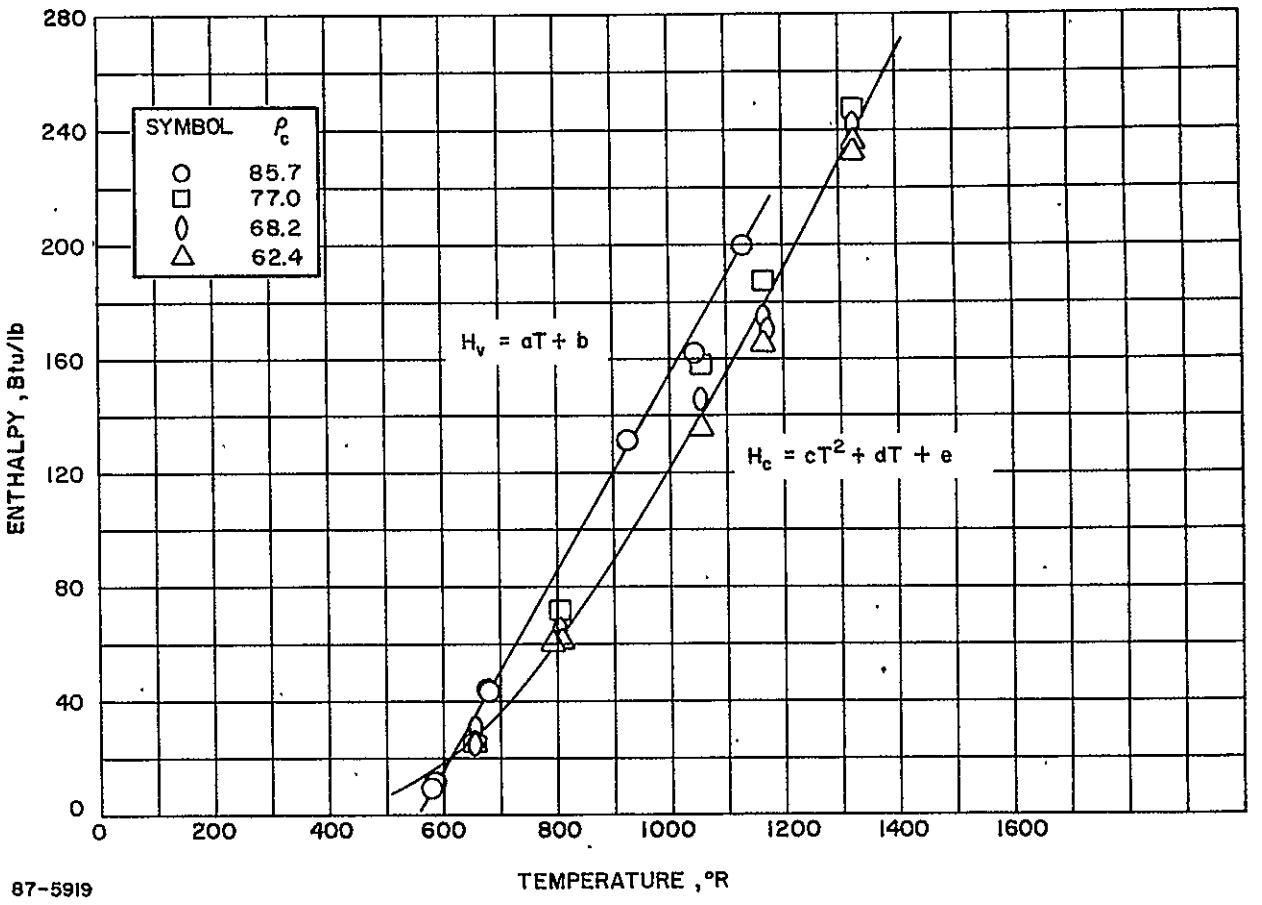
As in the case of thermal conductivity tests, measurements of enthalpy at various temperatures were made for both the virgin and precharred samples.

Calculation of the rate of change of enthalpy with temperature ($\partial H/\partial T$) is a measure of the specific heat of the material. Second order polynominals were derived for the existing data and the first derivative ($\partial H/\partial T$) was used to calculate specific heat values for each precharred condition at several temperatures. The expression ($\partial H/\partial T$) was not found to vary significantly with char density and so the average value of specific heat at each temperature is reported as the specific heat of char. A first degree fit of the virgin material test data resulted in a slope set equal to the virgin specific heat. The test data and curve fits are shown in



THERMAL CONDUCTIVITY FUNCTIONS AVCOR6300 - FULL SET OF SIMULATED FUNCTIONS

Figure 4.61



ENTHALPY-TEMPERATURE DATA AVCO. R6300

Figure 4.62

Figure 4.62. The resultant values of specific heat used for heat shield calculations are shown in Figure 4.63.

4.5.1.1.4 Density

Thermogravimetric analysis (TGA) data were used to compute char density which is an irreversible function of temperature. Exception was taken of the reported curve in that it indicated a 5 percent weight loss at 212°F. To ensure that R6300 tape-wrapped parts did not in fact contain this much moisture, samples were placed in an oven at about 230°F for 17 hours and measured weight loss was 0.80 percent. A tape-wrapped part was powdered (as in TGA tests) and this powder, under the same oven conditions, lost 4.5 percent of its weight in 10 minutes, indicating moisture pick-up from the atmosphere.

A plot of material density as a function of temperature, for R6300 reduced from the TGA data, is given as Figure 4.64. Density points from the thermal conductivity samples are also shown on this curve as well as a number of density points derived from ROVERS samples.

4.5.1.1.5 Correlation of Internal Properties(ROVERS Tests)

A series of eight samples were tested in the ROVERS facility so that a correlation between the material properties determined, as outlined above, and the transient thermal response of R6300 samples could be made. Results of the analysis performed on three of the tests are reported here with the test environments stated in Table 4.19. Thermocouple locations and sample dimensions are given in Table 4.20.

Calculations were performed on Avco Computer Program 1650 (a program in which a surface heating rate and internal temperature histories of a one-dimensional composite are calculated, given a surface temperature history - an inverse conduction problem - using the highest recorded

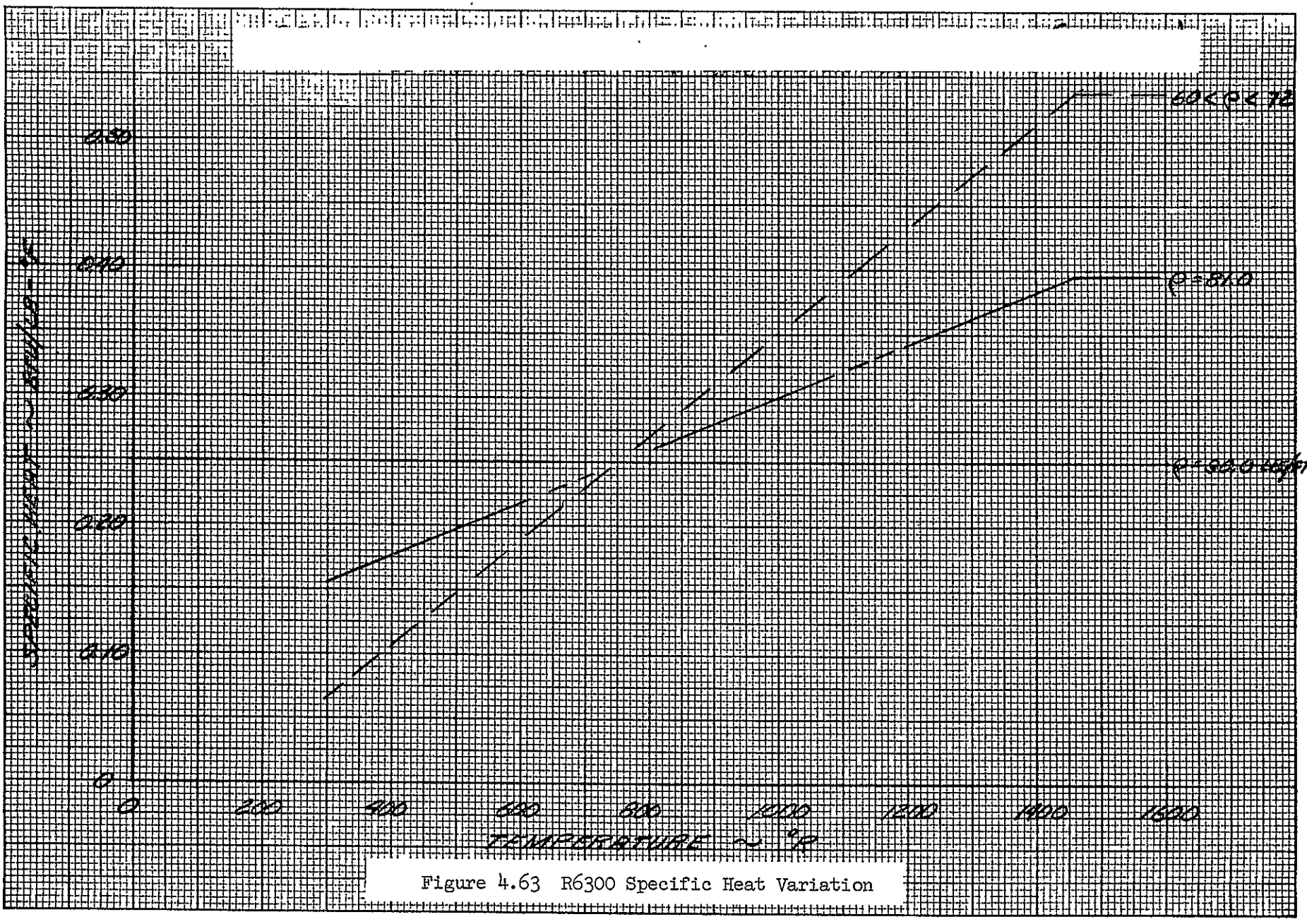
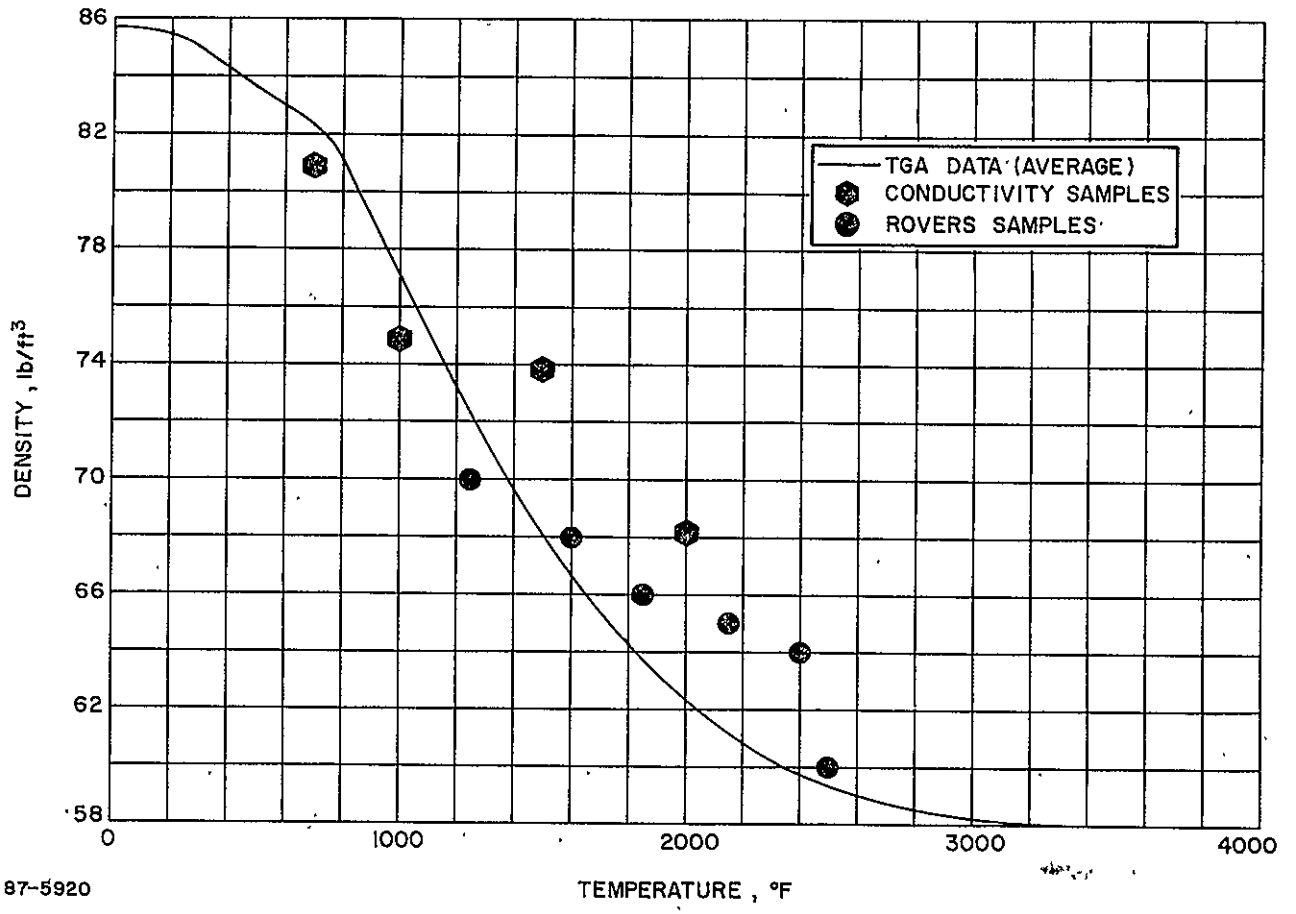
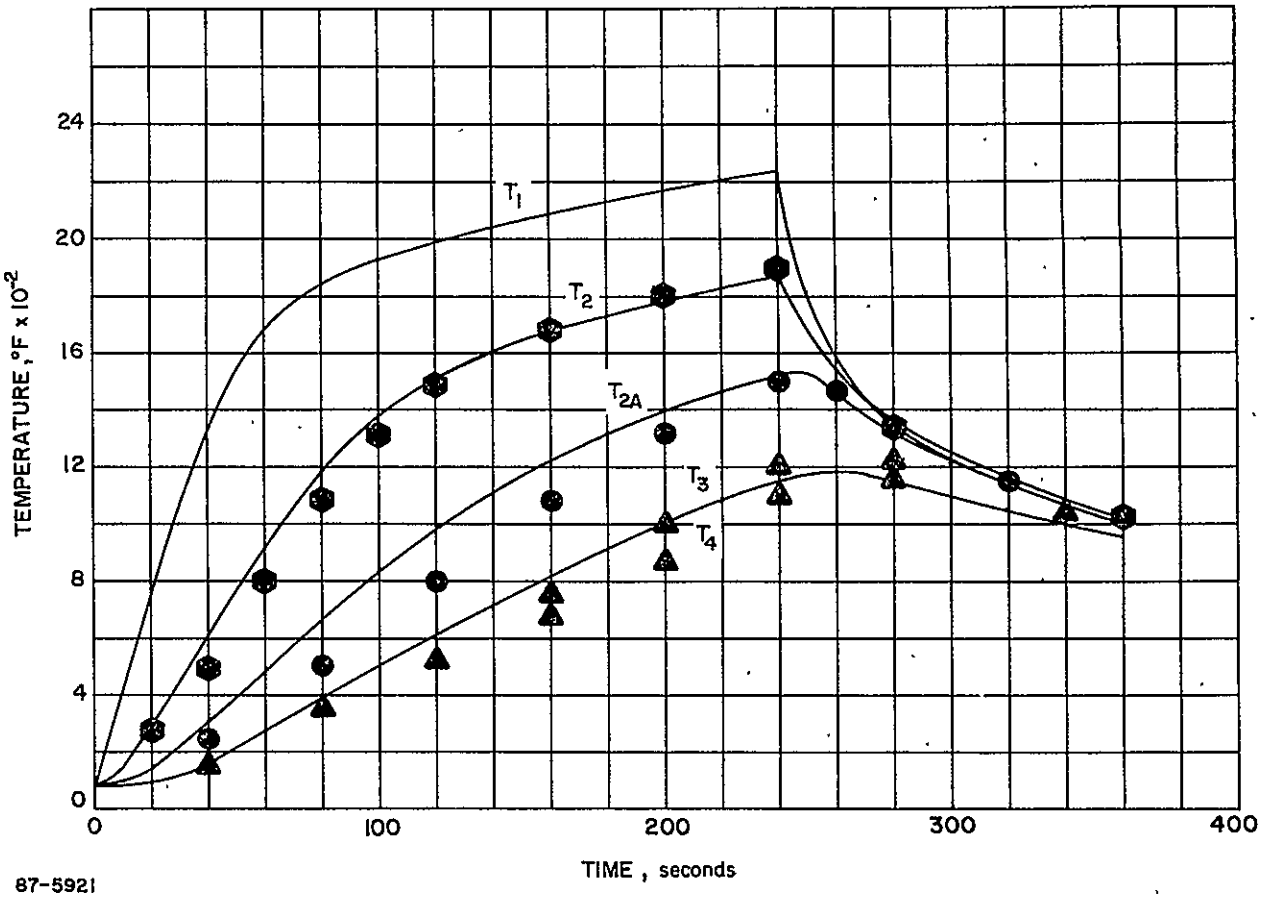


Figure 4.63 R6300 Specific Heat Variation



DENSITY-TEMPERATURE RELATIONSHIP R6300

Figure 4.64



COMPARISON OF PREDICTED AND MEASURED THERMAL RESPONSE
ROVERS TEST R6300-1

Figure 4.65

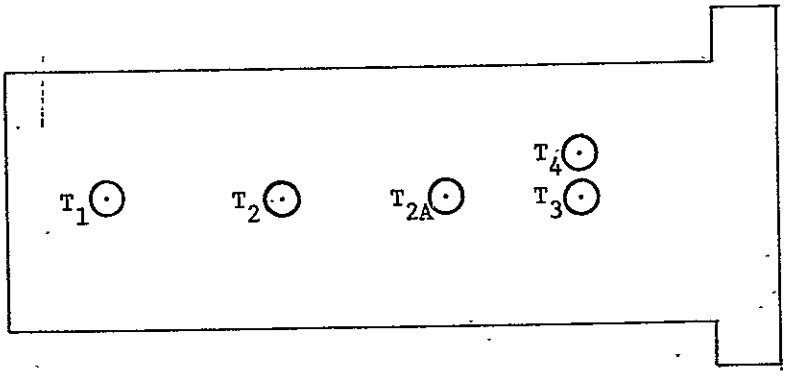
TABLE 4.19

ROVERS TEST ENVIRONMENTS -- R6300

Test No.	$\dot{q}_c$ (Btu/ft^2-sec)	H_s (Btu/lb)	Run Time (sec)
6300-1	42	9800	240
6300-3	100	10,300	180
6300-8	270	10,600	80

TABLE 4.20

THERMOCOUPLE LOCATIONS ROVERS TESTS - R6300



Thermocouple Number	Distance from Front Surface (inch)	Radial Displacement (inch)
1	0.10	0.062
2	0.20	0.062
2A	0.30	0.062
3	0.40	0.062
4	0.40	0.190

temperatures as the forcing functions. Results of calculations are shown in Figures 4.65 through 4.68 with the analytical predictions drawn as solid or broken lines (broken lines indicating estimated response) and experimental data shown as points.

The correlation shown in these figures indicate good agreement between test data and the analytical model. In addition to the temperature data, a final density profile for R6300-3 is shown in Figure 4.69. The predicted density profile was calculated using Program 1650.

4.5.1.2 Surface Recession Parameters Determination

4.5.1.2.1 Model 500 Arc Tests

Specimens of R6300 were tested in this facility to generate ablation and surface radiation data for material performance in a low heating environment. The assumption that material performance in the diffusion ablation regime is proportional to the heat transfer coefficient, as reviewed below, was sustained by experiment. In essence, the parameters evaluated under this analysis were TW and HC.

4.5.1.2.2 Data Reduction Technique

Bartle (Reference 59) has taken the expression for a diffusion controlled ablation rate.

$$\dot{S}_D = \frac{TW}{\rho} \times \frac{12}{16} \times \frac{W_e}{RT_o} \times h \times \phi_1 \phi_2 \qquad (24)$$

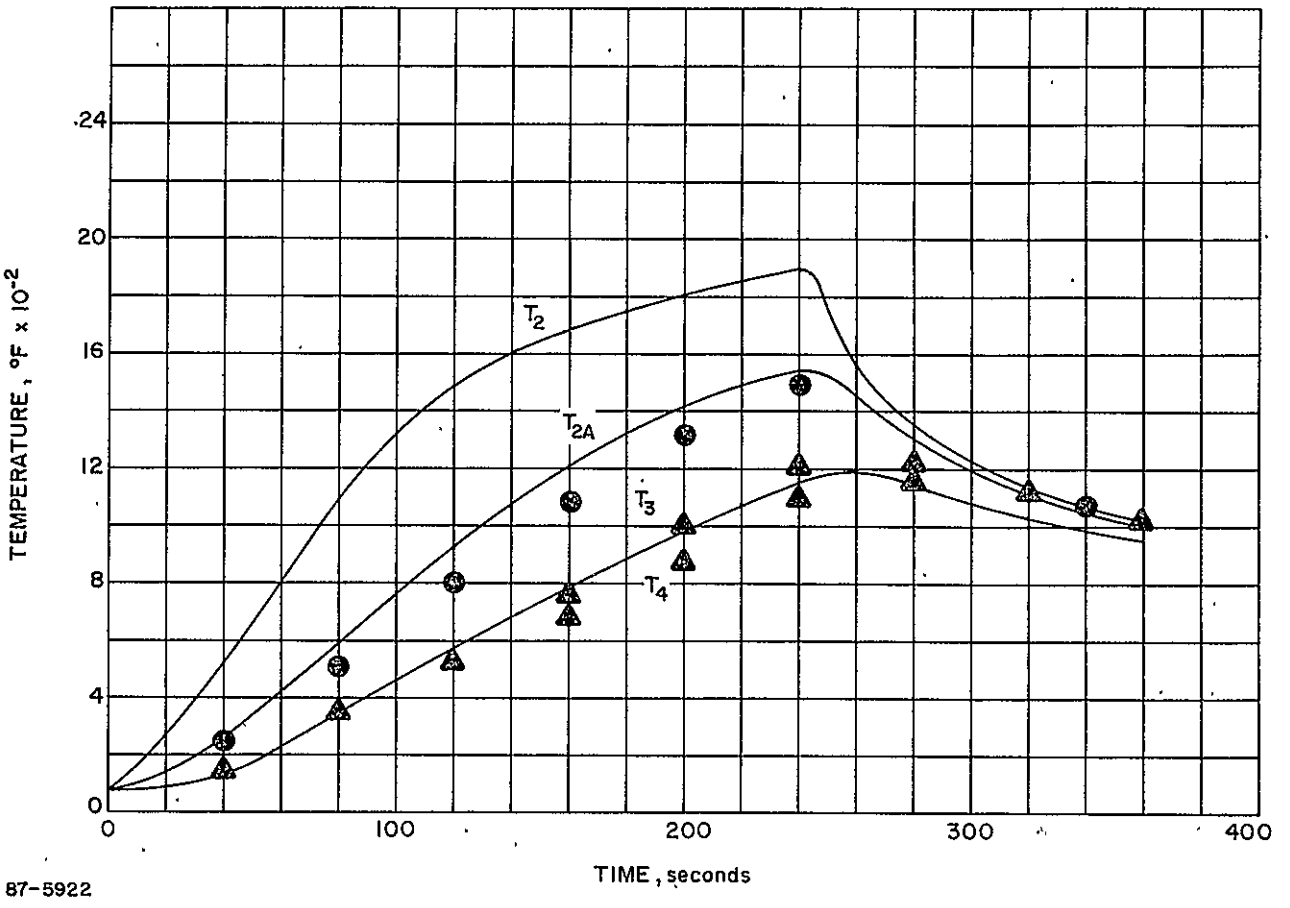
where:

$h = \dot{q}_c / h_s / RT_o$

ϕ_1 = Transpiration reduction

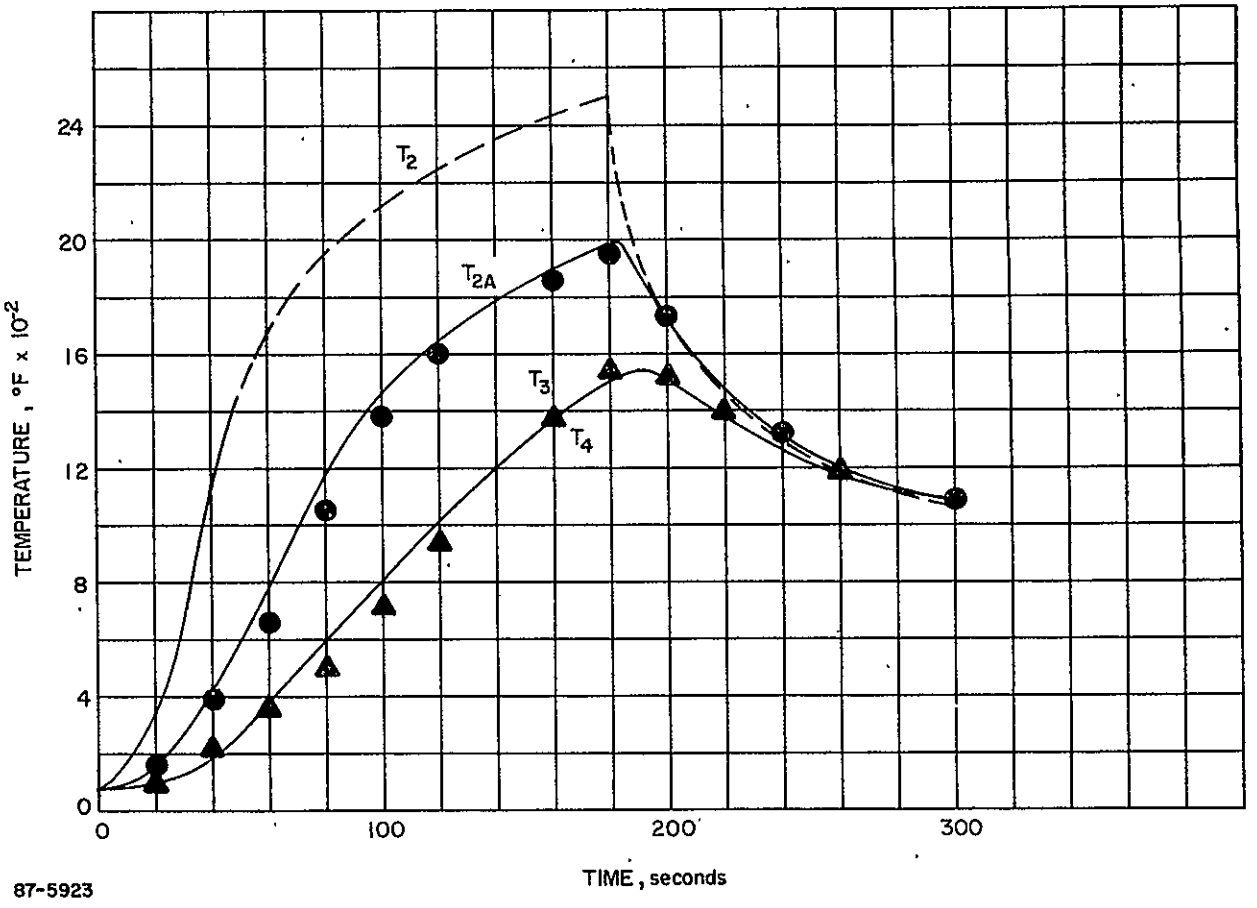
ϕ_2 = Calorimeter correction

and made the following assumptions:



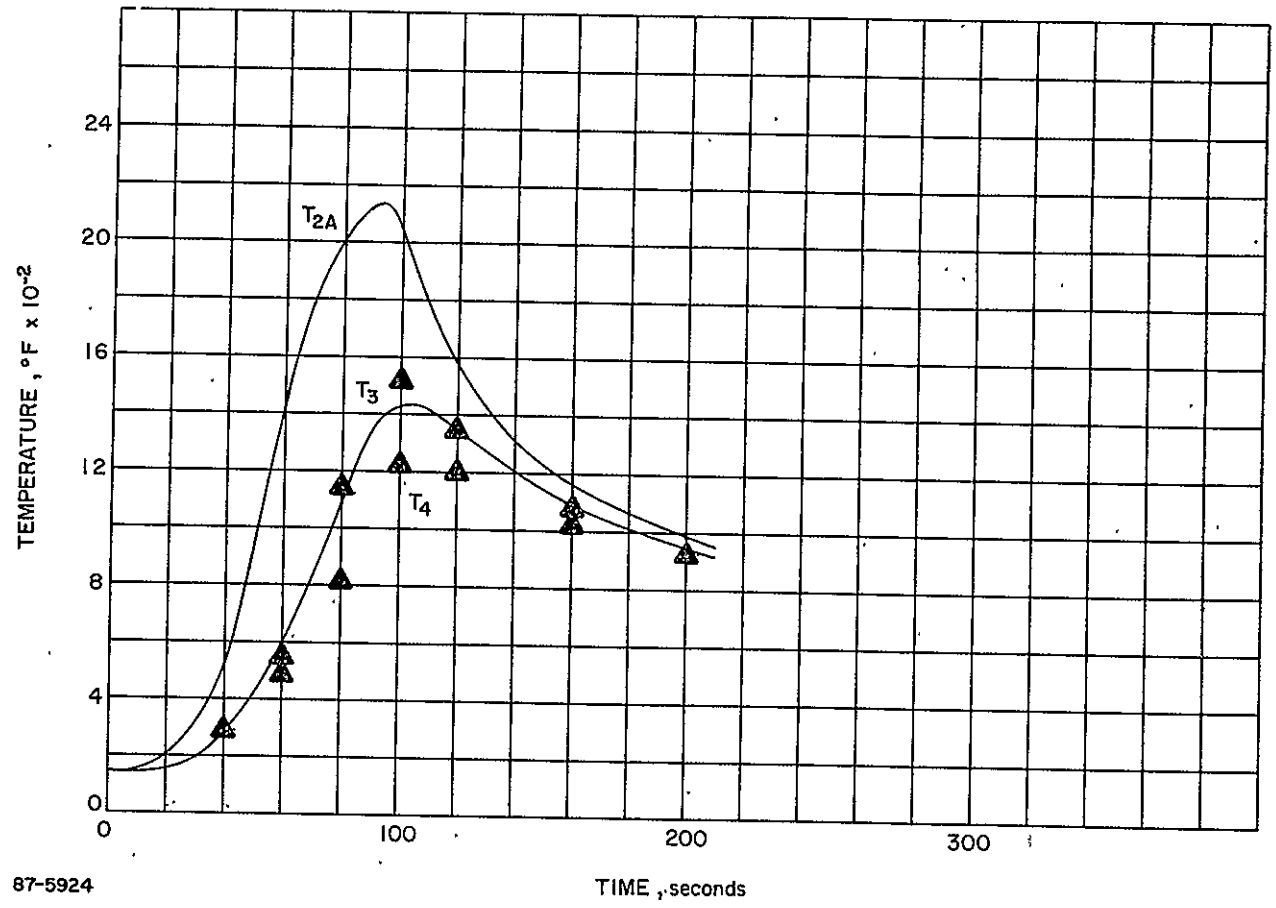
COMPARISON OF PREDICTED AND MEASURED THERMAL RESPONSE
ROVERS TEST R6300-1

Figure 4.66



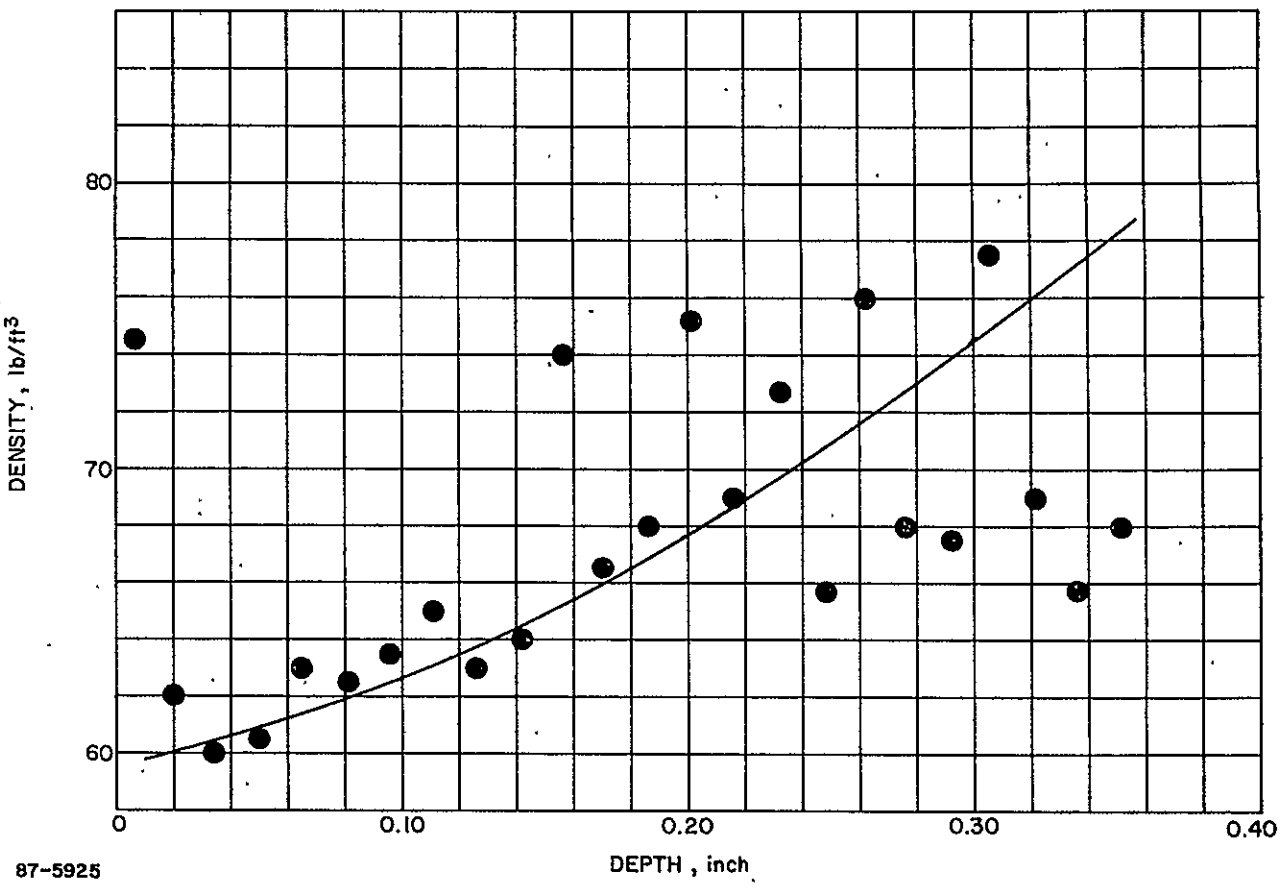
COMPARISON OF PREDICTED AND MEASURED THERMAL RESPONSE
ROVERS TEST R6300-3

Figure 4.67



COMPARISON OF PREDICTED AND MEASURED THERMAL RESPONSE
ROVERS TEST R6300-8

Figure 4.68



FINAL DENSITY PROFILE ROVERS TEST R6300-3

Figure 4.69

a. Linear reduction

b. Steady state

c. Fully charred surface

d. TW = 1.00

The above conditions enable a rewrite of the S_D equation as:

$$\dot{S}_D \left(\frac{W_{e_o}}{W_e} \right) = C \frac{h \phi_2}{\Psi} \tag{25}$$

where:

$$C = \frac{12}{16} \times \frac{1.00}{\rho_c} \left(\frac{W_{e_o}}{RT_o} \right)$$

$$\Psi = 1 + \frac{12}{16} \frac{\rho_o}{\rho} \eta (W_e) \phi_2$$

The simplifying assumptions (a - d) were determined to be reasonable by the series of Program 1600 calculations made both by Bartle in the original work and also for the work of reference 58.

A series of preliminary calculations were required in order to put the published data into the form of Equation 25 above. An example of the calculations of W_e, the local free-stream-oxygen fraction, may be found in Table 4.21 (for specimen RT 29-1). From such a calculation it is evident that W_e may be expressed as

$$W_e = \frac{0.2314 \dot{m}_{air} - \frac{16}{12} \dot{m}_c}{\dot{m}_{air} + \dot{m}_c} \tag{26}$$

Since there is a measurable m_c for each test specimen, due to carbon electrode comsumption, the value of W_e will differ from the W_{e_o} value of air.

Values of heating rates reported in the test data are average values from water-cooled calorimeter measurements and must be corrected for both hot wall effects and reference wall enthalpy. Equation 27 was used to produce the

TABLE 4.21

DETERMINATION OF FREE STREAM OXYGEN FRACTION (W_e)
(Rates in lbs/sec)

1.	O_2 content from $\dot{m}_{air}$ = 0.2314 x 4.79	= 1.1084
	N_2 content from $\dot{m}_{air}$ = 0.7686 x 4.79	= 3.6816
	C content expressed as $\dot{m}_c$ (electrode)	= 0.2330
	Total initial air stream + carbon	= 5.0230
2.	Amount of O_2 used for CO formation:	
	0.233 x 16/12 = 0.3107	
3.	Amount of CO formed:	
	0.233 x 28/12 - 0.5437	
4.	O_2 in gas stream = 1.1084 - 0.3107	= 0.7977
	N_2 in gas stream (unchanged)	= 3.6816
	CO formed and added to gas stream	= 0.5437
	Final stream total (unchanged)	= 5.0230
5.	O_2 fraction = W_e = 0.7977/5.0230	= 0.1588

cold-wall heat rates.

$$\dot{q}_{cw} = \dot{q}_o \left(\frac{h_s}{h_s - h_c} \right) \left(\frac{h_w}{h_c} \right)^{-0.037} \qquad (27)$$

where:

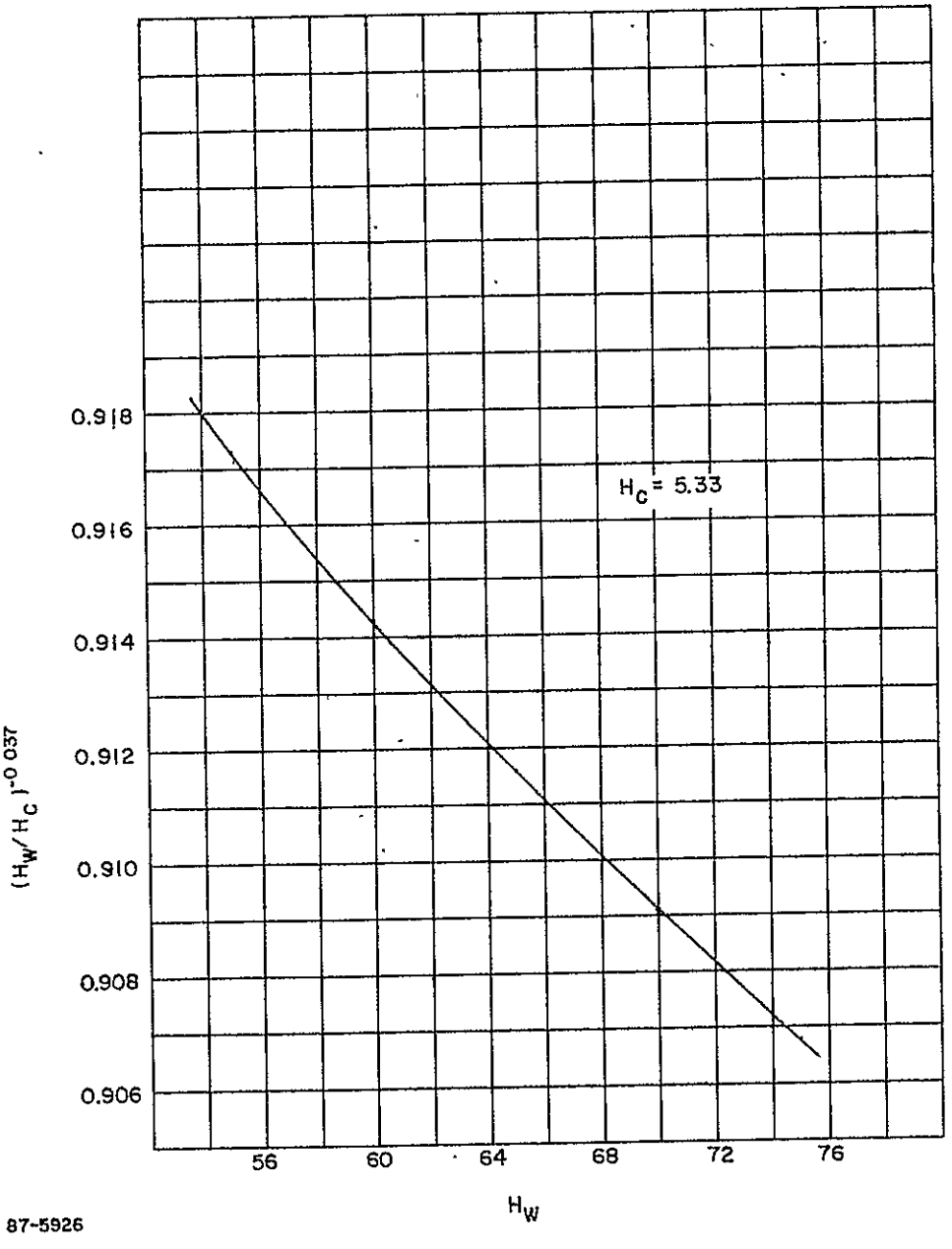
h_s = stagnation enthalpy

h_c = calorimeter wall enthalpy

h_w = ablating surface wall enthalpy

Since the value of h_w can only be approximated, the effect of the reference enthalpy correction was calculated over a range of possible h_w values. The results of this calculation are shown in Figure 4.70 and an approximate value of 0.91 was used for this correction.

Pertinent data for the ensuing analysis are contained within the data



ACTUAL WALL ENTHALPY CORRECTION AS A FUNCTION OF WALL ENTHALPY

Figure 4.70

of Table 4.16. It is now possible to plot the experimental results in the form of equation(25) and proceed with the analysis of the data.

4.5.1.2.3 Results of Analysis

An initial note should be made that the RT 28 specimen series were molded at 1000 psi while the RT 29 series were molded at 200 psi. As will be evident, this fact does not significantly alter the ablation behavior of the material and the internal properties, as noted, were determined for the RT 29 test series so that the resulting "set" of material properties will be for R6300 molded at 200 psi.

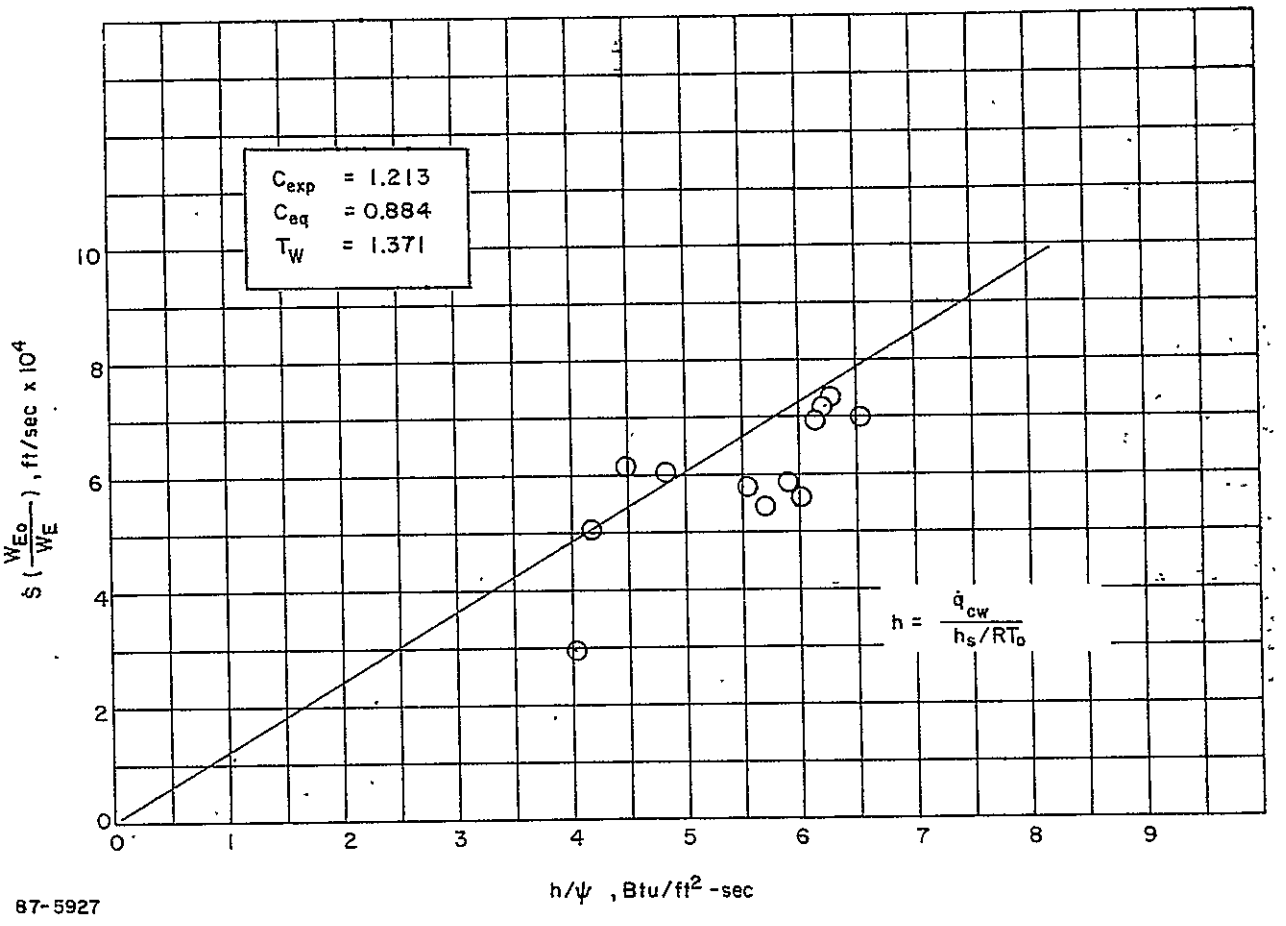
The plot of the data is shown as Figure 4.71 with a linear curve fit through all data points. The ratio of C_{exp} to C_{eq} yields a preliminary value of TW to be used for the Program 1600 calculations. Two objectives of calculations using Program 1600 are anticipated:

a. Match of specimen ablation

b. Match of surface re-radiation flux

To achieve objective 1), small variations in the value of TW are required to minimize the differences between calculated surface recession and experimental surface recession. To achieve objective 2), variations in HC (heat of combustion) are required until a value is found which results in minimum differences between values of surface re-radiation flux.

Figure 4.71 shows the data points with the best linear fit (TW = 1.371). Table 4.22 shows a summary of the $\dot{S}$ values and the values of HC required to match the test $\dot{q}_r$. A value of HC = 1.2×10^4 is a satisfactory choice for a constant value of this parameter derived from this test series and hence is the present value of HC used in the mathematical model for $\dot{S}_D$.



MODEL 500 ARC REDUCED DATA PLOT ABLATION RATE PARAMETER
VERSUS HEAT TRANSFER PARAMETER

Figure 4.71

TABLE 4.22

RESULTS OF DIFFUSION ANALYSIS

Test No.	$\dot{q}_r$ (Btu/ft^2-sec)	$\dot{s}_D$ (inches/sec)	$\dot{s}_{test}$ (inches/sec)	HC (Btu/lb)
15-1	578	0.0070	0.0073	1.38×10^4
28-4	555	0.0067	0.0076	1.22×10^4
16-1	472	0.0063	0.0065	1.23×10^4
28-5	452	0.0066	0.0062	1.17×10^4
16-2	394	0.0068	0.0066	1.21×10^4
28-6	(Considered replicate of 16-2)			

4.5.1.3 Reaction Rate Constants Bench Tests

4.5.1.3.1 Introduction

During both the ascent and terminal re-entry phases of a vehicle flight having an exposed carbon phenolic heat shield, an oxygen-rich boundary layer environment produces a surface recession rate which is controlled by chemical kinetics of the reaction:

$$3C + 2O_2 \rightarrow 2CO + CO_2 \qquad (28)$$

The mass loss rate (m) for such a system may be expressed in terms of the environment as:

(29)

where:

$$\dot{m} = A (P_{O_2})^n \exp (-B/T_w)$$

A, n, B = Reaction rate constants

P_{O_2} = Partial pressure of oxygen

T_w = Surface temperature

Euqation(29)is u

determining surface recession under a reaction controlled regime. As indicated by the form of Equation (29), values of m determined experimentally at various values of T_w will yield the data necessary to evaluate the rate constants.

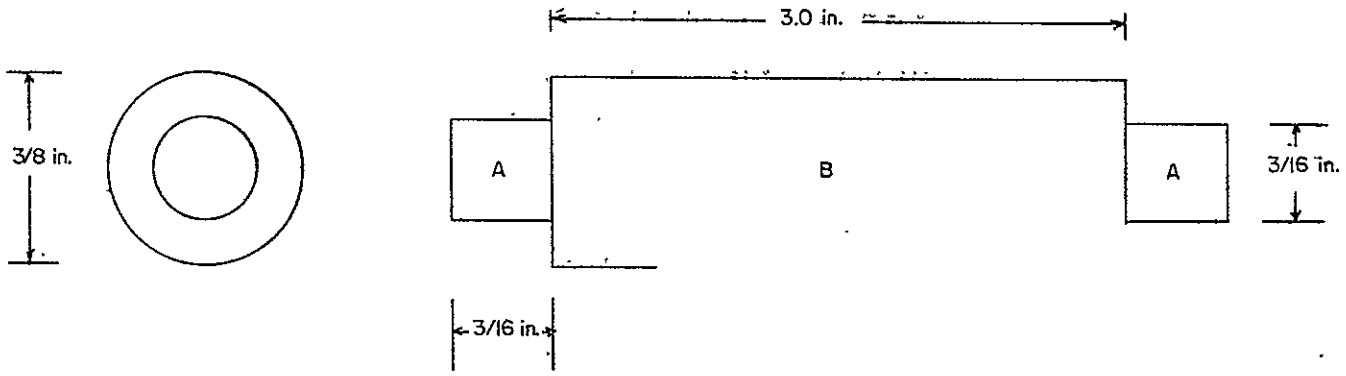
4.5.1.3.2 Test Method and Results

Precharred test specimens of R6300 (T_{char} - 1500°F) having the geometry shown in Figure 4.72 were heated electrically with the current controlled by a thermocouple sensor to maintain constant temperature. An infrared radiometer was used to measure the surface temperature of the test specimen and the resulting mass loss was measured gravimetrically.

Two series of tests were run with test specimens of R6300. Temperatures at which the test data has validity are constrained at both the high and low levels. At some high temperature level ($T_w \simeq 1040°F$) the energy produced by the exothermic chemical reaction is greater than the energy lost due to convection and radiation. When this phenomenon occurs, the surface temperature will continue to rise without any power input and the test data becomes invalid. Data below a wall temperature of 550°F shows an unexplained change of mechanism and so the test data used for determination of the reaction rate constants were obtained in the temperature range of 550-1040°F. Data in the form of m values versus values of $1/T_w$ are shown in Figure 4.73 for both test series.

4.5.1.3.3 Data Analysis

Use of Equation (29) for evaluating the reaction rate test data is accomplished by rewriting the equation in the following form:

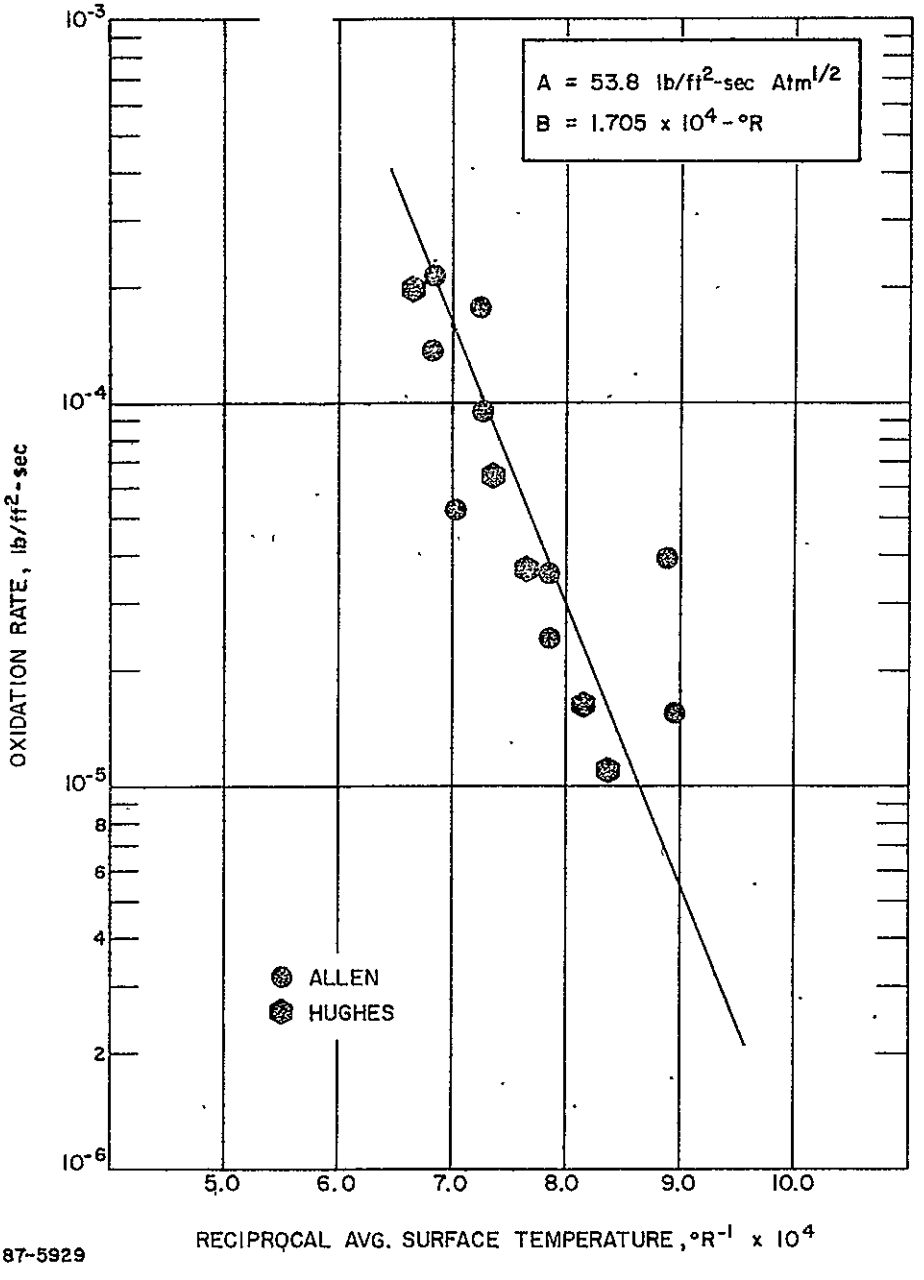


A. AREAS OF SUSPENSION
B. TEST SPECIMEN

87-5928

APPROXIMATE TEST SPECIMEN GEOMETRY REACTION RATE DETERMINATION
TESTS AVCO R6300

Figure 4.72



TEST SPECIMEN DATA REACTION RATE TESTS - AVCO R6300

Figure 4.73

$$\frac{\log \dot{m}}{0.4343} = \frac{\log (A\, p^n)}{0.4343} - B\, \frac{1}{T_w} \qquad (30)$$

A plot of Equation (30) results in a straight line and the line shown on Figure 4.72 is a least-squares fit of the applicable data. The slope of that line (B) is 1.705×10^4 °R.

By substitution in Equation (29), the value of the 1/T - 0.0 intercept A' ($A \left[P_{O_2}\right]^n$) may be calculated. The value of A' is 24.6. This value of A' divided by $\sqrt{P_{O_2}}$ is:

$$A = 53.8 \text{ lb/ft}^2\text{-sec-atm}^{0.5}$$

In summary, the reaction rate constants obtained by the above analysis are:

$$A = 53.8 \text{ lb/ft}^2\text{-sec-atm}^{0.5}$$

$$B = 17050.0^{\circ} \text{ R}$$

Having obtained a set of reaction rate constants by the methods discussed previously, a comparison of material behavior under an arc environment with behavior predicted by use of Program 1600 is required. Two test specimens of Avco R6300 were put in the Avco Model 500 arc facility and subjected to the following environments:

Specimen No.	H_s/RT_o	q_c (Btu/ft^2-sec)
6300-2	267	1180
6300-4	286	1321

The specimens were subjected to the above environments until a steady-state value of surface re-radiation flux was measured by a thrmopile. Upon achieving steady-state conditions the arc was shut down and the surface re-radiation recorded for a period of about 18 seconds.

Figure 4.74 shows the experimental points corrected for instrument response lag, and also the predicted surface response based on results from Program 1600. As indicated by Figure 4.74, a close agreement with experimental results was achieved by using the previously obtained rate constants.

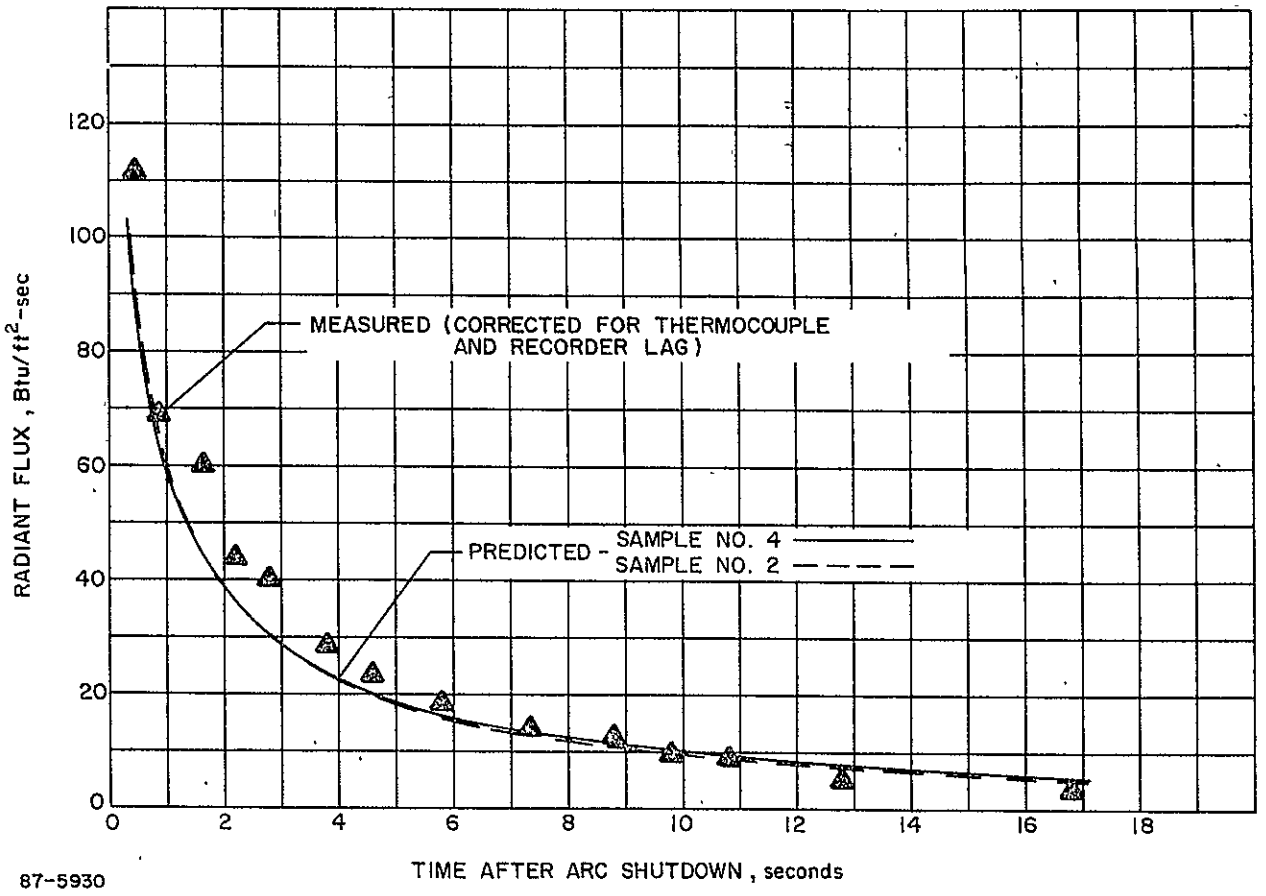
4.5.1.4 Carbon Sublimation

No ground test facilities are presently available in which tests can be run to obtain sublimation behavior for carbon-reinforced heat shield materials. Therefore, the mathematical model and thermochemical properties currently used for predicting ablation behavior in this range are subject to uncertainties inherent in the different theoretical approaches published to date.

As presented by Munson (Reference 60), the vapor pressure-temperature relationship for carbon has been calculated from the JANAF tables--a standard thermochemical reference. These data appear in error since they disagree by two orders of magnitude with a measured triple point of carbon. As shown in Figure 4.75, Avco has modified the P_v - T function to be consistent with the triple point data.

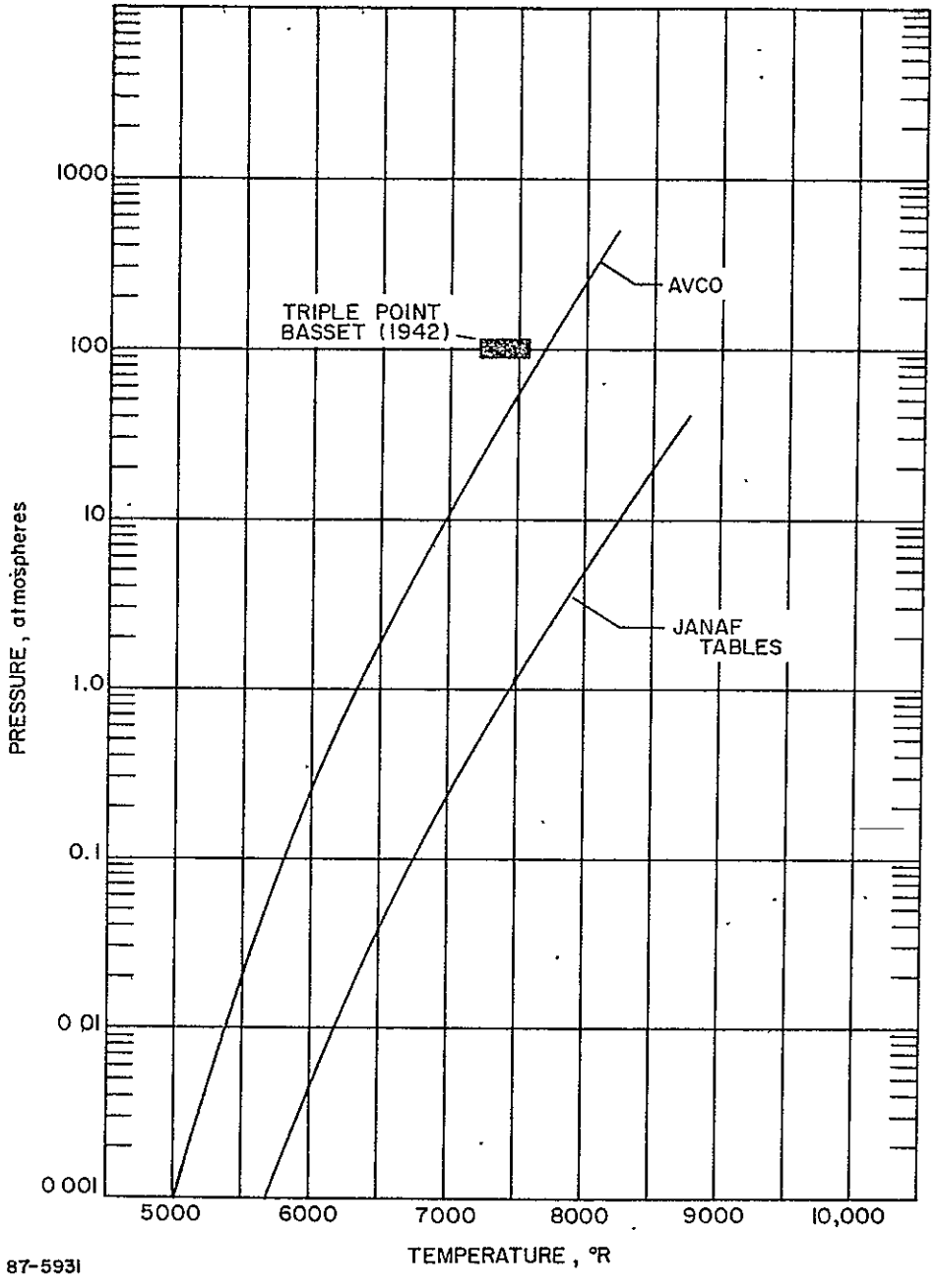
Using the revised P_v - T relationship, Figure 4.76 illustrates the axial tip recession of two-pointed, slender carbon cones tested in Avco's 10 MW facility. Accurate test predictions are extremely difficult due to the large shape change effects taking place throughout the test. Nevertheless, the calculated recession reasonably approximates the test results.

At this time, no flight test data are available to aid in



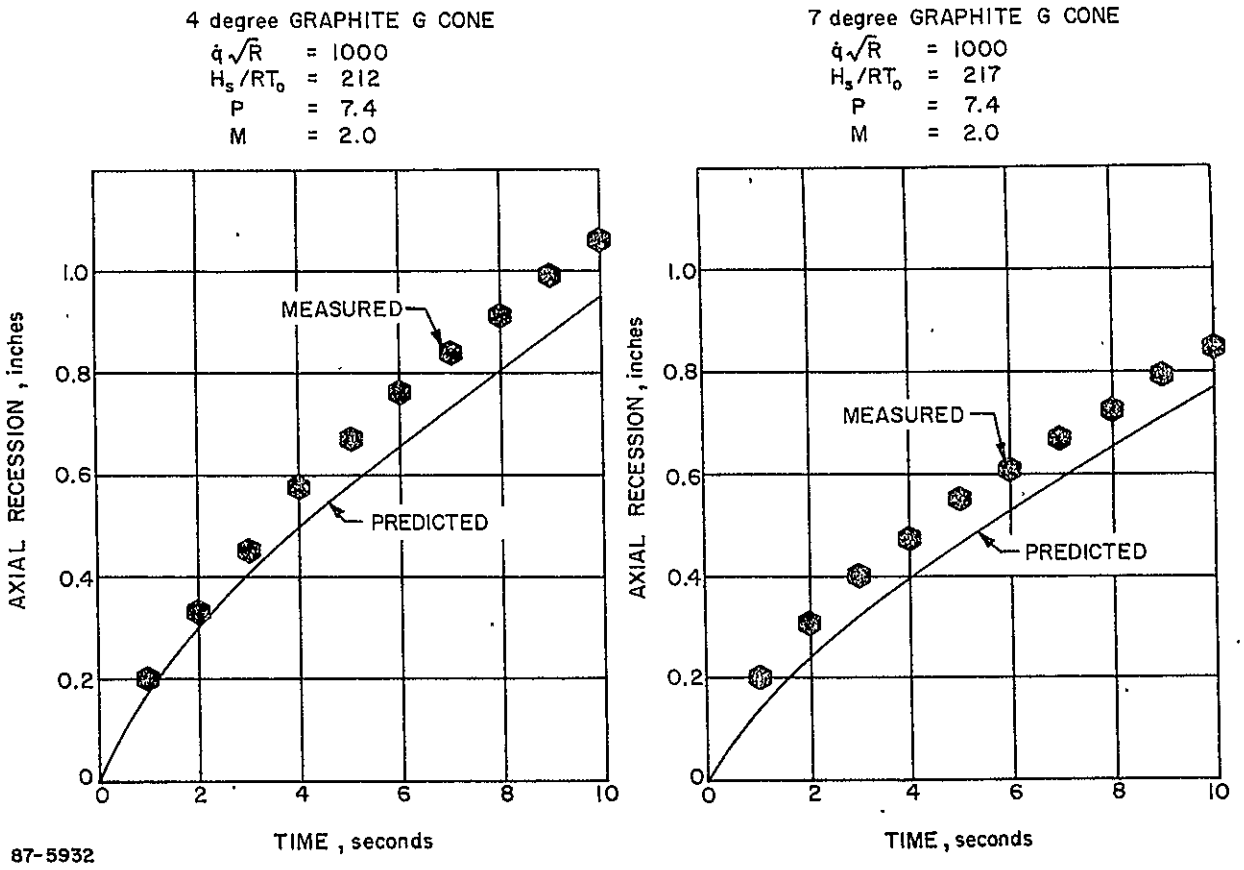
THERMAL RADIATION DECAY RESPONSE - SAMPLE NO. 2 AND 4 R6300

Figure 4.74



VAPOR PRESSURE OF CARBON

Figure 4.75



ABLATION HISTORIES COMPARISON WITH GROUND TESTS 10 MW ARC

Figure 4.76

determining how accurate is Avco's theoretical approach for predicting flight behavior. Rate constants for sublimation behavior are based on Avco's interpretation of the P_v - T relationship presented in Figure 4.75 and will be modified appropriately as future data shed light on this problem.

4.5.1.5 Flight Test Data

During the course of this study, flight test data on carbon phenolic were obtained from several re-entry vehicle programs. Sources for obtaining such data included the following:

a. Avco Corporation, Missile Systems Division

b. Aerospace Corporation

c. General Electric Corporation, Missile Systems Division

d. Air Force Flight Dynamics Laboratory, Wright-Patterson AFB

The documents which were obtained from the survey are listed as references 61 through 65 and apparently reflect the majority of flight information on carbon phenolic for vehicles where instrumentation was used. The four volume symposium report contains data from several contractors.

Review of all these documents indicated that the data are of no significant value relative to Venus entry probe design applicability. Almost without exception, surface recession data are only inferred from thermocouples going off scale or from optical signals. While information such as this may have some qualitative merit, it is much too sparse and unreliable for use in a quantitative fashion (e.g., to determine ablation constants for a design surface recession model). The thermocouple data are generally bondline temperature histories where the temperature responses are minimal. It is evident that the complex heat shield decomposition and conduction processes cannot be established with any certainty without temperature responses which attain elevated levels. Furthermore, it must be remembered that all of these

vehicles have been flown in the earth's atmosphere, a factor which would greatly complicate the interpretation of even well-defined ablation and elevated temperature histories. The data do indicate that the carbon phenolic is capable of sustaining the convective heating, pressures, and shears anticipated for the Venus entry probes being considered. Thus, the available flight data yield confidence of ablator capability but cannot be used for design information. For this reason, a detailed discussion of the data (as a classified addendum to this report) is not warranted.

4.5.1.5 Summary of Problem Areas

A review of the presently available data and that required for a mission into the Venus atmosphere indicates that there are several areas where more information is required. Table 4.23 summarizes the general problem areas and the reasons why testing and analysis work is considered necessary. Currently, it is virtually useless to attempt to estimate the effects of uncertainties in the present values of the parameters on the final results since the levels of these parameters may change in the Venus atmosphere. While Table 4.23 does not provide a list of all the parameters that are required, it is felt that the more significant items are included.

The data contained in Reference 66 should be compared to and evaluated with the carbon phenolic data discussed above. However, Reference 66 was not obtained in sufficient time to allow these comparisons.

4.5.2 Data Correlations: Avcoat 5026-39/HC-G

4.5.2.1 General

During the development test phases of the Apollo heat shield program, a vast amount of thermal test data has been generated. These data were compiled for purposes of the Venus entry probe investigations to provide a basis for generating ablator thicknesses and to serve as the basis for

TABLE 4.23

AREAS OF MATERIAL PROPERTY INVESTIGATION REQUIRED FOR CARBON PHENOLIC UTILIZATION IN THE VENUS ENVIRONMENT

	Area	Reasons for Investigation
	Reaction Rate Parameters (A, B, N)	1. Lack of data 2. Proper definition of surface temperature during terminal flight. 3. Aid in defining transition regime.
B.	Diffusion Parameters (TW, W_E)	1. To determine if expression holds for atmospheres other than for air (W_E) 2. Effect of radiation in diffusion equation. 3. Aid in defining transition regime.
C.	Sublimation Parameters	1. Present data virtually non-existent. 2. Determine point at which removal is by sublimation rather than diffusion.
D.	Thermal Conductivity and Specific Heat	1. Evaluate data at higher temperatures - required since insulation requirement is a significant amount of heat shield thickness.
E.	Heat of Combustion (or energy terms)	1. Effective value may change with atmosphere - needed for proper definition of surface energy effects including the case of radiant heating.
F.	Internal Conductive Parameters	1. Variation of char thickness and density due to different surface (and internal) reactions and radiant heating.

generation of a development test plan specifically for the Venus entry probe. It is recognized that all available data (e.g., NASA; MSC) are not included herein since these data were not received by Avco in time for interpretation and inclusion in this report. The following sections present pure radiant heating data, combined convective and radiant heating data, pure convective heating data, thermal properties data, and a discussion of flight test data correlations. Because of the environment for the capsule which utilizes Avcoat 5026-39/HC-G, it was not necessary to include the effects of shear and pressure on performance of this ablator.

4.5.2.2 Pure Radiant Heating Ablation Data

Avcoat 5026-39/HC-G was tested in a pure radiant heating environment at Southwest Research Institute (Reference 67), Giannini Scientific Corporation (Reference 68, Aerotherm (Reference 69), and Avco's Solar Furnace (Reference 70), The tests at the Southwest Research Institute were performed in five different atmospheric environments: air, nitrogen, argon; 5% O_2 - 95% N_2; and 10% O_2 -90% N_2. The tests at Giannini and Avco were run in air and the tests at Aerotherm were conducted in vacuum. All data are listed in Table 4.24.

The test results from SWRI, GSC, and Aerotherm are considered to be reasonably good data. However, the surface temperature data from the tests run in the Avco solar furnace are erroneous (as explained in Reference 70) since the measurement was made while the surface was being shuttered from the incident flux, and, as such, was rapidly cooling. The data were included for completeness but were not used for analysis purposes. (It is shown in Reference 70 that the reported surface temperatures are 2000-3000°R low depending upon the incident flux.)

The incident flux was plotted as a function of the measured surface temperature for each of the five atmospheric environments and is

ST-211

5026-39/HC-G ABLATION DATA - RADIATION TESTS

TABLE 4.24

Task No. 03.05.01

Specimen Identification			Geometry		Length			Density	$\dot{q}_c$	$\dot{q}_r$	H_s	P_{Surf}	Time	Shear Stress	Surface Temp.	q_{rr} / $\epsilon_\sigma T_c^4$	ϵ	Weight			$\dot{s}$	$\dot{m}$	Char Thick	Fluid Medium	Remarks
No.	Mat.	Config.	W	Dia.	Pre	Post	△											Pre	Post	△					Facility and Explanatory Notes
			Lbs.	In.	Inches			Lbs/Ft^3	BTU/Ft^{2}Sec		BTU/Lb	Atmos	Secs	Psf	$^\circ$R	BTU/Ft^{2}Sec		Grams			In/Sec	Lb/Sec	In.		
23	39/HC-G	Cylinder		0.625	1.950	1.710	0.040	33.0		21		0.1	128		1340					0.364	3.185×10^{-4}	6.378×10^{-6}	0.180	Air	SwRI Arc Image
45					1.950	1.840	0.110			81			189		3400					0.652	7.820×10^{-4}	7.615×10^{-6}	0.300		
30					1.950	1.750	0.200			145			216		3720					1.130	9.240×10^{-4}	1.16×10^{-5}	0.400		
81					1.950	1.650	0.300			270			183		4760					1.560	1.697×10^{-3}	1.58×10^{-5}	0.470		
92					1.950	1.700	0.250			490			133		5360					1.160	1.978×10^{-3}	1.925×10^{-5}	0.360		
107					1.950	1.680	0.270			975			51		6480					0.992	5.214×10^{-3}	4.21×10^{-5}	0.260		
196					1.950	1.810	0.140			1450			51		7360					1.310	2.745×10^{-3}	6.01×10^{-5}	0.370		
191					1.950	1.600	0.350			2050			31		7340					1.840	1.123×10^{-2}	1.31×10^{-4}	0.170		
22					1.950	1.950	0.000			19		0.5	116		2590					0.369	9.621×10^{-4}	7.00×10^{-6}	0.200		
55					1.950	1.830	0.120			78			192		3360					0.652	6.250×10^{-3}	7.58×10^{-6}	0.300		
66					1.950	1.610	0.340			147			191		3750					1.250	1.780×10^{-3}	1.44×10^{-5}	0.310		
82					1.950	1.640	0.310			285			121		4620					1.360	6.562×10^{-3}	2.49×10^{-5}	0.340		
93					1.950	1.530	0.420			473			137		5380					1.560	3.066×10^{-3}	2.51×10^{-5}	0.310		
108					1.950	1.700	0.250			780			52		6570					1.020	4.908×10^{-3}	4.325×10^{-5}	0.270		
195					1.950	1.640	0.310			1550			49		7110					1.790	6.327×10^{-3}	7.06×10^{-5}	0.190		
197					1.950	1.640	0.310			2.000			27		7360					1.280	1.149×10^{-2}	1.04×10^{-4}	0.190		
24					1.950	1.900	0.050			19		1.0	166		2580					0.454	3.012×10^{-3}	6.045×10^{-6}	0.230		
42					1.950	1.750	0.200			84			154		3420					0.850	1.300×10^{-3}	1.22×10^{-5}	0.300		
37					1.950	1.590	0.360			138			171		3680					1.590	1.985×10^{-3}	1.83×10^{-5}	0.410		
83					1.950	1.730	0.220			279			110		4490					1.280	2.000×10^{-3}	2.56×10^{-5}	0.470		
112					1.950	1.580	0.370			510			145		5410					1.620	2.552×10^{-3}	2.46×10^{-5}	0.370		
109					1.950	1.740	0.210			990			51		6660					1.080	4.118×10^{-3}	4.66×10^{-5}	0.240		
194					1.950	1.690	0.260			1550			51		7160					1.730	5.098×10^{-3}	7.50×10^{-5}	0.310		
198					1.950	1.680	0.270			2020			28		7380					1.300	1.643×10^{-2}	1.025×10^{-4}	0.220		

ABLATION DATA

TABLE 4.24 (CONT.) (2)

Task No. 03.05.01

Specimen Identification			Geometry		Length			Density	$\dot{q}_c$	$\dot{q}_r$	H_s	P_{Surf}	Time	Shear Stress	Surface Temp.	q_{rr} $\epsilon_\sigma T_c^4$	ϵ	Weight			$\dot{s}$	$\dot{m}$	Char Thick	Fluid Medium	Remarks
No.	Mat.	Config.	W	Dia.	Pre	Post	△											Pre	Post	△					Facility and Explanatory Notes
			Lbs.	In.	Inches			Lbs/Ft^3	BTU/Ft^2Sec		BTU/Lb	Atmos	Secs	Psf	°R	BTU/Ft^2Sec		Grams			In/Sec	Lb/Sec	In.		
124	39/HC-G	Cylinder		0.625	1.950	1.880	0.070	33.0		19		3.0	201		2610					0.515	3.423×10^{-4}	4.5×10^{-5}	0.340	Air	SwRI Arc Image
123					1.950	1.840	0.110			78			171		3260					0.510	5.751×10^{-4}	5.84×10^{-4}	0.320		
122					1.950	1.650	0.300			160			135		3760					0.964	1.875×10^{-3}	1.15×10^{-3}	0.250		
121					1.950	1.430	0.520			295			184		4610					1.510	2.974×10^{-3}	1.88×10^{-3}	0.310		
120					1.950	1.620	0.330			507			132		5370					1.420	2.520×10^{-3}	2.37×10^{-3}	0.390		
111					1.950	1.680	0.270			1005			53		4720					0.992	5.214×10^{-3}	9.125×10^{-5}	0.230		
113					1.950	1.800	0.150			1450			47		4760					1.360	3.061×10^{-3}	4.125×10^{-5}	0.400		
199					1.950	1.830	0.120			1920			20		4780					0.7737	4.030×10^{-5}	9.125×10^{-5}	0.220		
142					1.950	1.900	0.050			22		6.8	171		2670					0.340	2.924×10^{-4}	4.39×10^{-6}	0.210		
143					1.950	1.874	0.080			76			178		3260					0.539	1.494×10^{-4}	6.69×10^{-6}	0.310		
154					1.950	1.770	0.180			160			127		3810					0.539	1.497×10^{-3}	1.315×10^{-4}	0.230		
160					1.950	1.650	0.300			306			141		4660					0.936	2.123×10^{-3}	1.96×10^{-5}	0.290		
159					1.950	1.570	0.380			490			132		5360					1.220	2.377×10^{-3}	2.04×10^{-5}	0.270		
150					1.950	1.700	0.250			760			53		6660					0.709	4.717×10^{-3}	2.95×10^{-5}	0.230		
192					1.950	1.750	0.200			1500			40		11210					1.560	2.200×10^{-3}	1.28×10^{-5}	0.310		
200					1.950	1.730	0.220			1970			29		14430					0.992	9.584×10^{-5}	9.56×10^{-5}	0.230		
130					1.950	1.710	0.240			970		10.0	51		6690					0.765	4.704×10^{-3}	3.31×10^{-5}	0.250		

ABLATION DATA

TABLE 4.2A (CONT.) (3)

Task No. 03.05.01

Specimen Identification			Geometry		Length			Density	$\dot{q}_c$	$\dot{q}_r$	H_s	P_{Surf}	Time	Shear Stress	Surface Temp.	q_{rr} $\epsilon_\sigma T_c^4$	ϵ	Weight			$\dot{s}$	$\dot{m}$	Char Thick	Fluid Medium	Remarks
No.	Mat.	Config.	W	Dia.	Pre	Post	Δ											Pre	Post	Δ					Facility and Explanatory Notes
			Lbs.	In.	Inches			Lbs/Ft^3	BTU/Ft^2Sec		BTU/Lb	Atmos	Secs	Psf	°R	BTU/Ft^2Sec		Grams			In/Sec	Lb/Sec	In.		
41	39/12-6	Cylinder		0.625	1.950	1.950	0.000	33.0		18		0.1	182		2540					0.340	5.494×10^{-4}	4.12×10^{-4}	0.180	Nitrogen	SwRI Arc Image
61					1.950	1.940	0.010			77			190		3350					0.539	5.253×10^{-3}	6.26×10^{-4}	0.370		
45					1.950	1.920	0.030			139			179		3680					0.794	1.076×10^{-3}	9.75×10^{-4}	0.450		
63					1.950	1.870	0.080			306			176		4980					1.010	4.545×10^{-3}	1.35×10^{-3}	0.540		
89					1.950	1.870	0.080			510			134		5400					0.936	5.970×10^{-3}	1.54×10^{-3}	0.440		
99					1.950	1.790	0.160			985			54		6460					0.765	2.963×10^{-3}	3.12×10^{-3}	0.280		
176					1.950	1.750	0.200			1530			48		7210					1.190	4.167×10^{-3}	5.47×10^{-3}	0.330		
171					1.950	1.650	0.300			2050			26		7360					1.110	1.154×10^{-2}	9.395×10^{-3}	0.170		
21					1.950	1.950	0.000			19		0.5	162		2560					0.340	4.193×10^{-4}	4.63×10^{-4}	0.180		
46					1.950	1.940	0.010			75			195		3320					0.652	5.128×10^{-3}	7.395×10^{-4}	0.360		
39					1.950	1.920	0.030			147			173		3740					0.765	1.554×10^{-3}	8.75×10^{-4}	0.460		
53					1.950	1.900	0.050			300			168		4560					1.050	2.976×10^{-3}	1.375×10^{-3}	0.550		
131					1.950	1.850	0.100			490			148		5310					0.624	6.759×10^{-3}	9.31×10^{-4}	0.450		
100					1.950	1.800	0.150			1005			54		6560					0.765	2.777×10^{-3}	3.125×10^{-3}	0.290		
175					1.950	1.800	0.150			1500			47		7180					1.110	3.061×10^{-3}	4.975×10^{-3}	0.340		
182					1.950	1.620	0.330			2030			29		7410					1.160	1.138×10^{-2}	8.81×10^{-3}	0.190		
36					1.950	1.950	0.000			19		1.0	151		2600					0.369	6.249×10^{-4}	5.11×10^{-4}	0.180		
23					1.950	1.940	0.010			73			197		3300					0.624	5.125×10^{-3}	6.94×10^{-4}	0.390		
57					1.950	1.940	0.010			140			174		3685					0.765	5.155×10^{-3}	7.64×10^{-4}	0.520		
26					1.950	1.860	0.090			312			171		4425					1.050	5.263×10^{-3}	1.35×10^{-3}	0.540		
113					1.950	1.690	0.260			485			146		5360					0.879	1.781×10^{-3}	1.385×10^{-3}	0.350		
101					1.950	1.830	0.120			990			55		6640					0.737	2.132×10^{-3}	2.96×10^{-3}	0.340		
174					1.950	1.750	0.200			1470			48		7160					1.026	4.167×10^{-3}	4.67×10^{-3}	0.270		
181					1.950	1.700	0.250			2000			29		7410					1.020	9.621×10^{-3}	7.75×10^{-3}	0.230		

ST-211

ABLATION DATA

TABLE 4.2A (CONT.) (1)

Task No. 03 05.01

Specimen Identification			Geometry		Length			Density	$\dot{q}_c$	$\dot{q}_r$	H_s	P_{Surf}	Time	Shear Stress	Surface Temp.	q_{rr} $\epsilon_\sigma T_c^4$	ϵ	Weight			$\dot{s}$	$\dot{m}$	Char Thick	Fluid Medium	Remarks
No.	Mat.	Config.	W	Dia.	Pre	Post	△											Pre	Post	△					Facility and Explanatory Notes
			Lbs.	In.	Inches			Lbs/Ft^3	BTU/Ft^2Sec		BTU/Lb	Atmos	Secs	Psf	°R	BTU/Ft^2Sec		Grams			In/Sec	Lb/Sec	In.		
118	39/HC-6	Cylinder		0.625	1.950	1.940	0.010	33.0		21		9.0	207		2680					0.113	4.231×10^{-5}	1.21×10^{-4}	0.110	Nitrogen	SwRI Arc Image
117					1.950	1.940	0.010			77			204		3340					0.273	4.902×10^{-5}	3.66×10^{-4}	0.270		
116					1.950	1.930	0.020			143			188		3660					0.454	1.064×10^{-4}	5.32×10^{-4}	0.410		
115					1.950	1.900	0.050			307			162		4110					0.561	2.779×10^{-3}	7.72×10^{-4}	0.450		
114					1.950	1.770	0.180			515			146		5310					0.736	1.233×10^{-3}	1.41×10^{-3}	0.420		
102					1.150	1.050	0.100			970			51		7110					0.515	1.961×10^{-3}	2.525×10^{-3}	0.350		
173					1.950	1.710	0.240			1420			49		7160					0.964	4.236×10^{-3}	4.34×10^{-3}	0.230		
180					1.950	1.800	0.150			1990			30		7310					0.794	5.000×10^{-3}	5.83×10^{-3}	0.250		
137					1.950	1.950	0.000			20		6.8	166		2610					0.085	6.024×10^{-6}	1.13×10^{-4}	0.140		
136					1.950	1.940	0.010			77			179		3280					0.283	5.587×10^{-5}	3.49×10^{-4}	0.290		
145					1.950	1.950	0.000			137			149		3660					0.397	6.711×10^{-6}	5.875×10^{-6}	0.360		
156					1.950	1.890	0.060			325			135		4560					0.482	4.944×10^{-4}	7.875×10^{-6}	0.370		
158					1.950	1.860	0.090			510			129		5380					0.652	6.997×10^{-4}	1.11×10^{-5}	0.420		
146					1.950	1.870	0.080			960			52		6710					0.425	1.154×10^{-3}	1.80×10^{-5}	0.310		
177					1.950	1.890	0.060			1470			48		7240					0.709	1.467×10^{-3}	3.26×10^{-5}	0.330		
178					1.950	1.870	0.080			1920			26		7380					0.680	3.077×10^{-3}	5.97×10^{-5}	0.250		
126					1.950	1.910	0.040			1000		10.0	52		6960					0.367	7.672×10^{-4}	1.56×10^{-5}	0.330		

ABLATION DATA

TABLE 4.24 (CONT.) (5)

Task No. 08.05.01

Specimen Identification			Geometry		Length			Density	$\dot{q}_c$	$\dot{q}_r$	H_s	P_{Surf}	Time	Shear Stress	Surface Temp.	q_{rr} $\epsilon_\sigma T_c^4$	ϵ	Weight			$\dot{s}$	$\dot{m}$	Char Thick	Fluid Medium	Remarks
No.	Mat.	Config.	W	Dia.	Pre	Post	△											Pre	Post	△					Facility and Explanatory Note
			Lbs.	In.	Inches			Lbs/Ft^3	BTU/Ft^{2}Sec		BTU/Lb	Atmos	Secs	Psf	$^\circ$R	BTU/Ft^{2}Sec		Grams			In/Sec	Lb/Sec	In.		
59	39/HC-6	Cylinder		0.625	1.950	1.940	0.010	33.0		19		0.1	165		2660					0.312	6.661×10^{-5}	4.17×10^{-6}	0.210	Argon	SwRI Arc Image
68					1.950	1.930	0.020			79			222		3340					0.595	9.009×10^{-5}	5.91×10^{-6}	0.440		
72					1.950	1.930	0.020			139			211		3660					0.765	1.199×10^{-4}	7.00×10^{-6}	0.490		
74					1.950	1.910	0.040			275			188		4140					0.964	2.128×10^{-4}	1.13×10^{-5}	0.530		
86					1.950	1.870	0.080			478			132		5360					1.967	6.061×10^{-4}	1.51×10^{-5}	0.480		
94					1.950	1.670	0.280			970			55		6470					1.050	5.091×10^{-3}	4.21×10^{-5}	0.310		
167					1.950	1.670	0.280			1550			50		6460					1.110	5.600×10^{-3}	4.875×10^{-5}	0.280		
168					1.950	1.670	0.280			2110			25		7260					0.992	1.120×10^{-2}	3.75×10^{-5}	0.190		
129					1.950	1.950	0.000			18		0.5	176		2630					0.312	5.692×10^{-4}	3.91×10^{-6}	0.220		
73					1.950	1.930	0.020			144			190		3660					0.822	1.033×10^{-4}	9.56×10^{-6}	0.480		
75					1.950	1.860	0.090			285			176		4760					0.936	5.114×10^{-4}	1.17×10^{-5}	0.510		
87					1.950	1.780	0.170			525			132		5310					0.879	1.284×10^{-3}	1.47×10^{-5}	0.440		
96					1.950	1.880	0.070			985			55		6560					0.737	1.273×10^{-3}	2.96×10^{-5}	0.380		
169					1.950	1.680	0.270			2120			26		7330					1.220	1.038×10^{-2}	1.03×10^{-4}	0.230		
67					1.950	1.940	0.010			18		1.0	173		2570					0.340	5.464×10^{-5}	4.10×10^{-6}	0.220		
71					1.950	1.930	0.020			80			204		3290					0.595	9.804×10^{-5}	6.44×10^{-6}	0.400		
77					1.950	1.940	0.010			138			197		3610					0.709	5.076×10^{-5}	9.94×10^{-6}	0.490		
76					1.950	1.920	0.030			210			182		4670					0.936	1.648×10^{-4}	1.13×10^{-5}	0.550		
83					1.950	1.900	0.050			510			131		5380					0.822	3.917×10^{-4}	1.38×10^{-5}	0.490		
97					1.950	1.870	0.080			1040			53		6610					0.680	1.501×10^{-3}	2.83×10^{-5}	0.340		
166					1.950	1.780	0.170			1520			49		7160					0.879	3.469×10^{-3}	9.96×10^{-5}	0.340		
170					1.950	1.640	0.310			1710			27		7410					1.020	1.148×10^{-2}	8.31×10^{-5}	0.180		

ABLATION DATA

TABLE 4.2A (CONT.) (6)

125K No. 03.05.01

Specimen Identification			Geometry		Length			Density	$\dot{q}_c$	$\dot{q}_r$	H_s	P_{Surf}	Time	Shear Stress	Surface Temp.	q_{rr} $\epsilon_\sigma T_c^4$	ϵ	Weight			$\dot{s}$	$\dot{m}$	Char Thick	Fluid Medium	Remarks
No.	Mat.	Config.	W	Dia.	Pre	Post	△											Pre	Post	△					Facility and Explanatory Notes
			Lbs.	In.	Inches			Lbs/Ft^3	BTU/Ft^2Sec		BTU/Lb	Atmos	Secs	Psf	^oR	BTU/Ft^2Sec		Grams			In/Sec	Lb/Sec	In.		
78	39/no.a	Cylinder		0.625	1.950	1.950	0.000	33.0		18		3.0	183		2140					0.312	5.444×10^{-4}	3.96×10^{-4}	0.170	Argon	SwRI Arc Image
79					1.950	1.930	0.020			143			187		3660					0.709	1.010×10^{-3}	8.375×10^{-4}	0.480		
80					1.950	1.930	0.020			205			170		4540					0.907	1.053×10^{-3}	1.05×10^{-3}	0.560		
117					1.950	1.930	0.020			470			150		5340					0.707	1.333×10^{-3}	1.04×10^{-3}	0.530		
98					1.950	1.910	0.040			173			52		6690					0.534	2.547×10^{-3}	2.24×10^{-3}	0.360		
165					1.950	1.860	0.090			2000			26		7470					0.624	3.462×10^{-3}	5.29×10^{-3}	0.260		
134					1.950	1.940	0.010			21		6.8	184		2610					0.142	5.435×10^{-5}	1.7×10^{-4}	0.170		
135					1.950	1.940	0.010			77			187		3210					0.312	5.349×10^{-5}	3.675×10^{-4}	0.290		
144					1.950	1.940	0.010			149			171		3610					0.425	5.849×10^{-5}	5.48×10^{-4}	0.390		
155					1.950	1.930	0.020			305			95		4620					0.482	2.105×10^{-4}	1.12×10^{-3}	0.360		
157					1.950	1.900	0.050			502			110		5340					0.510	4.545×10^{-4}	4.025×10^{-3}	0.400		
147					1.950	1.930	0.020			760			52		6560					0.425	2.346×10^{-4}	1.86×10^{-3}	0.340		
163					1.850	1.920	0.030			1430			48		7130					0.482	4.250×10^{-4}	3.21×10^{-3}	0.320		
164					1.950	1.890	0.070			1840			25		7460					0.482	2.900×10^{-3}	4.25×10^{-3}	0.260		
125					1.950	1.950	0.000			1030		10.0	50		6760					0.340	2.000×10^{-3}	1.5×10^{-3}	0.370		

ABLATION DATA

TABLE 4.24 (CONT.) (7)

Task No. 03.05.01

Specimen Identification			Geometry		Length			Density	$\dot{q}_c$	$\dot{q}_r$	H_s	P_{Surf}	Time	Shear Stress	Surface Temp.	q_{rr} $\epsilon_\sigma T_c^4$	ϵ	Weight			$\dot{s}$	$\dot{m}$	Char Thick	Fluid Medium	Remarks
No.	Mat.	Config.	W	Dia.	Pre	Post	△											Pre	Post	△					Facility and Explanatory Notes
			Lbs.	In.	Inches			Lbs/Ft^3	BTU/Ft^2Sec		BTU/Lb	Atmos	Secs	Psf	°R	BTU/Ft^2Sec		Grams			In/Sec	Lb/Sec	In.		
58	39/HC-6	Cylinder		0.625	1.950	1.930	0.020	33.0		19		0.1	170		2540					0.425	1.176×10^{-3}	5.51×10^{-4}	0.190	5% Oxygen	SwRI Arc Image
52					1.950	1.940	0.010			77			201		3350					0.620	4.831×10^{-3}	9.25×10^{-4}	0.390	95% Nitrogen	
50					1.950	1.900	0.050			149			191		3400					0.539	2.619×10^{-3}	6.12×10^{-4}	0.460		
60					1.950	1.850	0.100			288			192		4360					1.050	6.208×10^{-3}	1.21×10^{-3}	0.500		
103					1.950	1.750	0.200			980			51		6460					0.907	3.922×10^{-3}	3.92×10^{-5}	0.280		
183					1.950	1.600	0.350			2050			30		7410					1.390	1.167×10^{-2}	1.02×10^{-4}	0.220		
38					1.950	1.950	0.000			19		1.0	167		2580					0.397	5.989×10^{-3}	5.24×10^{-4}	0.200		
33					1.950	1.880	0.070			83			196		3240					0.585	2.571×10^{-3}	6.69×10^{-4}	0.350		
34					1.950	1.870	0.080			148			191		3420					0.842	4.188×10^{-3}	9.50×10^{-4}	0.420		
32					1.950	1.870	0.080			280			195		4440					1.130	4.183×10^{-3}	1.28×10^{-3}	0.550		
164					1.950	1.770	0.180			990			54		6610					0.794	3.333×10^{-3}	3.24×10^{-3}	0.280		
184					1.950	1.650	0.300			2000			26		11360					1.130	1.154×10^{-2}	9.625×10^{-5}	0.180		
138					1.950	1.950	0.000			19		6.8	172		2660					0.142	5.314×10^{-4}	1.32×10^{-4}	0.150		
139					1.950	1.940	0.010			70			176		3210					0.340	5.622×10^{-3}	9.26×10^{-4}	0.310		
152					1.950	1.920	0.030			155			128		3760					0.340	2.344×10^{-3}	5.86×10^{-4}	0.320		
161					1.950	1.840	0.110			284			144		4560					0.397	7.639×10^{-4}	4.025×10^{-4}	0.330		
148					1.950	1.870	0.080			1030			52		6460					0.585	1.539×10^{-3}	2.525×10^{-5}	0.530		
190					1.950	1.860	0.090			1950			28		7360					0.652	3.214×10^{-3}	5.13×10^{-5}	0.240		
127					1.950	1.910	0.040			1020		10.0	53		6710					0.510	7.547×10^{-3}	2.125×10^{-5}	0.350		

ST-211

ABLATION DATA

TABLE 4.2.4 (CONT.) (6)

Task No. 03.05.01

Specimen Identification			Geometry		Length			Density	$\dot{q}_c$	$\dot{q}_r$	H_s	P_{Surf}	Time	Shear Stress	Surface Temp.	q_{rr} $\epsilon_\sigma T_c^4$	ϵ	Weight			$\dot{s}$	$\dot{m}$	Char Thick	Fluid Medium	Remarks
No.	Mat.	Config.	W	Dia.	Pre	Post	△											Pre	Post	△					Facility and Explanatory Not
			Lbs.	In.	Inches			Lbs/Ft^3	BTU/Ft^{2}Sec		BTU/Lb	Atmos	Secs	Psf	^oR	BTU/Ft^{2}Sec		Grams			In/Sec	Lb/Sec	In.		
48	39/K-G	Cylinder		0.625	1.950	1.950	0.000	33.0		18		0.1	167		2570					0.425	5.788×10^{-4}	5.41×10^{-6}	0.170	10% Oxygen-	SwRI Arc Image
51					1.950	1.900	0.050			37			165		3530					1.680	3.037×10^{-3}	9.09×10^{-6}	0.370	90% Nitrogen	
44					1.950	1.880	0.070			154			147		4770					0.850	5.389×10^{-4}	1.125×10^{-5}	0.410		
84					1.950	1.620	0.330			312			187		4130					1.160	1.715×10^{-3}	1.37×10^{-5}	0.340		
105					1.950	1.720	0.230			1010			53		6410					0.936	4.340×10^{-4}	3.89×10^{-5}	0.270		
189					1.950	1.650	0.300			2050			26		7320					1.160	1.154×10^{-2}	9.875×10^{-5}	0.180		
41					1.950	1.930	0.020			18		1.0	172		2590					0.425	1.163×10^{-4}	5.45×10^{-6}	0.180		
56					1.950	1.860	0.090			84			167		3270					0.652	5.319×10^{-4}	8.625×10^{-6}	0.340		
40					1.950	1.800	0.150			157			178		3441					0.922	8.429×10^{-4}	1.02×10^{-5}	0.380		
85					1.950	1.780	0.170			240			187		4270					1.360	9.091×10^{-4}	1.4×10^{-5}	0.440		
106					1.950	1.780	0.170			1060			52		6450					0.850	3.224×10^{-4}	3.61×10^{-5}	0.300		
187					1.950	1.750	0.200			1970			27		7360					0.936	7.407×10^{-3}	7.625×10^{-5}	0.260		
141					1.950	1.940	0.010			19		6.8	170		2082					0.170	5.582×10^{-5}	2.21×10^{-6}	0.180		
140					1.950	1.930	0.020			72			166		3280					0.369	1.205×10^{-4}	4.89×10^{-6}	0.300		
153					1.950	1.890	0.060			150			127		3960					0.425	4.722×10^{-4}	9.375×10^{-6}	0.310		
162					1.950	1.800	0.150			282			145		4710					0.624	1.034×10^{-3}	9.5×10^{-6}	0.320		
149					1.950	1.890	0.060			910			52		6680					0.567	1.154×10^{-3}	2.41×10^{-5}	0.380		
186					1.950	1.840	0.110			1930			26		7350					0.709	4.231×10^{-3}	6.01×10^{-5}	0.270		
128					1.950	1.840	0.110			990		10.0	47		6730					0.964	2.340×10^{-3}	4.52×10^{-5}	0.270		

ABLATION DATA

TABLE 4.29 (CONT.) (9)

Task No. 03.05.01

Specimen Identification			Geometry		Length			Density	$\dot{q}_c$	$\dot{q}_r$	H_s	P_{Surf}	Time	Shear Stress	Surface Temp.	q_{rr} $\epsilon_\sigma T_c^4$	ϵ	Weight			$\dot{s}$	$\dot{m}$	Char Thick	Fluid Medium	Remarks
No.	Mat.	Config.	W	Dia.	Pre	Post	Δ											Pre	Post	Δ					Facility and Explanatory Notes
			Lbs.	In.	Inches			Lbs/Ft^3	BTU/Ft^2Sec		BTU/Lb	Atmos	Secs	Psf	°R	BTU/Ft^2Sec		Grams			In/Sec	Lb/Sec	In.		
1970-27	3/4 HCG	Cylinder		3.5			0.083	35.42		312		0.0018	177.7		4230						4.471×10^{-4}			Air	GIANNINI SCIENTIFIC CORP.
1970-26	↓	↓		↓			0.055	34.88		312		0.0300	177.5		4350						3.099×10^{-4}			↓	
1970-22							0.016	30.07		313		0.0500	25.7		3660						6.226×10^{-4}				
1970-9							0.043	30.25		313		0.0500	100.1		3635						4.296×10^{-4}				
1970-32							0.029	35.81		313		0.0500	148.7		3630						1.950×10^{-4}				

ST-211

ABLATION DATA

TABLE 4.24 (cont) (10)

Task No. 03.05.01

Specimen Identification			Geometry		Length			Density	$\dot{q}_c$	$\dot{q}_r$	H_s	P_{Surf}	Time	Shear Stress	Surface Temp.	q_{rr} $\epsilon\sigma T_c^4$	ϵ	Weight			$\dot{s}$	$\dot{m}$	Char Thick	Fluid Medium	Remarks
No.	Mat.	Config.	W	Dia.	Pre	Post	△											Pre	Post	△					Facility and Explanatory Notes
			Lbs.	In.	Inches			Lbs/Ft^3	BTU/Ft^2Sec		BTU/Lb	Atmos	Secs	Psf	°R	BTU/Ft^2Sec		Grams			In/Sec	Lb/Sec	In.		
220							0.0121	34.0		96		0.0	20.8		3075					0.045	5.8×10^{-4}	4.77×10^{-6}			AEROTHERM CORP.
221							0.0320	↓		219		↓	20.0		3800					0.065	1.6×10^{-3}	9.15×10^{-6}		Vacuum	
222							0.0228			285			20.0		4150					0.047	1.1×10^{-3}	5.20×10^{-6}		↓	
223							0.589			487			15.0		4925					0.059	3.93×10^{-3}	9.67×10^{-6}			
224							0.104	↓		569		↓	15.1		4825					0.130	6.89×10^{-3}	1.90×10^{-5}			

ABLATION DATA

TABLE 4.24 (CONT.) (11)

Task No. 03.05.01

Specimen Identification			Geometry		Length			Density	$\dot{q}_c$	$\dot{q}_r$	H_s	P_{Surf}	Time	Shear Stress	Surface Temp.	q_{rr} $\epsilon_\sigma T_c^4$	ϵ	Weight			$\dot{s}$	$\dot{m}$	Char Thick	Fluid Medium	Remarks
No.	Mat.	Config.	W	Dia.	Pre	Post	△											Pre	Post	△					Facility and Explanatory Not
			Lbs.	In.	Inches			Lbs/Ft^3	BTU/Ft^2Sec		BTU/Lb	Atmos	Secs	Psf	°R	BTU/Ft^2Sec		Grams			In/Sec	Lb/Sec	In.		
SF2-81							0.0631	32.55		200.0		1.0	15.0		3410						4.54×10^{-3}			Air	AVCO SOLAR FURNACE
82																									
83																									
SF2-84							0.0311	32.32							3311						5.48×10^{-3}				
85																									
86																									
SF2-87							0.0192	32.23							3329						3.28×10^{-3}				
88																									
89																									
SF2-91							0.0720	32.91							3325						4.80×10^{-3}				
92																									
93																									
SF1-49							—	30.51		500.0					3572						—				
50																									
52																									
SF2-54							0.225	32.94							3682						1.50×10^{-2}				
56																									
59																									
SF2-58							0.178	32.57							3539						1.19×10^{-2}				
59																									
61																									
SF2-46							0.315	32.14		800.0					3972.						2.35×10^{-2}				
51																									
48																									
SF1-49							0.330	32.45							3900.						2.20×10^{-2}				
50																									
52																									

ST-2

ABLATION DATA

TABLE 4.24 (concl.) (12)

Task No. 03.05.01

Specimen Identification			Geometry		Length			Density	$\dot{q}_c$	$\dot{q}_r$	H_s	P_{Surf}	Time	Shear Stress	Surface Temp.	q_{rr} $\epsilon_\sigma T_c^4$	ϵ	Weight			$\dot{s}$	$\dot{m}$	Char Thick	Fluid Medium	Remarks
No.	Mat.	Config.	W	Dia.	Pre	Post	△											Pre	Post	△					Facility and Explanatory Notes
			Lbs.	In.	Inches			Lbs/Ft^3	BTU/Ft^{2}Sec		BTU/Lb	Atmos	Secs	Psf	$^\circ$R	BTU/Ft^{2}Sec		Grams			In/Sec	Lb/Sec	In.		
SF2-72							—	32.01		3000		1.0	15.0		3974.					—			Air	AVCO SOLAR FURNACE
73																								
74																								
SF2-5							2.522	31.18		1100.0					3974					3.42×10^{-2}				
7																								
8																								
SF2-10							2.399	32.02							3902.					2.53×10^{-2}				
12																								
14																								
SF2-43							2.277	32.92							3966.					1.76×10^{-2}				
44																								
45																								
SF2-15							2.205	30.65		1400.0					4062					1.37×10^{-2}				
18																								
19																								
SF2-21							2.323	31.56							4060.					2.22×10^{-2}				
24																								
25																								
SF2-26							2.411	32.74							4110.					2.74×10^{-2}				
28																								
30																								
SF2-33							2.462	31.73							4028					3.05×10^{-2}				
35																								
36																								
SF2-39							2.351	32.05							4010.					2.34×10^{-2}				
40																								
42																								

illustrated in Figures 4.77 - 4.81. The deviation of the solar furnace data from the other results is obvious. Examination of these plots leads to two conclusions:

a) the surface temperature is independent of environment; and

b) the surface temperature is a very weak function of surface pressure.

The surface recession data were examined and found to exhibit similar characteristics for all environments. A comparison of the nitrogen and argon data show about the same results at all temperatures. One could postulate that in these environments the mechanism controlling the surface recession is the melting and vaporization of the silica reinforcement. Comparison of those data with the 5% O_2-95% O_2 and 10% O_2-90% N_2 data shows that the surface recession rate increases with a proportionate increase in oxygen concentration in the temperature range from 3000 - 5000°R. The air data verify this observation. This leads to the conclusion that the surface recession is governed by a complex mechanism involving silica vaporization and carbon oxidation. However, for temperatures greater than 6000°R the data for all environments are essentially identical. It is postulated that in this temperature range the surface recession is controlled by the sublimation of carbon.

In examining the surface recession data, it was found that it was impossible to judge the extent of the pressure effect since it is inseparable from normal data scatter. However, when the data are compared on the basis of total mass loss per unit surface area, the scatter is radically reduced and the extent of a pressure effect becomes more evident. It appears that the total mass loss per unit area is inversely proportional to the surface pressure over the entire range of surface temperature. This observation leads one to conclude that the surface recession mechanism is most likely a vaporization or sublimation process.

An attempt was made to normalize the mass loss data for pressure.

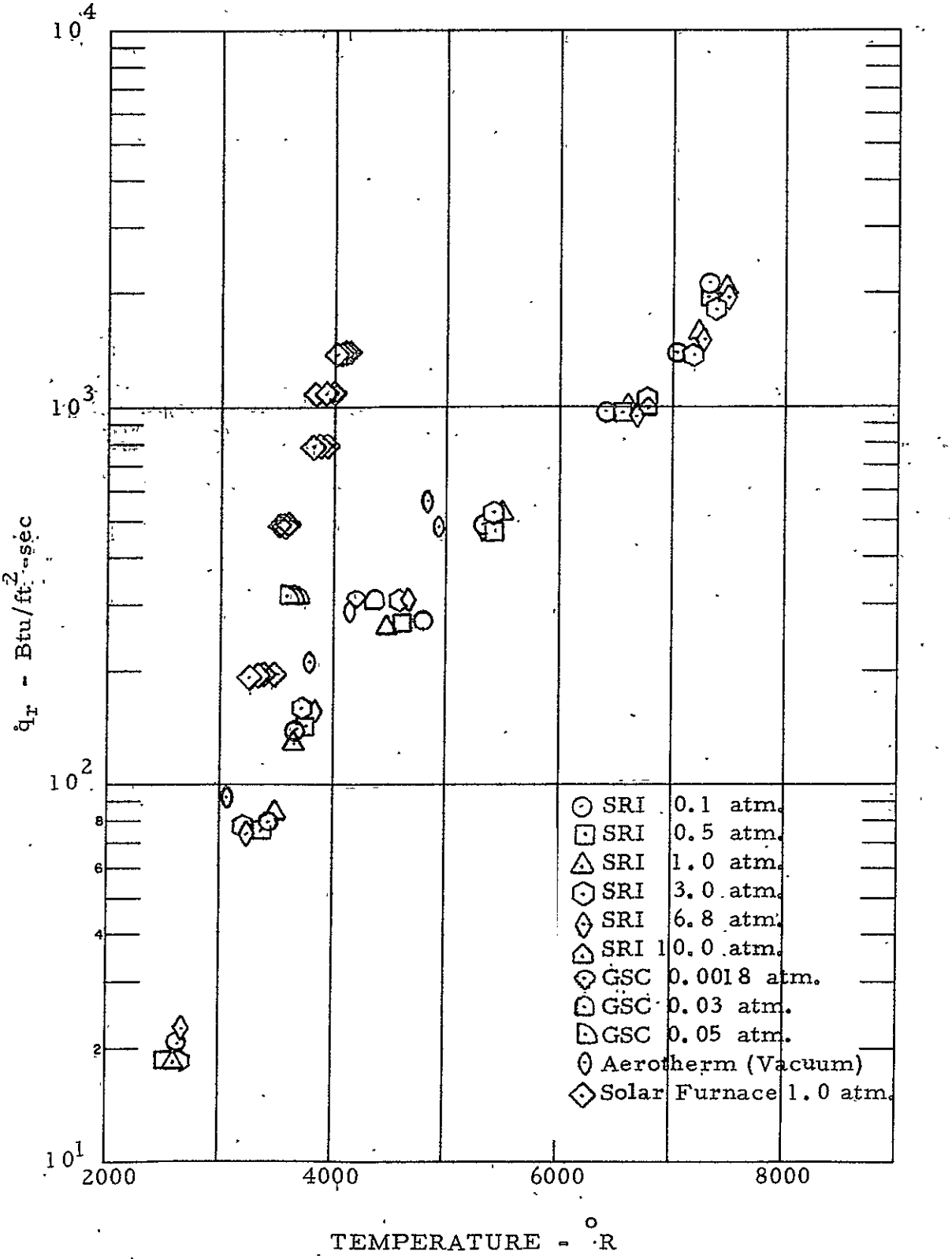


Figure 4.77

5026-39/HC-G Surface Temperature - Radiant Heating Tests - Air

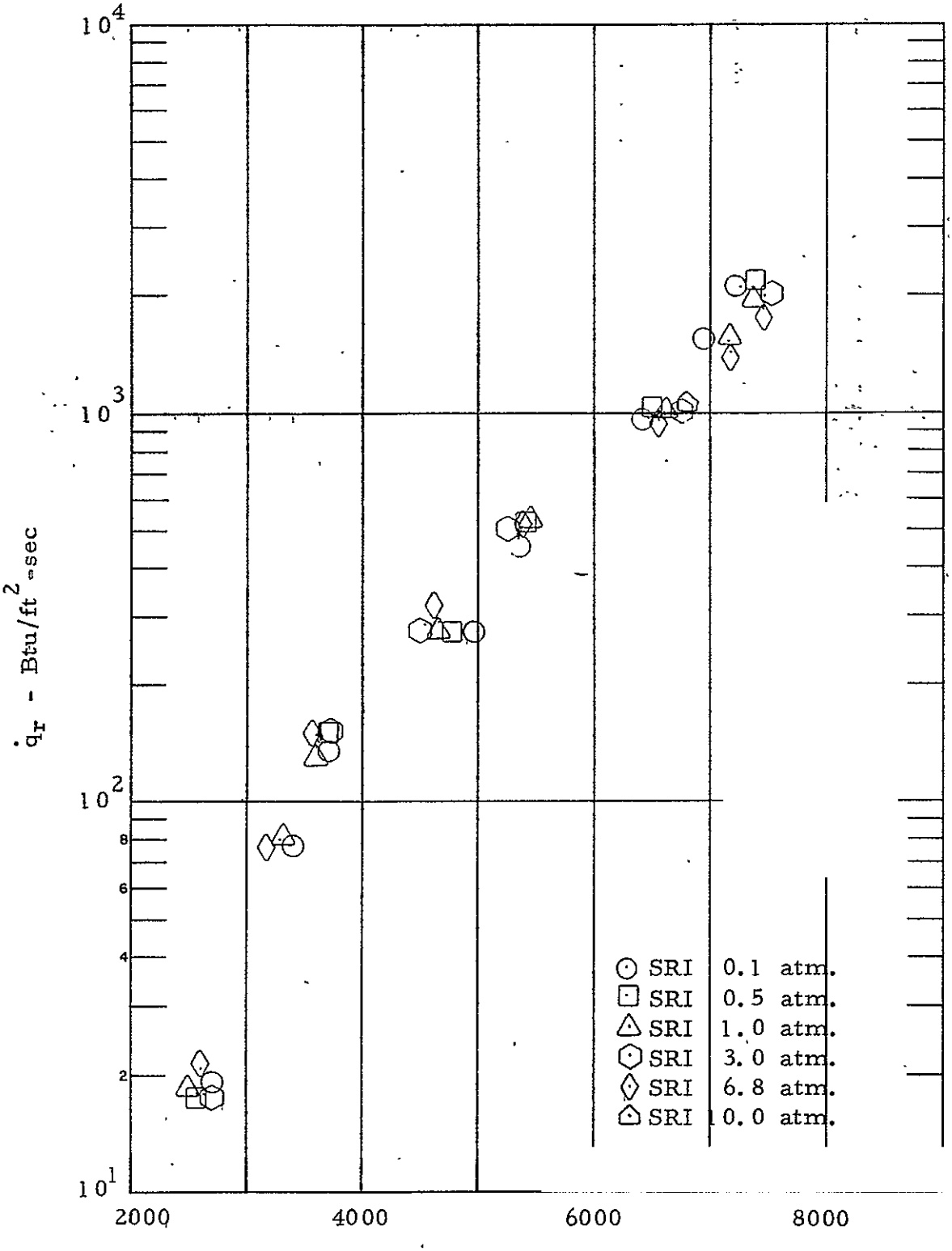


Figure 4.78

5026-39/HC-G Surface Temperature - Radiant Heating Tests - Argon

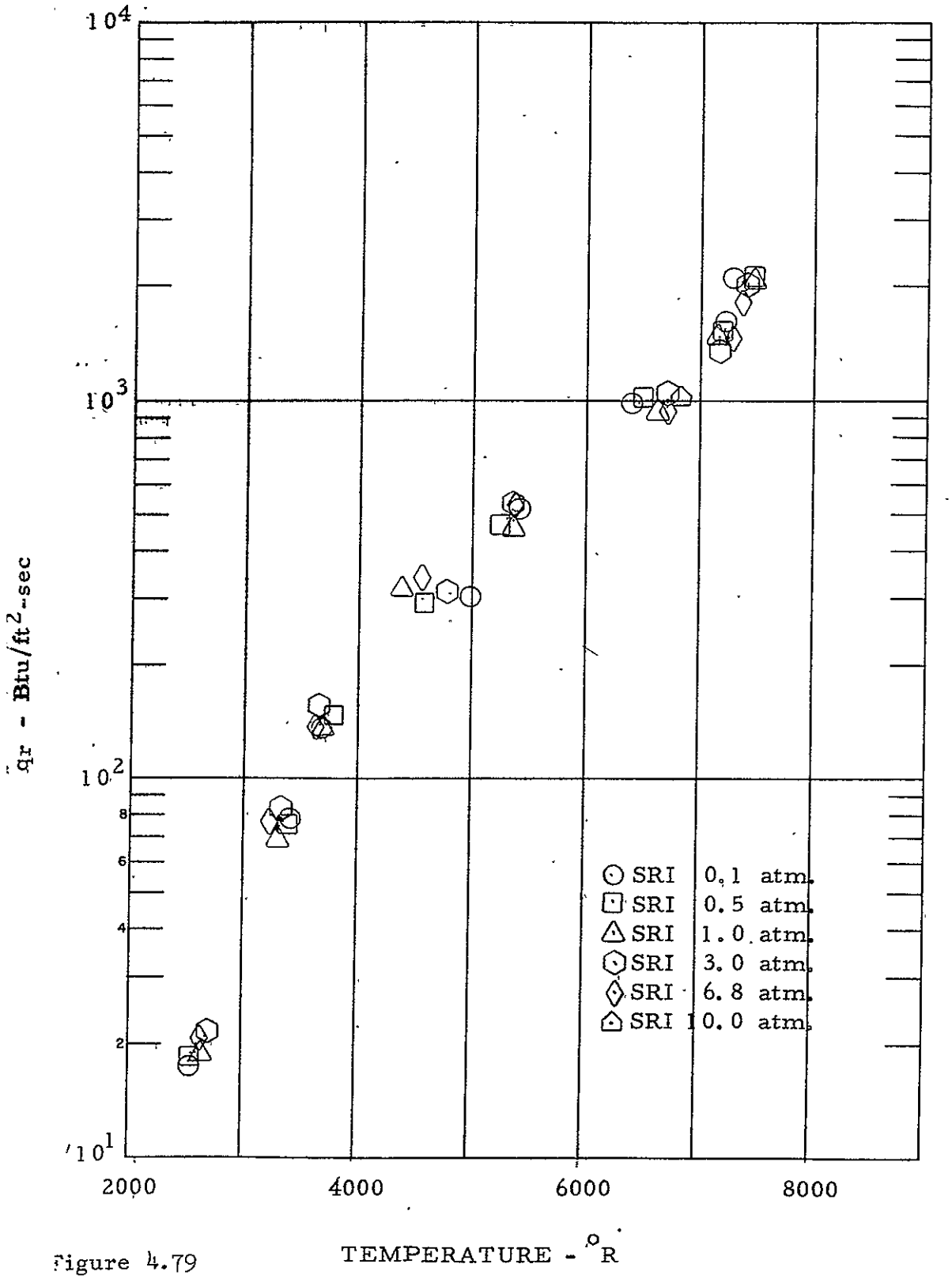


Figure 4.79 5026-39/HC-G Surface Temperature - Radiant Heating Tests - Nitrogen

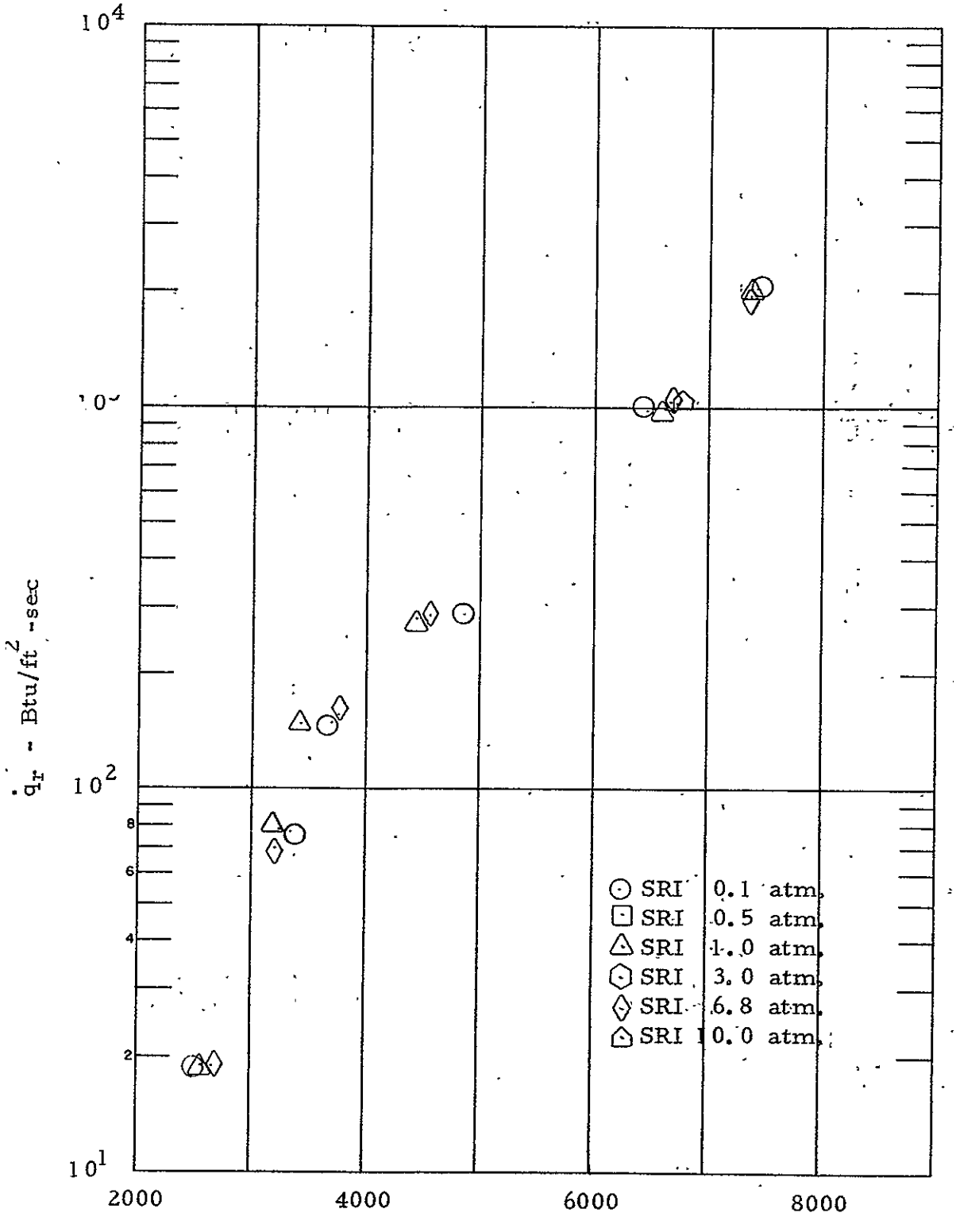


Figure 4.80

5026-39/HC-G Surface Temperature - Radiant Heating Tests - 5% O_2, 95% N_2

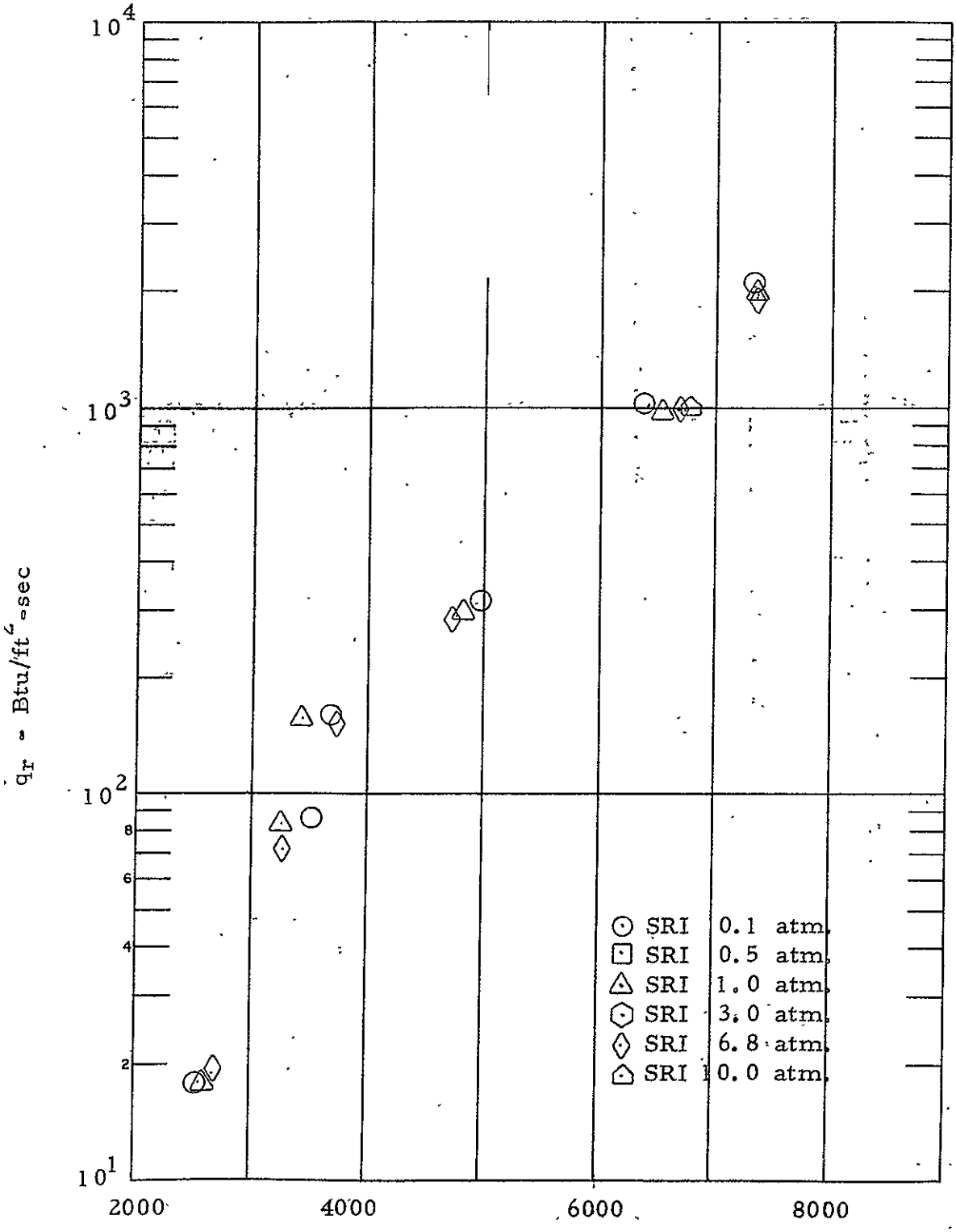


Figure 4.81

5026-39/HC-G Surface Temperature - Radiant Heating Tests - 10% O_2, 90% N_2

It was found that the mass loss data are inversely proportional to the two-tenths power of pressure.

The mass loss data, normalized for pressure, were plotted for each environment as a function of reciprocal temperature and is illustrated in Figures 4.82 - 4.86. Examination of these plots indicates that the total mass loss in the temperature range from 3000-5000°R is influenced by oxygen concentration but is not controlled only by this parameter. For temperatures greater than 6000°R, the data is independent of environment or oxygen concentration and is evidently good sublimation data.

In conclusion, the pure radiant heating tests that have been conducted on Avcoat 5026-39/HC-G have produced some interesting results. Certainly, the data at temperatures greater than 6000°R are sublimation data and are very valuable. However, the results at lower temperatures does not lead one to any immediate conclusions. These results indicate that the surface recession is affected by oxygen concentration but is not controlled by it. Whether this observation is consistent with convective or combined heating tests requires further study.

4.5.2.3 Combined Heating Tests

A series of combined convective and radiative heating tests of flat-faced specimens of Avcoat 5026-39/HC-G was conducted in the arc facility at Giannini (Reference 68). The objective of these tests was to determine the effects of a superimposed radiative environment upon ablation performance. Table 4.25 summarizes these data.

Upon examining the data, it was observed that the measured surface temperatures are in the range where diffusion controlled ablation would be anticipated for a carbonaceous material. Therefore, the data were correlated to a diffusion-controlled oxidation model. A plot of the

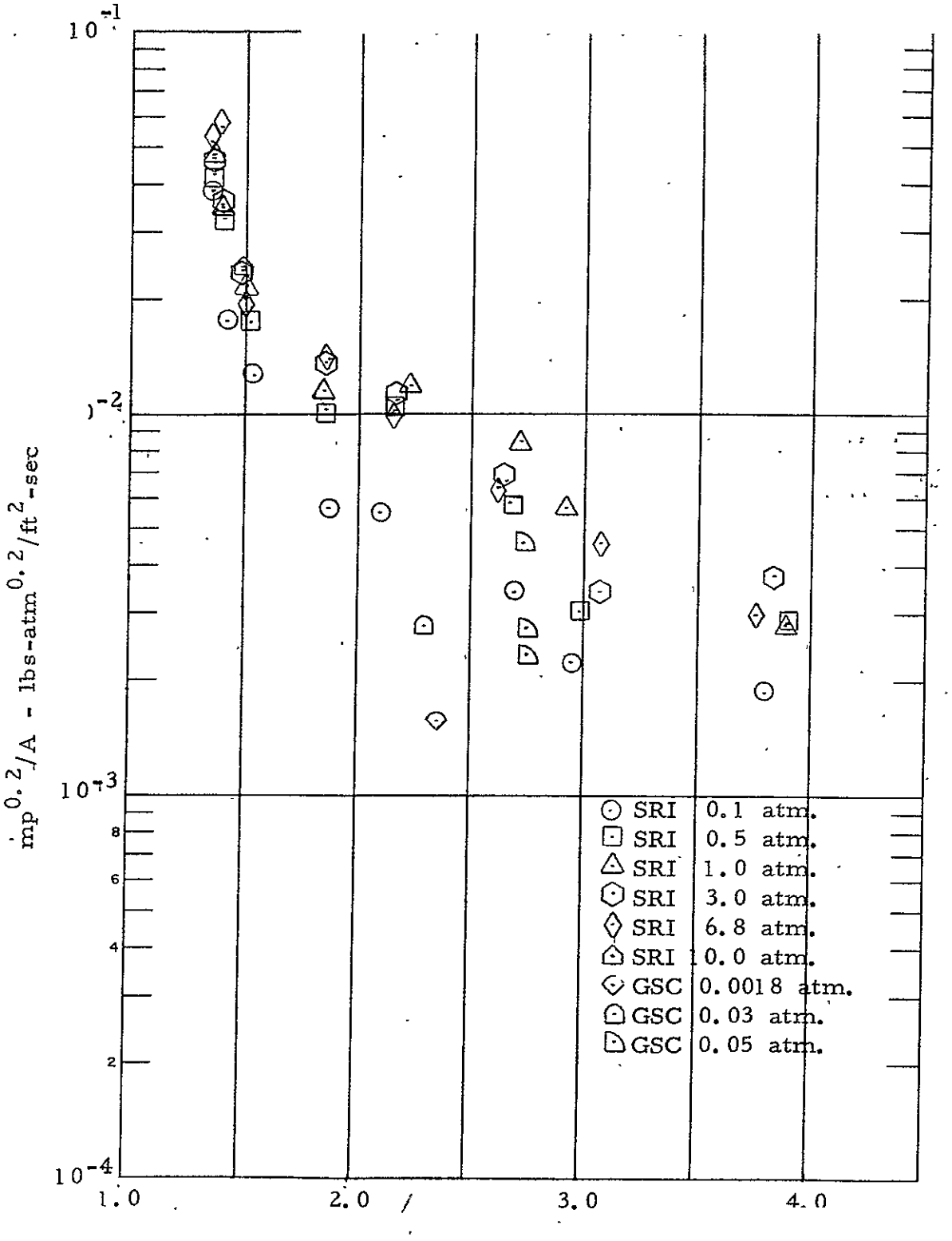


Figure 4.82

5026-39/HC-G Mass Loss Rate - Radiant Tests - Air

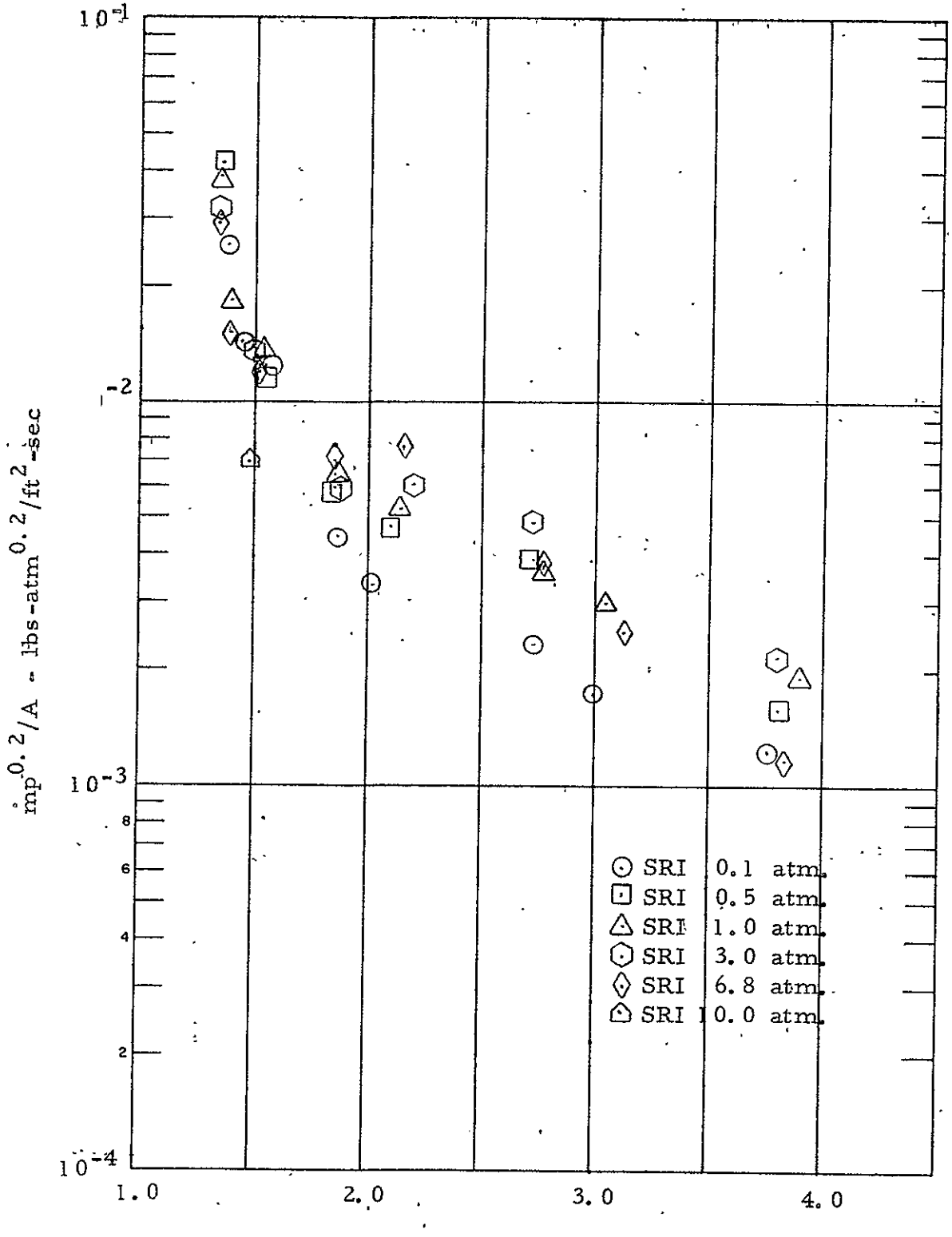


Figure 4.83 5026-39/HC-G Mass Loss Rate - Radiant Tests - Argon

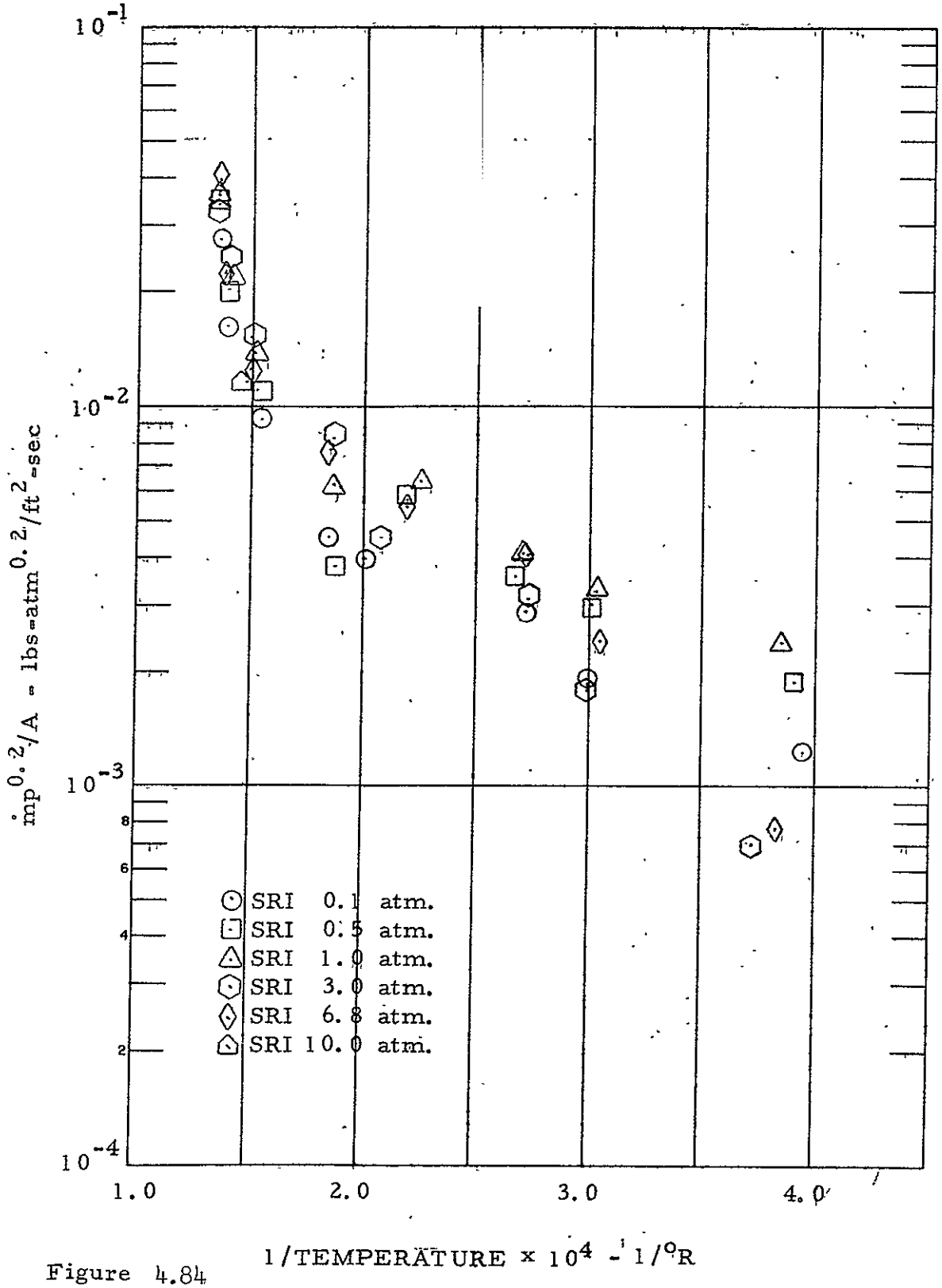


Figure 4.84 5026-39/HC-G Mass Loss Rate - Radiant Tests - Nitrogen

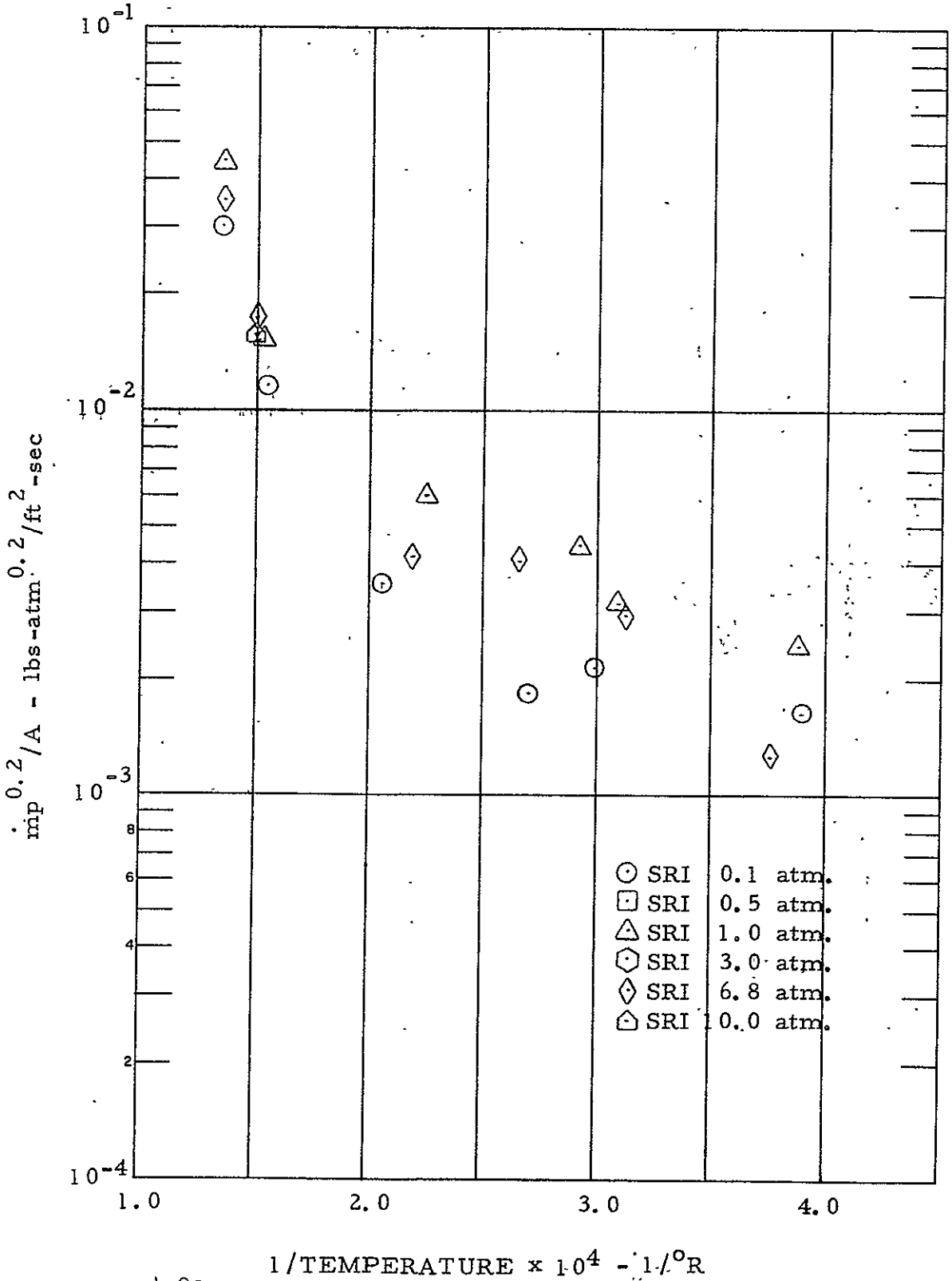


Figure 4.85

5026-39/HC-G Mass Loss Rate - Radiant Tests - 5% O_2, 95% N_2

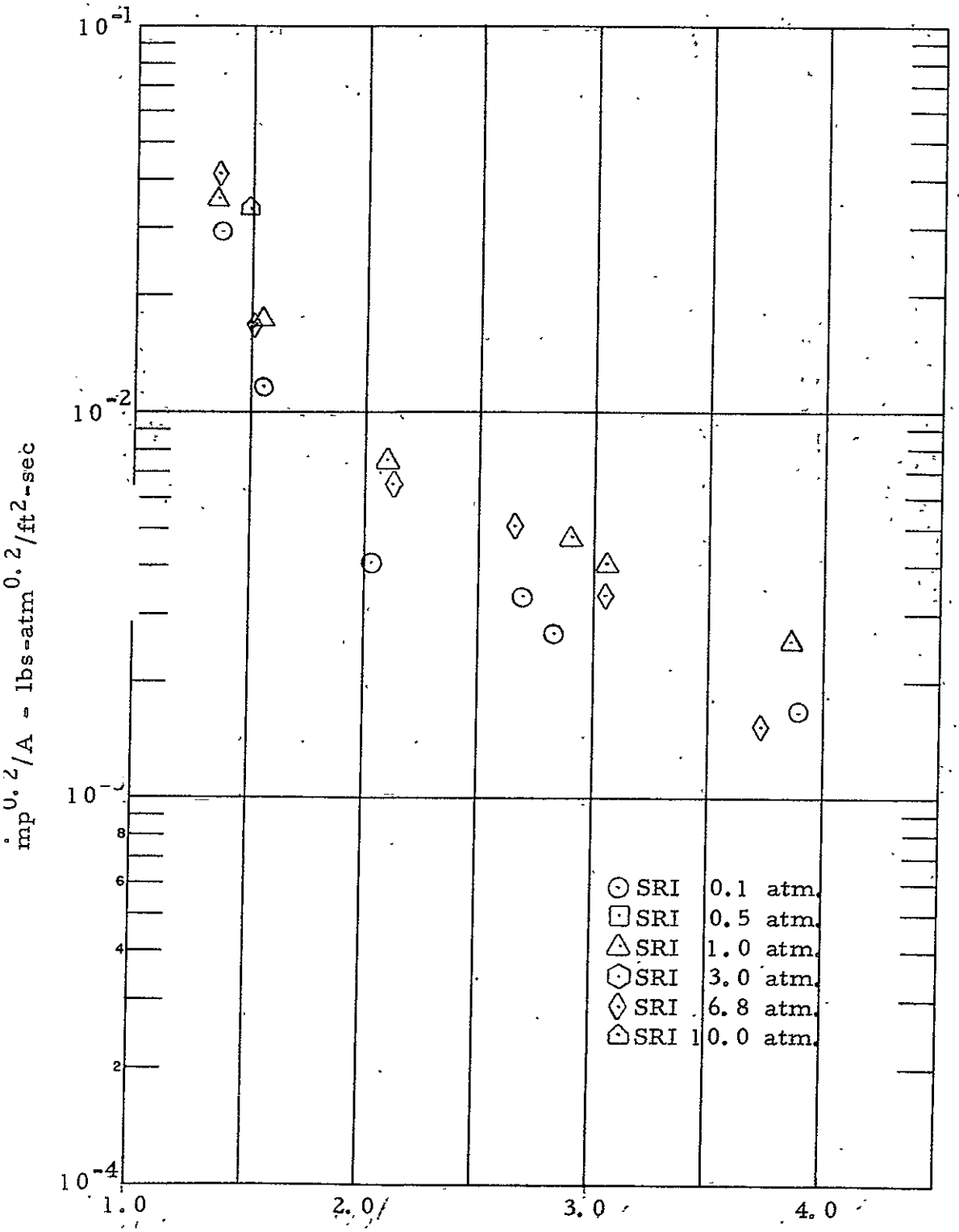


Figure 4.86

5026-39/HC-G Mass Loss Rate- Radiant Tests - 10% O_2, 90% N_2

5026-39/HC-G ABLATION DATA - GIANNINI TESTS

Task No 03.05.01

TABLE 4.25

Specimen Identification			Geometry		Length			Density	$\dot{q}_c$	$\dot{q}_r$	H_s	P_{Surf}	Time	Shear Stress	Surface Temp.	q_{rr} $\epsilon_\sigma T_c^4$	ϵ	Weight			$\dot{s}$	$\dot{m}$	Char Thick	Fluid Medium	Remarks
No.	Mat.	Config.	W	Dia.	Pre	Post	△											Pre	Post	△					Facility and Explanatory N
			Lbs.	In.	Inches			Lbs/Ft^3	BTU/Ft^2Sec		BTU/Lb	Atmos	Secs	Psf	°R	BTU/Ft^2Sec		Grams			In/Sec	Lb/Sec	In.		
1990-3	39/HC-G	CYLINDER		3.5			0.424	29.28	113	0	11,500	8.03×10^3	177.7		3585			227.75	200.96	26.79	2.39×10^{-3}	3.32×10^{-3}	–	AIR	GIANNINI SCIENTIFIC CORP
-14							0.183	28.43	119	0	12,500	8.17	77.3		3596			234.87	218.98	15.89	2.37	4.52	0.18		
-7							0.375	28.58	116	100	12,000	8.03	142.5		4442			233.53	203.40	30.13	2.63	4.65	0.28		
-24							0.354	28.15	119	200	11,500	7.90	118.7		4612			228.54	201.08	27.51	2.98	5.10	0.31		
-1							0.326	28.04	120	312	11,500	8.03	118.5		4771			228.93	200.04	28.89	2.75	5.70	0.28		
-17							0.155	29.01	183	0	14,000	16.1	40.0		3982			228.50	213.19	15.31	3.87	8.42	0.15		
-28							0.321	35.22	183	0	14,000	16.1	79.6		4244			313.86	287.72	26.14	4.03	7.22	0.15		
-8							0.489	29.62	180	0	14,000	16.1	127.8		4027			226.92	192.20	34.72	3.83	5.98	0.17		
-19							0.147	31.31	182	158	14,000	15.9	46.1		4591			236.52	217.87	17.65	3.19	8.42	0.16		
-13							0.315	29.06	178	158	14,000	16.1	79.0		4705			237.35	211.52	25.83	3.99	7.19	0.19		
-29							0.411	34.78	178	158	14,000	16.2	120.0		4688			314.28	276.90	37.38	3.43	6.85	0.23		
-18							0.165	28.62	180	312	14,100	16.1	40.0		4848			227.74	210.52	17.22	4.13	9.47	0.19		
-15							0.295	28.54	178	312	14,000	15.9	68.8		4848			224.46	198.33	26.13	4.29	8.36	0.20		
-25							0.583	34.70	181	312	14,200	16.5	140.0		4803			315.81	269.00	46.81	4.16	7.36	0.20		
-20							0.224	30.91	183	510	14,200	16.2	29.8		5360			229.30	211.05	18.25	7.52	13.47	0.11		
-11							0.329	31.30	180	510	14,200	16.1	59.2		5275			228.25	202.38	25.87	5.56	9.61	0.21		
-12							0.173	28.80	331	0	18,000	30.3	37.0		4527			235.95	217.45	18.00	4.68	10.70	0.12		
-16							0.344	28.08	334	0	18,000	30.3	73.7		4604			232.80	200.54	32.26	4.47	9.63	0.15		
-30							0.417	34.44	329	0	18,000	30.3	100.0		4602			314.99	273.85	41.14	4.17	9.05	0.18		
-23							0.167	29.15	322	300	18,000	27.7	30.2		5149			229.60	209.11	20.49	5.53	14.73	0.15		
-21							0.326	30.10	324	300	18,000	27.7	59.8		5120			238.00	202.14	31.86	5.45	11.72	0.21		
-31							0.328	34.10	320	300	18,000	27.7	79.0		5075			312.42	272.44	40.28	4.15	11.22	0.25		
-2							0.244	29.29	337	510	19,000	29.0	30.0		5440			224.05	204.72	19.33	8.13	19.17	0.16		
-10							0.340	33.91	335	510	19,000	30.0	60.0		5450			228.23	197.75	30.48	5.00	11.17	0.24		
-5							0.414	32.71	333	510	19,000	28.3	89.5		5300			249.75	197.43	43.32	4.63	10.65	0.25		
-4							0.193	29.81	460	0	21,000	35.6	44.8		4624			226.71	202.21	24.50	4.31	11.98	0.18		
-27							0.483	35.42	0	312	–	1.8	177.7		4495			313.80	290.32	23.48	0.47	2.91	0.57		
-26							0.055	34.88	0	312	–	30.0	177.5		4568			306.64	282.91	23.73	0.31	2.94	0.51		
-22							0.016	30.07	0	313	–	50.0	25.7		3560			249.54	249.90	8.64	0.62	7.40	0.17		
-9							0.043	30.25	0	313	–	50.0	100.1		3590			236.91	221.12	15.77	0.43	3.47	0.31		
-32							0.029	35.81	0	313	–	50.0	148.7		3588			309.70	290.40	19.30	0.20	2.86	0.39		

one-dimensional surface mass loss rate vs. the non-blowing heat transfer coefficient is illustrated in Figure 4.87. Diffusion-controlled oxidation theory predicts a linear relationship between the surface mass loss rate and the heat transfer coefficient. Inspection of Figure 4.87 shows that almost all of the data lie within 20% of a normal linear fit. Except for those few points that lie outside the 20% bounds, the data would indicate that the surface recession is diffusion-controlled for both the pure convective and combined convective-radiative heating environments.

Examination of the data for those few points that lie outside the 20% tolerance band shows that the measured surface temperatures for these particular tests were the highest. Thus, a plot was made of the surface mass loss rate normalized by the non-blowing heat transfer coefficient as a function of the observed brightness temperature and is shown in Figure 4.88. Diffusion-controlled oxidstion theory predicts that the normalized surface recession should be independent of surface temperature. Observation of Figure 4.88 indicates that the normalized mass loss rate is essentially a constant below temperatures of approximately 5200°R. Above 5200°R, a strong temperature dependency becomes apparent. The indication is that the mechanism of surface removal has changed from diffusion-controlled oxidation to surface sublimation, which is a strong function of temperature.

The data were inspected for evidence of some pressure or enthalpy dependency. Unfortunately, the two are inseparable for a given cold-wall convective heat flux and therefore, no dependency could be separated from the data. To summarize, analysis of the data indicates that the mechanism controlling the surface recession rate for surface temperatures greater than 3500°R, but less than 5200°R is diffusion-controlled oxidation of the carbonaceous char. Superimposition of a radiative heat flux on the convective conditions has no

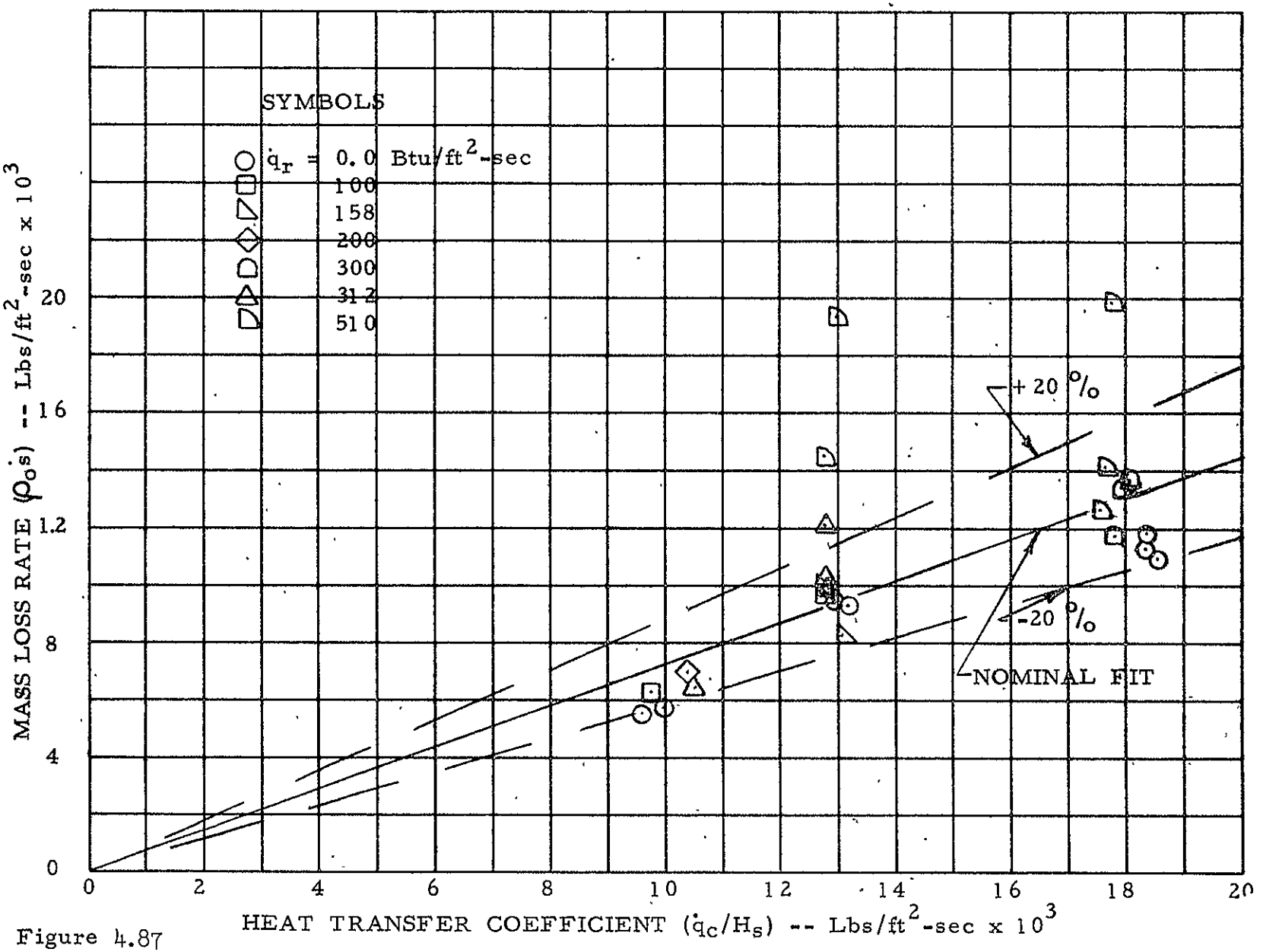


Figure 4.87

5026-39/HC-G Mass Loss - Giannini Splash Tests

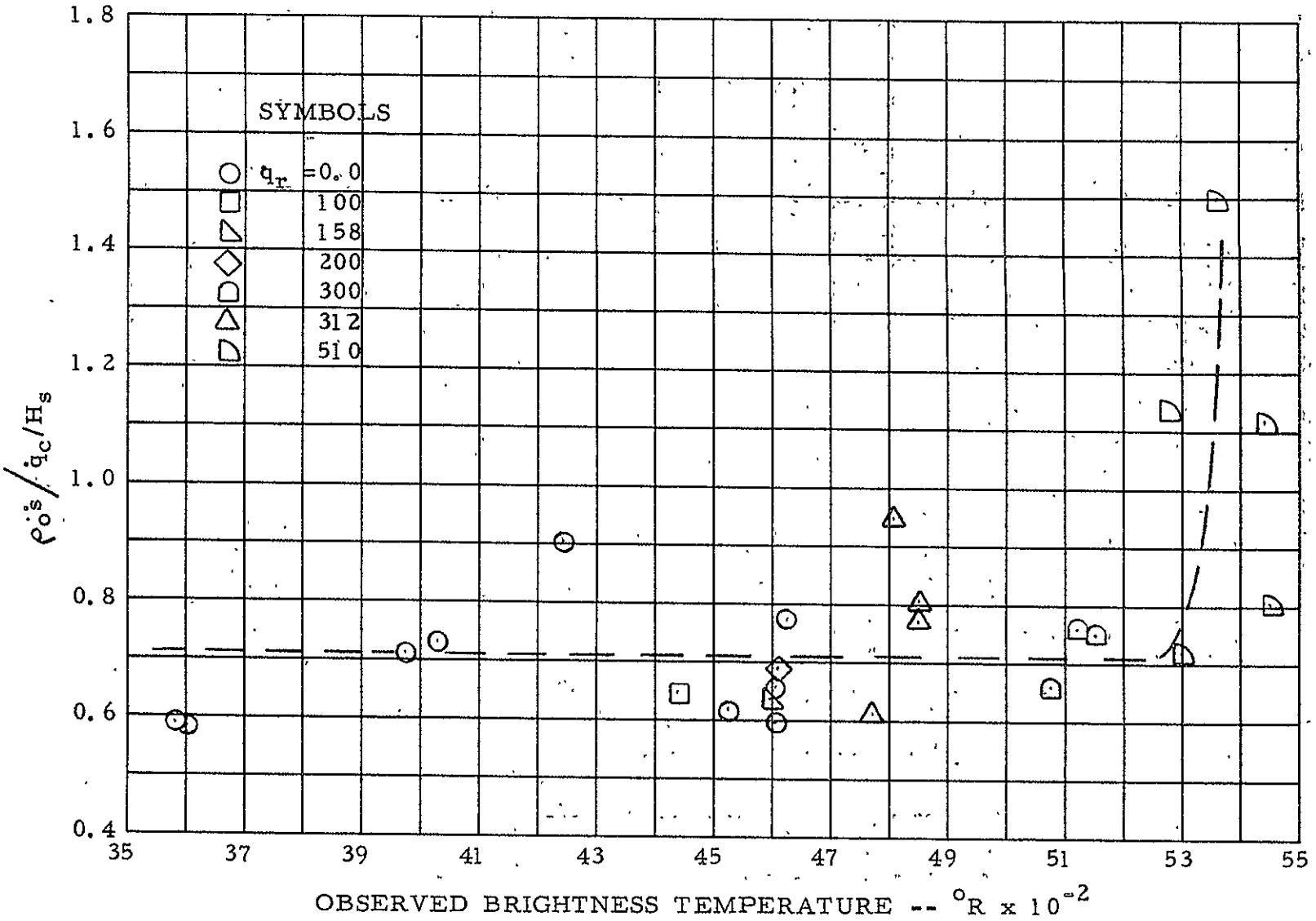


Figure 4.88 5026-39/HC-G Mass Loss - Brightness Temperature Correlations

appreciable effect upon the surface recession rate but merely tends to increase the surface temperature. However, when the surface temperature exceeds approximately 5200°R, the mechanism controlling surface removal changes to sublimation of the carbonaceous char and the actual recession rate becomes a very strong function of temperature. It is in this regime that the severity of the combined convective-radiative environment will have the most deleterious effects.

4.5.2.4 Convective Heating Test Correlations

Test data from the Avco OVERS facility have been analyzed to determine the enthalpy effect on ablator performance. The test conditions range from convective heat fluxes of 100 Btu/ft^2-sec to 432 Btu/ft^2-sec, over an enthalpy range of 4800 Btu/lb to 20,000 Btu/lb (See Table 4.26).

The fact that there is no apparent enthalpy dependence is indicated in Figure 4.89 which shows mass loss rate ($\rho_o \dot{s}$) as a function of heat transfer coefficient (q_c/H). The data demonstrate that the ablator performance correlates reasonably well with film-coefficient thus indicating that char removal is consistent with the diffusion-controlled regime.

Comparison of Figure 4.89 to Figure 4.87 indicates a significant difference of apparent performance when tested in two different facilities. At the time of this report, this difference has not been explained; however, it is considered that the problem is one of facility differences rather than one of ablator non-repeatability.

4.5.2.5 Thermal Properties Correlations

4.5.2.5.1 Thermal Conductivity

Figure 4.90 presents a series of curves for thermal conductivity of Avcoat 5026-39/HC-G pre-charred in an inert environment at a specific temperature and then tested up to that temperature. It must first be noted that actual test data include pre-chars and associated conductivity

ST-211

5026-39/HC-G ABLATION DATA - OVERS TESTS

TABLE 4.26

Task No. 03.05.01

Specimen Identification			Geometry		Length			Density	$\dot{q}_c$	$\dot{q}_r$	H_s	P_{Surf}	Time	Shear Stress	Surface Temp.	q_{rr} / $\epsilon_\sigma T_o^4$	ϵ	Weight			$\dot{s}$	$\dot{m}$	Char Thick	Fluid Medium	Remarks
No.	Mat.	Config.	W	Dia.	Pre	Post	Δ											Pre	Post	Δ					Facility and Explanatory Notes
			Lbs.	In.	Inches			Lbs/Ft^3	BTU/Ft^{2}Sec		BTU/Lb	Atmos	Secs	Psf	$^\circ$R	BTU/Ft^{2}Sec		Grams			In/Sec	Lb/Sec	In.		
1683-11	3/HC-G	CYLINDER		3.5			0.155	30.15	92	0	5,845	0.0217	60		3060	25	0.59	5.634	4.808	0.826	2.58×10^{-3}	3.04×10^{-5}	0.120	AIR	AVCO OVERS
-90							0.202	30.40	101		4775	0.0284	120		3710	68	0.76	5.710	4.717	0.993	1.68	1.82	0.160		
-27							0.390	30.28	92		5,130	0.0211	180		3240	45	0.85	5.665	3.909	1.756	2.11	2.15	0.190		
-18							0.584	30.28	92		5735	0.0211	240		3330	50	0.85	5.669	3.302	2.367	2.44	2.17	0.200		
-6							0.720	30.09	92		5060	0.0217	300		3060	34	0.81	5.633	2.901	2.732	2.90	2.01	0.230		
-10							0.132	30.47	99		7755	0.0105	60		3240	35	0.67	5.700	4.980	0.720	2.20	2.65	0.160		
-93							0.220	31.34	91		7245	0.0109	120		3635	–	–	6.260	5.082	1.178	1.84	2.16	0.180		
-2							0.348	30.51	99		7737	0.0105	180		3060	28	0.68	5.705	4.149	1.556	1.93	1.91	0.195		
-24							0.421	30.51	95		7,558	0.0105	240		3150	30	0.63	5.709	3.700	2.009	1.75	1.84	0.250		
-12							0.563	30.34	95		7810	0.0105	300		3060	31	0.73	5.669	3.328	2.341	1.87	1.72	0.257		
-15							0.086	30.71	101		9,720	0.0070	60		3060	33	0.80	5.795	5.107	0.638	1.43	2.34	0.150		
-91							0.189	30.51	94		9270	0.0071	120		3530	–	–			0.947	1.57	1.74			
-19							0.290	30.84	101		9755	0.0070	180		3330	36	0.62	5.769	4.388	1.381	1.61	1.69	0.227		
-14							0.264	31.03	92		10,370	0.0054	240		3330	40	0.68	5.815	4.384	1.431	1.10	1.31	0.293		
-7							0.301	30.65	92		10,370	0.0054	300		3330	41	0.70	5.726	4.144	1.582	1.00	1.16	0.320		
-3							0.095	31.09	95		9,460	0.0070	60		3060	34	0.81	5.820	5.162	0.658	1.58	2.42	0.173		
-99							0.180	31.21	106		10,115	0.0072	120		3655	62	0.73	5.862	4.805	1.056	1.50	1.94	0.200		
-23							0.241	31.27	99		9,540	0.0072	180		3060	25	0.60	5.841	4.382	1.462	1.34	1.79	0.237		
-5							0.348	31.27	99		9,555	0.0072	240		3150	33	0.70	5.859	4.076	1.778	1.54	1.63	0.243		
-9							0.445	31.03	95		9,455	0.0070	300		3060	30	0.72	5.807	3.711	2.096	1.49	1.54	0.270		
-8							0.075	31.71	99		10,240	0.0063	60		3060	29	0.70	5.925	5.297	0.628	1.25	2.31	0.170		
-88							0.152	31.71	107		10,600	0.0057	120		3618	68	0.84	5.947	4.941	1.006	1.27	1.85	0.200		
-30							0.345	31.78	100		10,110	0.0066	180		3200	–	–	5.944	4.385	1.559	1.92	191	0.220		
-22							0.412	32.54	100		10,110	0.0066	240		3200	–	–	6.082	4.135	1.947	1.72	1.79	0.287		
-4							0.399	31.65	99		10,260	0.0063	300		3150	34	0.72	5.917	3.901	2.016	1.33	1.48	0.340		
-26							0.050	33.29	102		12,445	0.00434	60		3600	57	0.71	6.222	5.631	0.591	0.83	2.17	0.150		
-96							0.154	30.51	95		11,145	0.00537	120		3510	–	–	5.731	4.819	0.912	1.28	1.68	0.190		
-25							0.185	33.29	101		12,340	0.00434	180		3420	49	0.76	6.224	5.029	1.195	1.03	1.46	0.240		
-21							0.252	32.72	101		12,305	0.00434	240		3150	39	0.83	6.122	4.690	1.432	1.05	1.31	0.260		
-28							0.338	32.54	102		12,425	0.00434	300		3420	55	0.85	6.085	4.254	1.831	1.13	1.34	0.270		

ABLATION DATA

TABLE 4.2k (CONCL.)

Task No. 03.05.01

Specimen Identification			Geometry		Length			Density	$\dot{q}_c$	$\dot{q}_r$	H_s	P_{Surf}	Time	Shear Stress	Surface Temp.	q_{rr} $\epsilon_o T_c^4$	ϵ	Weight			$\dot{s}$	$\dot{m}$	Char Thick	Fluid Medium	Remarks
No.	Mat.	Config.	W	Dia.	Pre	Post	△											Pre	Post	△					Facility and Explanatory Notes
			Lbs.	In.	Inches			Lbs/Ft^3	BTU/Ft^2Sec		BTU/Lb	Atmos	Secs	Psf	^oR	BTU/Ft^2Sec		Grams			In/Sec	Lb/Sec	In.		
1873-1	-39/FC-0	CYLINDER		3.5			0.555	30.59	96	0	7,500	0.0093	300		3815	81	0.70	–	–	–	1.87×10^{-3}	–	–	AIR	AVCO OVERS
1683-57							0.794	30.97	130		10,470	0.0087	500		3780	–	–	–	–	–		–	ALL		
1963-27							0.77	34.84	176		12,500	0.0105	400		4790	141	0.50	–	–	–	1.92	–	–		
-29							0.30	33.46	172		18,750	0.0172	135		4085	124	0.83	–	–	–	2.22	–	–		
1683-62							0.757	31.40	217		14,270	0.0103	400		4520	–	–	–	–	–		–	ALL		
-44							0.389	31.71	252		11,500	0.0208	150		4230	138	0.91	5.943	4.039	1.904	2.33	2.80×10^{-5}	0.26		
-55							0.957	30.40	262		12,985	0.0122	400		4880	–	–	–	–	–		–	ALL		
1727-1							0.778	29.75	280		17,915	0.0105	360		4670	168	0.69	–	–	–		–	0.33		
1683-50							0.326	30.53	432		20,000	0.0172	100		3995	79	0.65	5.714	4.225	1.489	1.81	3.28×10^{-5}	0.23		

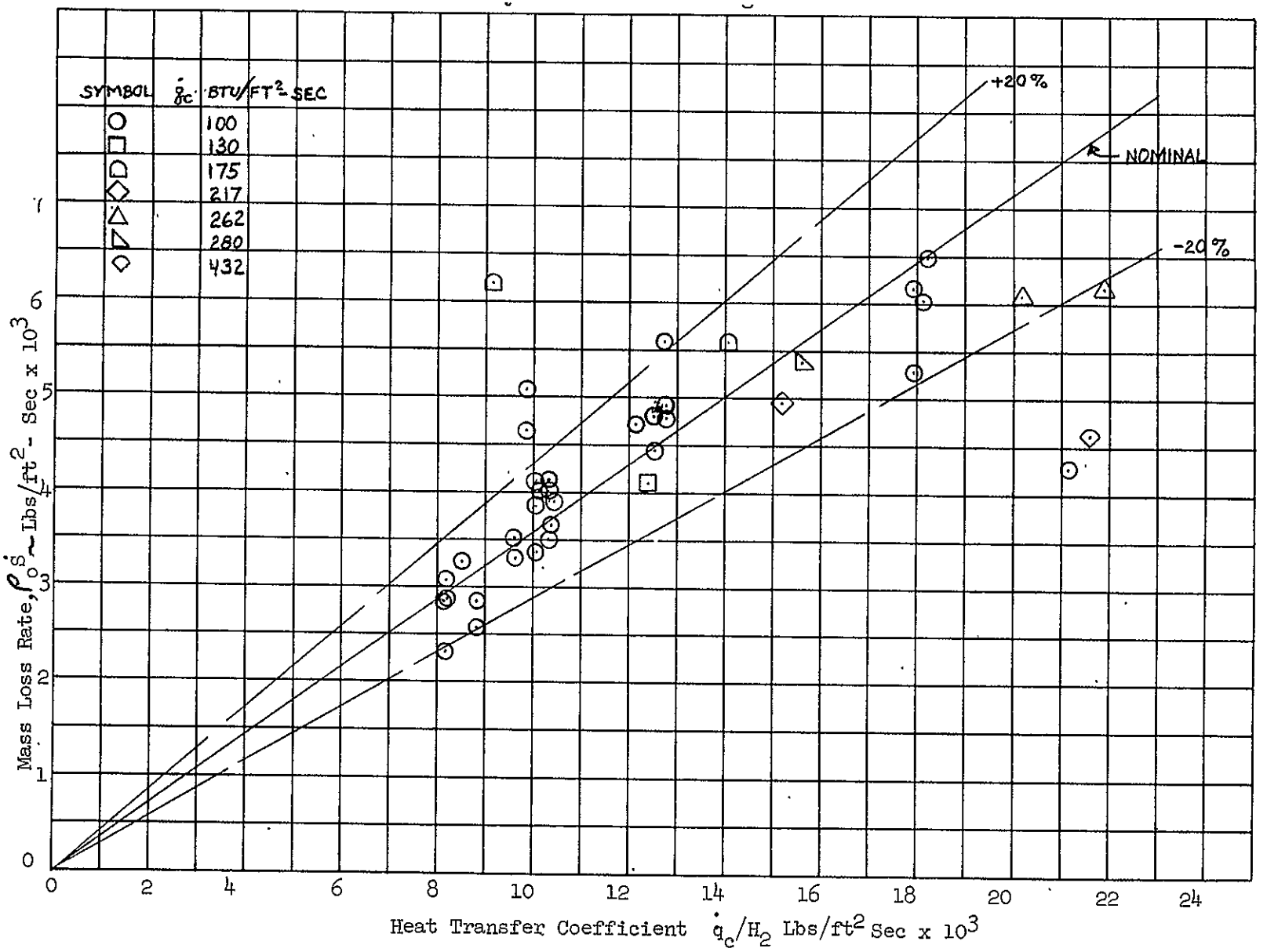


Figure 4.89 5026-39/HC-G Mass Loss - Overs Tests

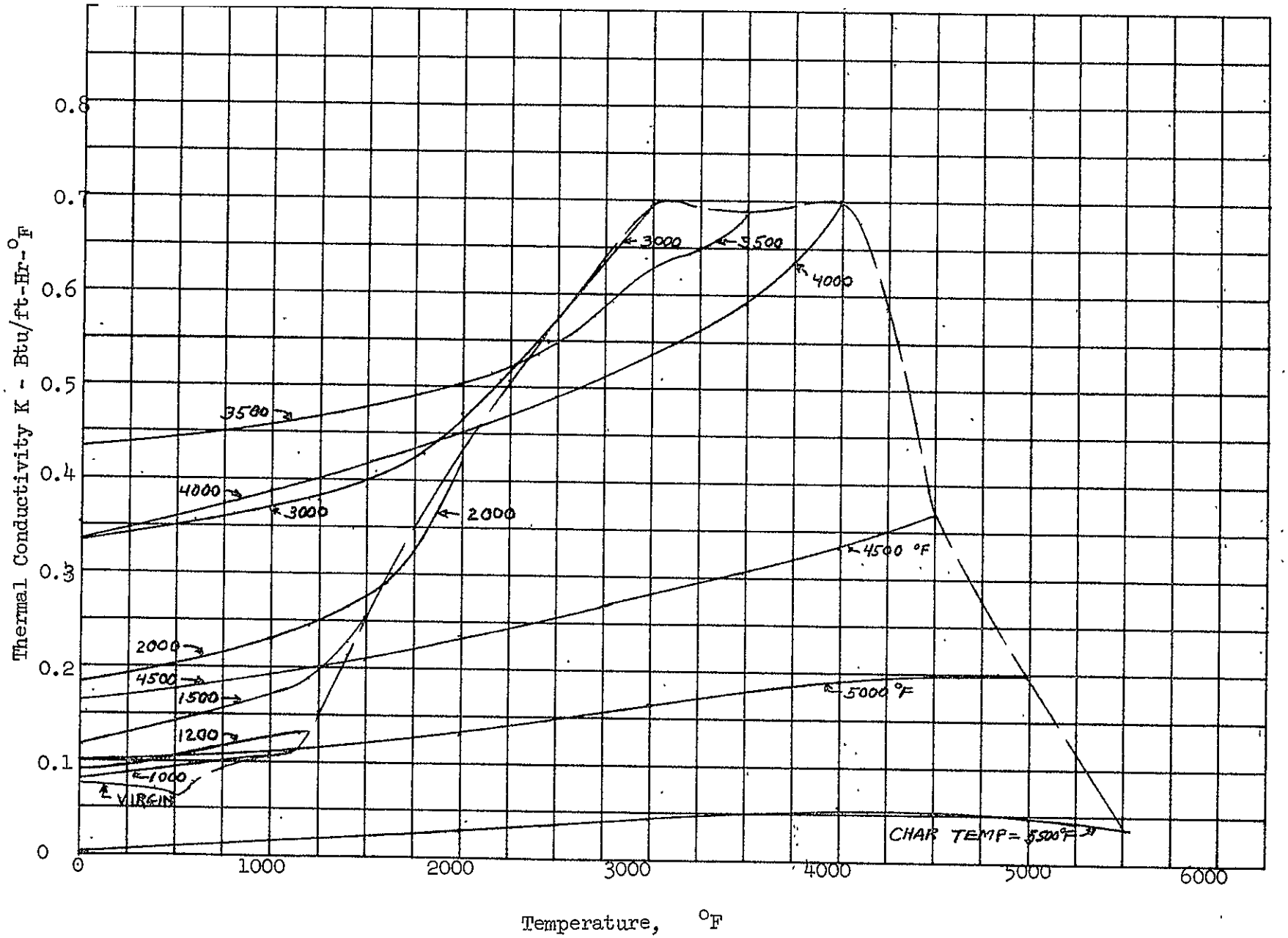


Figure 4.90 5026-39/HC-G Thermal Conductivity

measurements up to 3500°F. Beyond that point attempts were made to postulate char constituents (based upon chemical reactions) and to estimate conductivity for the combination of constituents. Because of the speculation of this approach above 3500°F, the thermal conductivity follows the envelope up to the maximum conductivity of 0.7 Btu/hr-ft-°F and then holds constant at higher temperatures. The data below 3500°F represent a combination of guarded hot plate measurements made at Avco and at Thermatest Laboratories. Individual test points are not shown for the sake of clarity on the curve.

It is apparent from Figure 4.90 that it is appropriate to use the envelope (the dashed line)as long as temperature is increasing. However, it is incorrect to allow the conductivity relationship to be reversible with temperature. Therefore, all heat shield calculations incorporate an irreversible dependence of thermal conductivity on temperature.

4.5.2.5.2 Specific Heat

Test measurements of specific heat for Avcoat 5026-39/HC-G have, in the vast majority of instances, shown that the value is approximately 0.35 Btu/lb-°F between room temperature and 1000°F (the upper limit to which data have been obtained). However, during the course of the flight evaluation of AFRM 011 (Reference 71) one set of measurements showed a significantly increasing value of specific heat with increasing temperature as shown on Figure 4.91. This functional relationship had no extreme effect upon correlations of measured with predicted temperatures but did improve slightly the overall correlation (as combined with all other parameters). It is for this reason that the specific heat of both virgin and charred ablator are used as given on Figure 4.91.

4.5.2.5.3 Decomposition Correlations

Linear thermogravimetric analysis data were obtained for Avcoat 5026-39/HC-G as shown on Figure 4.92. These data indicate weight

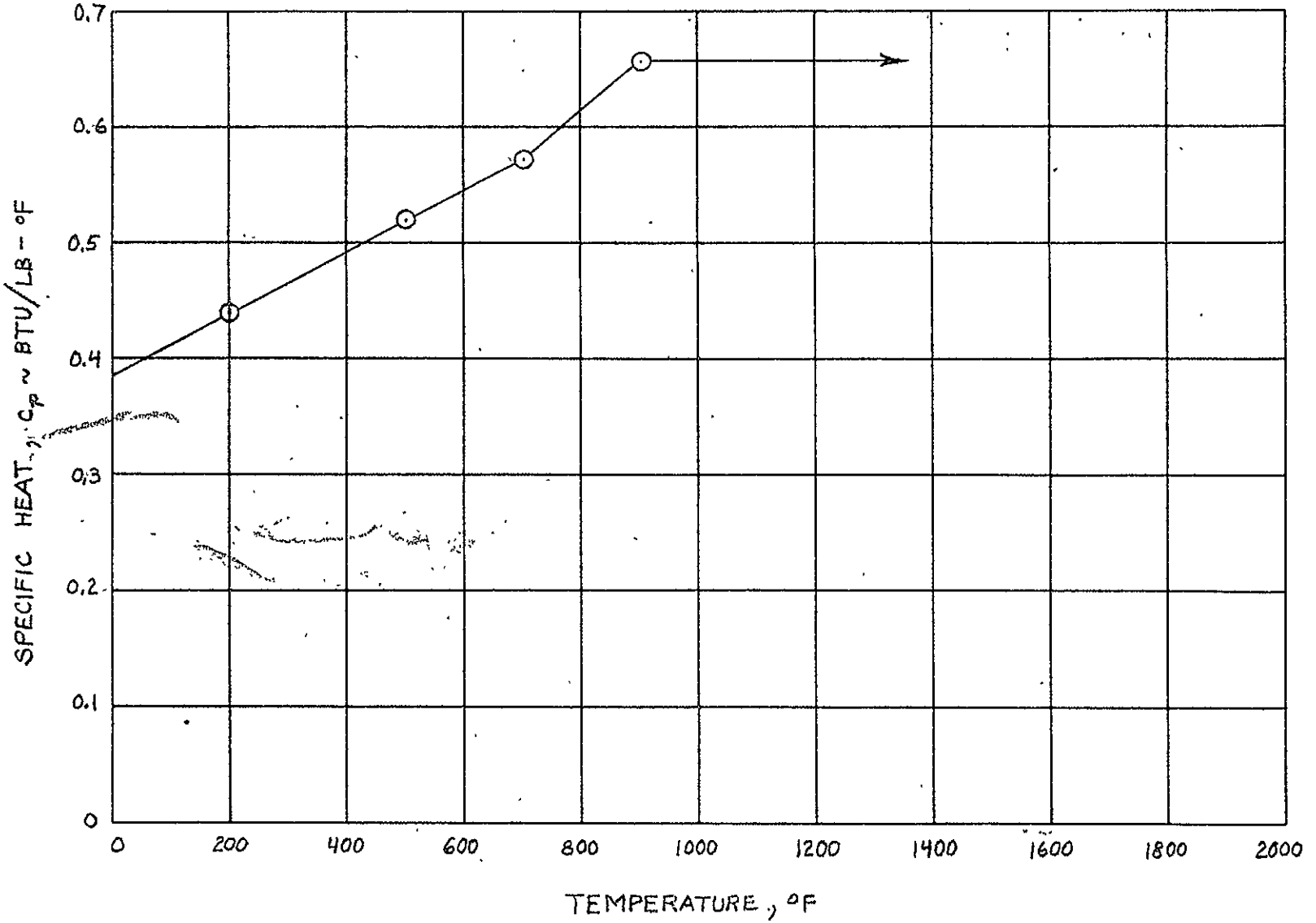


Figure 4.91
5026-39/HC-G Specific Heat

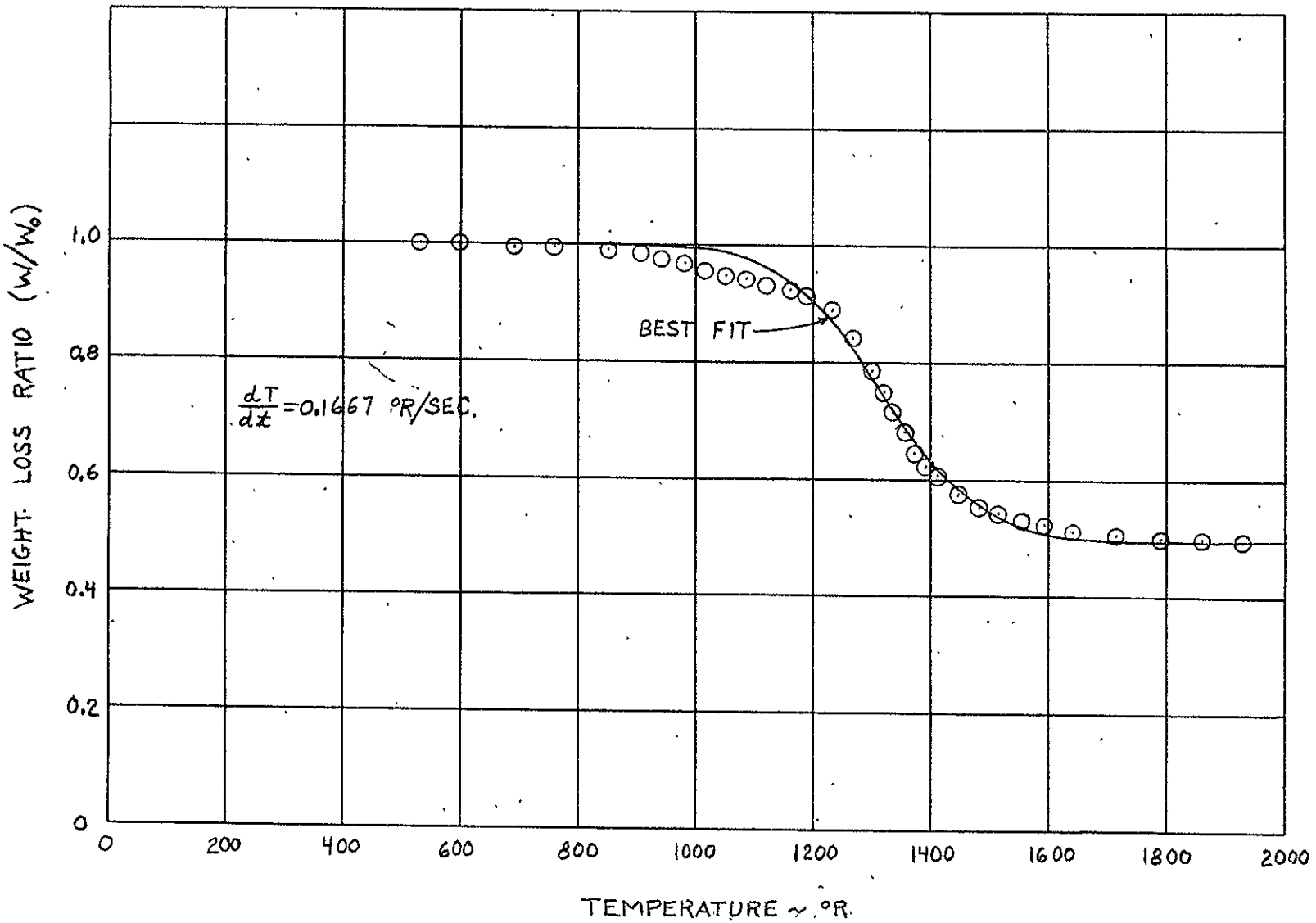


Figure 4.92
5026-39/HC-G Thermogravimetric Data

loss (which is assumed to be the same as density, thus neglecting any char shrinkage) as a function of temperature for a condition where the temperature is being increased linearly with time at a rate of 0.1677°R/sec. These data are reduced, along with similar data at other temperature rise rates, to establish the constants for the Arrhenius expression describing density reduction as a function of time and temperature.

4.5.2.4 Flight Test Correlations

Using the thermocouple data from the flight of Apollo AFRM 011, studies were performed as a part of a contract from NASA, MSC to correlate measured with predicted temperatures. The details of these studies are presented in Reference 67. It was found that by using a surface temperature as a driving force (in order to uncouple surface from subsurface phenomena) and after adjusting properties which are not measured in the laboratory, satisfactory agreement can be obtained between measured internal temperature responses and predicted values.

4.5.2.5 Summary of Problem Areas

A review of the available ground and flight test data on Avcoat 5026 indicates that additional testing is required to adequately define the thermal protection requirements for the Venus probe. Table 4.23 of Section 4.5.1, which indicates the additional testing required for carbon phenolic, is, in general, also applicable for Avcoat 5026 with a reduced level needed. It should be noted that for the trajectories indicated for the lower performance missions, the insulation requirements for Avcoat 5026 are significantly larger than the ablation requirements and therefore more stress is needed in the definition of internal properties than for the design using carbon phenolic. In general, the effect of atmospheric composition, radiant heating and the proper definition of ablation constants and energy terms must be determined. The amount of

testing for Avcoat 5026 should be less than carbon phenolic simply due to the availability of existing data provided, of course, that the effects of atmosphere can be easily correlated.

4.5.3 Heat Shield Performance Analysis

4.5.3.1 Scope of Analysis

The objective of this section is to present typical heat shield thermal responses for entry into the Venus atmosphere. Calculations are presented for both Avcoat 5026-30/HC-G and carbon phenolic. A scaling technique is derived for heat shield weights for other flight conditions and configurations.

4.5.3.2 Avcoat 5026-39/HC-G

Heat shield performance calculations were performed at the stagnation point of the entry probe which utilizes Avcoat 5026-39/HC-G as the ablative heat shield. The conditions for which this analysis was performed are as follows:

$$M/C_DA = 0.15 \text{ slugs/ft}^2$$

$$R_N/R_B = 0.25$$

$$\theta_c = 60^\circ$$

$$V_E = 35{,}600 \text{ ft/sec}$$

$$\gamma_E = -60^\circ$$

AV-50= atmospheric model

Table 4.27 gives the aerodynamic environment used for the thermal calculations. Figure 4.93 shows the surface recession history and indicates the ablation is first controlled by the surface reaction kinetics, then by the diffusion of oxygen to the wall (as surface temperatures increase) and then by sublimation of the carbonaceous char at the interval of maximum surface temperature. The process is essentially reversed as heating and surface temperature decrease, with a transition period where the ablation is governed to the same approximate

1-1394
R7-65

TABLE 4.27

AERODYNAMIC ENVIRONMENT FOR AVCOAT 5026-39/HC-G

PERFORMANCE CALCULATIONS

STAGNATION POINT

TIME ~ SEC.		CONV. HEAT FLUX ~ BTU/FT²-SEC.		RAD. HEAT FLUX ~ BTU/FT²-SEC.		PRESSURE ~ ATMOS.	
0.0		0.0		0.0		1.0×10^{-4}	
29.51		8.2		0.0		1.0×10^{-4}	
34.07		48.7		7.0		5.7×10^{-4}	
35.84		111.6		32.0		3.02×10^{-3}	
37.35		245.9		154.0		0.015	
39.56		841.5		400.0		0.183	
40.43		1169.3		225.0		0.45	
41.02		1257.6		45.0		0.74	
41.61		1120.9		20.0		1.02	
42.32		753.9		0.0		1.16	
43.26		306.7		↓		0.94	
44.32		86.8				0.56	
47.18		5.1				0.14	
49.91		0.9				0.06	
61.19		0.0				0.01	

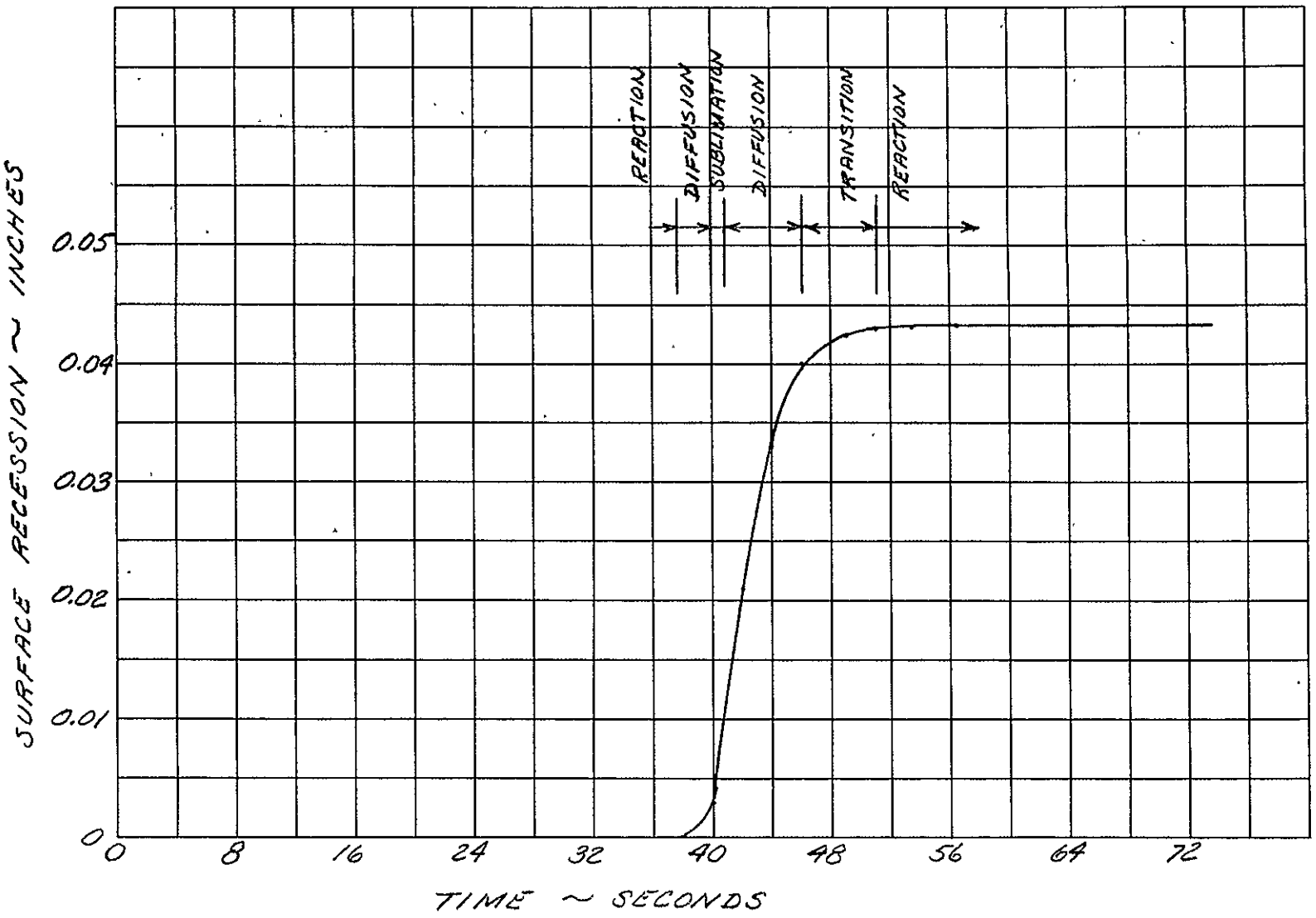


Figure 4.93 5026-39/HC-G Stagnation Point Surface Recession History

extent by both oxygen diffusion and reaction kinetics. It is seen that for this case, the total amount of char removal is 0.043 inch. Figure 4.94 presents temperature histories at the ablator surface, at the mid-point of the 0.15 inch of ablator, and at the bondline between the Avcoat and a 0.06 inch steel substructure. Design of the heat shield requires protection of the substructure to a 600°F maximum value at Mach 0.5. For this case, Mach 0.5 occurs at approximately 52 seconds, and it is seen that the 0.15 inch of ablator affords the proper thermal protection, assuming an initial entry temperature of 80°F.

Density profiles through the ablator at specific times are shown on Figure 4.95. Until 30 seconds, there is essentially no decomposition of the ablator as a consequence of the low heating up to this time. At 36 seconds the surface has charred to about one half of the fully charred conditic (16.5 lbs/ft^3). At later times the surface and some finite depth are fully charred. It is interesting to note the decomposition zone during the period of significant heating (at times later than 36 seconds) is relatively thin, indicating a condition which approaches steady-state.

The final capsule which employs Avcoat 5026-39/HC-G as the ablator has a ballistic coefficient of 0.20 slugs/ft^2 and a bluntness ratio of 1.0. Comparison of the environment for the actual capsule to that for which thermal responses were obtained shows that the quoted 0.30 inch thickness is sufficient to maintain the 600°F structure temperature limit. The 0.30 inch was selected as a probable minimum thickness for fabrication and is not derived from minimum thermal requirements.

4.5.3.3 Carbon Phenolic

During the initial heat shield parametric study to obtain ablator weights for many capsules and trajectories, only a limited number of

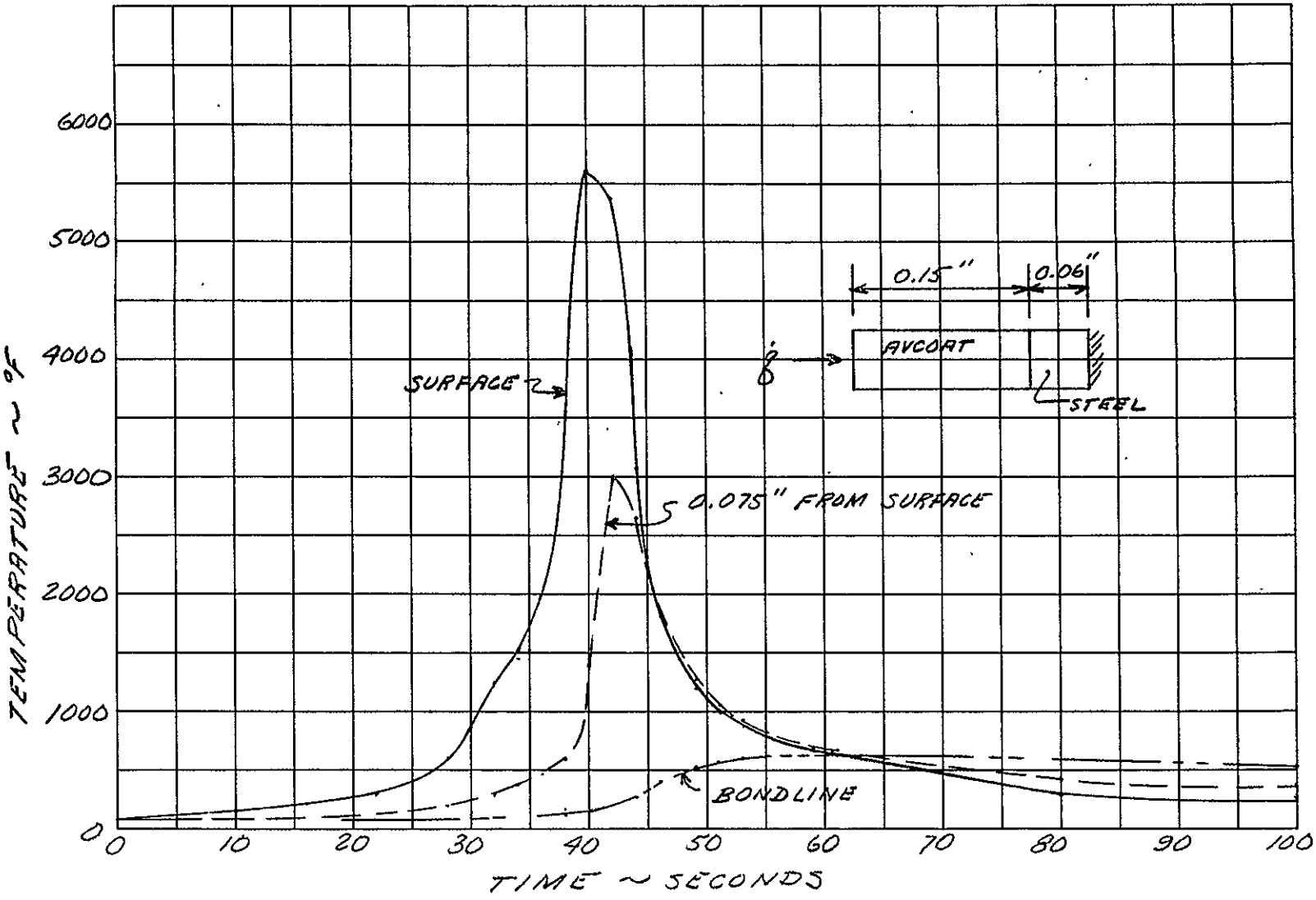


Figure 4.94 5026-39/HC-G Stagnation Point Temperature Histories

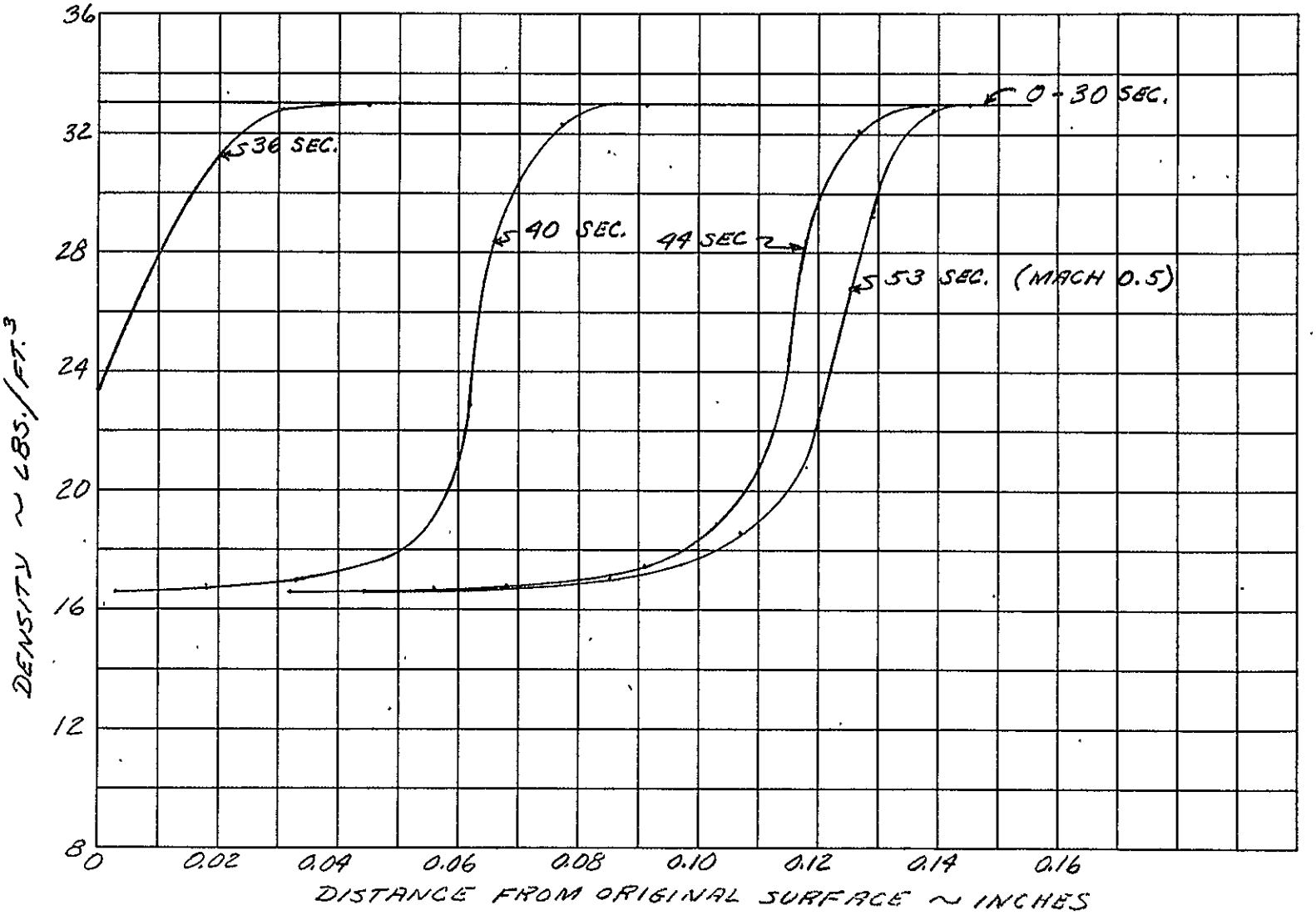


Figure 4.95 5026-39/HC-G Stagnation Point Density Profiles

transient 1600 calculations were performed. It was established from these calculations that the ablation process (and hence the mass of ablator removed) can be predicted by use of a quasi-steady surface boundary condition. Sufficient calculations were performed to establish that entry angle is the primary factor which influences insulation weight. Therefore, by studying the Program 1600 calculations and by performing a large number of quasi-steady calculations, the scaling process described in Section 4.5.3.4 below was employed to define heat shield weights for capsules not specifically contained within the initial parametric study.

A typical carbon phenolic thermal response calculation is presented in Figures 4.96 through 4.98 at the mid-cone point of a capsule having the following characteristics and entry conditions:

$$M/C_DA = 1.1 \text{ slugs/ft}^2$$

$$R_N/R_B = 0.25$$

$$\theta_c = 45^o$$

$$V_E = 38,254 \text{ ft/sec}$$

$$\gamma_E = -50$$

$$\text{AV-4} = \text{atmosphere model}$$

The surface recession (Figure 4.96) is dominated by the sublimation regime, a direct consequence of the high combined heating rates. The temperature histories of Figure 4.97 show the associated high surface temperatures and the fact that approximately 0.30 inch of ablator maintains the 600°F design limit. The char layer as indicated by the density profiles of Figure 4.98, remains relatively thin throughout the heating duration and does not begin to show significant transient effects until 80 seconds when heating is ended.

A performance analysis was also conducted for carbon phenolic at the conditions listed below, to duplicate an analysis of Jet Propulsion Laboratory.

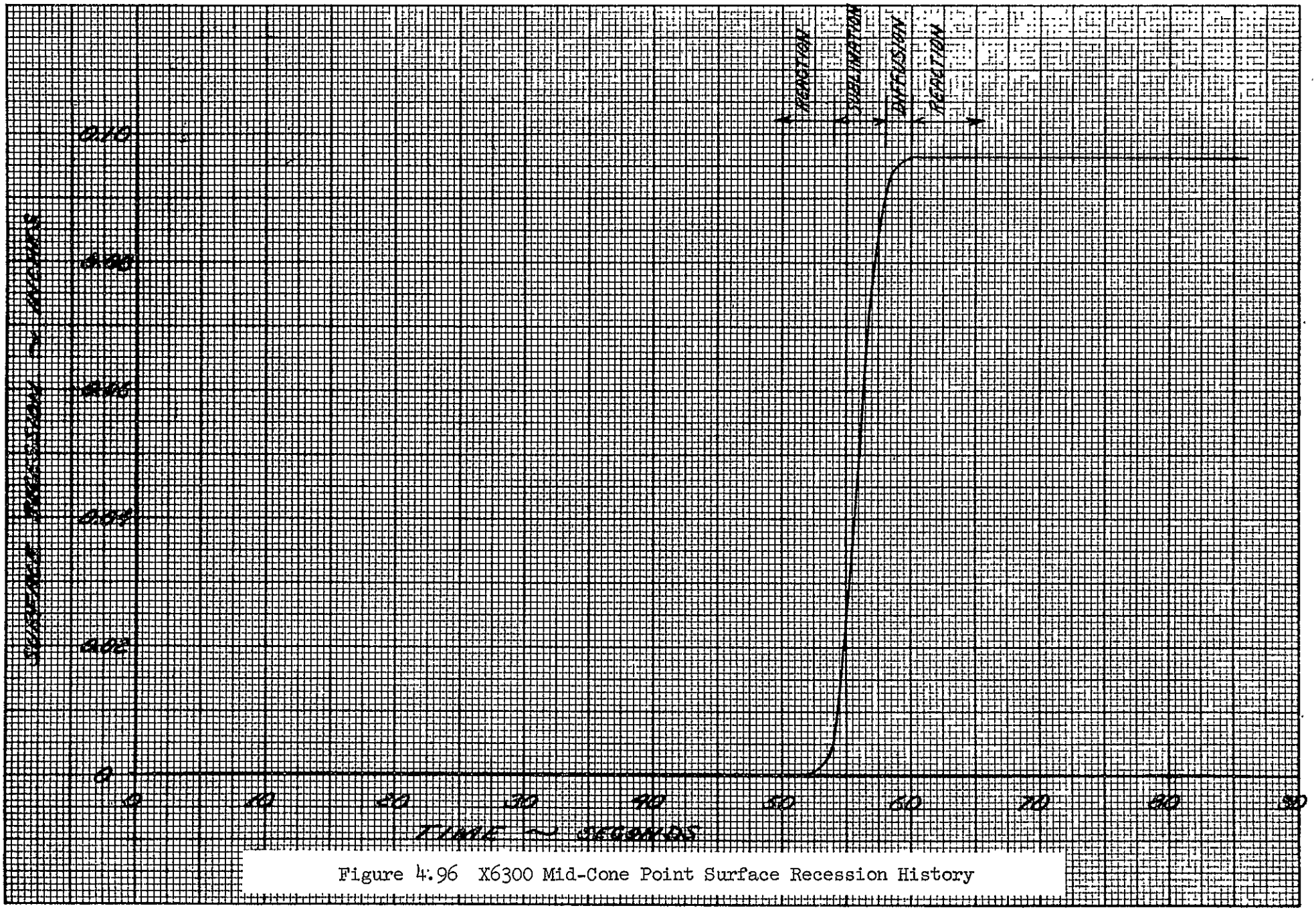


Figure 4.96 X6300 Mid-Cone Point Surface Recession History

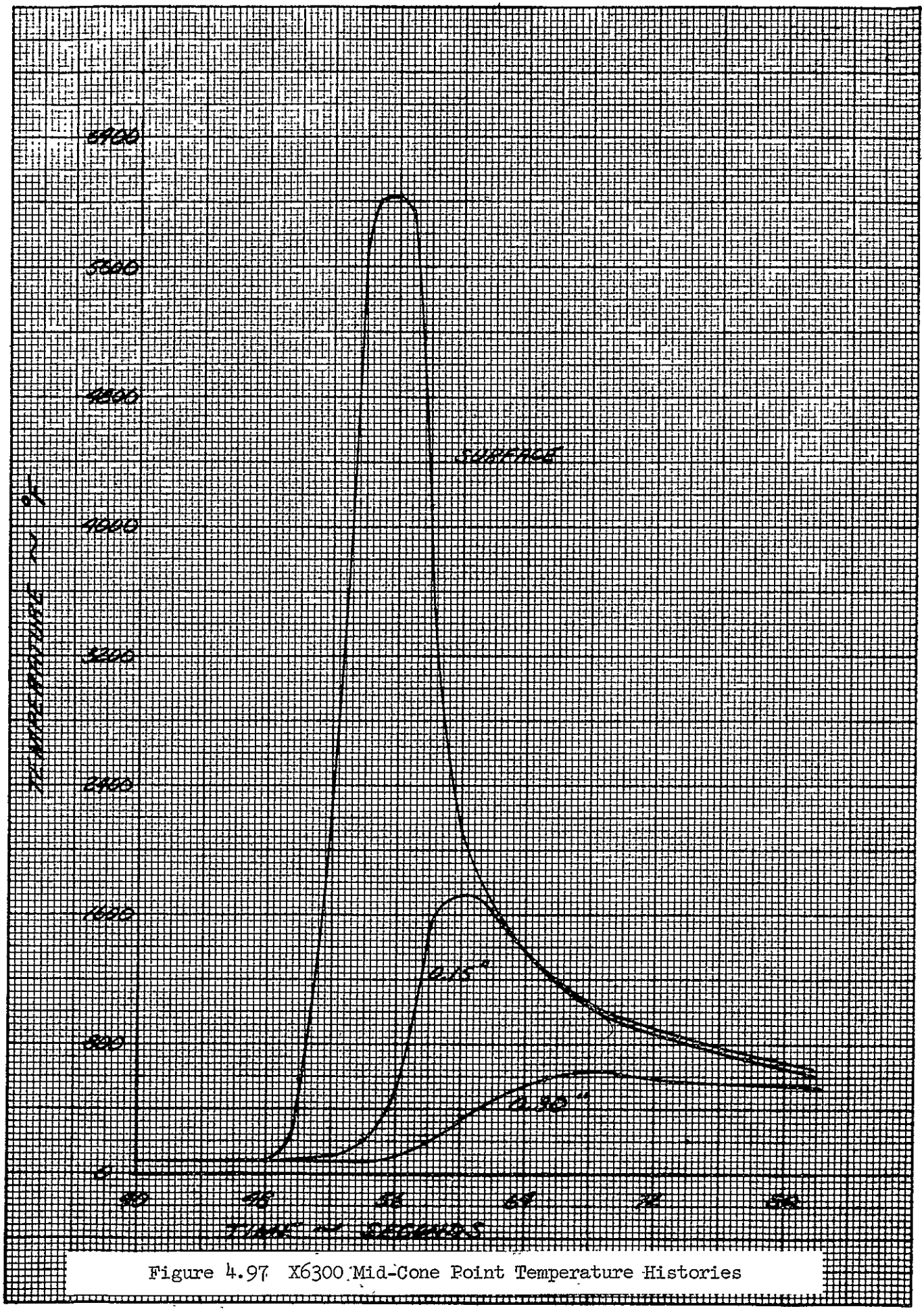


Figure 4.97 X6300 Mid-Cone Point Temperature Histories

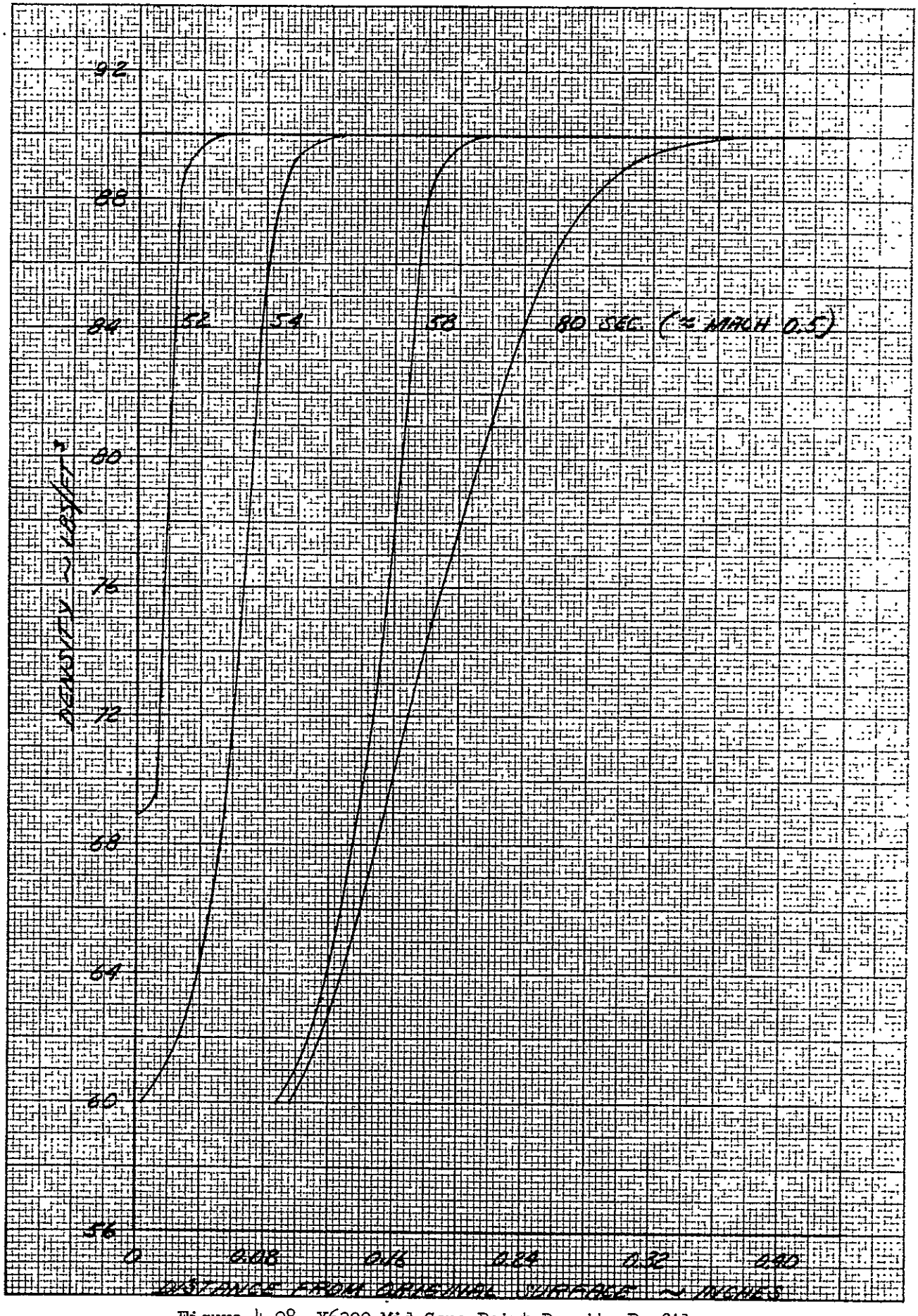


Figure 4.98 X6300 Mid-Cone Point Density Profiles

M/C_DA = 0.6 slugs/ft^2

Diameter = 4.0 ft

V_E = 36,000 ft/sec

γ_E = -30°

AV-50 = atmosphere model

The calculations were performed for the stagnation point using 0.43 inch of carbon phenolic. All environmental parameters were those supplied by Jet Propulsion Laboratory and are listed in Table 4.28.

The ablation history and modes of ablation are shown on Figure 4.99. It is noted that for this case, the removal is again primarily dictated by carbon sublimation.

Temperature histories for this analysis are given on Figure 4.100 at the surface, the ablator mid-point, and the backface. Assuming that protection to 600°F is required up to Mach 0.5 (which occurs at approximately 72 seconds) it appears that the 0.43 inch is more than sufficient since the backface is at 560°F at this time. It is noted that the 0.43 inch includes a simulation of a substructure, a technique employed by Jet Propulsion Laboratory in some heat shield calculations. It would thus appear that the Jet Propulsion Laboratory calculation is slightly conservative relative to the Avco approach. However, it must be realized that only one comparison has been made (due to time limitations) and no real trend can be established.

4.5.3.4 Heat Shield Scaling

Program 1600 calculations such as those discussed above for carbon phenolic were compared to calculations of surface recession using a quasi-steady form of the surface energy balance (Avco Program 1950). These comparisons, where were performed during the initial parametric study revealed that the quasi-steady approach to predictions of ablation agree almost exactly

1-1394
R7-65

TABLE 4.28

AERODYNAMIC ENVIRONMENT FOR JPL COMPARISON CASE

STAGNATION POINT

TIME ~ SEC.		CONV. HEAT FLUX ~ BTU/FT²-SEC.		RAD. HEAT FLUX ~ BTU/FT²-SEC.		PRESSURE ~ ATMOS.	
0.0		0.5		0.0		0.9×10^{-4}	
29.06		38.0		0.0		1.8×10^{-4}	
34.91		147.4		0.0		2.9×10^{-3}	
40.59		753.2		3.7		0.073	
43.08		1631.5		87.6		0.37	
44.5		2257.6		93.5		0.85	
45.55		2498.1		93.5		1.38	
45.93		2502.1		103.3		1.6	
46.54		2382.7		142.9		1.96	
47.07		2172.0		190.9		2.21	
47.54		1907.8		234.0		2.37	
48.0		1623.6		258.1		2.44	
49.95		617.5		28.5		1.97	
52.03		149.1		0.0		1.11	
55.17		22.8		↓		0.45	
57.02		9.0				0.28	
67.43		0.4				0.05	
72.22		0.0				0.023	

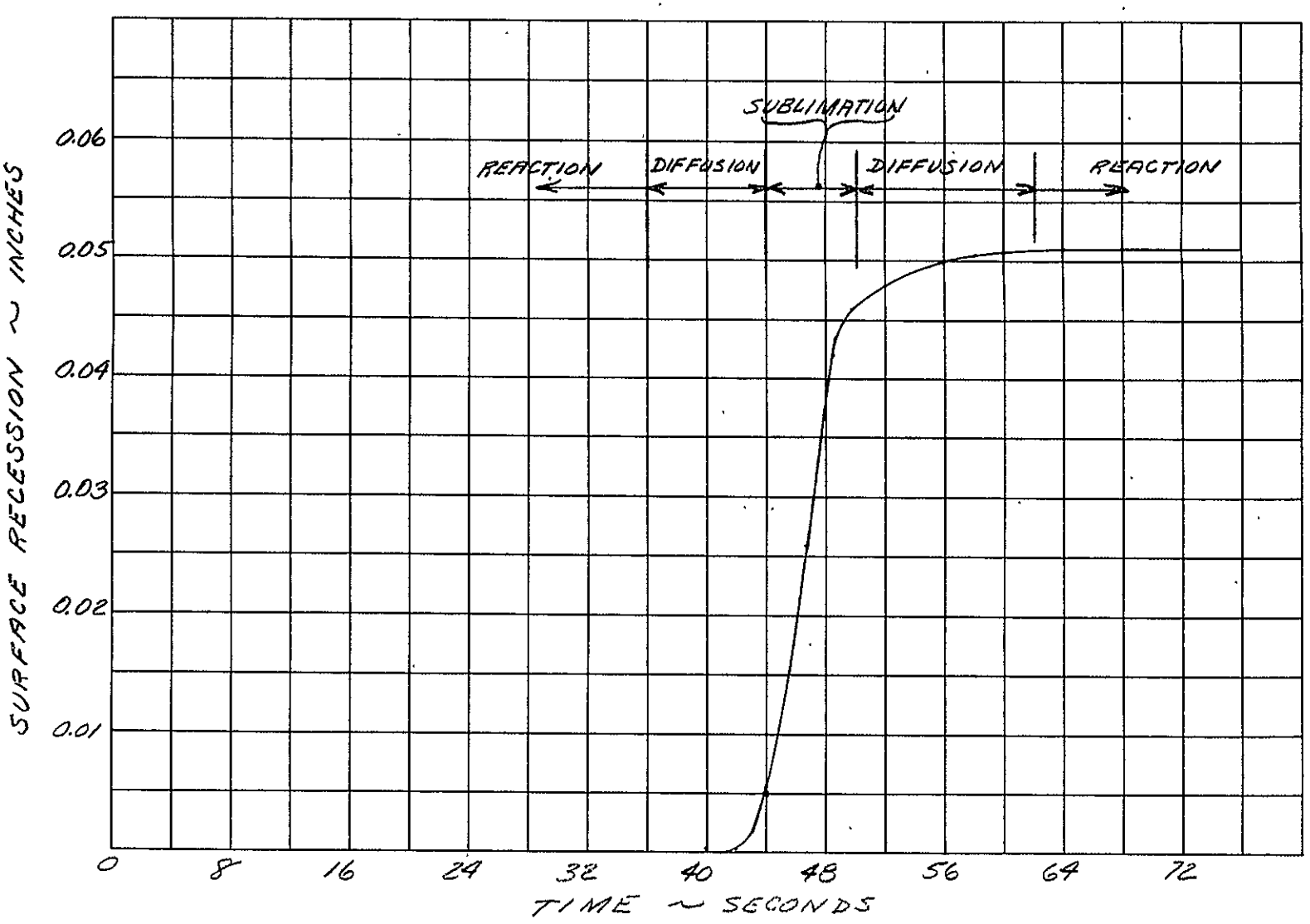


Figure 4.99 X6300 Stagnation Point Surface Recession History

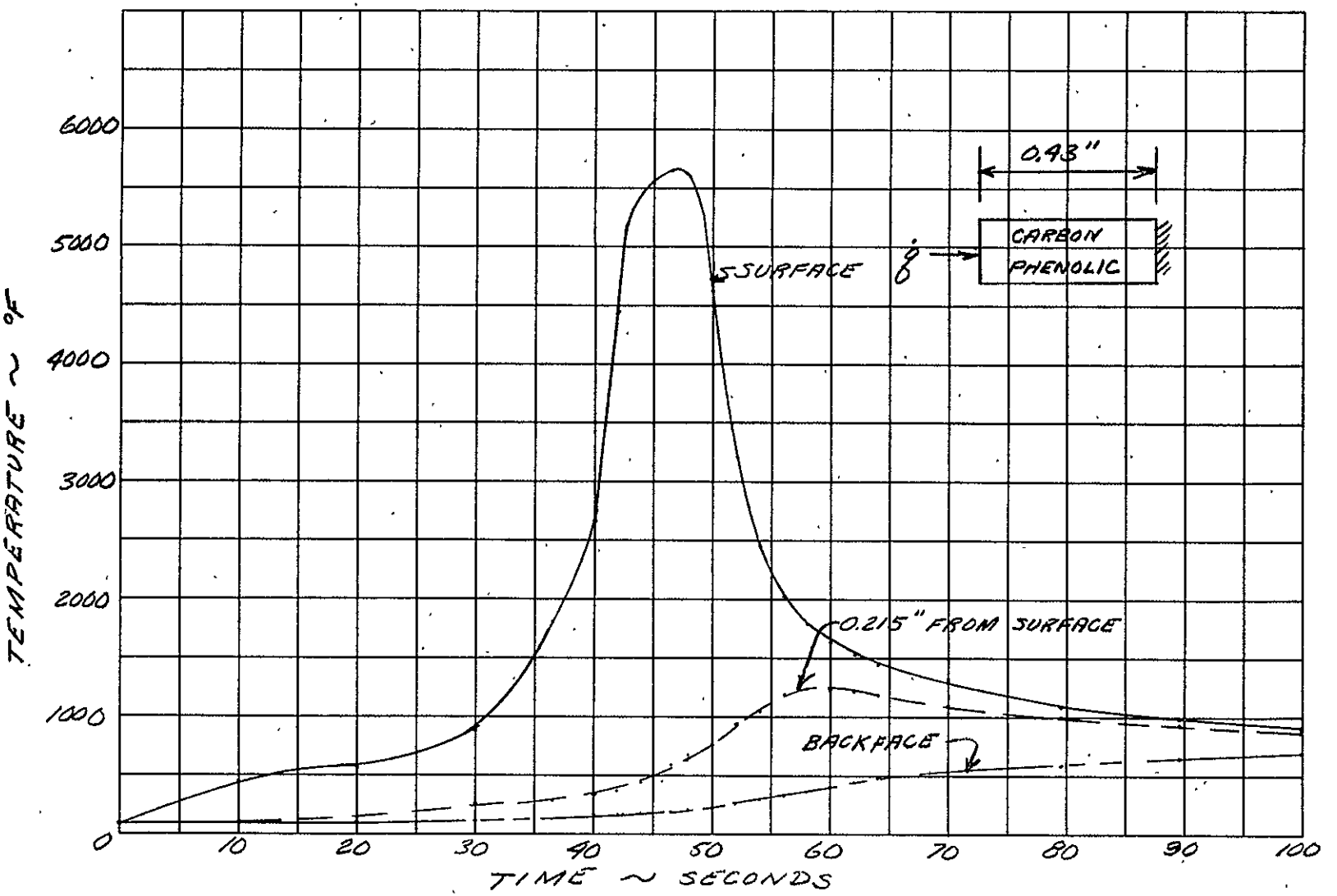


Figure 4.100 X6300 Stagnation Point Temperature Histories

with the Program 1600 calculations. It was further discovered that for the range of parameters being considered, entry angle was the dominating factor governing insulation requirements (i.e., the ablator which is not removed). Therefore, on the basis of these comparisons and observations from both the Program 1600 and the Program 1950 calculations, a heat shield scaling technique was developed. This scaling technique was employed to predict heat shield weights for the final capsule configurations.

The heat shield weight is divided into three elements:

$$W = W_{in} + W_R + W_c$$

where

W_{in} = insulation weight

W_R = ablated weight due to radiation heating

W_c = ablated weight due to convective heating

As noted above, the parametric studies on carbon phenolic showed that the insulation weight is primarily a function of the entry angle, and a variation was generated as shown in Figure 4.101. The insulation weight criteria used is that the backface temperature does not exceed 600°F prior to impact. Although the final capsules require protection only to Mach 0.5, the correlation is still very nearly correct since the structure temperature reaches its maximum value at a time very close to Mach 0.5.

The weight of ablator removed in order to dissipate partially the radiative heating component is estimated simply as

$$W_R = Q_R/H_V$$

where Q_R is the integrated incident radiative heating; use of the quantity H_V reflects the consideration that the primary heat rejection mechanism is by vaporization of the carbonaceous surface.

The ablation weight attributed to the convective heating component must account for the flow being laminar or turbulent and the effect

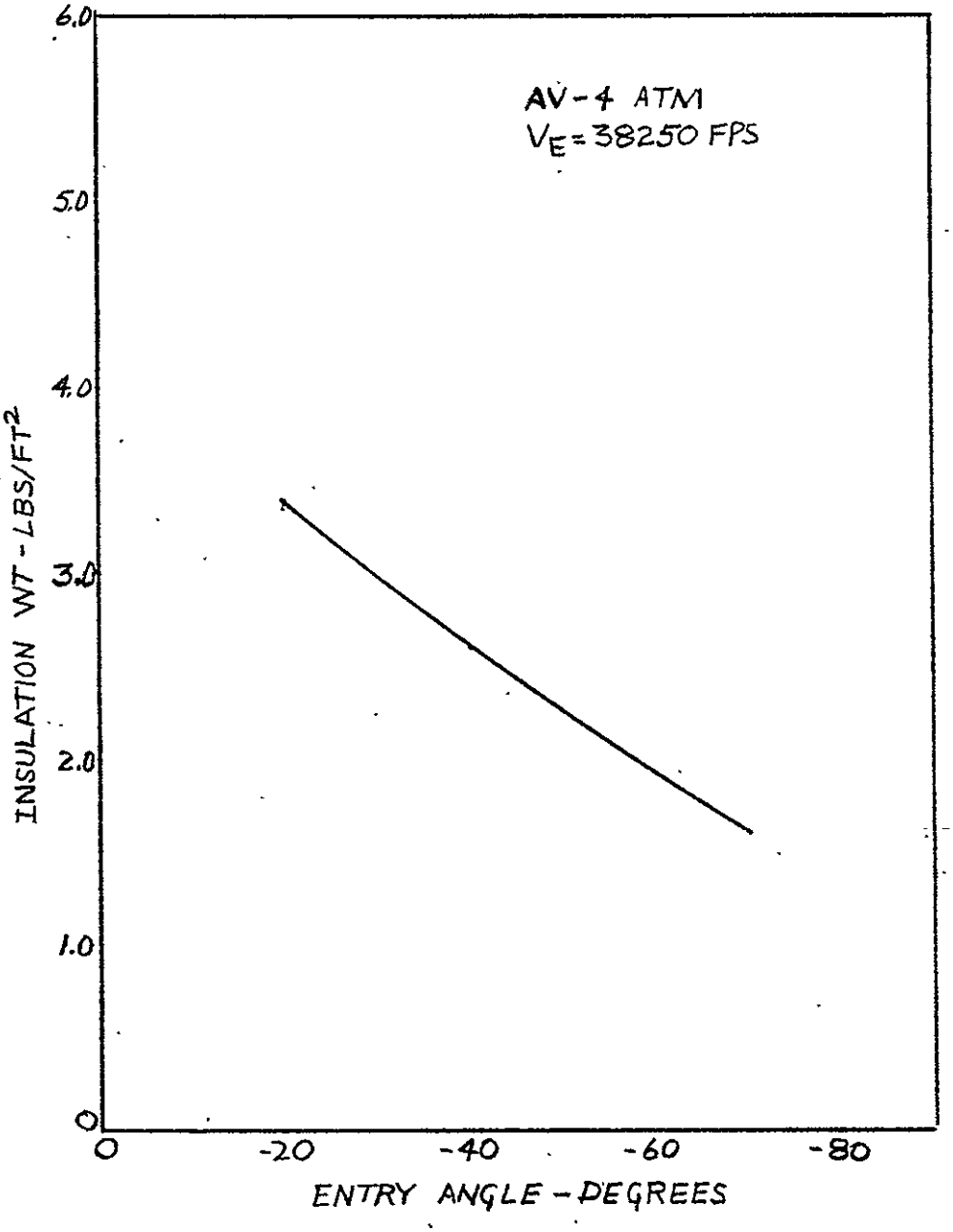


Figure 4.101 X6300 Insulation Weight

of radiation blockage. An elementary form is:

$$W_c = \frac{Q_c e^{-\frac{\omega_R \eta \bar{H}}{Q_c}}}{\eta \bar{H}} \qquad (31)$$

where $\bar{H}$ is an effective enthalpy, and the value of the enthalpy at peak heating is recommended, in which case,

$\bar{H}/H_e$ = 0.72 for laminar heating, and

$\bar{H}/H_e$ = 0.60 for turbulent heating

Q_c = the integrated cold wall convective heat transfer, and

η = the transpiration coefficient.

An example of use of this technique is as follows:

Material properties data are:

η_L = 0.76

η_T = 0.40

H_v = 11400 Btu/lb

$\bar{H}_L$ = 21600 Btu/lb

$\bar{H}_T$ = 18000 Btu/lb

$\eta_L \bar{H}_L$ = 16400 Btu/lb

$\eta_T \bar{H}_T$ = 7200 Btu/lb

The heating data on three configurations is taken from the parametric study results,

	Mid-Cone		Stag Point	
Vehicle	Q_c (turb)	Q_R	Q_c	Q_R
45 deg. cone	9100	2812	19560	14020
60 deg. cone	5280	9626	14000	9800
30 deg. cone	12600	3960	30000	29000

The insulation weight (unstaged) for this entry angle is 1.65 lbs/ft^2. The

heat shield weights calculated and given in the parametric study are,

Vehicle	Mid-Cone	Stag Point
45 deg. cone	2.55 psf	3.30 psf
60 deg. cone	2.85	2.79
30 deg. cone	3.30	4.65

The calculated weights using the scaling equation are:

Vehicle	Mid-Cone	Stag Point
45 deg. cone	2.93	3.31
60 deg. cone	2.72	2.82
30 deg. cone	3.43	4.65

Comparison of the approximate and numerical results indicate the stagnation point is fortuitously well predicted, and no more than 15 percent variation on the cone. On the cone, the combination of laminar and turbulent flow makes scaling difficult.

4.5.4 Shear and Pressure Gradient Effects on Avcoat 5026-39/HC-G

4.5.4.1 Effects of Aerodynamic Shear on Avcoat 5026-39/HC-G

The effects of shear upon Avcoat 5026-39/HC-G performance are best demonstrated by data such as those shown in Figure 4.102. The 10 MW arc downstream pipe configuration was used to perform tests for a range of aerodynamic shear stresses up to approximately 35 lb/ft^2. Previous studies of low-shear test data obtained in this facility have indicated that the ablation phenomena are most likely sublimation controlled; i.e., the surface temperatures (for this configuration) are apparently high enough for vaporization to control the surface mass-loss rate. Accordingly, Figure 4.102 shows a sublimation parameter that is a mass-loss rate normalized for pressure and plotted with measured surface temperature as the independent variable.

The significance of aerodynamic shear from 15 to 35 lb/ft^2

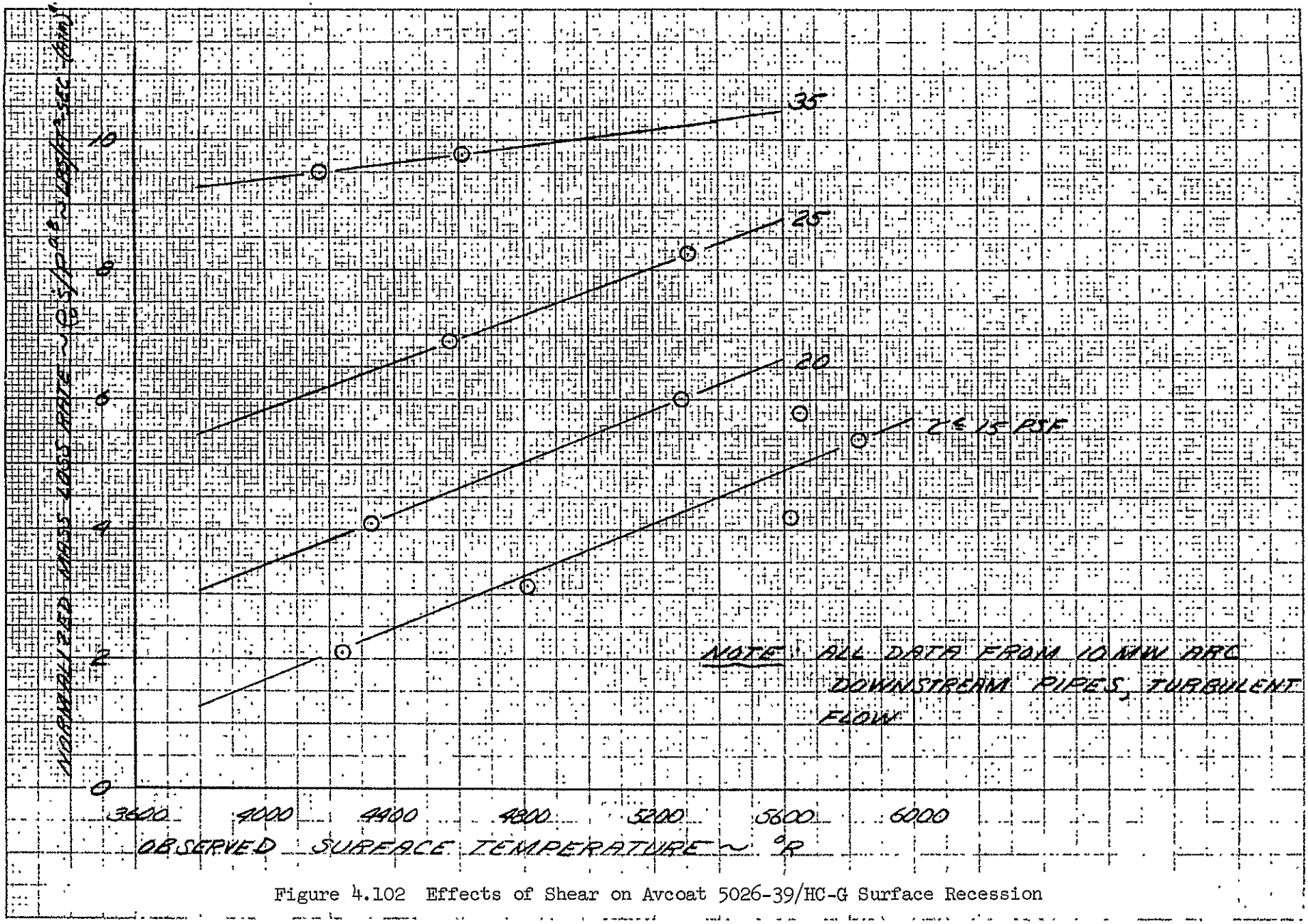


Figure 4.102 Effects of Shear on Avcoat 5026-39/HC-G Surface Recession

is evident. At 4000°R, the increased recession is close to a factor of 5, while at 5600°R, it is at least a factor of 2. (Data at 5600°R and 35 lb/ft^2 would probably be even higher than the indicated extrapolation.) The straight lines drawn do not represent functional relationships, but are shown only to indicate general trends of the data.

Although the data of Figure 4.102 are presented such that it appears possible to account for an apparently predictable recession increase, there are several reasons for adopting a more cautious approach. Up to 15 lb/ft^2, ablation data show no significant effects of shear. The surface of the char remains macroscopically smooth, and the surface recession is quantitatively repeatable and predictable. Beyond 15 lb/ft^2, serious char spalling occurs, creating self-aggravating, unstable, unpredictable surface recession and fluctuating surface temperatures. The measured mass-loss rate at shear levels above 15 lb/ft^2 is, at best, only partially indicative of actual performance.

4.5.4.2 Effects of Pressure Gradients on Avcoat 5026-39/HC-G

Besides the vulnerability to aerodynamic shear above 15 lb/ft^2, Avcoat 5026-39/HC-G erosion rates were observed to become excessive either where large surface pressure gradients exist or where the rear surface of the ablator is not sealed. In both of these cases, it is not evident that the hot plasma actually penetrates deep into the material. It appears that the gaseous products of decomposition do not transpire directly into the boundary layer; rather, if the pressure gradient is large enough to permit such flow, they follow a preferred path at least resistance through the porous ablator structure to a region of lower pressure than that at the ablating surface. In the resulting gas-starved area, energy dissipating reactions are reduced, and practically all of the heat-blocking transpiration effects are lost. The result is extremely rapid and irregular surface recession. This phenomenon

was observed from a series of 10 MW arc splash tests which were performed where specimens of identical thickness and with the honeycomb core aligned normal to the aerodynamic flow were subjected to identical test conditions. The only difference between a given set of two specimens was that one was sealed with an impervious material at the backface while the other had no seal. The results of these tests are summarized on Figure 4.103 where the difference of performance, as discussed above, is evident. It was concluded from these tests that the Avcoat 5026-39/HC-G is sensitive to significant pressure gradient as a consequence of the large open or inter-connected porosity. It is seen that further testing is required to establish the threshold of this sensitivity.

4.6 DEVELOPMENT TESTING SIMULATION

4.6.1 Introduction

The thermodynamics design of the heat shield for a Venus atmospheric entry capsule will contend with the customary problems associated with analysis and interpretation of ground test results, i.e., separation of variables such that the specific effects of enthalpy, pressure, heating rate, and shear stress can be properly evaluated and incorporated into the design analytical model. In addition, the Venus entry problem is complicated by two unique factors which have significant bearing on the nature and scope of the development test program. These are:

1. Large concentration of carbon dioxide in the Venusian atmosphere, and
2. Extremely high levels of convective and radiative heating emanating from the plasma sheath during entry.

Because of the complexity of the total problem, the development test program is to be accomplished in three distinct phases as follows:

Phase I: Two representative heat shield ablator materials (high and low

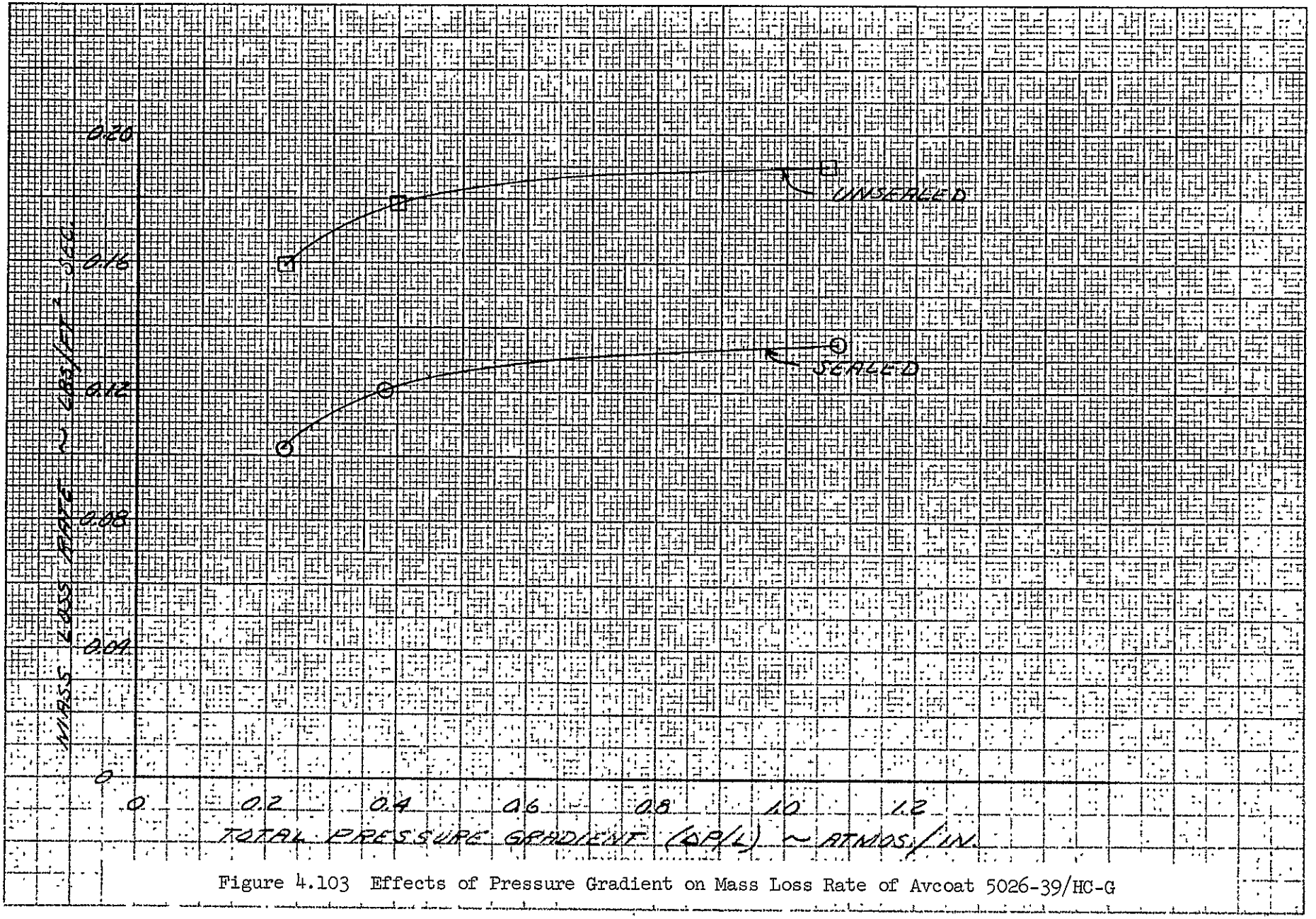


Figure 4.103 Effects of Pressure Gradient on Mass Loss Rate of Avcoat 5026-39/HC-G

density) will be tested over the widest possible range of applicable simulated flight conditions. The prime objectives of these tests will be to investigate the thermochemical phenomena associated with the complex ablation process. An important part of this effort will include tests which are specifically designed to resolve problems arising from certain simulation limitations inherent in the various ground test facilities.

Phase II: Thermodynamic properties tests and trajectory oriented ablation tests will be conducted to provide specific data for the design application. Statistical confidence in these data will be required. All Phase II tests will be conducted on the same materials utilized in Phase I.

Phase III: Based on the earlier work, meaningful screening tests will be selected and applied in evaluating the relative merits of several other candidate materials for the Venus entry application.

In the Phase I discussion, it will be shown that it is beyond the state-of-the-art to similate simultaneously in ground test facilities representative levels of flight heating rate, enthalpy, pressure, and shear. For the higher velocity entry trajectories described herein, it is beyond current facility capabilities to obtain in some cases even the appropriate level of a particular parameter of interest. The lack of accurate environmental simulation, coupled with the complexity of the thermochemical ablation phenomena over a wide range of conditions in a foreign atmosphere, makes it necessary to conduct for design support as comprehensive a parametric study as possible within the limitations of technical, economic, and schedule restraints.

4.6.2 Simulation Considerations

4.6.2.1 Mass Transfer Regimes

For the wide heating range of interest in this study, (Figures 4.104, 4.105, 4.106), the ablation of the carbonaceous charring materials will involve at least four distinct aerothermochemical regimes.

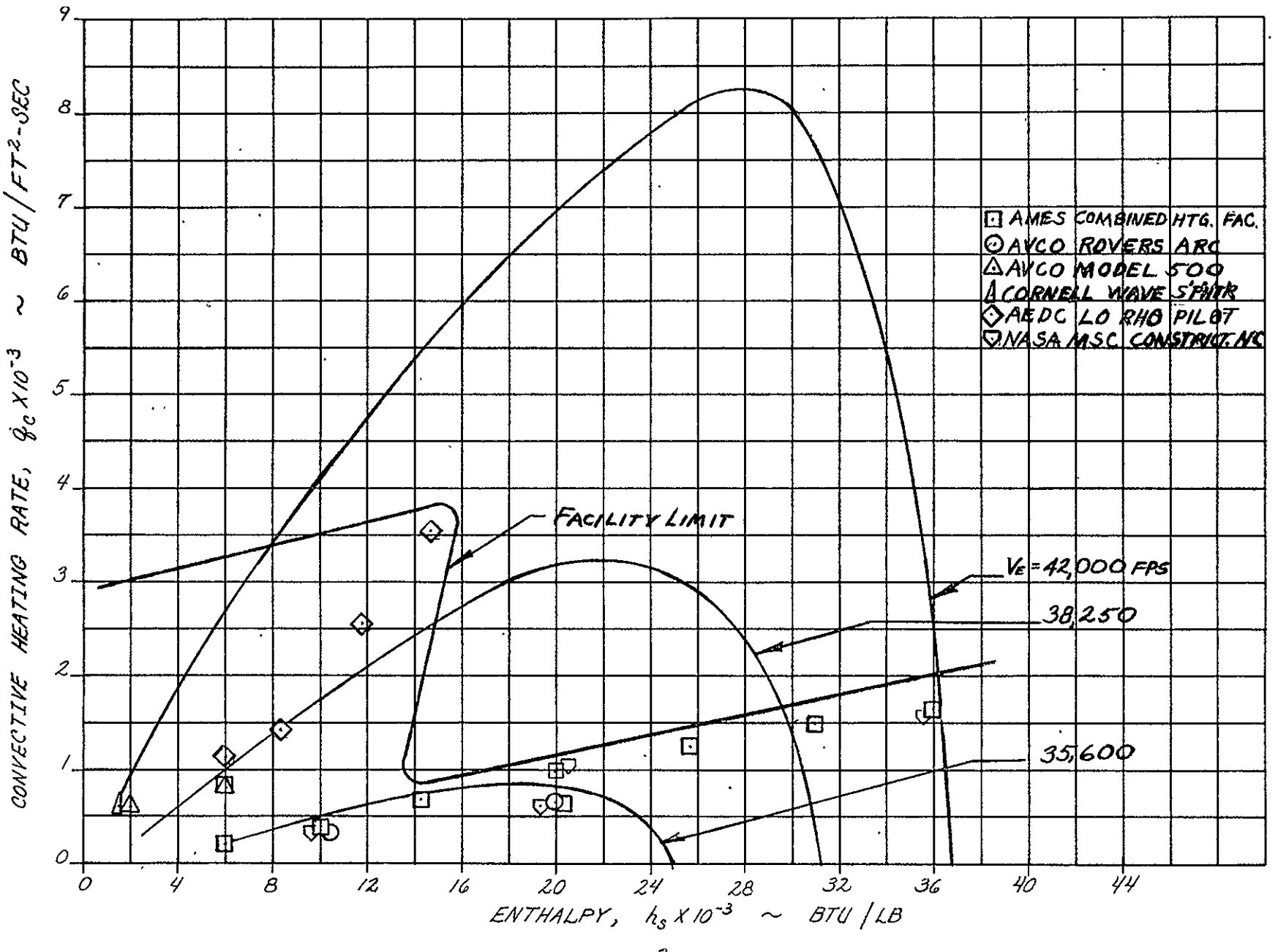


Figure 4.104 Stagnation Convective Heating - Gas Enthalpy Environment

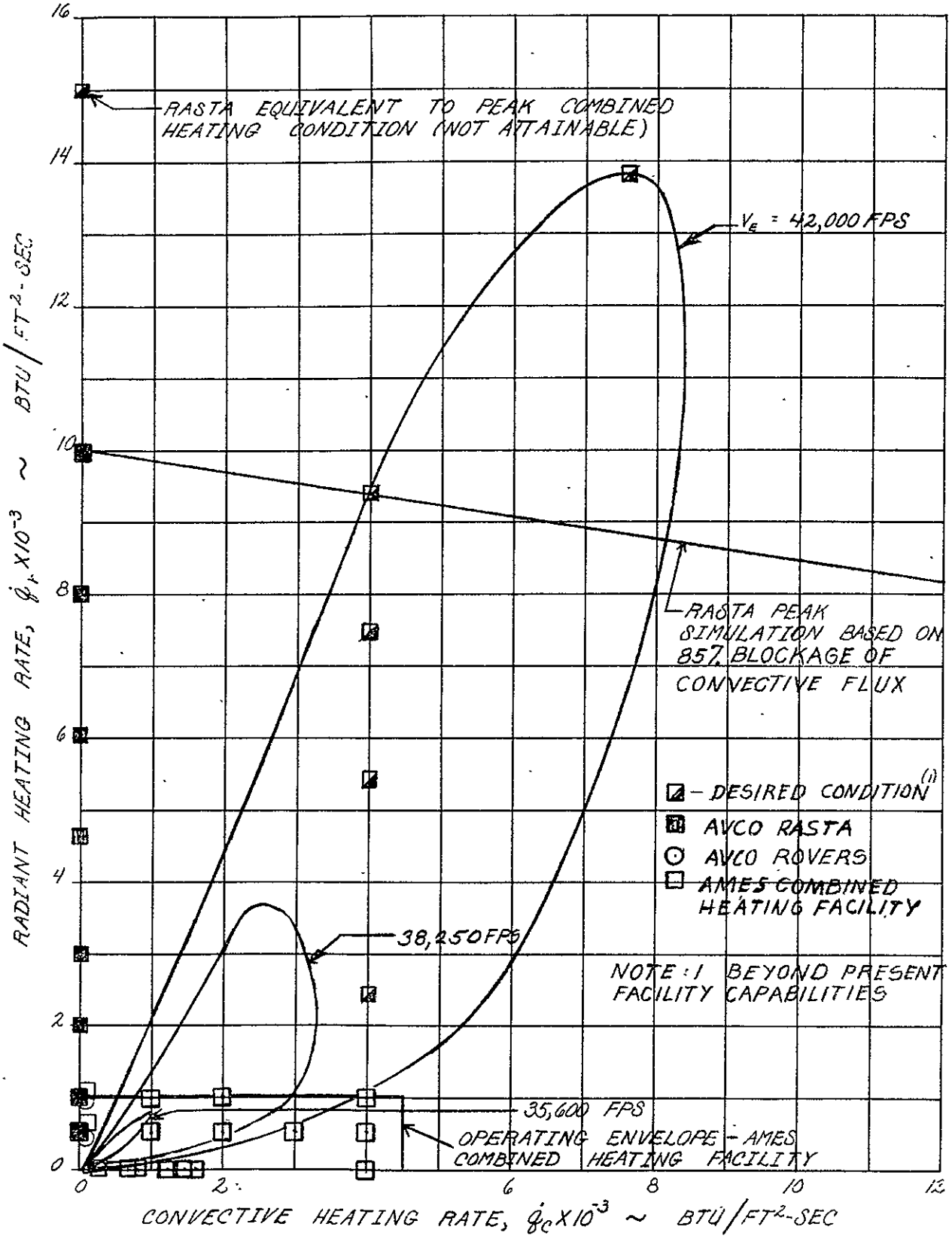


Figure 4.105 Stagnation Convective - Radiative Heating

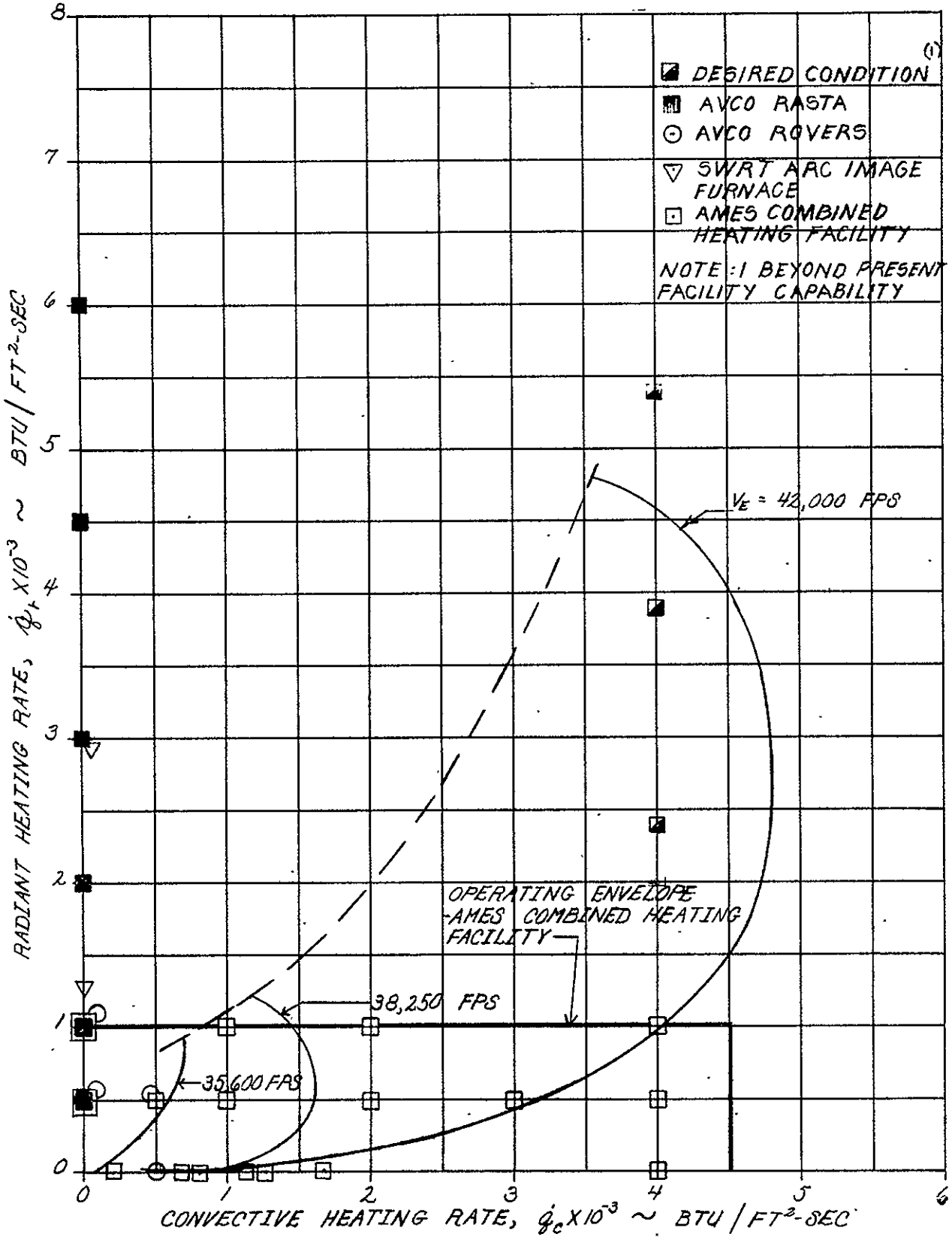


Figure 4.106 Convective - Radiative Heating on Cone

At the low fluxes, the mass transfer process is initially chemical "reaction rate controlled." As the heat flux and surface temperature increases, a "transition regime" exists where the speed of the chemical processes is comparable to the rate at which fresh reactant is brought to the surface and the products of reaction are removed by convection and diffusion. Thus, the overall process is a transition regime where both chemical and gas dynamic processes prevail. As the surface temperatures increase, the chemical oxidation processes are limited by the gas dynamic effects (diffusion-controlled regime). As the surface temperature increases further, the sublimation rate increases exceeding the surface oxidation rate, and atoms and molecules of the ablator are present in the gas phase; hence, the "sublimation regime".

In the rate controlled and transition regimes, the ablation rate of a carbonaceous material is a sensitive function of temperature. In the diffusion-controlled regime, the ablation rate is proportional to the square root of the pressure and is essentially independent of temperature. In the sublimation regime, the mass loss rate is a function of both surface pressure and temperature.

It should be noted that the foregoing disucssion applies directly to pure carbon or graphite materials and the presence of foreign materials such as phenolic or epoxy resin systems and glass fillers serve to complicate the problem of material ablation characterization.

4.6.2.2 Combined Radiative and Convective Heating

The high velocities associated with the Venus entry problem ($35000 \leq V_e \leq 42000$ fps) results in extremely high temperatures in the shock layer. The shock layer gases in this highly excited state act as a source of considerable radiant energy which augments and in some instances completely dominates the convective heating to the ablator surface during entry. Figures

4.105 and 4.106 show the combined heating rates for three representative entry trajectories. The influence of velocity on radiant heating level is quite severe. The peak rate for the 35,600 fps case is on the order of 1000 Btu/ft^2-sec as opposed to 14,000 Btu/ft^2-sec for the 42,000 fps case.

These heating values are considered realistic even though there is a considerable degree of uncertainty associated with prediction of the radiant heating rates. The several factors contributing to the large spreads in the predicted radiant heating levels are discussed in Section 4.2. One of the significant factors is prediction of the amount of radiant energy emitted from the hot gases in the ultraviolet spectrum. A spectrometry technique developed at Avco has been successfully employed to observe the nitrogen emission spectrum from an isothermal plasma (13,150°K) to approximately 900 angstroms. (72,73,74) Although not an integral part of this development test program, it is strongly recommended that similar measurements be made on CO_2 plasmas to improve the accuracy of the heating predictions.

4.6.2.3 Combustion Effects

The ablation performance of heat shield materials during Venus atmospheric entry will be affected by the amount of oxygen in the atmosphere available to support the combustion processes. Although there are uncertainties in the pressure profile and gas composition of the Venus atmosphere, it is now generally accepted that the gas composition is predominantly CO_2; probably over 90% by weight. The effects of this foreign atmosphere on the thermal and ablation performance of the heat shield material is of major concern in the development test effort.

4.6.2.4 Mechanical Erosion Due to Aerodynamic Shear Stress

Figure 4.107 illustrates the dependence of maximum shear stress on entry velocity. From quite nominal values of below 10 psf for the

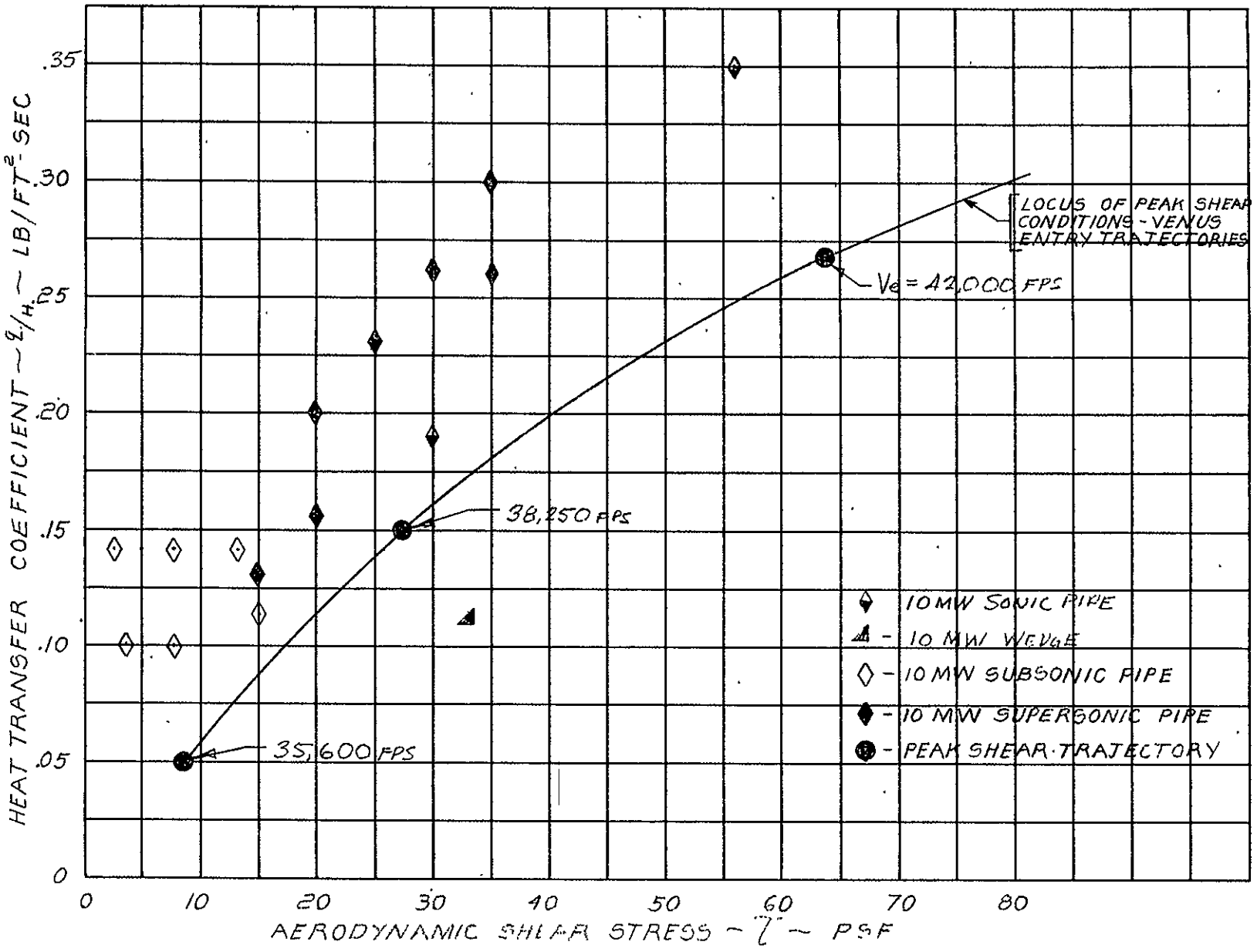


Figure 4.107 Turbulent Shear Stress Simulation

35,600 fps case the maximum shear values approach 70 psf at entry velocities around 40,000 fps. Although the conventional high density ablators are not detrimentally affected by shear values of these magnitudes, there is evidence that the low density classes of materials experience excessive irregular erosion at some point between the two shear stress levels indicated. Thus, for the lower velocity entry missions, shear stress is not considered a problem; but for the high velocity cases, the shear effects on the low density materials will be evaluated.

4.6.3 Trajectory Requirements and Facility Capabilities

4.6.3.1 Convective Heating

Figures 4.104 through 4.106 contain flight profiles of three selected entry vehicles* which describe the ranges of entry parameters to be encountered in a Venus atmospheric entry. On Figure 4.108, the range of operating conditions of presently operational convective heating facilities is represented by the cross-hatched area showing good coverage below one half atmosphere for a wide enthalpy range and for one to ten atmospheres below H/RTO = 400. The superimposed trajectory profiles on Figure 4.108 shows that although representative enthalpy and pressure levels can be achieved, simultaneous simulation of enthalpy and pressure near critical peak heating is well beyond the capabilities of currently available facilities. The peak heating points for the 38,250 and 42,000 fps entry trajectories actually fall outside

---

*

V_E fps	M/C_DA slug/ft^2	γ_E	θ_c	R_N/R_B	D
35,600	0.2	-60°	60°	1.0	43"
38,250	0.475	-60°	45°	0.25	4.5'
42,000	1.1	-50°	45°	0.25	2.5'

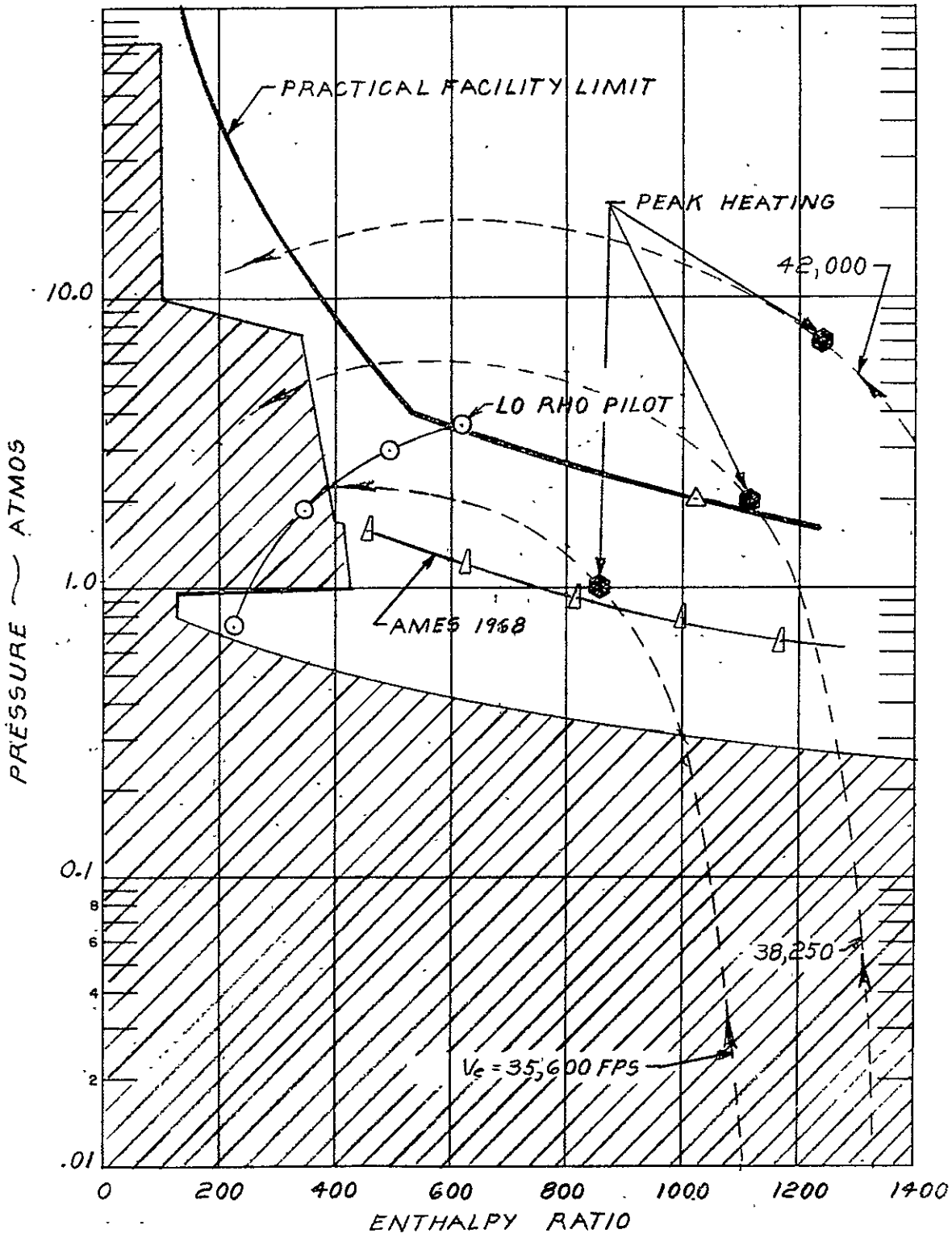


Figure 4.108 Future Ablation Test Facilities Capabilities

what is considered the practical facility limit for state-of-the-art arc plasma generators. The limit curve shown in Figure 4.108 is synthesized from References 75, 76, and 77. It shows that in a ground arc test facility, maximum attainable enthalpy decreases as pressure increases. At the low pressure side of the figure, the enthalpy limitation is based on the fact that increasing current produces a decrease in gas resistance and an increase in conduction and radiation losses such that the gas enthalpy does not increase with current flow. The enthalpy limits in the high pressure side of Figure 4.108 are due to extremely high heat transfer rates to the electrodes and nozzles which exceed the cooling capacities of forced convection techniques. Design capabilities of two test facilities which provide significantly better Venus entry test simulation than presently available facilities are shown in Figure 4.108. The Lo Rho Pilot facility at AEDC, Tullahoma, Tennessee, and the AMES Combined Heating facility are two of the test facilities recommended for use in the development test program and are discussed in detail later.

Figures 4.105 and 4.106 show the mission profiles with respect to enthalpy and convective heating rate for stagnation point and cone, respectively. The superimposed ground test facility capability boundary shows complete lack of simulation capability for the high velocity entry and reasonably good coverage for the low velocity entry. For the intermediate velocity profile, off design conditions are available which are not directly applicable to the trajectory conditions since level of heating and enthalpy can be achieved but not simultaneously.

Combined Radiative and Convective Heating

The combined heating levels associated with the stagnation point and cone of three representative Venus entry probes entering at typical velocities are shown in Figures 4.105 and 4.106, respectively. On Figure 4.105,

the ground test capability is shown to encompass a very small portion of the flight regime of interest. The half shaded points are desirable combined heating conditions which are beyond the capabilities of presently available facilities.

The best combined heating test capability is available in the AMES Combined Heating facility. (77) Because of reasons discussed in Section 4.6.4.1, the AMES facility employs external radiation sources in combination with a conventional arc jet to achieve the combined heating conditions. The external radiation technique is limited in this application because its radiant flux has a spectral distribution which is not representative of flight. The arc imaging sources provide no ultraviolet radiation. Ultraviolet energy may constitute a significant portion of the radiative flux to the flight vehicle. If the ablation material surface absorptivity is sensitive to the spectral distribution of incident radiation, it will have to be accounted for in interpreting the ground test data.

The plotted test conditions on Figure 4.105 indicate that the Avco RASTA facility, a pure radiant flux source, can provide heating rates up to 10,000 Btu/ft^2-sec. This level is equal in magnitude to the net heating of combined fluxes over a considerable range. At these high fluxes, the mass removal of the ablator will be sublimation controlled over the important portion of the heating pulse. If the ablation in the sublimation regime is sensitive only to surface temperature and pressure, the utilization of a pure radiant source to provide all of the energy to the test material is a reasonable means of circumventing the problem of lack of combined heating capability.

The effect of mode of heating on material ablation will be determined in the AMES Combined Heating facility by testing with parametric variations shown in Figures 4.105 and 4.106. From these results, the appropriate

levels of pure radiant heating to simulate combined heating levels will be established. It is expected that these tests will show the convective blockage factor to be very high in the high combined heating regimes. If the convective blockage factor is on the order of 85% then the RASTA test capability would embrace the area under the boundary shown in Figure 4.105.

The Avco ROVERS (78) and Southwest Research Institute (79) test conditions shown on Figure 4.106 will be utilized to provide a cross check on test techniques and to establish the relative ablation performance under identical heating rate levels but different spectral distribution of the three facility radiation sources.

4.6.3.3 Atmospheric Composition

The Venus atmospheric composition consists of approximately 90% CO_2 gas by weight. Unfortunately, all of the ablation test facilities cannot operate with these large concentrations of CO_2 gas in the test fluid. Problems such as oxidation of tungsten electrodes or chemical reactions between free carbon from degrading carbon electrodes and the oxygen in the test fluid must be solved through careful design and control of the tests.

The first step will be to establish the CO_2 equivalence of air in various facilities in terms of ablation and thermal response. This will afford a means of applying the results of already available ablation data in air to the Venus entry problem. Parametric variation of CO_2 concentration will show the relative performance of materials in the 90% CO_2 concentration range compared to the CO_2 concentration representative of air equivalence. The actual test conditions selected will, of course, depend on the results of the air equivalence runs and the maximum CO_2 capability of the facility. The concentrations suggested in Table 4.29 are preliminary estimates intended to indicate scope rather than tie down specific run conditions.

TABLE 4.29

VENUS ADDENDUM - DEVELOPMENT TEST PLAN - PHASE I

FACILITY DESCRIPTION	CONVECTIVE HEATING RATE (Btu/ft^2-sec)	RADIATIVE HEATING RATE (Btu/ft^2-sec)	ENTHALPY (Btu/lb)	PRESSURE (Atmos)	SHEAR STRESS (PSF)	MODEL GEOMETRY	TEST FLUID (% CO_2)	NO. OF TESTS	TEST OBJECTIVE
1. AMES Combined Heating Facility - Stagnation Tests (Thermocouples in depth)	0	500	---	0.2,1.0	---	Sphere	Variable	12	1. Effects of mode of heating and facility cross checks with ROVERS, SwRI, RASTA 2. Define Transition regime between diffusion and sublimation controlled ablation. Enthalpy effects at constant heat transfer coefficient and pressure. 3. Check pressure effects with Model 500.
	0	1000	---	0.2,1.0	---	Segment-Cylinder	Variable	12	
	1000	500	23,800	0.2	---		Maximum	3	
	1000	1000	23,800	0.2	---		Variable	6	
	2000	500	47,500	0.15	---		Maximum	3	
	2000	1000	47,500	0.15	---			3	
	3000	500	47,500	0.3	---			3	
	4000	0	47,500	0.5	---			3	
	4000	500	47,500	0.5	---			3	
	4000	1000	47,500	0.5	---			3	
	1650	0	36,000	0.2	---			3	
	1500	0	31,000	0.2	---			3	
	1250	0	25,700	0.2	---		Variable	6	
	690	0	14,300	0.2	---		Variable	6	
	200	0	6,000	0.2	---		Variable	6	
	800	0	6,000	0.4	---		Maximum	3	
2. AVCO RASTA Radiation Facility Stagnation Tests (Thermocouples in depth)	0	10,000	---	0.1,5,10	---	Sphere	Variable	18	1. High velocity entry simulation-sublimation data. 2. Intermediate velocity entry simulation 3. Low velocity entry simulation plus facility cross check conditions.
	0	6,000	---	0.1,5,10	---	Segment-Cylinder	Variable	18	
	0	4,500	---	0.1,5	---		90	6	
	0	8,000	---	0.1,5,10	---		90	9	
	0	3,000	---	0.1,1,5,10, 14	---		90	12	
	0	2,000	---	1.0	---		90	3	
	0	1,000	---	0.1,1.0	---		90	6	
	0	500	---	0.1,1.0	---		Variable	12	
							Variable	12	
3. Southwest Research Institute Arc Image Furnace-Radiation Only (Thermocouples in-depth)	0	500	---	1.0	---	Sphere	90	3	1. Facility cross check, AMES, ROVERS, RASTA 2. Intermediate-high velocity simulation
	0	1,000	---	1.0	---	Segment-Cylinder	Variable	6	
	0	1,500	---	0.1,5,10	---		90	9	
	0	2,000	---	1.0	---		90	3	
	0	3,000	---	0.1,1.0, 5,10	---		Variable	24	

TABLE 4.29 Cont.

FACILITY DESCRIPTION	CONVECTIVE HEATING RATE (Btu/ft^2-sec)	RADIATIVE HEATING RATE (Btu/ft^2-sec)	ENTHALPY (Btu/lb)	PRESSURE (Atmos)	SHEAR STRESS (PSF)	MODEL GEOMETRY	TEST FLUID (% CO_2)	NO. OF TESTS	TEST OBJECTIVE
4. LoRho Pilot Facility-Stagnation Tests (Thermocouples in-depth)	1130 1398 2570 3550 1150	--- --- --- --- ---	5,000 8,420 11,820 14,720 6,000	1.0 1.82 3.0 3.72 1.3	--- --- --- --- ---	Sphere Segment- Cylinder ↓	Air ↓	6 3 3 3 3	1. Best simulation enthalpy-heat rate for intermediate velocity. 2. Facility cross check Model 500
5. AVCO ROVERS Facility-Stagnation Tests (Thermocouples in depth)	0 0 500 500	500 1000 500 0	--- --- 20,000 20,000	1.0 1.0 .08 .08	--- --- --- ---	Sphere Segment- Cylinder ↓	Maximum Variable Variable Variable	3 6 6 6	1. Cross Check Ames, RASTA, SwRI. 2. Cross Check AMES
6. AVCO Model 500 Facility-Stagnation Splash Tests (Thermocouples in depth)	800 600 1,150	0 0 0	6,000 2,000 6,000	1.1 1.5 1.3	--- --- ---	Flat Faced Cylinder ↓	Variable 90 Air	6 3 3	1. Pressure Effects with AMES. 2. Pressure Effects with CWSH. 3. Check Effect of Model size on ablation data- cf. LoRho Data.
7. Cornell Wave Superheater-Stagnation Tests (Thermocouples in depth)	600	0	1500	6.0	---	Sphere Segment-Cylinder	Variable	6	1. Pressure Effects with Model 500.

TABLE 4.29 Cont.

FACILITY DESCRIPTION	CONVECTIVE HEATING RATE (Btu/ft^2-sec)	RADIATIVE HEATING RATE (Btu/ft^2-sec)	ENTHALPY (Btu/lb)	PRESSURE (Atmos)	SHEAR STRESS (PSF)	MODEL GEOMETRY	TEST FLUID (% CO_2)	NO. OF TESTS	TEST OBJECTIVE
8. 10 Megawatt Facility-Pipe Tests (Thermocouples in depth)	700	0	5100	2	2.5	Subsonic Pipe	90	3	1. Effects of shear on ablation in turbulent flow field. 2. Check internal vs. external surface.
	700	0	5100	2	5.0		90	3	
	700	0	5100	2.5	7.5		90	3	
	700	0	5100	5.0	13.0		90	3	
	665	0	5100	2.0	15.0		90	3	
	665	0	3400	2.8	20.0	Supersonic Pipe	90	3	
	866	0	5100	2.8	20.0		90	3	
	1100	0	6800	2.8	20.0		90	3	
	1150	0	5100	3.7	25		90	3	
	1300	0	5100	4.8	30		90	3	
	1550	0	5100	5.6	35		Variable	6	
	750	0	7200	2.0	4		90	3	
	750	0	7800	2.0	7.5		90	3	
	800	0	6800	5.0	15	Subsonic Pipe	90	3	
	2350	0	6800	10.0	56	Sonic Pipe	90	3	
	1200	0	6800	7.0	30		90	3	
	800	0	6800	1.3	33	Wedge	90	3	
9. NASA-Houston Constricted Arc Facility-Stagnation Tests (Thermocouples in depth)	650	0	20,000	.003	---	Sphere	Variable	6	1. Facility Cross checks AMES, ROVERS.
	1000	0	20,000	.011	---	Segment	Variable	6	
	400	0	10,000	.003	---	Cylinder	Maximum	3	
	1600	0	36,000	.02	---		Maximum	3	

4.6.3.4 Aerodynamic Shear Effects

Figure 4.107 shows the magnitude of the maximum shear stress encountered for the three selected Venus entry trajectories. The faired line between the three points of interest represents an approximate representation of the heat transfer coefficient-shear relationship. The plotted points in Figure 4.107 represent the test matrix to be used in establishing the effects or lack thereof of aerodynamic shear on the ablation performance of the materials. The range of test conditions available below 35 psf affords the flexibility of parametric variations such that shear effects can be quantitatively established. The point shown at 56 psf, however, is accomplished in a 10 MW (78) sonic pipe in which the given test condition represents the nominal initial test condition prior to any significant ablation in the pipe. The conditions change rapidly as the pipe ablates resulting in a transient, decreasing shear level during the run. This type of test is qualitative and yields useful go no-go results for a particular material or comparative results for screening various materials. If the ablators perform well up to 35 psf the sonic pipe will be utilized to determine their gross failure limit.

The 10 MW wedge point shown is from a recently developed test technique and will run to verify that the internal pipe configuration and an externally ablating model yield essentially the same results at similar conditions. The internal pipe configuration has two features which could result in misinterpretation of results. The first is its geometry which causes the char layer to form in a hoop in the internal surface of the pipe. Virgin material supports the char "hoop" which is probably in compression during the heating pulse. It is conceivable that char formed in this manner with its unique structural support would exhibit different mechanical integrity and resistance to erosion from the char formed on an external surface. Although

there is no real evidence that there is a significant difference between the two types of char, it is worthwhile to verify this now that the wedge test technique is available.

The second potential problem with the ten megawatt pipe is its inability to re-radiate energy to cold surroundings. The hot surfaces are driven to higher temperatures that would normally be experienced for a quoted cold wall heat flux. This is due to the fact that normally re-radiated flux is trapped within the pipe. This effect is easily compensated for by correlating the pipe surface temperature with the net heat flux, accounting for the the re-radiation peculiarity. Surface temperature measurements are accomplished for all supersonic pipe runs and the results are applicable to subsonic and sonic pipes.

4.6.4 Ground Test Limitations

4.6.4.1 Model Scale

Many of the problems associated with interpretation and correlation of ground test data can be avoided if the limitations of the instrumentation, equipment, and techniques are recognized and factored into the test planning.

A brief review of some of the problems associated with laboratory testing of heat shield materials as described in References 75 and 77 will serve as useful background for the succeeding discussion. Consider first, laminar heat transfer in the stagnation region (eq. 32) of a vehicle and the flat plate relationships for laminar heating (eq. 33) and shear (eq. 34).

$$q_L \sim \left(\frac{P}{R_n}\right)^{\frac{1}{2}} \quad H \qquad (32)$$

$$q_L \sim \left(\frac{\rho u}{X}\right)^{\frac{1}{2}} \quad H \qquad (33)$$

$$\tau_L \sim \left(\frac{\rho u}{X}\right)^{\frac{1}{2}} \quad u \qquad (34)$$

where P denoted pressure, ρ (density), H (enthalpy) R_n (nose radius), u (velocity), X (wetted length), q (heating rate), and τ_L (shear).

Fluid properties are taken at the boundary layer edge. Due to both technical and economical reasons, it is necessary to scale down test model sizes in ground test such effective nose radius of a test specimen is often as much as two orders of magnitude smaller than the flight article.

It can be seen that for laminar heating and shear the scale effect imposed by the necessity of testing small ablation models can be compensated for by adjusting pressure (or density) at a given enthalpy to achieve the proper simulation level. The small size of the test model, however, results in a relatively thin boundary layer with very little mass addition due to upstream ablation products. The cumulative effects of the upstream mass addition to the boundary layer are to cool the surface by means of convection, and reduce the net heat transfer to the surface by thickening of the boundary layer which reduces the boundary layer velocity gradient and thus results in a lower heat transfer coefficient. At a station remote from the stagnation point on a blunt body these effects can be considerable.

For turbulent heating and shear,

$$q_T \sim \rho u H / (R_e)^{0.2}$$

$$\tau_T \sim \rho u^2 / (R_e)^{0.2} \qquad (36)$$

where R_e denotes Reynolds number at the boundary layer edge, it is evident that the levels are only weakly dependent on scale, and unlike the laminar case, flight conditions are not easily duplicated by adjusting the density or pressure. Therefore, in order to achieve good simulation in turbulent flow, it is necessary to duplicate very nearly the flight pressure and

enthalpy. Unfortunately, for most of the pressure-enthalpy map of interest (Figure 4.108) simultaneous simulation of pressure and enthalpy is (for higher velocities) beyond the current state-of-the-art.

The radiative heating emanating from the plasma sheath is a strong function of pressure, enthalpy, and shock detachment distance. This can be represented approximately for thin isothermal layers as,

$$\dot{q}_r = \pi \int_0^\infty B_\lambda \left(1 - e^{-2\mu_\lambda \Delta}\right) d\lambda \qquad (37)$$

where:

B_λ = blackbody function

μ_λ = spectral absorption coefficient

Δ = shock stand off distance.

Since the shock standoff distance is a function of the effective nose radius of the test model, attainment of a representative level of the plasma sheath radiation, which is proportional to shock layer thickness, is possible on small test models only if the absorption coefficient is very large. Thus, for the missions of interest, the radiant flux levels desired require external sources such as arc lamps which are irradiated through the relatively thin shock layer; the extent to which the radiant energy is dissipated by means of scattering or absorption in the shock layer and boundary layer is not accurately simulated in the ground test.

4.6.4.2 Enthalpy Uncertainties

Reference 80 indicates the lack of correlation of ablation data among several selected facilities throughout the country. It appears from the data presented that the most doubtful measurement made, and, therefore, the greatest source of error is correlating data is that of the effluent enthalpy. Because of the possible inaccuracies involved in this measurement, it becomes difficult to correlate the data from even a single facility whose capability

extends over a large enthalpy range.

4.6.4.2.1 Arc-Heat Balance Enthalpy

In the majority of plasma arc facilities, the effluent enthalpy is determined by performing a heat balance at the arc head. Power to the arc is calculated from voltage and current measurements and net power to the air is obtained indirectly by measuring cooling losses from the arc head. (Measured mass flow rate and temperature rise of coolant fluid.) There are two major problems associated with this type of enthalpy determination. Frequently the power loss to the cooling fluid is of the same magnitude as the power to the arc. The power to the air, then, is determined by subtracting two large numbers to obtain a small number representing the net power to the air, i.e., enthalpy. Small percentage errors in the power in and power loss measurements result in large errors in calculated enthalpy. This effect is more significant at low enthalpies and lower pressures. For illustration, two typical ROVERS arc test conditions are shown where for the same nominal moderate enthalpy, power losses are in one case equal to and in the other 2.6 times net power to the air.

Test Condition	Enthalpy	Power to Arc	Power Losses (btu/sec)	Net Power to Air (btu/sec)
1	10,000	57.1	41.2c	15.9
2	10,000	116.0	58.8	57.2

A ten percent error in power loss measurement would bias the first test point enthalpy by 25% and the second by 10%. Even if the error were made in the same direction, a 15% discrepancy would be evidenced in a correlation of the two test points providing all other parameters were correct.

The second weakness in the heat balance technique

is that it yields a simple mass enthalpy which does not account for the spatial distribution of enthalpy in the jet or at the model surface. Thus, this enthalpy in many cases is not really compatible with the center line heating rate and pressure measurements which are localized measurements made with probes or small sensors located on non-ablating mockups of the ablation specimen.

4.6.4.2.2 Sonic Flow Enthalpy

The sonic flow measurement for evaluating enthalpy is described in Reference 81. This technique relies upon the measurements of plenum stagnation pressure and mass flow rate to calculate the enthalpy. It assumes that air flow up to the sonic point in the discharge nozzle can be represented by an isentropic expansion under equilibrium conditions. With certain limitations, the flow rate and plenum pressure uniquely describe enthalpy. The assumption of dissociation equilibrium introduces an error in the calculation where the flow at the throat is chemically frozen. The total enthalpy of air deduced from equilibrium sonic flow relations (81) will be low by about 7% at H = 2000 Btu/lb and 13% at H = 10,000 Btu/lb. These results cannot be extrapolated to higher enthalpies because the reaction studied considered oxygen dissociation only. Above 10,000 Btu/lb nitrogen begins to dissociate appreciably and would have to be factored in to yield accurate results.

The main limitations of the sonic throat technique are that

1. the extent of departure from dissociation equilibrium must be established and factored into the calculation, and
2. like the arc heat balance technique, the calculated enthalpy is a gross or average value that does not account for spatial distribution in the jet.

Although it would appear that this method should be more reliable than the arc head balance technique by virtue of its dependence on two presumably measurable parameters, it is concluded in Reference 80 that the sonic throat technique is a less suitable method of obtaining enthalpy insofar as it compares with the calculated enthalpy based on facility measurements of stagnation heating rate and pressure, which leads to a third technique of obtaining enthalpy.

4.6.4.2.3 Enthalpy from Fay-Riddell Relationship

The stagnation point enthalpy for a supersonic jet can be determined from the stagnation pressure and measured stagnation heating rate using the Fay-Riddell equation (82). This technique has the advantage of evaluating the enthalpy based on local measurements of heating, and pressure at the point where ablation data (surface temperature, recession, etc.) is to be obtained. The accuracy of the calculation is affected significantly by the geometry and relative size of the calorimeter used for the heat flux measurement. Ideally, the calorimeter used to calculate enthalpy should be a hemispherical tip much smaller than the jet diameter such that the radial distribution of enthalpy in the immediate vicinity of the probe is essentially flat. The actual size of the calorimeter depends on the particular facility but based on typical jet distributions such as those shown in References 80 and 83, it is recommended that the ratio of the calorimeter nose radius to jet radius be no greater than 1/3. The calorimeter used for enthalpy determination should be used in addition to a separate calorimeter to determine heat flux to the test specimen. This heat flux calorimeter should be contained in a non-ablating shroud with the identical size and shape of the test part.

In a supersonic plasma jet, great care must be taken in the heat flux and pressure measurements if the Fay-Riddell relationship is to be proven valid. It is extremely likely that one will find the constant

of proportionally between heating rate and enthalpy for measured values will be somewhat different than that given by the equation. If sufficient care has been taken in establishing the enthalpy, pressure, and heat rate measurements by using the proper instruments and techniques, the discrepancies have to be rationalized by other means. Low Reynolds number effects resulting from "viscous or merged shock layer" phenomena (84) and the possible influence of free-stream jet turbulence on the stagnation zone heating (85) are possible explanations for measured heating values exceeding theoretical values.

4.6.4.3 Stagnation Point Heating Rate-Calorimeters

Various facilities employ a variety of calorimeter types and designs. Reference 80 discusses the effects of shape, size of sensing area, and surface material on the indicated heating rate. Briefly, the shape and diameter of a calorimeter determine the velocity gradient over the surface and thereby the heat transfer to the surface. The size of the sensing area is important in that when a sensor is placed in a jet with a non-uniform enthalpy distribution, it tends to integrate or average the effect over the entire sensing surface. Thus, a very small sensor head will give an essentially point measurement while a large sensor head will average the flux over the sensing area. Two calorimeters of identical shape, but with different sized sensor heads, will give seemingly different results in the same environment.

Several different priciples of operation are employed in calorimeters used in various facilities. Basically, they can be divided into two categories employing one of two fundamental concepts; thermal capacity, and thermal gradient. The former includes the absolute water cooled calorimeter and the slug or slope calorimeter and the latter includes the uncooled transient and the asymptotic rapid response type calorimeters. (86) All of these different types of calorimeters are used in the facilities recommended

for these test programs. Since the principle of operation of the calorimeter sensor governs to a large extent its shape and size, comparison of results requires careful interpretation.

The foregoing is further justification for utilizing in this development test program a particular calorimeter design to make measurements in all facilities (in addition to the conventional facility heat rate measurement) so as to provide a common basis for comparison of data.

4.6.4.4 Specimen Geometry

The heat flux to an ablating surface in a ground test is largely dependent upon the type of specimen and particular geometry selected. In reviewing data from the various facilities mentioned in this program, the following types of geometries were encountered.

1. Stagnation Type
   a. Hemispherical tip
   b. Flat-faced cylinder
   c. Constant heat flux (Iso $\dot{q}$-surface (87))
   d. Pointed cone
2. Non-Stagnation Type
   a. Flat plate
   b. Wedge
   c. Pipe

To correlate data from a variety of model shapes is a difficult task, but is complicated to a much greater extent when the stagnation type models are different sizes with respect to the various plasma jet diameters. For instance, a flat-faced cylindrical specimen which is small with respect to a supersonic jet diameter will receive a stagnation heating rate level equivalent to approximately one half the heating rate to a hemispherical specimen (at

the same tunnel location) with a nose radius equal to the base radius of the flat-faced cylinder. (80,88) This "effective nose radius" effect holds only if the diameter of the specimen is not greater than the flat portion of the jet enthalpy "core". Increases in size beyond this relative dimension result in a decrease in heat rate until the flat-face diameter approaches a value equal to or greater than the jet diameter where it begins to respond as an infinite flat plate or "splash" configuration. Because of the uncertainties in enthalpy and pressure distributions in the various facilities studied, Reference 80 recommends that for a standard ablation test procedure the test jet be at least 50% greater diameter than the outer diameter of the test part.

Selection of stagnation specimen nose radius is a problem because of the shape change inherent in any stagnation heating test. Generally speaking, a blunt shape will become more blunt during the test, thus continually reducing the heating rate to the surface. Experimental work has been accomplished on the measurement of heating rate to spherical segment (convex and concave) and flat-faced cylinders (88,89). Unpublished data (90) is available at Avco showing the effects of various spherically concave configurations in the ROVERS test facility. Examination of these data and experience with various degrees of stagnation model bluntness ratio has indicated the following:

a. Extremely sharp models (sphere cones) are to be avoided since the rapid blunting of the nose and irregularities on the cone surface cause transient test conditions which are difficult, if not impossible, to define.

b. Concave and convex surfaces produce repeatable data which can be correlated to hemispherical or flat-faced values.

c. It is desirable to keep the blunted shape reasonably close the the flat-faced configuration since the heating rate is much less

sensitive to shape change in the $-0.2 \leq \frac{R_{BASE}}{R_{NOSE}} \leq +0.2$

region than from the $R_B/R_N = 1.0$ hemisphere to $R_B/R_W = +0.6$ region. A spherical segment-cylinder with a bluntness ratio near zero, then, seems desirable for stagnation testing. The test condition changes very little during test and can easily be bracketed by making measurements in the initial spherical segment and the limiting flat face configuration.

The question of the validity of the test data obtained in an internal pipe geometry was discussed earlier. The argument is based on the concept that mechanical integrity of the supported char in the internal configuration is different than that of the external configuration and therefore ablates differently for nominally similar conditions. Until recently, no good means of evaluating the worth of this argument has been available. It appears now that tests can be made to resolve this question and are shown in the test program.

The specimen nose radius and diameter relative to the jet should be selected based on previously discussed considerations, and performance of the particular shapes should be interpreted through data from imbedded thermocouple instrumentation. The instrumentation of "calibration" or "pilot" models should be carried out if the test part to be used does not require temperature instrumentation as an integral part of the test. This instrumentation is used to determine time resolved temperature gradients through the material for the following reasons:

a. provide basis for calculating heat flow through the material (conduction);

b. establish one-dimensionality of heat flow through a particular shape at various required test conditions; and

c. measure temperatures of various ablation zones (virgin, pyrolysis, char) throughout heating pulse.

The actual installation of thermocouples in ablation samples requires considerable care and certain techniques which are discussed in some detail in Reference 91.

4.6.4.5 Test Fluid

In order to simulate accurately the Venus entry environment, it is desirable to use a test gas mixture representative of the Venus atmosphere. Various personnel (92) were contacted in order to determine the established capability of each of the facilities to handle high mass fractions of CO_2 gas in the test fluid. Unfortunately, none of the facilities have been run with pure CO_2 and apparently there is no valid rule of thumb available to ascertain how much CO_2 a particular arc head configuration can handle before serious electrode deterioration occurs. Besides oxidation of electrode material, basic problems such as CO_2 gas storage and supply hardware exist for most facilities. The estimates of facility capability in this area, tabulated in Table 4.29, are engineering guesses made by the people contacted and by no means constitute a guarantee of any kind.

Because of the uncertainty in the amount of CO_2 concentration allowable in the various facilities, no attempt has been made to present the operating capabilities of the various facilities in a CO_2 environment. All enthalpy, pressure, and heating rate capabilities shown are accepted operating parameters of the various facilities in air. For purposes of these test plans, it is felt that the basic logic of the plans or even facility selection would not be significantly affected by the revised test conditions attainable in a CO_2 environment.

It is recognized that considerable work may have to be done in the area of CO_2 concentration effects in order to correlate data from facilities with grossly different capability in this area. However, it seems

unreasonable at this time to significantly perturb the test plans based on "best guess" information on untried procedures in (in some cases) as yet inoperable facilities. Trajectory information presented here is for AV-4 atmosphere (75% CO_2 - 25% N_2) and facility capabilities are based on air.

4.6.4.6 Recommended Procedures

Experience has shown that in far too many cases, the ablation test technology has been developed on a go no-go or simple comparative performance approach in a given test environment. The difficulties involved in correlation of data from various facilities are derived mainly from non-standardization of measurement devices and calibration techniques.

The stringent design requirements associated with the Venus entry problem require that the ablation data cover a wide range of environments and that quantitative results be obtained suitable for use in analytical models to predict ablation and thermal response with a relatively high confidence level.

In order to minimize the number and magnitude of the testing difficulties discussed earlier, the following recommendations are deemed important to the successful completion of the development test programs.

1. For each facility, all test procedures, measurement devices and techniques, and data reduction methods be well defined and identified prior to test. Specific areas of interest involve enthalpy determination techniques, data reduction programs for heating rate determinations, pressure measurement calibrations and any other particular test calibration that is carried out in test. Physical description of probes, sensors, and other measuring devices should be complete in detail.
2. All facility raw operating data should be reported along with

test performance results. For example, in the arc-head heat balance, power in, power loss, water and gas mass flow rates should be reported so that relative magnitudes and degree of uncertainty in the data can be established.

3. Wherever possible, a standard test geometry should be employed for all facilities. A spherical segment-cylinder is recommended with a nose radius of no less than one inch and a base radius no greater than 2/3 the jet radius.

4. Heating rate sensors used for performance data should be mounted in a non-ablating shroud with the exact external dimensions of the test article. The calorimeter measurements should be made prior to each individual test. "Bracketing" of spherical segment and flat-faced heating rates is recommended.

5. In addition to the normal performance heating rate and enthalpy determination, a jet center line measurement of impact pressure and hemisphere heating rate should be made for each test. The calorimeter used should be a hemisphere cylinder with a nose radius no greater than one third of the jet diameter. These measurements are made with the same calorimeter, pressure probe type and will provide measurements common to all facilities. This information will be used to resolve expected discrepancies in quoted test parameters.

6. All facilities should provide axial and radial jet heating rate and pressure distributions covering the range of influence on an ablating specimen. (Axial measurements sufficient to cover degree of surface recession of specimen surface is required.)

7. All ablation tests should be accomplished on instrumented (thermocouples in-depth) specimens and surface temperature (pyrometer) and emitted radiation (total radiometer) from the specimen should be

measured on all tests. These measurements are invaluable in providing quantitative cross-checks on measured test conditions with the surface boundary phenomena and internal temperature response.

4.6.5 Selection of Test Facilities - Phase I

Several test facilities have been chosen to accomplish the objectives of the Phase I test program. These facilities represent the most sophisticated and up-to-date developments in ablation testing technology. Many other facilities throughout the country have comparable capabilities but we are not cognizant of any facilities which extend the testing ranges beyond those represented by the facilities shown.

4.6.5.1 Lo Rho Pilot Facility (AEDC)

A BSD sponsored program is currently being carried out at Arnold Engineering Development Center, Tullahoma, Tennessee to develop a 600 megawatt Lo Rho facility (93). This facility is still in the planning stages, but presently work is being concentrated on a 40 megawatt pilot facility which is large enough to accomodate amply sized ablation test models. This facility consists of an MHD electrical generator, a conventional air arc heater, and an MHD channel which provides an energy "boost" to the test fluid. This boost consists essentially of a constant temperature acceleration of the plasma through the boost channel. Thus, kinetic energy in the gas exiting the accelerator is such that its "effective" total pressure and enthalpy are far beyond the capabilities of current arc heaters to develop in a true static plenum condition. Table 4.30 indicates estimated magnitudes of parameters that can be realized in this type of facility.

These conditions are based on an arc efficiency of 40% and an accelerator efficiency of 78%. This facility is actually a 0.1 scale version of the large facility whose power supply alone will cost $25,000,000 and whose arc system will consist of 5 or 6 fifty megawatt arc heads operating

TABLE 4.30

Lo Rho MHD Boost Performance

	Arc Nozzle Exit	MHD Accelerator Exit
Mach No.	2.0	7.4
H/RTo	150	435
T_s =	4000°K	3000°K
U =	4000 FPS	25000 FPS
$P_{T_{effective}}$ =	2.5	3900 ATMOS.

in parallel. The size of the pilot accelerator is 2.5 meters long with an inlet section of 7.5cm x 7.5 cm and an exit section of 12 cm x 12 cm . In order for the accelerator to be effective, the test gas must be seeded with from 0.1 to 0.5% mole fraction of potassium metal. The effect of the seed material on ablation performance of test materials will have to be proven negligible or somehow accounted for if the data is to be considered valid.

A calculated curve of operation for the Lo Rho pilot is shown on Figure 4.108. Notice that the Lo Rho pilot curve extends beyond the curve indicating the practical limit for arc heaters. Theoretically, there is no reason why this type of energy transfer cannot be utilized to obtain conditions much further into the previously unattainable regime. It is expected that this facility will be operational in the first half of 1968 and will be ready for test in the late summer of 1968.

4.6.5.2 Avco RASTA Facility

Figures 4.105 and 4.109 shows estimated maximum performance of the RASTA facility which will be operational at Avco in 1968. It is unnecessary at this time to describe this facility except that it will allow us to drive the surface of the test material to a very high temperature and

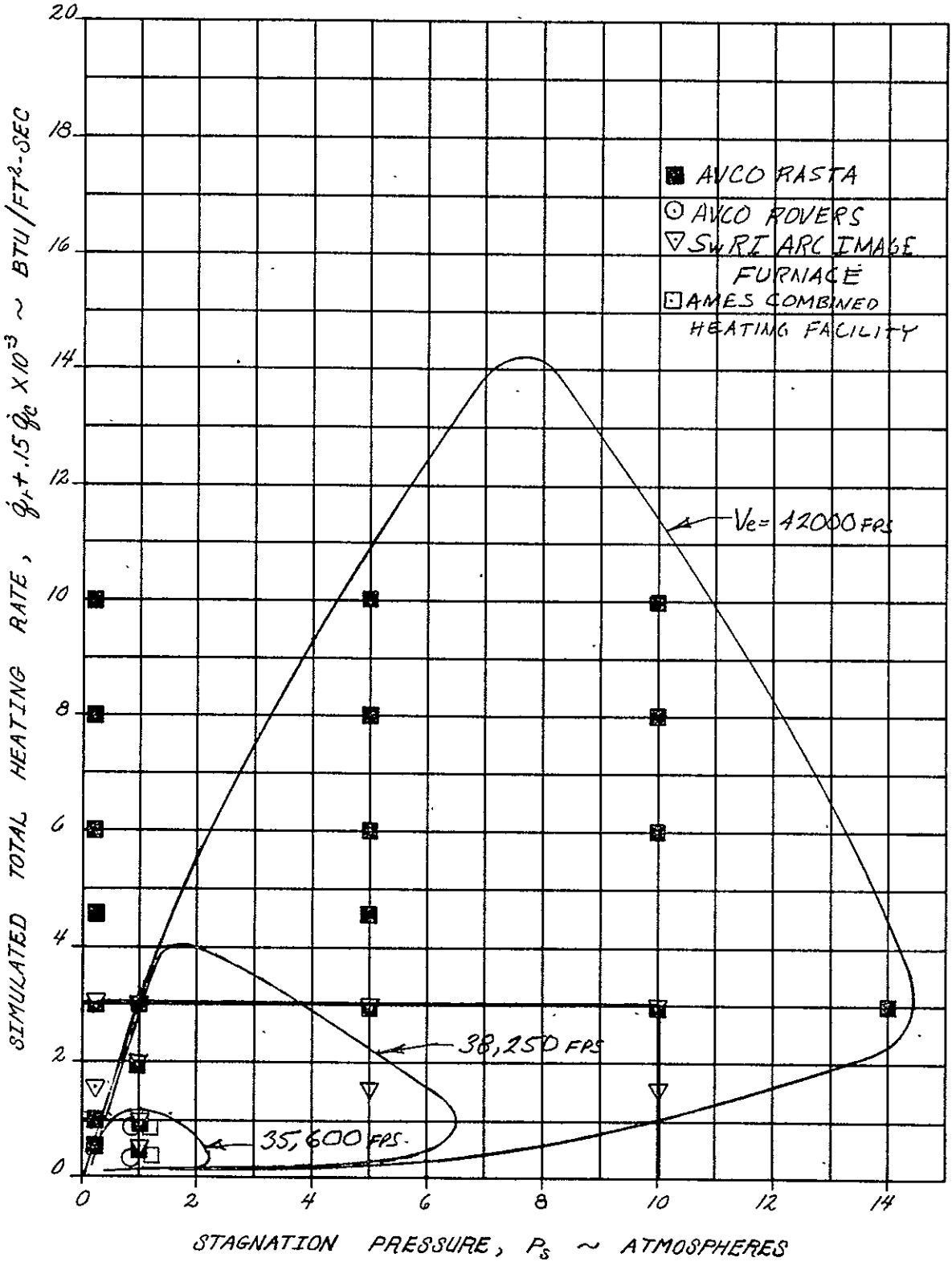


Figure 4.109. Stagnation Heating and Pressure Simulation

very likely obtain sublimation controlled ablation. The surface pressure and gas chemistry will be maintained by blowing cold gas over the surface of the model while irradiating the surface with the high radiant heat flux. It is clear from the figures that if it is possible to decouple the radiative and convective heating effects and if a large portion of the convective heating is blocked, then this facility affords us a means of getting meaningful ablation data for a wide range of conditions.

4.6.5.3 AMES Combined Heating Facility

Proposed operating conditions of the AMES Combined Heating Facility are described in Reference 77. In order to achieve the full range of test conditions indicated, the facility will employ a high pressure Linde type heater (94,95,96) and a high enthalpy constricted arc type heater (97,98, 99,100). Radiative heating will be provided by means of 14 radiation modules, each of which consist of an AMES 125 Kw radiation source (101) with associated equipment. The convective system will employ various arc heaters with a supersonic nozzle exhausting into a pressure cabin. The radiation sources are mounted external to the test cabin and although simultaneous operation of convective and radiative systems will be accomplished they will be controlled independently.

4.6.5.4 Avco Radiation Orbital Vehicle Re-entry Simulator (ROVERS)

The ROVERS facility is described in detail in Reference 78. Briefly, it consists of an electric arc gas heater supplying a supersonic nozzle for convective heating, a bank of four argon-arc imaging lamps for radiative heating, a 33,000 $ft^3/min.$ (10^{-1} torr) three stage vacuum pumping system, and a remotely controlled mechanism for positioning specimen, calorimeter, and a probe in the jet stream.

The convective system employs a thoriated tungsten cathode,

a copper water cooled anode, and a series of supersonic nozzles of various sizes. The design of the unit is based on a constricted arc configuration (102). Nitrogen is used for arc operation to hold electrode oxidation (and thus jet contamination) down to a minimum. Oxygen can be injected into the constricted section allowing controlled changes of the chemical composition of the test fluid. A variety of test gases, including CO_2, have been used in this facility. ROVERS will be utilized in Phase I mainly as a cross check for the combined heating and pure radiation tests recommended in the AMES, SWRI, and RASTA facilities.

4.6.5.5 Avco Model 500 Facility

The Avco model 500 plasma generator utilizes a subsonic jet from 1/4" to 3/4" diameter exhausting directly into the laboratory atmosphere. Air, N_2, CO_2, Argon, and O_2 have all been utilized as the working fluid in this facility. The electrode configurations used are either carbon-carbon or water cooled tungsten-copper.

The standard test specimen in the Model 500 test is a 3/4" diameter cylinder which violates the recommended test procedure number 3 in Section 4.6.4.6. Because of the backlog of available data in the Model 500 facility, tests are recommended in the Lo Rho facility at essentially the same test conditions as the Model 500 but with a larger size model with a model diameter to jet diameter ratio of 2:3. These data will be used for verification of the applicability of the Model 500 data.

4.6.5.6 Cornell Wave Superheater - Mach 3.0 Tunnel

The Wave Superheater (103) is a device that controls a direct transmission of energy from a high pressure gas to a low pressure gas. The energy exchange process is accomplished in a series of long narrow tubes mounted side by side in a rotating drum. The tubes, which are in reality

shock tubes, are progressively activated and discharged by rotating the drum at high speeds and exposing the ends of the tubes to fixed nozzles at the ends of the drum. During the cycle, each tube is filled with a low pressure charge gas (normally pure air) and then exposed to the high pressure driven gas (helium). Just as in a shock tube, the action of the driven gas creates a shock wave in the charge gas which compresses and heats the gas and drives it out of the tube at high velocity, where it is collected and expanded to a specific test condition.

The type of test condition achieved in the test cabin is controlled by the contour and size of the expansion nozzle which directs the test jet. The Mach 3.0 tunnel, of interest in this program, consists of a jet collector, throat, and contoured nozzle with a 2.45" exit diameter. This nozzle operates at approximately one atmosphere static pressure at the exit and functions as an open jet wind tunnel. Test models of up to 1.5" diameter can be accommodated in this test setup.

4.6.5.7 NASA MSC 1-MW High Enthalpy Constricted Arc Heater

This facility (104) has a very high enthalpy capability (40,000 Btu/lb mass averaged enthalpy at 1.2 atmosphere pressure). It has a single upstream cathode, a segmented 2-cm diameter constrictor, and 30 anode pins located in the supersonic nozzle which directs the test jet. Its function in this program will be to provide cross check data for the high enthalpy tests in the AMES Combined Heating Facility and low and intermediate checks of AMES CHF and Avco ROVERS facilities.

4.6.5.8 SWRI Arc-Image Thermal Flux Test Facility

The arc-image furnace (79) located at Southwest Research Institute utilizes twin parabolic mirrors to collect thermal radiation from a direct-current arc, and focus it on a test specimen held in a controlled environment. The arc is formed between a carbon cathode and an anode having a

misch-metal core. It is continuously blown by converging streams of sonic velocity air to oxidize and cool ionized matter. The air stream also serves the purpose of removing flame, ionized gas layers, and smoke from the area of the arc.

A set of 36" twin parabolic mirrors is used to collect and transmit the thermal radiation. The optical system is designed so the two mirrors are in perfect coaxial alignment with the rear mirror focused on the arc and the front mirror on the specimen. Since the magnification ratio of the optical system is unity, the image on the specimen is approximately 5/8" in diameter, the same cross section as the arc.

The arc and optical system are contained within a vessel designed to withstand internal pressures of 10 atmospheres. Running the arc under increased pressure helps to establish, maintain, and stabilize the high current arc. The specimen to be irradiated is housed in an independent pressure/vacuum tight chamber. An optically clear, hemispherical quartz dome forms the front of the housing so that the thermal radiation from the front mirror may focus on the specimen. Since the specimen chamber is remote from the pressurized arc chamber, it is possible to control the specimen environment without affecting or being affected by the arc chamber condition. This facility will be utilized to compare its wide emission spectrum data with the results of RASTA which generates monochromatic radiant energy. The SWRI facility is the only facility available to check to the reasonably high level radiant fluxes obtainable in RASTA. Fluxes up to 3000 Btu/ft^2-sec are available.

4.6.5.9 Ten Megawatt Facility

The 10 MW facility (78) consists of a four-inch diameter spherical plenum chamber into which flows plasma generated by the electric arcs of four carbon-copper electrodes systems. The plasma inlets are spaced at 90^o intervals around the plenum in a central plane. A fifth aperture

(exhaust) in the plenum is located such that its axis of symmetry is perpendicular to the electrode plane and passes through the center of the plenum. The plasma, after having mixed in the plenum, flows through this exhaust aperture into the test section which consists of a short water-cooled copper pipe (transition section), an ablating pipe (test specimen), and finally a nozzle section at which the flow becomes "choked" (i.e., sonic velocity is obtained). The flow in the cylindrical test specimen creates a high pressure, high shear, turbulent heating environment at the ablating surface.

Several types of pipe configurations are utilized to cover the full range of simulated flight environments possible in this facility.

The subsonic pipe test is accomplished by placing a water-cooled copper sonic nozzle downstream of the ablating pipe section. Since the flow is "choked" (sonic) downstream of the ablating pipe section, the flow in the ablating pipe remains subsonic throughout the run. The maximum attainable aerodynamic shear stress obtainable in the subsonic configuration is 18 lb/ft^2.

By eliminating the water-cooled sonic nozzle and substituting the material to be tested in the sonic section, shear values in excess of 100 lb/ft^2 can be realized. The sonic configuration also affords the opportunity to view the ablating surface directly, making direct measurement of surface brightness temperature and emitted radiation possible. It is also possible to photograph the ablating surface during the test with high speed color movies.

The supersonic pipe is located downstream of the transition section and water-cooled sonic nozzle. The plasma flow is choked at the nozzle and continues in a short supersonic expansion where a normal shock stands at the ablating pipe inlet. This configuration, like the sonic pipe, offers the advantage of direct viewing of the ablating surface and shear stress levels up to 35 psf are attained.

4.6.6 Phase I Test Program - Summary

The test conditions chosen for the evaluation of carbon phenolic and 5026-39/HC-G are summarized in Table 4.29. These recommended tests are based on considerations discussed in previous paragraphs. To summarize, the bases for selection of test points are:

1. Simulation of nominal flight conditions for a representative range of entry velocities.
2. Parametric variations to determine the nature of ablation phenomena within the environmental limits set by the range of flight conditions. This includes defining ablation modes, combustion effects, shear effects, pressure effects, and response to mode of heating.
3. Tests required to resolve data uncertainties due to physical peculiarities of the various facilities.
4. Limited tests to verify the applicability of data generated for the Apollo program in the Avco 10 megawatt, ROVERS, and Model 500 facilities. The effects of these Apollo tests which are in question are associated with the test model geometries.

The test conditions outlined in Table 4.29 are considered desirable test "points." Each test point is developed from a sufficient number of test runs to establish confidence in the validity of the data.

For instance, in order to adequately establish whether or not a flat pulse test at a particular test condition displays steady state ablation (i.e., surface recession rate equal to char interface velocity) it might be necessary to run three tests at successively increasing durations in order to separate the induction period from the steady state portion of the test. Another factor which effects the number of tests required is test failure due

to mechanical difficulty. Provision must be made to retest in certain areas to identify or verify "fliers", data points which do not make apparent sense in relation to other data. This type of problem will be more serious for the carbon phenolic as opposed to 5026-39/HC-G tests since the backlog of previous data is very sparse and provides a limited basis for extrapolating, interpolating, and, in general, predicting results of various tests.

Because of the uncertainties that exist in the gas composition of the Venus atmosphere and the lack of definition of facility capability to use CO_2 gas, parametric variation of gas composition are a necessary part of the test plans, and are defined in Table 4.29 in terms of CO_2 content by weight in the test gas. The 90% CO_2 concentration is considered nominal for the Venus atmosphere, but in many cases the variation of CO_2 concentration for various tests in a facility are necessary for two reasons. First, the CO_2 concentration equivalence of air for ablation performance must be established. Secondly, many of the facilities cannot handle large concentrations of CO_2 in the test fluid because of electrode oxidation problems and parametric variations in CO_2 concentration must be accomplished to provide a basis for extrapolation to the 90% CO_2 case. The notation in Table 4.29 indicates the need for this variation with the word "variable" - "maximum" indicates that the facility maximum capability is considered somewhat below the 90% CO_2 concentration desired.

Although the general model geometry is indicated in Table 4.29, the size is not defined since this will depend on jet size. All specimens will have a minimum frontal span of one inch. For consistency, all convective heating rates have been calculated based on a 1" nose radius except in the Model 500 facility (flat faced cylinder) and the 10 MW pipes and wedge.

The number of replicates of test runs to obtain a particular test point is arbitrarily set at 3. This number allows for uncertainties associated with steady state ablation and facility malfunctions. Where variable CO_2

concentrations are required, the number of runs per point has been doubled to six to account for the extra variable. The total numbers of tests shown in Table 4.29 are considered sufficient to accomplish the objectives stated for Phase I testing; however, this program should be considered a minimum effort. No contingency has been factored in for major program re-direction due to technical or other reasons.

4.6.7 Phase II - Characterization of Material for Design

4.6.7.1 Ablation Tests

The study of ablation phenomenology and facility limitations in Phase I forms the basis for a more specific Phase II effort which is design oriented to particular missions to be flown utilizing the carbon phenolic or 5026-39/HC-G material. The low and intermediate velocity missions described in Phase I are taken as examples of how the Phase II program will be developed. Figures 4.110 through 4.121 present the basis for the ablation testing portion of the Phase II program. The key features of the figures are tabulated below:

Description	Figure Number: $M/C_DA = .475$, $V_e = 38{,}250$ FPS	Figure Number: $M/C_DA = .2$, $V_e = 35{,}600$ FPS
1. Trajectory requirements and available ground test data.		
(a) Convective heat flux and enthalpy.	4.110	4.113
(b) Convective heat flux and pressure.	4.111	4.114
(c) Convective and radiative heat flux.	4.112	4.115
2. Trajectory requirements and available ground test facility capabilities		
(a) Convective heat flux and enthalpy.	4.116	4.119
(b) Convective heat flux and pressure.	4.117	4.120
(c) Convective and radiative heat flux.	4.118	4.121

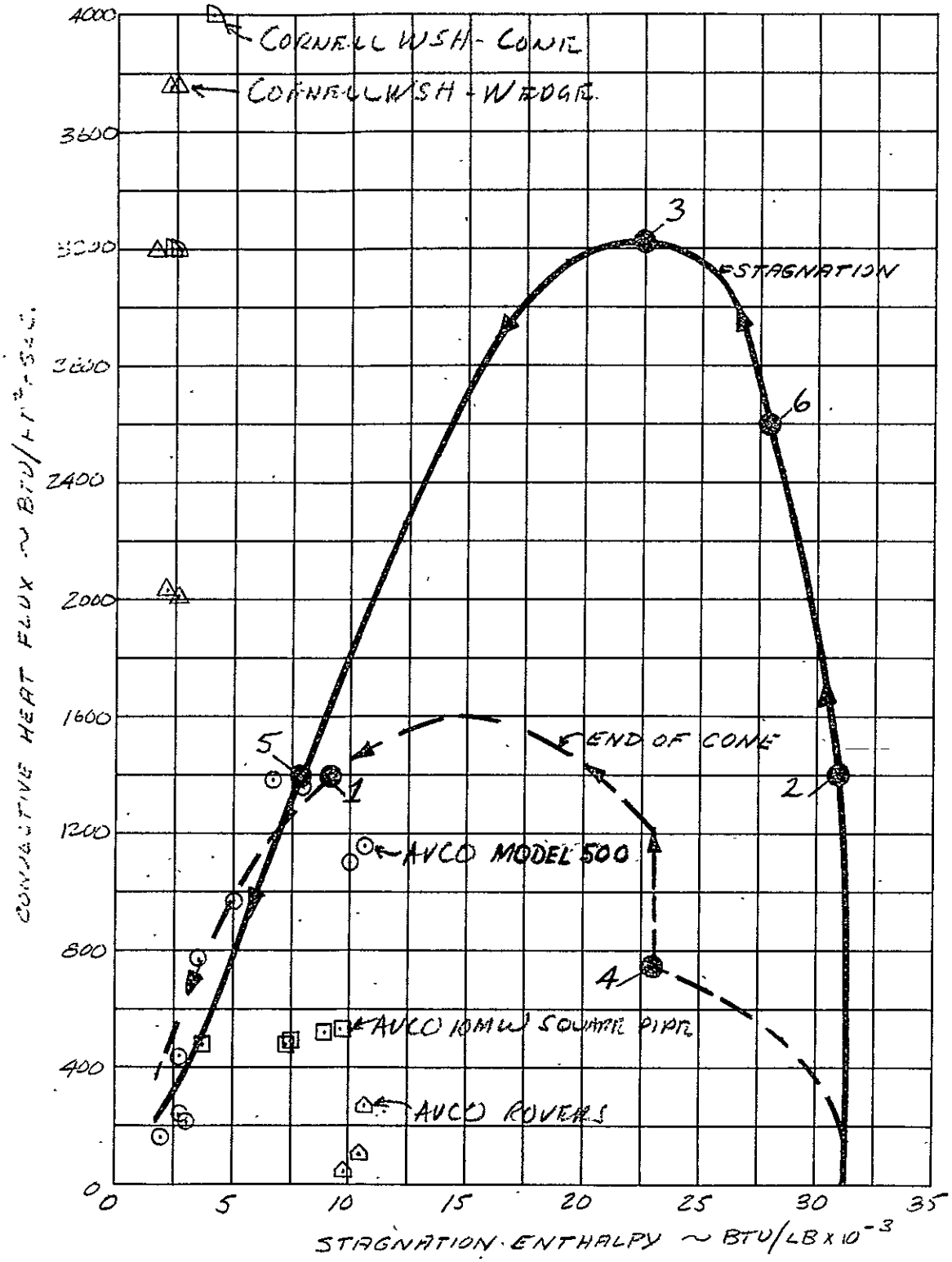


Figure 4.110 Convective Heating - Enthalpy Trajectory Profile, V_E = 38,250 fps γ_E = -60°

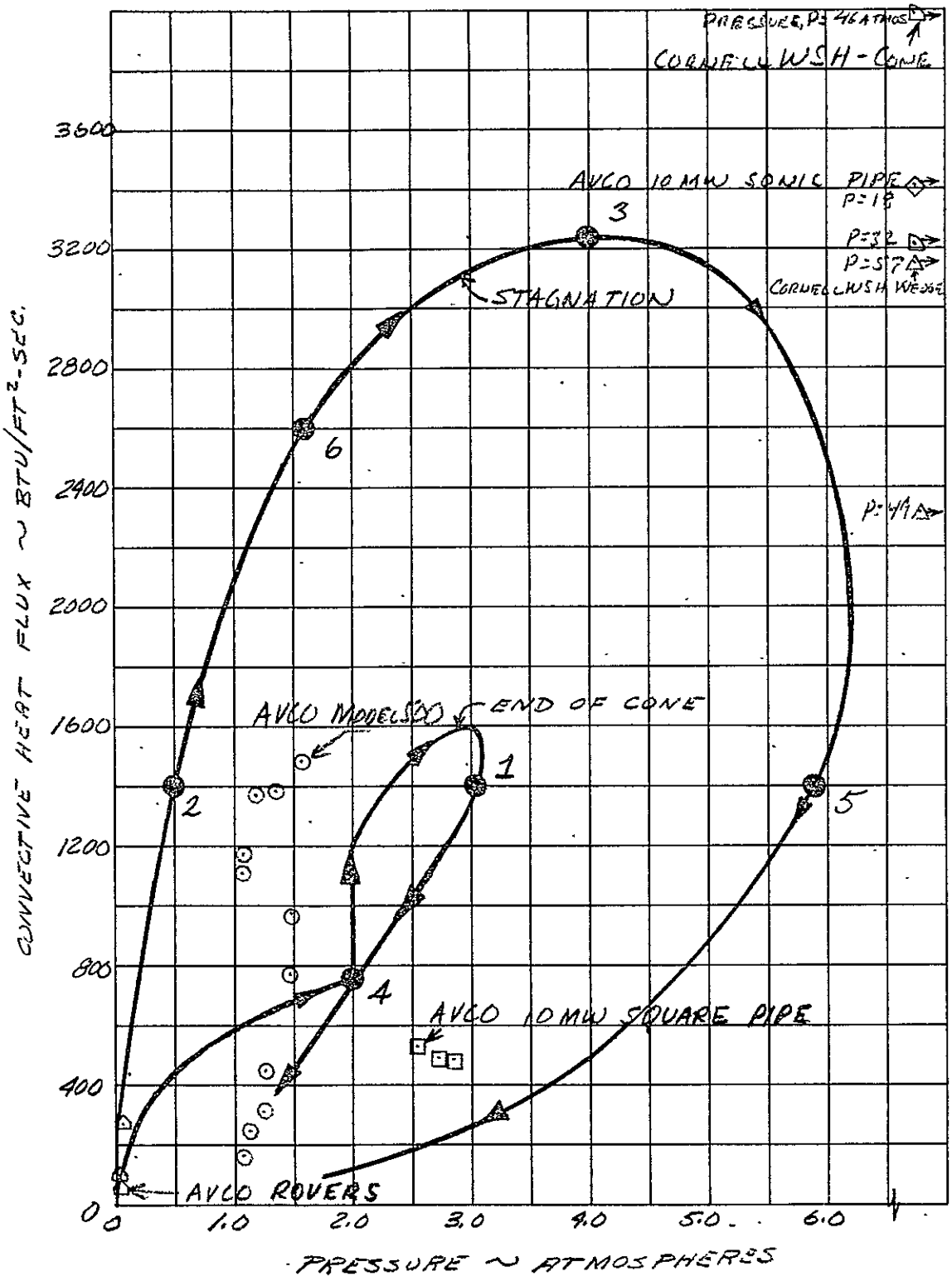


Figure 4.111 Convective Heating - Pressure Trajectory Profile, V_E = 38,250 fps, γ_E = -60°

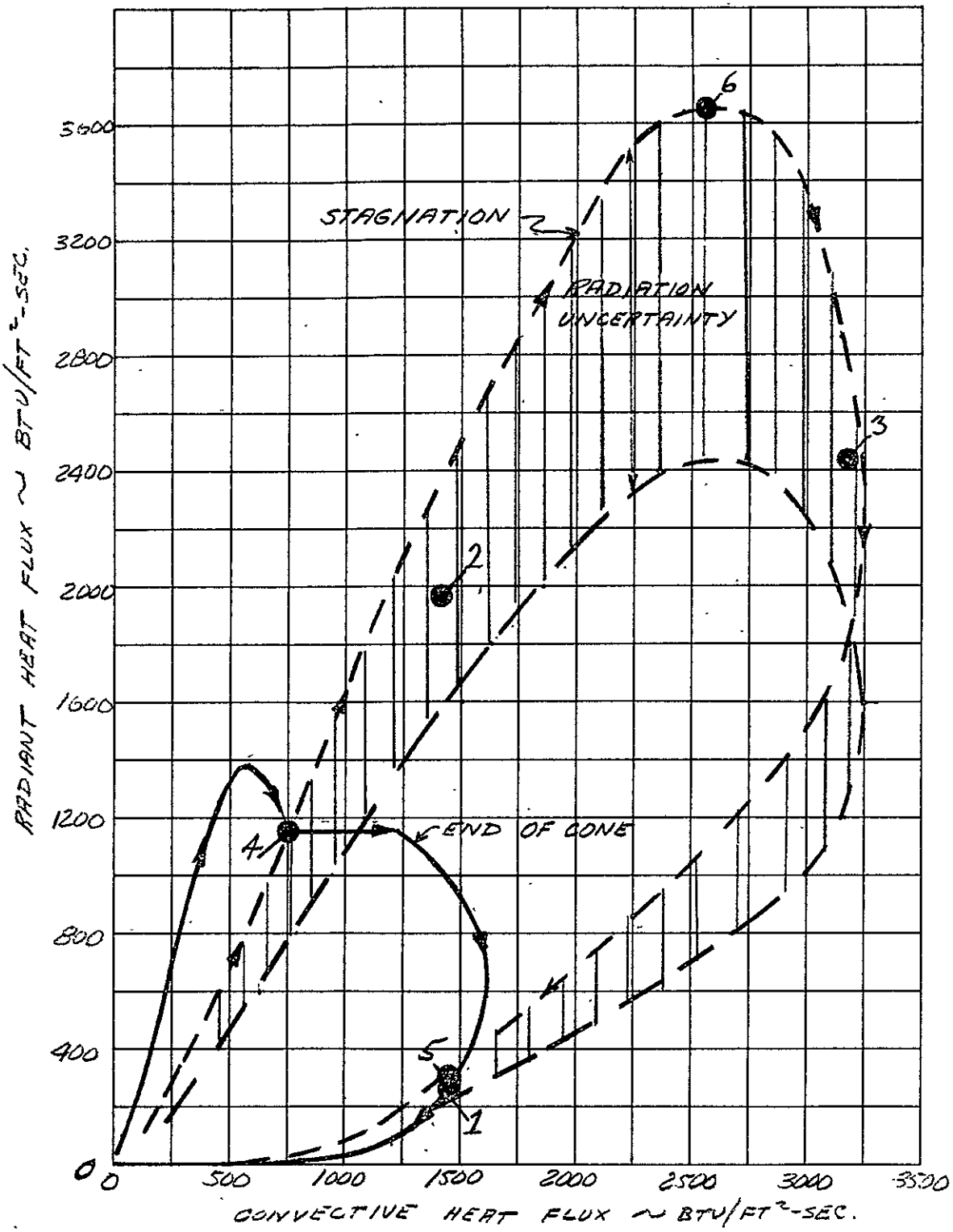


Figure 4.112 Convective - Radiating Heating Trajectory Profile, V_E = 38,250 fps, γ_E = -60°

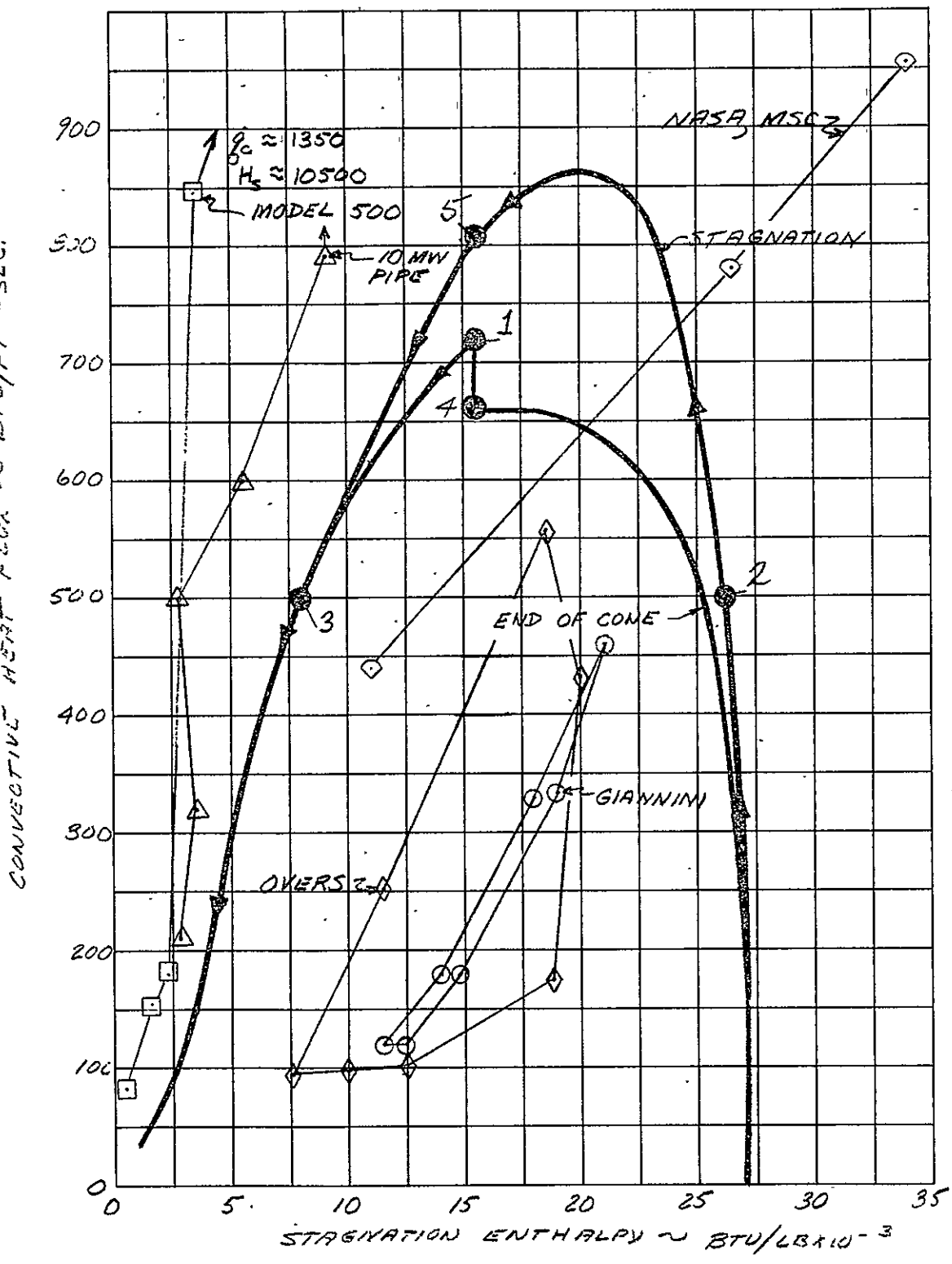


Figure 4.113 Convective Heating - Enthalpy Trajectory Profile, V_E = 35,600 fps, γ_E = -60°

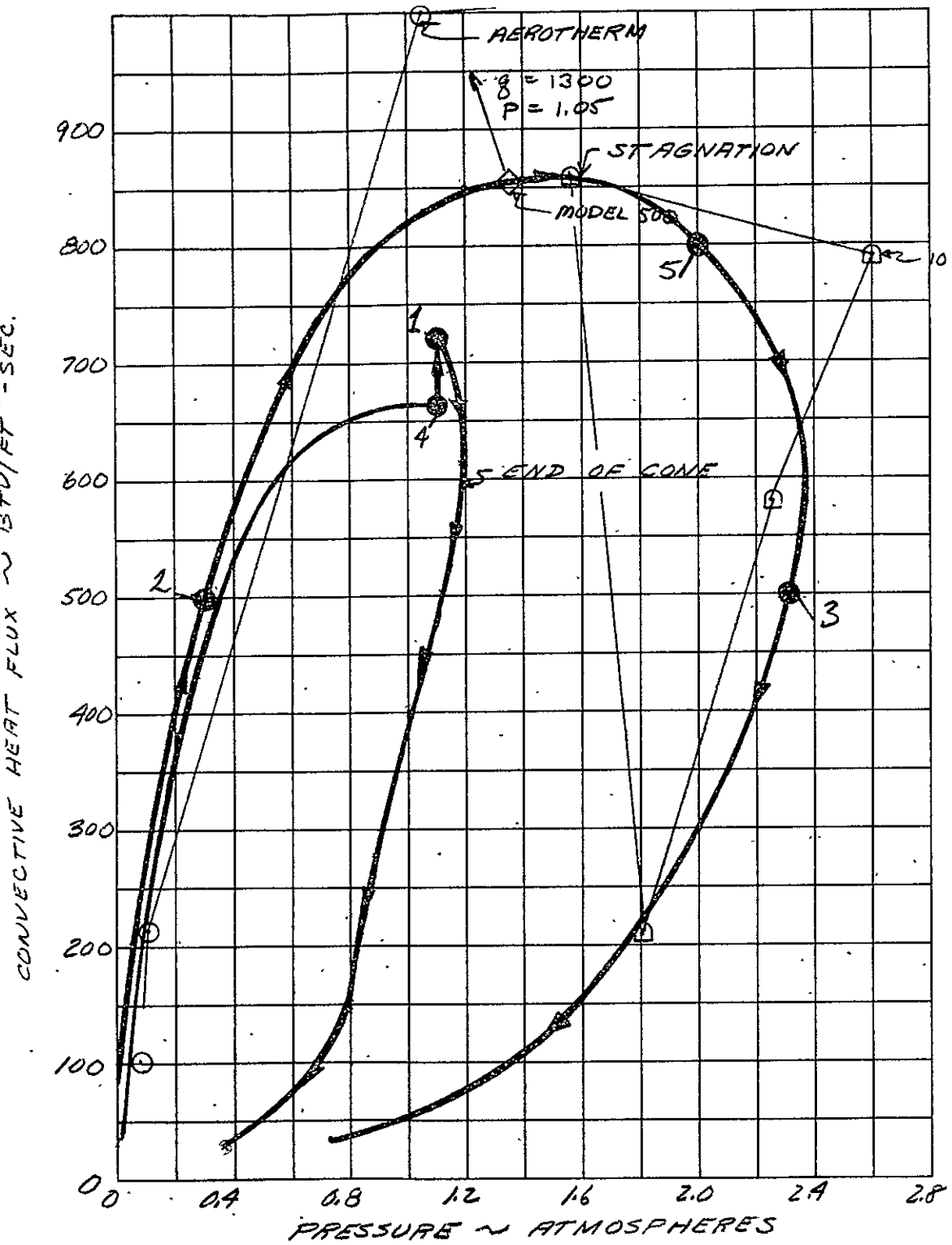


Figure 4.114 Convective Heating - Pressure Trajectory Profile, V_E = 35,600 fps, γ_E = -60°

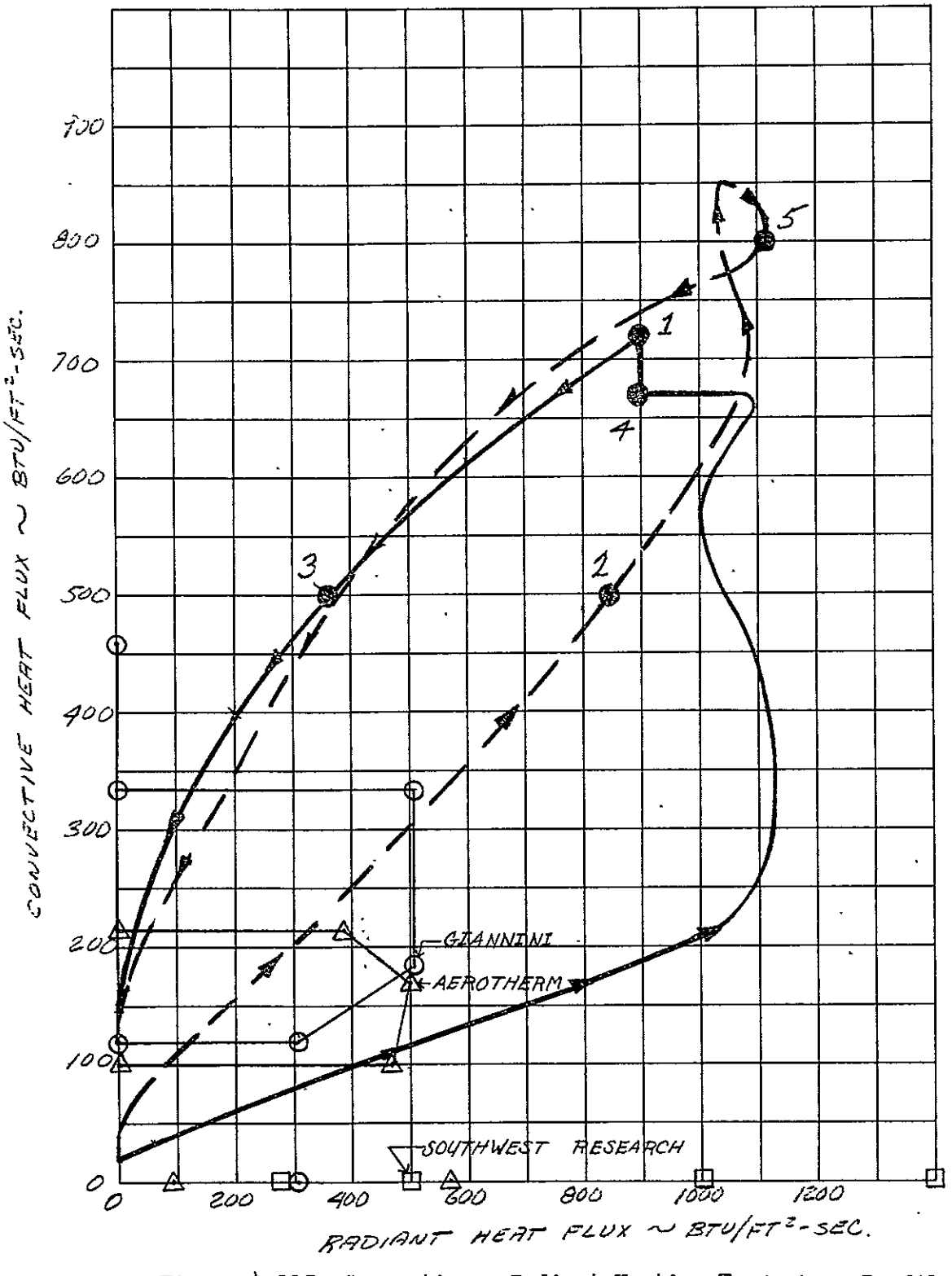


Figure 4.115 Convective - Radiant Heating Trajectory Profile, V_E = 35,600. fps, γ_E = -60°

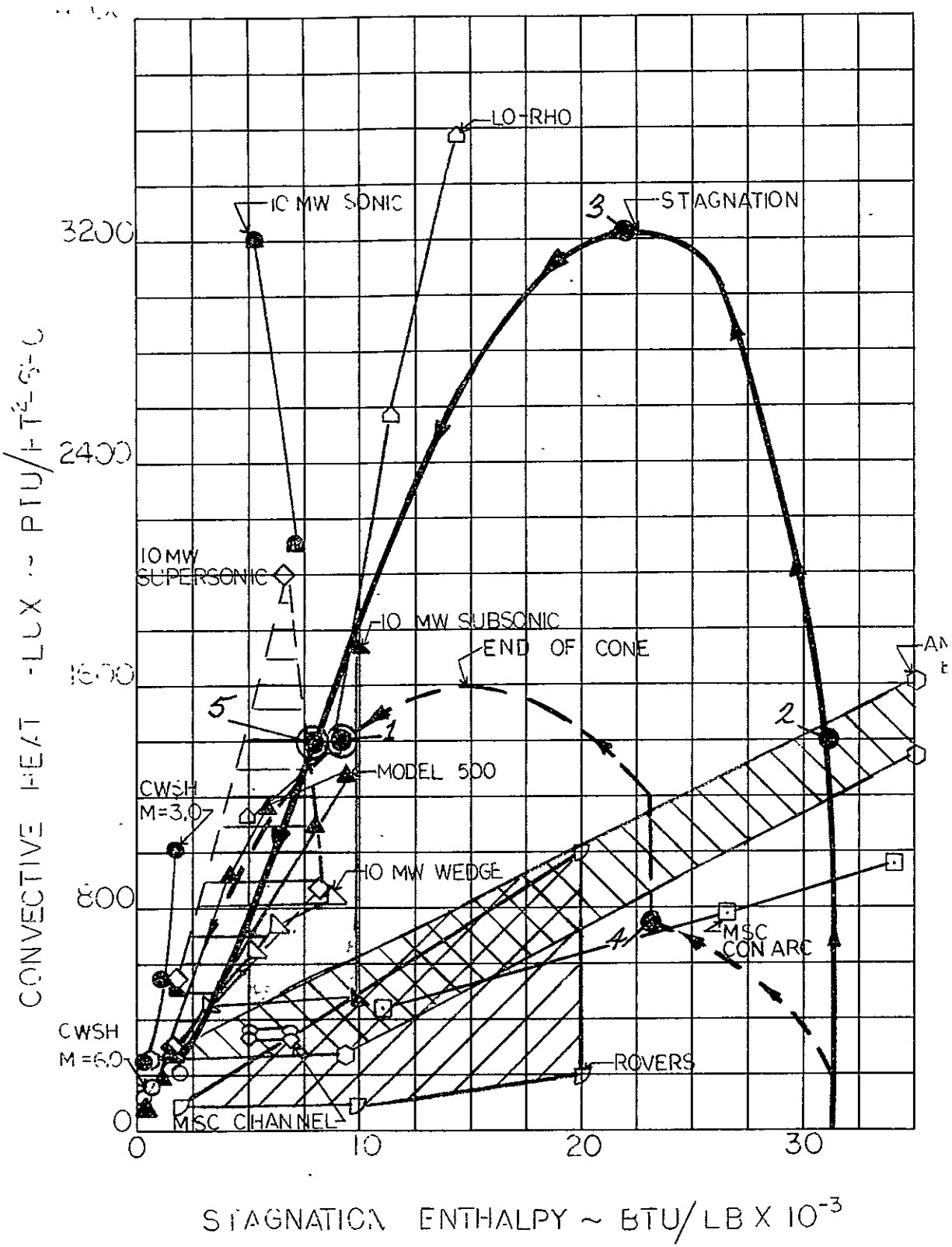
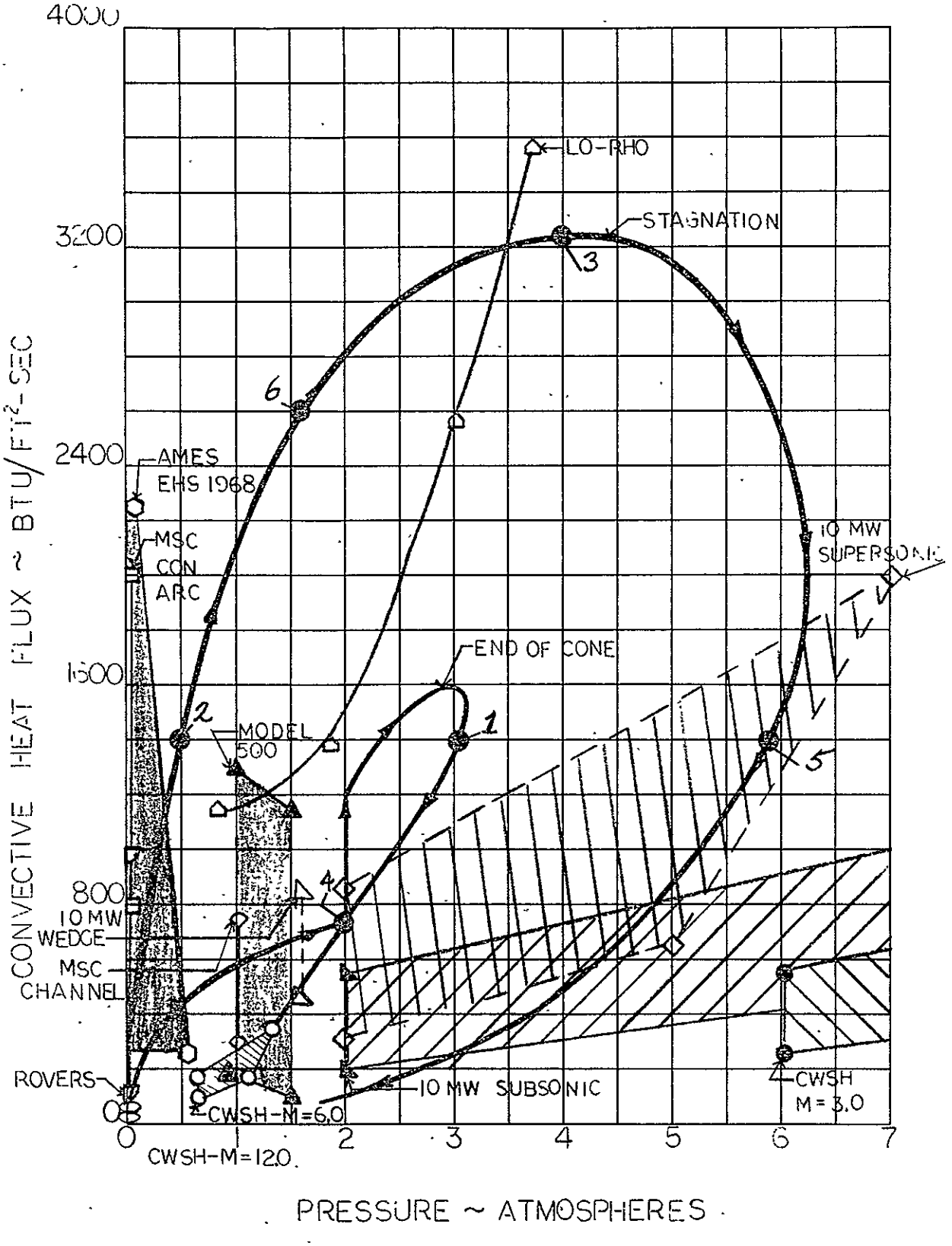


Figure 4.116 Convective Heating - Enthalpy Simulation,
V_E = 38,250 fps, γ_E = -60°

1 - 1650



1 - 1650

Figure 4.117 Convective Heating - Pressure Simulation, V_E = 38,250 fps, γ_E = -60°

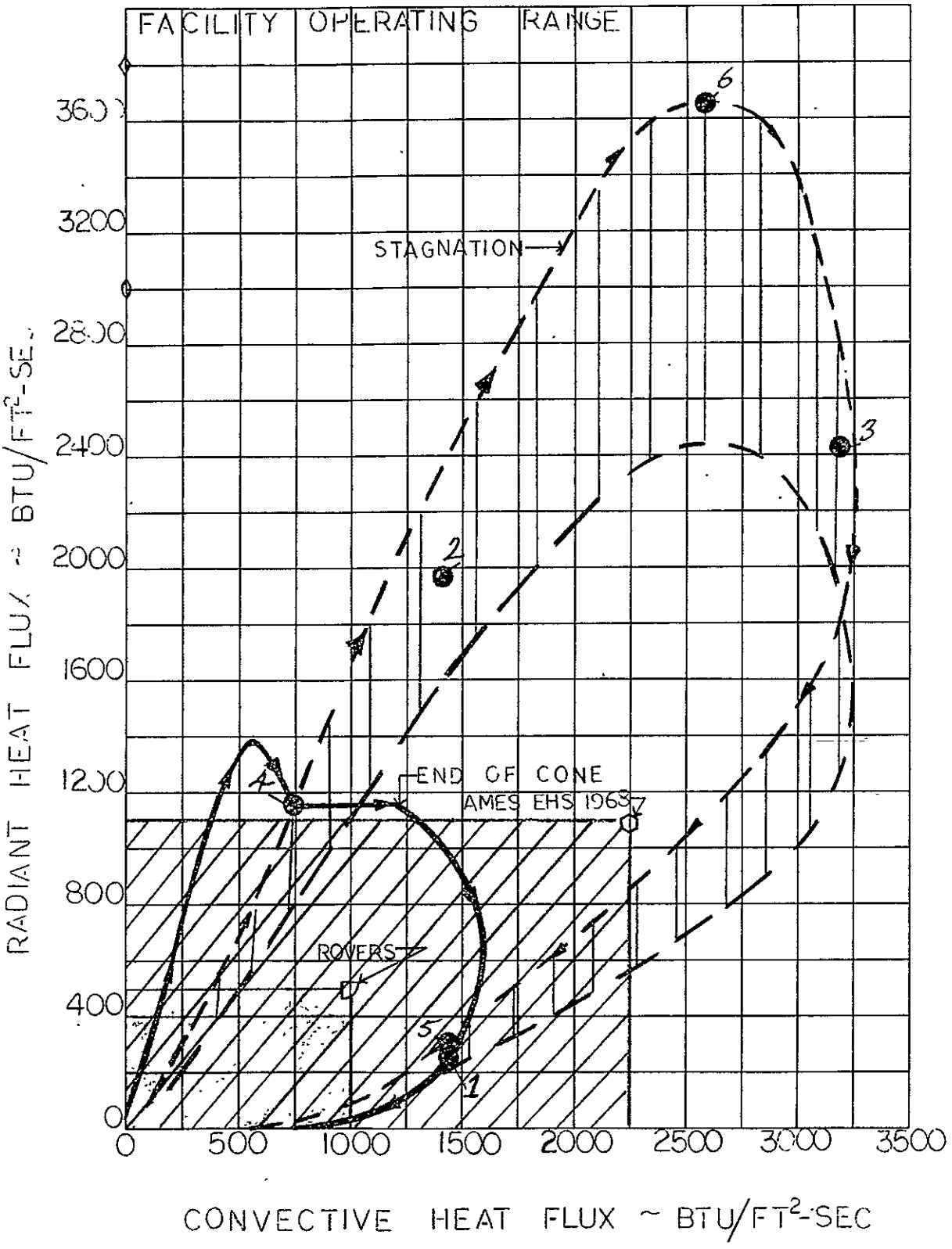


Figure 4.118 Convective - Radiative Heating Simulation,

V_E = 38,250 fps, γ_E = -60°

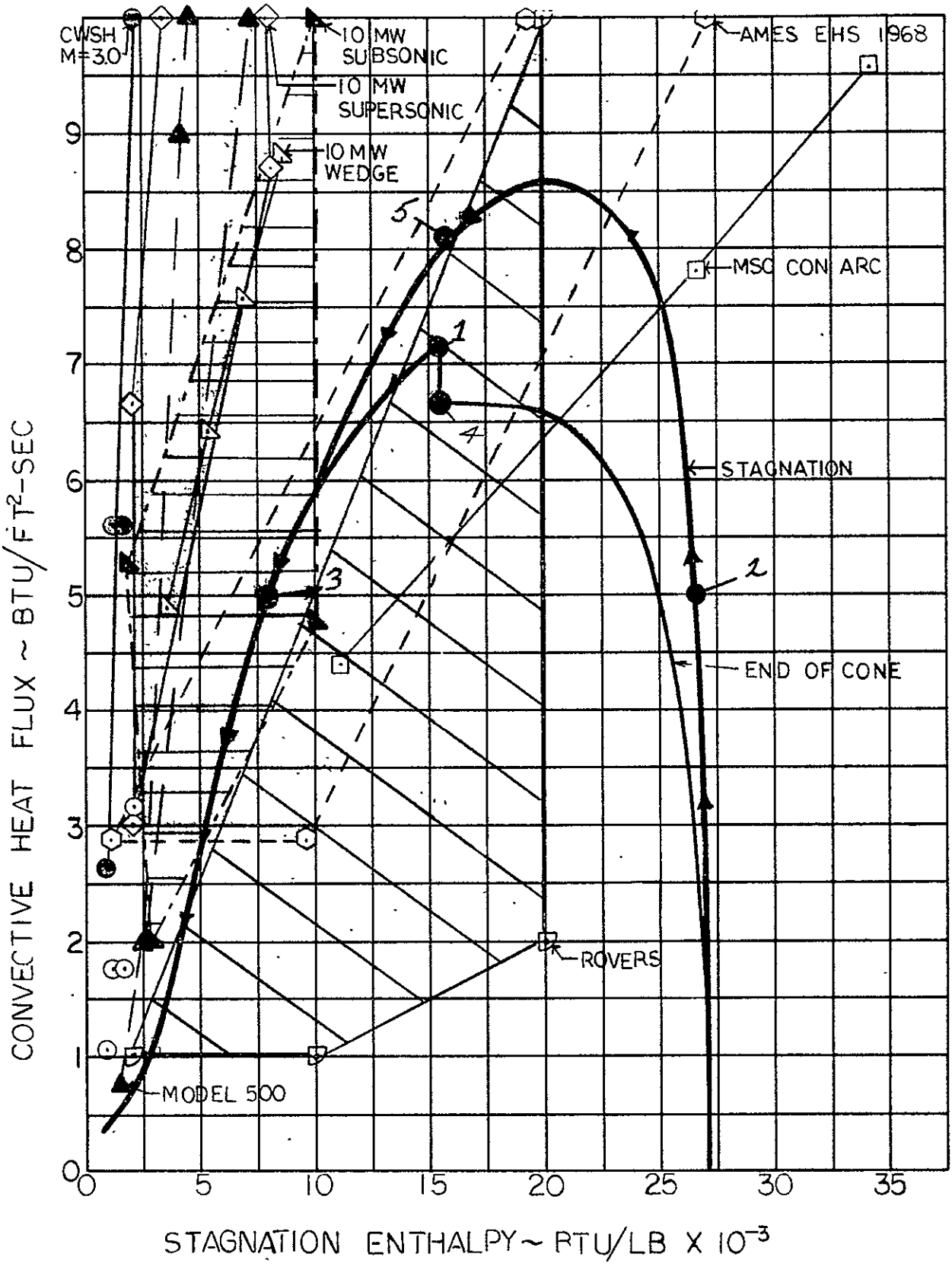


Figure 4.119 Convective Heating - Enthalpy Simulation,
V_E = 35,600 fps, γ_E = -60°

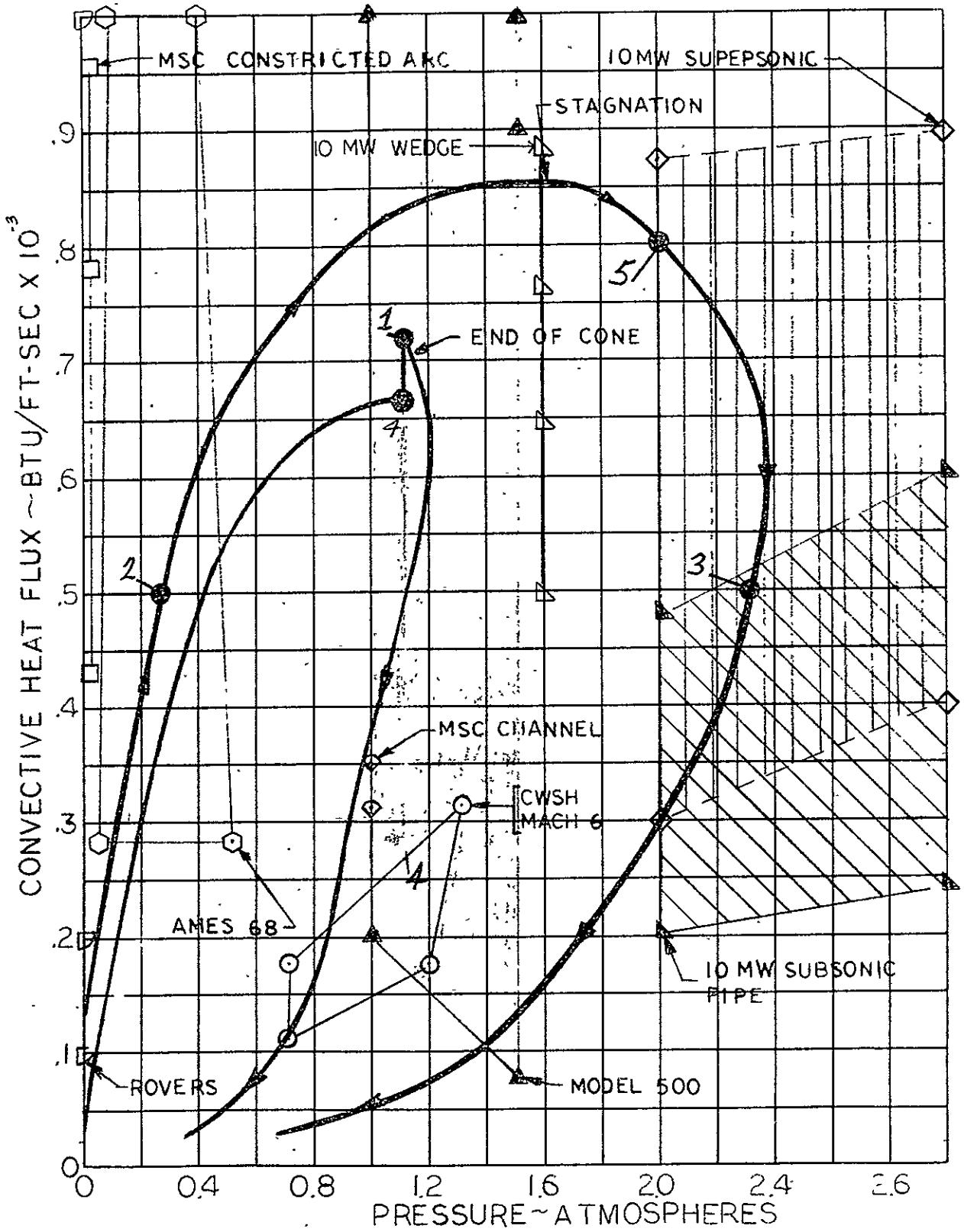


Figure 4.120 Convective Heating - Pressure Simulation,

V_E = 35,600 fps, γ_E = -60°

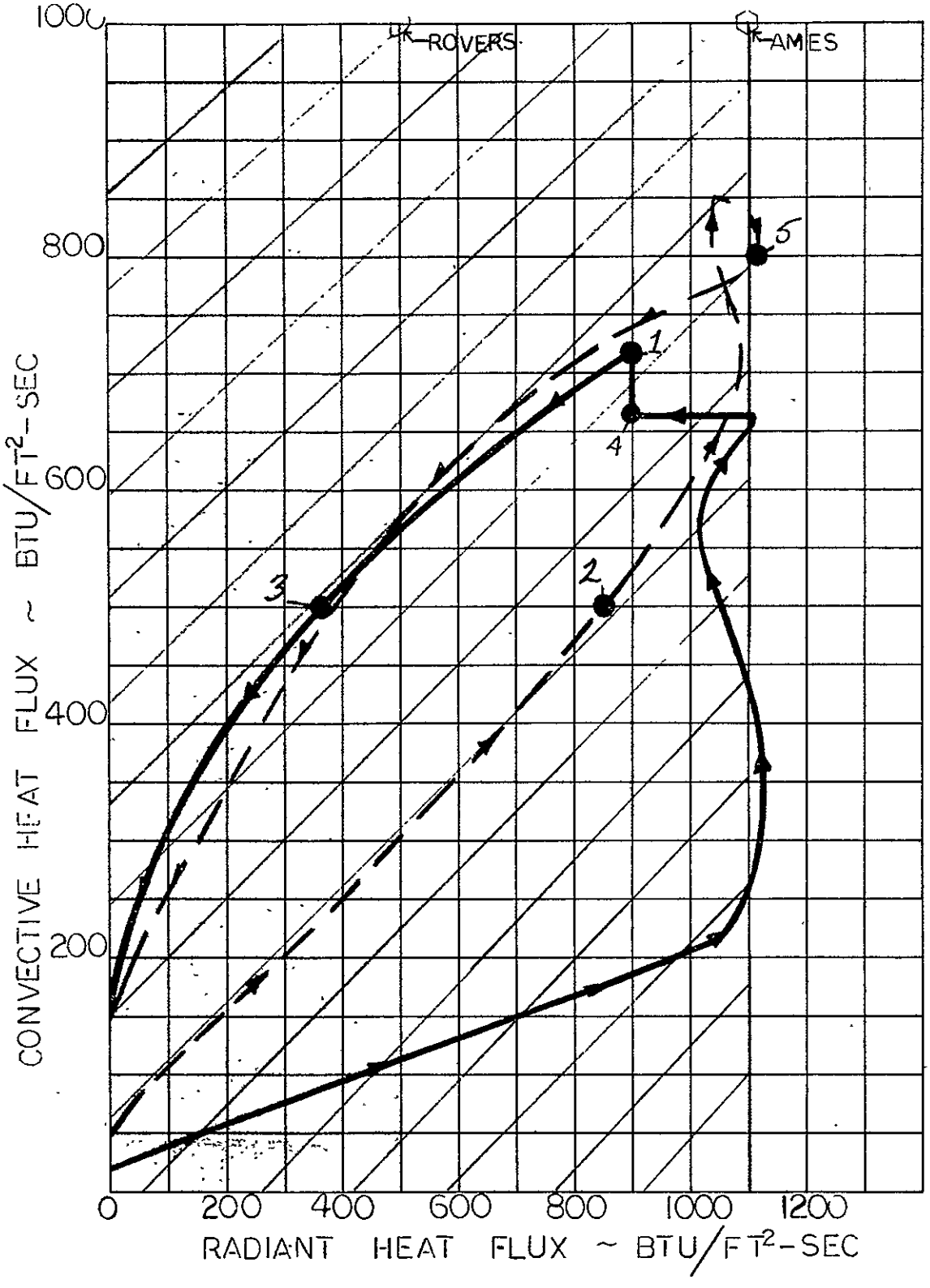


Figure 4.121 Convective - Radiative Heating Simulation, V_E = 35,600 fps, γ_E = -60°

1 - 1650

The first six figures (4.110 through 4.115) compare the trajectory parameters with presently available ground test data. All available data shown were conducted with air as the test gas. It is assumed that the carbon phenolic material is used for the high M/C_DA application and 5026-39/HC-G for the low M/C_DA application. These graphs aid in determination of requirement for additional data to clearly define performance in critical design environments. The last six figures (4.116 through 4.121) show the same trajectory information with superimposed facility maps representing the possible ranges of parameter combinations that can be simulated in presently available test facilities. Note that the trajectory profiles are common to all twelve figures and specific points (solid circle symbols) have been selected as the conditions most likely to control the designs of the heat shields. These "critical environments" have been tabulated in Tables 4.31 and 4.32 for the $M/C_DA = 0.2$ and $M/C_DA =$ .475 capsules, respectively.

From the information represented in the previously discussed figures and tables, Tables 4.33 and 4.34 were developed which show the best simulation possibility for each critical design point and the main limitation of the test. Even though there is a lack of complete simulation, the Phase I results should allow proper interpretation of ablation tests at the critical conditions. Comparison of the Phase II critical environments for ablative testing and the Phase I program shows that all required test points indicated in 4.33 and 4.34 have been fairly adequately covered in the Phase I program. Thus, ablation testing for these particular trajectories can be limited to design verification tests to check the analytical methods and material design properties.

4.6.7.2 Thermal Design Properties

Basic thermal properties tests on Avcoat 5026-39 such as thermal conductivity, specific heat and thermogravimetric analysis are not

SIMULATION REQUIREMENTS V_E = 35,600 fps, γ_E = -60°

TRAJECTORY POINT NUMBER	LOCATION-BOUNDARY LAYER STATE	CONVECTIVE HEATING (Btu/ft^2-sec)	RADIATIVE HEATING (Btu/ft^2-sec)	ENTHALPY (Btu/lb)	PRESSURE (Atmos.)	LOGIC
1	Cone-Turbulent	720	900	16000	1.1	Peak turbulent heating
2	Stagnation-Laminar	500	850	26500	0.3	Peak enthalpy
3	Stagnation-Laminar	500	360	8000	2.3	Enthalpy variation at constant heat rate-cf. point 2-also peak press.
4	Cone-Laminar	660	900	16000	1.1	Heat flux variation with constant enthalpy-cf. point 5.
5	Stagnation-Laminar	810	1100	16000	2.0	Essentially peak convective heating for stagnation point-also peak radiative heating.

TABLE 4.32

SIMULATION REQUIREMENTS V_E = 38,250 fps, γ_E = -60°.

TRAJECTORY POINT NO.	LOCATION-BOUNDARY LAYER STATE	CONVECTIVE HEATING (Btu/ft^2-sec)	RADIATIVE HEATING (Btu/ft^2-sec)	ENTHALPY (Btu/lb)	PRESSURE (Atmos.)	LOGIC
1	Cone-Turbulent	1400	250	10,000	3.0	Essentially peak turbulent heating on end of cone.
2	Stagnation-Laminar	1400	1950	31,000 (peak)	0.5	Peak enthalpy for stagnation point-enthalpy and pressure variation compared with point 5.
3	Stagnation-Laminar	3200	2425	22,000	4.0	Peak convective heating for stagnation point.
4	Cone-Laminar	800	1150	22,000	2.0	Heat flux variation at constant enthalpy cf. point No. 3.
5	Stagnation-Laminar	1400	300	6,000	5.8	Peak pressure -pressure variation at constant heat flux with point 2. Turbulent-Laminar heating comparison with point 1.
6.	Stagnation-Laminar	2600	3650*	28,000	1.5	Peak radiative heating and peak combined heating.

TABLE 4.33

COMPARISON OF GROUND TEST CAPABILITIES AND SIMULATION REQUIREMENTS,

V_E = 35,600 fps, γ_E = -60°

Trajectory Point Number / Facility	Boundary Layer	Convective Heating (Btu/ft^2-sec)	Radiative Heating (Btu/ft^2-sec)	Enthalpy (Btu/lb)	Pressure (Atmos.)	Remarks
1	Turbulent	720	900	16,000	1.1	Peak turbulent heating
AMES CHF-1968	Laminar	720	900	16,000	.05	Low pressure-laminar boundary layer
10MW Subsonic Pipe-AVCO	Turbulent	720	~	10,000	3.0	No radiant flux-high pressure
2	Laminar	500	850	26,500	0.3	Peak enthalpy
ROVERS-AVCO	Laminar	500	500	20,000	.08	Low Pressure
AMES CHF-1968	Laminar	500	850	26,500	.1	Low Pressure
3	Laminar	500	360	8,000	2.3	Peak pressure
Model 500-AVCO	Laminar	500	~	2,500	1.5	No radiant flux, low enthalpy
ROVERS-AVCO	Laminar	500	360	8,000	.08	Low pressure
4	Laminar	660	900	16,000	1.1	Heat flux variation
ROVERS-AVCO	Laminar	660	500	16,000	0.1	Low pressure
AMES CHF-1968	Laminar	660	900	16,000	.05	Low pressure
5	Laminar	810	1100	16,000	2.0	Peak radiative and combined heating
AMES CHF-1968	Laminar	810	1100	16,000	.04	Low pressure
AVCO-RASTA	Laminar	~	1100	~	2.0	No convective flux
10 MW Subsonic Pipe	Turbulent	810	~	10,000	4.0	No radiant flux-turbulent boundary layer

TABLE 4.34

COMPARISON OF GROUND TEST CAPABILITIES AND SIMULATION REQUIREMENTS,

V_E = 38,250 fps, γ_E = -60°

Trajectory Point Number / Facility	Boundary Layer	Convective Heating (Btu/ft^2-sec)	Radiative Heating (Btu/ft^2-sec)	Enthalpy (Btu/lb)	Pressure (Atmos.)	Remarks
1	Turbulent	1400	250	10,000	3.0	Near peak turbulent heating on cone
10 MW Subsonic Pipe - AVCO	Turbulent	1400	~	10,000	9.0	Internal pipe geometry.
LO-RHO Pilot Facility-AEDC	Laminar	1400	~	8,000	1.8	External specimen geometry but laminar flow
2	Laminar	1400	1950	31,000	0.5	Peak enthalpy
AMES CHF-1968	Laminar	1400	1100	28,500	.22	Low level of radiant heating
RASTA-AVCO	Laminar	~	1950	~	0.5	No convective flux
3	Laminar	3200	2425	22,000	4.0	Peak convective heating
LO-RHO Pilot Facility -AEDC	Laminar	3200	—	13,000	3.5	Low enthalpy-no radiant flux
RASTA-AVCO	Laminar	~	2425	~	4.0	No convective flux
4	Laminar	800	1150	22,000	2.0	Heat flux variation with point 2
AMES CHF-1968	Laminar	800	1100	22,000	0.12	Low pressure

TABLE 4.34 Cont.

Trajectory Point Number / Facility	Boundary Layer	Convective Heating (Btu/ft^2-sec)	Radiative Heating (Btu/ft^2-sec)	Enthalpy (Btu/lb)	Pressure (Atmos.)	Remarks
5	Laminar	1400	300	6000	5.8	Peak pressure
CWSH Mach 3.0	Laminar	600	~	1900	6.0	Low convective flux and low enthalpy
LO-RHO Pilot	Laminar	1400	~	8000	1.8	Low pressure
6	Laminar	2600	3650	28,000	1.5	Peak radiative and combined heating.
AMES CHF 1968	Laminar	1300	1100	28,000	.25	Low radiative convective fluxes and low pressure
RASTA-AVCO	Laminar	~	3650	~	1.5	No convective flux
LO-RHO Pilot	Laminar	2600	~	12,000	3.0	No radiative flux

required since sufficient data has been accumulated on the Apollo program and is available.

Limited data is available on carbon phenolic materials (see Section 4.5.1) including thermogravimetric analysis, specific heat data on virgin material, and thermal conductivity measurements on virgin and charred material (2000° char) up to temperatures of 1000°F. The amount of available specific heat and thermal conductivity data will have to be augmented to establish statistical confidence in the numbers, and the range of test conditions expanded to more completely over the range of interest.

Utilizing the method of mixtures for specific heat and a cut-bar conductivity apparatus as described in reference 105, data will be obtained on virgin and pre-charred material to at least 3000°F. The material will be pre-charred in 500°F intervals and tested under equilibrium temperatures up to the pre-char temperature.

It is possible to extend the testing beyond 3000°F but the problems introduced by the use of graphite standards and optical pyrometry in lieu of thermocouples impair the accuracy of the data. Data above 3000°F is recommended only if proven apparatus capabilities permit and a limited amount is required to aid extrapolation of other results.

No tests are recommended in the area of optical properties in either of the materials in these programs. Data on the Apollo materials (106) and carbon phenolic material (107) indicate that in the spectral area of interest, ($\lambda < 6\ \mu$) the absorptance of the charred materials is extremely high ($\alpha > 7.9$) at low temperatures. It seems unlikely that at higher temperatures and/or shorter wave lengths that the change in absorptivity would be significantly different and more than likely would be an approach to $\alpha = 1.0$. Development of sophisticated equipment to measure high temperature absorptance at short

($\lambda < .2\ \mu$) wave lengths does not seem warranted from both techanical and economic standpoints.

4.6.7.3 Test Program - Phase II Summary

The test conditions selected for the characterization for design of carbon phenolic and 5026-39/HC-G are summarized in Tables 4.35 through 4.38. The bases for selection of test points are:

1. Accumulation of thermal design properties for use in an analytical model predicting required design thicknesses.
2. Verification of design properties and analytical predictions through tests run as close to critical design conditions as possible.

The tests outlined in Tables 4.35 and 4.36 are at required test points. Each test point is developed from a sufficient number of test runs to establish confidence in the accuracy of the data. Three replicates per test point were required in the Phase I testing. The philosophy for the design verification tests (Phase II) is to run a limited number of test points at key conditions but allow for sufficient numbers of runs to provide statistical confidence in the results. For this reason, five replicates for each test point is required.

On Tables 4.35 and 4.36, the test points indicated with variable enthalpy and pressure are trajectory simulation tests. This type of test, a variable heat pulse (or pulses) simulating the transients experienced in the actual entry, is imposed on the model. This test technique has been developed on the Apollo test program to provide a means of evaluating the ability of the analytical model to predict the performance of the ablator undergoing time-temperature dependent phenomena. Since most of the thermal properties are generated in steady-state or equilibrium conditions, the trajectory simulation technique is an important part of the design verification

TABLE 4.35

VENUS ADDENDUM - DEVELOPMENT TEST PLAN

AVCOAT 5026-39/HC-G, $M/C_DA = 0.2$, $V_e = 35{,}600$ FPS

FACILITY	CONVECTIVE HEATING (Btu/ft^2-sec)	RADIATIVE HEATING (Btu/ft^2-sec)	ENTHALPY (Btu/lb)	PRESSURE (Atmos.)	MODEL GEOMETRY	TEST FLUID (% CO_2)	NUMBER OF TESTS	TEST OBJECTIVE
1. AMES Combined Heating Facility (Stagnation Tests-Thermocouples in-depth)	900 720 500 560 850	1100 900 850 900 1100	16,000 16,000 26,500 16,000 Variable	.2 .05 0.1 .05 Variable	Sphere-Segment Cylinder	Maximum " " " "	5 5 5 5	1. Verification of design properties and analytical model at critical conditions. (Points 1,2,4,& 5) 2. Trajectory Simulation.
2. AVCO 10 MW Arc Facility Pipe tests-thermocouples in-depth)	800	---	8,000	2.5	Subsonic Pipe	90	5	1. Verification of design at peak turbulent heating. (Point 1)
3. AVCO ROVERS Combined Heating Facility-Stagnation Tests-Thermocouples in-depth)	500 500 660	500 360 500	20,000 8,000 16,000	.08 .08 0.1	Sphere-Segment Cylinder	Maximum " "	5 5 5	1. Verification of design at peak enthalpy, peak pressure, heat flux variation (Points 2,3,4)
4. AVCO Model 500 Facility Splash Tests-Thermocouples in-depth)	500	0	2,500	1.5	Flat-faced cylinder	90	5	1. Verification of design at peak pressure. (Point 5)
5. AVCO RASTA Pure Radiant Facility-Tests-Thermocouples in depth.	----	1100		0.2, 2.0	Sphere-Segment Cylinder	90	10	1. Verification of design at peak radiant heating level. (Point 5)

TASK 4.36

VENUS ADDENDUM - DEVELOPMENT TEST PLAN

CARBON PHENOLIC - $M/C_DA = 0.475$, $V_e = 38,250$ FPS

FACILITY	CONVECTIVE HEATING (Btu/ft^2-sec)	RADIATIVE HEATING (Btu/ft^2-sec)	ENTHALPY (Btu/lb)	PRESSURE (Atmos)	MODEL GEOMETRY	TEST FLUID % CO_2	Number of Tests	TEST OBJECTIVES
1. AVCO 10MW Arc Pipe Tests-Thermocouples in depth.	1400	------	10,000	9.0	Subsonic pipe	90	5	1.Verification of design at peak turbulent heating (Point No. 1)
2. Lo Rho Pilot Facility-Stagnation Tests-Thermocouples in depth.	1400 2600 3200	------ ------ ------	8,000 12,000 13,000	1.8 3.0 3.5	Sphere-Segment Cylinder	Air	5 5 5	1.Verification of design at (a)peak turbulent heating-(point 1),(b) convective heating (point 3),(c) peak pressure (point 5),(d)peak combined heating (point 6).
3. AMES Combined Heating Facility-Stagnation Tests-Thermocouples in depth	1400 800 2250	1100 1100 1100	28,000 22,000 Variable	.22 .12 Variable	Sphere-Segment Cylinder	Maximum " "	5 5 5	1. Verification of design at (a)peak enthalpy (point 2), (b) heat flux variation (point 4),(c) peak combined heating(point 6).
4. AVCO RASTA Pure Radiant Facility-Stagnation Tests-Thermocouples in depth		2000 2425 3650		0.5,1.0 1.0,4.0 1.0,1.5	Sphere-Segment Cylinder	90 90 90	10 10 10	1. Verification of design at (a) peak enthalpy (point 2),(B) peak convective heating (point 3), (c)peak combined heating (point 6)
5. Cornell WSH Mach 3.0 Tunnel-Stagnation Tests-Thermocouples in depth	600	----	1900	6.0	Sphere Segment Cylinder	90	5	1. Verification of design at peak pressure (point 5)

program.

Tables 4.37 and 4.38 contain standard properties data required for design. The degree to which material is degraded has a significant effect on its thermal properties; therefore, it is desirable to obtain thermal properties data for as wide a temperature range as possible within the limits of current laboratory apparatus.

4.6.8 Phase III - Materials Screening

Various materials currently available, and others in planning and development phases, offer possible significant improvements over the Phase I and II reference materials for particular mission requirements. It would be prohibitive, from economic and schedule considerations, to include all of these materials in the Phase I and II studies. Results of the earlier work, however, is expected to form a sound basis for selection of key tests which will allow efficient screening and ranking of various materials for the Venus entry application.

Currently, several candidates from both the high and low density ablator classes are under consideration. Each of these offers a reasonable prospect of improved performance over the reference materials.

4.6.8.1 Low Density Ablator Candidates

4.6.8.1.1 Avcoat 5026-00

Low density (25 lb/ft^3) version of the present Apollo heat shield material possessing improved mechanical and thermal properties.

4.6.8.1.2 Low Density Ablator (16-20 lb/ft^3)

A new low density carbonaceous heat shield composition will be selected from the materials presently being developed under Contract AF 33(615)-3481, Ablative Composites for Lifting Re-entry Thermal Protection. Preliminary results of tests performed on the materials indicate they have excellent thermal properties and have performed well in ablative tests prescribed for the above program.

TABLE 4.37

CUT BAR THERMAL CONDUCTIVITY MEASUREMENTS

Carbon Phenolic

No. Tests	Pre-Char Temperature (°F)	Measurement Temperature Range (°F)	Data Availability
6	Virgin	Room Temperature-430	Yes
6	1000°F	R.T. - 1000	Yes
6	1500	R.T. - 1500	No
6	2000	R.T. - 2000	Partial
6	2500	R.T. - 2500	No
6	3000	R.T. - 3000	No
6	4000	R.T. - 4000	No

TABLE 4.38

METHOD OF MIXTURES SPECIFIC HEAT MEASUREMENTS CARBON PHENOLIC

No. Tests	Pre-Char Temperature (°F)	Measurement Temperature Range	Data Availability
	Virgin	Room Temperature -130	Yes
6	1000	RT - 1000	Yes
6	1500	RT - 1500	No
6	2000	RT - 2000	Partial
6	2500	RT - 2500	No
6	3000	RT - 3000	No
6	4000	RT - 4000	No

4.6.8.1.3 Low Density Prechar

Low density prechars (18-20 lb/ft^3) have been made from composites produced for Contract AF33(615)-3481. These chars possess excellent thermal properties and are expected to have good dimensional stability during ablation. One of the composites developed under the contract will be selected for evaluation.

4.6.8.1.4 Low Density Composite with Improved Filler

The continued development of new fillers for low density composites has resulted in new materials that should improve the thermal performance of present state-of-the-art low density ablators. The reference material for the ablative screening program will be reformulated to contain one of these new fillers (i.e. polyimide microballoons) and tested under this phase of the program.

4.6.8.1.5 Low Density Composite with Additives

Preliminary testing on AF33(615)-3923, Arc-Heater Characterization of Ablative Plastics and Composites has indicated that additives are available that will improve the radiative heat of ablation of low density ablators. The results of this program will be utilized to select additives and a composite formulation as a candidate material.

4.6.8.2 High Density Ablator Candidates

The reference material, RAD 6300, is a carbon/phenolic developed under the REST program (Contract AF04(694)-687). A complete description of this material along with fabrication techniques reported (Reentry Environment and Systems Technology (REST) Semi-Annual Progress Report, 1 January - 31 July 1965, Vol. IV, Materials (Task 4.0), Part 1 and Part 2, BSD-TR-65-406, Contract AF04(694)-687, 1 November 1965).

Modifications of this basic material would be made in an attempt to achieve improved ablative performance. These modifications would include:

4.6.8.2.1 Improved Resins

Several high char yield, thermally stable resins are available for this application. These include such resins as polyimides, polybenzimidazoles, and pyrrones. A resin of this type will be substituted for the phenolic in RAD 6300.

4.6.8.2.2 Graphite Fabric

RAD 6300 contains Pluton B carbon fabric. Graphite fabric has a higher thermal conductivity but may give better ablative performance at high heat fluxes.

4.6.8.2.3 Precharred Carbon or Graphite Phenolic

All of the above materials could be pyrolyzed prior to use to achieve dimensional stability and more shear resistant char layers. If this charring process is carried out at a low temperature (1000°F) thermal conductivity will not be adversely affected. Ablative efficiency can be improved by impregnating the precharred material with resin.

4.6.8.2.4 Reinforced Graphite

Fiber reinforced graphite in conjunction with insulation may offer a promising approach to a structural-ablative heat shield. To accomplish this two-dimensional (laminated) or three-dimensional reinforced graphite materials can be prepared with high modulus graphite reinforcements. This class of materials is currently under development and evaluation at AVCO.

4.6.8.2.5 High Performance Heat Shields with Additives

As with the low density materials, preliminary testing on AF33(615)-3923, Arc-Heater Characterization of Ablative Plastics and Composites, has indicated that additives can be used to improve the performance of high performance heat shield materials under radiative heating conditions. The results of this program will indicate which additives should be evaluated in one or more of the above concepts.

4.6.9 Evaluation of Flight Test Simulation

4.6.9.1 Objectives of Flight Test Simulation

Before discussing the details of the merits or lack of merits associated with flight simulation into the earth's atmosphere, it is necessary to establish those thermal objectives toward which such a program would be directed. For the current program, the flight simulation is a go no-go indicator relative to those parameters which are being simulated and does not serve any other real function. This fact is a direct consequence of such a test probably occurring well after the design has been frozen, and, therefore, irrespective of sophistication could not be used as the basis of a heat shield re-design. Needless to say, more than one flight test would be required to produce the confidence necessary for a re-design.

4.6.9.2 Flight Test Simulation Capabilities

It is likely that a flight test could reasonably simulate the cold wall convective heating, the unreduced (for absorbing and/or scattering) radiant flux, the pressure, the cold wall shear stress, and the enthalpy histories on the vehicle.

Although it may be possible to simulate the above parameters, the usefulness of an earth entry flight test becomes questionable when the following items are considered:

1. the difference of atmospheric composition
2. the current interest in lower entry velocities, and
3. available flight test data.

4.6.9.3 Effects of Atmospheric Composition on Simulation

Since both the carbon phenolic and the Avcoat 5026 produce highly carbonaceous chars, the mass injection rates into the boundary layer are governed by the free stream oxygen content. Therefore, the inability to simulate the oxygen mass fraction means that char formation and removal rates will not be simulated. This, in turn, means that boundary layer profiles cannot be simulated nor can the net convective heat flux, the shear stress at the wall, and the net radiant flux. Basically, the final result of all these non-simulated interactions is that the surface energy and mass balances will not be simulated and, hence, ablator performance will not be simulated.

4.6.9.4 Interest in Lower Entry Velocities

As the program proceeds, the initial interest in entry velocities exceeding 40,000 ft/sec has diminished and the current missions (with one exception) employ entry velocities at or below 36,000 ft/sec. This reduction greatly facilitates the abilities of ground tests to achieve over-test conditions on individual parameters and to approach more closely some of the combined parameters while using the correct atmospheric composition.

4.6.9.5 Available Flight Test Data

As indicated above, the principal thermal objective of a flight test simulation is to obtain go no-go information on the heat shield material. Both the carbon phenolic and the Avcoat 5026 have been subjected

to flight test programs. The carbon phenolic, neglecting the atmospheric composition and radiant heating, has survived environments far more severe than those anticipated for the Venus probe. On this basis, and, again, because composition cannot be simulated anyway, there seems to be no significant benefit to a flight test using carbon phenolic. Flight test data on Avcoat 5026 have included significant radiant heating but do not reflect the levels of all parameters expected for the Venus probe entry. However, extrapolation to these conditions is not extreme and, combined with over-tests on the ground, it is considered that this ablator is adequate for the low performance Venus entry probe.

4.6.9.6 Conclusion

Based upon the above discussion, it is concluded that a flight test simulation of the Venus probe into the earth's atmosphere is not justifiable from a thermal viewpoint. It is noted that other disciplines (e.g., structures or dynamics) may affect the overall significance of such a test. This conclusion is based upon data which are available and because of the inherent difficulty of extrapolating flight data to foreign atmosphere conditions.

4.7 References

1. Feldman, S., "Hypersonic Conical Shocks for Dissociated Air in Thermodynamic Equilibrium," Jet Propulsion, December 1957.

2. Lomax, H., and M. Knouye, "Numerical Analysis of Flow Properties About Blunt Bodies at Hypersonic Speeds in Equilibrium Gases," NASA-TR-R-204.

3. Lomax, H., and J. Rakich, "A Description of Numerical Methods and Computer Programs for Two Dimensional and Axisymmetric Supersonic Flow Over Blunt Nosed and Flared Bodies," NASA TN-D-2970.

4. Bobbitt, P.J. - Personal communication.

5. VanTassell, W., "Convective Heating in Planetary Atmospheres," Avco TM-63-72, 18 October 1963.

6. K. Wilson, W. Nicolet, "Spectral Absorption Coefficients of Carbon, Nitrogen, and Oxygen Atoms," Lockheed Palo Alto Research Laboratory, Lockheed Missiles and Space Company, November 1966.

7. W. Wiese, M. Smith, B. Glennon, "Atomic Transition Probabilities, Hydrogen Through Neon," NBS Report No. NSRDA-NBS4, Vol. I, May 1966.

8. J. Morris and R. Krey, "Radiation from Arc Heated Plasma," Quarterly Progress Report No. 2, Sept. 10, 1965 to December 10, 1965, Avco Document, December 10, 1965.

9. J. Morris and R. Krey, "Radiation from Arc Heated Plasma," Quarterly Progress Report No. 3, December 10, 1965 to March 10, 1966, Avco Document, March 10, 1966.

10. B. Kivel and K. Bailey, "Tables of Radiation from High Temperature Air," Research Report 21, Avco Everett Research Laboratory, December 1957.

11. "Mars-Venus Capsule Parameter Study," Volume I - Introduction and Analysis, RAD-TR-64-1, Avco, January 1964.

12. T. Wentink, Jr., E. Marram, L. Isaacson, and R. Spindler, "Ablative Material Spectroscopy, Volume I: Experimental Determination of Molecular Oscillator Strengths," AFWL-TR-67-30, Air Force Weapons Laboratory and Avco/SSD, November 1967.

13. H. Meyer, J. Ohrenberger, and T. Thompson, "Emission and Absorption of Radiant Energy in a Model Planetary Atmosphere," AIAA Journal, December 1965.

14. H. Hoshizaki and K. Wilson, "Convective and Radiation Heat Transfer during Superorbital Entry," AIAA Journal, January 1967.

15. Wolf, F., and J.M. Spiegel, "Status of Basic Shock Layer Radiation Information for Inner Planet Atmospheric Entry," AIAA Paper No. 66-421 (1966).

16. Gruszczynski, J.S. and W.R. Warren, "Experimental Heat Transfer Studies of Hypervelocity Flight in Planetary Atmospheres," AIAA, Vol. 2, No. 9 September 1964.

17. Gruszcynski, J.S. and W.R. Warren, "Study of Equilibrium Air Total Radiation," AIAA Journal, Vol. 5, No. 3, March 1967.

18. JPL Entry Vehicle Design Computer Program Users Manual, AVSSD-0001-66-RR, May 1966.

19. Allen, R.A., "Air Radiation Graphs: Spectrally Integrated Fluxes Including Line Contributions and Self Absorption," Avco Everett Research Laboratory, RR 230, September 1965.

20. Munson, T.R., Mascola, R.E., Brown, J.D., Spindler, R.J., and Klugerman, J., "An Advanced Analytical Program for Charring Ablators. Final Report. Volume II. Numerical Analysis, Program Description, Test Cases and Program Listing," AVSSD-0172-67-RR, Avco Space Systems Division, Lowell, Mass.

21. Graves, R.A., and Howser, L.M., "Charm: A Computer Program for Predicting the Thermal Response of Charring Ablation Materials," LWP-445, July 1967, National Aeronautics and Space Administration, Langley Research Center, Langley Station, Hampton, Va.

22. Curry, D.M., "An Analysis of a Charring Ablation Thermal Protection System," NASA TN D-3150, December 1965, National Aeronautics and Space Administration, Manned Spacecraft Center, Houston, Texas.

23. Swann, R.T., and Pittman, C.M., "Transient Numerical Analysis of Advanced Thermal Protection Systems for Atmospheric Entry," NASA TN D-1370, May 1962. National Aeronautics and Space Administration, Langley Research Center, Langley Station, Hampton, Va.

24. Kratsch, K.M., Hearne, L.F., and McChesney, H.R., "Theory for the Thermophysical Performance of Charring Organic Heat-Shield Composites, LMSC-803099 October 1963, Lockheed Missiles and Space Co., Sunnyvale, California.

25. Schaefer, J.W., Lundberg, R.E., Kendall, R.M., and McCuen, P.A., "A Study of Solid-Propellant Rocket Motor Exposed Materials Behavior," RTD-TDR-64-43, March 1964, Vidya, Palo Alto, California.

26. Rivers, W.J., Van Wyk, R., Seader, J.D., Friedman, H.A., and Chu, H.N., "Effect of Rocket Engine Combustion on Chamber Materials, Part I: One-Dimensional Computer Program," AFRPL-TR-65-13, January 1965, Rocketdyne Division, North American Aviation, Inc., Canoga Park, California.

27. Kendall, R.M., Bartlett, E.P., Rindal, R.A., and Moyer, C.B., "An Analysis of the Coupled Chemically Reacting Boundary Layer and Charring Ablator, Part I: Summary Report," Aerotherm Rept. No. 66-7, Part I, March 1967, Aerotherm Corporation, Palo Alto, California.

28. Moyer, C.B., and Rindal, R.A., "An Analysis of the Coupled Chemically Reacting Boundary Layer and Charring Ablator, Part II: Finite Difference Solution for the In-Depth Response of Charring Materials Considering Surface Chemical and Energy Balances," Aerotherm Rept. No. 66-7, Part II, March 1967, Aerotherm Corporation, Palo Alto, California.

29. Bartlett, E.P., and Kendall, R.M., "An Analysis of the Coupled Chemically Reacting Boundary Layer and Charring Ablator, Part III: Nonsimilar Solution of the Multicomponent Laminar Boundary Layer by an Integral Matrix Method," Aerotherm Rept. No. 66-7, Part III, March 1967, Aerotherm Corporation, Palo Alto, California.

30. Bartlett, E.P., Kendall, R.M., and Rindal, R.A., "An Analysis of the Coupled Chemically Reacting Boundary Layer and Charring Ablator, Part IV: A Unified Approximation for Mixture Transport Properties for Multicomponent Boundary-Layer Applications," Aerotherm Rept. No. 66-7, Part IV, March 1967, Aerotherm Corporation, Palo Alto, California.

31. Kendall, R.M., "An Analysis of the Coupled Chemically Reacting Boundary Layer and Charring Ablator, Part V: A General Approach to the Thermochemical Solution of Mixed Equilibrium-NonEquilibrium Homogeneous or Heterogeneous Systems," Aerotherm Rept. No. 66-7, Part V, March 1967, Aerotherm Corporation, Palo Alto, California.

32. Rindal, R.A., "An Analysis of the Coupled Chemically Reacting Boundary Layer and Charring Ablator, Part VI: An Approach for Characterizing Charring Ablator Response with In-Depth Coking Reactions," Aerotherm Report No. 66-7, Part VI, March 1967, Aerotherm Corporation, Palo Alto, California.

33. Swann, R.T.,Pittman, C.M., and Smith, J.C., "One-Dimensional Numerical Analysis of the Transient Response of Thermal Protection Systems," NASA TN D-2976, September 1965, National Aeronautics and Space Administration, Langley Research Center, Langley Station, Hampton, Va.

34. Fogaroli, R.P., and Saydah, A.R., "Turbulent Heat Transfer and Skin-Friction on a Porous Cone with Air Injection at High Mach Numbers," AIAA Journal, Vol. 4, No. 6, June 1966, pp. 1116-1117.

35. Woodruff, L.W., and Lorenz, G.C., "Hypersonic Turbulent Transpiration Cooling Including Downstream Effects," AIAA Journal, Vol. 4, No. 6, June 1966, pp. 969-975.

36. Pappas, C.C., and Okuno, A.F., "Measurement of Heat Transfer and Recovery Factor of a Compressible Turbulent Boundary Layer on a Sharp Cone with Foreign Gas Injection," NASA TN D-2230, Ames Research Center, April 1964.

37. Romanenko, P.N., and Kharchenko, V.N., "The Effect of Transverse Mass Flow on Heat Transfer and Friction Drag in a Turbulent Flow of Compressible Gas Along an Arbitrary Shaped Surface," Journal of Heat and Mass Transfer, June 1963.

38. Brunner, M.J., "Transpiration Cooling Test of a Sharp Sphere-Cone in a Rocket Exhaust Using N_2, He, and H_2O Coolants," ASME Paper No. 64-WA-HT-50, 1964.

39. Mickley, H.W., and Davis, P.S., "Momentum Transfer for Flow Over a Flat Plate with Blowing," NACA TN 4017, November 1957.

40. Bartle, E.R., and Leadon, B.M., "The Compressible Turbulent Boundary Layer on a Flat Plate with Transpiration Cooling," Convair Scientific Research Laboratory, Research Report 11, May 1961.

41. Tewfik, O.E., "Some Characteristics of the Turbulent Boundary Layer with Air Injection," AIAA Journal, June 1963.

42. Danberg, J.E., "Characteristics of the Turbulent Boundary Layer with Heat and Mass Transfer at M = 6.7," United States Naval Ordnance Laboratory, NOL TR 64-99, October 1964.

43. Rubesin, M.W., "An Analytical Estimation of the Effect of Transpiration Cooling on the Heat Transfer and Skin-Friction Characteristics of a Compressible Turbulent Boundary Layer," NACA TN 3341, December 1954.

44. Dorrance, W.H., and Dore, F.T., "The Effect of Mass Transfer on the Compressible Turbulent Boundary Layer Skin Friction and Heat Transfer," Journal of the Aeronautical Sciences, June 1954.

45. Van Driest, E.R., "On Mass Transfer Near the Stagnation Point," North American Aviation, Inc., Report No. AL-2553, June 1957.

46. Kelley, J.B., and L'Ecuyer, M.R., "Transpiration Cooling-It's Theory and Application," Jet Propulsion Center, Purdue University, Report No. TM-66-5, June 1966.

47. Culick, F.E.E., "The Compressible Turbulent Boundary Layer with Surface Mass Transfer," Massachusetts Institute of Technology Naval Supersonic Laboratory, TR-454, August 1960.

48. Bartle, R.E. and Leadon, B.M., "The Effectiveness as a Universal Measure of Mass Transfer Cooling for a Turbulent Boundary Layer," Proceedings of the 1962 Heat Transfer and Fluid Mechanics Institute, Stanford University Press, Stanford, California, 1962, pp. 27-41.

49. Stewart, J.D., "Transpiration Cooling: An Engineering Approach," General Electric Co., Missile and Space Vehicle Department, GE-TIS- R59SD-338 May 1959.

50. Spalding, D.B., Auslander, D.M., and Sandarum, T.R., "The Calculation of Heat and Mass Transfer Through the Turbulent Boundary Layer on a Flat Plate at High Mach Numbers With and Without Chemical Reaction," Supersonic Flow, Chemical Process and Radiative Transfer, Edited by D.B. Olfe and V. Zakkay, Pergamon-MacMillan, 1964, pp. 211-276.

51. Rubesin, M.W., and Pappas C.C., "An Analysis of the Turbulent Boundary Layer Characteristics on a Flat Plate with Distributed Light-Gas Injection," NACA TN 4149, February 1958.

52. Munson, T.R., Mascola, R.E., Brown, J.D., Spindler, R.J., and Klugerman, J., "An Advanced Analytical Program for Charring Ablators. Final Report, Vol. I, Analytical Formulation, Data Interpretation and Flight Simulation," AVSSD-0172-67-RR, Avco Space Systems Division, Lowell, Massachusetts.

53. Gross, J.F., Hartnett, J.P., Masson, D.J., and Gaxley, Jr., C., "A Review of Binary Laminar Boundary Layer Characteristics," Int. J. of Heat and Mass Transfer, ' Vol. 3, pp. 198-221, 1961.

54. Mascola, R.E., "A Review of the State of Knowledge Concerning the Reduction of Convective Heating Rates by Mass Injection," Avco Internal Release, S230-REM-558, March 1963.

55. Fillio, D.N., "Effect of Stabilization and Sterilization on Selected Properties of Avcoat 5026-39/HC-G," Avco Report, TR R210-8-64-50 (13 November 1964).

56. Bishop, W.M., "An Experimental Study of Ablation Materials Under High-Stress Environments," Avco Report AVMSD-0178-66-CR (23 September 1966).

57. Gatewood, Thermal Stresses, McGraw-Hill Publications in Aeronautical Science.

58. KHDR-AVMSD-67-10, "Mathematical Model and Thermal Material Properties of Carbon Phenolic (Avco R6300)." July 1967.

59. S230-65-RSB -71, Bartle, R.S., "On the 500 Arc Splash Tests - Carbon Materials," April 1965.

60. AVMSD-0172-66-CR, "Minutes of Mark 17 TD Meeting No. 2," (u) June 1966. SECRET Restricted Data.

61. G.E. - RSD Doc. #66SD 882, "Minuteman Mark 12 Re-entry System, Flight Test Evaluation Report (R/V #612005)," (u) July 1966 SECRET Restricted Data.

62. G.E. - RSD Doc. #66SD 9287, "Minuteman Mark 12 Re-entry System, Flight Test Evaluation Report, Mod 1 Re-entry Vehicle (S/N 6120006)," (u) SECRET Restricted Data.

63. G.E. - RSD Doc. #66SD9170, "Minuteman Mark 12 Re-entry System, Flight Test Evaluation Report, Mod 1 Re-entry Vehicle (S/N 6120007), (u), November 1966. SECRET Restricted Data.

64. G.E. - Doc. #67SD 5221, "Flight Evaluation Report, Atlas 35D," May 1967 SECRET Restricted Data.

65. Aerospace Report No. TR-1001 (S2815-20)-1, "Re-entry Nosetip Technology Symposium," (u), Volumes 1 through 4, October 1966, SECRET Restricted Data.

66. Sallis, D.V., H.E. Sparhawk, H.H. Hotchkiss, "Evaluation of Ablative Materials," AFML-TR-66-348, September 1967.

67. Baker, E.J., Jr., "Thermal Radiation Testing of Ablative Heat Protective Materials with an Arc-Image Furnace," Volume II, August 1965, Southwest Research Institute, Houston, Texas.

68. "Ablative Material Splash Tests in the GSC Hyperthermal Test Facility," FR 026-317, February 1966, Giannini Scientific Corporation, Santa Ana, Calif.

69. Schaefer, J.W., Flood, D.T., Reese, J.J., Jr., Clark, K.J., "Experimental and Analytical Evaluation of the Apollo Thermal Protection System Under Simulated Re-entry Conditions," Rept. No. 67-16, Part I, July 1967. Aerotherm Corporation, Palo Alto, California.

70. McCandless, W.J.C., "Ablation Data from Solar Furnace Testing of Avcoat 5026-39/HC-G,"Avco Internal Release VE/WJCM/23, January 1967, Avco Space Systems Division, Lowell, Massachusetts.

71. AVSSD-0375-67-RR, "Evaluation of the Thermophysical Properties of th Apollo Heat Shield," Volumes I and II, Final Report, August 1967.

72. Morris, J.C., and G.R. Bach; NS 11 (109) IEEE Trans. Nucl. Sci. (196

73. Morris, J.C., R.U. Krey, and R.W. Liebermann; ARL Report on Radiation 65-164, August 1965, Aerospace Research Laboratories Office of Aerospace Research, USAF (AF 33(615) -2976).

74. Morris, J.C., R.L. Garrison; "Note on Nitrogen Recombination Continuum in the Vacuum Ultraviolet", J. Quant. Spectrosc. Radiat. Transfer, Vol. 6, PP 899-902, Pergamon Press Ltd., Printed in Great Britain.

75. Adams, M.C., S. Georgiev, P. Levine and R.R. John. Some Recent Studies of New Reentry Problems. 9th Anglo American Aeronautical Conference.

76. Eschenback, R.C., J.R. McLeod, E.F. Stresion, et. al. "Performance Improvement of Arc Heaters for Aerodynamic Wind Tunnels, AFFDL-TR-65-87.

77. Gowen, F.E., J.H. Lundell, and B.H. Wick; "Facilities for Simulating Combined Convective and Radiative Entry Heating Environments" AMES Research Center, NASA, Moffett Field, California, 94035.

78. "Avco Hyperthermal Simulation Capabilities" Avco SSD. Technical Operations AVSSD-0021-68-A.

79. Baker, E.J., Jr. "Thermal Radiation Testing of Ablative Heat Protective Materials with an Arc-Image Furnace" NASA CR-65-124, Vol. 1, August 23, 1965.

80. Hiester, N.K., C.F. Clark, "Feasibility of Standard Evaluation Proceaures for Ablating Materials", Stanford Research Institute, Report Number 8 Prepared for Office of Research Grants and Contracts, NASA, May 31, 1965.

81. Winovich, W., "On the Equilibrium Sonic Flow Method for Evaluating Electric Arc Air Heater Performance," NASA TN D-0132, March 1964.

82. Fay, J.A., and F.R. Riddell, "Theory of Stagnation Point Heat Transfer in Disassociated Air, J. Aero Sci. February 1958.

83. Grindle, S.L., and Todd, J.P. "Evaluating Thermal Protection Systems Under Simulated Reentry Conditions". ML-TDR-64-293 February 1965 - Prepared by AF Materials Laboratory, Wright-Patterson Air Force Base, Ohio.

84. Probstein, R.F. and Kemp, M.H., "Viscous Aerodynamic Characteristics in Rarefied Gas Flow," Avco Everett Research Laboratory RR (revised) 48, December 1959.

85. Weeks, T.M. First Lieutenant, "Influence of Free Stream Turbulence on Hypersonic Stagnation Zone Heating," AFFDC, Wright-Patterson Air Force Base, Ohio. Presented at 28th Semi Annual Meeting of Supersonic Tunnel Association, Denver, Colorado, October 30-31, 1967.

86. Stempel, F.C., "Application and Advancements in the Field of Direct Heat Transfer Measurements," ISA 18th Annual ISA Conference and Exhibit, September 9-12, 1963, Chicago.

87. Hankey, W.L. Jr., and Hooks, L.E., "Constant Convection Heating Rate Surfaces for Lifting Re-entry Vehicles," AIAA Journal, July 1963, ASD, Wright-Patterson AFB, Ohio.

88. Nestler, D.E. and I. Musser, "Correlations for Convective Heat Transfer Pressure Distribution, and Shock Detachment Distance for Blunt Axisymmetric Forebodies," GE-MSVD-AETM No. 149, January 1960.

89. Boisson, J.C. and H.A. Curtiss, "An Experimental Investigation of Blunt Body Stagnation Point Velocity Gradient," ARS Journal, Feb. 1959.

90. Stein, E., Unpublished Avco ROVERS Data.

91. AVSSD-0233-66-CA, "Thermal Sensor Group and Laboratory Facilities, "Avco Space Systems Division, 21 October 1966.

92. Personal Communications - Henry Hoercher, Avco, Dr. Joseph Teno, Avco Everett Laboratories, John Lundell, NASA Ames, Donal Tillian, NASA MSC, Houston.

93. Personal Communications - Dr. Joseph Teno, Avco Everett Laboratory.

94. Eschenbach, R.C., Skinner, G.M. et al; "Development of Stable High Power High Pressure Arc Air Heaters for a Hypersonic Wind Tunnel," WADD-TR-61-100, July 1961.

95. Smith, R.I., and Kachek, Werner, A., "Design and Performance of a High Pressure Continuous Flow Arc Heater," AFFDC TR-66-48, May 1966.

96. Sarlitto, R.J., Eschenbach, R.C., Dryson, D.A., Laakaniemi, R.H. and Troue, H.H., "Development of High Enthalpy, High Power Arc Air Heaters."

97. Shepard, C.E., and Watson, V.R., "Performance of a Constricted Arc Discharge in a Supersonic Nozzle," Fifth Biennial Gas Dynamic Symposium, Northwestern University, Technological Institute, August 14-16, 1963.

98. Stine, Howard A., "The Hyperthermal Supersonic Aerodynamic Tunnel," Proc. High Temperature Technology, Asiloniar, Pacific Grove, California, September 8, 1963, Butterworth, 1964.

99. Vorreiter, J.W., and Shepard, C.E., "Performance Characteristics of the Constricted Arc Supersonic Jet," Proc. 1965 Heat Transfer and Fluid Mechanics Institute, Stanford University Press, 1965.

100. Shepard, C.E., Ketner, D.M., and Vorreiter, J.W., "A High Enthalpy Plasma Generator for Entry Heating Simulation," 13th Annual Institute of Environmental Sciences Technical Meeting and Equipment Exposition, Washington, D.C., April 10-12, 1967.

101. Sorensen, Carl and Camacho, S., "Experimental Results of Radiation Source Development by AMES Research Center, AIAA Preprint 66-185, 1966.

102. RAD, Theoretical and Experimental Investigation of Arc Plasma-Generation Technology, (AVCO/RAD-SR-61-26) 15 February 1961.

103. Carpenter, J.E., "Wave Superheater Hypersonic Tunnel-Description and Capabilities", August 1966, Cornell Aeronautical Laboratory, Inc.

104. Richter, R. and Buhler, R.D., "Final Report - High Enthalpy Gas Heater," Prepared for NASA Manned Spacecraft Center, Contract No. NAS 9-3564, EOS 6320-Final, 30 December 1965.

105. "Experimental Capabilities of the Thermal Properties Measurements Group," Materials Department, Research Directorate, Avco, Wilmington, Mass.

106. "Apollo Heat Shield, Design Status Report," (u), Volume III, Thermodynamics RAD-SR-64-137, 1 June 1964.

107. Wood, M.J., "Optical Properties - Final Report," Avco Internal Technical Release, W330-23 of 27 September 1967.

V. FLYBY PROBE SYNTHESIS

5.0 FLYBY PROBE SYSTHESIS

In consonance with the study guidelines (Section 1.2.0) the flyby probe study was aimed at defining the essential modifications to a Mariner Mars 1969 spacecraft in order for it to be usable for the 1972 Venus mission. Many of the mission and study constraints have already been discussed in Sections 1.0, 2.0, 3.0 and only a brief recapitualtion is given here. Furthermore as detailed descriptions of the basic flyby subsystems are documented in the Mariner Mars 1969 Functional Requirements Document, the presentation here is given in a summary manner. Supporting analyses of the flyby probe system and subsystems definition are contained in the Flyby Probe Synthesis Supplement.

5.1 System Requirements and Constraints

5.1.1 Mission Invariant Requirements and Constraints

Table 5.1 lists those requirements and constraints which the flyby probe must adhere to regardless of the trajectory and scientific experiments on board.

Table 5.1

Invariant Requirements and Constraints

Requirements	Constraints
o Utilize MM '69 basic spacecraft system where possible.	o Retention of MM '69 design concepts
o Atlas/Centaur SLV-3C launch capability	o Experiment view angles, weight volume and data rate requirements
o Carry one or more atmospheric entry probes	o Atlas/Centaur-Surveyor shroud
o Uplink communication required through low gain antenna during all mission phases	o Entry probe functional and physical requirements
o Provide engineering data during cruise	o Thermal control adequate for Venus environment
o Provide science data during encounter	o Venus quarantine requirements
o Two launches during the opportunity	
o Utilize DSN for command, control, communications, and tracking	

5.1.2 Best RF Occultation (Baseline) Mission Requirements and Constraints

In addition to the mission invariant requirements and constraints, those associated with the baseline system are summarized in Table 5.2.

Table 5.2

Best RF Occultation Mission
Requirements and Constraints

Requirements	Constraints
Mount single 54" diameter entry probe under octagon	o Magnetically clean S/C
Encounter geometry compatible with both entry probe release and RF occultation	o Maximum separation weight of 1665 lb.*
Provide cruise and science data; Trapped Radiation Detector and Magnetometer	o Entry probe θ_{op} of 135° requires additional low gain antenna
Attidue change maneuver at encounter minus 12 days for probe deployment	o Far side flyby with nominal 16 July 1972 arrival
	o Maintain Sun and Canopus lock while pointing spacecraft experiments to desired look angles

*Includes additional adapter weight also

5.1.3 Alternate Mission Requirements and Constraints

Table 5.3 summarizes the alternate mission requirements and constraints. The alternates in general have less requirements than the baseline system.

Table 5.3

Alternate Mission Requirements and Constraints

Requirements	Constraints
Common to Both Alternates	
o Mount single entry probe under octagon	o Near side flyby 3 August arrival geometry
o Entry probe diameter: Minimum Flyby/Entry Mission 43" Best Entry Probe Mission 48"	o Body fixed experiments
	o Maintain Sun and Canopus lock during encounter
	o Maximum separation S/C + probe weight of 1245 lb.*
Alternate 1	
o Support baseline science complement less magnetometer and trapped radiation detector (RF occultation experiment optional)	
Alternate 2	
o Support wide angle TV, periapsis on light side of Venus	

*Includes additional adapter weight also.

5.2 System and Configuration Design

5.2.1 Best RF Occultation Mission

From a Mariner Venus 1972 spacecraft system standpoint, the two main influences on spacecraft design are:

1. Total spacecraft weight at launch
2. Conditions at Venus encounter

Maximum spacecraft weight is dictated by booster capability to insert a given payload into the proper trajectory to intercept Venus. The basic mission allows a maximum approach velocity (V_∞) to Venus of 6.22 km/sec. This results in

a booster energy requirement of C_3 = 14.7 km^2/sec^2 or a maximum injected payload weight of 1665 pounds. Lower planet approach velocities require higher C_3 values which in turn reduce total injected weight. (See Section 2.9 for mission selection rationale).

5.2.1.1. Alternate Configuration Approaches and Selection

Twenty-three basic spacecraft configurations have been developed and studied to determine their degree of applicability in supporting a Mariner Venus 1972 flyby mission. The basic Mariner Venus 1972 mission provides for cruise science as well as planet encounter science along with one or two Venus atmospheric entry probes released from the flyby several days before encounter.

All of the basic configurations that were analyzed are discussed in detail in the Flyby Probe Synthesis Supplement. Table 5.4, showing ten representative configurations, is presented as a summary of the results of this study. The configuration study was accomplished within the framework of the following constraints:

1. The flyby/entry probe package must fit inside the existing Atlas/Centaur-Surveyor shroud.
2. Maximum payload weight at liftoff = 1665 pounds.
3. Science experiment view angle requirements must be met.
4. Antenna view angle and placement requirements must be met.
5. Entry probe functional and physical requirements must be met.

In addition, flyby probe solar panel, propulsion and attitude control system physical and functional requirements were taken into account.

Of the configurations studied, two (Figs. 5.1 and 5.2) were selected as being most suitable to fulfill mission requirements and still require a minimum of modification to the basic Mariner Mars 1969 spacecraft design. Each mounted a single entry probe below the basic structure and a two position high gain antenna. Both configurations utilize one fixed low gain antenna, and one articulated low gain antenna. The second (articulated) low gain antenna is used during the entry probe

Table 5.4

CONFIGURATION TRADE ANALYSIS
REPRESENTATIVE CONFIGURATIONS

	DESCRIPTION						ADVANTAGES	DISADVANTAGES
No.	NO. OF ENTRY PROBES	LOCATION	LOW GAIN ANTENNA	HIGH GAIN ANTENNA	SCAN PLATFORM	OTHER		
1	One (35" Dia. 26" Deep)	Below	Mtd on Scan Platform	Mtd on Scan Platform	Yes	Near Side Flyby	No View Angle Constraints	Reduced Reliability, Temporary Loss of Down Link
5	One (35" Dia. 26" Deep)	Above	Articulated	Articulated	Yes	Microwave Antenna Articulated	Increased Capsule Depth Available	Reduced Reliability, High Cost, Compromised Performance
7	Two (35" Dia. 26" Deep)	One Above One Below	Articulated (~170°)	Two Position	No	Near Side Flyby	Two Capsules	Very Marginal on Weight, Articulated Low Gain
8	Two (35" Dia. 26" Deep	Below	Articulated (30°)	Two Position	Yes (Offset Exp.)	Far Side Flyby	Two Capsules, High Performance	Weight Marginal, Articulated Low Gain
10	One (35" Dia. 26" Deep)	Below	Fixed	Two Position	Yes	Platform Cantilevered. Far-Side Flyby	Increased Reliability, High Performance	Small Microwave Antenna (36 x 36), View Angle Interference
10a	One (43" Dia. 36" Deep)	Below	One Fixed One Articulated	Articulated Two Position	Yes	Platform Cantilevered. Far-Side Flyby	Increased Reliability High Performance	Microwave Antenna View Angle Interference, Articulated Low Gain

Table 5.4 cont.

	DESCRIPTION					ADVANTAGES	DISADVANTAGES
NO.	NO. OF ENTRY PROBES / LOCATION	LOW GAIN ANTENNA	HIGH GAIN ANTENNA	SCAN PLATFORM	OTHER		
14	One (78" Max. Dia. 39.5" Deep. 60° Half Cone) Below	Articulated	Two Position	Yes	Shortened Solar Panels, Far-Side Flyby	Large Capsule, Simple Scan Platform	Microwave Antenna View Angle Interference. Articulated Low Gain
18	One (63" Max.Dia. 42.5" Deep 45°Half Cone) Below	Fixed	Two Position	No	Shortened Solar Panels, Far-Side Flyby	Large Capsule, Decreased Complexity, High Reliability	Reduced Performance
20	One (43" Dia. 26" Deep 60° Half Cone) Below	Fixed	Two Position Solar Panel Mounted	Yes (Offset Exp.)	Far-Side Flyby	High Performance, Increased High Gain Antenna View Angle Clearance	One Solar Paddle has Unique Assy. Redundant Solar Panel Deployment for Equal Reliability.
20a	One (43" Dia. 26" Deep 60° Half Cone) Below	One Fixed One Articulated	Two Position Solar Panel Mounted	Yes	Platform Cantilevered, Far Side Flyby	High Performance, Increased High Gain Antenna View Angle Clearance	One Solar Paddle has Unique Assy. Redundant Solar Panel Deployment for Equal Reliability.

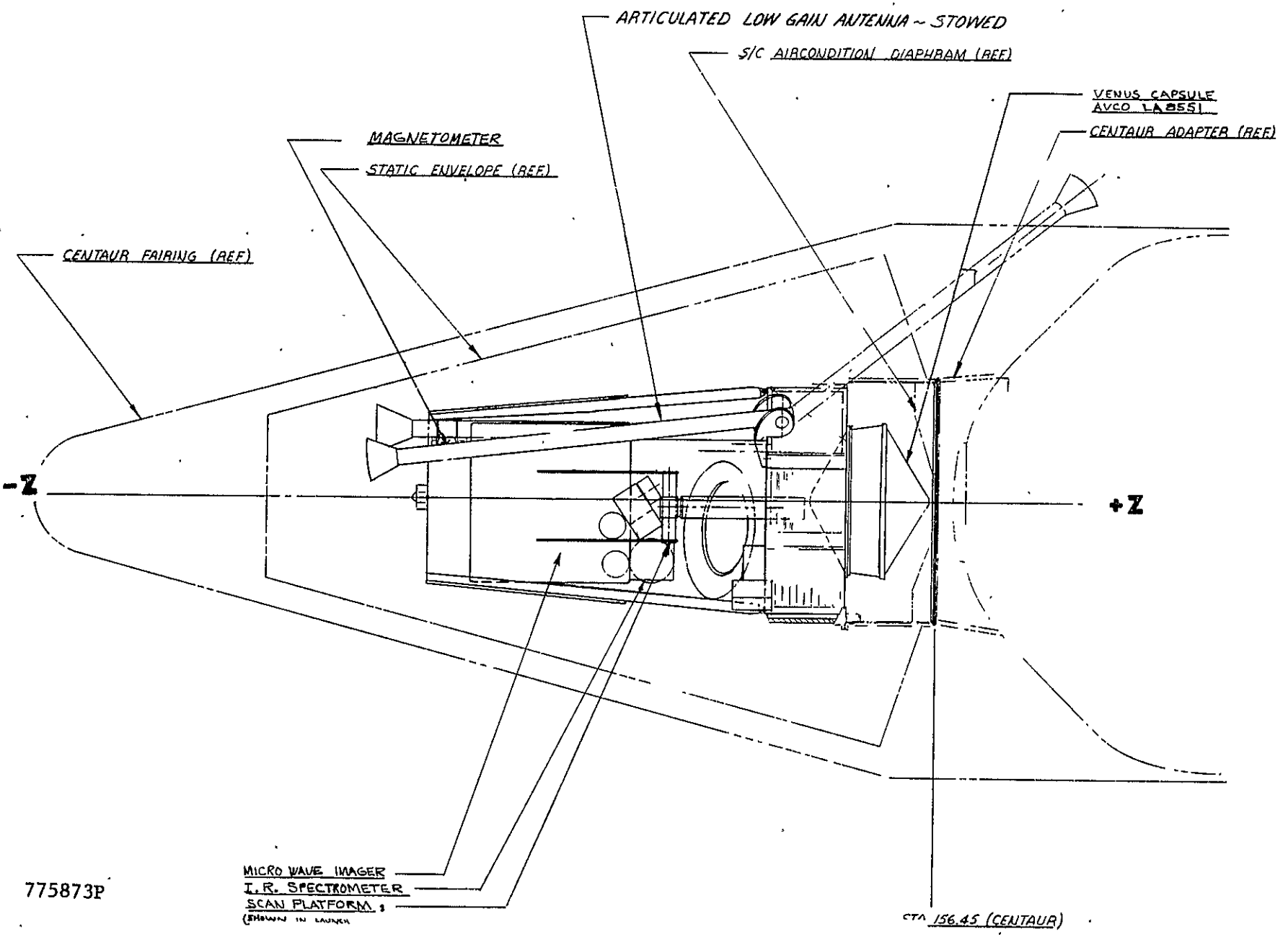


Figure 5.1a: Flyby Configuration 10a, Stowed

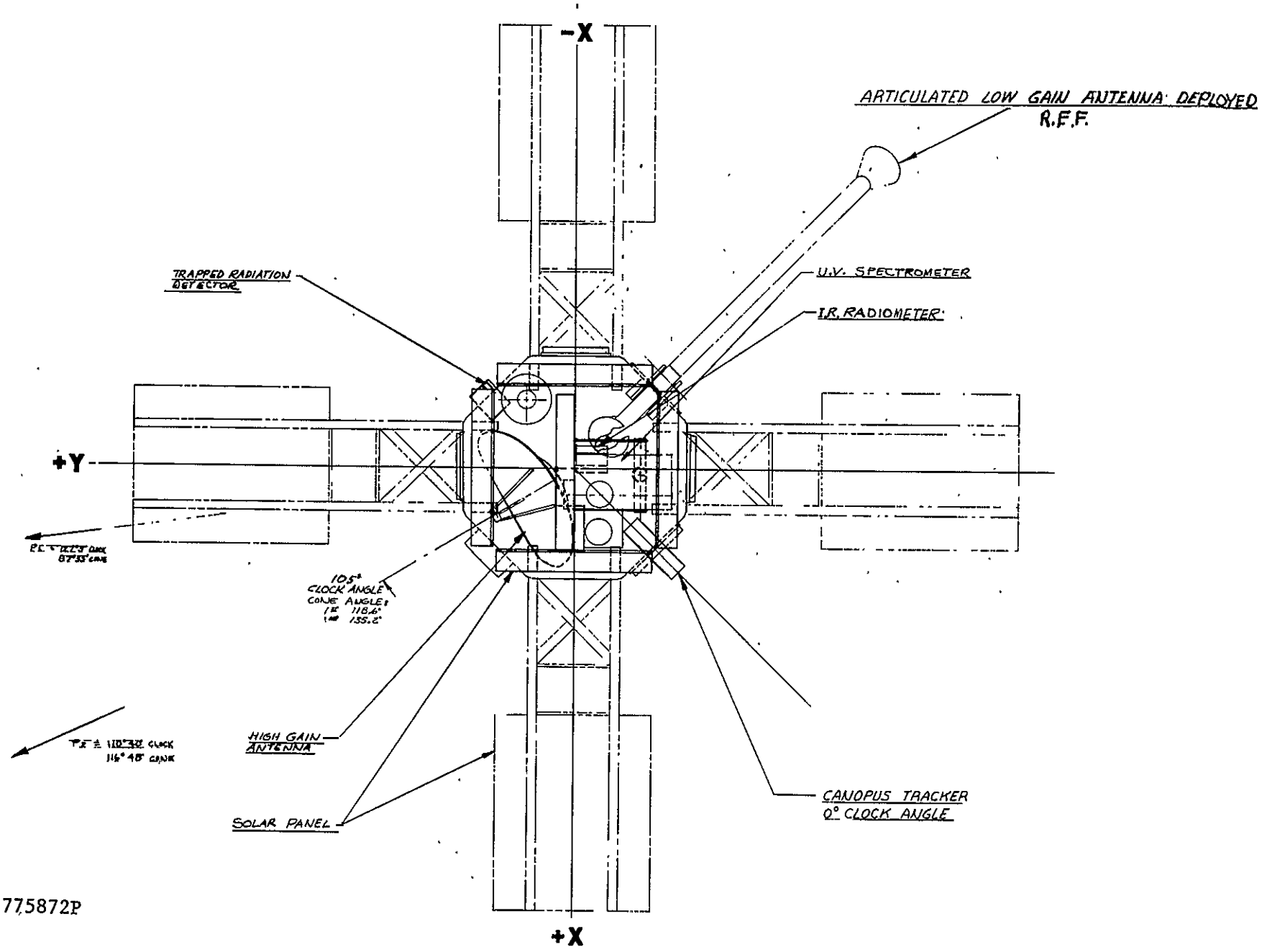


Figure 5.1b: Flyby Configuration 10a, Deployed

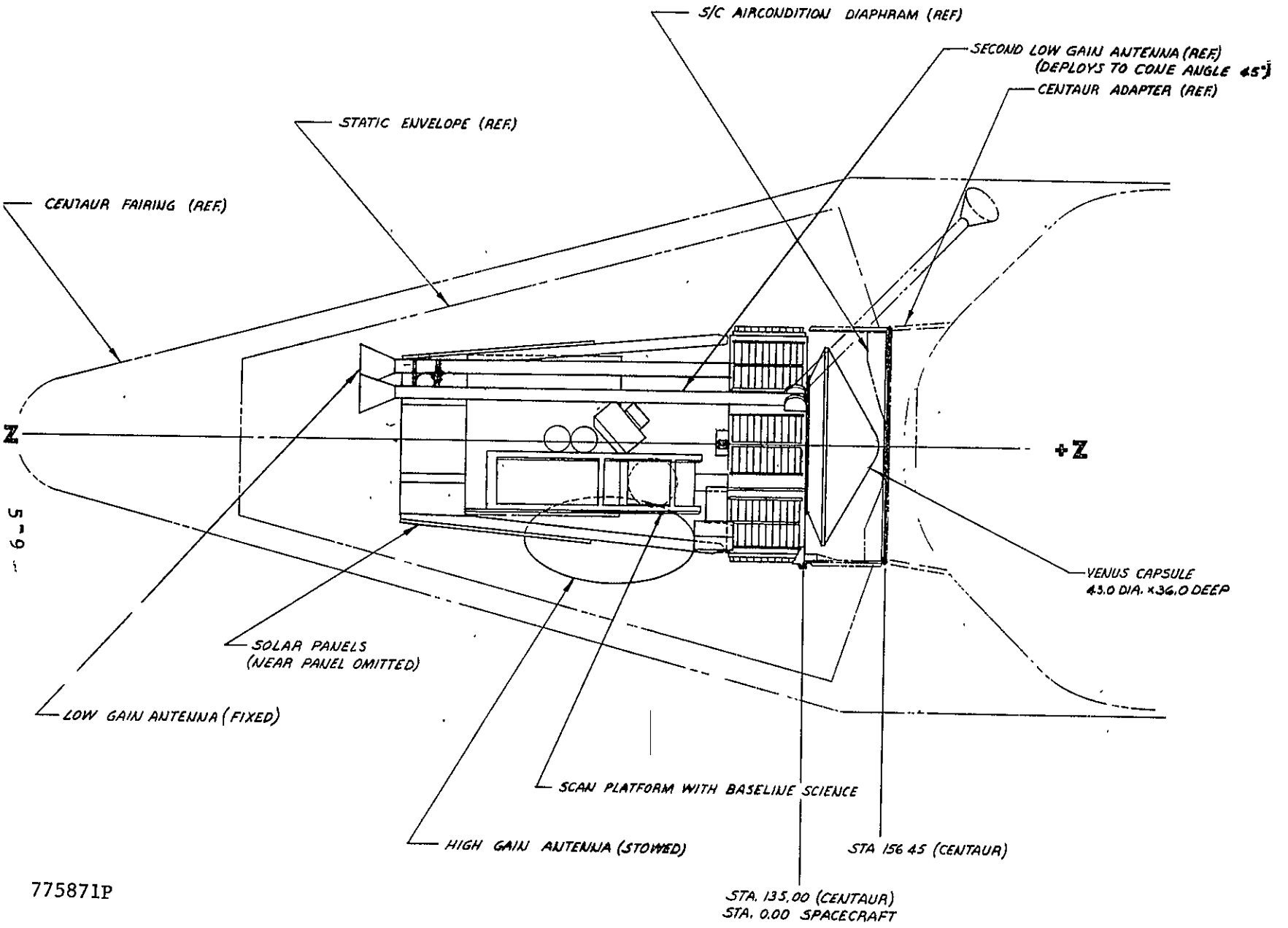
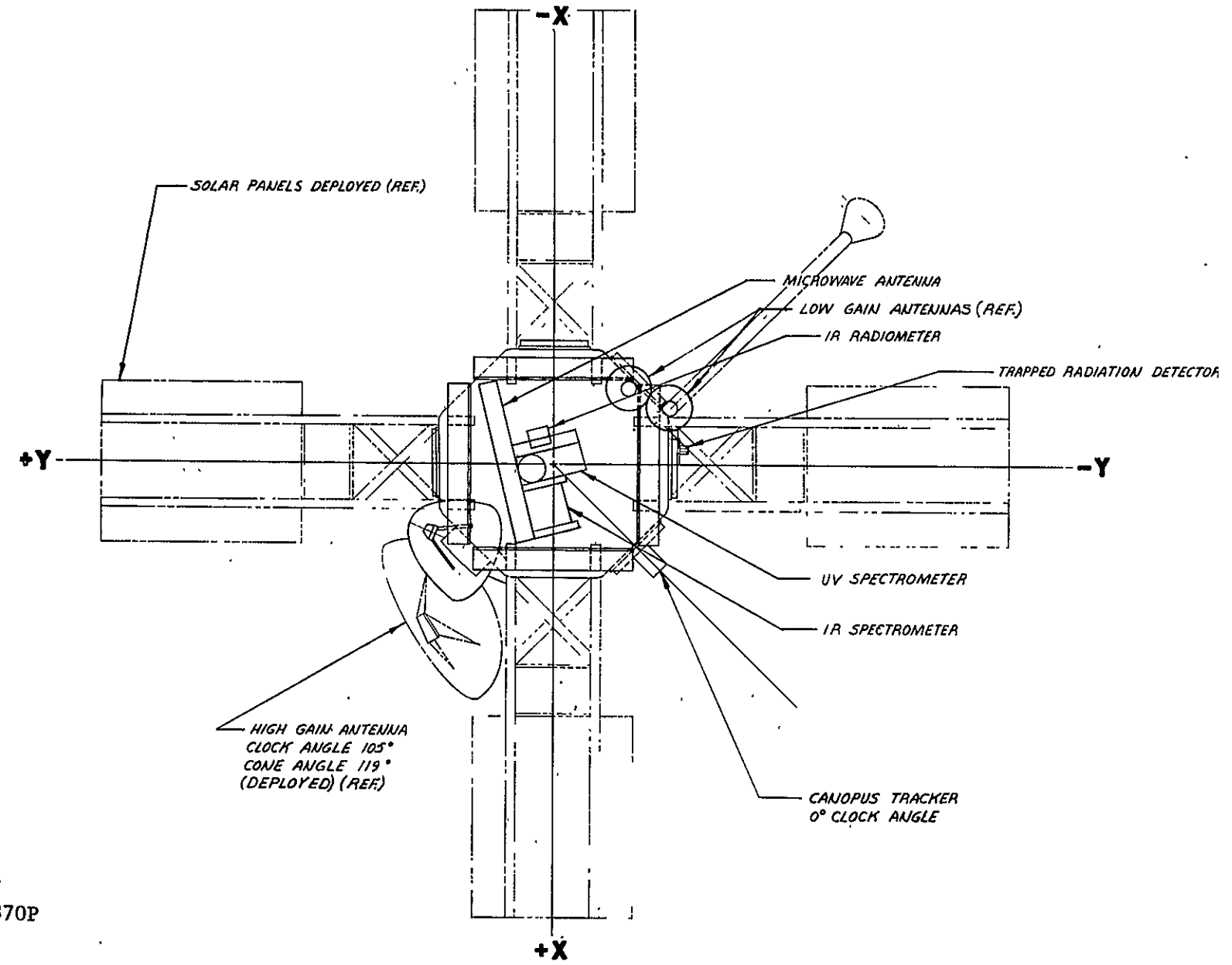


Figure 5.2a: Flyby Configuration 20a, Stowed



775870P

Figure 5.2b: Flyby Configuration 20a, Deployed

deployment maneuver. The fixed antenna view angle to earth is zero (0) degrees (very deep Null) during entry probe separation necessitating use of the second low gain antenna.

Configuration number 20a is the selected baseline. This is the only configuration that meets all of the science and communications view angle requirements completely and does not violate physical or weight constraints and affect a practicable structural arrangement. In addition, configuration number 20a utilizes a maximal number of Mariner 1969 structure assemblies. The scan platform of configuration number 20 mounts close to the flyby probe octagon which provides benefits in structure rigidity not available with the competing configurations.

5.2.1.2 Description of Entry Probe Configuration (No. 20A)

A single (43 inch diameter by 36 inch deep) is mounted under the Mariner Mars 1969 spacecraft octagon. The baseline science is on the scan platform; mounted above the spacecraft octagon. The 40 inch (major axis) by 23 inch high gain antenna is mounted on one of the solar panels. The flyby probe attitude maneuver during entry probe deployment requires two low gain antennas in order to maintain communications. The primary low gain antenna is fixed on the upper side of the octagon while the back-up low gain is articulated about a hinge mounted on the side of the octagon to point at a cone angle of 45 degrees and a clock angle of 270 degrees. The Mariner Mars 1969 solar panel design (solar cell area reduced to 44.8 ft^2), is applicable to this configuration with minimal modification. The major portion of the scan platform is cantilevered from its supporting structure. Figure 5.2 depicts two-views of this configuration.

5.2.1.3 Best RF Occultation Mission Configuration Selection

The entry probe for the Best RF Occultation Mission has a nose mounted rocket to satisfy encounter trajectory requirements, and is 54" in diameter to ease heat shield development. Following the approach of configuration 20a, the articulated high gain and low gain antennas are retained. As a result, of the larger adapter and increased requirements of the entry probe, the solar panel

hinge points are moved to the base of the octagon and both low gain antennas must be articulated to stay within the dynamic launch envelope. The launch configuration is shown in Figure 5.3.

The increased adapter size adds 48 lbs to the spacecraft, so that the total separated weight is 1235 lbs. The spacecraft weight summary is shown in Table 5.5

5.2.2 Alternate Missions

Alternate missions, embodying later arrival type I trajectories were considered to effect a low Venus approach velocity. The low Venus approach velocities (4.5 km/sec) are desired to confine the entry probe heating to valu not exceeding that demonstrated with Apollo technology. Trajectories having low approach velocities at Venus have relatively high injection energy requirements ($C_3 \approx 18.8$ km^2/sec^2) and, correspondingly lower available spacecraft injected weight capabilities. The late (August 3, 1972) arrival trajectory selected for the alternate missions restricts the maximum combined flyby and entry probe weights to 1245 pounds. The change is maximum permissible spacecraft weight (from 1665 to 1245 lbs) and changes in encounter trajectory geometry (from far side to near side encounter), were reflected in configuration studies described i the following paragraphs.

5.2.2.1 Configuration Approaches and Selection

The approach used in selection of alternate mission configuration consisted of selecting a configuration from the twenty-two studied during the baseline mission analysis and then modifying this design to fulfill the requirements and constraints of the alternate mission. The basic alternate mission constraint of a 1245 lb flyby/entry probe launch weight and the desire to reduce mission costs dictated that the flyby science complement be reduced and simplified. The approach taken to meet these revised objectives, was to

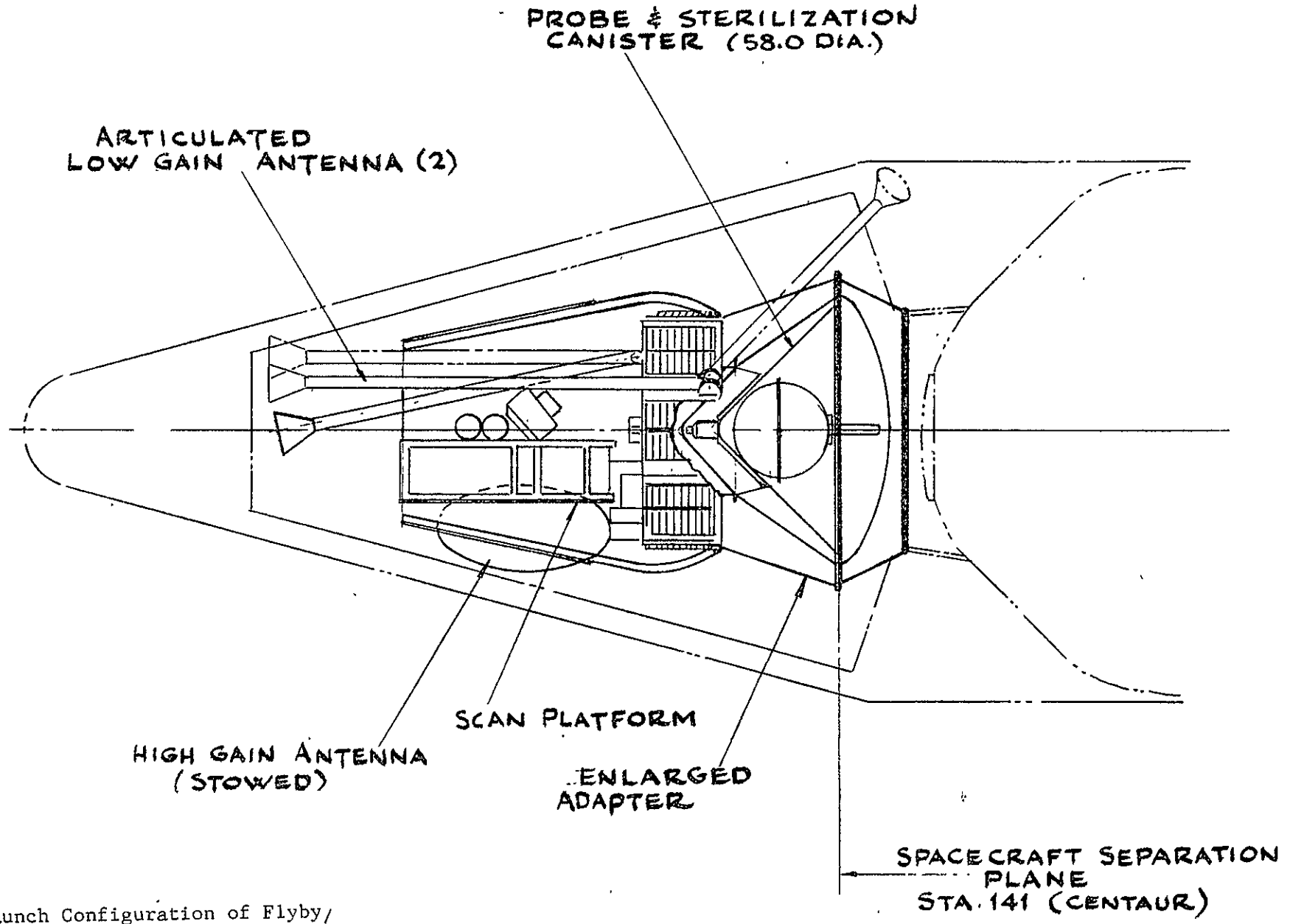


Figure 5.3: Launch Configuration of Flyby/ Entry Probe - Best RF Occultation Mission

Table 5.5

Baseline Mariner 72 Weight Table

	SUBSYSTEM	MM '69 ACTUAL WEIGHT, LBS.	BASELINE MV 72 WEIGHT, LBS
001	Structure	200.00	205.00
002	Radio Frequency	48.73	49.00
003	Command	9.50	9.50
004	Power	118.10	94.00
005	Central Computer and Sequencer	18.00	18.00
006	Flight Telemetry	23.80	23.80
007	Attitude Control	62.00	62.00
008	Pyrotechnics	13.00	13.00
009	Cabling	58.80	68.50
010	Propulsion	50.00	50.00
011	Temperature Control	29.11	29.00
012	Devices	43.50	27.30
014	Approach Guidance	-	-
016	Data Storage	42.00	22.00
020	Data Automation	23.00	23.00
	S/C Weight Less Science	739.54	89.00
031	Scan Control	14.50	24.50
034	Ultraviolet Spectrometer	30.00	30.00
036	Television	47.00	
037	Infrared Spectrometer	31.00	31.00
038	Infrared Radiometer	5.00	5.00
	Magnetometer		6.25
	Trapped Radiation		2.15
	Microwave Spectrometer/Imager		36.00
	Body Fixed Structure		
Total System Weight		867.40	829.00
S/C Adapter Increase			48.00
Probe			358.00
	TOTAL SEPARATED WEIGHT	867.40	1235.00

constrain the selected science complement to operate and deliver useful scientific information while mounted, body fixed, to flyby probe. In addition, the selected configuration must accommodate an entry probe below the flyby probe octagon and provide the proper probe release environment several days before planet encounter. A trade off study analysis of the various baseline spacecraft configurations resulted in the selection of Number 20a, as now the entry probe diameter was constrained to avoid adapter modifications. This configuration was selected as the alternate mission starting point because it required the least number of changes. Configuration 20a features a basic Mariner Mars 1969 octagon structure along with Mariner Mars 1969 solar panel structures reduced in size for the Venus mission. A single 43 inch diameter entry probe is located below the octagon, and a scan platform with associated baseline science is positioned above the octagon. A 40 inch high gain antenna is attached to one of the solar panel structural beams and is deployed when the solar panels are deployed. A low gain antenna is fixed to one of the top corners of the octagon and a second low gain antenna is articulated from a mounting structure attached to the side of the octagon.

Based on the starting point configuration Number 20a and a late arrival (August 3, 1972) near side flyby trajectory, a basic baseline science experiment complement was selected for a Minimum Mission and considered as Alternate No. 1. The changes to the baseline science complement consisted of:

1. Omitting the cruise science (Magnetometer and Trapped Radiation Detector).

2. Spacecraft body mounting the planet encounter science complement (IR and UV Spectrometers, IR Radiometer and Microwave Spectrometer/Imager).

Omitting the cruise science instruments and removing the scan platform in favor of spacecraft body fixing the planet encounter science instruments resulted in a flyby probe launch weight of 790.5 lbs and a flyby/entry probe launch weight of 931 lbs. The subsystem weights are summarized in Table 5.6. The decision

Table 5.6

Minimum Mission
Weight Table
(Alternate 1)

Subsystem	Weight, lbs.
Structure	205.00
Radio Frequency	50.00
Command	9.50
Power	94.00
Central Computer & Sequencer	18.00
Flight Telemetry	25.00
Attitude Control	62.00
Pyrotechnics	13.00
Cabling	60.00
Propulsion	50.00
Temperature Control	30.00
Devices	12.50
Data Storage	22.00
Data Automation	23.00
S/C Weight Less Science	674.00
Ultraviolet Spectrometer	30.00
Infrared Spectrometer	31.00
Infrared Radiometer	5.00
Microwave Spectrometer/Imager	36.00

Table 5.6 (cont.)

Subsytems	Weight
Body Fixed Structure	14.50
Total System Weight	790.50
Minimum Probe	141.00
Total Separated Weight	931.50 lbs.

Table 5.7

Minimum Mission Weight Table
(Alternate 2)

SUBSYSTEM	WEIGHT, LBS.
Structure	205.00
Radio Frequency	49.00
Command	9.50
Power	94.00
Central Computer and Sequencer	18.00
Flight Telemetry	25.00
Attitude Control	64.00
Pyrotechnics	12.00
Cabling	58.50
Propulsion	50.00
Temperature Control	29.00
Devices	27.30
Data Storage	42.00
Spacecraft Weight Less Science	683.30
Television	17.00
Total System Weight	700.30
Probe	141.00
TOTAL	841.30 LBS.

to omit the Trapped Radiation Detector and Magnetometer was based on:

1. The reduced effectiveness of these experiments from the early (baseline) arrival trajectory to the late arrival mission (70% to 40% for the magnetometer and 50% to 25% for the trapped radiation detector).

2. The relatively small loss of total scientific data obtained from the mission.

In addition, inclusion of a magnetometer would have required a magnetically clean flyby/entry probe resulting in additional expense for little additional scientific data return.

A second alternate configuration Minimum Mission Alternate No. 2, was also analyzed. This configuration consisted of a modified baseline Number 20a with the entire science complement and the scan platform removed and a single flyby probe body fixed wide angle television experiment installed on the top of the octagon. This flyby television configuration would weigh 700.3 lbs at launch, while total launch weight (flyby, television and entry probe assembly would weigh 841 lbs.). The subsystem weights are summarized in Table 5.7.

5.2.2.2 Description of Selected Configurations

Two Minimum Mission flyby probe configurations have been selected as follows:

1. Alternate No. 1 - body fixed encounter science only and one atmospheric entry probe.

2. Alternate No. 2 - body fixed television experiment and one atmospheric entry probe.

Both of these alternate configurations are based on a Mariner Mars 1969 spacecraft structure, a Mariner Mars 1969 solar panel design (solar cell area reduced to 44.8 ft^2) and a single 43 inch diameter atmospheric entry probe mounted below the octagon.

However, both of the alternate configurations differ from the baseline in the following areas:

1. The high gain antenna was moved from one of the solar panel support beams to a fixed position on top of the octagon.

2. The science scan platform was omitted.

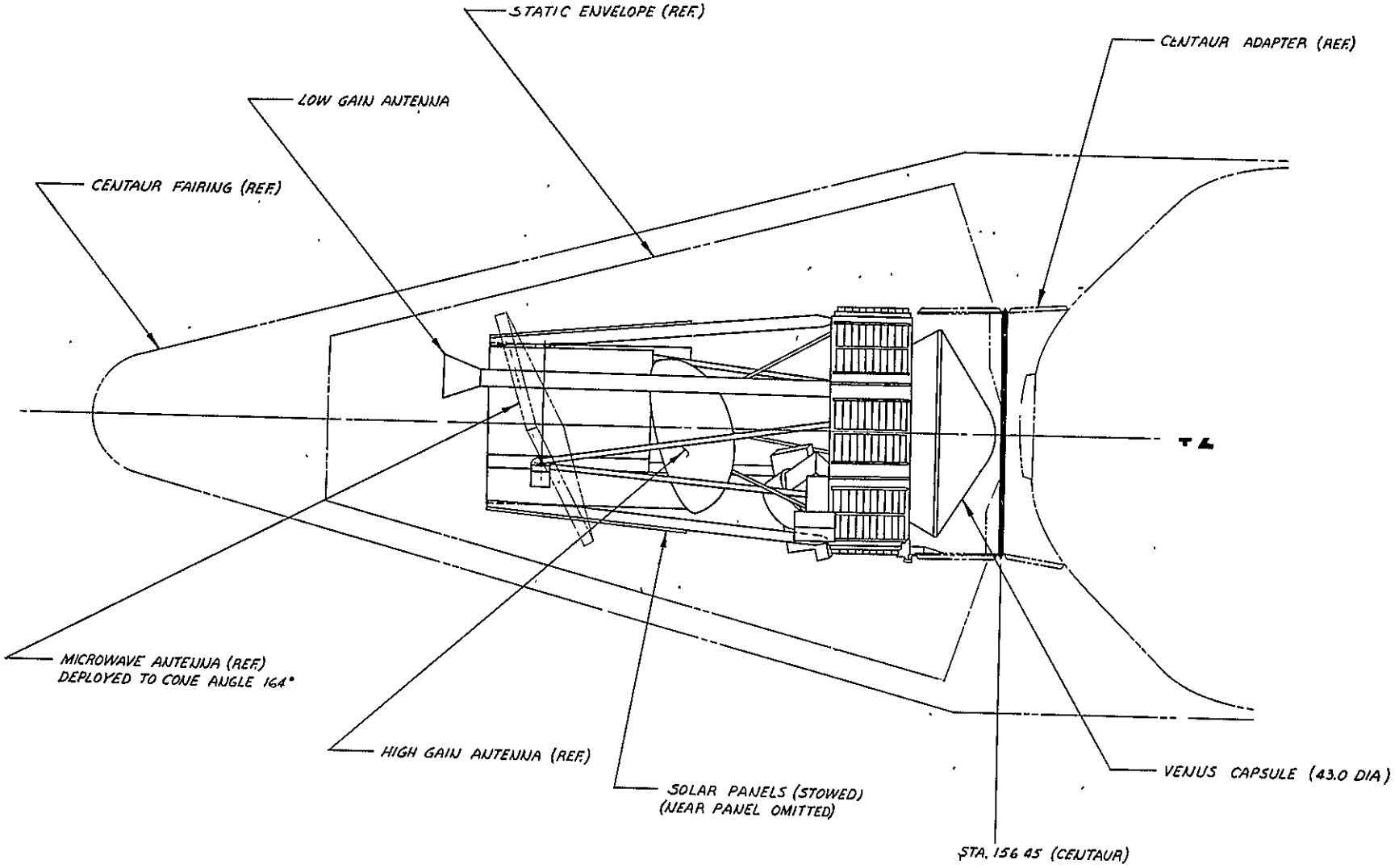
3. The articulated low gain antenna was omitted.

Moving the high gain antenna to a fixed position above the octagon was made possible by omission of the scan platform. For the baseline mission, the high gain antenna and the scan platform along with the science instruments all require nearly the same cone angle, approximately 90°. This required a physical separation of the two assemblies (Configuration 20a, Figure 5.2). For the alternate mission trajectory, the science instruments as well as the T.V. experiment require approximately a 164° cone angle, while the high gain antenna only requires a 110° cone angle. The combination of body fixing the science complement (Alternate No. 1) and the T.V. (Alternate No. 2), resulting in a lower height for these devices along with the more favorable cone angle requirements, allowed the high gain antenna relocation.

In the case of the articulated low gain antenna, the Best RF Occultation Mission trajectory (far side flyby) required a 135° cone angle change for entry probe deployment resulting in the need for a second low gain antenna in order to maintain communication links. The Minimum Mission trajectory (near side flyby) only required a cone angle change of approximately 45°, a value capable of being handled by a single low gain antenna.

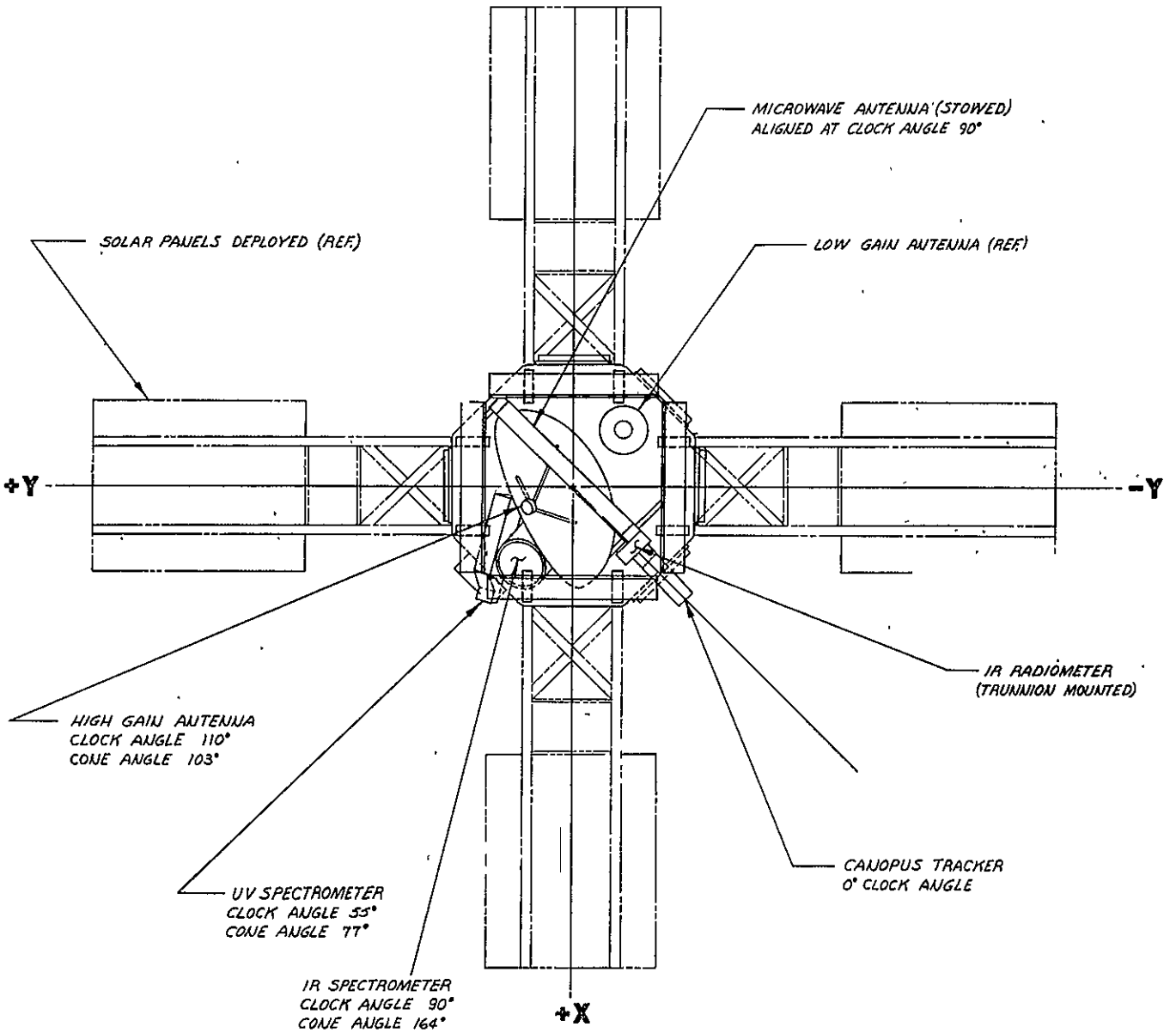
5.2.2.2.1 Minimum Mission Flyby Probe Alternate No. 1

Flyby Alternate No. 1 (Configuration No. 21, Figure 5.4) carries four body fixed science experiments for use at Venus encounter in addition to a 43 inch diameter entry probe mounted under the basic octagonal structure. IR and UV spectrometers, and IR radiometer and microwave spectrometer/imager make up the science complement. The low gain antenna is mounted rigidly to a top corner



775875P

Figure 5.4a: Flyby Configuration
Minimum Mission - Alternate 1,
Stowed



775874P

Figure 5.4b: Flyby Configuration - Minimum Mission Alternate 1, Deployed

of the octagon, and the high gain antenna is fixed to the upper surface of the octagon but above the two spectrometers and below the microwave antenna. The microwave antenna is trunnion mounted to permit stowing for launch and is deployed to a 164° encounter cone angle after launch. The radiometer is fixed to one side of the microwave antenna trunnion where a simple cam drive mechanism induces it to scan limb to limb. The IR radiometer, the IR spectrometer, and the microwave spectrometer/imager all require view angles along the nadir at periapsis--a cone angle of approximately 164°. The UV spectrometer requires a view angle along the negative of the velocity vector at periapsis--a cone angle of approximately 77°. The instrument slit is oriented normal to the trajectory plane--a cone angle of approximately 99°.

5.2.2.2.2 Minimum Mission Flyby Alternate

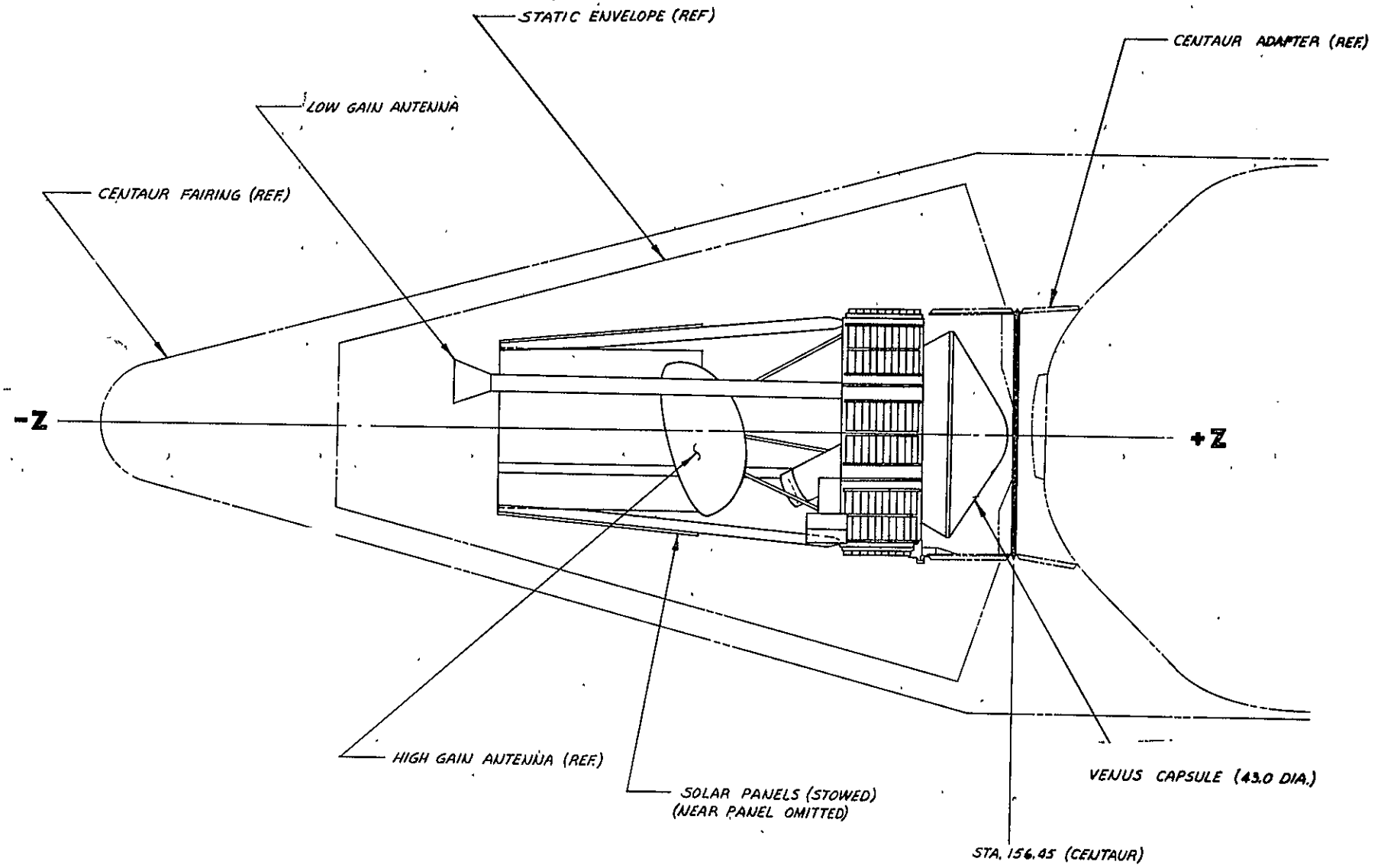
Flyby Alternate No. 2 (Configuration No. 22, Figure 5.5) is identical to Configuration No. 21 except that a single wide angle television experiment is carried in place of the planet encounter science complement. The camera and associated electronics are located at the same position on the octagon top as are the spectrometers carried on Configuration No. 21 in order to provide the camera with the same 164° cone viewing angle. Body fixing the camera at this position allows 17 pictures to be taken over a period of 20 minutes at Venus encounter (10 minutes before and 10 minutes after periapsis).

5.3 Subsystem Design

5.3.1 Structure and Mechanical Subsystem

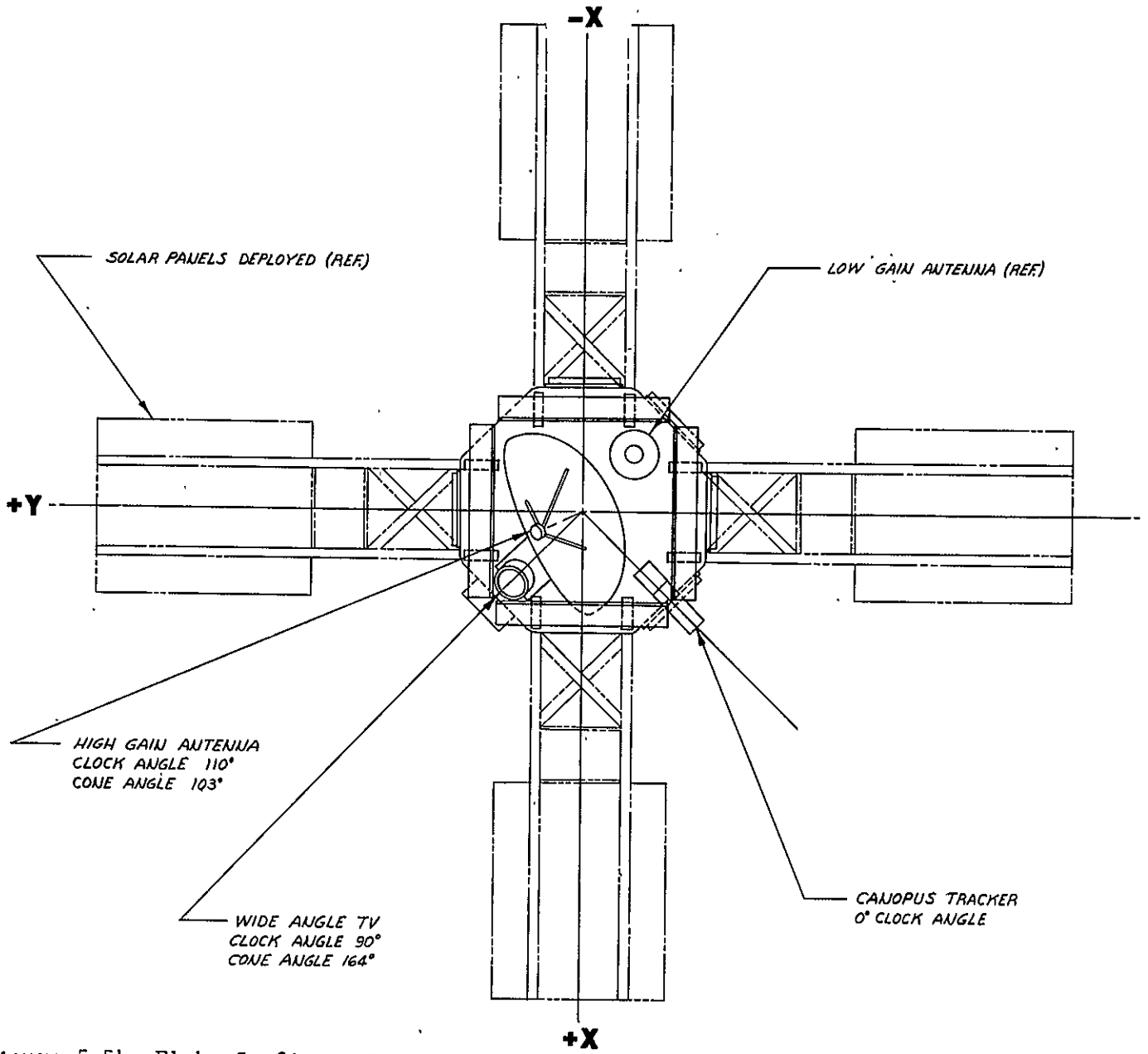
In accordance with study guidelines, all Mariner Mars 1969 structure was used where practical.

The interplanetary and encounter trajectory differences between the Mars and Venus missions causes the communications antennas and the scan platform to require mounting on the same side of the fylby probe. As a consequence of



775877P

Figure 5.5a: Flyby Configuration - Minimum Mission - Alternate 2, Stowed



775876P

Figure 5.5b: Flyby Configuration - Minimum Mission - Alternate 2, Deployed

these requriements, the major structural modifications to Mariner 1969 for effecting the Mariner 1972 system are (1) relocating the scan platform and its supporting structure to the top of the octagon, (2) providing a structural interface for the capsule on the lower side of the octagon, and (3) providing structure to support and position both low gain and the high gain antennas. All Mariner Mars 1969 mechanical devices are usable and required by the Mariner 1972 Venus configuration with the exception of the scan platform latch. The latch for the Mariner 1972 need not be as sophisticated due to the scan platform taking the launch loads in compression. In addition, two new devices are required, one to position the high gain antenna (RF occultation experiment) and the second to deploy and latch the second low gain antenna.

5.3.1.1 Functional Requirements

The structure subsystem supports all the other subsystems throughout the life of the flyby probe; before, during, and after launch.

The mechanical subsystem functionally provide all necessary mechanical motions which separate flyby/entry probe from booster, deploy all articulated equipments and position all mechanical devices such as the positional scan platform.

5.3.1.2 Functional Description

The principal structure is the Mariner Mars 1969 octagon with provisions to accommodate the solar panels, capsule, scan platform, and communications antennas geometrically arranged to provide the required functional interactions between subsystems for the Venus mission. Mariner Mars 1969 electronic packaging, cabling, and other internal subsystems are duplicated in the Venus 1972 spacecraft to the maximum extent practicable.

The mechanical subsystem consists of all pin pullers, thrusters, spring devices, and their associated mechanical latches, locks, and

dampers required to deploy, position, release, and perform such other movements necessary to accomplish the spacecraft mission.

5.3.1.3 Functional Modifications from Mariner Mars 1969

The structure and mechanical subsystems of the baseline Mariner Venus 1972 spacecraft differ functionally from Mariner Mars 1969 in that (1) the high gain antenna is positionable for RF occultation, (2) a second, articulated low gain antenna is added to maintain communications during capsule deployment, and (3) the atmospheric entry capsule is added. The modifications to the Mariner 1969 which result in the Mariner Venus 1972 are graphically shown in Figures 5.2 and 5.3. The rearrangement of the Mariner 1969 scan platform attachment spider to act as the capsule attachment is shown in Figure 5.6.

Modifications of the Mariner 1969 structure to serve the functional requirements of the Venus 1972 alternate missions are similar to those for the baseline mission with the following exceptions:

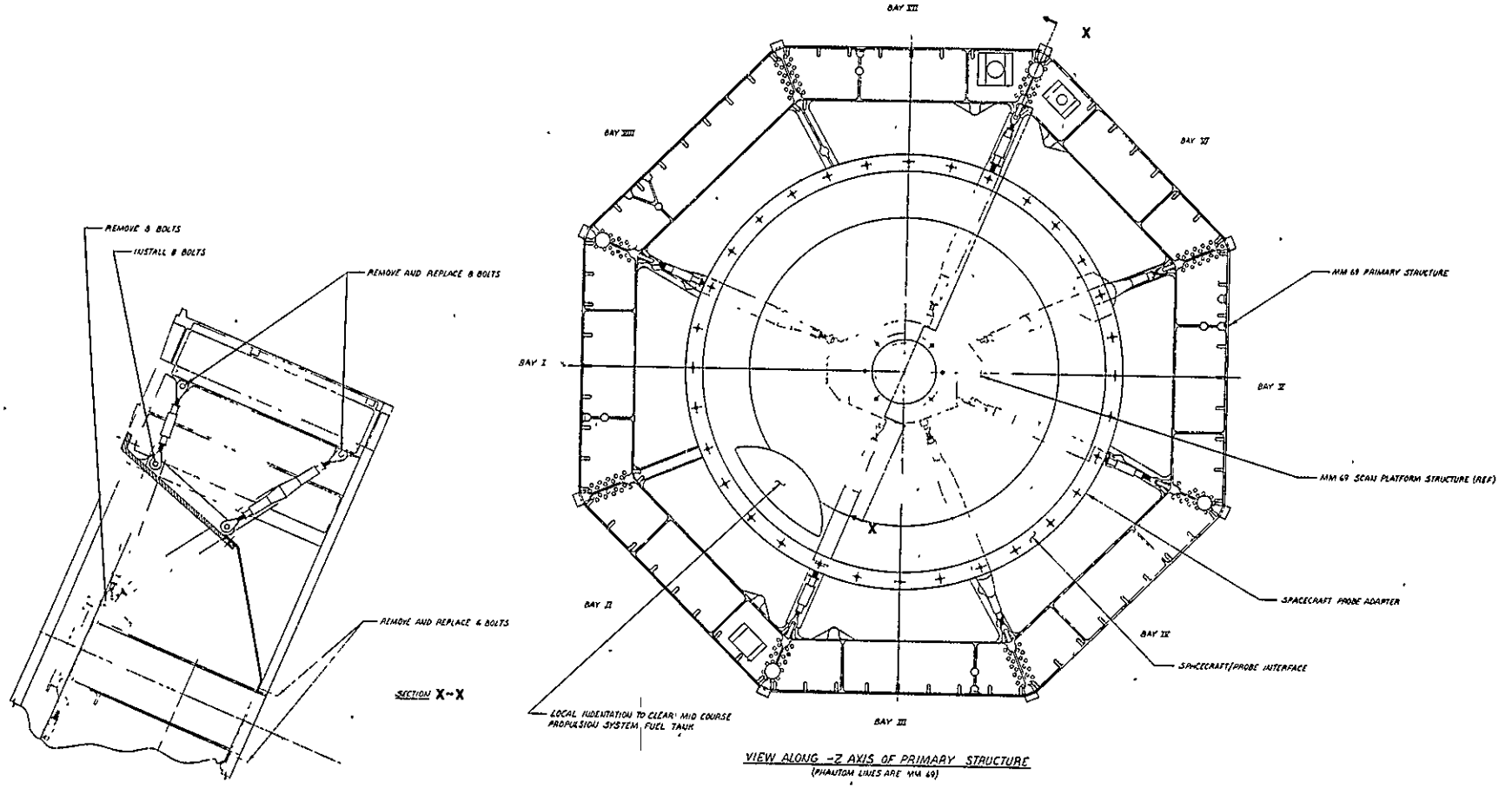
a. The scan platform and its structural support are deleted, and the flyby probe experiments are affixed to the primary and superstructure elements;

b. The articulated (second) low gain antenna, its support trunnion and deployment mechanisms are deleted.

5.3.2 Scan Platform Subsystem

5.3.2.1 Functional Requirements

The scan platform enables the flyby probe to maintain Sun-Canopus lock while pointing the experiment sensors in the desired direction during the encounter phase of the mission. The scan platform control electronics must have the capability to update the platform cone and clock angles through the flight command system (FCS). The scan platform positions are derived from the following look angle requirements.



775878P

Figure 5.6: Structural Interface of Flyby/Entry Probe

a) Position the UV spectrometer slit parallel ($\pm 3^{\circ}$) along its length to the tangent to the planet at the sub-image point.

b) Erect the scan platform perpendicular to the trajectory at periapsis.

c) Position the microwave imager-spectrometer to view along the nadir.

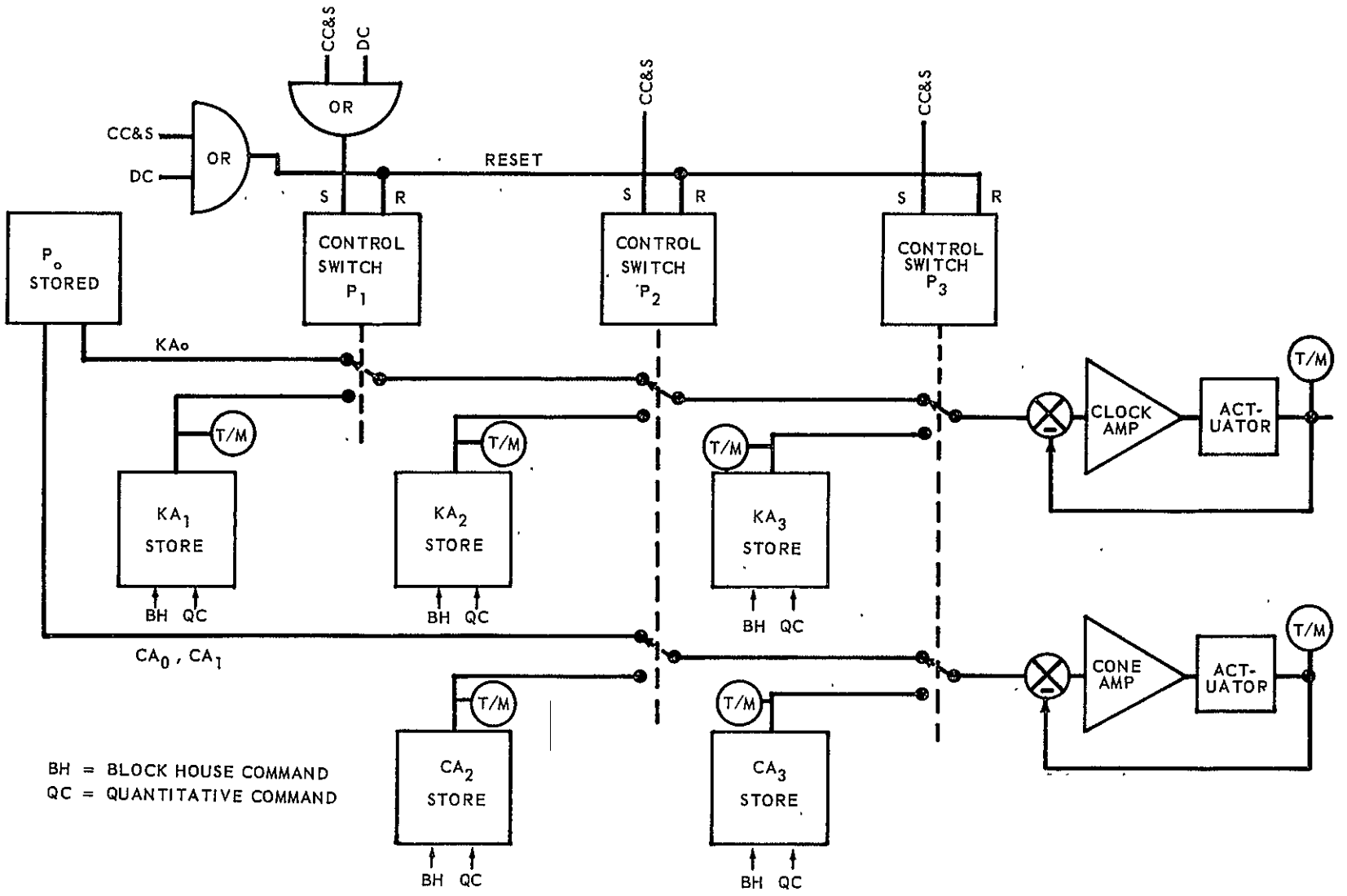
5.3.2.2 Functional Description

The scan platform converts stored information which is in the form of electrical signals, into angular positions on command. The electrical signals are entered into storage prior to launch by blockhouse command (BH) and updated during the course of the mission via the FCS by quantitative command (QC). The platform is commanded to the near encounter position either by direct command or by the commands stored in the central computer and sequencer (CC&S). The commands to slew the platform to the remaining two positions are originated in the CC&S. Figure 5.7 presents the scan platform functional block diagram.

5.3.2.3 Functional Modification from Mariner 1969

The major change in the scan platform subsystem is the deletion of the far encounter control circuitry required for planet tracking by the Mariner 1969 television subsystem. The Mariner Venus 1972 scan platform control circuitry is, therefore, a simplified version of that used on Mariner 1969.

Baseline Mariner Venus 1972 cone and clock scanning angle requirements, which differ from those of Mariner 1969, are accommodated with minor modifications. The clock angle capability of 25° through 145° is required for Mariner Venus 1972; the Mariner 1969 capability is 90° to 305°. The cone angle capability of Mariner 1972 is 68° to 167°; the Mariner 1969 capabilities are 101° to 165°. The scan platform and its associated control electronics are deleted for the alternate missions.



775939 P

Figure 5.7: Scan Platform
Functional Block Diagram

5.3.3 Attitude Control Subsystem

The attitude control subsystem orientes the spacecraft during all portions of the Mariner Venus 1972 mission. It provides stellar reference orientation during the cruise portion of the mission. Prior to midcourse propulsion and probe deployment maneuvers, the attitude control system provides previously calibrated commanded turns. During midcourse propulsion phases and during flyby separation sequence, the attitude control system maintains a constant orientation of the spacecraft. The attitude control system provides control torques, control logic, and attitude sensing during cruise, commanded turn, and probe deployment modes. During the midcourse maneuver, the jet vanes on the midcourse maneuver engine provides the necessary control torques.

5.3.3.1 Functional Requirements

Functional requirements of the attitude control subsystem are a direct function of the Mariner Venus 1972 mission profile. This is illustrated in Figure 5.8. The release of one or more entry probes and the resultant variations in slyby probe mass properties strongly affect attitude control requirements.

During the cruise limit cycle mode, the attitude control system is required to keep the roll, pitch, and yaw axes alinged to the steller reference axes within 8 milliradians. Following separation from the launch vehicle the attitude control system is required to stabilize in a limit cycle mode from any orientation within a period of thirty (30) minutes and from an initial tumbling rate of up to 50 milliradians per second. The attitude control system must also acquire the primary stellar references following all midcourse and entry probe deployment manuevers or disturbances such as meteoric impacts.

Midcourse propulsion maneuvers are carried out at two (2) to ten (10) days following launch and again approximately midway along the Earth

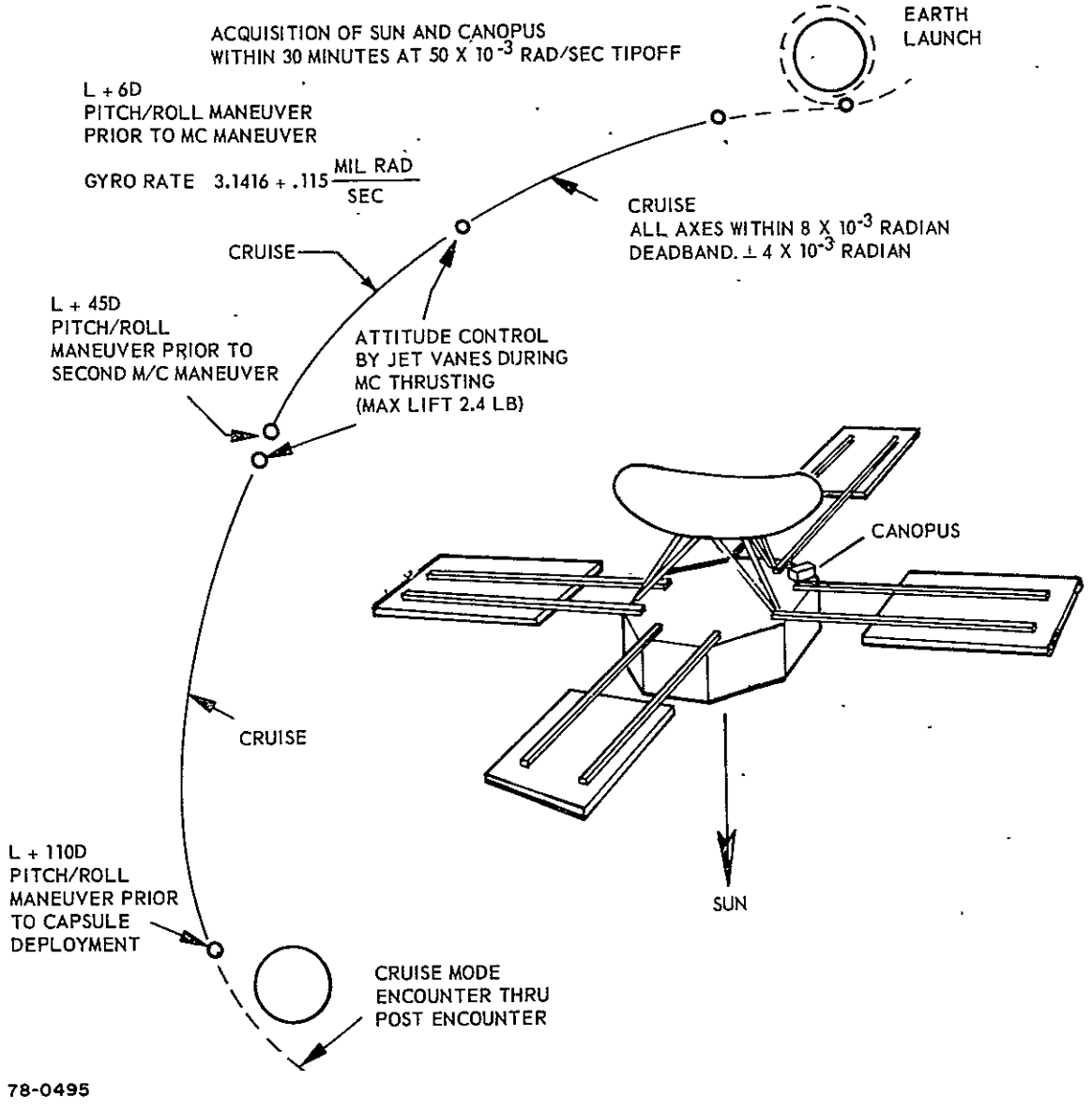


Figure 5.8 Attitude Control Requirements

Venus heliocentric trajectory (approximately 50 days after launch). The midcourse maneuvers are preceded by a sequential commanded turn which is implemented by the attitude control system.

The attitude change sequence is a calibrated pitch maneuver followed by a calibrated roll maneuver. The turn command is transmitted to the spacecraft from earth with CC & S backup stored command provided. During commanded turns, the three axis gyro system becomes the primary reference, and the rotational rate is constant at 3.1416 $\pm$ .155 milliradians per second. Gyro drift is limited to no greater than .003 t_I milliradian; where t_I is the time for the midcourse propulsion maneuver. The attitude control system must control the jet vanes on the midcourse engine in order to hold the flyby/entry probe attitude during the midcourse propulsion sequence. Attitude control torques are to be provided by the proportional deflection of the midcourse propulsion engine jet vanes.

The entry probe deployment maneuver is initiated approximately six (6) days prior to encounter (nominally 116 days for encounter). Commanded turns are accomplished by the attitude control system similar to that for a midcourse propulsion maneuver. The attitude control then must hold the flyby probe attitude within 1^o for the period required for each entry probe deployment.

5.3.3.2 Functional Description

Attitude control subsystem mechanization is illustrated in Figure 5.9. The limit cycle is acquired by means of cold gas nitrogen jets sized to the inertial requirements of the Mariner Venus 1972 mission. The attitude control jets produce angular accelerations of .83 milliradian/second^2 about the pitch and yaw axes and .91 milliradian/second^2 about the roll axis. The Mariner Venus 1972 attitude control subsystem utilizes derived rate feed back to provide stable limit cycle acquisition and to inhibit spurious signals from causing

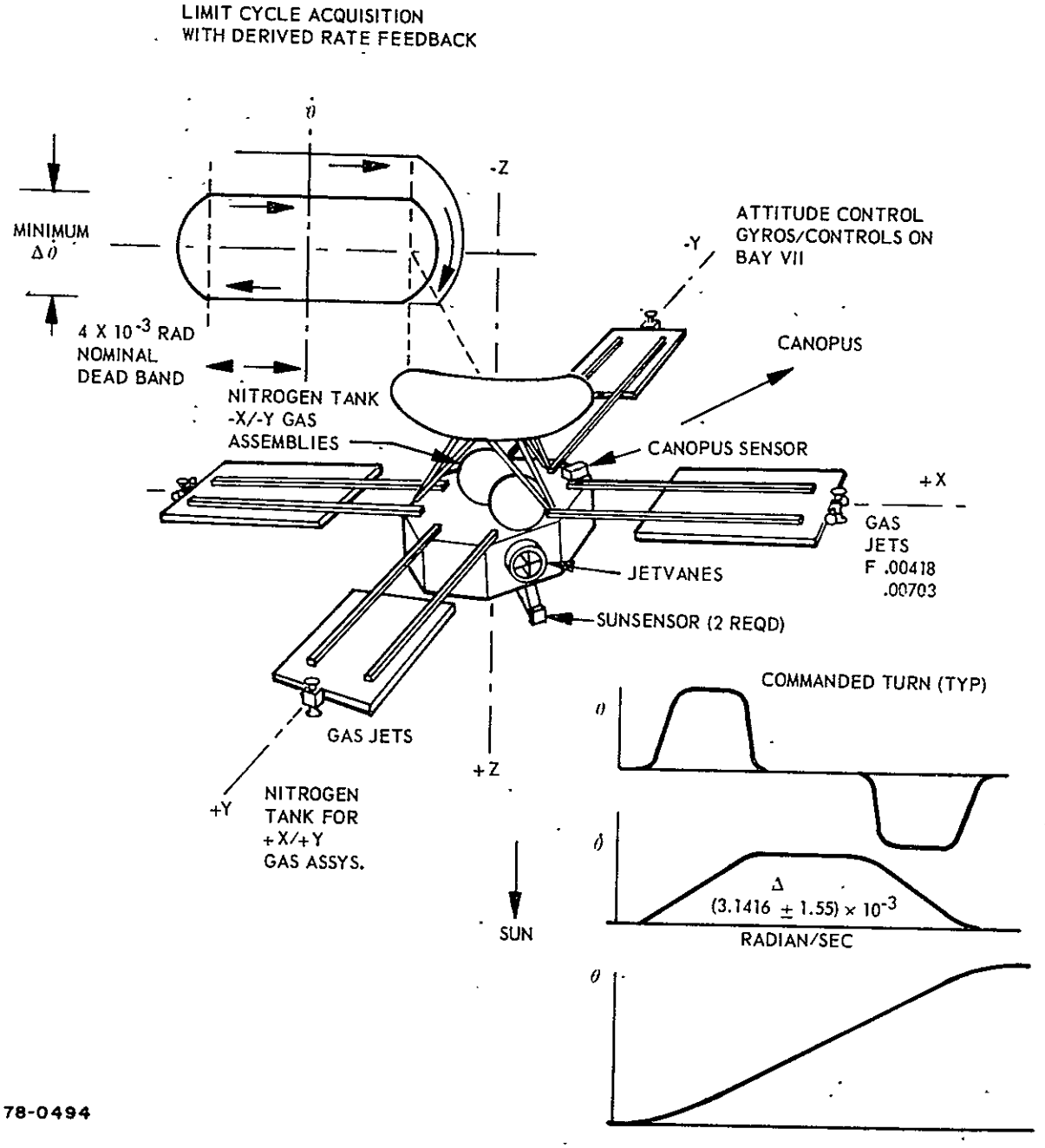


Figure 5.9 Attitude Control Mechanization

unnecessary opening of the gas jets. The flyby probe rotational drift velocity is predicted and the gas valves receive a signal to close early. During cruise the limit cycle is maintained at $\pm$ 4 milliradian with the Sun and the star Canopus as references.

The nitrogen gas for the attitude control system is contained in two tanks. The tanks are connected to the gas jets to create two parallel systems working together. Failure of a single gas system results in thrust being applied by a single jet instead of two jets. A slight translational motion is imposed on the spacecraft when single jet operation occurs. Either tank has sufficient gas to complete the mission.

Flyby/entry probe moments of inertia were estimated for several configurations. These are tabulated in Table 5.8 and and a direct function of capsule configuration.

Table 5.8

Principal Inertial Characteristics of Mariner Venus 1972 Spacecraft

Principal Moments of Inertia slug ft^2	Baseline Configuration and Probe (1350 lbs.)	No Probe (956 lbs)	Two Probes (1200 lbs)
Izz	160	140	82
Ixx	100	80	155
Iyy	100	80	73

The baseline attitude control gas system weighs 64 pounds; and has a volume of 2500 cu inches. Five (5) pounds of pure N_2 gas are stored within the two nitrogen tanks.

Commanded turns for midcourse and entry probe deployment maneuvers are accomplished at constant rotational rate; first about the pitch axis, and then about the roll axis. The fixed rotational rate of 3.1416 $\pm$ 0.155 milliradian per second is reached within 4 seconds. Primary reference for commanded turns is the three axis gyro system.

Flyby/entry probe attitude is controlled by the midcourse propulsion unit jet vanes during midcourse engine firing. The primary reference is the three axis gyro system. Attitude control gas jets remain active during midcourse propulsion operation. This has an advantage of supplying additional control torques about the engine thrust axis. It is, however, somewhat wasteful of attitude gas.

Flyby/entry probe attitude is controlled by the gas jets during entry probe deployment phases. The allowable uncertainty in attitude is $\pm 1^{o}$. The primary reference during capsule deployment is the three axis gyro system up to entry probe separation. This is 12 minutes after completion of the required commanded turns.

The single probe baseline configuration is devoid of attitude control problems. Configurations with two probes and asymetric loading of the spacecraft exhibit tip off rates that require an increase in attitude control thrust level for proper control. The effects of asymetry result in gas volume increases to 2400 cubic inches. Attitude control gas system size increases correspondingly, from 2500 cubic inches and 64 pounds to 3700 cubic inches and 72 pounds.

5.3.3.3 Functional Modifications from Mariner 1969

The Mariner Mars 1969 exhibits a lower moment inertia than is estimated for the Mariner Venus 1972 spacecraft. The Mariner Venus 1972 gas jets have, therefore, increased thrust level to compensate for the higher moments of inertia. The Mariner Venus 1972 mission profile is of shorter duration than Mariner 1969 mission compensating for the increased thrust or sizes. As a consequence, propellant loadings and nitrogen gas system component sizes and design are the same for Mariner 1972 as for Mariner 1969.

The Mariner Venus 1972 mission has the +Z axis towards the Sun as contrasted to Mariner Mars 1969 with the -Z axis toward the Sun. The sola sensors and Sun gates are located on the opposite side of the spacecraft octagon as compared to Mariner 1969.

The Mariner Venus 1972 attitude control system must have a provision for a third commanded turn prior to entry probe separation and must control flyby probe attitude during entry probe deployment. This is not required by the Mariner Mars 1969 mission.

For a trajectory that results in Canopus occultation, provision must be made to provide gyro redundancy during the occultation period. This is accomplished by:

Having the gyro slaved to the Canopus sensor prior to occultation to compensate for gyro drift.

Providing for a gyro error signal during occultation for roll control.

The above functions can be accomplished in the manner depicted in the functional block diagram presented as Figure 5.10.

5.3.4 Thermal Control Subsystem

The thermal control subsystem maintains flyby probe temperature within the acceptable operational and survival limits established for experiments and spacecraft components. The flyby probe is isolated from solar and planetary inputs by means of thermal insulation blankets as required to maintain the requisite thermal balance. Heat generated internal to the flyby probe is transferred along transfer paths to radiating surfaces that are decoupled as much as possible from solar inputs. Temperatures are regulated by modulating radiator emissive characteristics with temperature controlled louvers. The temperature control system maintains flyby probe temperature relatively constant with the

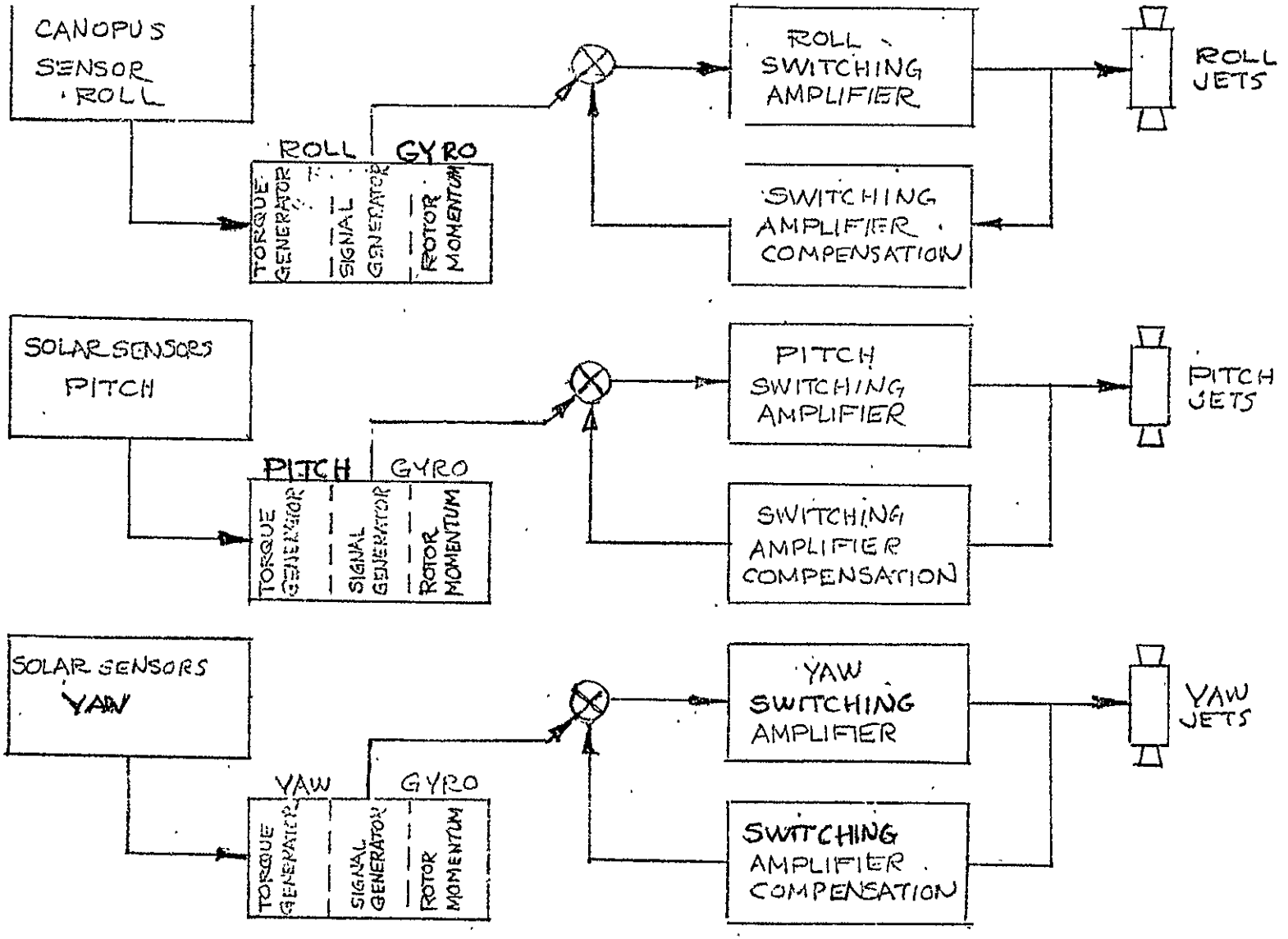


FIGURE 5.10 ATTITUDE CONTROL FUNCTIONAL BLOCK DIAGRAM WITH CANOPUS OCCULTATION AT PLANET

variable heat rejection rate and changing solar distances associated with the Mariner Venus 1972 mission.

5.3.4.1 Functional Requirements

The Mariner Venus 1972 flyby probe will carry an entry probe to the planet Venus. The presence of the probe's biological shield modifies heat transfer paths within the spacecraft structure. For the Mariner Venus 1972 mission, the flyby probe attitude is oriented with the +Z axis facing the Sun. Figure 5.11 illustrates the significant thermal requirements that evolve as a result of the Mariner Venus 1972 mission profile.

Following entry probe deployment, the flyby probe must remain isolated from the entry probe biological shield. Excessive heating of the flyby probe by conductance of the heat flux from the capsule shield could otherwise occur.

The relatively small amount of heat generated within the entry probe during heliocentric transfer must be radiated to space. Only a small amount of heat can be permitted to leak through the biological shield into the flyby probe structure.

The louvers must be isolated from direct solar inputs as well as reflected and re-radiated inputs from adjacent solar panels. The panels are a particularly significant heat source at Venus distances where they reach temperatures of 250° F.

During the mission, wide variations in heat load occur on bays V, VI, and VII. The highest heat dissipation rate occurs on bay VI during post encounter transmission of data to Earth. At Venus encounter, the insolation and reflection from the planet are both high. This represents the most severe thermal environment of the mission. Solar irradiation is 840 BTU/ Hr Ft^2, and because planetary abbedo of Venus is high, a large quantity of heat is reflected

MARINER VENUS 72
SIGNIFICANT THERMAL SUBSYSTEM REQUIREMENTS

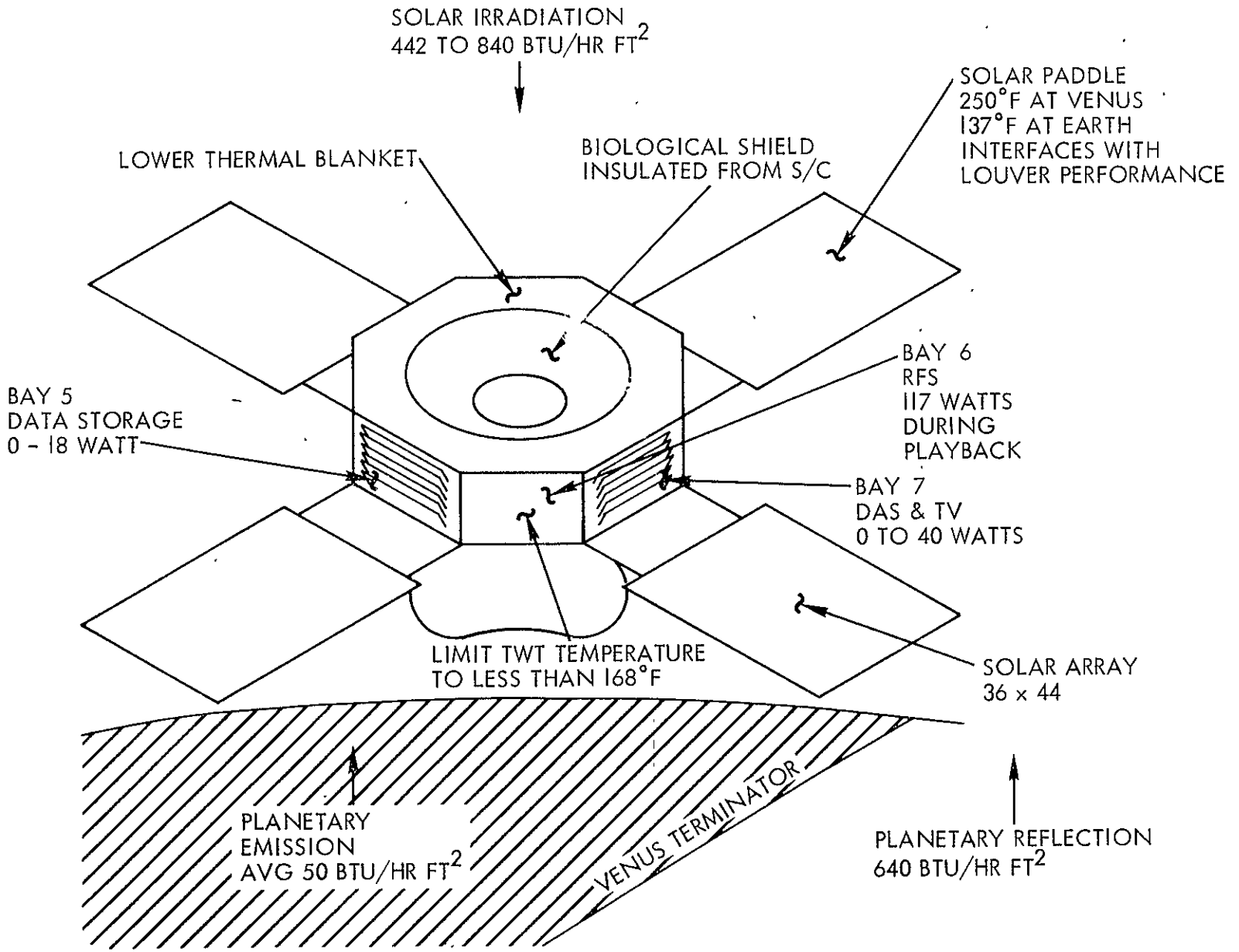


FIGURE 5.11 THERMAL CONTROL SUBSYSTEM REQUIREMENTS

back to the flyby probe (640 BTU/Hr Ft^2). Planetary emission is expected to be relatively small (50 BTU/Hr Ft^2).

During all portions of the mission, the temperature of the flyby probe must never go below 40° F nor above 125° F. The battery temperature must remain above 40° F. The propulsion system monoprepellant should be kept below 125° F. The only exception to these temperature limits is the radio transmitter bay (Bay VI). The temperature of the TWT must be kept below 168° F.

5.3.4.2 Functional Description

The Mariner Venus 1972 flyby probe thermal control subsystem is designed to use the techniques used for thermal control of earlier Mariner spacecraft to a maximum extent. The solar and planetary heating inputs are minimized to a maximum extent by coatings and insulation so as to permit louvers mounted to electrical/electronics equipment bays to regulate the flyby probe temperatures within narrow limits. The louvers compensate for variations in electrical power losses. Thermal blankets completely enclose the lower and upper portions of the flyby probe. The lower thermal shield on the +Z side of the flyby probe is extended over the edge of the octagon. This prevents solar irradiation inputs to radiating surfaces when the solar cone angle is off zero. Thermal blanket performance is expected to be at least as good as that for Marine Mars 1969 and Mariner Venus 1967 blankets. The latter is equivalent to a black body radiator with an area of 0.7 square feet.

The effect of thermal blanket performance upon flyby probe temperature is illustrated in Figure 5.12. Normally with the louvers closed flyby probe temperatures increase until a pre-adjusted temperature is reached. The louvers then open, maintaining a relatively constant temperature until the louvers are wide open. Increase in I^2R power loss beyond the condition where louvers are fully open will result in an increase in flyby probe temperature.

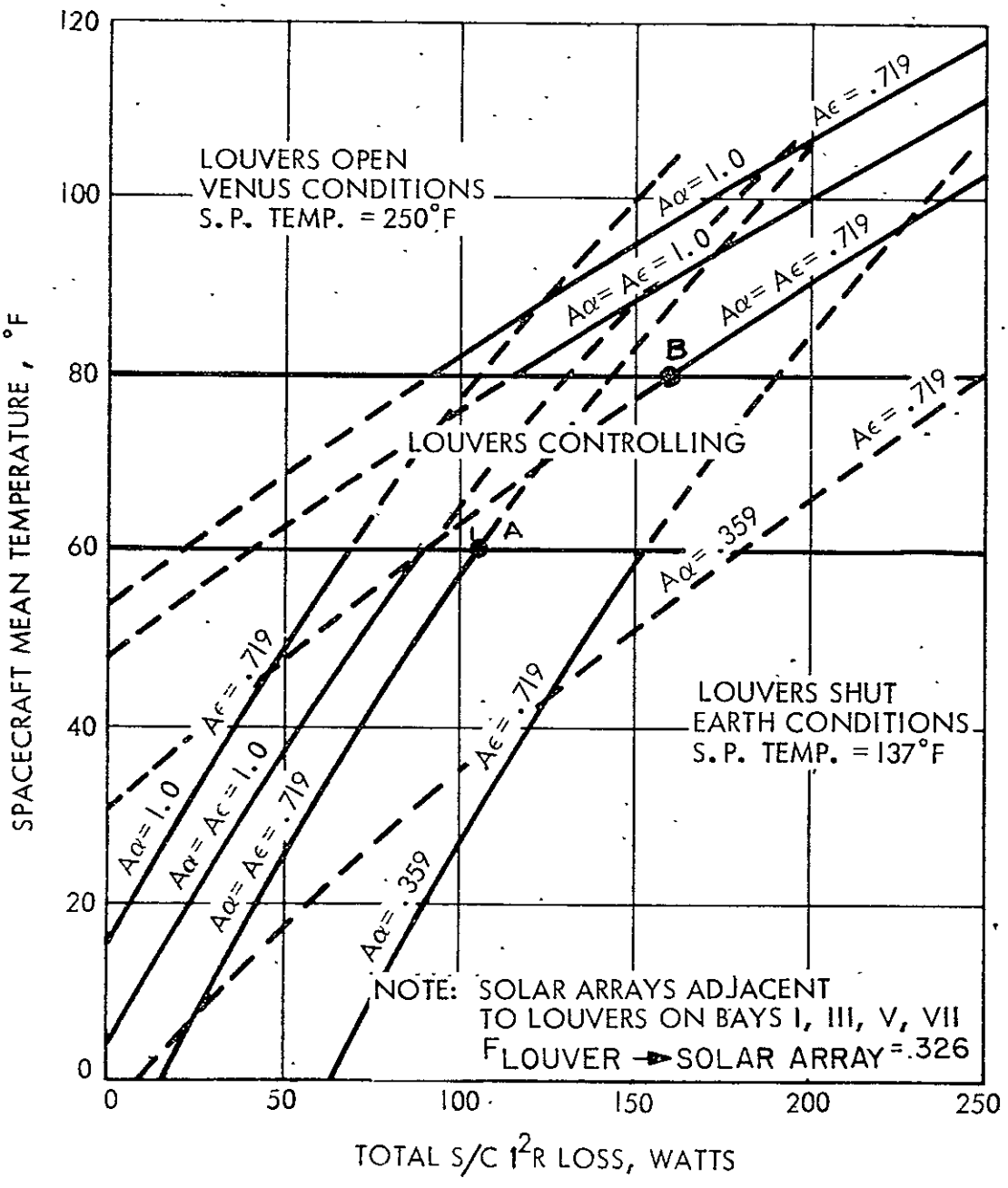


FIGURE 5.12 THERMAL BLANKET PERFORMANCES

For example, if $\alpha A = \epsilon A = 0.716$ ft^2, the louvers will begin to open at Point A and will be completely open at Point B. Increasing ϵ and decreasing α will increase the range of allowable heat dissipation for which the louvers can control flyby probe temperatures. This is done by using a thin plastic (Teflon) coating for the outside layer of the thermal blanket..

The presence of the solar arrays interferes with the performance of the louvers particularly during periods when the flyby probe is close to Venus. During the encounter and post-encounter phases, the flyby probe must reject the largest quantity of heat. At this time, the solar panels are at their highest temperature of 250° F and are an additional heat source to adjacent louvered radiator surfaces. Figure 5.13 illustrates the influence of solar array heat inputs upon flyby probe temperature at Venus encounter. In order for flyby probe temperatures to remain below 80° F with the louvers wide open, the solar arrays must be 19-inches or more from the nearest louvered radiator surface.

During the playback mode, following planetary encounter, the RF transmitter will be operating at 20 watts of radiated power. This results in a total heat loss of 83 watts from the TWT amplifier and its power supply. When this is added to the rest of the RFS losses, just under 120 watts of heat energy must be removed from Bay VI and radiated to space. The temperature of the TWT collector is only a few degrees less than its upper limit at this time. In order to maintain RFS temperatures within acceptable levels, it is necessary to improve the shear plate design, increase contact resistance between the heat dissipation elements, and provide adequate heat paths behind the radiator and within the flyby probe. Bay VI temperatures are shown in Figure 5.14.

The most significant features of the Mariner Venus 1972 thermal control subsystem design are illustrated in Figure 5.15. The thermal blanket will be modified to accommodate the entry probe and biological shield. The

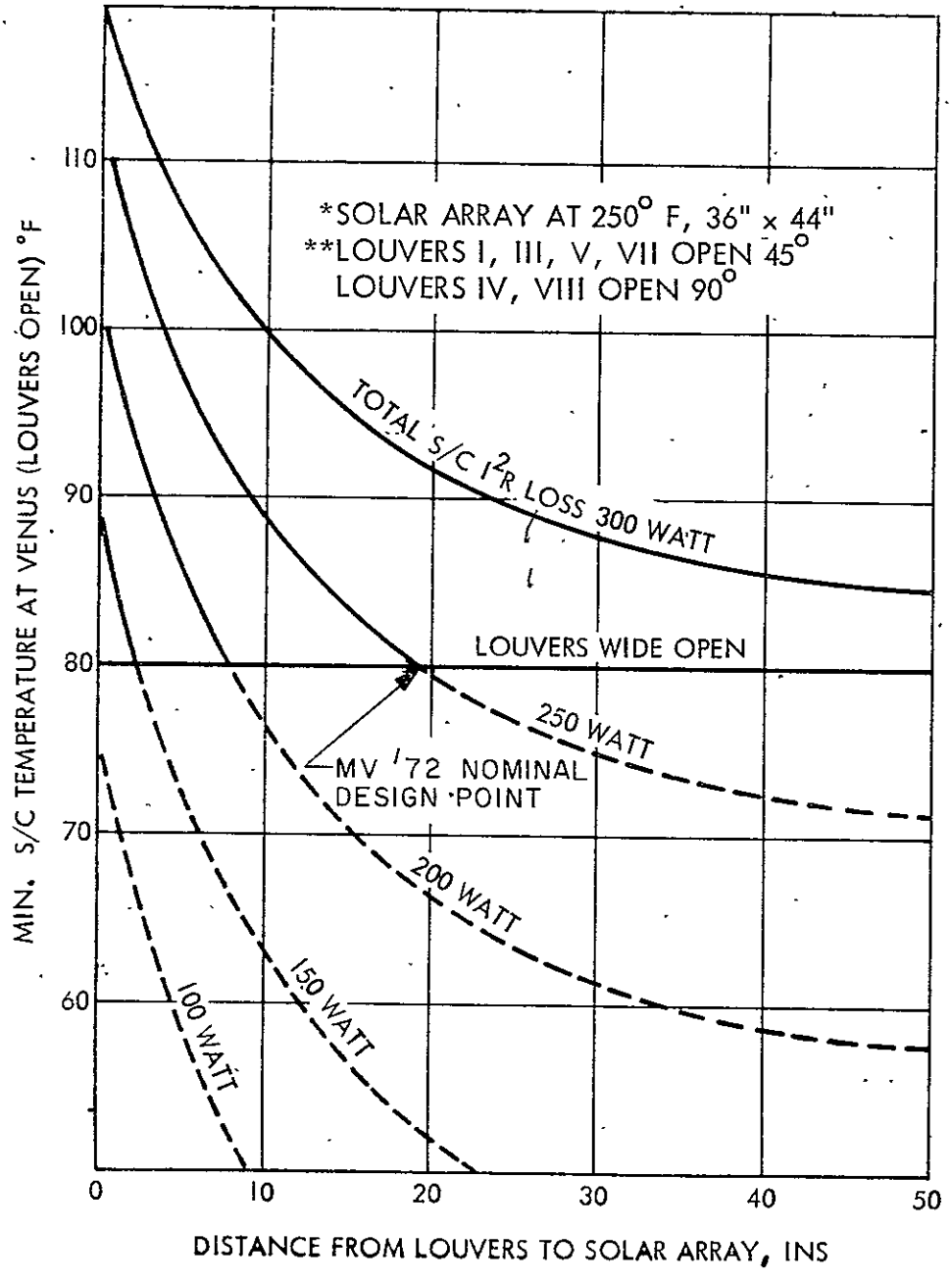


FIGURE 5.13 . EFFECT OF SOLAR ARRAY ON LOUVERS

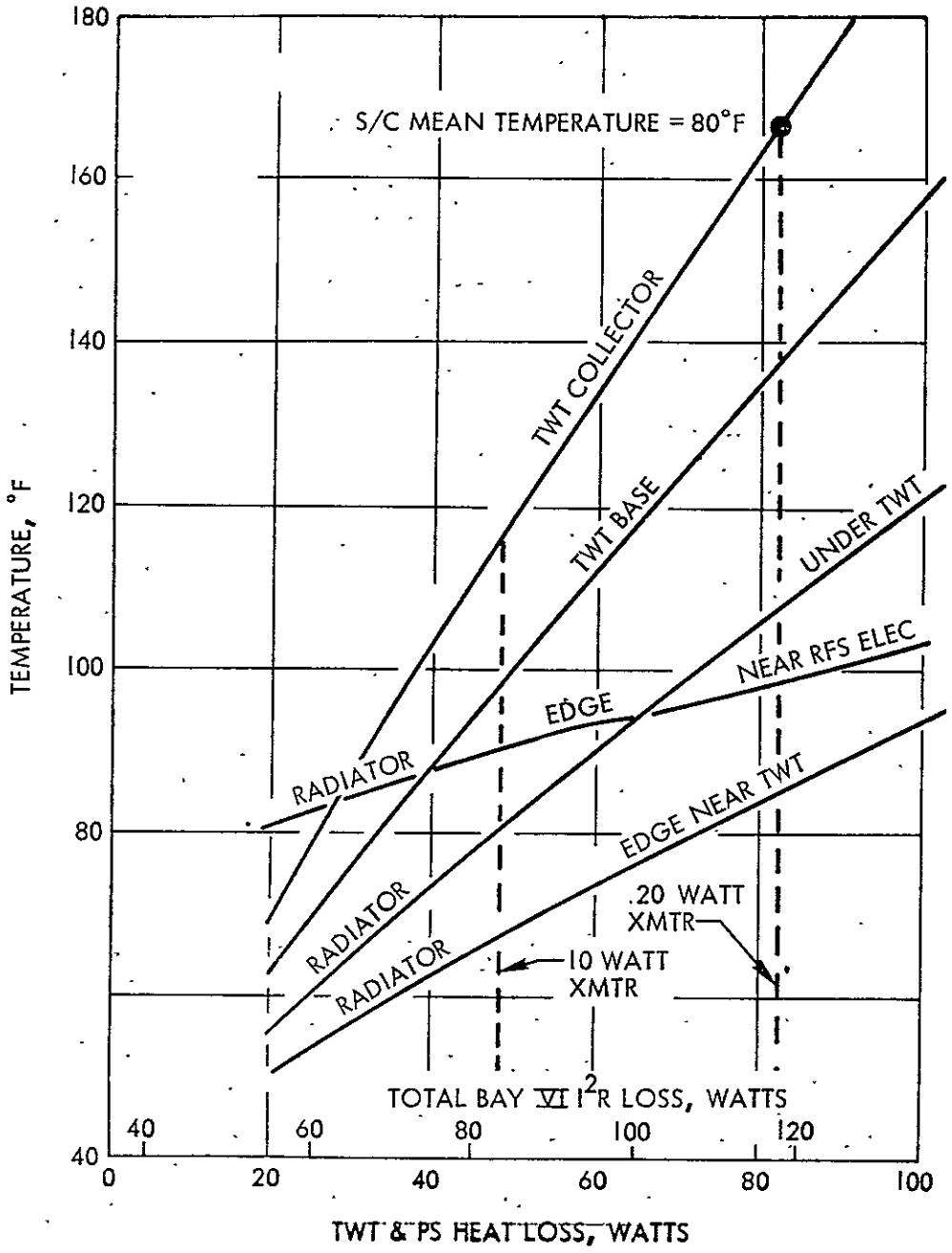
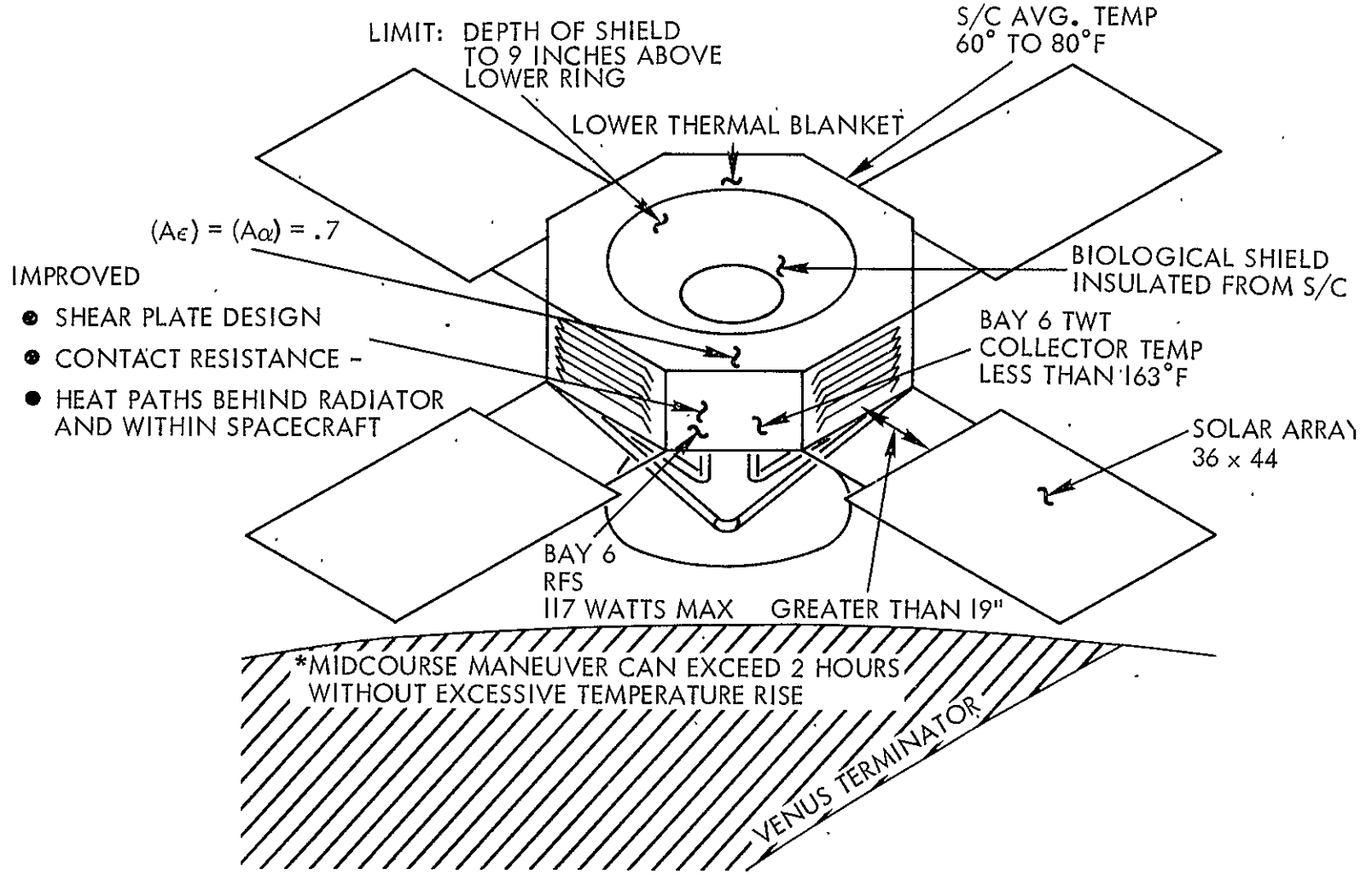


FIGURE 5.14 BAY VI TEMPERATURES



775941P

FIGURE 5.15 THERMAL CONTROL SUBSYSTEM SUMMARY

biological shield will be insulated from the flyby probe and will be restricted to penetration depths of less than 9-inches into the flyby probe structure. The solar panels will be kept an adequate distance from the louvered bays to prevent heat input into the louvers. By means of improved shear plate design, improved contact resistance and by providing adequate heat paths from the shear plate to the rest of the flyby probe, the TWT temperature at the collector will be held below 163° F at 117 watts of dissipated power. By improving contact resistance between the shear plate and major heat capacity elements of the RFS system, the midcourse maneuver in excess of two hours (at Earth) without excessive temperature rise.

5.3.4.3 Functional Modifications from Mariner Mars 1969

The Mariner Venus 1972 thermal control system differs from the Mariner Mars 1969 in the range of planetary and solar irradiation experienced and by the inclusion of a entry probe in 1972. The larger solar irradiation of the Venus 1972 mission permits use of smaller solar arrays. To insure these do not interfere with heat rejection from the louvers, the solar arrays are displaced out from the octagon structure to the same distance as those of Mariner 1969. The RFS system bay is somewhat improved for the 1972 Venus mission. Thermal blanket performance is expected to be improved for the Mariner 1969 mission and $\alpha = \epsilon = .7$ will be attained in lieu of the Mariner 1969 value of 1.0. The midcourse and entry probe deployment manuever is limited to one hour for the Mariner Venus mission to preclude excessive thermal control problems at the relatively close-to-sun distance of capsule deployment. The Mariner Mars 1969 midcourse maneuver duration is not limited by thermal considerations.

Power Subsystem

5.3.5.1 Functional Requirements

The power subsystem provides a central supply for the lyby/entry probe. It conditions the raw power from the solar array-battery

source and distributes this conditioned power to the subsystem. Flyby probe central timing is derived from the closely controlled frequency of the 2.4 KHz main inverter.

Battery chargers are required in the power subsystem to maintain the flyby probe and entry probe batteries fully charged.

5.3.5.2 Functional Description

The Mariner Venus 1972 Power Subsystem is functionally illustrated in Figure 5.16. The basic source of power is solar panels. A silver zinc battery augments the solar panels. The solar panels have an area of 44.8 ft^2 and provide 400 watts of power near earth and 524 watts of power at Venus encounter. The battery is maintained fully charged for use during launch midcourse and entry probe deployment manuevers, and exigencies.

The raw DC power is regulated in the booster-regulator and fed to the inverters. There are four inverters; a 2.4 KHz main inverter, a 400 Hz-1ϕ inverter, a 400 Hz-3ϕ inverter, and a 2.4 KHz maneuver inverter. The main inverter powers most of the subsystems and provides the timing function. The 400 Hz-3ϕ and maneuver inverters power the attitude control subsystem. The 400 Hz-1ϕ inverter provides power to the DSS, scan and IRS subsystems.

5.3.5.3 Functional Modifications from the Mariner Mars 1969

The power subsystem conditioning components for the baseline mission are identical to those of Mariner Mars 1969 with the exception of the 2.4 KHz main inverter. The power output of the main inverter has been increased to 175 watts (Mariner Mars 1969 main inverter power output = 155 w) due to the increased science load.

The magnetometer and trapped radiation detector experiments are not included in the Alternate No. 1 configuration. Consequently, the main inverter load is less than for the baseline. The main inverter output for the Alternate No. 1.

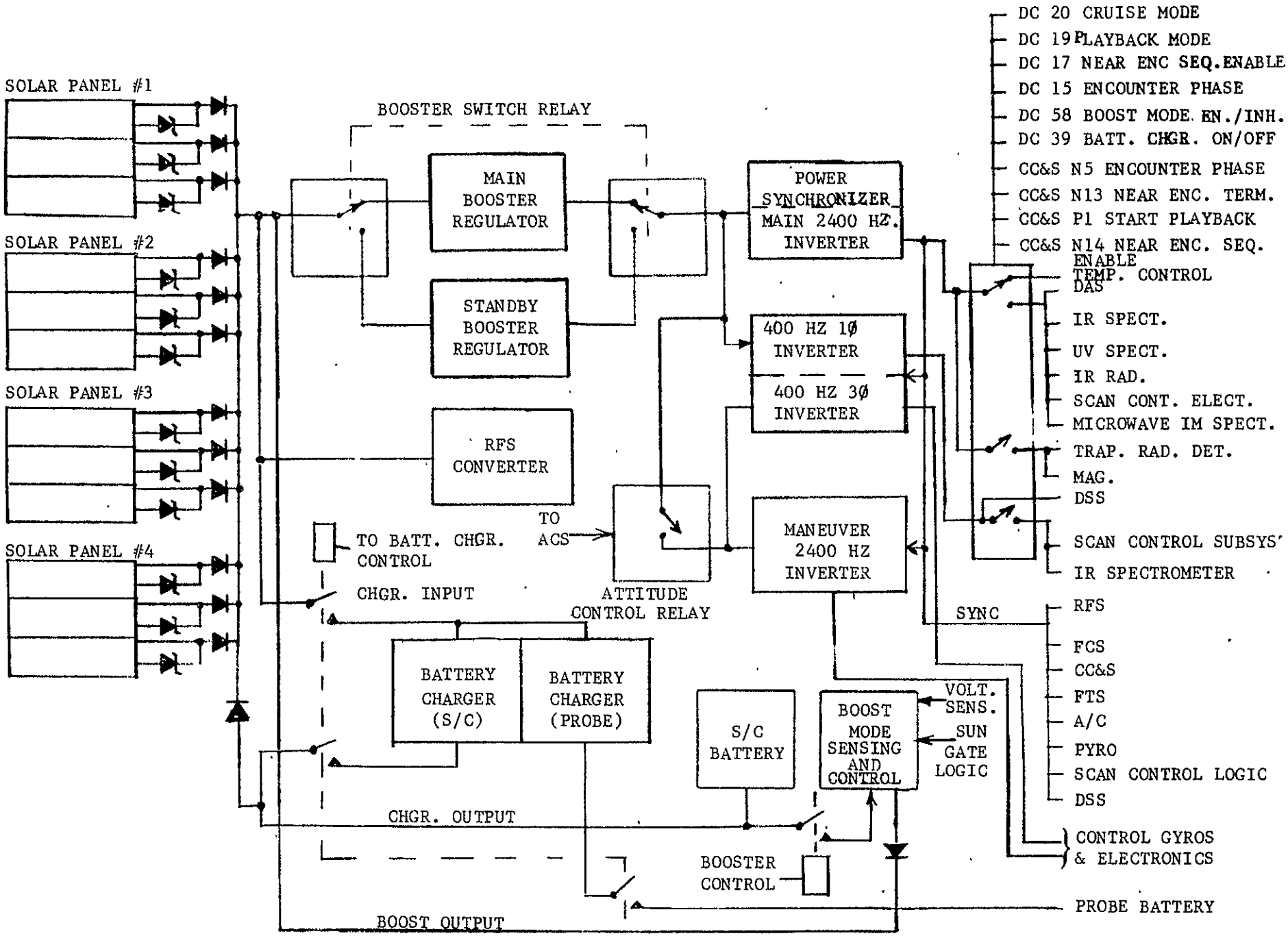


FIGURE 5.16 MARINER VENUS 1972 POWER SUBSYSTEM FUNCTIONAL BLOCK DIAGRAM

configuration is 165 watts. The Alternate No. 2 configuration substitutes a T.V. experiment for the baseline science experiment complement. The power requirement of the T.V. system is less than that of the baseline science (20 watts vs. 67 watts). Therefore, the Alternate No. 2 main inverter power output is identical to Mariner Mars 1969.

The flyby probe battery is unchanged (capacity 1200 wt-hr).

The Mariner Venus 1972 solar panel area is approximately one-half that of Mariner Mars 1969. The panel area reduction is made possible by the increase in solar panel power as the flyby probe approaches Venus. The Mariner Venus 1972 solar array will have an output of approximately 400 watts near Earth and 524 watts at encounter.

An entry probe battery capable of two charging rates--180 ma and 40 ma (trickle) has been added to the flyby probe power subsystem.

For the post encounter phase, the silicon cells will provide sufficient power margin. For this Venus mission, tilting the solar paddles or utilization of gallium arsenide cells is not required.

5.3.6 Midcourse Propulsion Subsystem

The Mariner Venus 1972 Midcourse Maneuver Propulsion subsystem supplies one or two corrective velocity increments in order to remove trajectory errors and satisfy entry probe deployment and planetary flyby experiment requirements. The propulsion thrust level is fixed. The duration and direction of firing are accurately controlled by the CC & S to obtain the desired trajectory at Venus encounter.

5.3.6.1 Functional Requirements

The Mariner Venus 1972 midcourse propulsion subsystem supplied a first midcourse maneuver velocity increment of 26.1 meter/second

(maximum) (see section 2.8.3 for requirement) several days after launch in order to remove the injection aim point bias (for planetary quarantine) and injection errors. Entry probe deployment and flyby experiments encounter trajectory accuracy requirements can impose the requirement for a second midcourse maneuver of 0.9 meters/second (maximum) approximately midway along the heliocentric trajectory. The resulting total maximum velocity increment is 27 meter/second.

The Mariner Venus 1972 flyby/entry probe may have a mass ranging between 841 pounds (Minimum mission) and 1750 pounds, the maximum launch mass for acceptable Type I trajectories. The baseline configuration, having a single probe with flyby and cruise experiments has an estimated mass of 1235 pounds. The heavier flyby/entry probe require additional total impulse capability for achieving a fixed velocity increment of 27 meters per second.

The impulse imparted by the midcourse propulsion system must be accurately directed through the spacecraft mass center to avoid rotation of the flyby/entry probe.

5.3.6.2 Functional Description

The Mariner Venus 1972 midcourse propulsion system is a monopropellant bydrazine unit sized to supply 27 meter per second velocity increment. The propellant requirements of the heavier Venus 1972 Mission flyby/entry probe satisfied by using the Mariner Mars 1969 fuel tank and nitrogen pressurant tank. A nitrogen gas pressure regulator reduces the nitrogen pressure from 3300 psia to 300 psia upstream of the pyrotechnic squib actuated valves and propellant. The 300 psia nitrogen is fed to the propellant tank and, by exerting pressure through a bladder, expells the propellants.

The velocity increments obtainable with the existing Mariner 1969 propulsion subsystem are shown for the baseline and alternate missions in Table 5.9.

MARINER VENUS 1972 VELOCITY INCREMENT WITH MARINER 1969 SUBSYSTEM

Mariner Venus 1972 Configuration	Flyby/Entry Probe Mass pounds	Velocity Increment Meters/Second	ΔV Margin abov 27m/sec
Baseline Mission	1350	35.4 max. 0.059 min.	8.4
Alternate Mission One	1064	36.8 max. 0.062 min.	9.8
Alternate Mission Two	956	50.2 max. 0.084 min.	13.2
Maximum Possible Injected Mass (C_3 = 13.4)	1750	27.4 max. 0.046 min.	0.4
Mariner 1969	800	60.0 max. 0.100 min.	33.0

The Mariner 1969 subsystem provides adequate velocity increments for all Mariner flyby/entry probe Venus 1972 Missions, more than satisfying the 27 meter/second required to achieve accurate flight path control and satisfy the $\overline{10^{-5}}$ probability of Venus contamination (see Sections 2.64 and 2.83 for details).

5.3.6.3 Functional Modifications from Mariner 1969

The existing Mariner 1969 subsystem hardware can be used for the baseline or alternate missions. The velocity increment available to the Venus 1972 flyby/entry probe with use of the Mariner 1969 subsystem is previously presented in Table 5.9.

5.3.7 Flight Telemetry Subsystem

5.3.7.1 Functional Requirements

Functional requirements for the Mariner Venus 1972, flight telemetry subsystem (FTS) are similar to those on the Mariner Mars 1969 and are:

- o Accept analog and digital measurement signals from the spacecraft
- o Accept and keep a cumulative count of event pulses from the spacecraft
- o Condition and encode the preceding signals into a seven-bit digital word format
- o Insert unique codes into the data to identify the beginning of sequential frames and subframes of commutated data
- o Accept serial digital data from other flyby probe subsystems for transmission to earth during the appropriate data modes
- o Provide change of data rate to make use of available bandwidth in the radio frequency communications system to planetary distances; and amplify, during the launch phase, signals from two accelerometers mounted on the spacecraft. The amplified signals will be rounted across the spacecraft-launch vehicle interface to the Centaur telemetry unit.

The baseline and alternate missions contain the same functions with minor mechanization alternations.

5.3.7.2 Functional Description

Figure 5.17 presents a functional block diagram of the FTS for the Mariner Venus 1972 missions. The system will generate a baseband consistin of one or two subcarriers. During cruise where data rates are relatively low, a mixture of scientific and engineering data will be multiplexed and encoded in a PCM format on a single subcarrier. At encounter, or when a greater transmission capability is required, one subcarrier will be reserved for scientific data and the other for engineering data. Table 5.10 presents anticipated data rates for baseline and alternate Venus mission.

5.3.7.3 Functional Modifications from Mariner Mars 1969

The changes in multiplexing schedules and data rates shown in Table 5.10.can be mechanized using modules and packaging techniques that are being used on the Mariner Mars 1969 mission. It is anticipated that the physical parameters will change slightly from Mariner 1969. Maximum weight is anticipated to be 25 pounds, volume 1100 cubic inches, and power 10 watts of 2.4 KHz power.

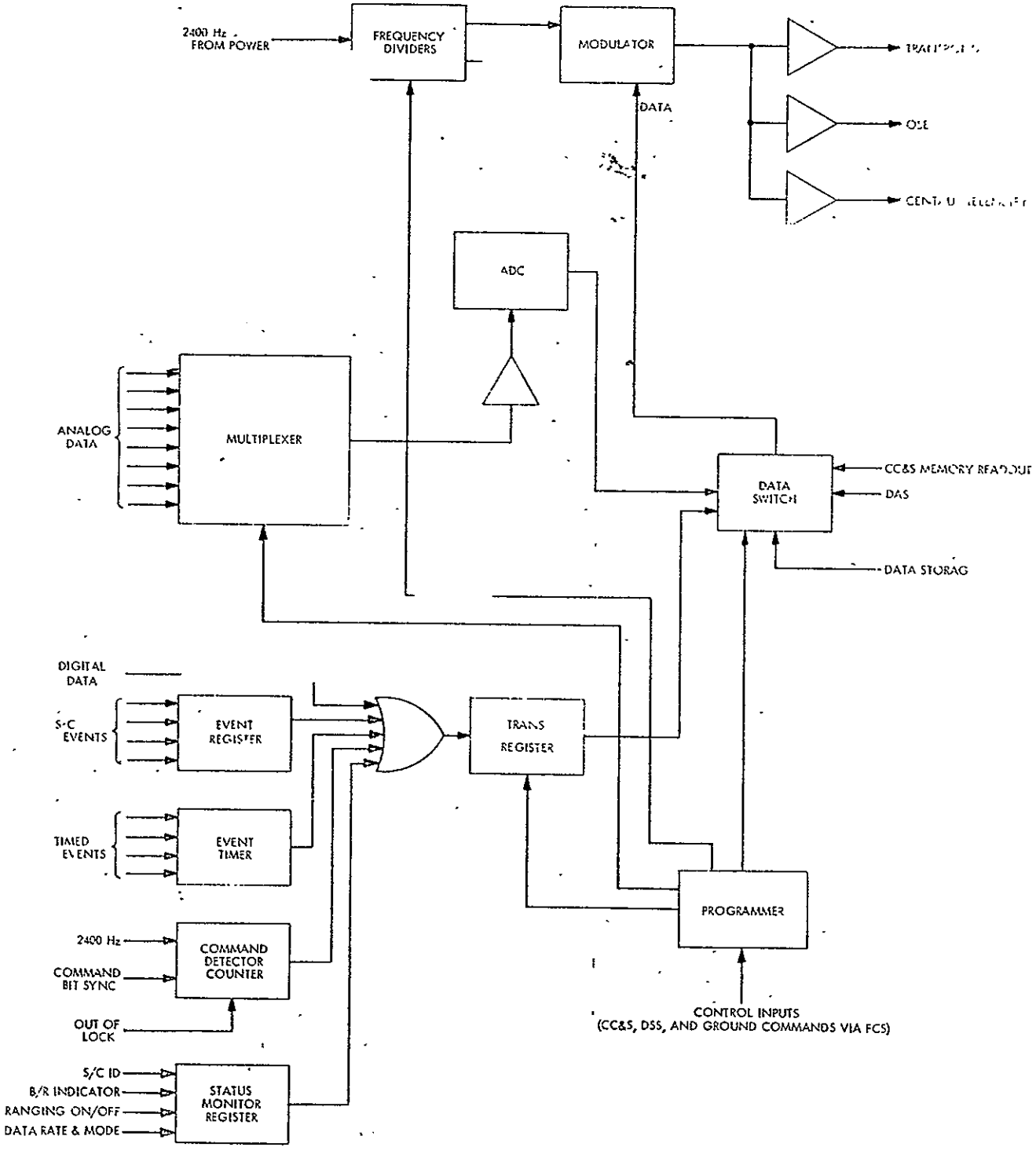


FIGURE 5.17 FTS. Block Diagram

Table 5.10

FUNCTIONAL MODIFICATIONS FROM
MARINER 1969 FLIGHT TELEMETRY SUBSYSTEM

OPERATING MODE BIT RATES	MARINER 1969	MARINER VENUS - 1972		
		Baseline	Alternate #1	Alternate #2
1. Cruise	8-1/3	33-1/3	8-1/3	8-1/3
2. Encounter	CH #1 33-1/3 CH #2 270	Ch #1 8-1/3 Ch #2 133-1/3	Ch #1 8-1/3 Ch #2 133-1/3	Ch #1 8-1/3 Ch #2 270
3. Post Encounter	CH #1 8-1/3 CH #2 270	CH #1 8-I/3 CH #2 133-1/3	Ch #1 8-1/3 Ch #2 133-1/3	Ch #1 8-1/3 Ch #2 270
4. CC&S Memory Readout	8-1/3	33-1/3	33-1/3	33-1/3

Note: Channel #1 Engineering & Minimal Science
#2 Science Only

5.3.8 Flight Command Subsystem

5.3.8.1 Functional Requirements

The Flight Command Subsystem (FCS) acquires phase coherence with the synchronization information from the Radio Frequency Subsystem and demodulates the command word information from which the command word data bits are detected and reconstructed. Direct, quantitative and coded commands are decoded from the command word bits. The decoded commands are then routed by the FCS to the appropriate subsystem.

5.3.8.2 Functional Description

The FCS has two major functional elements are shown in Figure 5.18. These elements are the command detector and the command decoder.

The command detector receives the command signals from the Radio Frequency Subsystem. The command word information is demodulated and detected and the command word bits are reconstructed. The command word data bits are fed to the decoder where discrete momentary switch closures are provided to the proper user subsystem (direct command channel). The coded command channel directs coded command data to the CC&S to update event timing and enter maneuver data int the CC&S. The quantative command channel provides a variable length pulse train to the scan subsystem which contains scan platform cone and clock angle data. The detector lock status signal indicates whether or not detector synchronization with the received signal has been established.

5.3.8.3 Functional Modifications from Mariner 1969

The command detector unit will be identical to that of Mariner 1969.

The command decoder will require minor modification to accommodate changes made in command outputs. These changes will consist of adding isolated switches to increase the command output capability and reassignment of

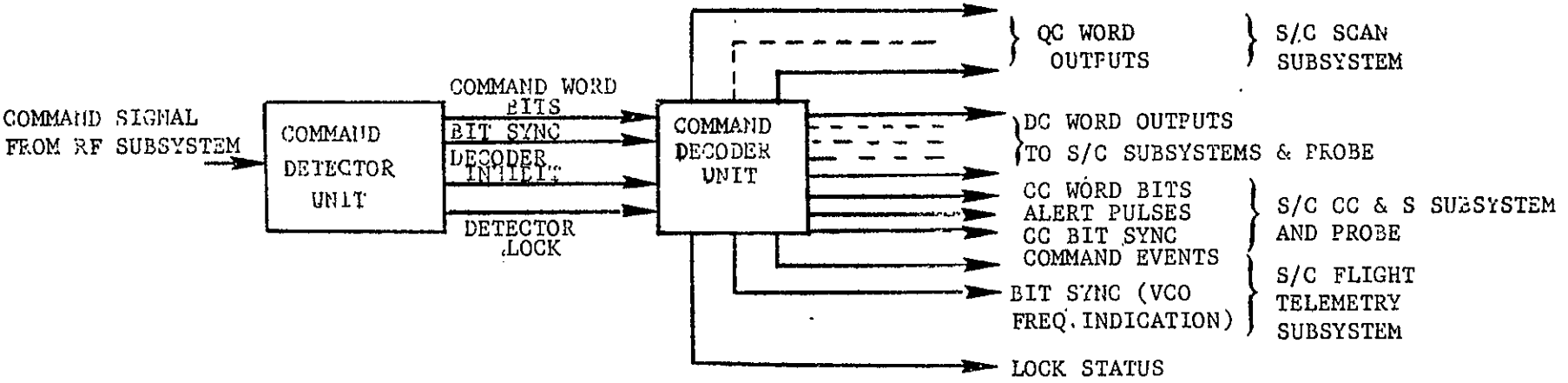


FIGURE 5.18 - FLIGHT COMMAND SUBSYSTEM - FUNCTIONAL BLOCK DIAGRAM

existing isolated switches. Table 5.11 lists the number of commands required by the baseline, alternate configurations and Mariner Mars 1969 missions.

Table 5.11

Command Requirement Comparison

Mission	Direct Commands	Quantitative Commands	Coded Commands
Mariner Mars 1969	52	4	1
Mariner Venus Baseline	57	4	1
Mariner Venus 1972 Alt. #1	55	0	1
Mariner Venus 1972 Alt. #2	53	0	1

5.3.9 Radio Frequency and Antenna Subsystem

5.3.9.1 Functional Requirements

The Radio Frequency Subsystem (RFS) functional requirements are summarized as follows:

Receive radio frequency signals from the DSIF

Coherently translate the frequency by a ratio compatible with the DSIF

Demodulate and separate command signals from the up-link baseband

Send command signals to the FCS

Detect ranging signal from the DSIF

Modulate telemetry data stream(s)

Modulate detected ranging signals

Transmit a modulated radio frequency signal that is phase coherent with either received signal or an internal frequency source

Transmit signals to the DSIF with proper polarization characteristics and have nearly isotropic pattern coverage with low gain antenna system

5.3.9.2 Functional Description

The functional description of the baseline system is shown in Figure 5.19 in block diagram form. The ability to automatically switch between two low gain antennas during entry probe deployment is required to perform the baseline mission. Since transmission time is significant at this part of the mission, the switching function receives its stimuli from the receiver AGC level. In the event that the AGC level is below an acceptable threshold on either antenna, the switching unit will search by switching between the two antennas one time each second until a suitable signal is received from the DSIF. The function is backed up by both the CC&S and the FCS. This capability is only required in missions where the cone angle changes more than 90 degrees.

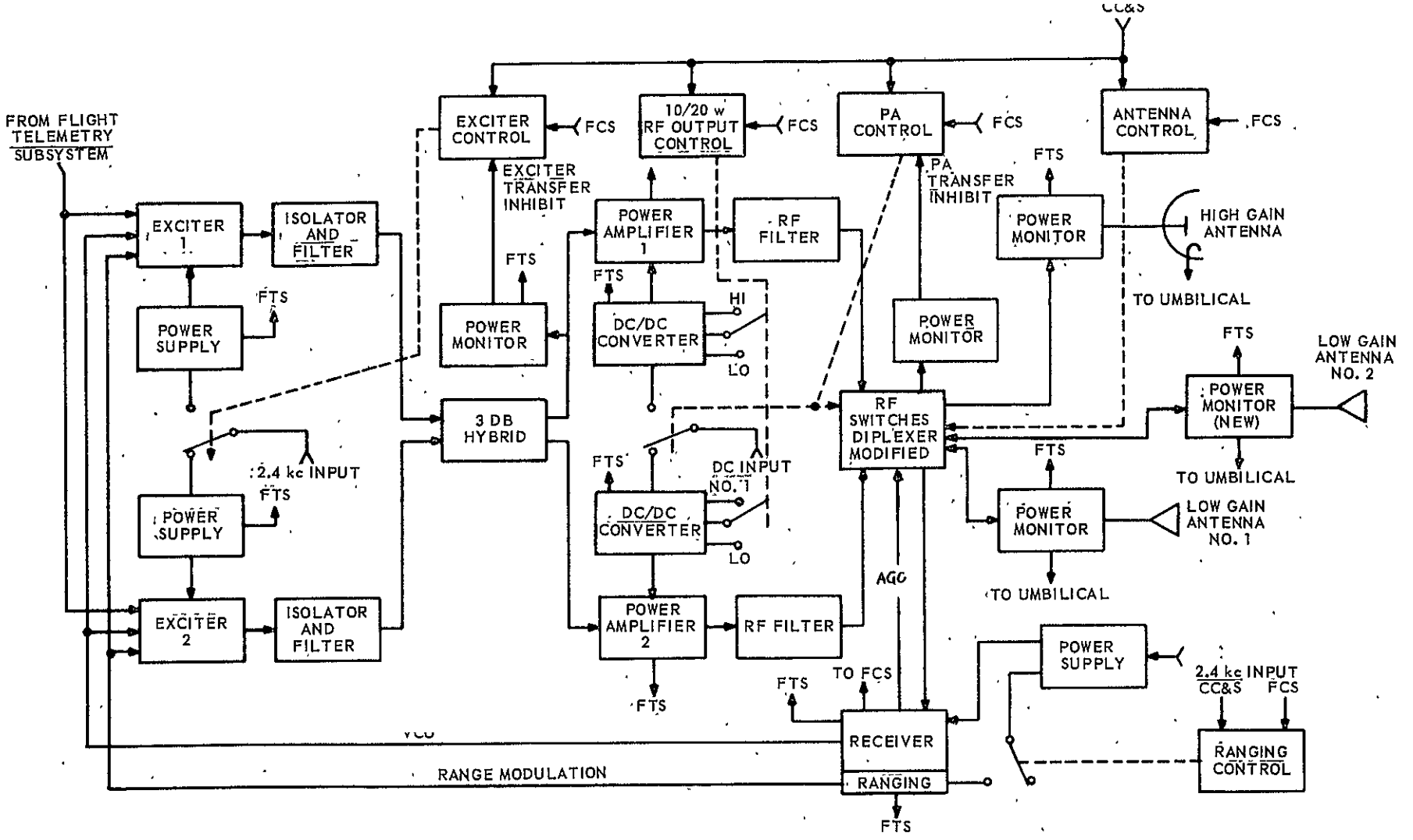
5.3.9.3 Functional Modifications from Mariner Mars 1969

The high gain antenna configuration for the baseline mission is similar to the Mariner Venus 1967 with two boresight positions. The antenna gain is +23.5 db above a circular polarized isotropic reference source. The baseline mission involves flyby probe cone angle changes over 90 degrees for capsule deployment. resulting in use of a second low gain antenna. The addition of the second low gain antenna, its switching circuitry, and logic requires a new design for the baseline mission. The low gain antennas will be similar to the Mariner Mars 1969 configuration with modified mounting fittings.

The alternate Mariner Venus 1972 missions do not require a movable high gain antenna, since the R.F. occultation experiment is not conducted. The second low gain antenna is also not required on the alternate missions since the flyby probe cone angle does not exceed 90 degrees during entry probe deployment.

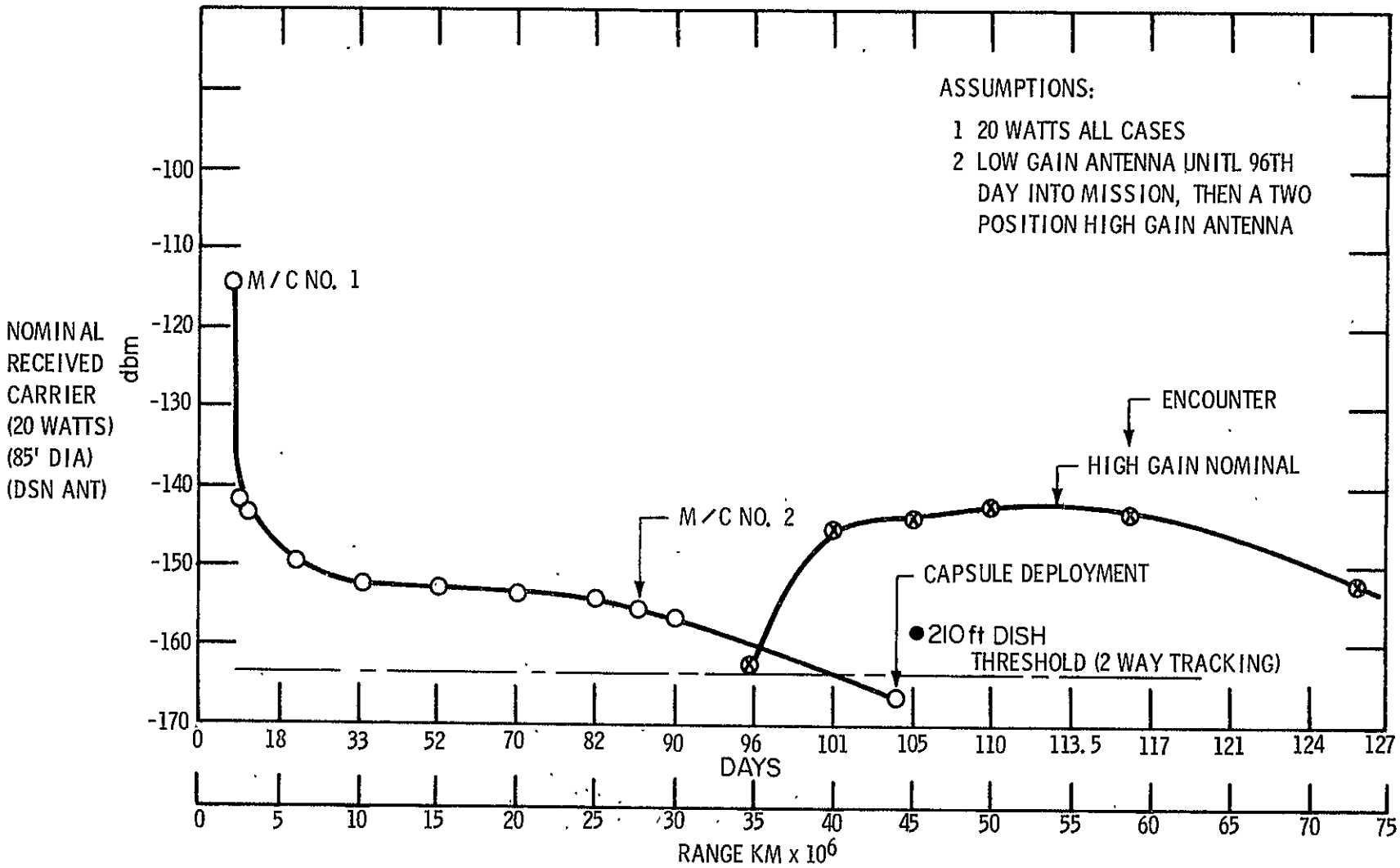
5.3.9.4 Performance of Radio Frequency Subsystem

The normalized receiver carrier power levels throughout the mission using a transmitter power of 20 watts nominal and both high and low gain antennas is shown in Figure 5.20. The computed signal margins



775945P

FIGURE 5.19 RFS BLOCK DIAGRAM



775926P

FIGURE 5.20 NORMALIZED CARRIER PERFORMANCE

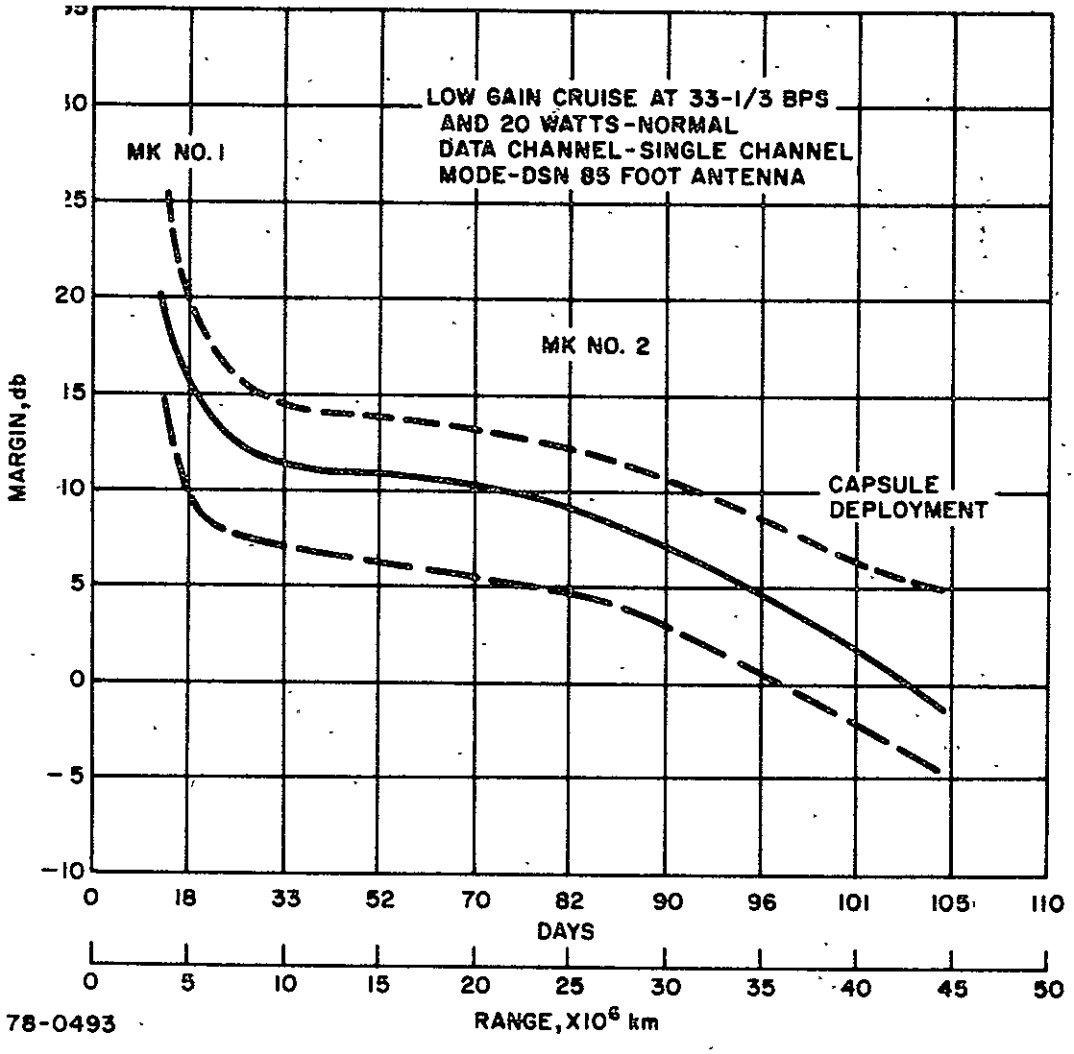
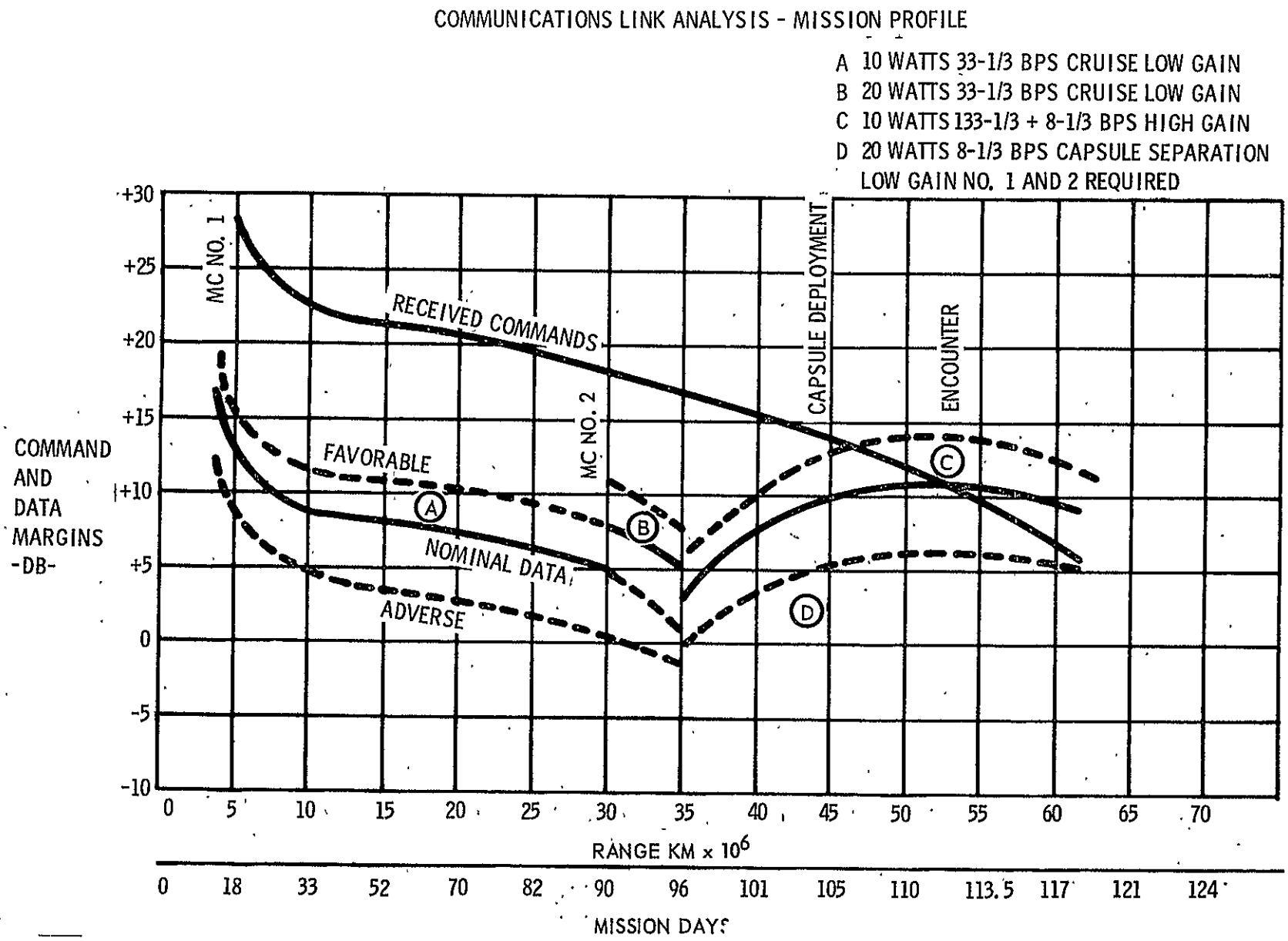


Figure 5.21 Cruise Data Subcarrier Margin



775925 P

FIGURE 5.22 DATA MISSION PROFILE

for the single channel cruise case is shown in Figure 5.21. A recommended mission profile is shown in Figure 5.22. Design control tables for two periods in the mission are given in Tables 5.12 and 5.13.

The "far side" trajectory has cone angles approaching zero degrees at the time of entry probe deployment. Preliminary data indicates that a very severe antenna pattern null exists in this area and prevents satisfactory reception of commands from the Deep Space Network; and prevents satisfactory signals to be transmitted to the Deep Space Network using either the primary low or high gain antennas. To overcome this problem it is necessary to include a second low gain antenna which has maximum gain at a zero degree cone angle and at least isotropic gain at cone angles of ninety degrees. Antenna testing would be required to optimize the pattern.

Recent information obtained in EPD 283, Revision 2, dated 1 January 1967 and performance data of the Mariner 1969 traveling wave tube amplifiers indicates that DSN antenna gains are 0.3 db higher than shown on the design control tables and the system noise temperatures have been reduced from anominal $55^{\circ}K$ to $42^{\circ}K$. Transmitting circuit losses presented on the design control tables are 1.3 db as compared to 1.990 on the Mariner 1969. Assumptions made that the ground antenna losses are 0.5 db were proven to be overly conservative. The net effect of these changes indicate that the performance of the Mariner Venus 1972 will be approximately 0.4 db better than indicated on the previously referenced figures insofar as total received power at the DSN is indicated.

The most critical part of the mission, considering the RFS, will occur at entry probe separation. If antenna gains of the low gain antennas never exceed isotropic level adequate system margins are possible. Command margins are slightly better but timely switching between the two low gain antennas will be of paramount importance.

If the "far side" trajectory (Type I with nominal July 16, 1972 arrival) is flown, it is necessary to have a second low gain antenna which has

TABLE 5.12

Design Control Table
Day 104 - Entry Probe Deployment
Mariner Venus 1972

Entry Probe Deployment, Day 104, 33-1/3 BPS Single Ch. Low Gain #2 20 watts

	PARAMETER	VALUE	TOLERANCE	
1	Total Transmitter Power 20 watts	+43 dbm	+0.5	-0.5
2	Transmitting Circuit Loss	-1.3 db	+0.2	-0.3
3	Transmitting Antenna Gain Lo gain #2	0		
4	Transmitting Antenna Pointing Loss			
5	Space Loss @ 2298 MC, R = 44 x 10^6 KM	-252.5 db		
6	Polarization Loss	-3 db	+3	-0
7	Receiving Antenna Gain	+53 db	+1.0	-0.5
8	Receiving Antenna Pointing Loss			
9	Receiving Circuit Loss	-0.5 db	+0.2	-0.2
10	Net Circuit Loss	-204.3 db	+4.4	-1.5
11	Total Received Power	-161.3 dbm	+4.9	-2.0
12	Receiver Noise Spectral Density (N/B) T System = 55 $\pm$ 10°K	-181.2 dbm	.9	+0.7
13	Carrier Modulation Loss	-5.0 db	+0.6	-0.6
14	Received Carrier Power	-166.3 dbm	+5.5	-2.6
15	Carrier APC Noise BW ($2B_{LO}$ = 12 HZ)	+10.8	-0.5	+0.0
	CARRIER PERFORMANCE-TRACKING (one-way)			
16	Threshold SNR in $2B_{LO}$	0.0 db	-0.0	0.0
17	Threshold Carrier Power	-170.4 dbm	1.4	+0.7
18	Performance Margin	+4.1 db	+6.9	-3.3
	CARRIER PERFORMANCE-TRACKING (two-way)			
19	Threshold SNR in $2B_{LO}$	2.0 db	-1.0	+1.0
20	Threshold Carrier Power	-168.4 dbm	-2.4	+1.7
21	Performance Margin	+2.1 db	+7.9	-4.3
22	Threshold SNR in $2B_{LO}$	6.0 db	-1.5	+1.5
23	Threshold Carrier Power	-164.4 dbm	-2.9	+2.2
24	Performance Margin	-1.9	+8.4	-4.8
	DATA CHANNEL θ = 1.45 rad			
25	Modulation Loss	-2.0 db	+0.3	-0.3

TABLE 5.12 (cont'd)

Mariner Venus 1972

Entry Probe Deployment, Day 104, 33-1/3 BPS Single Ch. Low Gain #2 20 watts

	PARAMETER	VALUE	TOLERANCE	
	DATA CHANNEL			
26	Received Data Subcarrier Power	-161.3 dbm	+5.2	-2.3
27	Bit Rate (1/T) 33-1/3	+15.2 db	+0.0	-0.0
28	Required ST/N/B	5.6 db	-0.2	+0.2
29	Threshold Subcarrier Power	-160.4 dbm	-1.1	+0.9
30	Performance Margin	-0.9 db	+6.3	-3.2

COMMENTS:

+3.7 db additional gain is required.

(1) The 210' dish antenna must be used during time of maneuver.

(2) A second low gain antenna similar to existing one must be installed with correct polarization.

TABLE 5.13
Design Control Table
Post Encounter
Mariner Venus 1972

Past Encounter 133-1/2 + 8-1/3 BPS + 10 days - 20 watts - +10 days
High Gain Position #2

	PARAMETER	VALUE	TOLERANCE	
1	Total Transmitter Power 20 watts	+43.0 dbm	+0.5	-0.5
2	Transmitting Circuit Loss	-1.3 db	+0.2	-0.3
3	Transmitting Antenna Gain	+22 db	+1.0	-1.0
4	Transmitting Antenna Pointing Loss	-1.0 db	+0.0	-1.0
5	Space Loss @ 2298 MC, R= 73 x 10^6 KM	-262.9 db		
6	Polarization Loss			
7	Receiving Antenna Gain	+53.0 db	+1.0	-0.5
8	Receiving Antenna Pointing Loss			
9	Receiving Circuit Loss	-0.5 db		
10	Net Circuit Loss	-190.7 db	+2.2	-2.8
11	Total Received Power	-147.7 dbm	+2.7	-3.3
12	Receiver Noise Spectral Density (N/B) T System = 55°K $\pm$ 10°K	-181.2 dbm	-0.9	+0.7
13	Carrier Modulation Loss	-5 db	+0.6	-0.6
14	Received Carrier Power	-152.7 dbm	+3.3	-3.9
15	Carrier APC Noise BW ($2B_{LO}$ = 12 HZ)	10.8 db	-0.5	+0.0
	CARRIER PERFORMANCE-TRACKING (one-way)			
16	Threshold SNR in $2B_{LO}$	0.0 db	-0.0	+0.0
17	Threshold Carrier Power	-170.4 dbm	-1.4	+0.7
18	Performance Margin	+17.7 db	+4.7	-4.6
	CARRIER PERFORMANCE-TRACKING (two-way)			
19	Threshold SNR in $2B_{LO}$	2.0 db	-1.0	+1.0
20	Threshold Carrier Power	-168.4 dbm	-2.4	+1.7
21	Performance Margin	+15.7 db	+5.7	-5.6
22	Threshold SNR in $2B_{LO}$	6.0 db	-1.5	+1.5
23	Threshold Carrier Power	-164.4 dbm	-2.9	+2.2
24	Performance Margin	+11.7 db	+6.2	-6.1
	DATA CHANNEL A SCIENCE			
25	Modulation Loss θ = 1.38 rad	-2.5 db	+0.3	-0.3
26	Received Data Subcarrier Power	-150.2 dbm	+3.0	-3.6
27	Bit Rate (1/T) 133-1/3 BPS	+21.2 db	+0.0	-0.0
28	Required ST/N/B	+5.6 db	-0.2	+0.2

TABLE 5.13 (Cont'd)

Design Control Table
Post Encounter
Mariner Venus 1972

Past Encounter 133-1/2 + 8-1/3 BPS + 10 days - 20 watts - +10 days

High Gain Position #2

	PARAMETER	VALUE	TOLERANCE	
29	Threshold Subcarrier Power	-154.4 dbm	-1.1	+0.9
30	Performance Margin	+4.2 db	+4.1	-4.5
	SYNC CHANNEL ENGINEERING			
31	Modulation Loss $\theta = 0.46$ rad	-14.6 db	+0.3	-0.3
32	Receiver data Subcarrier Power	-162.3 dbm	+3.0	-3.6
33	Bit Rate (1/T) 8-1/3 BPS	9.2 db	+0.0	-0.0
34	Required ST/N/B	5.6 db	-0.2	+0.2
35	Threshold Subcarrier Power	-166.4 dbm	-1.1	+0.9
36	Performance Margin	+4.1 db	+4.1	-4.4

maximum gain at a cone angle of from zero to forty-five degrees and is equal to or above isotropic at a cone angle of ninety degrees.

Since the cruise mode science and engineering data rates are low, they should be multiplexed upon a single subcarrier and transmitted at a rate of 33 1/3 bits per second. Encounter science and engineering data would be transmitted on separate subcarriers.

The following radio frequency subsystem transmitter modes are recommended for the nominal baseline mission:

0 to 90 days into the mission - 10 watts and low gain antenna

25 days prior to encounter - 20 watts and low gain antenna

20 days prior to encounter - 10 watts and high gain anntena in position one

12 days prior to encounter at capsule separation - 20 watts and second low gain antenna thence back to high gain antenna configuratio

1 day after encounter - high gain antenna in position two and 10 watt

5.3.10 Central Computer and Sequencer Subsystem

5.3.10.1 Functional Requirements

The Mariner Venus 1972 Central Computer and Sequencer (CC&S) is required to provide timing and sequencing of flyby probe events. The CC&S issues discrete commands to sequence the flyby probe subsystems. Programming of the mid-course maneuver and attitude change maneuver for entry probe deployment is achieved via the FCS by coded command. CC&S provides redundant control of flyby maneuvers to minimize the probability of a catastrophic mission failure.

5.3.10.2 Functional Description

The major portion of the CC&S consists of a programmable special purpose computer and a maneuver fixed sequencer. Three modes of maneuver sequencing are possible; the tandem mode (normal), the fixed sequencer mode, and the programmable sequencer mode. The computer and fixed sequencer are operated in parallel during flyby probe maneuvers. Figure 5.23 is a functional block diagram of the CC & S.

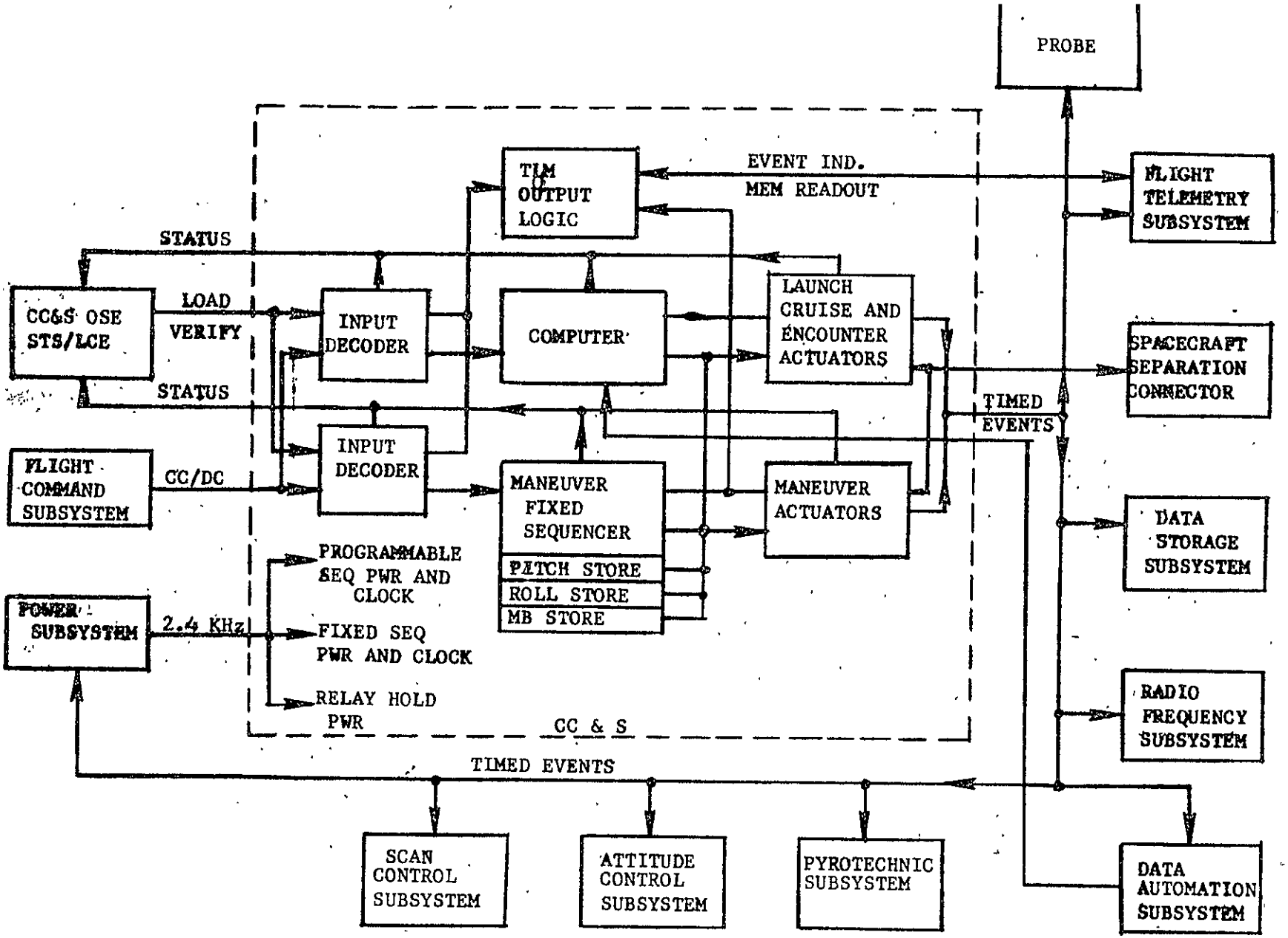


FIGURE 5.2.3 CC&S FUNCTIONAL BLOCK DIAGRAM

The CC & S has the capability to automatically control all spacecraft events except those involving spacecraft maneuvers. In the event that the mission deviates from the nominal, midcourse correction information in the form of attitude control and propulsion parameters are entered into the CC & S by coded command. The flyby probe executes the maneuver under control of the CC & S Subsystem timing and sequencing information is derived from the CC & S.

The computer controls flyby probe event times which can be updated by coded command if the mission deviates from the nominal. As presently conceived, the sequencer program on the entry probe is fixed, assuming that the time of arrival, and the entry probe separation event are adjusted (if necessary) by a midcourse propulsive maneuver. If detailed trajectory perturbation and failure mode studies show that a fixed entry probe sequencer program is inadequate, then the flyby computer program will have to update the separation event for both the flyby and entry probe by means of coded commands.

5.3.10.3 Functional Modifications From Mariner Mars 1969

The changes required to the Mariner Mars 1969 CC & S are minor. The Mariner Mars 1961 CC & S presently has the capability to store and control 40 events excluding the maneuver events. Additional relays are required to interface with the increased command outputs to the subsystems for the baseline mission which has 41 CC & S commands.

The Mariner Venus 1972 mission differs from the Mariner Mars 1969 mission in that a flyby probe maneuver is a part of the nominal mission (entry probe release maneuver). A nominal mission is herein defined as one which does not require any maneuvers for the purpose of using the propulsion subsystem to make a trajectory correction. In view of this definition, two non-nominal maneuvers, first and second midcourse corrections, are possible, however the likelihood of these are anticipated before launch and the program contains provision for both the maneuvers. The Mariner Mars 1969 fixed sequencer mode must

be modified to inhibit the propulsion burn logic during the entry probe deployment maneuver.

The Alternate No. 1 configuration requires 32 CC & S commands (Mariner Mars 1969 has 32 CC & S commands) and requires the reassignment of some CC & S output relays with associated changes in the CC & S logic circuitry. No additional relays are required.

The Alternate No. 2 configuration requires 31 CC & S commands. CC & S changes similar to those of Alternate No. 1 are required.

5.3.11 Data Automation Subsystem

5.3.11.1 Functional Requirements

The Mariner Venus 1972 Data Automation Subsystem (DAS) is required to sample, time multiplex, encode and process scientific data from the flyby probe science subsystem.

Data from the magnetometer and trapped radiation detector is processed ruing cruise to the planet Venus in the baseline mission. During encounter additional scientific instruments are active; the microwave imager, the ultraviolet spectrometer, infrared spectrometer, and infrared radiometer. During cruise the DAS transfers the data to the Flight Telemetry Subsystem; during encounter DAS processed data is stored in the digital tape recorder. The data rates to the DAS during encounter are summarized below;

Table 5.14
DATA RATE SUMMARY

Experiment	Data Rate (Bits/Sec)
UV Spec.	3200
IR Spec.	1330
TRD	8
Mag.	30
IR Radio	9.5
Microwave Image	60

Delection of the magnetometer and trapped radiation detector experiments for alternate mission number one removes the requirement that the data output of these experiments be processed. Alternate Venus 1972 mission number two provides television data only. All other spacecraft science is deleted, leaving data coding as the only requirement on the DAS.

5.3.11.2 Functional Description

A functional block diagram of the DAS is shown in Figure 5.24. Data from the science instruments flows through the interface to the analog-to-digital counters whereupon it is selected by the dump matrix for transfer through the output shift registers. The output shift registers control the data flows to either the flight telemetry system interface for real time transmission or to the buffer system for storage in the digital tape recorder

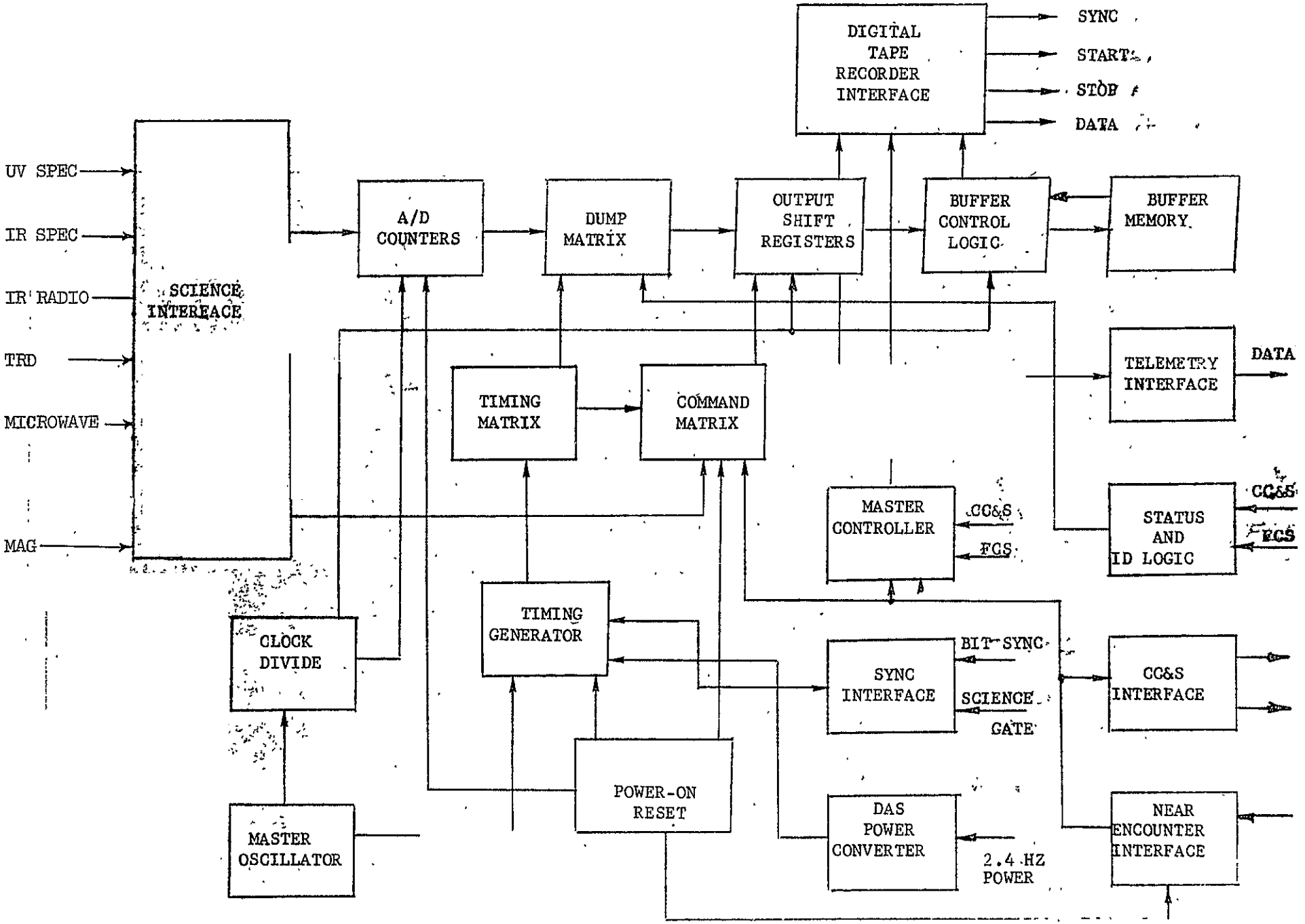


Figure 5.24DAS -- Functional Block Diagram

and real time telemetry through the dump matrix and elements following it. The shifting and transfer of information through the DAS is controlled by the timing matrix and command matrix, which in turn are controlled by the master oscillator and timing generator chain. The near encounter interface determines the start of the near encounter sequence and notifies the command matrix and the CC&S interface of the event. The real time output of the DAS is synchronized to the telemetry bit rate by bit sync from the flight telemetry system through the sync interface. Control inputs from other flyby probe susbsystems are handled through the master controller. The digital tape recorder will be commanded to start recording by the command matrix and will also be commanded to change its speed at different times. The 2.4 KHz power will be received by the power converter and will be converted to DC voltages and distributed throughout the system. The KHz voltage will also be reduced in amplitude and used as one of the sync sources of the DAS. At power turn on, a power-on-reset circuit will initialize all of the pertinent logic.

5.3.11.3 Functional Modifications from Mariner 1969

A review of the 1969 DAS functional capability and the baseline 1972 requirements indicated that the 1969 subsystem mechanization was adequate for use in the 1972 mission. Modification of the DAS is required to handle the increased number of scientific data channels and perform the time multiplexing required by the experiment sampling rates. Modifications in data format are also required as indicated by the changes in data channels and multiplex.

The Alternate configuration No. 1 also is accomodated by the Mariner 1969 DAS with the same modifications employed for the baseline mission. The DAS console can be deleted for Alternate configuration No.2 where flyby probe science consists of the television only. The data coding function required by the television can be embodied in the T.V. subsystem.

5.3.12 Data Storage Subsystem

5.3.12.1 Data Storage Subsystem Functional Requirements

The Mariner Venus 1972 data storage subsystem (DSS) performs the functions called out under the following mission phases in the baseline mission

(a) Fly-by-Science - Store data from the Data Automation System at 4500 bits per second for 50 minutes. At the completion of this recording sequence the recorder will contain the required 1.8×10^7 bits of science data.

(b) Playback Phase - The playback sequence shall begin after flyby. This sequence consists of the following: reproduce all stored data from the digital recorder and send it to the flight telemetry subsystem (FTS). Playback of the data shall be at 133-1/3 bits/sec synchronously with the FTS. The digital recorder data stored shall be played back until the telemetry link performance falls below threshold.

The DAS requirements for Alternate configuration No. 1 the same as those for the baseline mission but without the magnetometer and trapped radiation detector data storage requirements. Alternate configuration No.2, which carries only a television aboard the flyby produces a requirement for storage of analog data at a rate of 18.9 KHz and storage of 10.6×10^8 data bits. Additionally, the television data should be played back at a rate of 270 bits/sec after Venus encounter.

5.3.12.2 Functional Description

The baseline mission Mariner 1972 flyby probe data storage subsystem will consist of one digital tape recorder, power conditioner and controller. The bit error probability will be 1 in 10^5 bits. One major record mode will be required; the flyby science mode. The record bit rate for the flyby science mode is 4500 bits/sec. The required storage capacity for the baseline and alternate mission unumber one flyby science is 1.8×10^7 bits.

The television experiment of alternate configuration No. 2 requires data storage at a rate of 18.9 KHz and storage of analog data equivalent to 1.6×10^8 data bits. The high data rate and storage requirements is accommodated with use of both an analog and a digital tape recorder. The functional block diagram of Figure 5.25 presents the configuration of the DSS for alternate configuration No. 2; the most complex DSS of the three alternatives. All video data are stored in the analog tape recorder during data acquisition. Subsequent to encounter the analog data are transferred to the digital tape recorder via the analog-to-digital converter until capacity of the digital recorder is reached. The digital recorder, when filled, plays back the data to the F.T.S. When emptied, the digital recorder is reloaded from the analog tape recorder. The cycle is repeated until all analog data are transmitted to earth.

5.3.12.3 Functional Modifications from 1969

The Mariner Mars 1969 Data Storage system was studied for compatibility with the Mariner Venus 1972 mission requirements. The general characteristics of the 1969 data storage system are the presence of two tape recorders; one analog and one digital, with analog to digital conversion equipment for transfer of data from the analog tape recorder to the digital tape recorder. The large data storage capacity of both tape recorders was demanded by the TV experiment, which stored 1.57×10^8 bits in the analog tape recorder.

The playback speed of the Mariner 1969 tape recorder is 270 bits/sec. The record and playback speed of the Mariner Mars 1969 digital tape recorder must be modified to 133-1/3 bits/sec for the 1972 baseline and alternate configuration No. 1. The analog tape recorder used in the 1969 mission may be deleted for the baseline and alternate No. 1 configurations.

Alternate configuration No.2 uses the Mariner 1969 DSS unaltered, and at less than its maximum capacity.

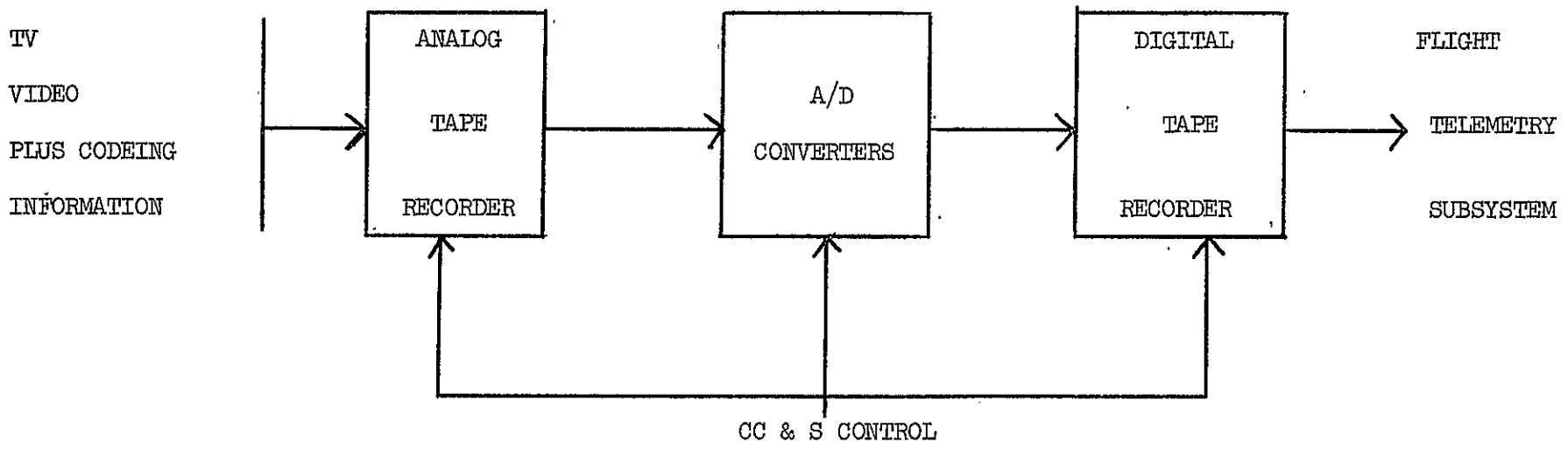


Figure 5.25

MARINER VENUS 1972 DATA STORAGE SUBSYSTEM FUNCTIONAL BLOCK DIAGRAM

(Alternate No. 2)

5.3.13 Cabling Subsystem

5.3.13.1 Functional Requirements

The cabling subsystem is the electrical interface between the spacecraft subsystems. Hence, it must transfer electrical signals throughout the spacecraft with minimum degradation by minimizing magnetic and electrostatic interference, IR drop in conductors, power losses, and cross coupling between conductors.

5.3.13.2 Functional Description

The major portion of the cabling subsystem consists of the upper and lower ring harnesses. Extending radially from the ring harnesses are assembly harnesses which interconnect the flyby probe subsystems. The entry probe/flyby probe cabling interface will be through an in flight separation connector.

5.3.13.3 Functional Modifications From Mariner Mars 1969

The basic ring harness design philosophy used on Mariner Mars 1969 will be retained for Mariner Venus 1972. Changes in the location of subsystem assemblies on the flyby probe together with the inclusion of the probe at the bottom of the octagonal structure dictate that a new cabling detail design be accomplished for Mariner Venus 1972.

5.3.14 Pyrotechnic Subsystem

5.3.14.1 Functional Requirements

The pyrotechnic subsystem (PCU) is required to remotely activate electro-explosive devices required for the performance of various mission events as tabulated in Table 5.15 below for the baseline and alternate missions.

Table 5.15

Pyrotechnic Subsystem Functional Requirements

Functional Requirement	Baseline	Alt. #1	Alt. #2
o Spacecraft separation	X	X	X
o Solar panel deployment	X	X	X
o Science (or TV) cover deployment	X	X	X
o Midcourse propulsion start & shutoff			
o IRS cooldown and motor start	X	X	
o High gain antenna pointing angle change	X		
o Articulated low gain antenna deployment	X		
o Scan platform unlatching	X		
o Canister cover deployment	X	X	X
o Probe Separation	X	X	X

The functional requirements on the pyrotechnic subsystem of the Mariner Venus 1972 are more numerous than on Mariner 1969 as a result of antenna pointing and entry probe release events.

5.3.14.2 Functional Description

Two identical pyro control units perform the function of energy storage, command control and power switching to initiate pyro events. The PCU's are armed via a mechanically actuated switch which closes upon flyby/entry probe separation. The PCU's receive input commands from the CC&S, FCS or separation initiated timer. Upon receipt of a command, the PCU's momentarily switch energy storage capacitors to the proper pyrotechnic device for firing. Telemetry confirmation of firing current is provided to the FTS. The functional block diagram of the pyrotechnic subsystem is shown in Figure 5.26.

5.3.14.3 Functional Modification from Mariner Mars 1969

The basic Mariner 1969 PCU can be retained for the Mariner 1972 mission with only minor modifications required to increase the input/output function capability. Proven pyrotechnic actuators used on Mariner 1969 for solar

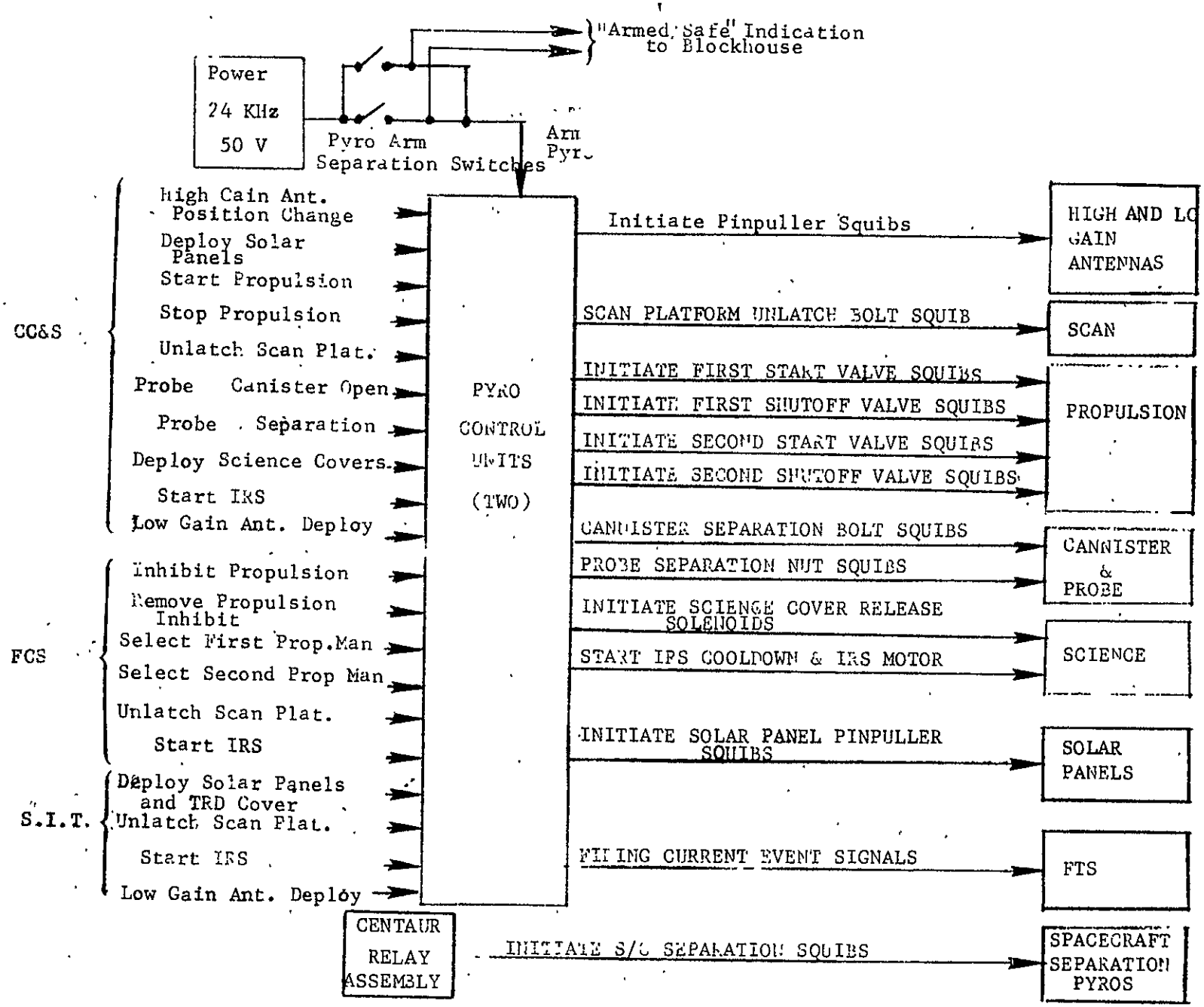


FIGURE 5.26 - PYROTECHNIC SUBSYSTEMS - FUNCTIONAL BLOCK DIAGRAM

panel deployment, S/C separation, propulsion control, and IRS cooldown, etc. will be retained for the Mariner 1972 missions. A summary of the variations from Mariner 1969 pyrotechnic subsystem, to accommodate the Mariner 1972 Venus missions, are presented below in Table 5.16.

Table 5.16

Pyrotechnic Subsystem Variation from MM '69

Functions	Baseline	Alt. #1	Alt. #2
High gain antenna pointing angle change	X		
Articulated low gain antenna deployment	X	X	X
Canister cover deployment	X	X	X
Probe separation	X	X	X

VI. PROGRAM SCHEDULE, COST, EFFECTIVENESS AND RISK SUMMARY

6.0 PROGRAM SCHEDULE, COST, EFFECTIVENESS AND RISK SUMMARY

6.1 Introduction

The mission analyses resulted in three alternatives; however, from the point of view of program costs the Best RF Occultation Probe Mission is considered the Baseline Mission, using the baseline science experiments. The differences between the entry probes for the Best RF Occultation Probe Mission and Best Entry Probe Mission are relatively minor and offsetting factors between the two concepts result in comparable costs for the two. For the cost analysis, therefore, only the Baseline Mission and Minimum Flyby/Entry Probe Missions are considered; they being representative cost-wise of the mission alternatives considered.

The Best RF Occultation Probe Mission (Baseline Mission) utilizes two launches to achieve the program goal of 10% risk, whereas the Minimum Flyby/Entry Probe Mission and Best Entry Probe Mission consider either a dual or a single launch with an associated increased risk of 30% for the dual launch. Schedule, cost, effectiveness, and risk analyses are herein presented covering the alternative systems commensurate with the missions.

6.2 Work Breakdown Structure

To develop the Flyby Probe System and Entry Probe System portion of the overall program schedule and cost, the first step was to identify the Venus 1972 Project activities in a Work Breakdown Structure (WBS). The WBS, shown in Figure 6.1, presents an example of some of the various primary activity areas which were considered in the definition of the

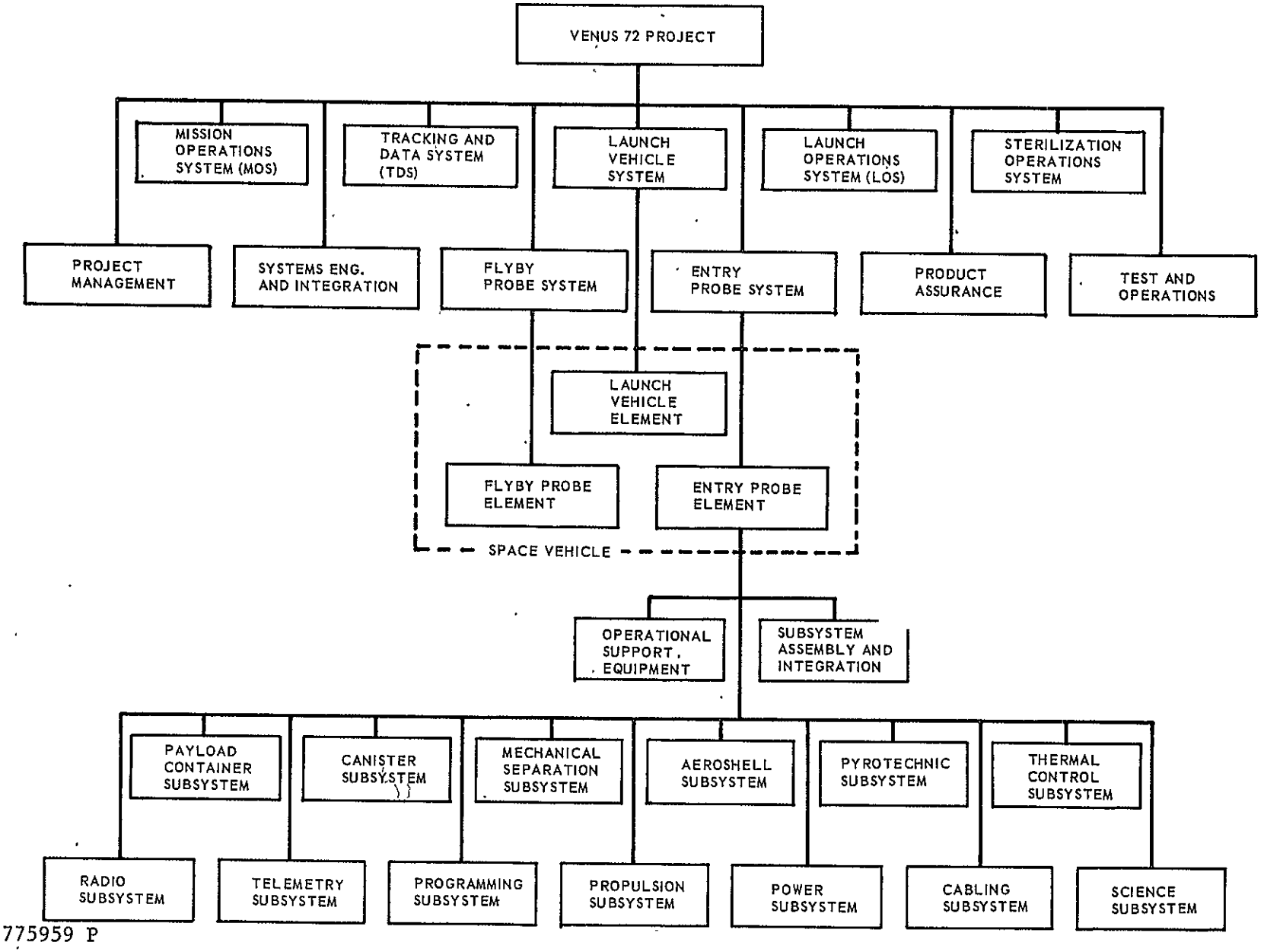


Figure 6.1 ENTRY PROBE SYSTEM - WORK BREAKDOWN STRUCTURE

Entry Probe System as a part of the overall project. A more detailed WBS which includes lower level subsystem breakdowns for both the flyby probes and the entry probes was the basis for the actual cost and schedule analyses. It was assumed that the Launch Vehicle System, the Flyby Probe System and the Entry Probe System would each be a separately contracted package to be integrated by a NASA selected agency. The Mission Operations System (MOS), the Tracking and Data System (TDS) and the Launch Operations System (LOS) would be funded and coordinated according to existing procedures. Separate tasks are expected to be defined, funded, and coordinated within the Launch Vehicle System, Flyby Probe System, and Entry Probe System contracts for the integration with the MOS, TDS and LOS. Sterilization of the Entry Probe Element would be accomplished at the JPL Experimental Assembly Sterilization Laboratory (EASL) and Sterilization Assembly Development Laboratory (SADL) facilities. Planned integration and operations tasks to accomplish this sterilization are to be included in an activity area of the Entry Probe System contract.

Each of the primary activities areas are further divided into subtasks to define work packages in sufficient detail to identify levels of manpower required and subcontract hardware requirements. These work packages are then time phased with an anticipated schedule for a 1972 launch opportunity and an estimate of breadboard, engineering development, prototype test and flight hardware, to result in an estimated Entry Probe System cost.

6.3 Schedule Ground Rules

Schedule analyses were performed on both the flyby probe and the entry probe systems using recent programs as a basis for comparison and

judgement wherever possible. It was assumed that, although program element time spans have varied between programs, the present Mariner Mars 1969 program schedule is the composite of experience gained on all Mariner programs and, as such, it provides the most meaningful basis for the Mariner Venus 1972 flyby probe schedule analysis. Departures from this Mariner baseline were made only where analyses disclosed a significant program element difference. For the Entry Probe System the schedule was based on the feasibility studies of a Mars Atmospheric Probe reported in NASA CR530 dated 1 September 1966 (NASA Contract NAS2-2970) and updated as a Mars Atmospheric Probe for 1971 reported in NORT 67-242 dated September 1967.

Schedule time elements were started from the 1972 launch opportunity and worked backwards without consideration of premium time for development. It was assumed that each subsystem design will be able to take maximum advantage of space qualified hardware. Where this availability is not possible, modifications to space qualified hardware or the selection of components which can be qualified by virtue of their similarity to space qualified hardware was assumed.

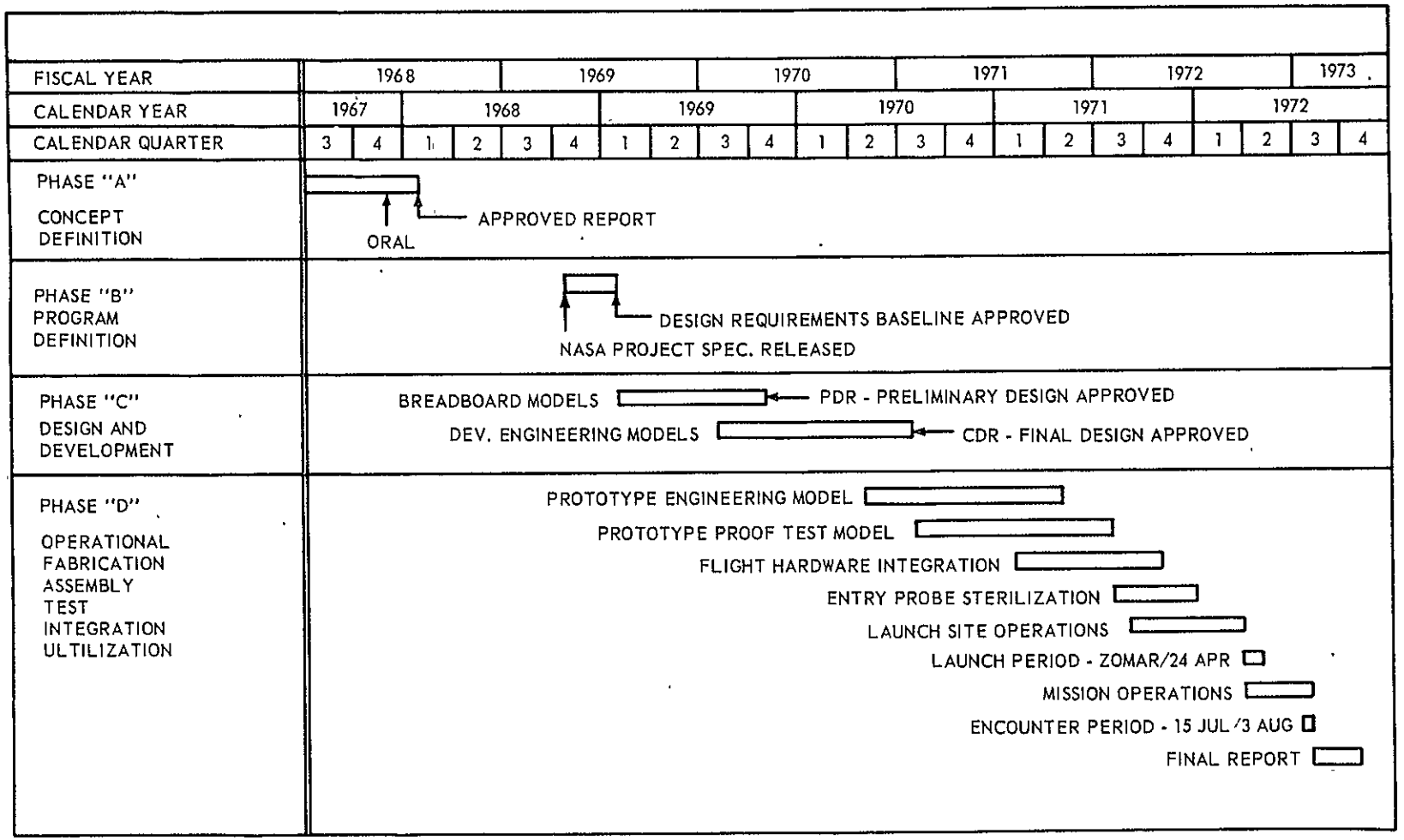
The Science Subsystems on both the entry and flyby probes are expected to be long lead items. To avoid any potential problem, firm specifications must be finalized and issued as early as possible, together with the application of careful vendor selection procedures, to maintain tight subsystem integration and control resulting in maximum overall system compatibility.

6.4 Program Schedule

6.4.1 Total Program Considerations

The Venus 1972 Project Flyby/Entry Probe Schedule shown in Figure 6.2 is a summary evolved from detailed application of the above ground rules and other program criteria. This nominal program schedule is based on an assumed NASA Venus 1972 Project Specification release in Fiscal Year 1969 which is part of the proposal-preparation contractor-selection cycle prior to the "Go-Ahead" of a Program Definition-Phase B during the 4th calendar quarter of 1968. This specification would be derived from an approach developed as a result of the studies conducted during the Concept Definition-Phase A. The primary objectives of Phase A have been the demonstration of feasibility, mission definition, flyby probe synthesis, entry probe synthesis, program requirements, technology requirements, and a reliability approach. Eight months are shown between the completion of Phase A and the beginning of Phase B to allow adequate preparation of a Request for Proposal package by NASA, the preparation of proposals by suitable contractors and a Phase B contract award and negotiation. Further development activities of the program have also been considered in terms of sequential program Phases B, C and D.

Program Definition-Phase B--This phase includes system level tradeoff studies, subsystems analysis, systems engineering baseline definition, systems and subsystems specification preparation, program management documentation, development of the Program Plan and integration meetings with participating contractors. Preparation of this documentation is



775960 P

Figure 6.2 VENUS 72 PROJECT FLYBY/ENTRY PROBE SCHEDULE

approximately four months in duration including customer evaluation, customer coordination and baseline definition approval before the Phase C start. Some long lead item procurement may also be originated during this period if any subsystem can be shown to require more than the 38 months from subsystem specification release to integrated launch readiness with the flyby entry probe.

Design and Development-Phase C--This phase includes the generation of final mission, system, subsystem and component specifications and ends with the release of manufacturing drawings for the flyby/entry probe. Phase C includes breadboarding and engineering model activities required to finalize component or subsystem specifications. During this period, technical efforts will consist of detailing and finalizing the design for which configuration and performance objectives have been established during preliminary design. The end product will be a set of documents providing complete identification and definition of all subsystem and system parameters, interfaces, specifications and drawings.

Operational Phase-D--This phase of the development cycle encompasses the procurement and fabrication of components and/or subsystems, assembly and integration of each Entry Probe System and Flyby Probe System, integration of Flyby Probe Element with Entry Probe Element and the Launch Vehicle Element to make up the Space Vehicle, including evaluation, qualification and acceptance tests. Phase D also includes the demonstration test of and Engineering Test Model (ETM) assembled with prototype hardware, the qualification test of the Proof Test Model (PTM) (including selected subsystem Type Approval Models-TAM) and the integration of these entry

and flyby probe models with the launch vehicle, launch complex, Deep Space Network, etc. These tests will verify the final design prior to the flight hardware acceptance and sterilization of the Entry Probe Element. The launch period and encounter period shown, bracket the nominal dates considered in the Phase A studies. The final report would be submitted three months after the latest encounter date considered, to result in a schedule end date of 31 October 1972, a total of 52 months after initiation of Phase B.

6.4.2 Special Flyby Probe Considerations

The nominal period of time shown from the beginning of Phase C to the first considered launch window on 20 March 1972 is approximately 38 months representing the comparable period of 37 months from the beginning of detailed "Analysis/Design" of the flyby probe through to "Launch" shown on the Mariner Mars 1969 schedule in Figure 6.3. An analysis of schedule changes was performed to evaluate the program phasing relationships and time spans for Venus 1972 Flyby Probe Baseline, Alternate No. 1 and Alternate No. 2 configurations. This analysis was related to the present Mariner Mars 1969 program schedule to obtain established time spans and program element concurrencies. Mariner Mars 1969 data were used because it is believed that this program represents the latest composite of experience gained by JPL on Mariner programs and is, therefore, the most meaningful criteria available.

Baseline and Alternate No. 1 Configurations--Comparative analysis disclosed close similarities between the Baseline and Alternate No. 1

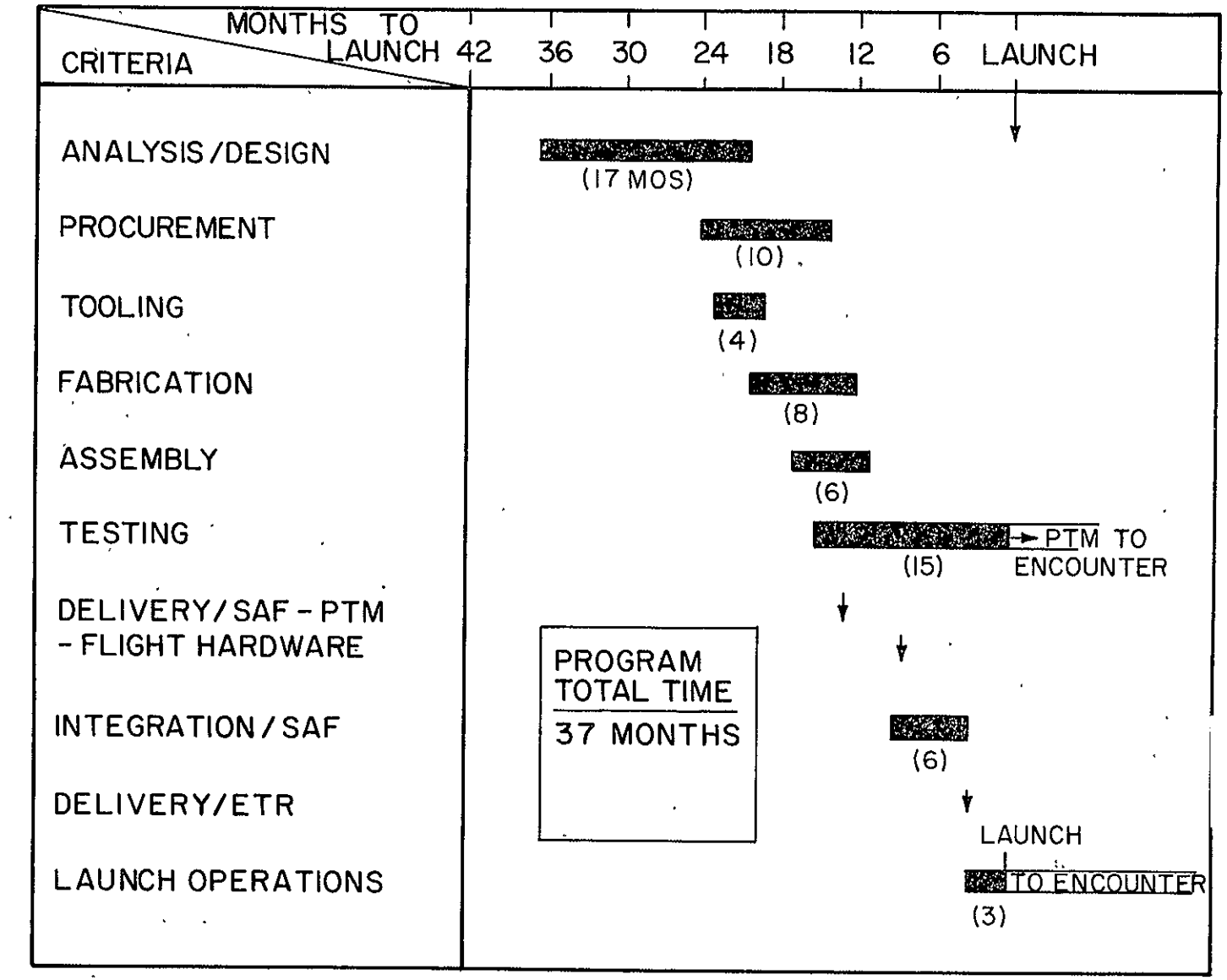


Figure 6.3 FLYBY PROBE PROGRAM SCHEDULE REFERENCE - MARINER MARS 1969

Configurations. Accordingly, a single master schedule was developed for these programs, shown in Figure 6.4. This schedule compares very closely with the Mariner Mars 1969 schedule except in the areas of procurement and integration activities. Because of the early developments status of the microwave spectrometer/imager an additional three months procurement time has been included. Also, an additional three months integration time has been included in the schedule for Flyby Probe Element/Entry Probe Element integration and microwave spectrometer/imager integration. However, since this schedule programs the initiation of procurement earlier in the analysis/design period, only three months are added to the total program time. This results in a total time of 40 months for the Baseline and Alternate No. 1 Configurations as compared with a total program time of 37 months for the Mariner Mars 1969.

Alternate No. 2 Configurations--This mission also compares very closely with the Mariner Mars 1969 schedule. The relative simplicity of this alternative poses no new problem areas, and the addition of two months for Flyby Probe Element/Entry Probe Element integration as shown in Figure 6.5, yields a program total time of 39 months.

6.4.3 Special Entry Probe Considerations

The entry probe technology study, Section 4.0, indicated that a severe lack of data exists on applicable candidate heat shield materials for Venus entry. As materials characterization arc test data is needed for Phase C, it is imperative that materials testing begin no later than FY 1969, preferably sooner. The heat shield must be assumed to be the most critical schedule controlling subsystem due to the present lack

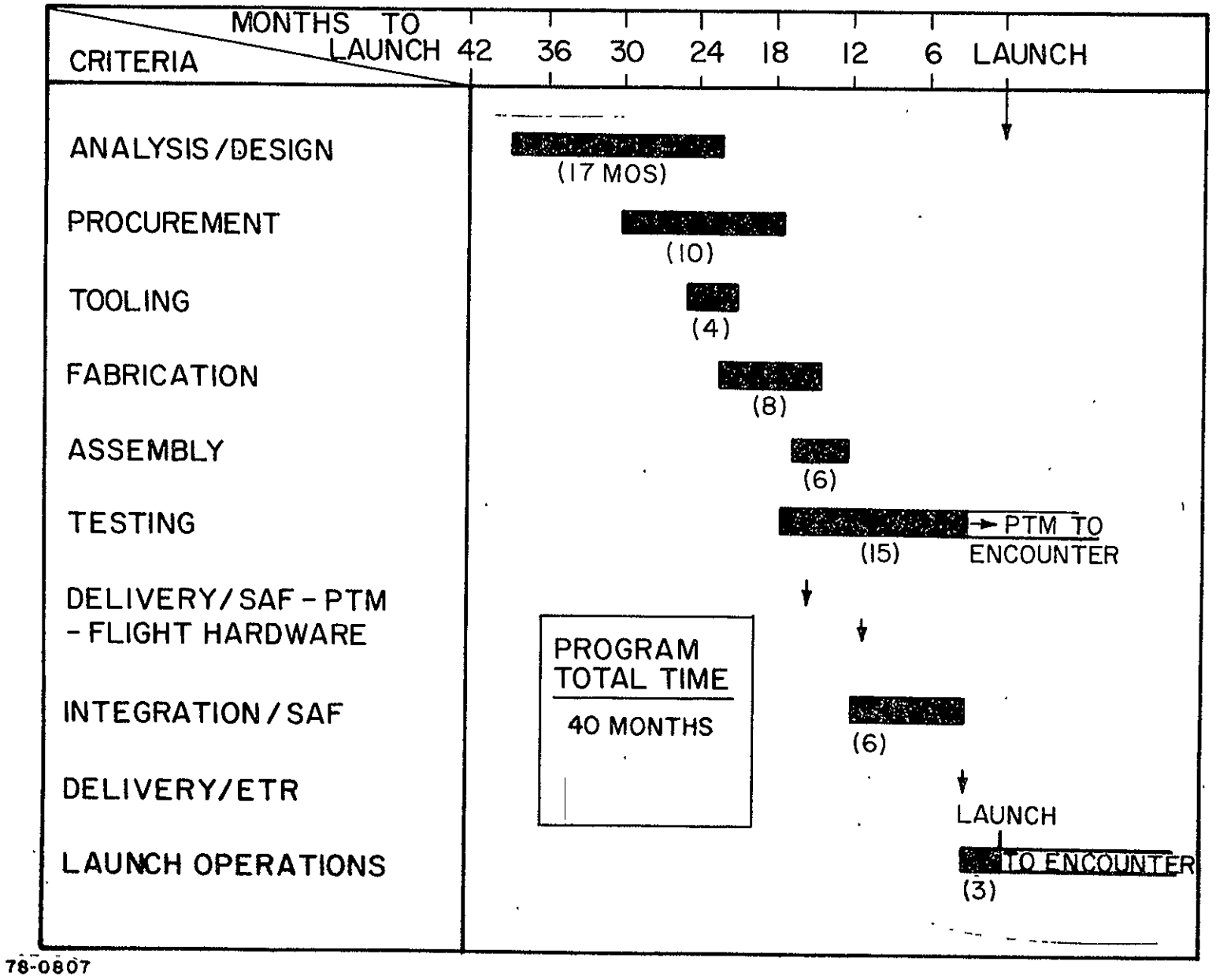


Figure 6.4 1972 FLYBY PROGRAM SCHEDULE - BASELINE AND ALTERNATE I CONFIGURATIONS

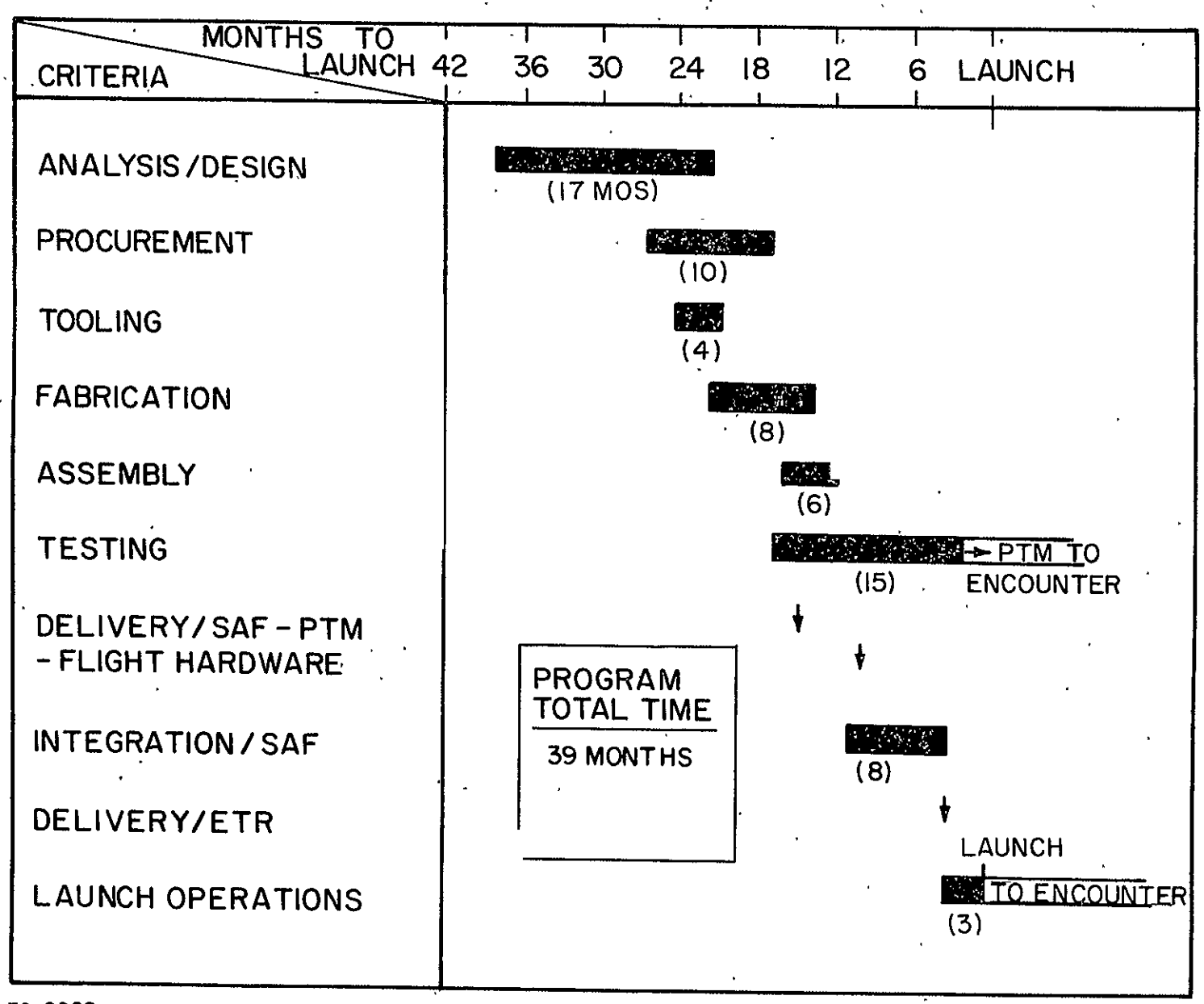


Figure 6.5 1972 FLYBY PROGRAM SCHEDULE - ALTERNATE 2 CONFIGURATION

of test data, and the complexity of the ground test program needed. A minimum of 18 months is needed to provide the necessary heat shield design data required. If R and D is initiated by Fiscal Year 1969 in the critical subsystems areas as the science payload, heat shield, sterilizable batteries, sterilizable transmitter that can operate in a high G environment, and design definition activities continued, Phase C, could start as late as the third calendar quarter of 1969 (beginning of Fiscal Year 1970).

6.4.4 Summary

In summary, there is no schedule limitation for the Venus 1972 mission regardless of which design alternatives are selected for either the flyby probe or the entry probe, if the Design and Development Phase can be underway early in calendar year 1969, based on an approved Desig.. Requirements Baseline. If the beginning of the Design and Development Phase is delayed until the middle of calendar year 1969 (beginning of Fiscal Year 1970), then special long lead item procurement activities will be required before the start of Phase C or "Crash" activities may be necessary in some of the subsystems areas depending on which flyby probe or entry probe configurations are selected. The importance of a timely NASA Project Specification cannot be overemphasized in order that these long lead items or "Crash" efforts can be identified as early as possible.

6.5 Costing Ground Rules

Both the Flyby Probe System and Entry Probe System costs are presented independently to be compatible with expected system contractual

arrangements whereby the Project will be coordinated by a central NASA agency. Therefore, only integration between these two systems with all other systems has been considered in the flyby probe and entry probe system cost analysis and subsequent estimates. Costs of the Launch Vehicle System, Launch Site Activation, Mission Operations System, etc., are not included at this time, although at least two sets of all flight hardware are included for each probe, including appropriate OSE to support two launch complexes and two launch vehicles. Availability of a launch complex or its cost are not part of this cost analysis.

6.5.1 Primary Entry Probe System Ground Rules

1. The Entry Probe System cost includes the integration costs with other systems.
2. All entry science instrumentation (development and production) is GFE, but estimated costs are provided.
3. Mission Operation System, Tracking and Data System, Launch Vehicle System and Launch Operations System costs include only the entry probe contractors coordination and integration requirements.
4. Sterilization operations facilities at JPL will be operated by the entry probe contractor.
5. An estimated cost is provided for the transmitter in the Radio Subsystem (development and production).
6. An estimated cost is provided for the batteries in the Power Subsystem (development and production).

7. Three flight hardware Entry Probe Elements plus two complete sets of spare parts would be provided for a two launch program or one flight vehicle plus two complete sets of spare parts for a single launch.
8. Aerodynamic tests on the entry vehicles to be conducted by NASA engineering teams at NASA facilities in coordination with the entry probe contractors test and field operations.
9. Period of performance includes from the beginning of Phase B to the end of the final report.

6.5.2 Primary Flyby Probe System Ground Rules

1. Flyby Probe to be a new procurement.
2. Modify existing Mariner Mars '69 Operational Support Equipment.
3. No requalification required when Mariner Mars 1969 designs are used.
4. Hardware deliverable end items include:

   3 Flight Flyby Probes, plus 20% discretionary spares (2 launches)

   1 Flight Flyby Probe, plus 20% discretionary spares (1 launch)

   1 Proof Test Model

   1 Structural Test Model

   1 Thermal Control Model

   2 Sets of Modified Mariner Mars 1969 OSE
5. Magnetic cleanliness required for baseline mission.
6. Use cost factors derived from historical Mariner approach.
7. All subsystem costs to be derived at the functional level.
8. Cost integration with all other systems.
9. Period of performance runs from the beginning of Phase B to the end of the final report.

6.6 Program Costs

6.6.1 Cost Summary

The Venus 1972 Program costs were analyzed and estimated for the Flyby Probe System and the Entry Probe System according to the above ground rules. A cost summary for a selected series of alternate configuration combinations is shown in Table 6.1. A factor of eight million dollars was added to the baseline entry probe subtotals to approximate the cost of GFE items, the batteries and transmitter. Four million dollars was added to the entry probe alternate mission to cover the costs of these same items for the reduced payload.

6.6.2 Flyby Probe Configuration Summary

The baseline and alternative flyby probe configuration recurring, non-recurring, management and operations costs are comparatively shown in Table 6.2. The reasons for the cost differences are discussed below.

6.6.2.1 Baseline Flyby Probe

The Baseline Flyby Probe cost is relatively low, due to maximum use of previously qualified equipment and minimum revision to Mars Mariner 1969 spacecraft subsystems. The Baseline Flyby Probe includes cruise science, two low gain antennae and a scan platform.

6.6.2.2 Alternate Flyby Probe No. 1

This alternate flyby probe will delete the scan platform, the deployable low gain antenna and cruise science. The deletion of the magnetometer relaxes the magnetic cleanliness requirements and reduces some of the

N68-21888

Table 6.1

Flyby Probe/Entry Probe Costs
(Millions of Dollars)

	Flyby/Entry Probe Summary	Flyby Probe Sub Total	Entry Probe Sub Total
1. Baseline Flyby Probe Baseline Entry Probe (2 launches)	98.81	56.71	42.10
2. Alternate No. 1 Flyby Probe	94.37	52.27	42.10
Baseline Entry Probe (1 launch)	80.79	42.47	38.32
3. Alternate No. 2 Flyby Probe	90.81	48.71	42.10
Baseline Entry Probe (1 launch)	77.65	39.33	38.32
4. Alternate No. 1 Flyby Probe	86.06	52.27	33.79
Alternate Entry Probe (1 launch)	72.85	42.47	30.38
5. Alternate No. 2 Flyby Probe	82.50	48.71	33.79
Alternate Entry Probe (1 launch)	69.71	39.33	30.30

Table 6.2

Baseline and Alternate Flyby Probe Configuration Cost Summary
(Millions of Dollars)

Configuration	Non-Recurring	Recurring	Management	Operations	One Flyby Probe	Three Flyby Probe
Baseline	27.26	5.45	4.0	9.1	45.81	56.71
Alternate No.	25.32	4.95	3.7	8.5	42.47	52.37
Alternate No. 2	22.27	4.69	3.47	8.9	39.33	48.71

expense associated with the requirement. Because of the reduced subsystem complements, program costs are somewhat less than the baseline mission.

6.6.2.3 Alternate Flyby Probe No. 2

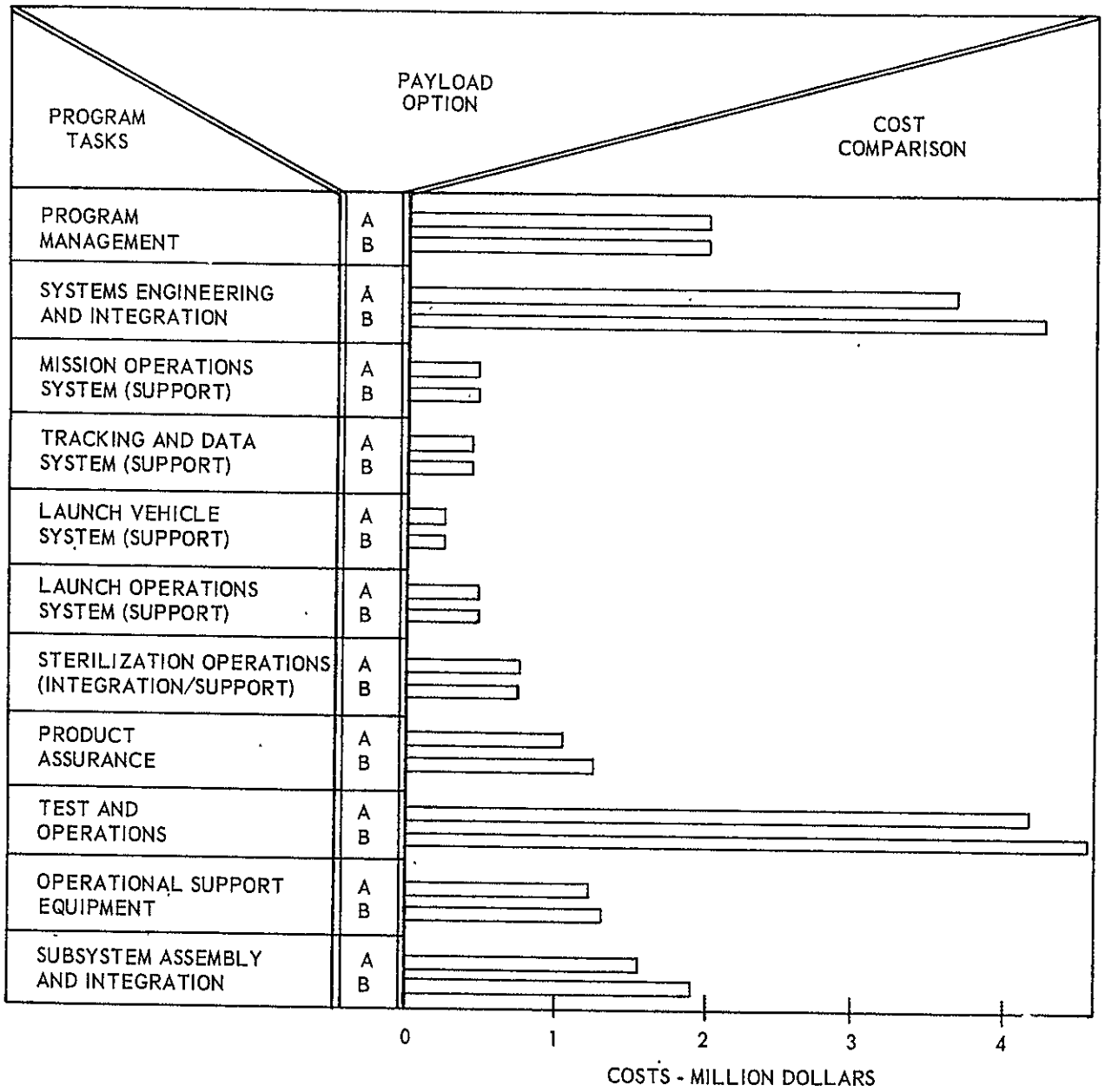
This second alternate flyby probe differs from alternate number one by having TV as the only science experiment. This change results in reduced cost because the cameras to be used are presently qualified and available. The operations cost will increase slightly because of the complexity of TV data processing equipment. The data storage system cost will increase because of the addition of an analog tape recorder to the subsystem. Total program costs are less than either the Baseline Flyby Probe or Alternate Flyby Probe No. 1.

6.6.3 Entry Probe Configuration Summary

The estimated cost for each major program task shown in the Work Breakdown Structure is compared in Figure 6.6 for the "A" (Minimum) and "B" (Baseline) options. The primary reasons for increased cost to accomplish the "B" option, if any estimated difference is identifiable, is indicated in Table 6.3. The estimated cost for each subsystem shown in the Work Breakdown Structure is compared in Figure 6.7 for the "A" and "B" option. The primary reasons for an increased cost for the "B" option, if any estimated difference is identifiable, is indicated in Table 6.4.

6.6.3.1 Baseline Entry Probe

The Baseline Entry Probe includes all of the suggested Best RF Occultation Probe Mission experiments plus associated data collection



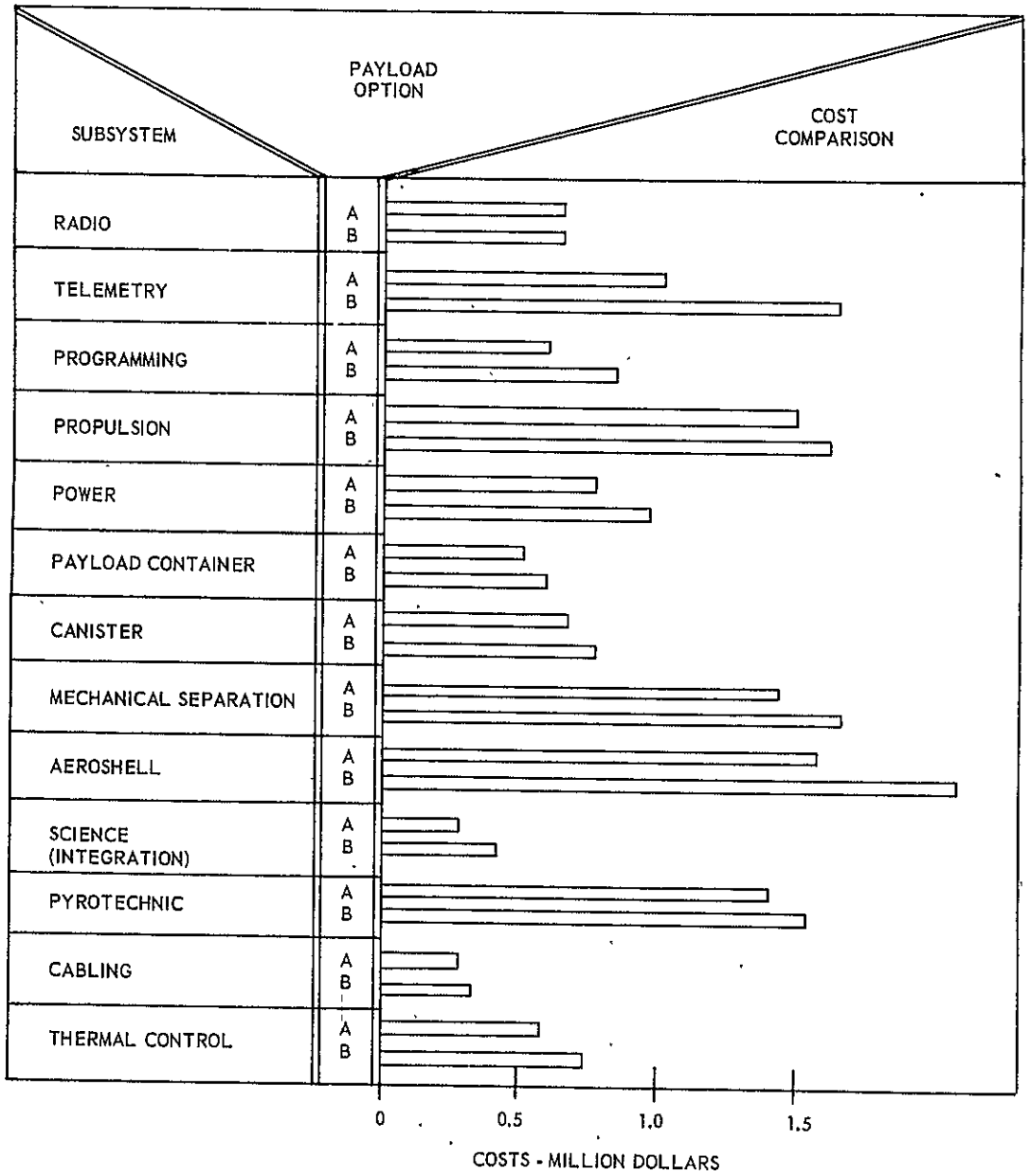
775962P

Figure 6.6 ENTRY PROBE PROGRAM TASK COMPARISON - COST/PAYLOAD OPTION

Table 6.3

"A" and "B" Entry Probe Task Comparisons

Program Management	No difference
Systems Engineering and Integration	Increased design, analysis, integration and test
Mission Operations Systems	No difference
Tracking and Data Systems	No difference
Launch Vehicle System	No difference
Launch Operations System	No difference
Sterilization Operations	No difference
Product Assurance	Increased hardware handling and test analysis
Test and Operations	Increased scope of systems, quality and integration test operation
Operational Support Equipment	Larger size system plus increased test equipment support
Subsystem Assembly and Integration	More complex subsystems to assemble and integrate



775963P

Figure 6.7 ENTRY PROBE SUBSYSTEM COMPARISON - COST/PAYLOAD OPTION

Table 6.4

"A" and "B" Entry Probe Subsystem Comparison

Radio	No difference (transmitter GFE)
Telemetry	Increased data handling and storage requirement
Programming	Increased events and functions
Propulsion	Increased vehicle weigh requires higher impulse
Power	Added regulation and increased distribution
Payload Container	Larger volume and weight required for science instruments
Canister	Larger volume and weight of Entry Probe
Mechanical Separation	More separation functions and added weight and size to be separated
Aeroshell	Larger structure and increased entry heating environment
Science	More experiments to integrate
Pyrotechnics	More devices require S & I and explosive functions
Cabling	Greater wiring and connections
Thermal Control	Large areas and more equipment

and playout requirements. The more difficult set of entry conditions are accommodated by use of advanced heat shield material concepts. Specific science subsystem includes a three (3)-axis accelerometer, two (2) temperature transducers, two (2) pressure transducers, mass spectrometer, acoustic densitometer, beta densitometer, visual photometer and impact detector.

6.6.3.2 Minimum Entry Probe

The Minimum Entry Probe science subsystem deletes the mass spectrometer, acoustic densitometer, beta densitometer, visual photometer and impact detector plus reduces the associated data collection and playout requirements. Reduced heat shield requirements are also included due to the lower entry velocities and low M/C_DA of the probe.

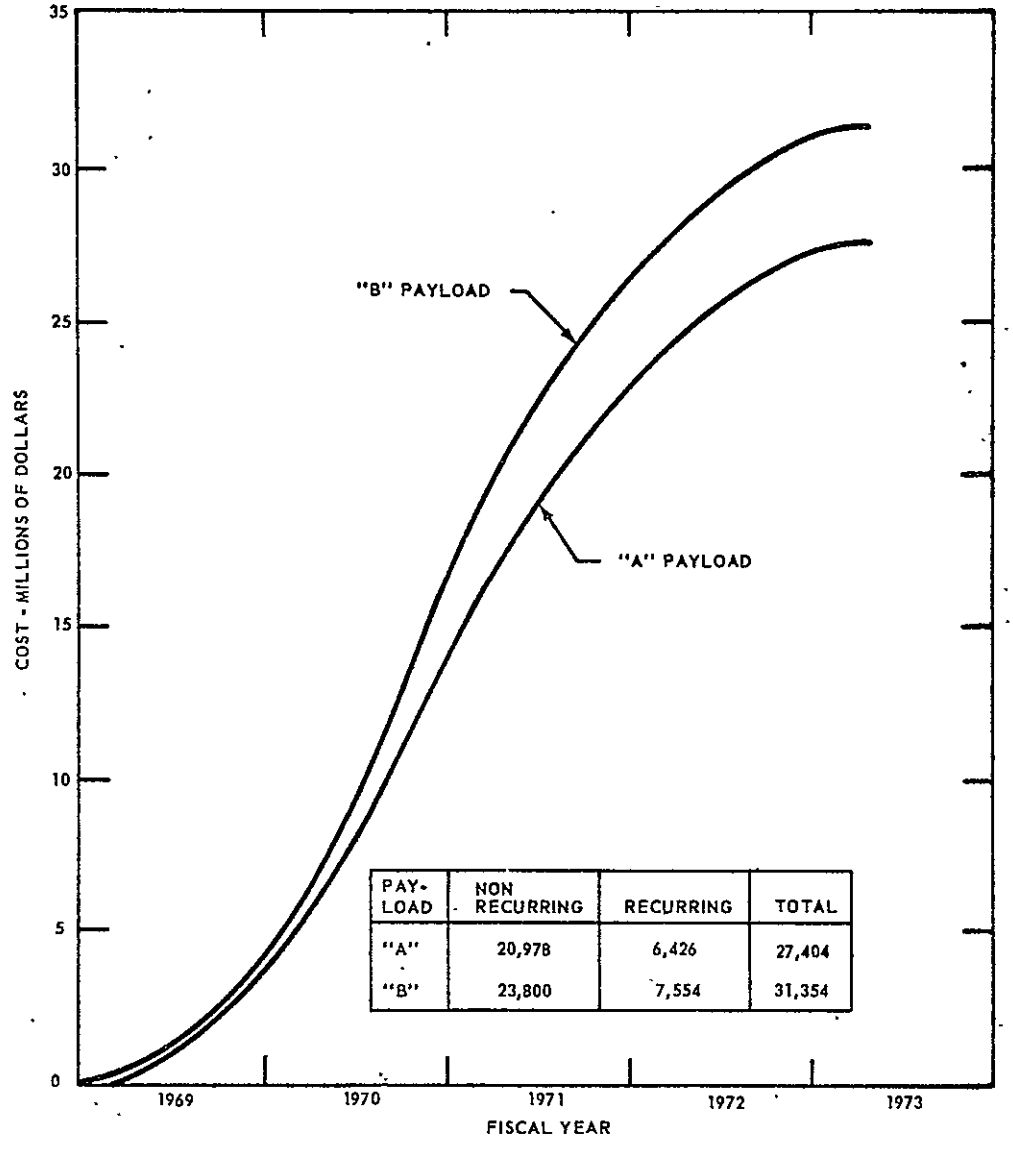
6.6.4 Expenditure Plan

The yearly expenditure requirements for the entry and flyby probes are shown in Figures 6.8 and 6.9. The entry probe expenditures shown do not inlcude science, battery or transmitter costs. The maximum yearly expenditure occurs in FY 1971, 15 million on the entry probe and 20 million on the flyby probe.

6.7 Cost Effectiveness for Alternate Approaches

6.7.1 Effectiveness Criteria

The criteria used in evaluation of the system effectiveness of the baseline and alternate missions are:



PAY-LOAD	NON RECURRING	RECURRING	TOTAL
"A"	20,978	6,426	27,404
"B"	23,800	7,554	31,354

775961 P

Figure 6.8 ENTRY PROBE EXPENDITURE PLAN

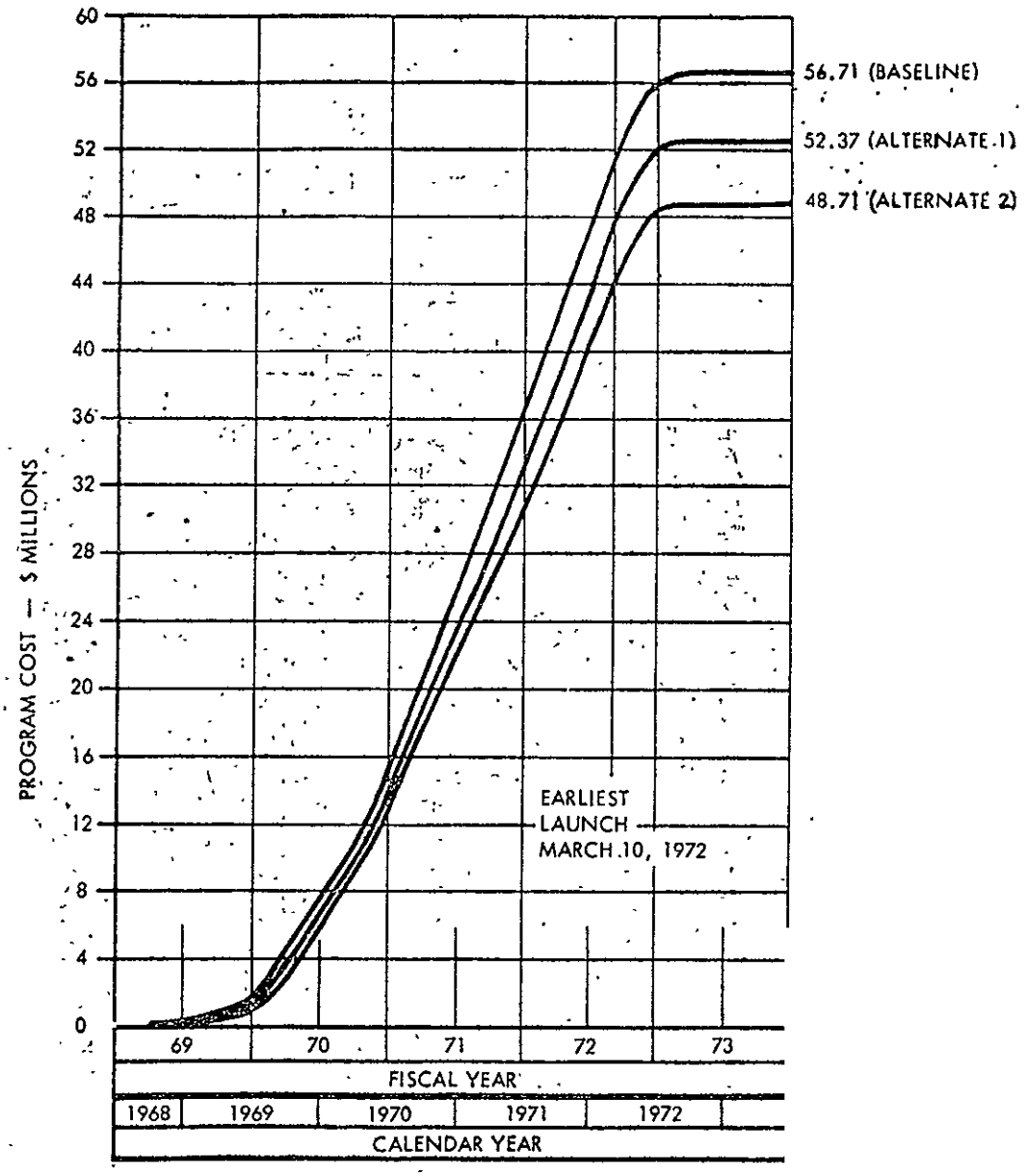


Figure 6.9 FLYBY PROBE EXPENDITURE PLAN

1. Achievement of mission objectives
2. Availability
3. Dependability

The configurations are rated on their capability for achieving the mission science objectives. Availability and dependability factors relate schedule implications and engineering complexity of the configurations to the total system effectiveness.

Achievement of the mission objectives is directly related to the mission value results given in Section 2.4.2. Normalizing the mission values for alternate missions (refer to Tables 2.9, 2.10, 2.11) with those for the baseline, i.e., Best RF Occultation Probe Mission, yields the results shown below:

Mission	Normalized Mission Value
Best RF Occultation Probe Mission	1.00
Minimum Flyby/Entry Probe Mission	0.67
Best Entry Probe Mission	0.91

The schedule analysis indicates that the Best RF Occultation Probe Mission is more difficult due to the higher entry velocities for this mission and poses a more difficult heat shield development problem. The schedule shows ample time for the development of any of the missions provided a FY 69 start is made for heat shield material testing. Although the missions having the lower entry velocity are felt to have an edge in mission effectiveness from the viewpoint of schedule, no quantification of these effects is given. One should of course bear

Table 6.5

Summary of Major System Differences for Alternate Missions

Best RF Occultation Probe Mission	Minimum Flyby/Entry Probe Mission	
	Alternate No. 1 Flyby Probe Minimum Entry Probe	Alternate No. 2 Flyby Probe Minimum Entry Probe
Early Arrival	Late Arrival	
High V_∞ ($\approx$ 6.7 km/sec)	Reduced V_∞ ($\approx$ 4.3 km/sec)	
20 day launch period (2 launches)	12 day launch period (1 or 2 launches)	
Entry Probe Science - Baseline	Entry Probe Science - Alternate	
Flyby Probe Science - Baseline (JPL 161-01 including magnetometer and trapped radiation cruise science)	Flyby Probe Science - reduced (delete trapped radiation and magnetometer)	Flyby Probe Science - minimum (include wide angle TV)
Flyby Probe Configuration - Scan Platform - Two low gain antennas - Articulated high gain antenna	Flyby Probe Configuration - No Scan Platform - One Low Gain Antenna - Fixed High Gain Antenna	Flyby Probe Configuration - No Scan Platform - One Low Gain Antenna - Fixed High Gain Antenna
Magnetic Cleanliness Required on EP and FP	Reduced Magnetic Cleanliness Required on EP and FP	

in mind the scheduling problem when evaluating the cost effectiveness results.

The aspect of dependability, or reliability, favors the simpler Minimum Flyby/Entry Probe Mission and Best Entry Probe Mission. The major system differences are summarized in Table 6.5, wherein the lesser complexity of the Minimum Flyby/Entry Probe Mission is apparent. Here again, no quantification of the effect of system complexity on the overall mission effectiveness is presented, but this aspect of mission selection must be borne in mind when evaluating the overall mission effectiveness.

6.7.2 Cost Effectiveness Summary

The overall cost and system effectiveness results are summarized in Table 6.6. Included in Table 6.6 are several additional configurational alternatives for which mission value calculations were performed as described in Section 2.4. The normalized measure of cost effectiveness is the normalized cost (mission cost divided by Best RF Occultation Probe Mission cost) divided by the normalized mission effectiveness.

The results shown in Table 6.6 indicates that the Best RF Occultation Probe Mission is the most effective mission. Contained within the results of Table 6.6 is the trend of mission effectiveness with cost. The variation of mission cost and effectiveness is further illustrated by plotting the results of Table 6.6 in bar graph form in Figure 6.10. From the cost effectiveness trends in Figure 6.10, it can be seen that the cost differences are relatively small for a wide range of effectiveness, but a large cost reduction appear possible if a truly austere high risk single launch mission were to be attempted.

Table 6.6

Cost Effectiveness Comparison

	Missions	EP & FP Systems Cost - M$	Normalized Mission Effectiveness (M)	Normalized Cost/Mission Effectiveness
1.	Best RF Occultation Probe Mission (Baseline Entry Probe and Baseline Flyby Probe)	98.81[2]	1.00	1.00
2.	Best Entry Probe Mission * (Alternate No. 1 Flyby Probe)	94.37[2] 80.79[1]	0.91	1.05 0.90
3.	Best Entry Probe Mission * (Alternate No. 2 Flyby Probe)	90.81[2] 77.65[1]	0.77	1.20 1.02
4.	Flyby/Entry Probe Mission (Minimum Entry Probe and Alternate No. 1 Flyby Probe)	86.06[2] 72.85[1]	0.67	1.30 1.10
5.	Flyby/Entry Probe Mission (Minimum Entry Probe and Alternate No. 2 Flyby Probe)	82.50[2] 69.71[1]	0.62	1.35 1.14

* Entry probe costs for the Best RF Occultation Probe Mission and Best Entry Probe Mission are assumed identical.

1 One launch

2 Two launches

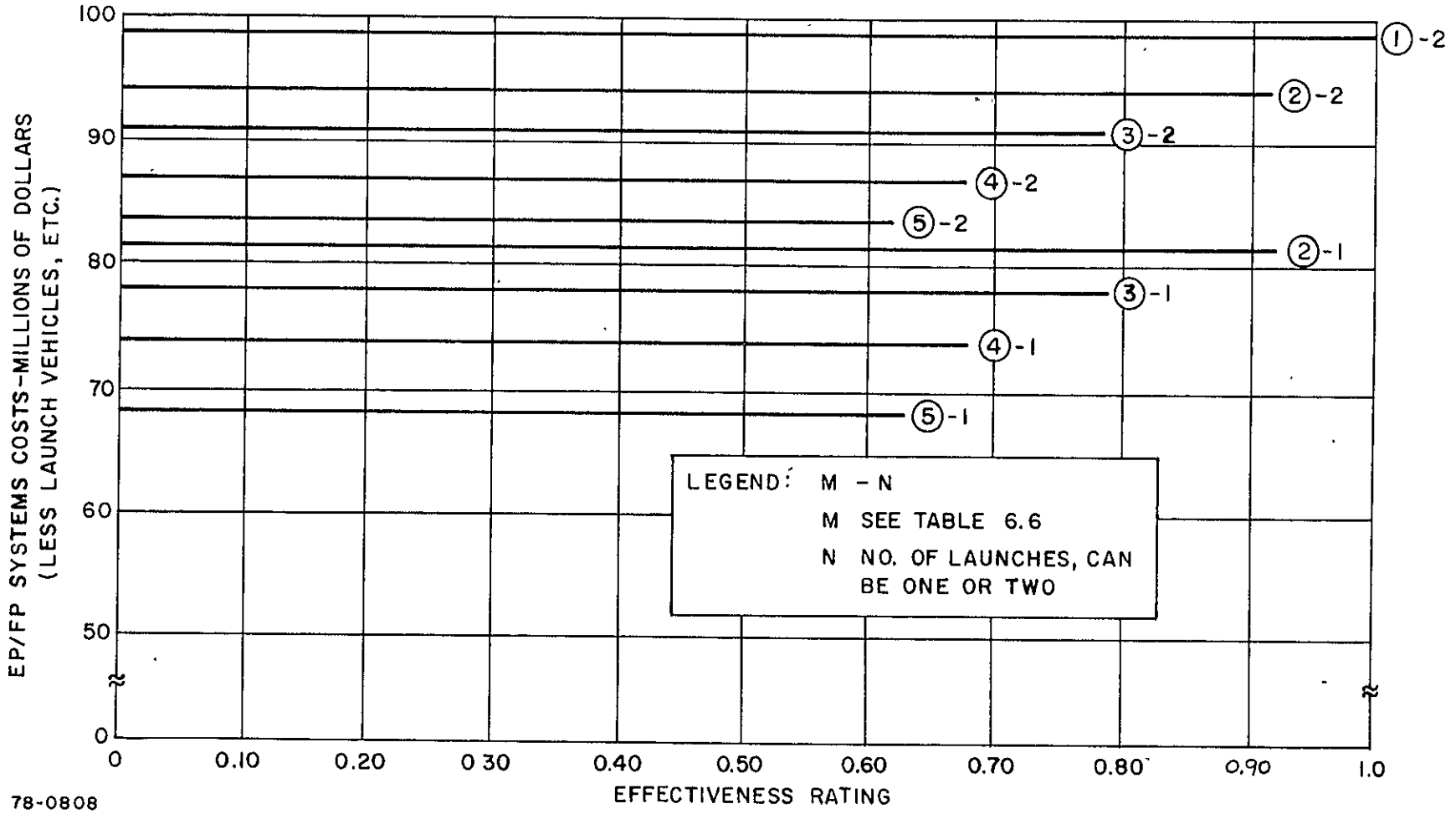


Figure 6.10 ALTERNATE MISSION COST AND EFFECTIVENESS

On the basis of cost effectiveness, a single launch (high risk) Best Entry Probe Mission with an Alternative No. 1 is superior. The effect of mission risk on the effectiveness must be considered as a two-launch mission has a more favorable risk factor. The mission risk analysis (Ref. Section 2.5.2) shows a 10 percent risk for the two-launch mission versus a 30 percent risk for the single launch mission. The risk differences are felt to be pessimistic as the recent Mariner V and Venera 4 missions were both successful and both have provided additional information regarding the problems of Venus entry and direct link communications.

Under the philosophy of a two-launch mission, both launches must occur prior to the critical separation and entry phases which occur late in the mission and as both entry probes are direct link, they both are targeted for the same point; hence, if both work, one only reinforces the results already obtained. It therefore appears that due to the targeting inflexibility with the direct link, two launches are not as effective as they might be if they could be targeted for alternative sites. The cost difference between one or two launches for the Best Entry Probe Mission is 13.6 million plus an additional increment of 10 million for one vs. two Atlas/Centaur vehicles. For the single launch mission, additional funding in the area of reliability, test, and quality control could improve the mission risk.

In conclusion, the recommended mission is the Best Entry Probe Mission with the Alternate No. 1 flyby probe configuration. Considering the single launch successes to date in the Mariner program, and the limited

funding projected for planetary exploration, a single launch mission appears most attractive.

APPENDIX I

STATEMENT OF WORK

APPENDIX I

STATEMENT OF WORK

ARTICLE 1. STATEMENT OF WORK

(a) The Contractor shall conduct a study on the definition of a flyby spacecraft/entry probe system combination, for the 1972 launch opportunity, (with potential application to the 1973 launch opportunity), capable of accomplishing the science measurements of the attached Document 161-01, Exhibit No. 1, within the capability limits of the Atlas/Centaur SLV-3C launch vehicle. The results of the study should be of sufficient depth to permit mission and spacecraft system and subsystem definition and evaluation of program and technology requirements.

The general areas of effort to accomplish the above objectives are:

(1) Synthesis of a capsule system design, based on capsule instrumentation specified in JPL TM 33-282, consistent with sterilization and entry requirements. The capsule system is not required to survive Venus surface impact.

(2) Synthesis of a spacecraft flyby system design based on the Venus baseline science measurements given in JPL Document 161-01 and compatible with the capsule system interface requirements. The spacecraft flyby system shall be based where practical on Mariner Mars '69 project concepts and functional designs as defined in Mariner Mars '69 Functional Requirements.

(3) Evaluation of spacecraft mechanization effects of alternate science payloads based on JPL TM 33-282, decreasing the allowable weight and complexity to a reasonable minimum and increasing the allowable weight and complexity to utilize the full capability of the launch vehicle.

(4) Development of technology and program requirements, and estimates of mission effectiveness, of the baseline system compared with the alternatives of Item (a)(3)above, for the 1972 launch opportunity.

(b) In the performance of this effort the Contractor shall:

(1) Define the interplanetary, planetary flyby and planetary entry trajectories, consistent with mission scientific requirements, including but not necessarily limited to the following considerations:

(i) Definition of approach trajectories (capsule deflection mode, not spacecraft deflection) for a capsule and flyby spacecraft compatible with a relay telecommunication link and/or a direct telecommunication link to Earth.

) Definition of capsule entry and descent trajectory parameters affecting capsule design shall be traded-off to determine the most desirable entry conditions for the capsule mission (e.g., Aerodynamic heating and deceleration as a function of entry path angle; telecommunication geometry, etc.).

(A) The atmospheric models defined in NASA SP 3016, extended to a range of 4-50 Earth atmospheres surface pressure, shall establish the range over which capsule analysis shall be made. The atmospheric parameters range for which the capsule system shall be capable of accomplishing mission requirements shall be determined by tradeoff of subsystem design penalties and the most probable ranges of parameters. Final selection of the baseline range for the capsule system design shall be reviewed and approved by JPL.

(B) Insure deceleration of the capsule to subsonic velocity at an altitude and time before impact compatible with science measurement and data transmission requirements.

(iii) Definition of Venus flyby geometry information (e.g., distance of closest approach, relationship to terminator, Earth occultation, etc.) to mechanize flyby science measurements of JPL Document 161-01.

(iv) Definition of interplanetary transfer trajectories (consistent with launch vehicle constraints) and mission requirements (e.g., items (b)(1)(i) through (b)(1)(iii), and consistent with the planetary quarantine criterion that there be less than a 10^{-3} probability of contaminating Venus with a survivable organi

(2) Define spacecraft/capsule system and subsystem reliability requirements, consistent with mission lifetime and operational sequence requirements, including the following:

(i) Development of representative reliability goals for the major phases of the mission. Results shall be submitted to JPL for review and approval.

(ii) Estimates of part and/or subsystem failure rate allocations consistent with item (b)(2)(i) above and the projected state-of-the-art (Hi-Rel programs). For this study, these items do not imply the development of detailed prediction models and parts count analysis.

(iii) Evaluation of system and subsystem functional reliability requirements by preliminary failure mode, effect, and criticality analysis for spacecraft and capsule operations. The objectives and intent of this analysis are specified in Section 3.4 of NASA NPC 250-1.

(iv) Specification of mission and system considerations resulting in greatest relative reliability for given alternatives and tradeoffs.

(3) Define a capsule system consistent with the capsule instrumentation specified in JPL TM 33-282. The capsule system is not required to survive impact. Results and conclusions shall be documented by system and subsystem functional descriptions and block diagrams, operational sequences, configuration drawings and weight and power summaries. Definition of the system shall include but not necessarily be limited to the following:

(i) Definition of the data system design based on mission requirements, including tradeoff between a relay telecommunication link with the flyby spacecraft and direct transmission of data to Earth.

(ii) Design mechanization of science instrument sampling and/or data gathering including physical arrangement of instruments, ducting and/or sensor exposure required, and possible deployment from or ejection of the heat shield to obtain meaningful measurements of the Venus environment.

iii) Definition of design and technological implications of capsule sterilization to the criteria established in Section (b)(6)(v).

(iv) Definition of qualitative design considerations to achieve reliability goals developed in Item (b)(2).

(v) Definition of capsule engineering subsystems requirements and system configuration (e.g., attitude control, heat shield) to achieve the entry and descent conditions consistent with scientific objectives, based on analyses specified in Item (b)(1).

(vi) Evaluation of major technology developments necessary for the capsule system.

(4) Define a flyby spacecraft system consistent with the interplanetary and flyby science instrumentation specified in JPL Document 161-01. Spacecraft system design shall be based on Mariner 1969 project concepts as defined in the JPL Mariner '69 Project Functional Requirements. Results and conclusions shall be documented by system and subsystem functional descriptions and block diagrams, operational sequences, configuration drawings and weight and power summaries.

N68-21888

Definition of the system shall include but not necessarily be limited to the following:

(i) Design mechanization of planetary encounter operations including planetary scan requirements and planetary science instrumentation based on the trajectory analyses of Item (b) 1

(ii) Definition of the telecommunication system mechanization (including antenna pointing requirements) based on interplanetary, planetary encounter and capsule relay link (if required) data requirements.

(iii) Definition of spacecraft orbit determination, trajectory correction and capsule injection requirements (including accuracy requirements) to achieve spacecraft flyby and capsule entry conditions consistent with mission (e.g., sterilization) and scientific requirements.

(iv) Definition of the flyby spacecraft engineering subsystems requirements (e.g., attitude control, structure, thermal control, power and sequencing subsystems) consistent with capsule interface, scientific and subsystem requirements specified in Items (b)(4)(i) through (b)(4)(iii).

(v) Qualitative design considerations to achieve reliability goals developed in Item (b) 2.

(vi) Synthesis of a spacecraft system configuration, based on overall system, subsystem, and interface requirements.

(vii) Evaluation of the effect on the flyby spacecraft design and/or mission operations to comply with the planetary quarantine policy that there be less than 10^{-3} probability of contaminating Venus with a survivable organism.

(viii) Evaluation of major technology developments necessary for the flyby spacecraft system.

(5) Provide information necessary for evaluation of program requirements. This information shall include but not necessarily be limited to:

(i) Estimated schedule for accomplishment of the above described project with launch of two (2) spacecraft during the 1972 Venus opportunity.

(ii) Estimated costs to accomplish this project (exclusive of launching vehicles and DSN operation) including spacecraft and facilities development, testing, flight operations, project management, flight equipment, and sufficient spares. The cost evaluation shall be broken down to at least the major subsystem level.

(iii) Major variations in schedule and cost which may be peculiar to alternate system concepts (e.g., reduced or increased science objectives).

(6) Observe the following constraints:

(i) Mission accomplishment shall be during the 1972 launch opportunity, with analysis of the resulting system design applicability to the 1973 mission opportunity. System state-of-the-art will be as of January, 1969, and for this study should be based on Mariner 1969 Project Concepts as defined in JPL Mariner '69 Functional Requirements.

(ii) Spacecraft requirements shall be compatible with the Deep Space Net (DSN) capability as described in EPD 283.

(iii) Launch energy requirements shall be based upon use of an Atlas/Centaur SLV-3C. The vehicle capability assumed for this study shall be defined by JPL-supplied information.

(iv) Program planning shall be based on two (2) launches in the 1972 opportunity.

(v) Capsule operations shall be consistent with NASA planetary quarantine policy specified in NASA Management Manual 4-4-1, "NASA Unmanned Spacecraft Decontamination Policy," September, 1963, which for purposes of this study, requires the following:

(A) The lander will be assembled in "clean rooms" at specific levels of assembly.

(B) All hardware included in a planetary lander must be capable of withstanding both heat sterilization and ethylene oxide (ETO) exposure. These environments are defined in "Compatibility Test for Planetary Dry Heat Sterilization," JPL Environmental Test GMO-50198-ETS-A, September, 1964.

(C) The landing assembly will be enclosed in a bacteriological barrier to maintain cleanliness and sterility. After decontamination, the enclosure will not be opened within any portion of the Earth's atmosphere which might re-contaminate the landing assembly.

(vi) Trajectory-related constants shall be as defined in JPL TR No. 32-604 dated 6 March 1964 and any subsequent addenda specified by JPL.

(7) Utilize the following information:

(i) EPD 283, "System Compatibility and Development Schedule of the Deep Space Net."

(ii) Atlas/Centaur launch vehicle performance information.

(iii) JPL generated trajectory data (tabulated) for the 1972 and 1973 launch opportunities for Venus flyby missions. This does not include capsule approach trajectory information.

(iv) JPL TM 33-282, Revision 1, "Venus: Preliminary Science Objectives and Experiments for Use in Advanced Mission Studies, " August 1, 1966.

(v) JPL Specification No. X SO-30275-TST-A, "Compatibility Test for Planetary Dry Heat Sterilization Requirements," dated May 24, 1964.

(vi) JPL Specification No. GMO-50198-ETS-A, "Compatibility Tests for Ethylene Oxide Decontamination Requirements," dated September 3, 1964.

(vii) NASA NPC 250-1, "Reliability Program Provisions for Space System Contractors," Section 3.4.

viii) NASA SP-3016, "Venus and Mars Nominal Natural Environment for Advanced Manned Planetary Mission Programs," 1965.

(ix) JPL Mariner '69 Functional Requirements.

(x) Mariner '69 Mission Plan and Requirements.

(xi) JPL Document 161-01, "Venus Flyby/Entry Probe Mission Baseline Science Instruments."

(8) Provide the following reports and documentation:

(i) One (1) reproducible and twenty-five (25) print copies of a Monthly Technical Progress Letter Report which shall include but not necessarily be limited to the following:

(A) The detailed technical progress made during the reporting period.

(B) A brief discussion of technical problems encountered and their solution.

(C) A brief review of the detailed program for the ensuing month.

(D) An evaluation of conditions which may affect completion of the study Contract.

(ii) One (1) reproducible and six (6) print copies of a Monthly Financial Report which shall include but not necessarily be limited to the following:

(A) Cost reports JPL Form No. 0330 (July, 1962).

(B) A graphic presentation indicating rate of actual expenditures and projected expenditures to completion of Contract.

(iii) One (1) reproducible and twenty-five (25) print copies of an Interim Technical Progress Report which shall include but not necessarily be limited to the following:

(A) A summary of the detailed technical progress made during the reporting period.

(B) A summary of technical problems encountered and their resolution.

(C) A summary evaluation of conditions which may affect timely completion of the study effort.

(iv) A Midterm Oral Presentation at JPL to include but not necessarily be limited to the progress of the work performed during the reporting period. The Contractor's key personnel on this study shall be present at this Midterm presentation.

(v) One (1) reproducible and seventy-five (75) print copies of a Final Summary Technical Report covering all effort accomplished in the performance of the Contract. The report shall be presented in the following general format:

(A) Definition of task.

(B) Definition of terms.

(C) Assumptions and constraints.

(D) Method of approach.

(E) Results and conclusions.

(vi) A Final Oral Presentation at JPL to include but not necessarily be limited to the results of all work performed under this Contract. Twenty-five (25) copies of the slide material shall be delivered to JPL one (1) week before the presentation.

(9) A technical meeting between the Contractor and JPL shall be held at Contractor's facility two (2) weeks after date of Contract, at which time the Contractor shall present a detailed study plan.

(10) At the request of either JPL or the Contractor, informal discussions shall be held at Contractor's facility to review the progress of the study, or any other matter pertinent thereto.

(c) The Jet Propulsion Laboratory will furnish to the Contractor, within five (5) calendar days after date of Contract, the data shown under paragraph (b)(7). A bibliography of relative study information and reports (e.g., Ames/Avco Capsule Study, etc.) will be compiled for supplemental information and will be supplied when available.

EXHIBIT NO. 1

Document 161-01

Venus Flyby/Entry Probe Mission
Baseline Science Instruments

The instruments listed in this table comprise the baseline payloads for which the capsule and spacecraft shall be mechanized. The instrument selections are taken from the Mariner '69 project science payload with alterations required due to the significant difference in conditions at Venus from those at Mars. Consistent with the Mariner '69 project philosophy and the fact of a previous mission to Venus, the baseline mechanizations will not provide for interplanetary (cruise) science measurements.

The instrument descriptions and the discussion of mechanization requirements and the type of information to be obtained are given in JPL TM 33-282, revision 1, and/or the Mariner '69 project Functional Requirements. Where conflicts in information exist, the Mariner '69 Functional Requirements take precedence.

A. Capsule Instruments

As shown in Table A-3 of JPL TM 33-282, Revision 1.

B. Spacecraft Planetary Instruments

*Microwave Spectrometer (Combined Atmospheric Sensor and Surface Imager)	50#
**Magnetometer	7.2
**Trapped Radiation Detectors	2.6
RF Occultation (Since this measurement constrains the near planet trajectory, its mechanization is conditioned upon tradeoff with other important factors.)	-
Ultraviolet Spectrometer	30
Infrared Spectrometer	25
Infrared Radiometer	5

* This instrument is substituted for the television instruments because of the Venus application.

** Not included on Mariner Mars '69 - these instruments are being flown on Mariner/Venus '67.